Forschungszentrum Karlsruhe
Technik und Umwelt

Wissenschaftliche Berichte
FZKA 6462

Proceedings of the 4th IEA International Workshop on Beryllium Technology for Fusion

September 15–17, 1999
Karlsruhe, Germany

F. Scaffidi-Argentina (Ed.)
Institut für Kern- und Energietechnik

April 2000

Forschungszentrum Karlsruhe

Technik und Umwelt

Wissenschaftliche Berichte

FZKA 6462

Proceedings of the 4th IEA International Workshop on Beryllium Technology for Fusion

September 15-17, 1999
Karlsruhe, Germany

Francesco Scaffidi-Argentina (Ed.)

Institut für Kern- und Energietechnik

Forschungszentrum Karlsruhe GmbH, Karlsruhe
2000

Als Manuskript gedruckt

Forschungszentrum Karlsruhe GmbH
Postfach 3640, 76021 Karlsruhe

Mitglied der Hermann von Helmholtz-Gemeinschaft
Deutscher Forschungszentren (HGF)

ISSN 0947-8620

Content


Be
4th IEA INTERNATIONAL
WORKSHOP ON BERYLLIUM
TECHNOLOGY FOR FUSION

Fourth IEA International Workshop on Beryllium Technology for Fusion September 15-17, 1999, Karlsruhe, Germany

The Fourth "International Workshop on Beryllium Technology for Fusion" was held – under the auspices of the International Energy Agency Implementing Agreement for a Program of Research and Development of Fusion Materials (IEA-FM) – in Karlsruhe, Germany on September 15-17, 1999. The workshop was attended by 69 registered participants, and 38 papers were orally presented. The workshop participants came from many different countries, including Japan (7), Russian Federation (14), Republic of Kazakhstan (7), USA (6), Israel (1) and European Union (34).

General chairman of the workshop was Dr. Francesco Scaffidi-Argentina from the Forschungszentrum Karslruhe, Germany. Co-chairs were Dr. Hiroshi Kawamura from the Japan Atomic Energy Research Institute, Oarai, Japan; Dr. Glen Longhurst from the Idaho National Engineering and Environmental Laboratory, Idaho Falls, USA; and Dr. Vladimir Shestakov from the Science Technical Center of Controlled Thermonuclear Fusion, Almaty, Kazakhstan.

This workshop is the fourth of a sequence of meetings convened under provisions of the IEA-FM, the first being held in Karlsruhe (1993), the second in Jackson (1995) and the third in Mito city (1997). Prior to IEA-FM sponsorship, similar workshops were held in Idaho Falls, Idaho (1988) and at Clearwater Beach, Florida (1991) in the USA.

The main objective of the workshop was to support the advancement of the international development of fusion power through communication and dissemination of information on progress made in beryllium technology. This has been accomplished through presentation of original research on issues of current interest to the fusion beryllium community.

The workshop was divided into 10 technical sessions that addressed the general topics of (a) Production and Characterization; (b) Health and Safety; (c) Forming and Joining; (d) Chemical Compatibility; (e) Thermal-Mechanical Properties; (f) Pebble Bed Behavior; (g) High Heat Hlux Performance; (h) Irradiation Effects; (i) Plasma/Tritium Interaction; (j) Molten Beryllium-Bearing Salts.

In the Production and Characterization session, D. Schmidt presented the status of the Japanese production of beryllium pebbles made by inert gas atomization, while V.A. Gorokhov presented the status of production of porous beryllium for the Russian DEMO breeding blanket design. The distribution of impurities in beryllium pebbles produced by the rotating electrode method was presented by T. Iwadachi, while H. Kleykamp reported on phase equilibria, compatibility studies and thermal properties of beryllium systems. characterization of the materials the fabrication design of the ITER Plasma Facing Components. Production of each type of beryllium was discussed in detail, including also perspectives on production on an industrial scale.

In the Health and Safety session, N. Bitkolov described protection against beryllium aerosols for air in premises and the environment. The health effects of beryllium particles on humans was also discussed and the necessity of a systematic experimental study on the effects of sub-micron beryllium particles on the human health was stressed.

In the Forming and Joining session, the many issues associated with the fabrication and joining of beryllium to itself and other materials, particularly for components subjected to high heat fluxes, such as those in the divertor were discussed. T.N. McKechnie presented the experimental results on a brush like structure for plasma facing components as an alternative to the conventional planar bonding technique. The brush armor materials fabricated to date have been made with preformed tungsten and beryllium rods, which are backed with specific matrix materials. These matrix materials are then used to bond the armor to copper alloy and aluminum alloy heat sinks. The results of high heat flux testing experiments by Sandia National Laboratories in their Electron Beam Testing System showed that the tungsten brush armor survived cyclic loading (10s beam on, 10s beam off) for 500 cycles each at 5, 10, 15, 22 and 30 MW/m^2 with no damage to the heat sink and little or no damage to the armor.

On the other hand, A. Gervash presented the results for a Russian fast brazing process for joining beryllium to Cu-alloy that allows it to successfully surviveheat fluxes higher than 10 MW/m^2 during thousands of heating/cooling cycles without serious damage in the armour material. A precipitation hardened CuCrZr alloy and the dispersion strengthened GlidCop alloy were used as heat-sink materials. The results of comparative tests showed that the Russian fast brazing technique is a very promising joining technique, able to provide good Be/CuCrZr and Be/GlidCop joints for ITER applications.

In the Chemical Compatibility session, R.A. Anderl presented the results of experiments to measure the chemical reactivity of Be pebbles (0.2 to 2-mm diameter) and Be powder (~14 to 30-mm diameter) exposed to steam at elevated temperatures. H_2 rates, based on BET surface area measurement, for the powder samples were in good agreement with the results for fully-dense, consolidated powder metallurgy (CPM) Be cylinders and discs. Corresponding rates for the Be pebbles were systematically lower than the CPM-Be rates, especially for temperatures above 600°C. Smaller differences were noted for temperatures below 600°C. The observed differences in the derived H_2 rates for the pebble Be and the CPM Be can be accounted for by surface and bulk impurities and other microstructural and surface features that contribute to the measured BET surface area and influence the oxidation process at the material surface.

F Druyts presented the results on experiments performed in both air and steam for vacuum hot pressed grade S-200 F beryllium with three different irradiation histories: (1) unirradiated fully-dense; (2) irradiated fully-dense; (3) irradiated porous (97.2% of the theoretical density). In steam, the same kinetic regimes as in air were observed: i.e. parabolic kinetics at low temperatures (600°C and 700°C for unirradiated dense and irradiated dense material, 600°C for irradiated porous material) and

accelerating/linear kinetics at high temperatures (800°C for unirradiated dense and irradiated dense material, 700°C and 800°C for irradiated porous material).

In Thermal and Mechanical properties session, R. Chaouadi presented the correlation between the tensile properties and fracture initiation toughness of beryllium. A micromechanical model associated with detailed finite element calculations allowing one to better understand the correlation between the flow and the fracture properties in the presence of helium bubbles was also presented.

D.E. Dombrowski reported on the elevated temperature thermomechanical properties of modern beryllium grades, thus contributing to expanding the database from simple tensile and physical properties to more complicated mechanical tests. The elevated temperature (ambient to 648°C) thermomechanical properties of two beryllium grades made by Hot Isostatic Pressing (HIP) were compared: S-65H (made from impact ground powder) and O-30 (made from gas atomized (GA) powder). The elevated temperature properties (UTS, YS, percent elongation, reduction in area) of S-65-H generally exceed those of HIP'd GA Be up to 650°C. Successful measurements of elevated temperature smooth and notched fatigue were presented for the first time on modern beryllium grades. Valid beryllium K_{IC} fracture toughness results were obtained for the first time at temperatures above room temperature, and elevated temperature creep, tensile, electrical resistivity and thermal conductivity were also presented and critically discussed. Fracture toughness, as measured by either K_q or K_{max}, continues to increase with temperature until it reaches a plateau at approximately 315-540°C. HIP'd GA beryllium clearly has significantly lower stage II creep rates for 480-650°C. Finally, A.M. Khomutov presented the advancements in production and mechanical characterization of Russian beryllium semi-products (grade DShG-200) produced by powder metallurgy. The mechanical tensile properties in two orthogonal directions were presented for a wide temperature and strain rate range (i.e. 20–600 $^{\circ}C$ and 10^{-4}–1 s^{-1} respectively).

In the Pebble Bed Behavior session, M. Dalle Donne reported on the measurements for a binary bed of large ($\Phi \approx$ 2 mm) and small ($\Phi \approx$ 0.1-0.2 mm) beryllium pebbles. Measurements on the heat transfer parameters of such a binary pebble bed, namely the thermal conductivity and the heat transfer coefficient to the containing wall, were presented and correlated with the effect of the bed temperature and of the constraint exerted by the containing walls. Empirical correlation for wall heat transfer coefficients and pressures on the containing walls as a function of temperature and mechanical constraint were also provided and critically discussed. Moreover, experiments to determine the heat transfer parameters of single size beryllium beds made by 2 mm beryllium pebbles were also presented. Although these beds have considerably lower thermal conductivity than binary beryllium pebble beds, they have been investigated because for certain blanket designs the high thermal conductivity obtained with a binary bed is not required. Furthermore, these beds are simpler to handle during the filling of the pebbles.

J. Reimann presented results on uniaxial compression tests with monosized and binary beryllium pebble beds over the temperature range between ambient temperature and 480 °C and pressures up to 8 MPa. Empirical correlations for the moduli of deformation for the different bed types as well as first measurements on thermal creep were also discussed. Additionally, results for triaxial compression tests for monosized and binary beds were reported. The experiments showed that the initial state of consolidation of the pebble bed is very important for the stress-strain dependence.

E. Alves presented the results of the measurements on the effective electrical resistivity of both single-size and binary beryllium pebble beds. The presence of a certain amount of BeO distributed on the pebble external surface as well as along the grain boundaries strongly contributes in increasing the effective electrical resistivity of the pebble bed. At room temperature, the lowest resistivity values were found for the case of a binary pebble bed. After a mechanical cycling, the electrical resistivity of the bed never reached its initial value for zero pressure but it remained about one order of magnitude below the original value. After the first loading cycle succeeding loading/unloading resistivity curves do not show any significant change. For the same applied load, the pebble bed electrical resistivity increased almost linearly with the temperature.

The status of experimental activities aimed at investigating the out-of-pile thermal and electrical behaviour (e.g. thermal conductivity, wall heat transfer coefficient, electrical resistivity) of a binary beryllium pebble bed under ITER breeding blanket module relevant conditions was presented by G. Dell'Orco. Finally, three dimensional finite element analyses both in steady state and in cyclic conditions aimed at better understanding the thermal and mechanical behaviour of medium scale blanket mock-up for the European HCPB-DEMO blanket were presented by A. Di Maio. The calculations showed that the mock-up is able to withstand the loads it will undergo during the experimental working cycles and suggested possible hints for a further mock-up design optimization.

In the High Heat Fux Performance session, M. Yamada first and then A. Cardella presented the rationale of the ITER design choices for the application of beryllium to the blanket first wall and gave an overview of the R&D performed and the results achieved. As a result of this R&D, Be S-65C (or equivalent) has been selected as the reference material for all the components, and significant new data have been generated on Be performance under expected ITER conditions. A HIP process with specific interlayers (Ti or AlBeMet) is the preferred joining technology for the primary and baffle FW, while a special high performance fast brazing technology with the use of amorphous braze (CuInSnNi) is the preferred method for the limiter.

Recent results obtained in Russia with beryllium as a plasma facing armour material were presented by I. Mazul. Aiming at investigating the beryllium behavior under normal and off-normal reactor conditions, the results of several experiments with different Russian Be grades (DShG-200, TGP-56, TShG-56, TR-30, Condensed Be) as well as S-65C (ITER reference grade) at simulated disruption loads (~5 MJ/m^2) and subsequent thermal cycling (~5 MW/m^2, 1000 cycles) were discussed.

Experiments have revealed no macroscopic damage of the tested grades, although significant differences in crack formation and propagation were observed.

R. Giniaytulin reported on tests with several Be-mockups fabricated using a brazing technique and tested at electron-beam facilities in Russia and the USA. The purpose of the testing was to find the number of thermal cycles required for armor debonding for several heat flux values. The mockup with the tile dimensions of 5x5x5 mm demonstrated best results during the tests and during thousand cycles by heat flux density of 13.5 MW/m^2 no damages in the Be/CuCrZr joint was observed. The results of the comparison of long- and short-pulse cyclic loading for beryllium armoured small-scale assembles were also presented and discussed.

A. Lodato presented experimental results on thermal shock behaviour of different beryllium grades before and after neutron irradiation. All materials showed higher erosion after neutron irradiation. The effect is ascribed to the decreased ductility after irradiation. No large differences were observed for two different irradiation temperatures. The comparison between different beryllium grades indicated the ITER grade S65C and the condensed Be as the material with the lowest erosion after neutron irradiation.

In the Irradiation Effects session, R. Chaouadi reported on irradiation tests on beryllium grades of ITER interest performed in the BR2 reactor at various temperature and neutron spectrum conditions (temperatures from 200-600°C; neutron damage from 0.8 to2.5 dpa; helium content from 250 to 750 appm). Analysis of the experimental data showed that irradiation induces an increase of the tensile properties accompanied with a significant loss of ductility, in particular in the region 250 to 600°C. Fracture toughness exhibits a same pattern. Damage accumulation is affected not only by the accumulated dpa but also by the irradiation temperature. The latter plays an important role in the recovery of the flow properties. However, the main damage mechanism that drastically reduces the fracture toughness results from the helium production.

D.R. Harries made a comprehensive assessment of the ambient and elevated temperature tensile and fracture toughness properties of unirradiated, aged (~2000 h at temperatures in the range 185 to 605 C) and irradiated ($2.1x10^{25}$ nm^{-2} (>1 MeV) at 200, 400 and 600 °C) hot isostatic (HIP) and vacuum hot (VHP) pressed S-65 and S-200F beryllium grades. The effects of material (powder consolidation method, beryllium oxide and elemental impurity contents and grain size), test (temperature) and irradiation (temperature, atom displacement dose and helium concentration) variables were analysed to further the development of composition - structure - property relationships for unirradiated and irradiated beryllium. The results of the analysis demonstrate that the tensile and ultimate strengths of the unirradiated and aged beryllium grades at a given test temperature increase with the inverse square root of the grain diameter. The beryllium grades do not differ significantly in their resistance to radiation damage at the lower test temperatures; however, the S-65 VHP and, in particular, the S-200F HIP grades are more ductile and marginally tougher at temperatures higher than 435 .

C. L Coheur presented microstructural analyses by means of transmission electron microscopy of four Be samples irradiated in the BR2 reactor at 200, 400 and 600°C and fluence between 2 and 3 dpa. A comparison between the experimental results and theoretical calculations made by means of molecular dynamics and concerning the stability of various types of defects (e.g. dislocation loops) susceptible to occur in Be was also presented and discussed. The formation of helium during irradiation seems to have an influence on the microstructure only for the samples irradiated at 400°C and 600°C. At 200°C, there is only a small change with respect to the unirradiated samples.

V.P. Chakin presented the results of investigations on irradiated Russian beryllium grades, including metallography, measurements of swelling, microhardness, mechanical tensile and compression tests. During mechanical tensile tests at room temperature and at 200°C, all irradiated specimens failed while they were still in the elastic region without any rest elongation. Ultimate tensile stress for all marks of beryllium was 120-320 MPa. The compression tests on samples irradiated at 20-200°C showed that the specimens failed at rest elongation of a few per cent at 200°C only. In other cases the samples failed in brittle fracture. The ultimate tensile stress increases from 600 to 1400 MPa with increasing the testing temperature.

I. Kupryianov reported on the effect of a neutron irradiation on helium and tritium mobility and swelling from three Russian beryllium grades. He showed that the first signs of helium release were detected at about 700°C, while tritium release occurred also at lower temperatures. Tritium mobility increases significantly when swelling increased, and it is approximately three orders of magnitude higher than that of helium, which does not significantly change with the swelling. Finally, A. Polyakov presented results on both the nature and the kinetics of irradiation defects as well as on microhardness and electrical resistance changes in gamma-irradiated beryllium ceramics.

In the Plasma/Tritium Interaction session, P. Goldstrass reported on the surface reactions and adlayer formation on beryllium after carbon and oxygen bombardment. The experimental data are in good agreement with results calculated by the kinematic Monte Carlo code simulations. The interaction of the incoming ions with the target is fully explained by kinematic processes like implantation, reflection and sputtering. A carbon layer of increasing thickness is formed on top of the beryllium metal, but after a fluence of approximately 1×10^{18} cm^{-2} no more Be is eroded. Both the composition and the thickness of the formed layer depend on the energy of the incoming CO^+ ions. The absolute amounts of C and O reach constant values for extended CO^+ implantation, which in combination with the continuing weight loss of the target during borbardment means that the Be target surface is continuously eroded. The underlying chemical processes for this behavior, which may imply the formation of BeO, Be_2C and additional compounds in the ternary layer and the formation and transport of CO molecules as the desorbing species in the erosion process, are not yet identified and subject to further studies.

R.G. Castro presented results on plasma deposition of beryllium carbide via magnetron sputtering into a methane/argon plasma at an audio frequency. Be_2C is the dominant phase in the films, and "free" beryllium exists in the Be-rich films. The films were exposed in laboratory environments for 30 days

without weight change and little or no change in appearance of the samples. This confirms that the films are air stable at ambient temperature. The films that come the closest to meeting the ICF capsule requirements have a hydrogen permeation coefficient of 7.0 $cm^3Acm/cm^2AsecAcmHg$. Defect stress analysis and tensile stretching experiments indicate the thin films tensile strength to be in the range of about 70 to 700 MPa. At room temperature the thermal conductivity is 1.95 W/m°C. Furthermore, experimental studies show that beryllium carbide has an extremely low sputtering rate, which would suggest the use of beryllium carbide coating as a first wall material.

Korshunov reported on erosion and deuterium retention in mixed W-Be layers on beryllium. The mixed W-Be layers were prepared by depositing Be and W atoms upon a Be substrate under simultaneous sputtering of Be and W targets by 20 keV Ar^+-ions and further irradiated by a pulsed deuterium plasma flux. After irradiation by two plasma pulses, the W-Be film was melted and removed completely from the local surface over areas up to 30 μm in diameter, while the element distributions in a mixed layer after subjection to the pulsed plasma are essentially changed. The integral deuterium concentrations are equal to $0.6 \cdot 10^{20}$ and $2.2 \cdot 10^{20}$ m^{-2} for the removed film areas and for the retained melted film ones, respectively.

Investigations on deuterium trapping in ion implanted thin beryllium oxide films, both thermally grown and prepared by ion sputtering technique were presented by A. Markin. It was shown that for thermally grown BeO films implanted in the range 300-900 K the total deuterium retention is practically the same whereas the thermal desorption spectra depend markedly on the irradiation temperature. For implantation at room temperature, the deuterium is released in a wide range of temperature (i.e., 400-1000 K). On the contrary, at implantation temperatures above 600 K, deuterium is released in a desorption peak at about 1000 K from both ion implanted thermally grown BeO films and co-deposited D/BeO layers. This suggests that under conditions when oxygen is available in the divertor plasma, the tritium and beryllium co-deposition will contribute significantly to the total tritium retention in the redeposited layers, especially at elevated temperatures.

Results on hydrogen release tests from deposited beryllium layers were presented by E.V.Chikhray. Beryllium coatings were deposited on the samples by magnetron sputtering in an equal mixture of hydrogen and argon. The thickness of the deposited beryllium layer was 25 microns. The analysis of hydrogen retained in deposited beryllium layers showed two release peaks at the temperatures 760-800 K and 920-970 K. Average hydrogen concentration in the beryllium samples loaded in the process of magnetron sputtering was equal to 3800±200 appm. The experiments with beryllium layers, enriched with carbon, revealed the increase of retained hydrogen concentration up to 9600±200 appm.

R.G. Castro reported on transferred-arc (TA) cleaning method for roughening and removing surface contamination from beryllium. Results of TA cleaning tests show that during TA cleaning, arc attachments on the surface of beryllium, tungsten and stainless leaves surface craters that were formed by the displacement of melted material. Type III arc attachments leave large (>10μm) connected

craters. These are desirable to maximize the mechanical interlocking and bond strength between a plasma sprayed coating and the underlying material. In any case, TA cleaning was shown to be an effective method for removing carbon and hydrogen isotopes from the surface of beryllium, tungsten and stainless steel.

A. Zimin presented results on an investigation study on redeposited layers produced at interaction of H and D ions with beryllium. A mode of operation with an effective return of sputtered particles to the Be-target surface under its bombardment by high-rate hydrogen and deuterium ion fluxes was presented to model beryllium redeposition in conditions similar to those in ITER reactor. Results of studies of hydrogen isotope accumulation in beryllium, as well as of chemical and physical composition and microstructure of re-deposited and sputtered beryllium layers were presented.

In the Molten Beryllium-Bearing Salts session, G.R. Longhurst dealt with an emerging issue relative to beryllium technology in fusion involving tritium interactions with molten beryllium-bearing salts. Innovative designs for fusion reactors, both magnetic and inertially confined, feature the molten mixture of Li,F, and BeF_2 commonly called Flibe, as a tritium breeder and coolant. Among the issues to be resolved for such coolant systems, the potential loss of tritium from the Flibe coolant to the walls of the system, particularly through heat exchanger tubes, and from there into secondary coolants or working fluids and the environment was presented and discussed. Corrosion by evolved TF was also discussed. Results of analyses performed to estimate the fractional loss of tritium through heat exchanger tubes in molten Flibe systems suggest that unacceptably large losses of tritium from the Flibe coolant may be possible. The gravity of the implications of these estimates calls for experimental verification to determine if tritium losses through molten Flibe heat exchangers or other Flibe systems can really be so high. The status of several experiments presently being planned to address these issues including experiments to induce tritium in Flibe using spontaneous fission neutrons, experiments in flowing loops to evaluated tritium losses through heat exchanger walls, and exploration of schemes for tritium extraction from molten Flibe was also presented.

In summary, it was recognized that swelling and He/T release of beryllium pebble irradiated up to high He content, effective thermal conductivity of pebble bed, tritium permeation and coating and fabrication cost of pebble were important for the pebble bed type blanket. For plasma facing components, life time estimation of beryllium and coated beryllium by erosion, dust and particle production, joining and waste, mechanical properties and deformation by swelling were recognized by attendees as important. Especially, it was recognized that relative estimation by other researchers was important because the reliability of data is increased. Methods of international collaboration should be presented by the Organizing Committee in near future. Finally. the International Organizing Committee accepted the proposal of the Russian representative, Dr. A. Khomutov from the Bochvar Research Institute of Inorganic Materials, Moscow, Russia, to hold the "5th International Workshop on Beryllium Technology for Fusion" in Russia in October 2001.

Trial production of beryllium pebbles made by Inert Gas Atomization and the results of basic characterization

T. Iwadachi[a], H.Uchiyama[a] D. Schmidt[b]

[a] NGK INSULATORS,LTD.,
1 Maegata-cho, Handa-city, Aichi-ken 475-0825 Japan

[b] NGK Deutsche Berylco GmbH,
Postfach No.1620,61406 Oberursel, Germany

The particle size distribution of beryllium pebbles produced by the inert gas atomization method (IGA) was investigated selecting production parameters. Fine powder under 0.1mm is easy to produce by this method. Maximum ratio between 0.1mm to 0.2 mm to total powder amount was about 60% in this experiment. Some irregularly shaped pebbles mixed in with the 0.1 mm to 0.2 mm pebbles. Pebbles under 0.2 mm were difficult to handle and individually inspect.

The amount of oxide in the pebbles between 0.1 mm to 0.2 mm in size was 0.049 weight percent. The smaller the particle size becomes, the larger the increase in oxide in the pebbles.

BET specific surface was evaluated in each size of IGA pebbles compared to REM pebbles.

1. INTRODUCTION

The 0.1- 0.2 mm beryllium pebbles produced by the inert gas atomization method (IGA) are supposed to be one of the candidate materials for small size pebbles for use in neutron multiplier applications. Although IGA is well known as a suitable process for the production of fine powder of up to 0.1mm in diameter, only a few studies on size distribution of beryllium pebbles have been reported. [1]

Therefore, we tried to produce IGA beryllium pebbles by selecting production parameters, and we examined their size distribution, particle shape, impurities and relative specific surface.
Based on these results, optimum selection of pebbles' size for use in breeding blanket of fusion reactors was discussed.

2. EXPERIMENTAL

2.1. Trial Production of beryllium pebbles

Inert gas atomization apparatus involves vacuum induction furnace, vacuum chamber and a nozzle that injects inert gas to dropping melt.
The outline of this method is shown by Fig.1.

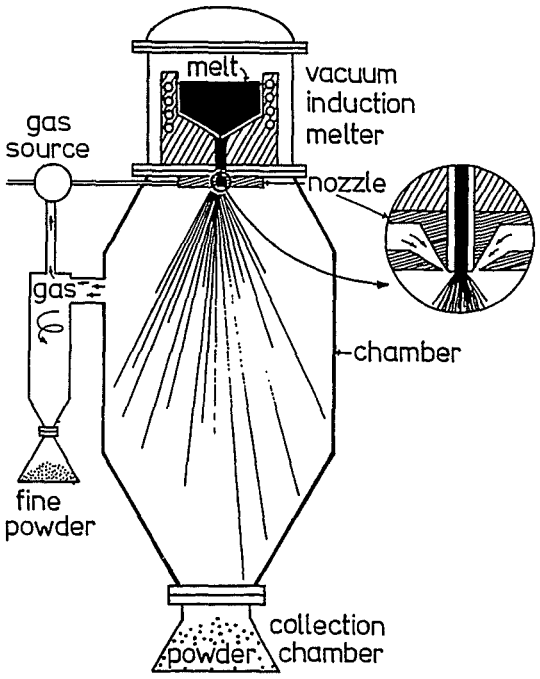

Fig.1. Inert Gas Atomizing Method [2]

Vacuum casted beryllium ingot was used as raw material for atomizing. After melting beryllium ingot, argon gas was injected to melt stream through the nozzle. Process parameters, such as temperature of melt, injection gas pressure and location of nozzle were changed to get the various particle size distribution of beryllium pebbles. Particle distribution of the beryllium pebbles produced by each production condition in inert gas atomizing method was examined through a sieve.

2.2. Shape and surface microstructure observation

Sieved pebbles' shape and surface microstructure were observed by SEM and magnified photographs.

2.3. Impurities content

Pebbles in each size range were provided to chemical analysis. The amount of beryllium oxide was measured by iodine-bromomethanol method. Other impurities such as magnesium, aluminum, silicon, iron were measured by plasma emission spectochemical analysis.

2.4 Specific surface area

Specific surface area of beryllium pebbles produced by IGA was measured by BET method in each size. The results were compared with the measured values of beryllium pebbles produced by the rotating electrode method (REM) . Gas used for measuring was mixed gas consist of krypton of 10 percent and helium of 90 percent. Evaluated pebbles' sieving ranges of IGA pebbles are shown in Table 1 and that of REM pebbles are shown in Table 2.

Table 1
Sieving range of evaluated IGA pebbles (mm)

IGA		
0.044 -0.075	0.075 - 0.100	0.10 - 0.18

Table 2
Sieving range of evaluated REM pebbles (mm)

REM			
0.18 - 0.25	0.25 - 0.30	0.85 - 1.18	1.7 - 2.36

3. RESULTS

3.1. Particle size distribution

Typical particle size distribution plots are shown in Fig. 2

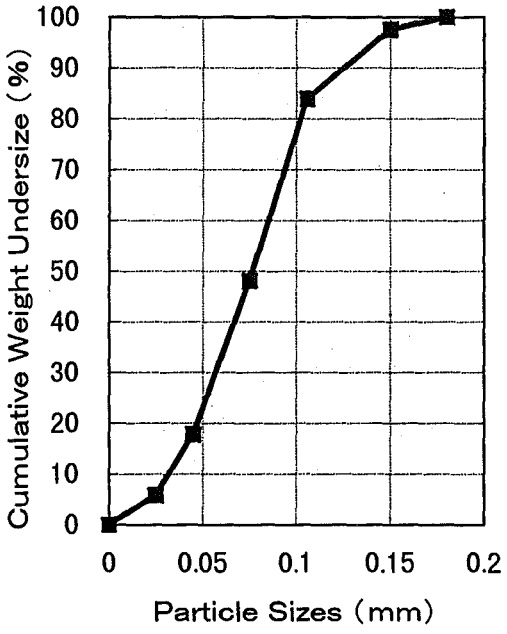

Fig.2. Typical particle distribution of IGA Pebbles

Average particle size was approximately 0.075 mm and the ratio between 0.1mm and 0.2mm was 20 percent by weight of the total amount of product. Particles smaller than 0.1 mm were easy to produce using this method. We tried to produce pebbles coarser than 0.1 mm in diameter by changing process parameters.

Fig.3 shows the typical particle distribution and that of largest sized ones.

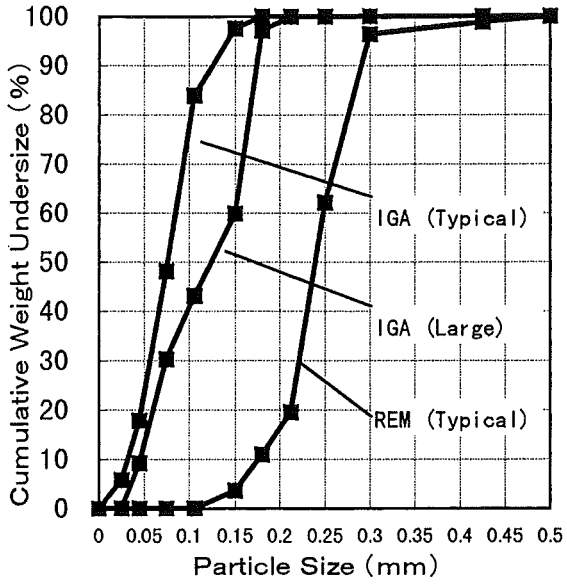

Fig.3. Typical and large particle size distribution of IGA pebbles and REM pebbles

By optimizing process parameters, maximum ratio of pebbles between o.1 mm and 0.2 mm to the total amount of pebbles became about 60 percent. However it is still a low ratio from production point of view.

3.2. Shape and surface observation

Fig.4 shows the SEM image of the beryllium pebbles between 0.1 mm and 0.2 mm in size. Fig.5 and Fig.6 shows the enlarged photograph. It shows that irregularly shaped pebbles were mixed with regularly shaped pebbles in this size range.

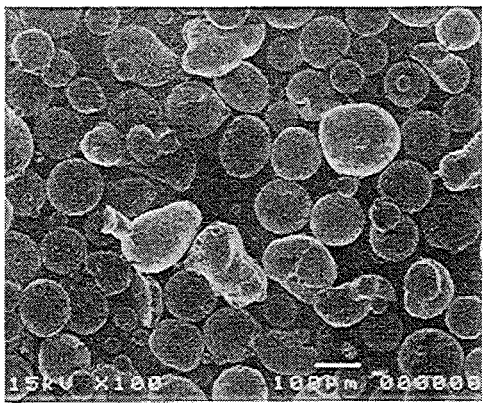

Fig.4. SEM image of IGA Pebbles (ϕ 0.1-0.2 mm)

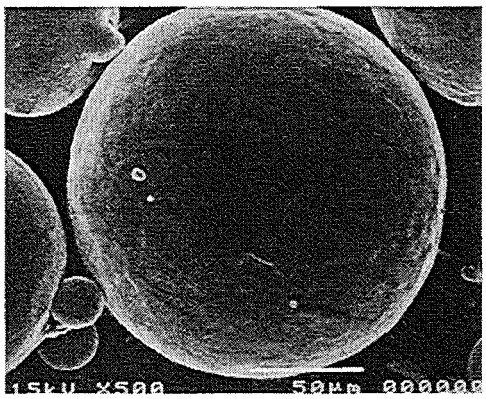

Fig.5. SEM image of IGA good shape Pebbles (ϕ 0.1-0.2 mm)

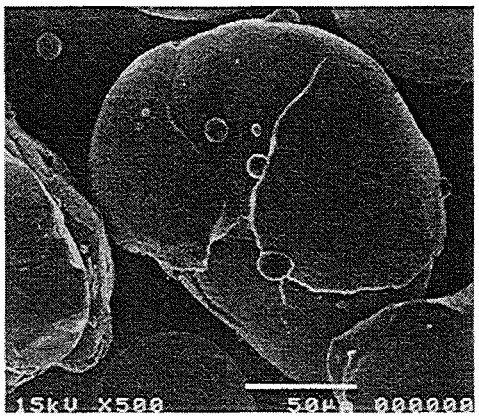

Fig.6. SEM image of IGA irregular shape Pebbles (ϕ 0.1-0.2 mm)

BET specific surface area is the measurement of the amount of gas adsorbed on the powder surface versus the partial pressure.

The specific surface area is expressed in terms of the are per unit mass (m^2/g). For monosized spheres, the area per sphere A and the volume per sphere V are given as,

$$A = \pi D^2 \quad (1)$$

$$V = \pi D^3 / 6 \quad (2)$$

with the weight W given in terms of the volume and metallic density ρ m

$$W = \rho m V \quad (3)$$

Consequently, the area per unit weight can be given as

$$S = 6 / (\rho m D) \quad (4)$$

where S is the specific surface area.

If a different particle shape is assumed in in deriving Equation (4), then the relation between particle size and surface area would be different. A general form of Equation 4 would be as follows:

$$S = k / (\rho m D) \quad (5)$$

where k is termed a shape factor. It is possible to make a rough determination of shape by comparing independent measurements of particle size and specific surface area through the calculated proportionality constant k. [2]

Based on these idea, specific surface area measured in this experiment was compared with the calculated line in the case of a perfect spherical particle in Fig.12.

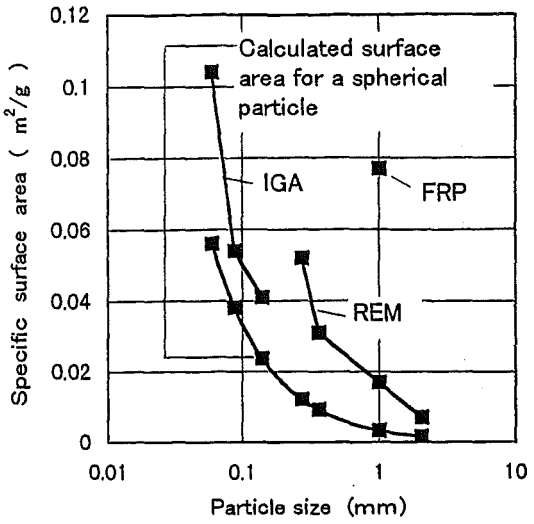

Fig. 12. Specific surface area versus particle size

Each specific surface area of IGA pebbles is near the calculated line for complete spherical particles.

Calculated k value is shown in Table 6.

Table 6
k - factor of various pebbles

Pebbles	k - factor
IGA 0.10 - 0.18 mm	10
IGA 0.075 - 0.10 mm	9
IGA 0.044 - 0.075 mm	11
REM 1.70 - 2.36 mm	26
REM 0.84 - 1.19 mm	31
REM 0.30 - 0.425 mm	21
REM 0.25 - 0.30 mm	26
FRP 0.84 - 1.19 mm	139

K - factors of the IGA produced pebbles obtained in this experiment is relatively small. This means IGA produced beryllium pebbles in this experiment have good sphericity compared to pebbles produced by other methods.

Fig.7 and Fig.8 shows a SEM micrograph of IGA pebbles between 0.044 and 0.075 mm in size. Some irregularly shaped pebbles were found, but the ratio was smaller than that of 0.1-0.2 mm IGA pebbles. Sphericity is good for the pebbles in this size range.

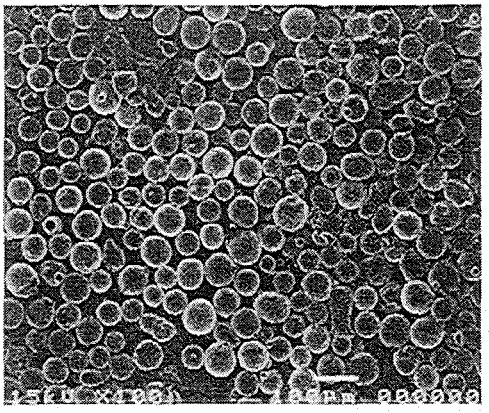

Fig.7. SEM image of IGA Pebbles
(ϕ 0.044 - 0.075 mm)

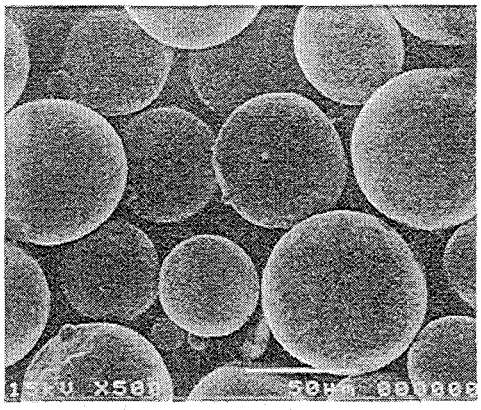

Fig.8. SEM image of IGA Pebbles
(ϕ 0.044 - 0.075 mm)

Fig.9 shows a magnified image of IGA pebbles. For the purpose of comparison, large size pebbles produced by REM in the range, between 0.18 and 0.25 mm, are compared in Fig.10. Fig.11 shows the 1 mm in diameter REM pebbles.

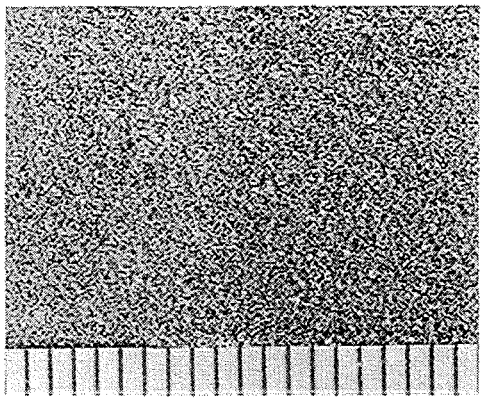

Fig.9. IGA Pebbles (ϕ 0.1 - 0.18 mm)

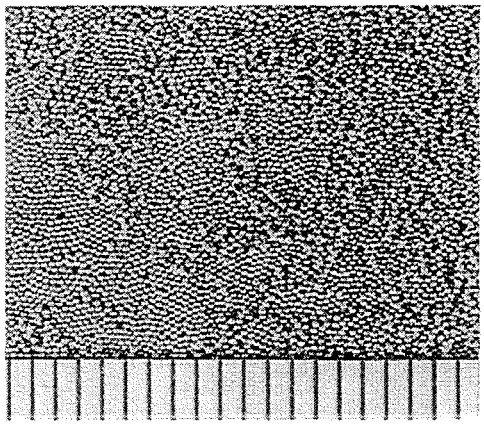

Fig.10 REM Pebbles (ϕ 0.18 - 0.25 mm)

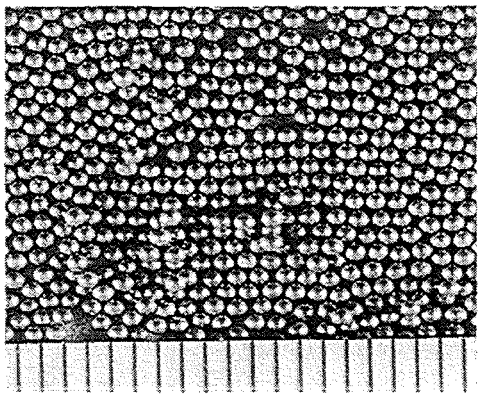

Fig.11. REM Pebbles (ϕ 0.84 - 1.19 mm)

IGA pebbles 0.1 - 0.2 mm in size couldn't be handled individually. Pebbles that can be handled individually are about 0.2 mm at minimum.

3.3. Impurities content

Table 3 shows the chemical composition of IGA pebbles in each size range.

Table 3
Chemical composition of IGA pebbles in each size range (wt %)

Particle size	Be	BeO	Mg	Al	Si	Fe
0.1-0.2	99.7	0.049	0.030	0.030	0.010	0.060
0.044-0.075	99.6	0.12	0.033	0.028	0.012	0.060
< 0.044	99.5	0.27	0.076	0.047	0.014	0.065

Relatively high purity beryllium pebbles between 0.1-0.2 mm pebbles can be obtained. Oxide content was 0.049 percent in 0.1 - 0.2 mm pebbles but the smaller the pebbles size, the higher the increase in oxide content. Other impurities were also plentiful in small size pebbles.

3.4 BET specific surface area

Table 4 shows the specific surface area measured by the BET method.

Table 4
BET specific surface area of IGA produced pebbles

Particle Size	BET specific surface area (m^2/g)
0.1mm-0.18mm	0.041
0.075mm-0.1mm	0.054
0.044mm-0.075mm	0.104

The specific surface area increased relative to decrease in the size range.

For comparing this data, the BET specific surface area of REM produced pebbles and the pebbles produced by the Fluoride Reduction Process (FRP) were also measured and the results are shown in Table 5.

Table 5
The BET specific surface of REM and FRP pebbles

Particle Size	BET specific surface area (m^2/g)
REM : 1.70 - 2.36 mm	0.007
REM : 0.84 - 1.19 mm	0.017
REM : 0.30 - 0.425 mm	0.031
REM : 0.25 - 0.30 mm	0.052
FRP : 0.84 - 1.19 mm	0.077

4. DISCUSSION

4.1. Particle size distribution

Beryllium pebbles between 0.1 mm and 0.2 mm are supposed to be small size pebbles in double size bed concept in bleeding blanket for fusion application. Beryllium pebbles produced by IGA method in this experiment shows the relatively high quality of sphericity, chemical composition and specific surface area. However, production yield of the pebbles in this range is low. From the production point of view, IGA method is suit for smaller size range. For example, the size range from 0.044 mm to 0.15 mm is recommended from the production yield point of view.

4.2. Specific surface area of the IGA produced pebbles

For small size pebbles, such as the size range in this experiment, it is difficult to evaluate the property of each individual pebble. The surface area is an average measure of the external surface of a large number of particles. It is considered that surface area is useful powder characteristic because it often correlates with various kinetic and geometric characteristics such as chemical activities and adsorption. [2]

4.3. Handling problem

If safety problems are not considered, the recommended size range is between 0.044 mm and 0.15 mm, from the production point of view.

However, small size pebbles smaller than 0.2 mm couldn't be handled individually because the size is too small. This is considered the problem from the safety point of view.

Optimum size ranges and production methods for small size pebbles for bleeding blankets should be evaluated again .

5. CONCLUSIONS

1) Maximum ratio of the pebbles between 0.1 mm and 0.2mm to total pebbles was 60 percent in this experiment.
2) Fine powder under 0.1 mm was easy to produce by IGA method. Optimum size range in IGA method is from 0.044 mm to 0.15 mm, from the production point of view.
3) Oxide content in the pebbles between 0.1 mm and 0.2 mm was 0.049 percent in weight.
4) Specific surface area of 0.1 mm - 0.2 mm IGA produced pebbles was 0.041 m^2/g in this experiment.
5) Pebbles under 0.2 mm couldn't be handled individually.

6. REFERENCE

1. Veselkov N. A et al., 1st Cordi. Meeting on a proposal for benchmark tests on beryllium pebbles,Kazakstan, May 1998
2. Randall M. German, Powder Metallurgy Science, Metal Powder Industries Federation, Princeton, New Jersey

Materials and fabrication of the porous beryllium multiplier zone element for the DEMO breeding blanket model

D.A.Davydov, M.I.Solonin, Yu.E. Markushkin, V.A.Gorokhov, V.V.Gorlevsky

NRC-A.A.Bochvar Research Institute of Inorganic Materials (NRC RF- VNIINM),123060 Moscow, P.O.Box 369, Russia, fax: +(095) 196 - 6671, tel.: +(095) 190 - 8085, E-mail: chernovv@bochvar.ru or vniinm.400@g23.relcom.ru

Russian Federation considers a porous beryllium as a promising multiplier material for domestic conception of DEMO breeding blanket.

Main requirements to the manufacturing technique and porous beryllium multiplier for the breeding blanket are: 1) industrial experience and low cost technique; 2) inherently open porosity in an item within 15-30% for more easy removal of radioactive gases; 3) high thermal conductivity; 4) close contact with SS shell to provide high heat transfer; 5) low swelling under neutron radiation.

A unique low temperature pressing (LTP) method designed in NRC RF-VNIINM (Russia) provides for a production of porous beryllium items conforming to the requirements mentioned above.

For comparison with EU Helium Cooled Pebble Bed (HCPB) beryllium multiplier a technique was also designed to fabricate the pebble bed multiplier with specified density (78-80%).

Porous beryllium multiplier fabricated has shown an apparent advantages in comparison to pebble bed one: specified level (21.9%) of inherently open porosity was attained; thermal conductivity was a factor of 10-15 higher; porous beryllium tightly adjoined the SS shell without visible clearances; high compression mechanical properties were demonstrated etc.

Using the designed low temperature pressing (LTP) process the porous samples, mock-ups and beryllium multiplier of DEMO breeding blanket model for fission (IVV–2M reactor) tests have been manufactured at NRC RF-VNIINM.

The experimental results obtained gave strong support for RF proposal to consider the porous beryllium as a candidate material for the reference ITER breeding blanket.

1. INTRODUCTION

One of the basic problems at development and making of a of a helium-cooled blanket of the DEMO with a ceramic breeder and of its experimental module for testing in the composition of the blanket of ITER is the experimental substantiation of the design, material-science and technological solutions, including reactor tests of the models.

For these purposes in Russia State Unitary Enterprise Research and Development Institute of Power Engineering and NRC of the Russian Federation All-Russia Research Institute of Inorganic Materials (NRC RF-VNIINM) there was developed a construction of model of a unit of the breeding zone of the experimental module of the helium-cooled blanket of the DEMO with tritium-breeding ceramics and a beryllium multiplier of neutrons.

This report presents the properties of materials, methods of production, used by the NRC RF-VNIINM, for manufacture of models of the breeding zone.

2. CONSTRUCTION OF THE BERYLLIUM MULTIPLIER OF THE MODEL OF THE BREEDING ZONE OF THE DEMO BLANKET

The breeding sector of the model (fig. 1) of a DEMO blanket represents two coaxial cylindrical channels 1 and 2 with diameters 46 and 26 mm and wall thickness of 1 mm. The annular gap between them is used for filling the multiplier 3 as porous beryllium (porosity 20 %) or granular beryllium fill. On to one end face of the channels there is welded a ring fuse 4, which creates space for delivery of the gas-carrier of tritium into the breeder, and to

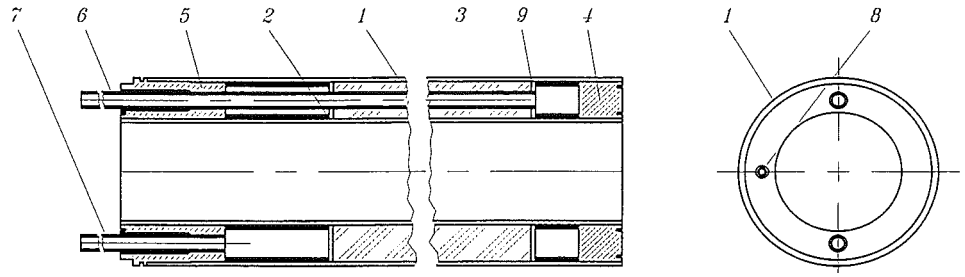

Figure 1. Construction of a beryllium neutron multiplier of the model of a breeding zone.

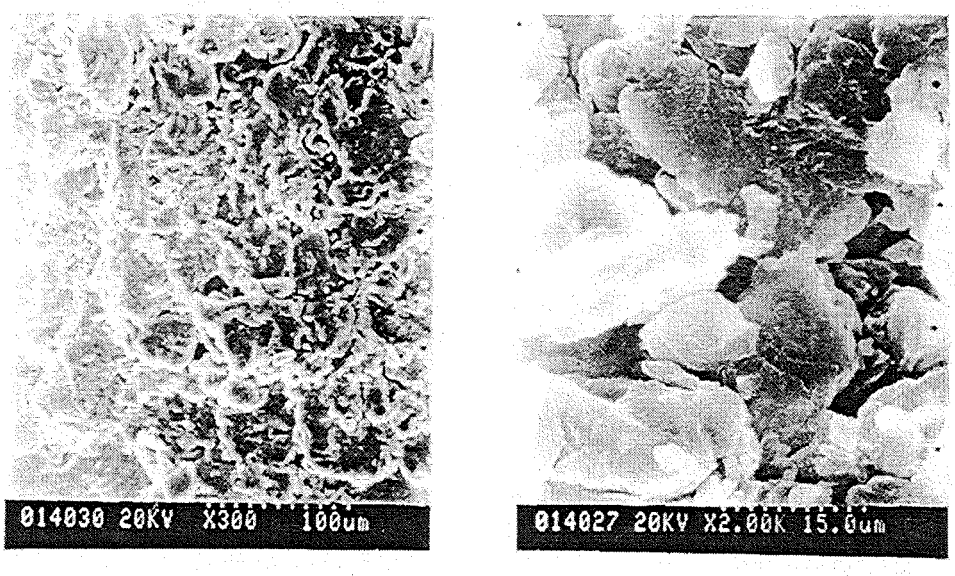

Figure 2. SEM picture of structure of surfaces of fractures of the comparison (attestor) samples of a porous beryllium tested for tension.

the other end face - a fuse 5 with nipples of delivery 6 and withdrawal tap 7 - gases carrier and thermoelectric couple 8. Between the fuses and the breeder mesh elements 9, preventing entry of possible beryllium particles in the channel of the gas-carrier are placed.

3. SOME PERFORMANCE OF A MATERIAL FOR A POROUS BERYLLIUM MULTIPLIER

A beryllium multiplier can be manufactured by two methods:

1. low-temperature pressing of porous articles from beryllium with guaranteed open porosity, designed and licensed in NRC RF- VNIINM;
2. binary filling of the zone of the neutrons multiplier with granules of beryllium of different particle size.

3.1. Manufacture of porous beryllium

Investigations and technological experiments demonstrated feasibility in principle of manufacture of porous beryllium in one stage from filling of the blend ($Be+BeH_2$) up to obtaining a finished article from beryllium of preset geometry and porosity [3,4]. There was designed and tested a two-stage method an expedient of manufacture of the comparison (attestor) samples and of a porous article. At the first stage by pressing there were made separate elements of preset geometry from the blend ($Be+BeH_2$). At the second stage

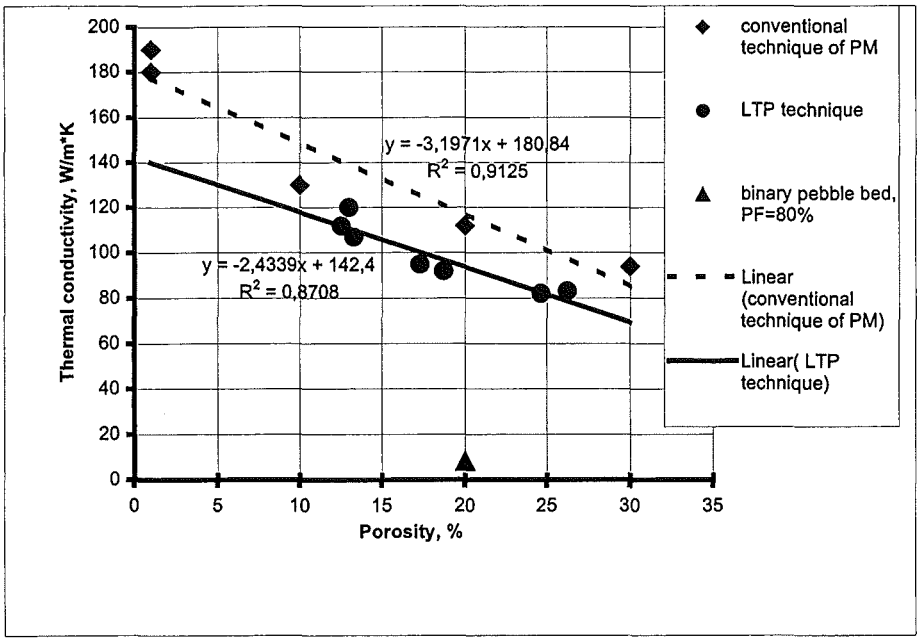

Figure 3. Thermal conductivity of porous beryllium obtained by conventional methods of powder metallurgy (PM), low-temperature pressing (LTP) and binary filling (packing factor - PF=80%)[5], depending on the level of porosity at temperature 50°C.R^2-assurance of an linear approximation.

by share pressing of separate elements at particular temperature there was obtained a finished article with simultaneous forming of guaranteed open porosity.

At the second stage as a result of thermolysis of BeH_2 at temperature 250-350°C there is formed chemically highly active ultra fine beryllium, which plays the role of a binder between larger particles of a beryllium powder, and hydrogen released in great amount ensures shaping of a homogeneous microporous structure with fully open pores [3,4].

There were produced comparison (attestor) samples, which were excised from mock-ups obtained by modes of manufacture of models, and there was performed measuring of their functional properties.

3.2. Structure

With use of a scanning electronic microscope (SEM) the surfaces of fracture of porous beryllium samples after tension test were explored (Fig. 2).

From the analysis of structure it was found, that:

- the pores are uniformly distributed on volume of samples and mock-ups;
- the porosity formed is characterized by a complex combination of pores of different sizes from 1-2.5 micron up to 25-30 micron and a developed system of point-to-point channels pairing the pores among themselves and ensuring formation of guaranteed open porosity.

3.3. Mechanical properties

Samples for tension and compression tests were produced from comparison (attestor) samples.

Samples for compression testing were 6 mm in diameter and 9 mm in height. Testing of the samples took place at room temperature with rate of movement of the entrapments of 2 mm/min.

At tests for compression the medial values of σ_B and ε_p of porous beryllium at room temperature respectively equaled 315 MPa and 2.2%.

As in previous investigation [4], beryllium with open porosity behaves like a typical sintered material. There is observed good correlation of mechanical properties with the volume of open porosity.

3.4. Coefficient of linear thermal expansion

Measuring of coefficient of linear thermal expansion (CLTE) was conducted on a high-temperature dilatometer ("Adamel" corporation, France, model DHT- 60 with furnace CT-60) in medium of helium. Heating rate of samples during measuring was a 5-6°C/min. The precision of measuring was 1-3 %. Measuring was conducted in the range of temperatures from 20 up to 820°C. In the indicated temperature range three measurings for each sample were conducted. For samples with porosity 22±0.5% the medial values of CLTE for two temperature ranges were:

$\alpha_{20\text{-}400°C}$ (1/°C) = 13.5±0.5 x10^{-6},
$\alpha_{20\text{-}800°C}$ (1/°C) = 17.6±0.5x10^{-6}.

As was noted earlier, the value of CLTE for porous beryllium is close to values for a dense material [4].

3.5. Thermal conductivity

Thermal conductivity of porous samples of a beryllium was determined in vacuum of 10^{-4} Pa by measuring a gradient rate of temperature after heating of one of end faces of a sample by an electron beam.

To obtain the reference point there was defined the thermal conductivity of a sample of beryllium of grade S-65B produced by method of hot pressing, in the corporation Brush Wellman (USA), for which the thermal conductivity is reliably determined.

Thermal conduction of porous beryllium depending on the method of manufacture, and level of porosity and binary filling [5] at temperature 50°C is presented in Fig. 3.

4. MANUFACTURE OF NEUTRONS MULTIPLIER FROM POROUS BERYLLIUM FOR THE MODEL OF THE BREEDING ZONE OF A BLANKET

To manufacture the neutrons multiplier there was used a two-stage technology of obtaining a porous material including heat treatment of preliminary pressed intermediate semiproducts from a blend of beryllium powders and beryllium hydride.

As a result of the work done, there was demonstrated feasibility in principle of manufacture by two-stage low-temperature pressing of articles from sintered porous beryllium:

- of composite shape, including those containing technological channels;
- by full sintering between separate intermediate semiproducts making up the full-scale article;
- with a tight contact between the article and steel tubes of the shell;
- a preset level of open porosity and heteroporosity on the volume of an article not exceeding ±5%.

Some performances of the porous multiplier of neutrons are presented in Tab. 1 and in Fig. 3.

The NRC RF-VNIINM executed the total complex of material-science and technological operations on manufacture of specific components, parts and the model of the breeding zone of a blanket with a porous beryllium multiplier.

As a structural material for the mockup and models ferrite-martensite steel EP-450 (1Cr12Mo2NbVB) was selected. It possesses thermal cycle strength, radiation and corrosion resistance, small activatability under irradiation and shows a high level of serviceability in industrial and experimental fast-neutron reactors BN-600, BN-350, BOR-60, etc. [1]. The thin-wall pipes for outside and inner shells of the models were manufactured from the

Table 1.
Performances of a full-scale article

Complete mass, g	Mass of steel tubes, g	Mass of Be, g	Inner diameter of outer tubes, mm	Outer diameter of inner tubes, mm	Heig ht, mm	Volume, см3	Porosity, %
1038.0	614.34	423.66	44.0	26.0	300.	293.6	21.9

indicated steel.

There have been designed technologies of assembling, soldering, welding and checking of lithium and beryllium blocks.

A series of welding alloys containing no argentum were explored and one of them, of Cu-Ni-Mn composition, was used in the technology of manufacture of models for high-temperature (1050-1070°C) vacuum soldering.

There was designed a series of procedures of check of the technological operations of quality of models as a whole, including for hermeticity; there was held certification of models before reactor tests.

Development of methods and manufacture of multiplier from porous beryllium and by binary filling have allowed to estimate advantages and deficiencies of materials and technologies for their production.

From [3,4] and results of the work done it follows, that the technology of low-temperature pressing of porous beryllium by technological modes has essential advantages as contrasted with the technology of obtaining granulated beryllium. The low temperatures, small number of operations, opportunity to conduct the process in the air using simple production equipment, high reproducibility of the performances of articles, relatively low price of the gained porous beryllium, etc., demonstrate efficiency of the designed process.

The porous beryllium has advantages under the basic requirements as compared with filling: thermal conductivity is 10-15 times

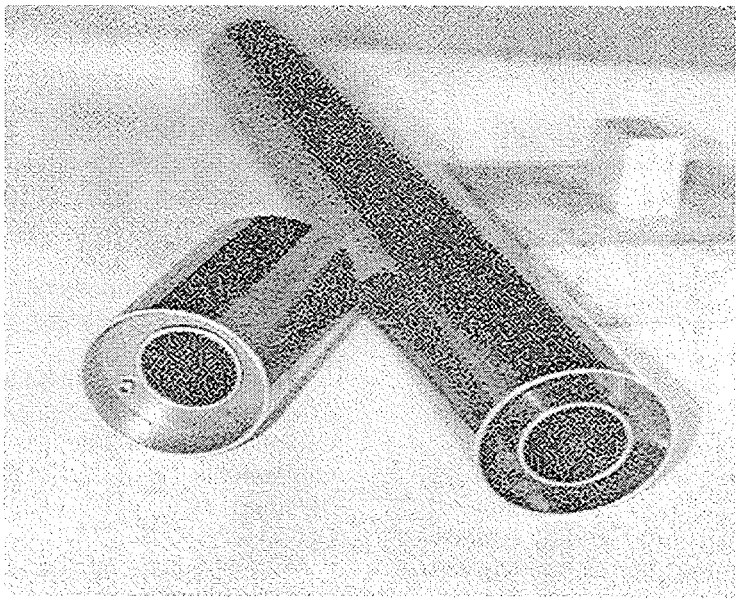

Figure 4. Multiplier of neutrons (on the right) and a trial mock-up (on the left) in steel tubes without trailer flanges manufactured by the method of low-temperature pressing of porous beryllium

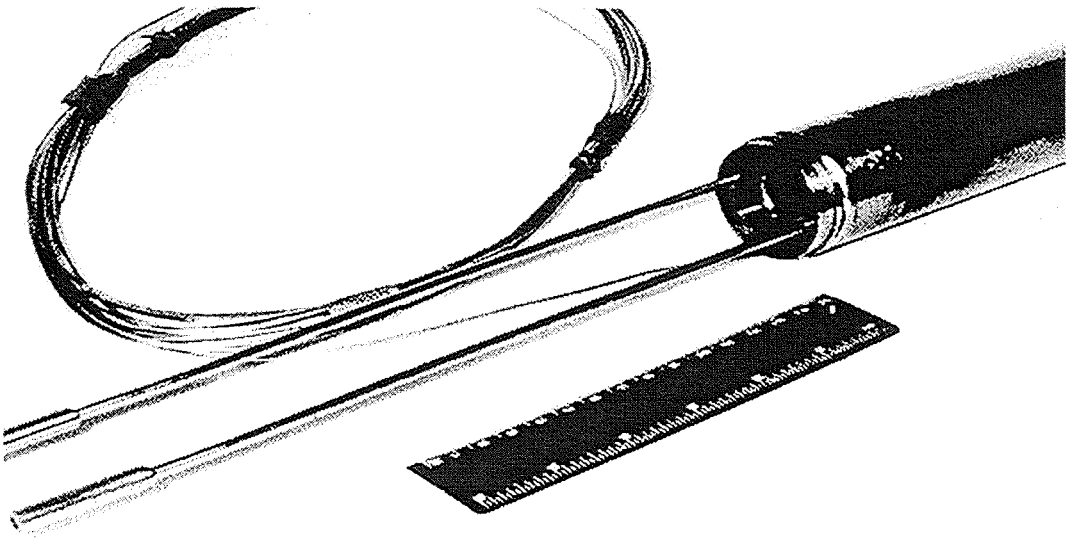

Figure 5. Porous beryllium multiplier in SS shell

higher; the maximally close contact with the steel shell is accomplished as well as the most effective heat transfer through the contact stratum, maintenance of the preset structure of the material at vibrations is ensured, opportunity of reference definition of any performances of the material is provided, etc.

The method of an atomization of the rotated electrode to obtain granules requires more complex production equipment, separate technology of manufacture of electrods with a high accuracy. It has poor efficiency and high cost [5]. The process of manufacture of large fraction of 1-2 mm, similar to the process of manufacture offered by the corporation Brush Wellman (USA), according the information of the representatives of the corporation (July 1998) requires further examinations and has not been completed yet [5].

Russia is not only developing methods of obtaining materials for realization of the ITER project, but is also looking for opportunities of their industrial duplicating in demanded volumes.

By now, to perform work there have already been accumulated reserves of metal beryllium in the amount of several tens of tons, including that from beryllium components put out of operation.

So, now to obtain for deriving porous beryllium the NRC RF-VNIINM has an opportunity to make initial materials and is ready to deliver articles with production volume up to 300-350 kg per year.

Russia proposes described above methods and technologies of manufacture of beryllium components for realization of the ITER project.

5. CONCLUSIONS

1. There has been designed a waste-free method of low-temperature pressing at temperature 250 - 300°C of porous articles from beryllium in the air with a preset level of porosity (≈20 %) and heteroporosity by volume not exceeding ±5%.

1.1. The porosity formed in beryllium is characterized by a complex combination of pores of different sizes from 1-2.5 micron up to 25-30 micron and a well developed system of point-to-point channels pairing these pores among themselves and providing forming of guaranteed open porosity.

1.2. There has been achieved good reproducibility of the method of a low-temperature pressing by structure and properties of porous beryllium and shown feasibility in principle of manufacture of articles of complex, also of tubular shape, containing also technological channels.

1.3. The medial values of σ_B and ε_p of porous beryllium at a room temperature under compression testing were 315 MPa and 2.2% respectively.

1.4. For samples with porosity 22±0.5% the medial values of CLTE for two temperature ranges correspond to values for a compact material and are:

$\alpha_{20\text{-}400°C}$ (1/°C) = 13.5±0.5 x10^{-6},

$\alpha_{20\text{-}800°C}$ (1/°C) = 17.6±0.5 x10^{-6}.

1.5. With level porosity of 19-20% thermal conductivity of porous beryllium is more then 90 W/m•K, which 11-12 times higher than thermal conductivity of binary filling of similar porosity.

2. Using the designed materials and methods, the NRC RF-VNIINM has made:

- multiplier elements from porous (21.9%) beryllium and of filling type (with density of binary filling 78%);
- two models of breeding zone of the blanket of DEMO, composed from tritium- breeding and multiplier elements;
- a mock-up for ampoule-physical measuring.

At present there are conducted experiments on irradiation of the model with binary filling of ceramics and beryllium on a reactor IVV-2M.

REFERENCES

1. M.I.Solonin. Proc. 8th Int. Conf. On Fusion Reactor Materials (ICFRM-8), J. Nucl. Mater. 258&263(1998) 30-46.
2. V. Kovalenko, L. Kiryiak, A. Lopatkin et al. Ceramic breeding zone models of DEMO ceramic helium cooled blanket test module for testing in IVV-2M reactor. Proc. 5th Int. Symp. Fusion Nucl. Technol.

(ISFNT-5), September 19-24, 1999, Roma, Italy.
3. Yu.E. Markushkin, M.I. Solonin, V.V. Gorlevskyi et al. Pat 2106931 (RF). Manufactory technique of the parts of porous berillyum. NRC-All Russia Research Institute of Inorganic Materials (VNIINM); Publ B. №8, 1998, ICI B 22 F 3/14.
4. D.A. Davydov, M.I.Solonin, Yu.E.Markushkin et al. Proc. 8th Int. Conf. On Fusion Reactor Materials (ICFRM-8), J. Nucl. Mater. 271&272(1999) 435-439.
5. Y.Gohar, F. Scaffidi-Argentina, D.Dombrowski et.al. Materials Assessment Report. ITER material properties handbook for Breeding Blanket. Garching Joint Work Site, Germany, July 14, 1998.

The distribution of impurities in beryllium pebbles produced by Rotating Electrode Method

T. Iwadachi[a], D. Schmidt[b], H. Kawamura[c]

[a] NGK INSULATORS,LTD.,
1 Maegata-cho, Handa-city, Aichi-ken 475-0825 Japan

[b] NGK Deutsche Berylco GmbH,
Postfach No.1620,61406 Oberursel, Germany

[c] JMTR, Oarai Establishment, JAERI
Oarai-machi, Higashi Ibaraki-gun, Ibaraki-ken 311-1394, Japan

Oxygen and other impurities' distribution in the beryllium pebbles produced by the rotating electrode method (REM) was investigated by EPMA and AES.

Oxygen is rich on surface of the beryllium pebbles produced by REM. The thickness of the surface oxide was estimated at approximately 200 nm. A peculiar oxide pattern was observed on the surface of the pebbles. Oxygen was in existtanc throughout the grains of the beryllium pebbles not located at grain boundaries.

Surface oxide was removed by acid cleaning. The thickness of the oxide was estimated at approximately 50 nm. Oxide content was reduced to half of that before acid cleaning.

Other impurities such as magnesium, aluminum and silicon were not localized at grain boundaries but were more or less segregated throughout the grains also iron was not localized in grain boundaries.

1. INTRODUCTION

Rotating Electrode method (REM) is one of the candidate methods for use as the neutron multiplier in pebble-bed-type bleeder blanket.

The nature of beryllium pebbles is estimated to be extensively affected by both manufacturing methods and production conditions.

Recently it has been reported that beryllium oxide and iron might influence the material behavior such as tritium release and swelling under neutron irradiation. [1] Furthermore, surface oxides of beryllium are considered to affect the reactivity to the steam and structure material such as stainless steel. [1] Therefore, it is important to evaluate the distribution of impurities in the beryllium pebbles.

In this study, the distribution of impurities such as oxides and others was examined by Electron Probe Micro Analysis (EPMA) and Auger Electron Spectroscopy (AES).

2. EXPERIMENTAL

2.1. Specimens

Specimens used were beryllium pebbles produced by the Rotating Electrode Method of NGK INSULATORS, LTD.. The diameter of evaluated pebbles were about 1 mm. The chemical composition of the pebbles is shown in Table 1.

Table 1
Chemical composition of beryllium pebbles

Element (wt%)					
Be	BeO	Fe	Al	Si	Mg
99.7	0.21	0.062	0.037	0.025	0.026

Two type of samples were prepared. One was REM produced samples. The other was surface - etched samples with acid. Mixed acid of Phosphoric acid;100 ml and sulfuric acid;10 ml was used for etching. Etching time was 10 minutes at 40 ℃.

2.2. EPMA Analysis

The samples for EPMA were molded in a resin mold and then polished in cross-section with diamond paste. Polished samples were cleaned with deionized water and acetone and dried.

The microstructure of the pebbles was observed by using polarized light micrograph.

JEOL-JXA-880 was used in examining the distribution of the impurities in beryllium pebbles. Accelerating voltage was 15kV and beam current was 0.3 μ A. Pixel No is 420 x 400.
The EPMA results were compared with the microstructures and component image by SEM.

2.3 AES Analysis

Surface structure and atomic depth profile was examined by AES. Equipment used was AES-680 of Physical Electronics Inc. Accelerating voltage was 15Kv and beam current was 20 nA. The tilt angle was 30°. Surface structure was observed by both SEM images and Auger electron images. After measuring the Auger spectrum of the surface, depth profile of each element was examined with Argon sputtering. Argon sputtering was carried out in the condition of 1 keV. Etching rate at this condition is 1.18 nm/min for SiO_2. Etching rate on beryllium oxide is unknown but beryllium etching rate can be calculated using sputter ratio of a solid beryllium atom, a solid silicon atom and the ratio of solid metal and oxide (Si/SiO^2) The value used is in Table 2.

Table 2 [2,3]
Used value on sputter ratio (Ar 1keV)

Be	Si	Be/Si	Si/SiO_2
0.95 atoms/ion	0.76atoms/ion	1.25	0.65

1.4nm/min was used as etching rate for metallic beryllium in this work.

3. RESULTS and DISCUSSION

3.1. Microstructure

Fig. 1 shows the polarized light micrograph of the beryllium pebble for EPMA analysis.

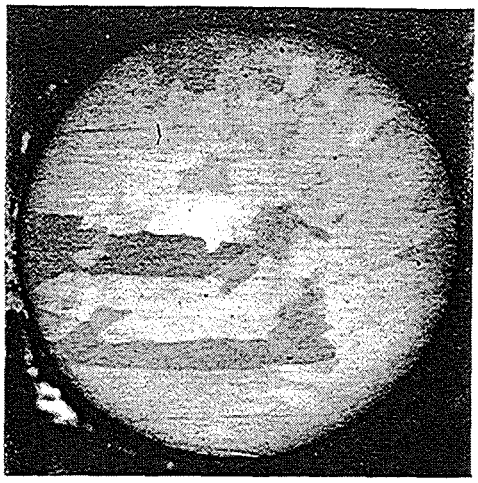

Fig.1. Microstructure of a beryllium pebble

The microstructure is multigranular and relatively coarse grain can be seen.

3.2. EPMA results

Fig. 2 shows the oxygen distribution in a beryllium pebble by EPMA mapping.
Oxygen exists uniformly throughout the grain, not localized in grain boundaries.

Fig.3 shows the magnesium distribution in the beryllium pebble by EPMA mapping. Magnesium is more or less segregated in the pebble, although it is not localized in grain boundaries.

Fig.4 shows the aluminum distribution in a beryllium pebble by EPMA mapping. Aluminum is also segregated in the pebble, and not localized in grain boundaries.

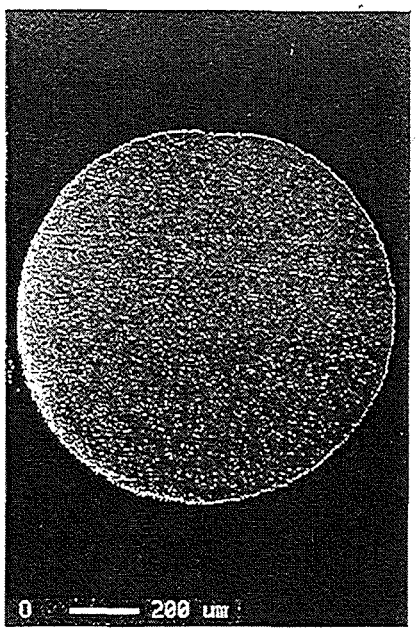

Fig.2. EPMA mapping image of oxygen

Fig.4. EPMA mapping image of aluminum

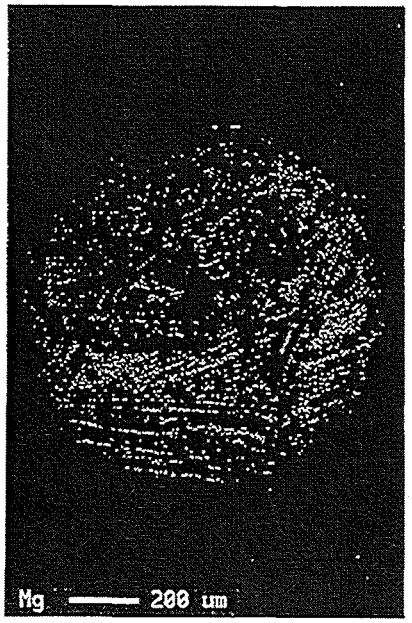

Fig.3. EPMA mapping image of magnesium

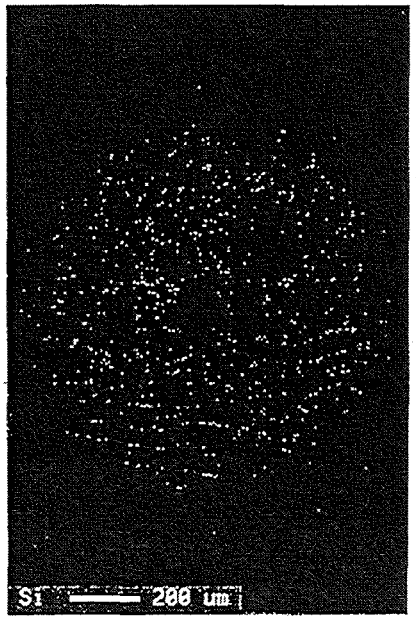

Fig.5. EPMA mapping image of silicon

Fig.5 shows the silicon distribution in a beryllium pebble by EPMA. Silicon is segregated in the pebbles, and not localized in grain boundaries.

Fig.6 shows the iron distribution in a beryllium pebble by EPMA mapping. Iron isn't observed to be segregated in the pebble and distributed uniformly.

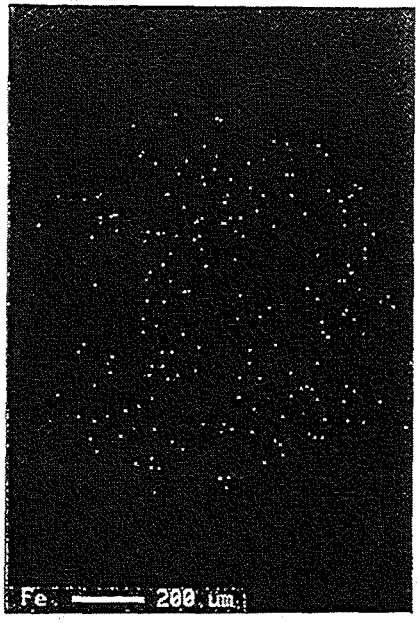

Fg.6. EPMA mapping image of iron

As a results of observing these EPMA images, magnesium, aluminum and silicon images show the same pattern, but iron doesn't correspond to that pattern.

Fig.7 shows the component image of the same beryllium pebble. Precipitate that can be seen as bright images corresponded to the same location that magnesium, aluminum and silicon were detected. Therefore this precipitates is estimated to be complex precipitation consisting of magnesium, aluminum and silicon.

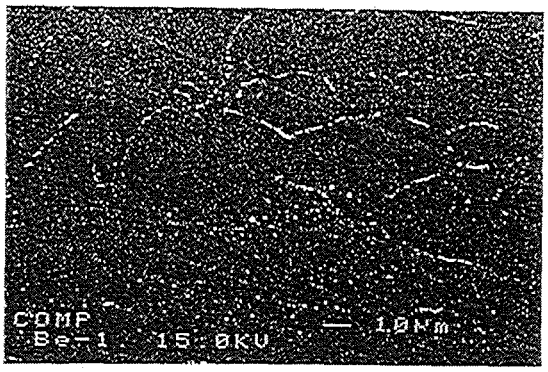

Fig.7.Component image of SEM in a beryllium pebble

3.3. AES analysis results of REM produced pebbles

Fig.8 shows the SEM micrograph of a beryllium pebble of about 1.0mm in diameter. The shape of the pebble are spherical and a peculiar pattern can be observed on surface.

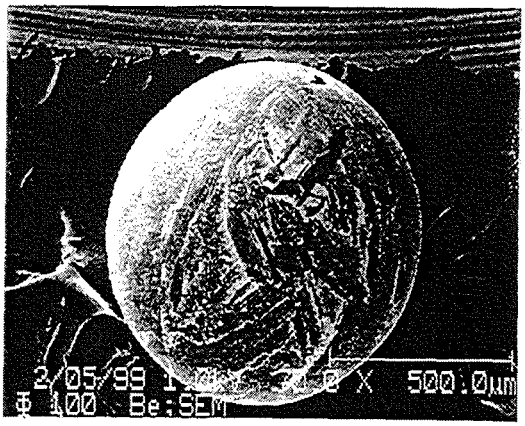

Fig.8. SEM image of a beryllium pebble for AES analysis

Fig.9 shows the SEM and Auger electron images of the pebbles after 5 minutes of sputter etching. The peculiar pattern was also observed in the SEM micrograph and this pattern was found to correspond to the oxide pattern in Auger electron images.

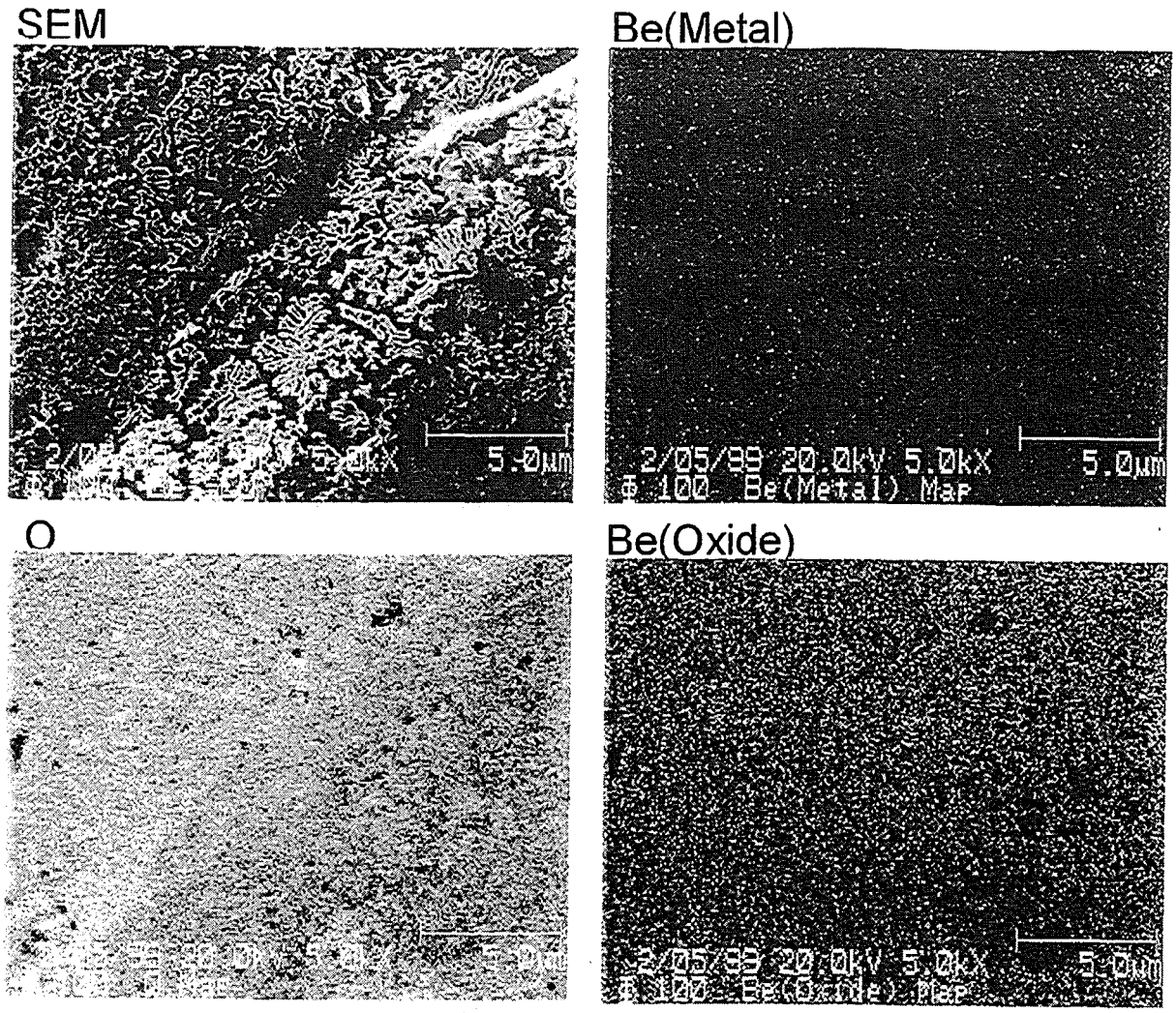

Fig.9. SEM and Auger electron images of a beryllium pebble after 5 minutes argon etching

Fig.10 shows the Auger spectrum of the surface of the beryllium pebble. Oxygen, beryllium oxide and carbon can be observed on the surface.

3.4 Depth profile of each element from surface

Fig.11 shows the depth profile that is derivative peak height changes of each elements of oxygen, beryllium and carbon versus sputter time by argon .

Fig.12 shows the depth profile that atomic content ratio versus depth from surface. Sensitive factors used in these analysis are shown in Table 3.

Table 3
Sensitivity Factors used in analysis

Oxygen	0.212
Beryllium	0.108
Carbon	0.076

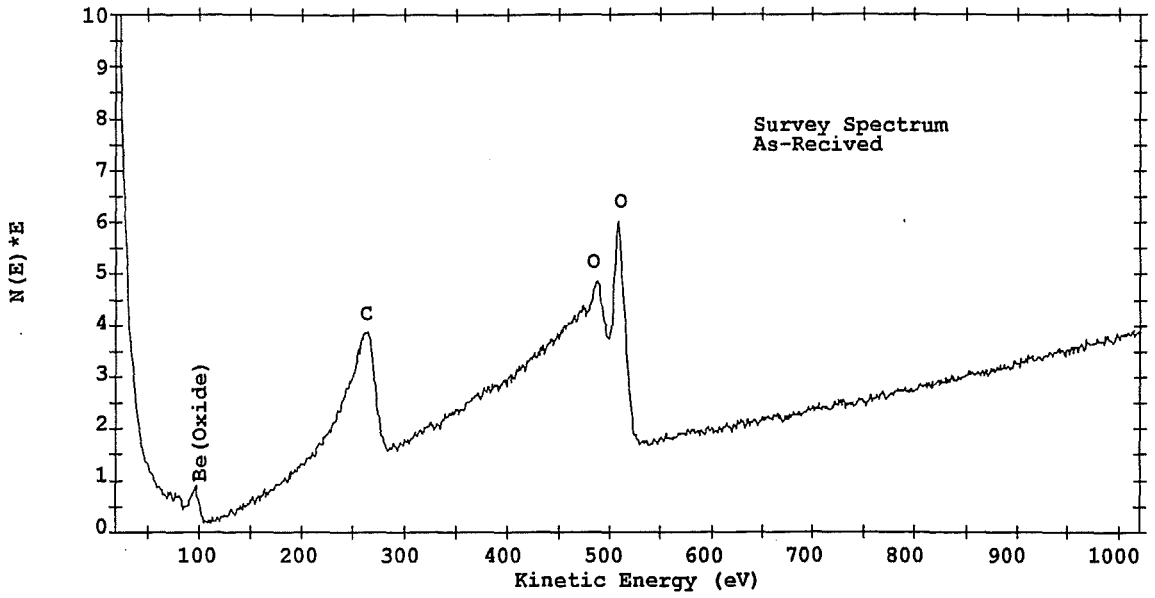

Fig.10. Auger spectrum of the surface in a REM produced beryllium pebble

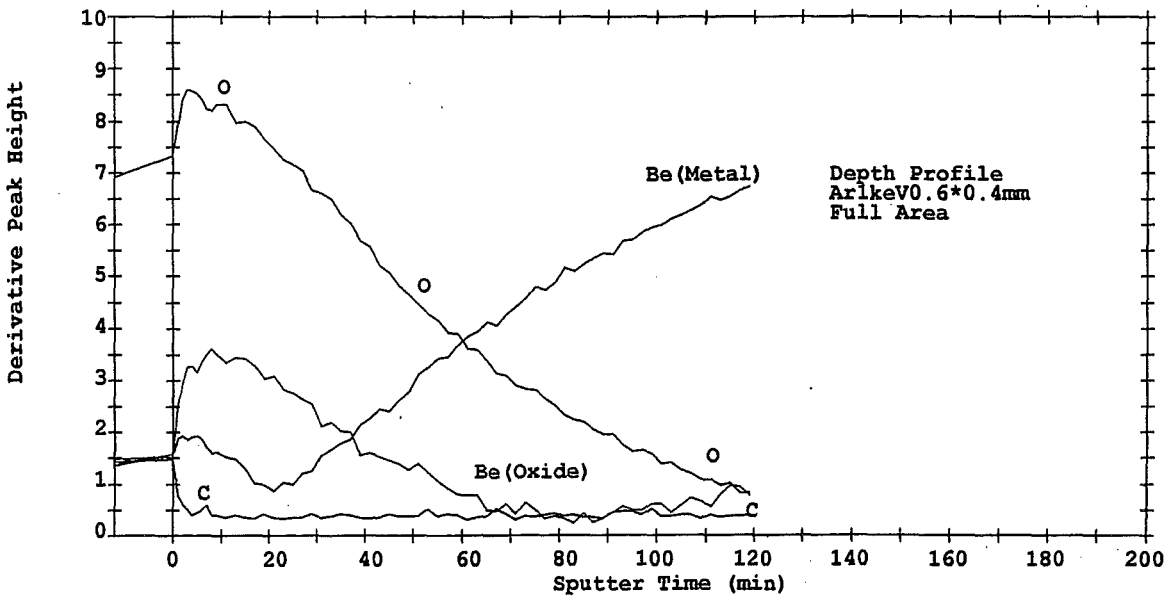

Fig.11. Derivative peak height changes of elements in a REM produced pebbles with argon sputter time

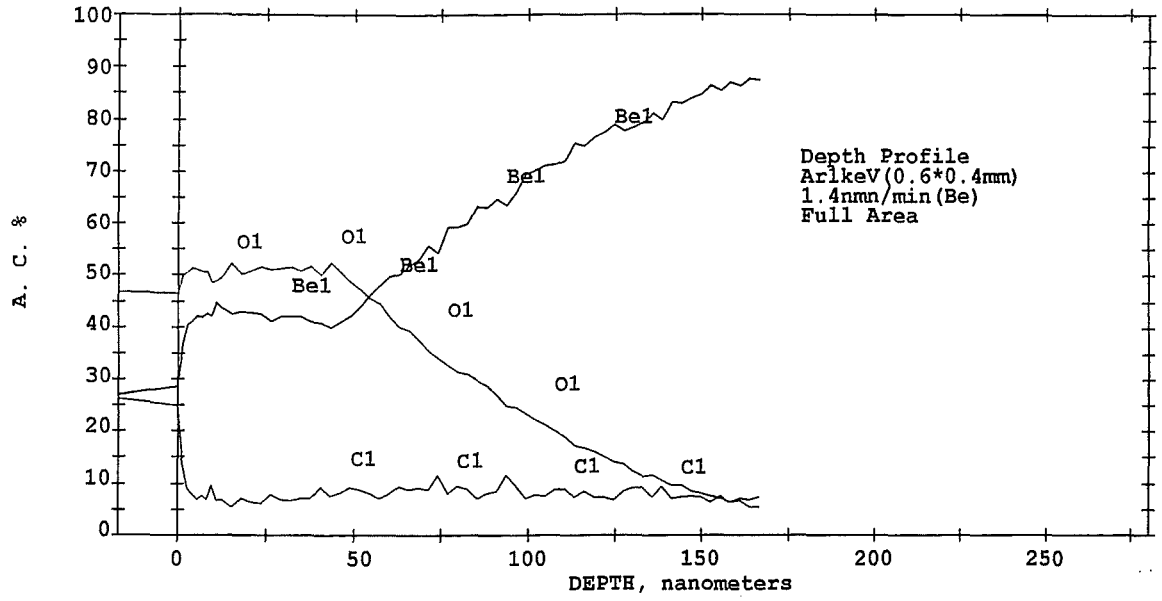

Fig. 12. Depth profiles of elements in a REM produced pebble.

3.5. Surface observation after argon sputtering

Fig. 13 shows a SEM micrograph of a beryllium pebble after 140 minutes of argon sputtering.

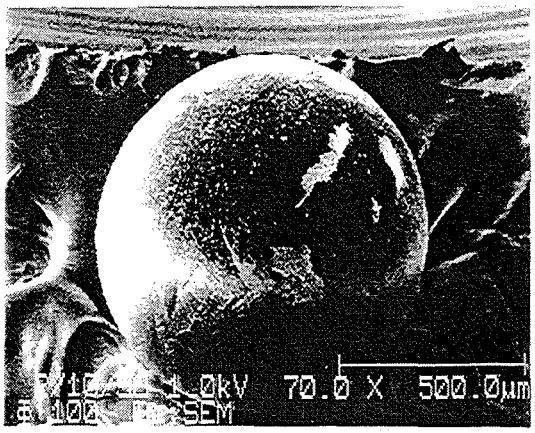

Fig. 13. SEM image of a beryllium pebble after 140 minutes by argon sputtering

The peculiar pattern that was observed in the REM Produced pebble disappeared mostly after argon etching. Therefore the peculiar pattern is considered to be the oxide on the surface.

Fig. 14 shows the SEM and Auger electron images of the pebbles after 140 minutes sputter etching. The peculiar pattern also disappear in SEM micrograph and beryllium metal is detected mainly.

According to these data, oxide thickness was estimated to be approximately 50 - 150 nm calculated from the etching rate of beryllium.
Oxygen was in existence in the inner area and oxygen content in the inner area was estimated to be 1-2 atomic percent.

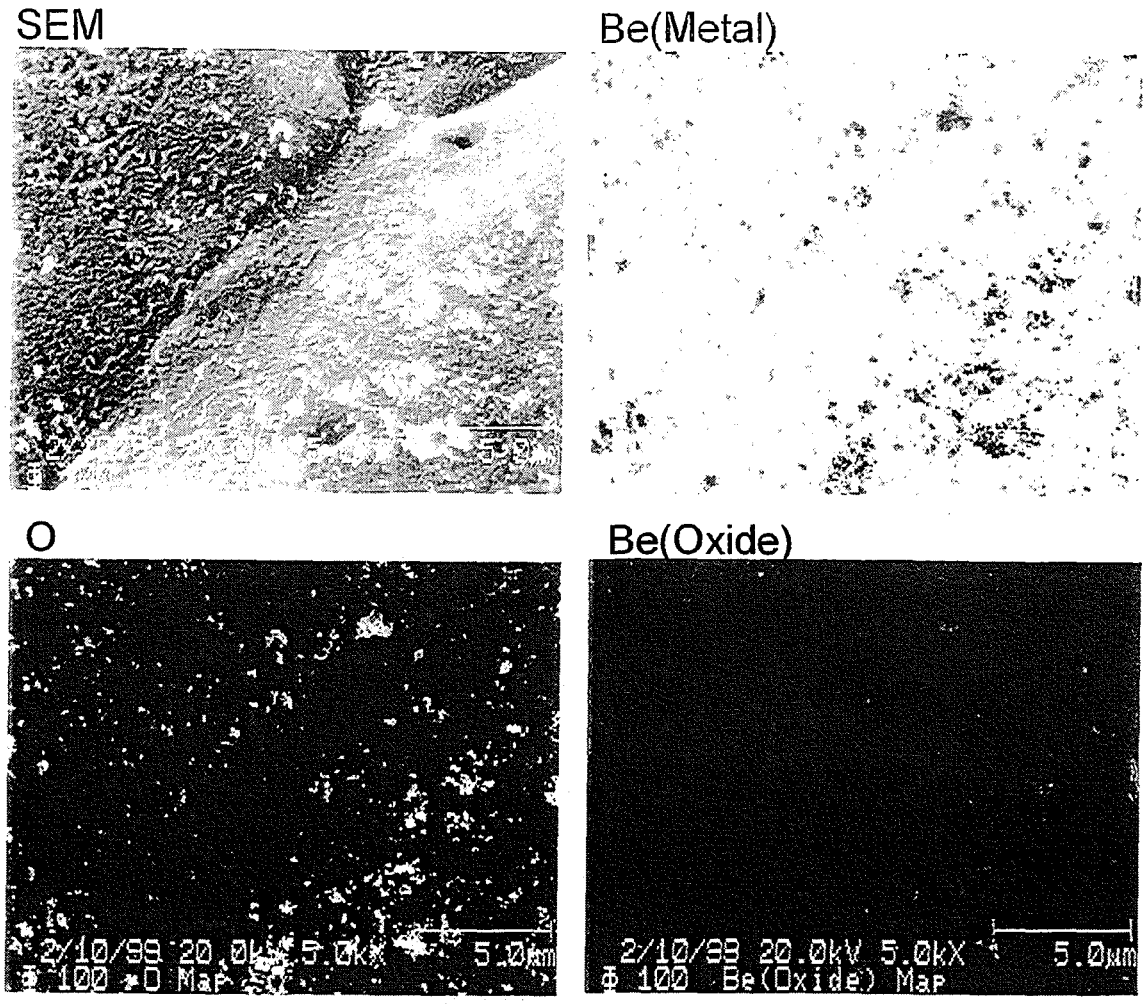

Fig.14. SEM and Auger electron images of a beryllium pebble after 140 minutes argon etching

3.6. AES analysis results of as etched pebbles by acid

Fig.15 shows the SEM micrograph of a beryllium pebble after etching by a mixed acid made of phosphoric acid and sulfuric acid.

The surface is smooth and the peculiar pattern that can be seen in REM produced pebbles can't be observed in an etched pebble. Etched pits are observed in some area.

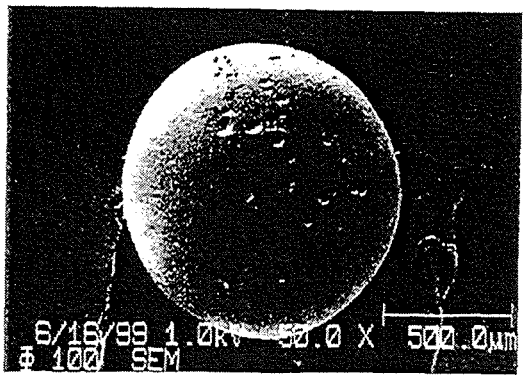

Fig.15. SEM image of REM pebbles after etching

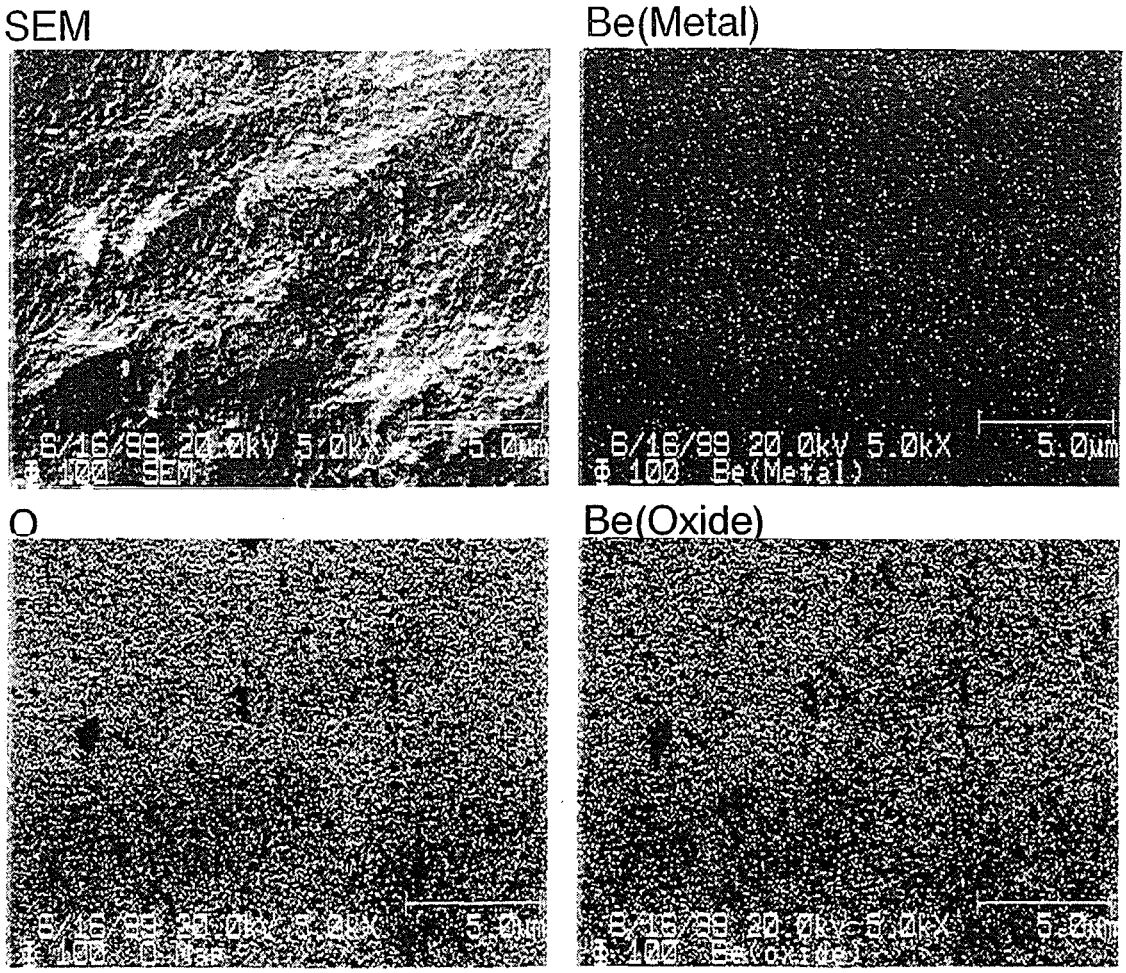

Fig. 16. SEM and Auger electron images of chemically etched REM pebbles

Fig. 16 shows the SEM and Auger electron images of etched, pre-argon sputtered pebbles Oxygen was detected mainly from the surface of the pebble.

Fig. 17 shows the depth profile that atomic content from the surface calculated from the etching ratio of beryllium. It is assumed that the surface is covered with a thin oxide, but the thickness is thin. Estimated oxide thickness is approximately 20 - 40 nm.

Table 4 shows the oxide content of beryllium pebbles after etching compare with that before etching. The oxide content of beryllium pebbles after etching was half of that before etching and the oxide content was 0.11 wt %.

From these analysis, it is found that oxygen in the beryllium pebbles produced by the rotating method is thick in surface area. By etch and chemical cleaning, oxygen content can be decreased.

Table 4

Oxide content of beryllium pebbles (wt %)	
as produced	0.21
as chemical etched	0.11

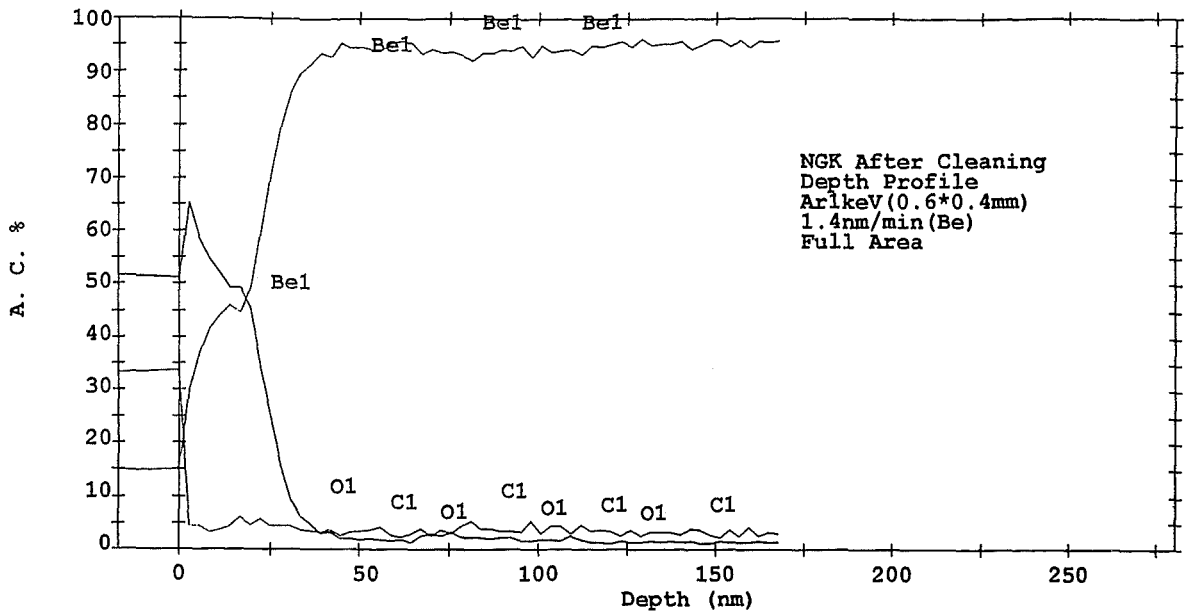

Fig. 17. Depth profiles of elements in a chemical etched REM pebble.

Therefore there is a possibility that oxide can be decreased by controlling processing atmosphere of REM, even if no etching is applied.

4. CONCLUSIONS

It was found by EPMA and AES that beryllium pebbles' surface produced by the rotating electrode method is covered with a thin oxide layer. The thickness of the oxide is estimated to be about 50 - 150 nm by AES depth analysis. Oxide in the cross-section isn't segregated in the grain boundaries, and is distributed throughout the grains.

By chemical etching, surface oxide can be decreased and total content of oxide decreases to half of that before chemical etching. Existing oxygen in the inner area of the beryllium pebble is estimated to be 1-2 atomic percent by AES.

Magnesium, aluminum and silicon in the beryllium pebbles produced by REM is estimated to make precipitates in the grain and these are not segregated in the grain boundaries.

5. REFERENCE

1. E.Ishituka, H. Kawamura, T.Terai and S.Tanaka, Proceedings of the third IEA international workshop on beryllium technology for fusion October 22-24,1997, MITO, Japan
2. Atomic Data and Nuclear Data, 31(1984)1-80.
3. Veeco, Brochure V60

PHASE EQUILIBRIA, COMPATIBILITY STUDIES AND THERMAL PROPERTIES OF BERYLLIUM SYSTEMS

H. Kleykamp[1]
Forschungszentrum Karlsruhe
Institut für Materialforschung I
Postfach 3640, 76021 Karlsruhe, Germany

The quality control of commercial beryllium, the examinations of the phase equilibria in beryllium systems as well as the broad field of incompatibility and the reaction kinetics of beryllium with other materials necessitate a sophisticated method for the analysis of this element in micrometer areas. A powerful tool is the wavelength dispersive X-ray microanalyser. Therefore, a commercial synthetic Mo-B_4C multilayer X-ray diffracting device with 2 d = 22.2 nm periodicity was used to extend X-ray microanalysis to the ultra-light elements Be and B in an existing instrument. The spectrometer covers a wavelength range between 5.2 and 13 nm. The wavelength of the Be Kα emission line from elemental Be is λ = 11.35 nm and the full width at half maximum is ΔE = 7.2 eV. The optimum working voltage U_o is 10 kV for moderate X-ray mass absorption of the targets. The determination of Be in oxides is less favourable owing to the high mass absorption. U_o has to be reduced to 5 kV. The chemical shift of the Be Kα line in BeO is $\Delta\lambda$ = + 0.3 nm relative to pure Be [1].

Beryllium pebbles are foreseen as neutron multipliers in future fusion reactor blanket concepts. Industrial intermediate Be products which had been produced by a modified Kroll process and subsequent reduction of BeF_2 using Mg were investigated by X-ray microanalysis. The following precipitates in the Be matrix of 2 mm pebbles partially annealed up to 790°C could be detected: (Mg, Zr, U) Be_{13}, $MgBe_{13}$, Mg_2Si, Al_2Mg_3 and (Fe, Cr) alloys. The maximum solubility of selected metallic impurities in beryllium annealed at 800°C is: 0.06 mass % Fe, 0.03 mass % Al, 0.02 mass % Si, < 0.01 mass % Mg and $\approx$ 0.01 mass % Cr. The purification of Be by vacuum distillation reduces the amount of highly volatile Mg resulting in a lower precipitation density of Mg containing phases. These 0.2 mm Be pebbles were manufactured by the melt atomising process. Al_5Fe_2, Be_2C and Cr-Fe-Si were observed in specimens annealed between 870 and 690°C. It is interesting that Al_5Fe_2 precipitates were observed; however, the phase $AlFeBe_4$ that would have been expected according to the phase diagram of the ternary Al-Be-Fe system was not found. Probably the Fe/Al ratio is too low for $AlFeBe_4$ formation. The high annealing temperature starting at 870°C could also be a reason for the disappearance of $AlFeBe_4$ because this phase decomposes above 850°C. In order to avoid a liquid Al(Be) phase, the Fe/Al atomic ratio of the impurity elements should be higher than one because in this case a solid intermetallic phase stable to high temperatures is formed [1,2].

[1] Corresponding author,
Tel: +(49)7247-82-2888, Fax: +(49)7247-82-4567, e-mail: heiko.kleykamp@imf.fzk.de

Compatibility studies of Be with the fusion breeder materials Li_4SiO_4 and Li_2SiO_3 have shown that Be reacts with Li_4SiO_4 by the formation of Li_2Si, BeO and $Li_2Be_2O_3$. In previous blanket concepts, Li_4SiO_4 and Be pebbles were mixed and irradiated in the HFR Petten. After 10 % Li burn-up the following reaction takes place: 10 Li_4SiO_4 + 2 Be = 8 Li_4SiO_4 + 2 Li_2SiO_3 + 4 He + 2 T_2 + 2 BeO followed by a secondary reaction in direct contact of both phases: BeO + Li_2SiO_3 = Li_2BeSiO_4. All these phases were proven by X-ray microanalysis on irradiated fusion blanket materials [3].

SiC fibre reinforced SiC fabrics are considered for structure materials of advanced fusion blanket concepts. A priority task are compatibility studies of SiC with Li breeder ceramics and the neutron multiplier Be. Solid state reactions were studied between SiC and Be pellets by capsule experiments. The reaction products Be_2C and Si were observed at 800 and 900°C between the initial phases by X-ray microanalysis. A parabolic time law and a chemical diffusion coefficient of Be in the products were deduced at 900°C which gives $D = 2.6 \cdot 10^{-15}$ m²/s. The presence of oxygen releasing SiO_2 without direct contact with the reactants results in the oxidation of the reaction product surface by formation of a Be_2SiO_4 layer. All reactions are kinetically hindered below 700°C [4].

Hcp Be has a first order transition to bcc Be at about 13 degrees below melting. The temperatures of transformation T_{tr} and melting T_m and the enthalpies of transformation $\Delta_{tr}H$ and melting Δ_mH were measured by difference thermal analysis and by anisothermal calorimetry. The results for the hcp-bcc transformation of Be are T_{tr} = (1269 ± 1)°C and $\Delta_{tr}H$ = (6100 ± 500) J/mol and those for the melting process are T_m = (1282 ± 2)°C and Δ_mH = (7200 ± 500) J/mol, resp. The kinetic aspects of the bcc-hcp back-transformation of Be indicate a strong delay of transformation during cooling. When liquid Be falls in drops through pierced sieves during the manufacturing process of small pebbles and becomes solid during further fall down to the base-plate, an incomplete bcc - hcp transformation of Be cannot be excluded [5].

References

[1] H. Kleykamp, J. Anal. At. Spectrom. 14 (1999) 377

[2] H. Kleykamp, H. D. Gottschalg, internal reports (1998)

[3] H. Kleykamp, J. Nucl. Mater. 273 (1999) 171

[4] H. Kleykamp, 9th Int. Conf. Fusion Reactor Mater., Colorado Springs, USA, 1999; J. Nucl. Mater., to be submitted

[5] H. Kleykamp, Thermochim. Acta (1999), in print

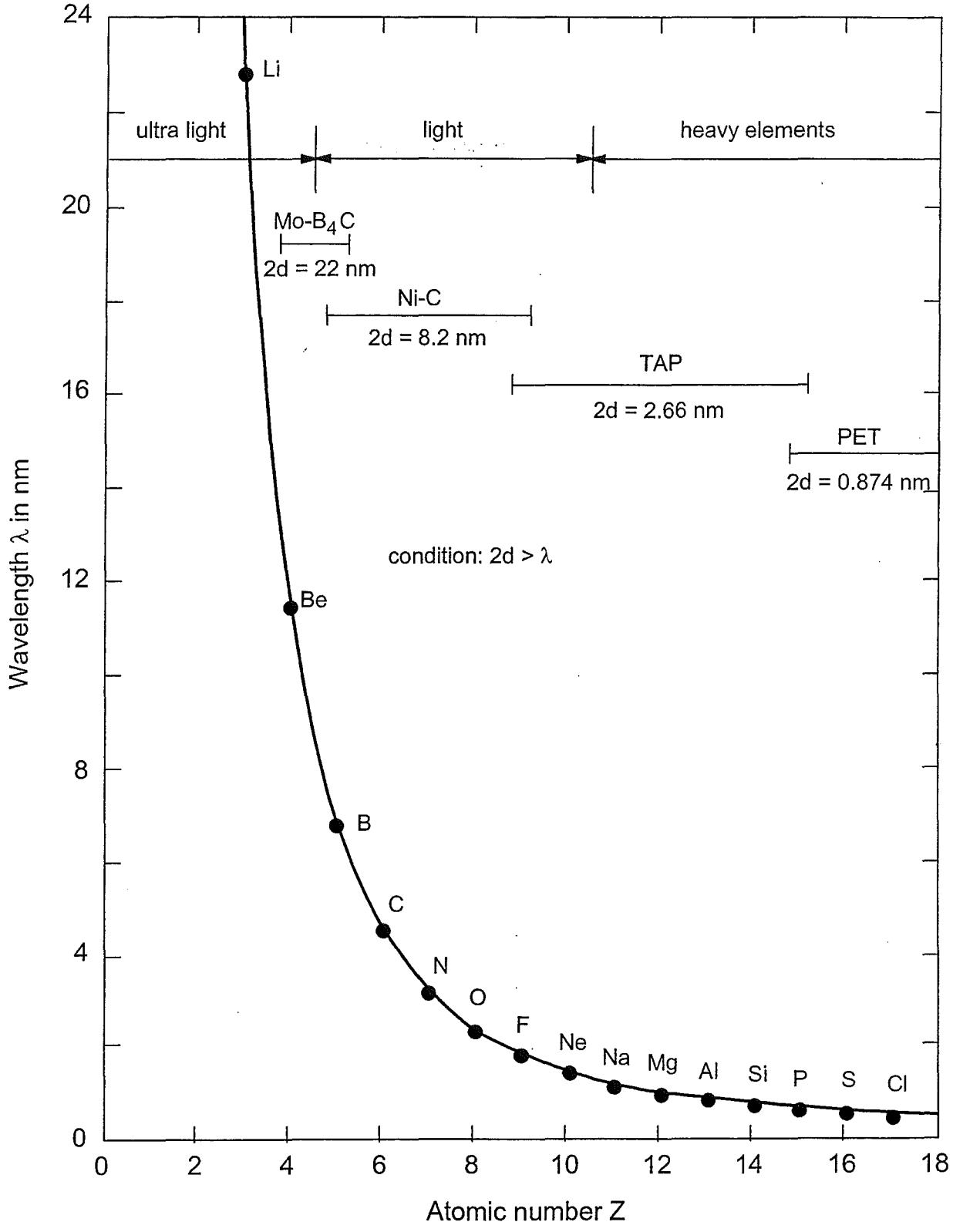

Use of X-ray diffraction crystals in the periodic system

hkl29.pre 29.1.98

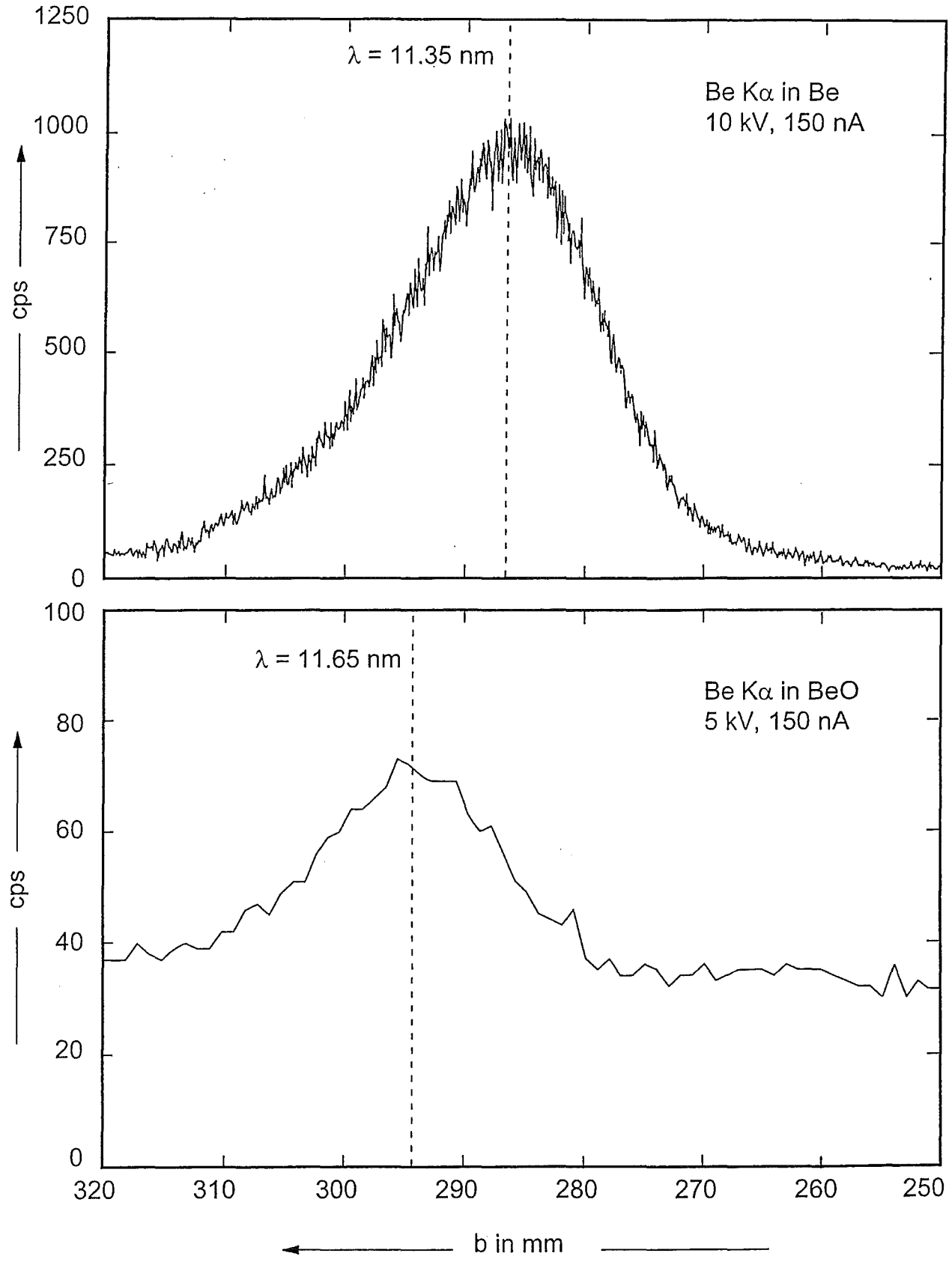

Be Kα spectra in Be metal and in BeO

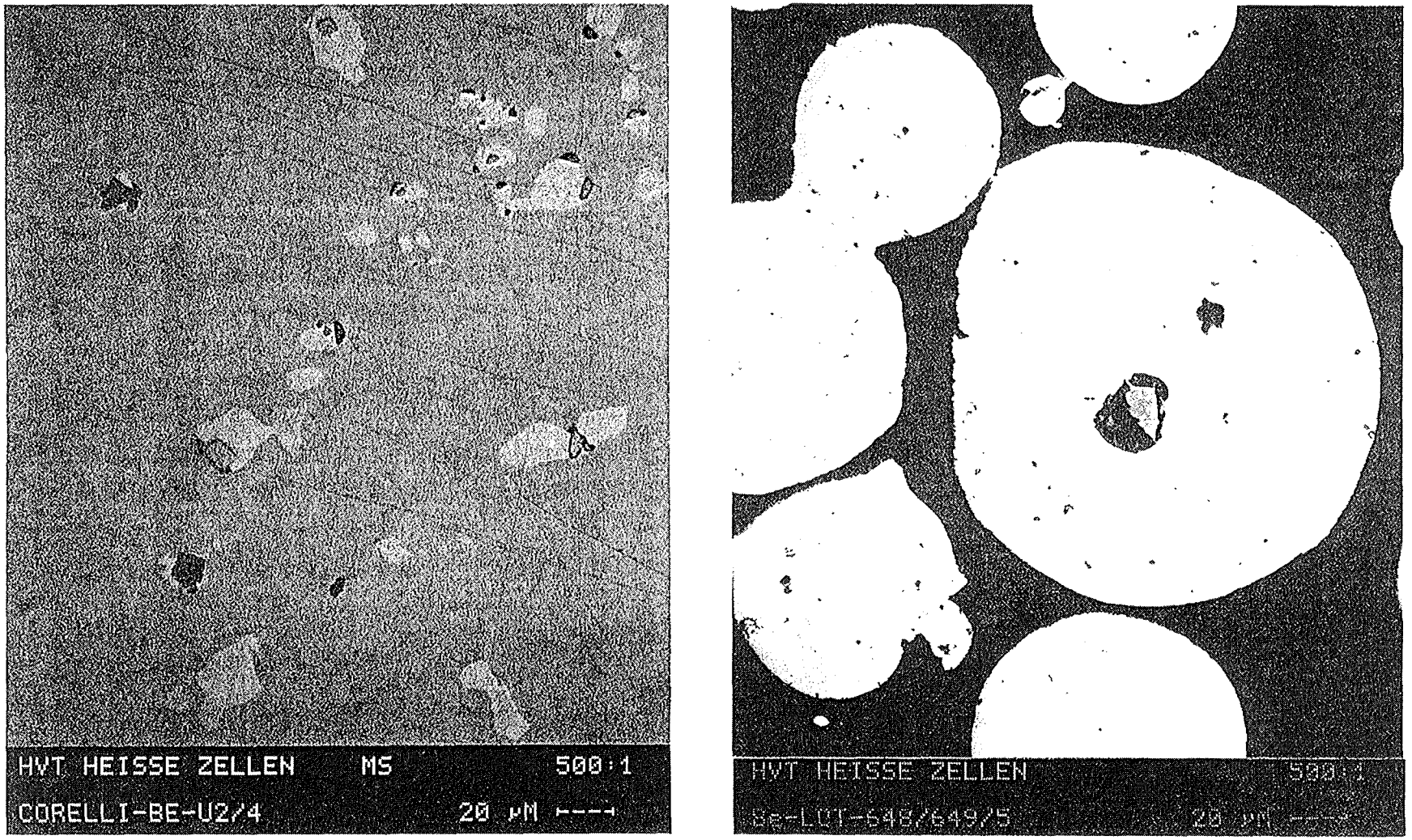

Impurities in beryllium pebbles: left: Be_{13}(Mg,U,Zr), Mg_2Si and Al-Mg in Be intermediate product; right: Al_5Fe_2 and SiC in melt-atomized product.

kl53.pre 17.08.98

Precipitates and maximum solubilities in beryllium

preparation method	annealing	precipitates		
intermediate product	≤ 790°C	$(Mg, Zr, U)Be_{13}$, $MgBe_{13}$, Mg_2Si, Al_2Mg_3, Fe-Cr		
vacuum distillation, melt atomising	≤ 870°C	Al_5Fe_2, Be_2C, Fe-Cr silicides		
		element	composition (mass %)	max. solubility (mass %)
vacuum distillation, melt atomising	≤ 870°C	Be	99.4	balance
		O	0.22	-
		Fe	0.09	0.06
		C	0.07	-
		Al	0.04	0.029
		Si	0.04	0.019
		Mg	≤ 0.01	< 0.01
		Cr	-	≈ 0.01

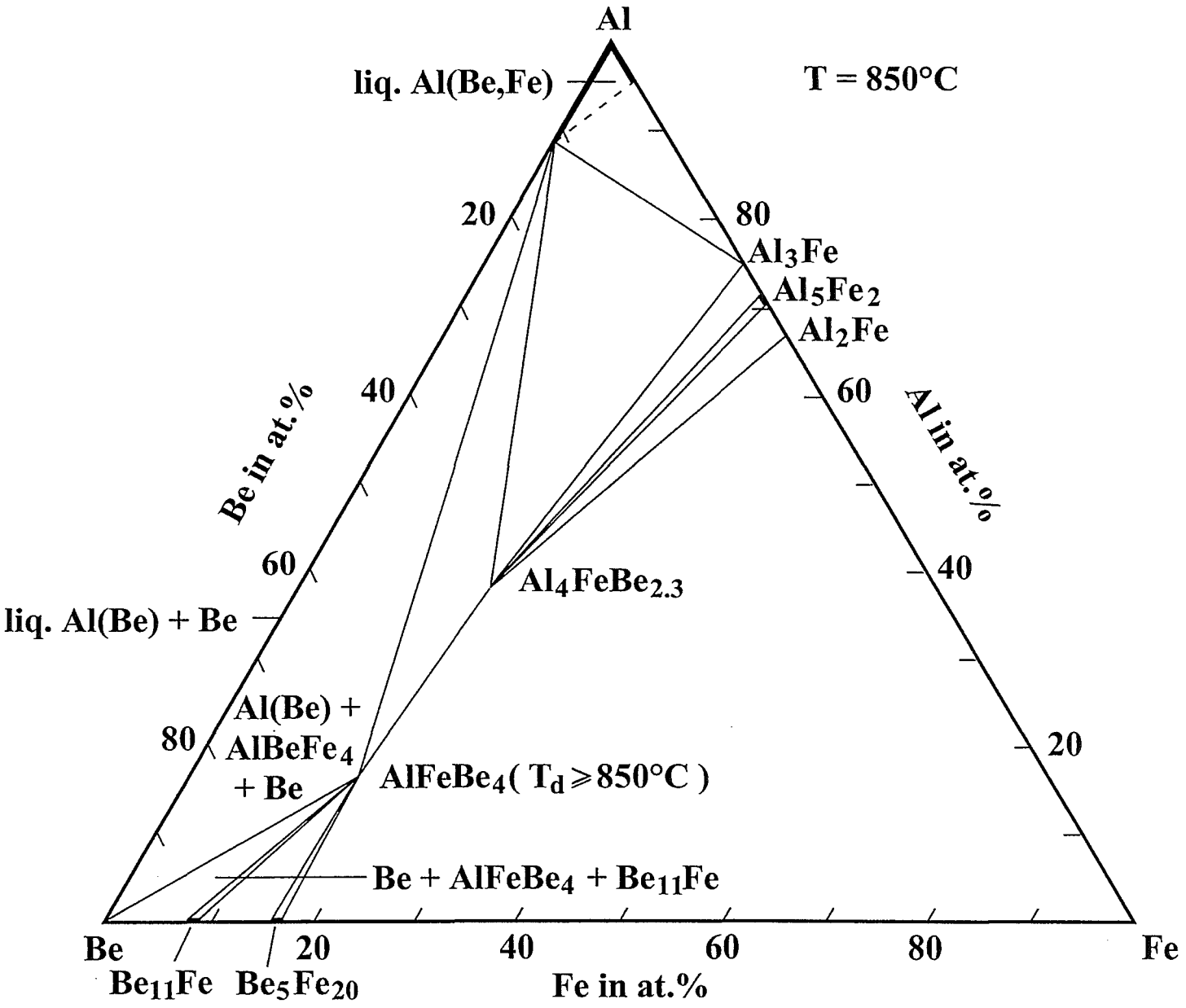

Phase diagram of the Al - Be - Fe system at 850°C

hkl76.pre 28.07.1999

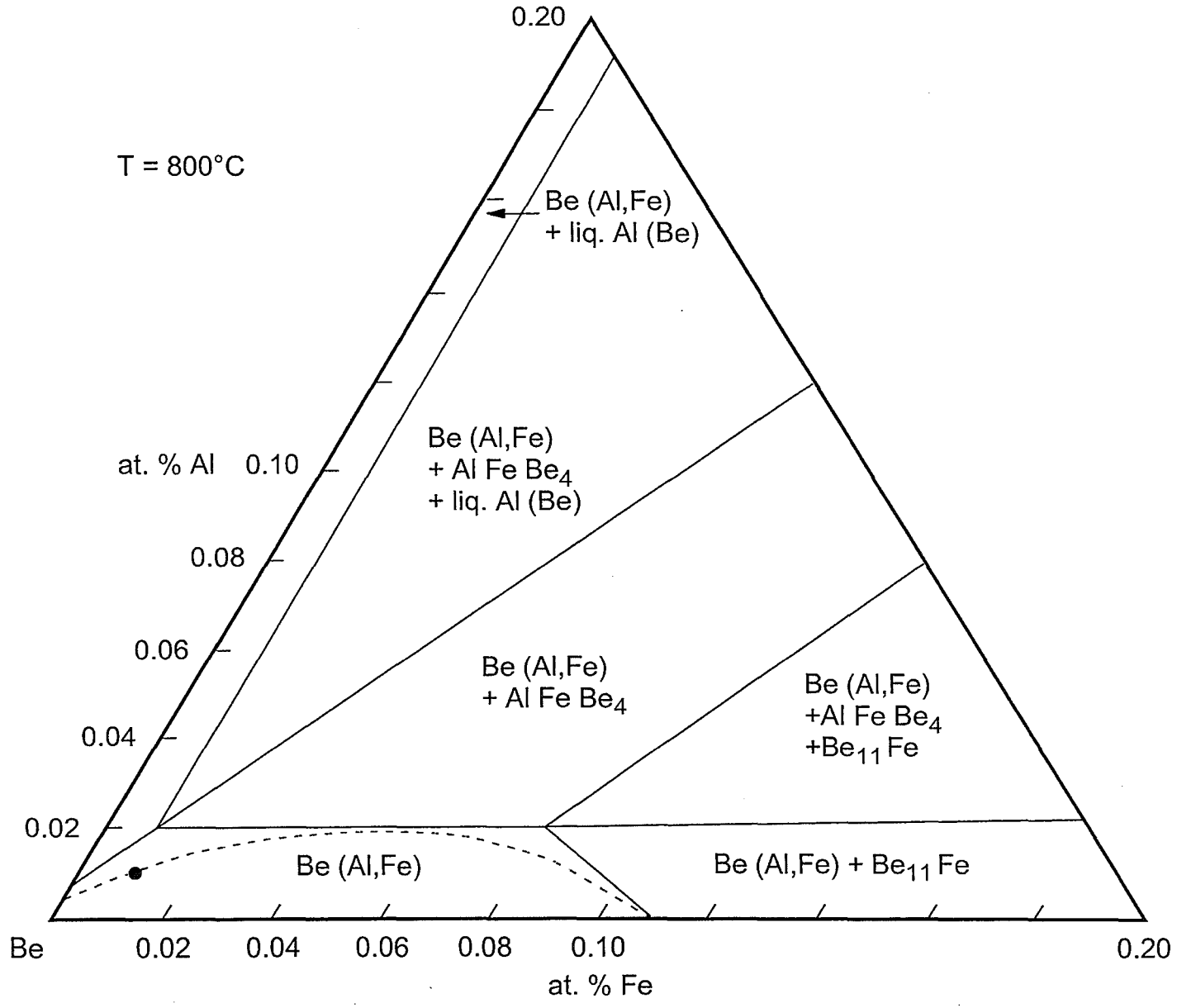

Isothermal section of the Be - Al - Fe system at 800°C (from Myers and Smugeresky),
• : solubility limit by X-ray microanalysis, this study.

hkl49 03.08.98

Be-Li_4SiO_4 irradiation experiment EXOTIC-7 with 18 % Li burn-up

Be-Li_4SiO_4 reaction behaviour after 18 % burn-up:

1. Li_4SiO_4 burn-up process in presence of beryllium:

   100 Li_4SiO_4 + 36 Be = 64 Li_4SiO_4 + 36 Li_2SiO_3 + 72 He + 36 T_2 + 36 BeO
   Secondary reaction: Li_2SiO_3 + BeO = Li_2BeSiO_4
   parallel reaction: 3 Be + Li_4SiO_4 = Li_2Si + BeO + $Li_2Be_2O_3$

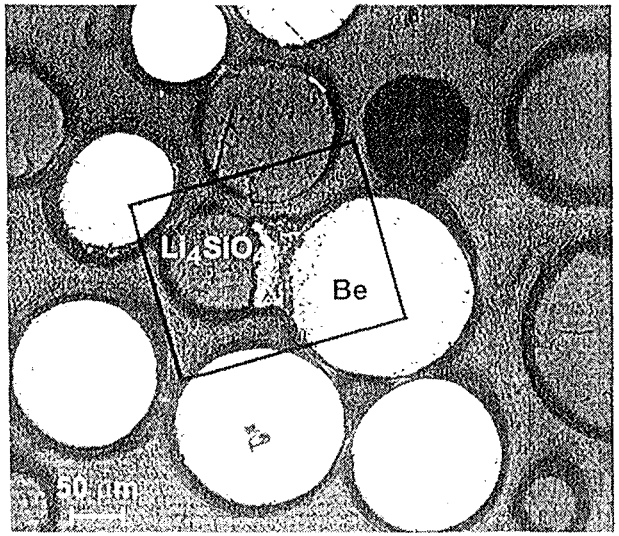

light-optical microstructure

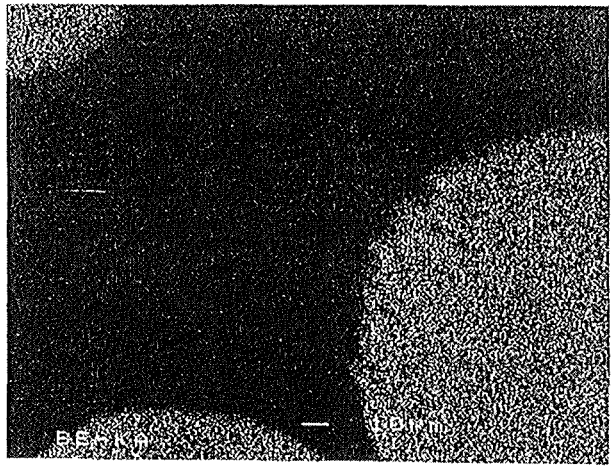

beryllium distribution

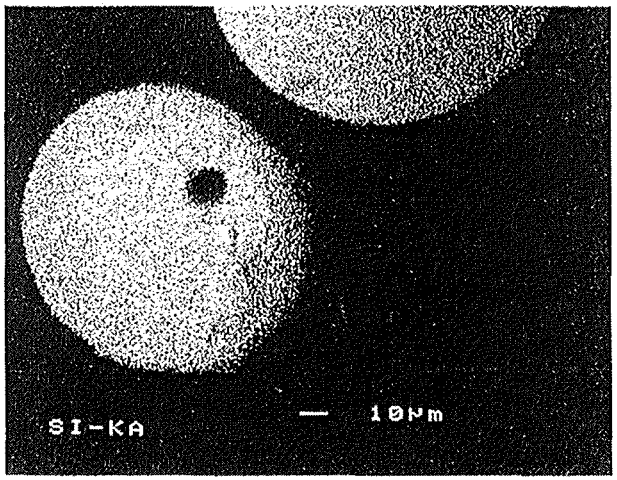

silicon distribution

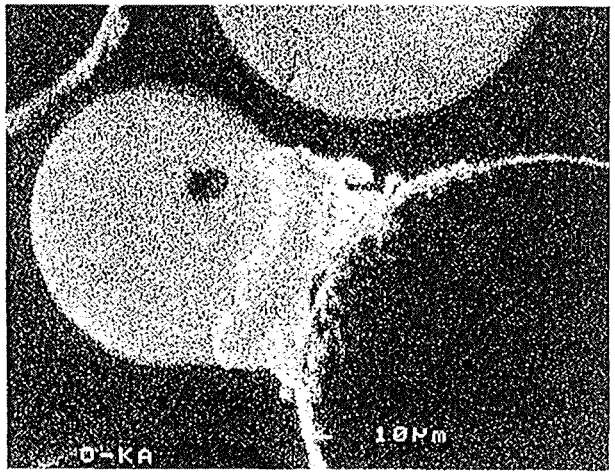

oxygen distribution

$Li_4SiO_4(Li_2SiO_3)$ - Be interaction in a fusion blanket after irradiation in the HFR to 18% Li burnup

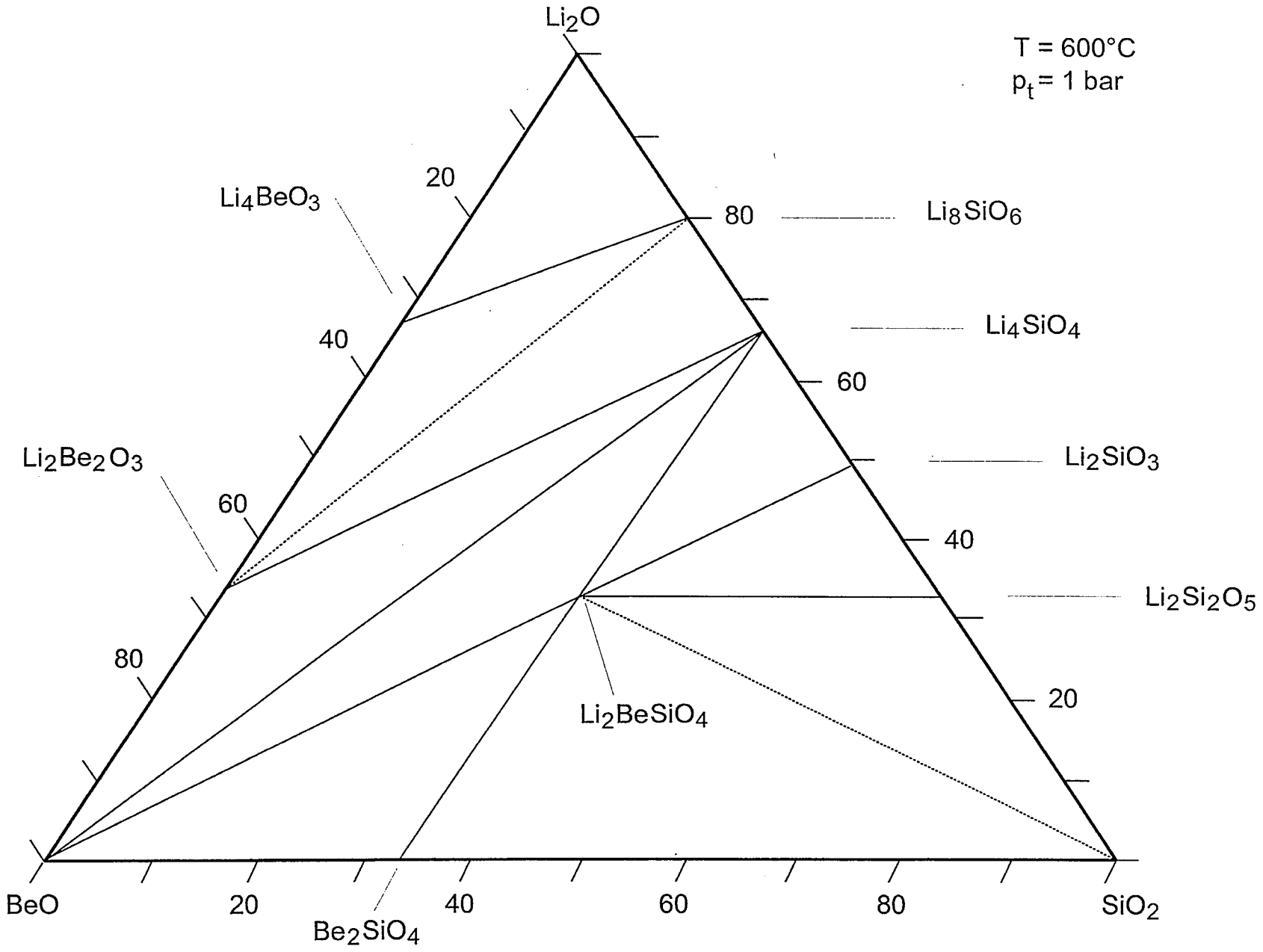

Isothermal section of the pseudo-ternary Li_2O - BeO - SiO_2 system (co-ordinates in mol %)

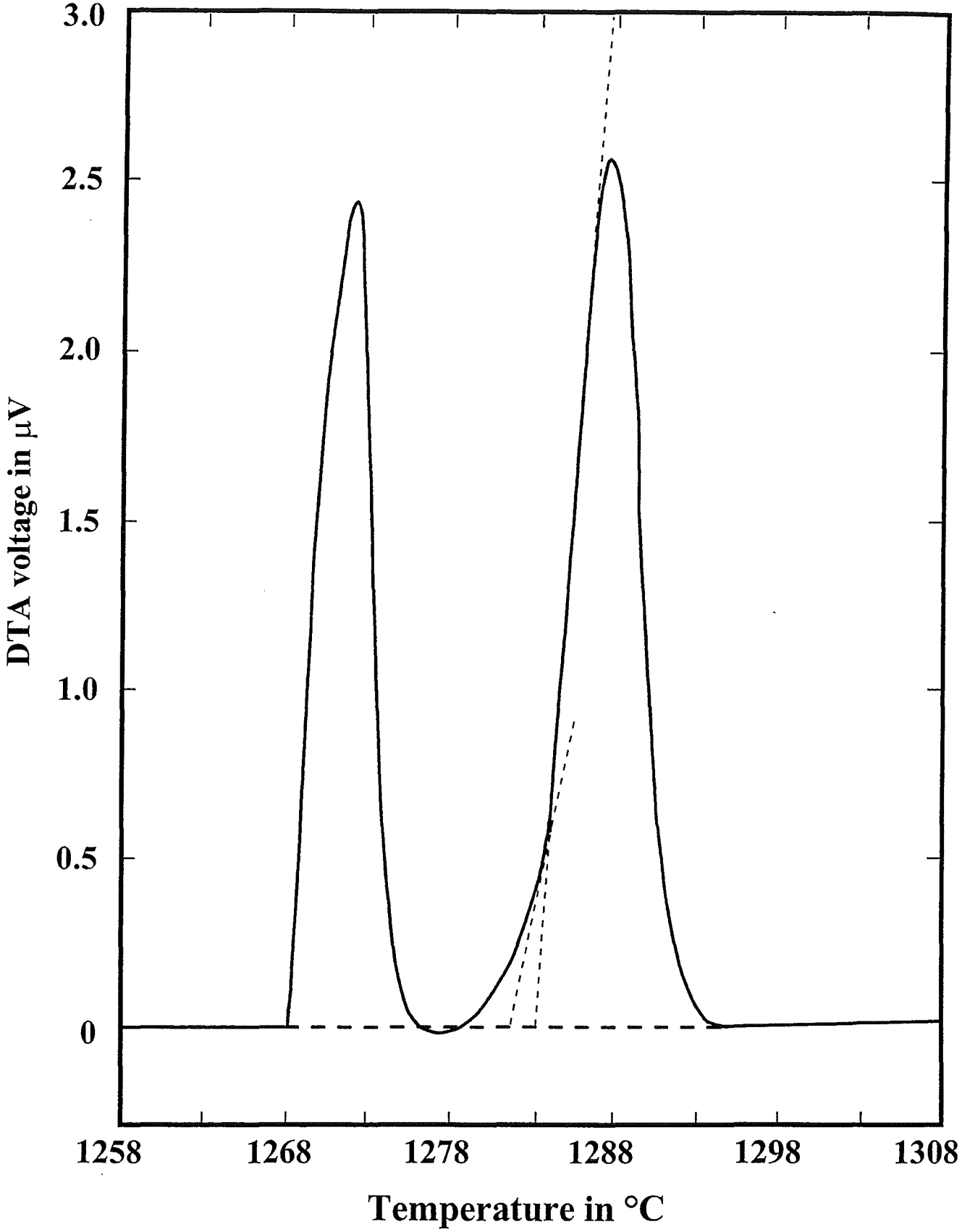

Temperatures of transformation and melting of beryllium by DTA

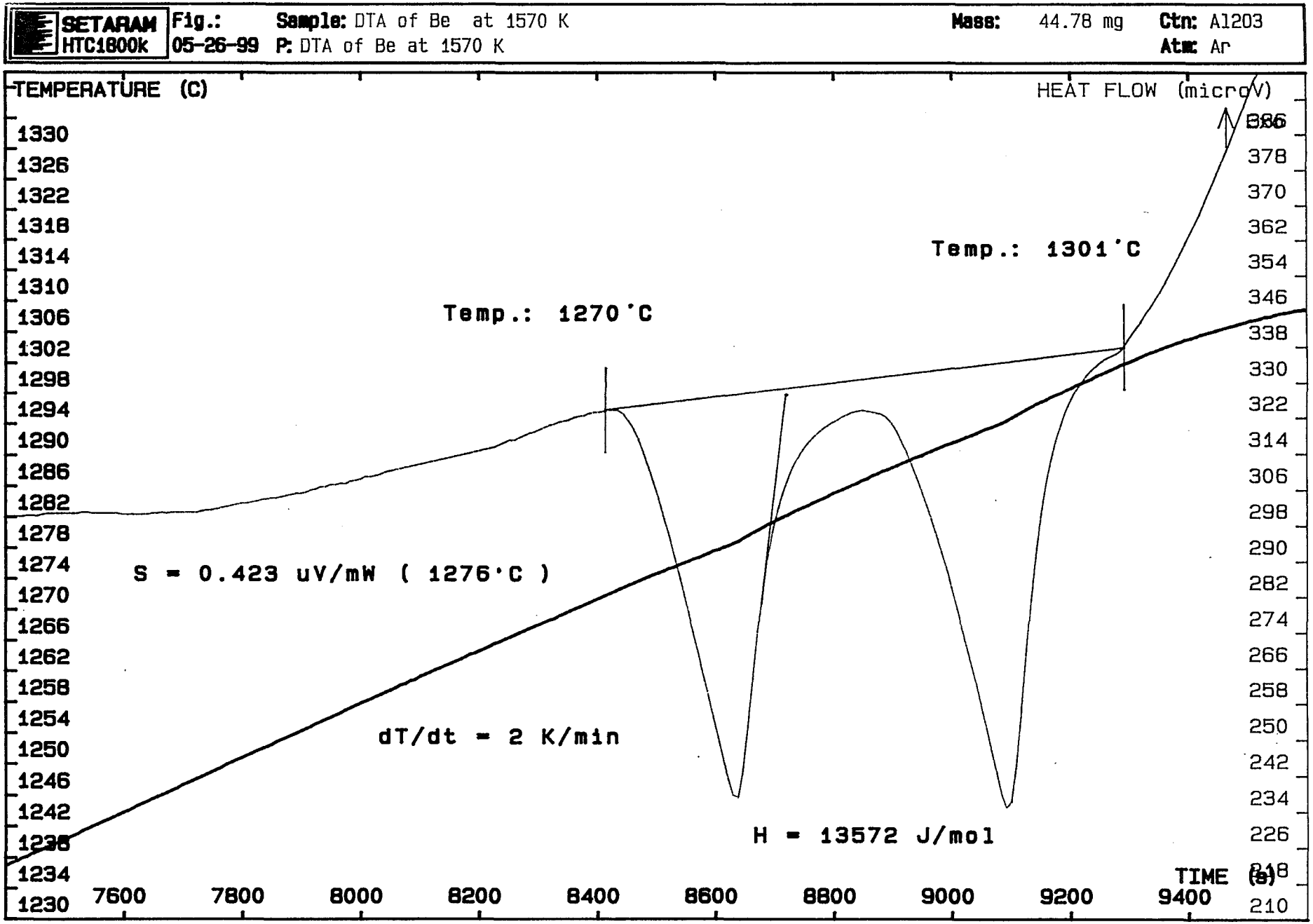
SETARAM
HTC1800k
Fig.:
05-26-99
Sample: DTA of Be at 1570 K
P: DTA of Be at 1570 K
Mass: 44.78 mg
Ctn: Al203
Atm: Ar
TEMPERATURE (C)
HEAT FLOW (microV)
Temp.: 1270°C
Temp.: 1301°C
S = 0.423 uV/mW (1276°C)
dT/dt = 2 K/min
H = 13572 J/mol
TIME (s)
1330
1326
1322
1318
1314
1310
1306
1302
1298
1294
1290
1286
1282
1278
1274
1270
1266
1262
1258
1254
1250
1246
1242
1238
1234
1230
386
378
370
362
354
346
338
330
322
314
306
298
290
282
274
266
258
250
242
234
226
218
210
7600
7800
8000
8200
8400
8600
8800
9000
9200
9400

Temperatures of transformation T_{tr} and melting T_m of beryllium.

T_{tr} in °C	T_m in °C	method	author (year)
1263	1278	thermal analysis	Teitel, Cohen (1949)
1271	1290	DTA (Be by zone refining)	Martin, Moore (1959)
-	1287	drop calorimetry	Kantor et al. (1960)
1254	-	electrical resistivity	Amonenko et al. (1962)
1260	1285	electrical resistivity	Francois, Contre (1965)
1279	1290	DTA	Loasby, Dearden (1977)
1263	1285	DTA	Abey (1984)
1268 ± 1	1282 ± 2	DTA	Kleykamp (1999)
1270 ± 1	(1283 ± 2)	anisothermal calorimetry	Kleykamp (1999)

Enthalpies of transformation $\Delta_{tr}H$ and melting Δ_mH of beryllium.

$\Delta_{tr}H$ in J/mol	Δ_mH in J/mol	$\Delta_{tr}H + \Delta_mH$	method	author (year)
-	-	14800	drop calorimetry	Kantor et al. (1960)
7500	14600	(22100)	Clausius-Clapeyron ($(T_{tr}, T_m) = f(p)$)	Francois, Contre (1965)
-	- 9050[a]	-	anisothermal calorimetry	Radenac, Berthaut (1972)
2100	2400	(4500)	DTA (peak area integration)	Loasby, Dearden (1977)
7950	9200	(17150)	DTA (peak area weighing)	Abey (1984)
6100 ± 500	7200 ± 500	(13300)	anisothermal calorimetry	Kleykamp (1999)

[a] Enthalpy of solidification

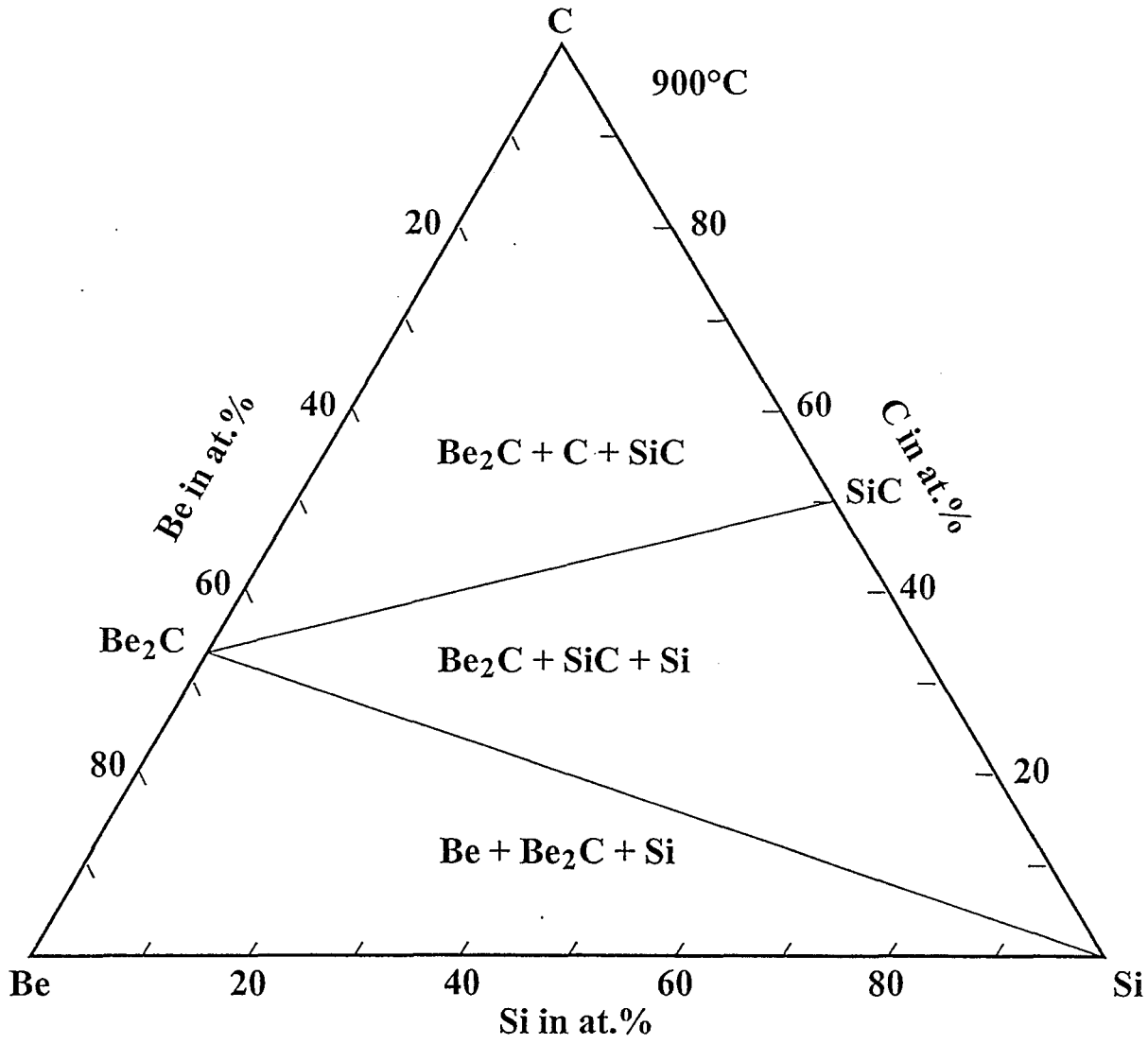

Isothermal section of the Be - C - Si system at 900°C

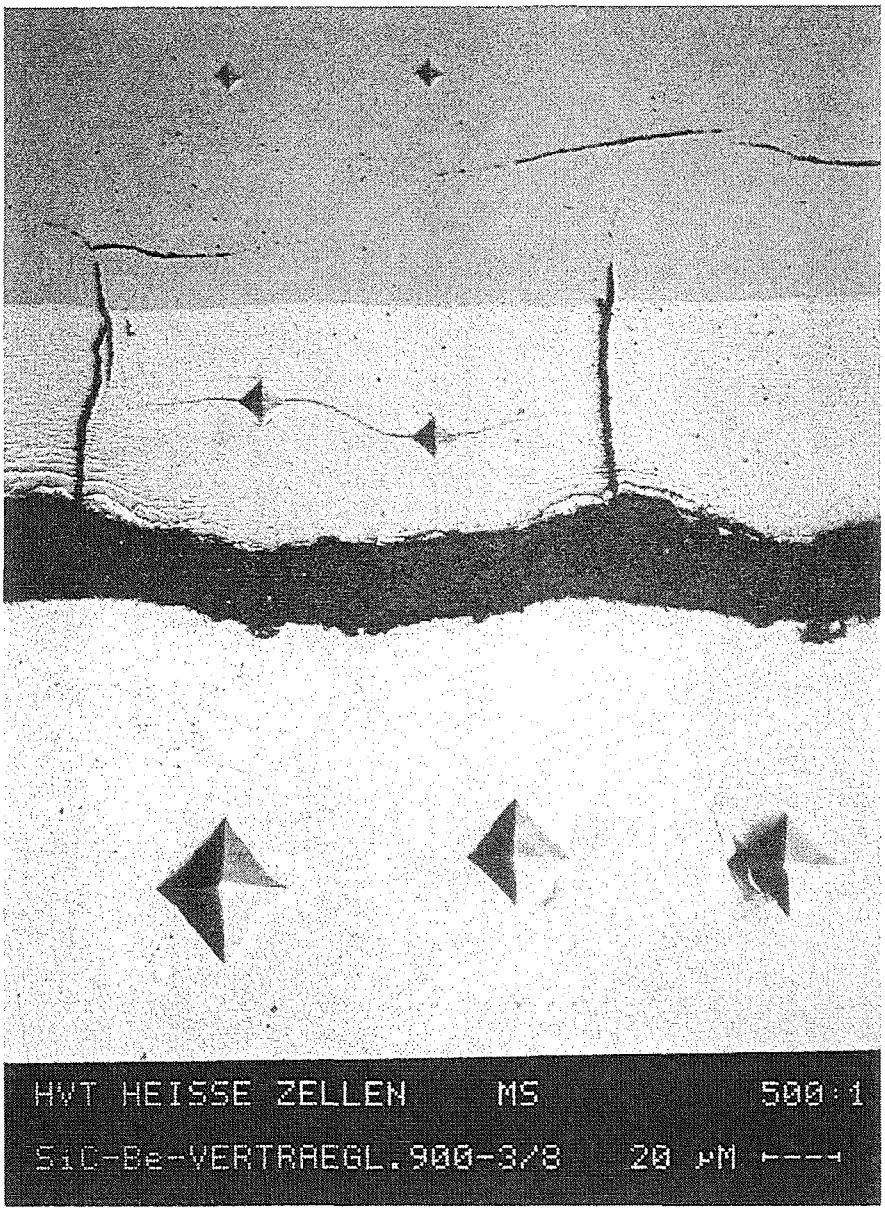

Microstructure of the two-phase Be_2C - Si layer after reaction between SiC and Be at 900°C / 34d

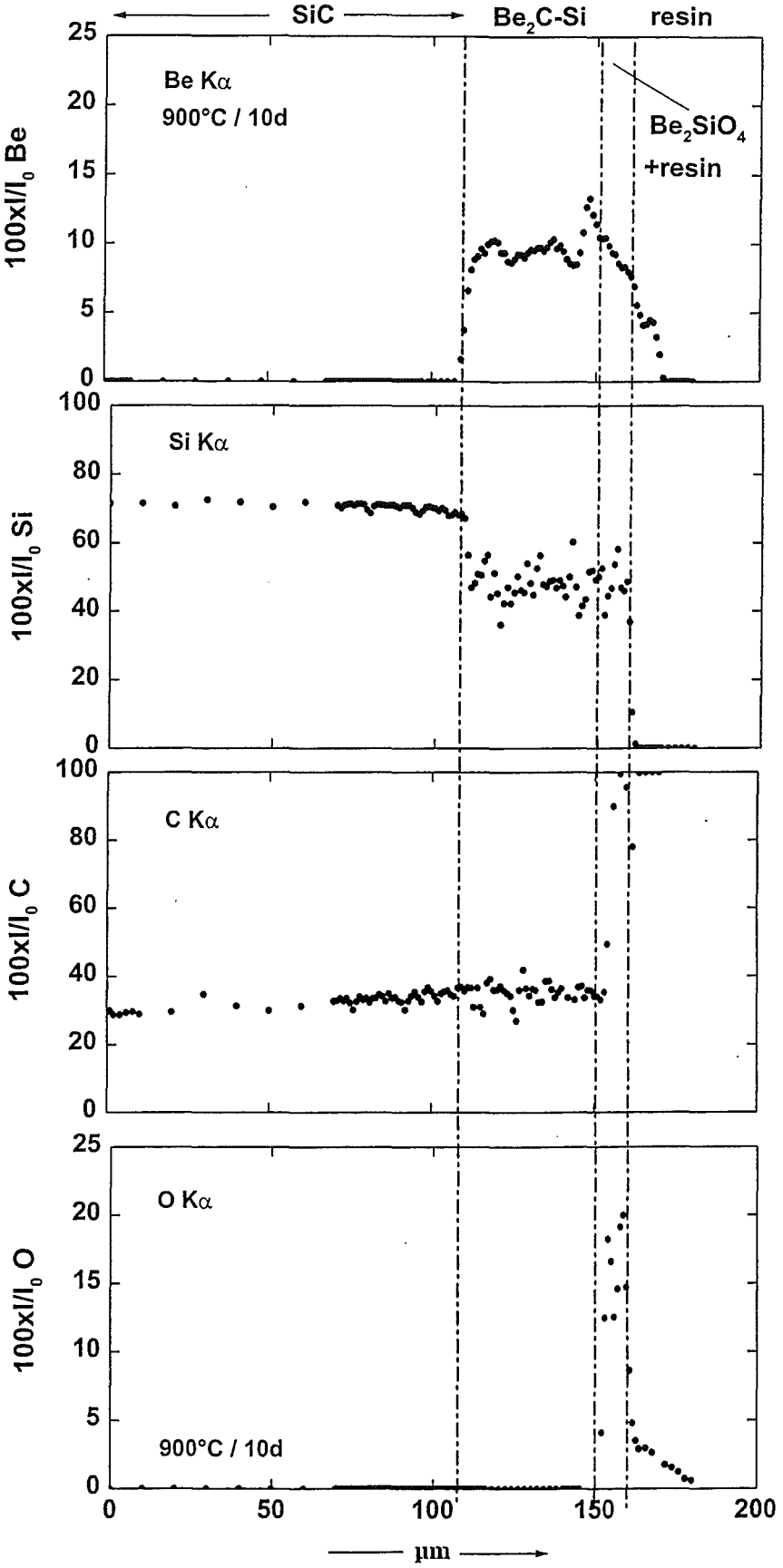

Reaction behaviour between SiC and Be

292-#1.opj 26.07.1999

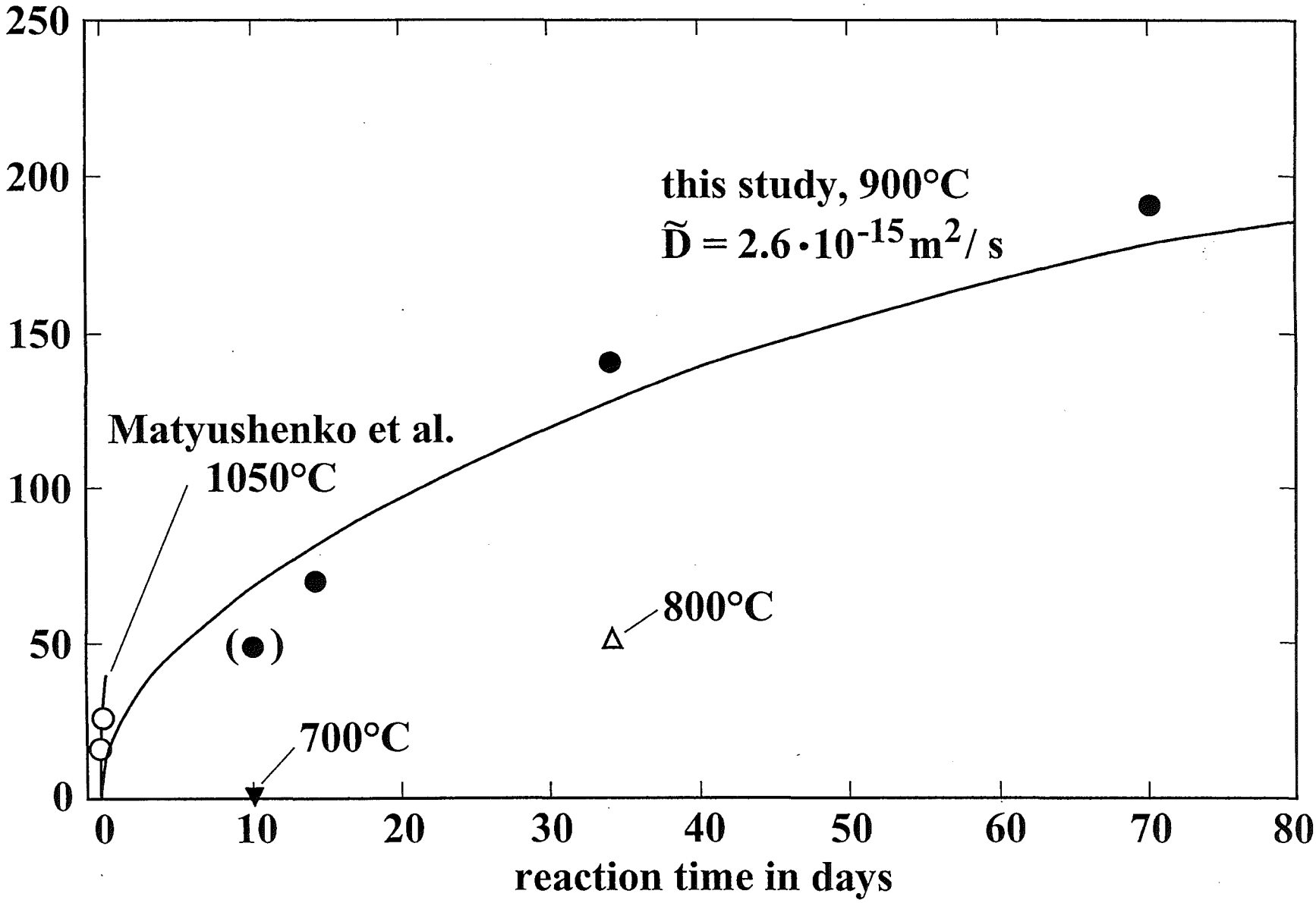

Be_2C - Si layer formation of the Be - SiC diffusion couple

Some aspects of the control and management of air pollution by beryllium aerosols

Bitkolov Noor

Research Institute of Industrial and Marine Medicine
Gagarina ave., 65/67, St.-Petersburg, 196143, Russia
Ph. (812) 127-20-00, fax: (812) 126-75-83
e-mail: bitkolov@vozduh.spb.ru

ABSTRACT

The concentration of beryllium aerosols in air of rooms and environment is determined by technological operations which are carried out on ITER and can be rather various. It determines differentiated the approaches to means and methods of the air pollution control.

It is expedient to classify concentration Be, arising in air. Criterion of classification can be concentration of an impurity and its exposition.

In tests of various duration are determined different on value of concentration Be in air of a working zone. At non-stationary processes of allocation the short-term tests have significant dispersion and allow to reveal both low and high meanings of concentration. This difference in conditions of astable allocation Be in air of a working zone can make the order and more.

The long test in many respects smooths possible bursts of concentration, that does not allow to estimate real danger of technological operation or process.

The high concentration Be can render decisive toxic astion on a human organism at high levels of pollution. The presence of submicronal particles Be, formed at work ITER presumably should strengthen effect of influence on organism. It is possible to explain it to that alongside with traditional toxic effect of aerosols Be, in addition can impose the mechanism action of a submicronal dust.

With the purpose of increase information of tests and opportunity of the forecast of the air pollution levels the mathematical model of logarithmic normal distribution can be used.

Submiting data of sampling in logarithmic probable grid, it is possible to carry out the analysis on two parameters: the median and the logarithmic standard.

The existing standards and rules of the contents Be with reference to conditions ITER are expedient for differentiating with the account toxicity, exposition, affection on a human organism.

The distinctions in allowable concentration Be in air on different sites in rooms allow to create more effective and economic methods of protection of air environment.

INTRODUCTION

Beryllium is widely used in various industries, however its high toxicity and volatility permitting it to penetrate easily into a human organism with the air requires to make precauti

ons against dangerous concentrations of in indoor and outdoor air.

It should be noticed that the diseases caused by affections are quite often. At the same time the low concentrations of Be in an organism complicate diagnostics thus imposing special requirements for safety norms and standards and defining the necessity to estimate extremely small concentrations of Be in the air or in the sample.

Be concentrations in the air are stipulated in the State Standard GOST 12.1.005-88 "Indoor Air. Requirements for measurement techniques of toxic substances concentrations". In compliance with this documents the only one norm for Be indoor the maximum concentration for 8-hour working shift is 1 $\mu g/m^3$ is adopted in the Commonwealth (Russia and other republics). Germany – 2 $\mu g/m^3$.

In the USA the following standards are adopted:
-average allowable concentration during 8-hour working shift – 2 $\mu g/m^3$;
-maximum concentration for 8- hour working shift - 5 $\mu g/m^3$;
-maximum (overlimit) concentration for the period not longer than 30 min of the 8- hour shift - 25 $\mu g/m^3$.

For the outdoor air the concentration shall be 0.01 $\mu g/m^3$ – 100 times less than the indoor concentration.

Similar American standards:
-for the non-continuous ingresses of Be the average outdoor concentrations shall not exceed 75 $\mu g/m^3$ for the period from 10 to 60 min per fortnight within any area where the toxic affection on a man is possible;
-for the continuous ingresses the maximum allowable concentration shall not exceed 10 g/day or 0.01 $\mu g/m^3$ of the monthly average concentration.

In the Commonwealth countries there are valid several standards for Be compounds: $BeSO_4$, BeF_2 – 2 $\mu g/m^3$, $BeCl_2$ - 1 $\mu g/m^3$ and for Be concentrates - 1-2 $\mu g/m^3$. Germany for compounds – 5 $\mu g/m^3$.

BACKGROUND AND PROCEDURE

The standards and regulations above need unification considering the complex effect of various factors such as toxicity, exposition, chemical properties, affection on human organism. In particular it would be reasonable to stipulate Be concentrations for the following cases:
indoor:
-average for 8 hours;
-maximum allowable for the working shift;
-maximum one-time concentration for the working shift provided that the limits for the working shift should not be exceeded;
-maximum allowable one-time concentration;
outdoor:
-average for one day (24 hours);
-maximum allowable for one day (24 hours);
-maximum one-day provided that the maximum allowable one-day concentration should not be exceeded;
-maximum one-time concentration.

At the same time we consider it reasonable to classify the outdoor concentrations of Be in accordance with their affections on a human organism:
-safe;
-safe for work;
-non dangerous;
-causing chronic diseases with long-term affection;
-dangerous for short-time affection;
-lethal.

The concentrations and their expositions can be served as criteria of the classification proposed. The list of supposed standards shown above determines the standards and regulations for the samples preparing. In accordance with the GOST standards of the Commonwealth only the shift average concentrations can be served as the samples. The similar American standards consider also 30-min-taken sample along with the shift average.

The difference between the sample preparetion periods determines that between the indoor concentrations of Be. The short-time samples usually results in the higher concentrations than those got from the long-term samples. This difference may be of about an order and even higher if Be ingresses are not continuous.

Samples of various duration τ and τ_0 related as follow:

$$\frac{S_\tau}{S_0} = \left[\frac{\tau}{\tau_0}\right]^{-\alpha} \quad \exp\ [-\beta\,(\tau - \tau_0)] \qquad (1)$$

where:

$$\alpha = \frac{1}{2}(1 - a_0) \qquad \beta = \frac{1}{2}a_1$$

a_0, a_1 – (it is determinate empirically in practice) Taylor's expand coefficients of follow expression

$$\frac{\int_0^\tau \lambda \cdot K_\tau(\lambda) \cdot d\lambda}{\tau^2 \cdot K_\tau(0)} \qquad (2)$$

where:
$K_\tau(\lambda)$ – autocorrelation function of the random variable C (τ)

In many cases the average sample "smooths" possible peak concentrations during a working shift thus preventing to estimate real danger of this or that production process. Perhaps, the analysis of the danger of the production process is necessary to be conducted as well as sanitary analysis of environment, especially

when processing the substances featured with accumulative effect.

Beside, a sample represents high-intelligent subject, as a lot of various information on the production process can be extracted from it after the appropriate processing, e.g. planning and ventilation of the premises, organization of works and so on. That is why appropriate information processing and interpretation of the results is of primary emphasis in the analysis of the concentrations and especially in making predications for safety.

In this respect the estimation of the results proceeding from the mean values can not regarded as an accurate method as it does not consider the whole range of the maximum (peak) values. The high concentrations can be of crucial importance in affection on a human organism when working on the toxic substances such as beryllium. In order to increase the set of information extracted from the samples analysis and to make the predications for the toxic substances concentrations in the air another model was proposed for the computations – the lognormal distribution.

If the samples analysis data are presented in the scale of the probability logarithm the mathematical analysis can be carried out with the two parameters of the distribution: the median and the logarithmic standard.

The mean values method of statistic processing supposes the use of the absolute values only, in this case the average values is determined mainly by the peaks and the rest data set is found out of less statistic significance. Meanwhile the median estimation does not consider the absolute values of the concentrations, but the fact of the peaks presence, i.e. each of the measurements is of its own probability. So all the samples contribute equally in determination of the parameter, in the other words the whole set of the data is effectively used.

The logarithmic standard determines the variance of the concentrations which grows with the decrease of the inclination angle and with "stress-increase" of the environment situation and vice versa.

Ideally, when $\alpha=90^0$ the pollutions ingress into the atmosphere is uniform and continuous. The experience indicates (fig. 1) that the straight line shifts to the left, to the zone of the lower concentrations, as the ergonomic and safety measures are being taken. As for the inclination angle, it does not change being resulted from the set of the various technological conditions. The significant deviations of the angle take place only in the cases of the complete modification of the production process, replacement or updating of the equipment.

This model permits to make predication for the extremely high values and their frequency. The number of the factors to be taken into consideration is determined by the some parameters:

-the logarithmic standard, e.g. the level of the danger of each particular process;

-relative measurements error;

-confidence coefficient of the probability of obtaining the results with the specified measurement error;

-the "density" of control, i.e. the relationship of the real time necessary for the samples preparation to the maximum allowable time for the period of experiments.

The similar results obtained during the previous revision are served as the initial data. In doing so the of which distribution scaling becomes the main factor determining the range of the control.

The range of the control is calculated as following:

$$n = \frac{N}{(N-1)\cdot\left[\frac{arcsh\cdot(\varepsilon/100)}{(t\alpha+1)/2\cdot k\ln\delta}\right]^2+1} \qquad (3)$$

where:

ε – the specified relative accuracy of determination of the centre of distribution, %;

δ – real scale factor of the distribution;

$(t\alpha+1)/2$ – Student's factor;

k – number of freedom degrees (in this case k = n-2);

α- specified confidence coefficient.

The maximum calculated number of samples:

$$N = T_{hrs}/T_s \qquad (4)$$

where:

T_{hrs} – working period (working hours);

T_s – sample period, hrs.

If N>>n>>1 (non-repeated samples) the formulas will be as following:

$$n = \left[\frac{(t\alpha+1)/2\cdot k\ln\delta}{arcsh(\varepsilon/100)}\right]^2 \qquad (5)$$

SUMMARY

It would be reasonable to accept the differentiated norms which would guarantee the safety when processing Be as well as the safety of environment of the neighbourhood zones.

The methods and organizations of the samples preparation shall be adapted to the norms and standards for allowable Be concentrations.

The number of samples be sufficient to provide all the necessary information.

About the probable part of the beryllium microdispersive fraction in the berylliosis growth

Saenko Swetlana

Research Institute of Industrial and Marine Medicine
Gagarina ave., 65/67, St.-Petersburg, 196143, Russia
Ph. (812) 127-20-00, fax: (812) 126-75-83

1. FOREWORD

According to the data obtained by Russian and Japanese scientists, in the process of air purification by means of the aerosol filters system in the tokamak thermonuclear reactor outlet submicron metal beryllium dust is detected, which is not retained by the impactor. Similar data were obtained with respect to the air of beryllium production working zone, involving high temperature beryllium conditioning processes, which result into formation of aerosol condensation [1]. Due to the joint work performed by the Moscow Physical Chemistry Institute and the Saint Petersburg Industrial and Maritime Medicine Research Institute, the fact was established that dealt with the presence of a "penetrating" fraction of beryllium aerosols not retained by aerosol filters in the zones of manufacturing method high temperature stages. Thus it was determined by the Moscow Physical Chemistry Institute that at the section of magnesium thermal beryllium reduction during various operations aerosol evolves, having the range of particle dimensions about 0.01 μm and lower. Dispersion composition was determined by means of the electron microscope.

2. MAIN PART

The beryllium microdispersive fraction can enter the bodies of working people together with inhaled air, however biological effectiveness of this process has not been studied so far and the part of this stage in the berylliosis growth is not taken into account.

In the process of man's professional activity his respiratory organs are the main duct of beryllium entry into the body. It is generally admitted that macrodispersive aerosols are retained in the upper respiratory tract, in the trachea and in the main bronchi, from which, due to the activity of the ciliated epithelium, they enter the digestive tract through deglutition. Depth of aerosol particles penetration into the lungs increases as they reduce in size [2]. Thus particles of 0.01 to 1 μm in size deposit in the inferior lobes of the lungs. The smallest particles (less than 0.01 μm) penetrate into the alveoli. According to calculations performed by individual authors, aerosols retain in the alveoli, having median aerodynamic diameters of the following percentage: 10 μm and larger – 5%, 1 μm – 25%, 0.2 μm – 50%, 0.1 μm – 60%. Consequently, the higher aerosol dispersity is, the more aerosol deposits in the alveoli.

Submicron particles of insoluble beryllium compounds are assumed to cause more expressed lung affection, since they have significantly larger total surface area than larger particles. Apart from that, there is an increase in the number of particles themselves, which penetrate into virtually all lobes of the lungs, causing generalized affection. This fact is consistent with the indication of individual authors made with respect to an increase in toxicity of insoluble beryllium compounds with their dispersity growth [3]. At the same time, due to the Brownian motion, the submicron particles may penetrate from the alveoli into the circulatory system and later into the liver and other organs, evoking more expressed general and specific responses of the body. It is probable that the same submicron particles that have penetrated through the bloodstream into the liver, the spleen, the glands constitute the centres round which granulomas develop, being characteristic of chronic berylliosis.

The unaccounted effect of the microdispersive fraction may explain pronounced pathogenic influence of beryllium and its compounds in the lungs, where they accumulate in the amount significantly exceeding the content of this metal in the body as a biological element, even in the case of its inhaling at the concentration rate exceeding ambient air standard only 2 times. Sensitization of the body may be ascribed to the effect of the same microdispersive fraction, as well as some functional

disturbances in people exposed to the long-term beryllium effect at the level of ambient air standard.

There is an opinion that by their biological effectiveness the submicron particles will be close to the aerosols that are present in the inhaled air in their ionization state [3].

3. RESUME

Accordingly, the aforementioned goes to prove that we cannot pretend that the microdispersive fraction problem, its part in the berylliosis growth does not exist. It is essential that we should start exploring experimentally the role of submicron fractions of insoluble beryllium compounds in the development of beryllium affections.

REFERENCES

1. A.I. Burnazyan (ed.), Clinical study of acute and chronic beryllium affections, Moscow, Meditsina, 1983, 176 p.
2. K.P. Molokanov (ed.), Berylliosis, Moscow, Meditsina, 1972, 247 p.
3. A.I. Burnazyan, S.A. Keizer (eds.), Beryllium. Toxicology, hygiene, prophylaxis, diagnostics and treatment of beryllium affections, Moscow, Energoatomizdat, 1985, 160 p.

Beryllium and Tungsten Brush Armor for High Heat Flux Applications

J.S. O'Dell and Timothy N. McKechnie

Plasma Processes, Inc.
4914 D Moores Mill Road, Huntsville, Alabama 35811, USA

The joining of low thermal expansion armor materials such as beryllium and tungsten to high thermal expansion heat sink materials has been a major problem in plasma facing component (PFC) development. Conventional planar bonding techniques have been unable to withstand the high thermal induced stresses resulting from fabrication and high heat flux testing. Thermo-mechanical modeling has shown the ability to reduce the stress at the armor/heat sink interface using a brush like structure for plasma facing component armor. Small-scale divertor mockups have been fabricated with beryllium and tungsten brush armor. The brush armor materials fabricated to date have been with preformed tungsten and beryllium rods, which are backed with specific matrix materials. These matrix materials are then used to bond the armor to copper alloy and aluminum alloy heat sinks. The results of high heat flux testing experiments by Sandia National Laboratories (SNL) in its Electron Beam Testing System (EBTS) of this revolutionary armor concept have been outstanding. PFC mockups using the tungsten brush armor have survived cyclic loading (10s beam on, 10s beam off) for 500 cycles apiece at 5, 10, 15, 22 and 30 MW/m^2 with no damage to the heat sink and little or no damage to the armor. A discussion of the methods used during the fabrication of beryllium and tungsten brush structures is presented. Items of particular interest include measurement of the bond strength between the brush and its matrix material, and techniques for joining the brush structures to heat sink materials. The latest high heat flux test results and an analysis of these results is also included.

1. INTRODUCTION

Magnetic fusion energy devices require plasma facing components (PFCs) that must survive long pulse (tens of seconds to steady state) high heat fluxes for first wall components (0.1 to 2 MW/m^2) and for limiter and divertor components (5 to 50 MW/m^2). In addition, these materials must survive short pulse (about one thousandth of a second) heat fluxes due to plasma disruptions (10 to 500 MW/m^2).[1]

PFCs are comprised of an armor material, which is in contact with a high energy plasma, and a heat sink, which is actively cooled by high velocity fluids passing through internal cooling channels. Two of the leading candidate materials for PFC armor are beryllium and tungsten.[2,3] Each of these materials have intrinsic properties which are desired for PFC armor, i.e., beryllium armor used in relatively low heat flux areas such as the first wall to reduce plasma poisoning potential and tungsten armor used in relatively high heat flux areas for melt layer, erosion and disruption resistance. Presently, copper alloys are considered the primary candidate for the actively cooled heat sink because of their relatively high thermal conductivities.[4] However, thermal expansion mismatch between the low expansion armor materials and the high expansion heat sink materials is a major concern.

Thermo-mechanical modeling by Sandia National Laboratory has shown the desirability of using a "brush" structure (cluster of small rods or filaments) for armoring PFCs as a method of reducing stress.[5] Figure 1 is a schematic representation of the ABAQUS model showing a 5mm thick tile with a uniform 1 MW/m^2 heat flux and the positions of interest. Figures 2 and 3 are plots showing the results of the study on beryllium and tungsten tiles, respectively. These figures show by reducing the tile width (effectively the cross-sectional area) of an individual tile that the stress the tile encounters under a 1 MW/m^2 heat load is significantly reduced. Utilizing this information, small scale mockups with beryllium and tungsten brush armor have been fabricated. Several joining techniques have been developed for attaching the brush armor to PFC heat sinks. High heat flux testing of brush armored mockups have produced excellent results.

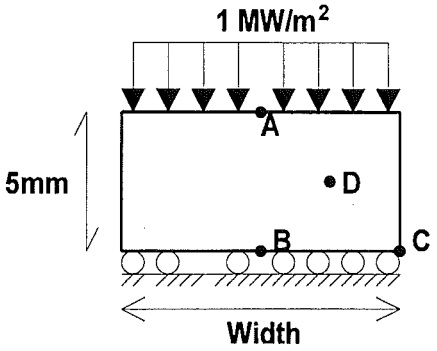

Figure 1 - Schematic representation of model.[5]

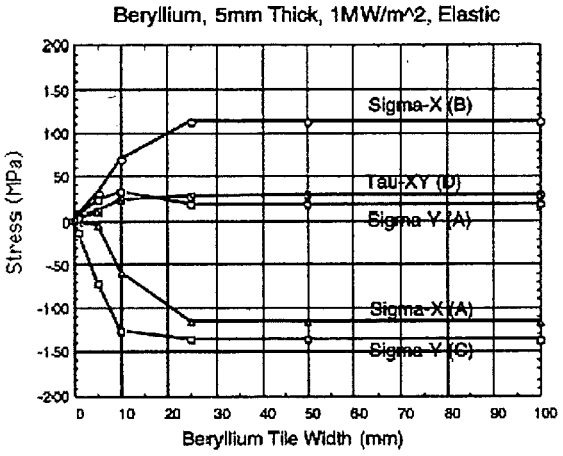

Figure 2 - Plot showing the results of the model for a beryllium tile.[5]

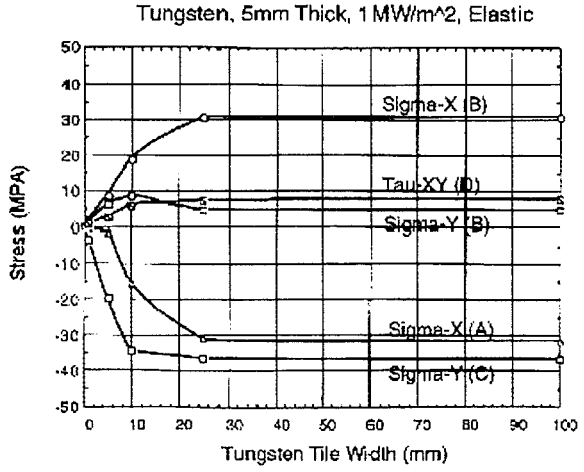

Figure 3 - Plot showing the results of the model for a tungsten tile.[5]

2. FABRICATION OF BRUSH ARMOR

Many of the fabrication techniques are common to both beryllium and tungsten brush. The basic fabrication process can be described in three steps: 1) individual rods are made and stacked in a close-packed configuration, 2) Vacuum Plasma Spray (VPS) is used to deposit a matrix material on one end of the rods forming the armor, and 3) the matrix material is then bonded to a heat sink using conventional bonding techniques such as brazing, diffusion bonding or welding. A schematic representation of these steps is shown in Figure 4.

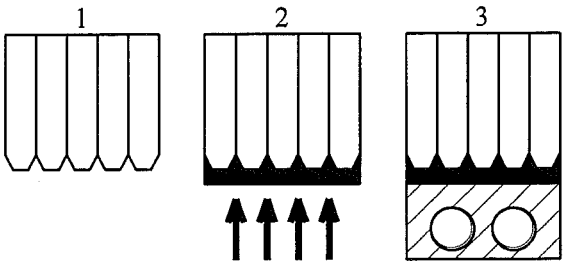

Figure 4 - Schematic representation of brush fabrication process.

Pointed and conical tip configurations have been used to eliminate stress concentration at a planar bond line. To prevent excessive penetration of the VPS matrix down the rods, damming techniques have been developed. Protrusion of the tips above the dam can be varied to allow variation of the amount of embedding of the rods into the backing material. Prior to deposition of the matrix, the tips of the rods are grit blasted to expose a fresh, clean surface. The fixture rod assembly is loaded into a large vacuum chamber, evacuated and backfilled with argon. The brush is preheated with the plasma gun (no powder on) to a predetermined temperature. This temperature is monitored using an optical pyrometer. Negative transferred arc cleaning is used to clean the surface of the tips prior to coating.

Utilizing high efficiency, bell contoured plasma spray nozzles (U.S. Patent 5,573,682), a diffusion barrier or a bond coat can be deposited followed by deposition of the brush backing material to the desired thickness. VPS deposition of the matrix results in low oxygen content, high density deposits that enhance thermal conductivity. In addition, fine grained microstructures are produced which are highly resistant to low cycle fatigue.

2.1. Beryllium Brush Armor

Beryllium brush structures have been produced with both copper and aluminum matrices. The copper backed beryllium brush required a diffusion barrier between the beryllium and the copper matrix to prevent the formation of brittle Be-Cu intermetallics during fabrication and subsequent high heat flux testing. Figure 5 shows a beryllium brush structure with VPS copper matrix. This sample is comprised of 1.5mm diameter, S-65 grade beryllium rods and 1.7mm diameter, S-200F grade beryllium rods with a proprietary diffusion barrier between the rods and the copper matrix. Figure 6 is a photomicrograph showing the high density of the VPS copper deposit and fine grain size (16-22μm).

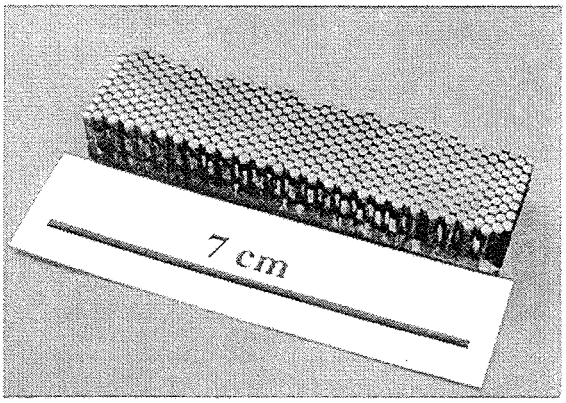

Figure 5 - Beryllium brush with VPS copper matrix.

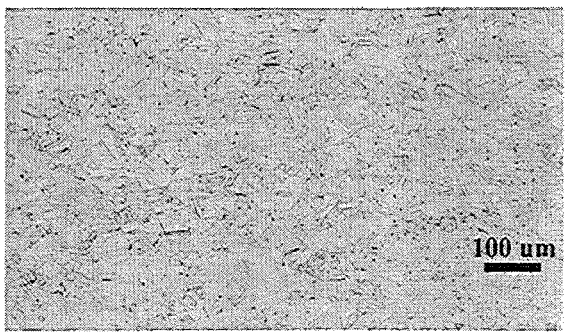

Figure 6 - Microstructure of as-sprayed copper matrix. Note average grain size is 16-22 microns.

As an alternative to copper backed beryllium brush armor, beryllium brush armor with an aluminum matrix has been developed. Because aluminum and beryllium do not form any brittle intermetallic compounds, the need for diffusion barriers is eliminated. Figure 7 shows a beryllium brush structure with aluminum matrix. The use of square cross sectional rods (2mm x 2mm) allowed a packing density of near 100%. Rolled, S-200F graded beryllium sheet was used to make the rods. Figure 8 shows the excellent bond between the VPS aluminum and the beryllium rod.

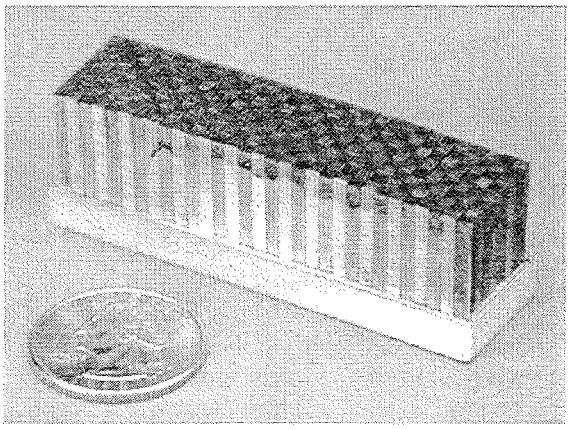

Figure 7 - Beryllium brush with square cross sectional rods and aluminum matrix.

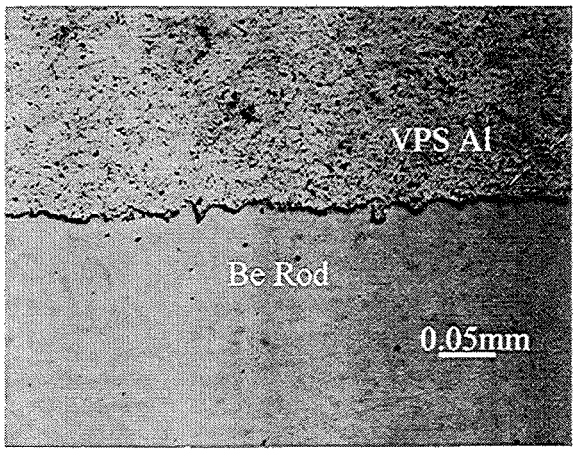

Figure 8 - Photomicrograph showing the excellent bond between the VPS Al and Be rod.

2.2. Tungsten Brush Armor

Similar to the fabrication of the beryllium brush, tungsten brush structures have been produced. Figure 9 shows a tungsten brush comprised of 3.2mm diameter, 1.5% lanthanated tungsten rods and VPS copper matrix. Both pure and lanthanated tungsten have been used in the fabrication of brush armor with 1.5mm and 3.2mm diameter rods. Tungsten brush armor as thick as 25mm has been manufactured.

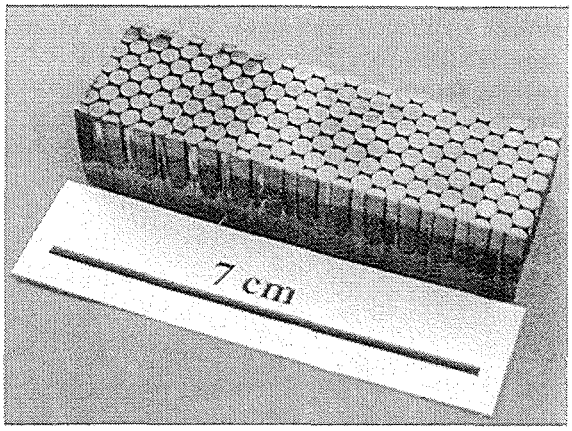

Figure 9 - Tungsten brush armor (3.2mm dia. rods) with VPS copper matrix.

Microscopic examination of the tungsten tips and VPS copper matrix revealed complete coverage by the sprayed material and high density. Figure 10 shows the tips embedded in the copper matrix as well as the interface between the matrix and a CuCrZr heat sink after a low temperature HIP diffusion bonding process.

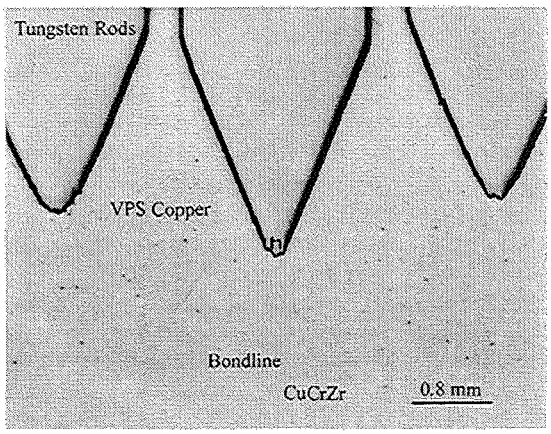

Figure 10 - Photomicrograph showing complete coverage of the tungsten tips by the copper matrix. Note the lack of a distinct bond lone between the copper matrix and a CuCrZr heat sink after bonding.

2.3. Bond Strength Measurements

To evaluate the bond strength between the brush rod tips and the matrix materials, tensile tests have been performed. This test has also been used to evaluate the effectiveness of various bonding agents and diffusion barrier materials. Figure 11 is a schematic representation of the test configuration. A single rod protruded out the end opposite the deposited material and a Universal Test Stand (UTS) machine is used to pull the rod from the deposit. The load at failure is then used to determine the bond strength. The results of beryllium-copper and beryllium-aluminum pull-out tests are shown in Tables I and II.

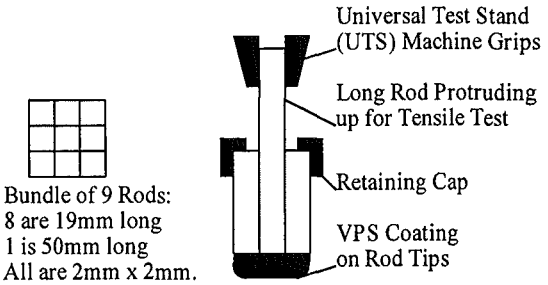

Figure 11 - Schematic representation of tensile pull test. Both round and square rods have been tested using this technique.

Table I
Results of Be-Cu tensile pull tests

Interface Material	Test Temp. (°C)	Stress at Slippage (MPa)	Failure Location
None	25	268	Grip Slippage
V98-13A*	25	310	Grip Slippage
V98-12*	25	322	Grip Slippage

* - proprietary diffusion barrier coating

Table II
Results of Be-Al tensile pull tests

ID No./ Interface Material	Test Temp. (°C)	Failure Stress (MPa)	Failure Location
17A/None	25	176	Al matrix
17B/None	25	185	Al matrix
17C/None	25	260	Al matrix
17D/None	25	177	Al matrix
17E/None	25	112	Al matrix

Figure 12 is a scanning electron microscopy image showing one of the beryllium pull rods after removal for the aluminum matrix. Failures of the beryllium pull test samples have all occurred in the ductile matrix material. This indicates that the bond strength at the interface is equal to or greater than the ultimate tensile strength of the aluminum matrix.

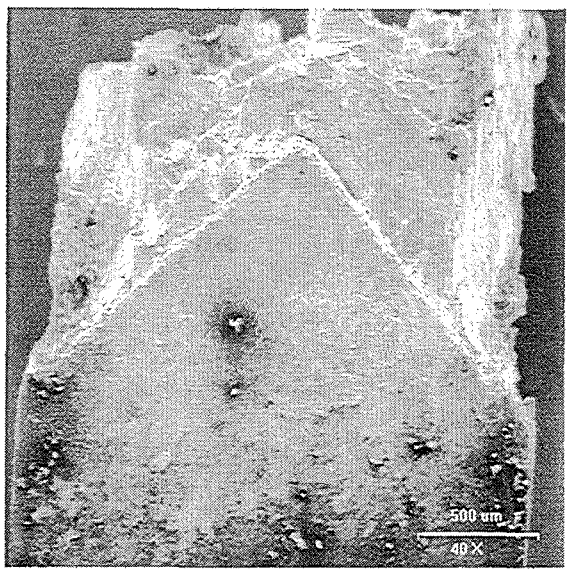

Figure 12 - SEM secondary electron image of beryllium pull rod showing failure in aluminum matrix.

Tungsten-copper pull test results are shown in Table III. Several bonding agents have been evaluated to increase the bond strength between the tungsten tips and the copper matrix. To date, the best bond strengths have occurred when using a rhenium bond coat.

Table III
Results of W-Cu tensile pull tests

Interface Material	Test Temp. (°C)	Max. Failure Stress (MPa)	Avg. Failure Stress (MPa)
None	280	207	179
Fine Ni	280	148	114
Coarse Ni	280	119	95
PPI-1*	280	164	134
PPI-2*	280	77	46
Rhenium	280	286	264
V98-11*	280	190	175
V98-28B*	280	41	28
V98-29A*	280	154	132
V98-29B*	280	129	92

* - proprietary bond coating

3. JOINING OF BRUSH ARMOR TO HEAT SINK MATERIALS

Since the mismatch in thermal expansion is overcome at the rod/matrix interface, conventional joining techniques can be used to bond the brush matrix to heat sink materials of similar composition. Currently, three joining techniques have been developed for joining brush armor to heat sinks.

3.1. Diffusion Bonding of Beryllium and Tungsten Brush to Copper Alloy Heat Sinks

This technique, which was developed by the US Home Team for joining copper to copper alloy heat sinks, uses a low temperature diffusion bonding (450-550°C) to prevent over-aging of the precipitation hardened CuCrZr alloy. Parts to be joined are placed in a can and hot isostatically pressed (HIPed) at 207 MPa for 3 to 6 hours at the appropriate temperature. Both beryllium and tungsten brush structures have been joined to copper alloy heat sinks using this technique. Figure 10 showed the good bond achieved between the VPS copper matrix and CuCrZr when using this process.

3.2. Vacuum Brazing of Beryllium Brush to Aluminum Alloy Heat Sinks

Prior to brazing all samples are vacuum baked-out at 300°C for one hour. The surfaces to be brazed are then chemically cleaned and etched in an acid solution. A braze foil (aluminum-silicon composition) is placed between the surfaces to be joined. Fixturing is used during brazing to maintain a uniform pressure of 21 to 55 kPa. The braze temperature is ~595°C and the hold time at temperature is <5 minutes.

Figure 13 is a photograph showing a beryllium brush after brazing to an aluminum alloy heat sink. Note the tight packing of the rods even after brazing. Figure 14 is a polarized image showing the grain structure at the bond line. This figure shows grain growth occurred for the aluminum matrix near the braze joint. This grain growth in the matrix material near the bond line is consistent with the increased diffusion that would be present due to the wetting of the grains by the filler metal.

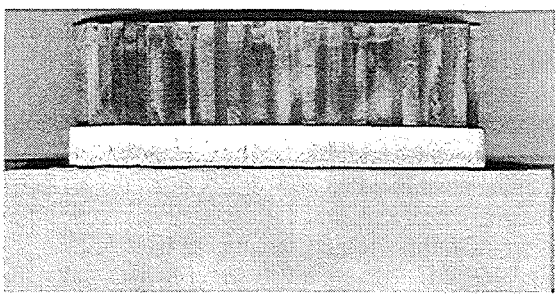

Figure 13 - Beryllium brush after brazing to aluminum alloy heat sink.

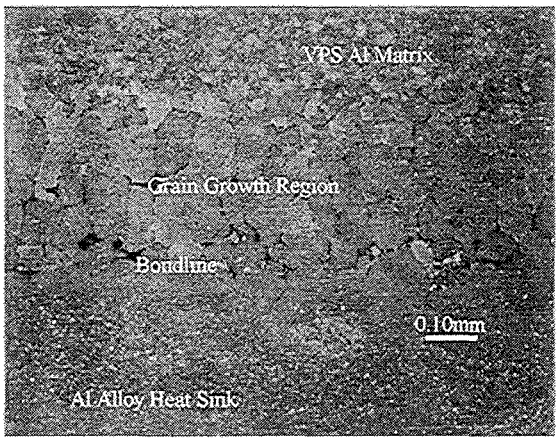

Figure 14 - Polarized image showing grain growth in the aluminum matrix adjacent to the braze joint.

3.3. Deep Penetration Electron Beam Welding of Beryllium and Tungsten Brush to Copper Alloy Heat Sinks

Electron beam welding has been evaluated for joining brush armor with copper matrix to CuCrZr heat sinks. The objective was to produce 100% penetration butt welds from one side with no porosity in the joint region. Figures 15 and 16 are photomicrographs of the weld region near the middle of the joint. These figures show a good, dense weld was achieved. Welds 19mm deep have been produced. Measurements of the heat affected zone (HAZ) in the CuCrZr show that it is less than 0.5 mm. The thickness of the weld was ~1.4 mm with essentially equal parts of the VPS Cu material and CuCrZr materials consumed to make the weld. Present brush design leaves, ~3 mm of the VPS Cu unaffected by the electron beam for incorporation of the brush tips.

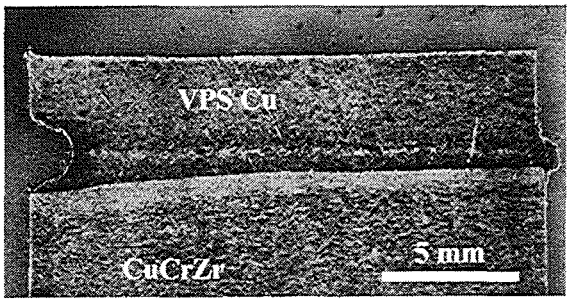

Figure 15 - Micrograph showing the electron beam weld used to join VPS Cu to CuCrZr. Penetration depth is 19mm. Beam direction is from left to right.

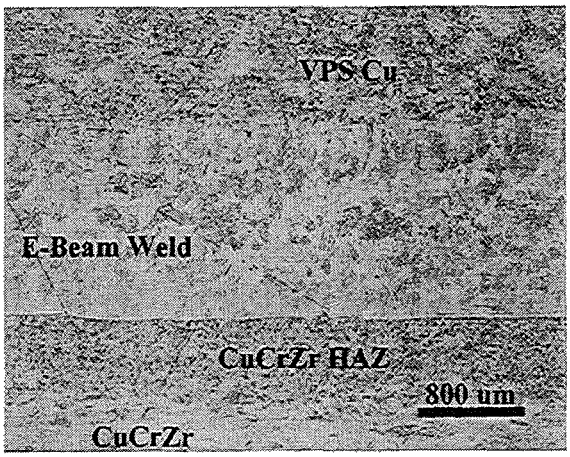

Figure 16 - Micrograph of the e-beam weld near the middle of the joint. The weld is free of voids, and the HAZ in the CuCrZr material is small. Thickness of the e-beam weld zone is ~1mm.

4. HIGH HEAT FLUX TEST RESULTS

Figure 17 shows two small-scale mockups armored with 12mm thick tungsten brush on CuCrZr heat sinks. The results of high heat flux testing experiments by Sandia National Laboratories (SNL) in its Electron Beam Testing System (EBTS) of this revolutionary armor concept have been outstanding. Plasma facing component mockups using the tungsten brush structure have survived cyclic loading (10s beam on, 10s beam off) for 500 cycles apiece at 5, 10, 15, 22 and 30 MW/m^2 with no damage to any joints (rod tips/metal matrix and metal matrix/substrate) or the heat sink. During the last 500 cycles of testing, surface temperatures between 2500°C-2700°C have been observed for tungsten brush structures at the 30 MW/m^2 heat flux which resulted in some erosion of the tips of the tungsten rods due to evaporation (see Figure 18).

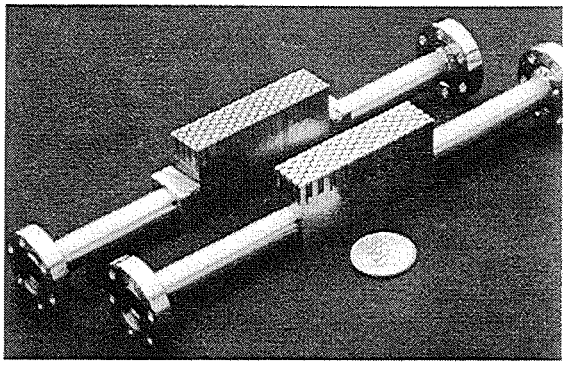

Figure 17 - Tungsten brush armor (3.2mm dia. x 12mm thick) bonded to CuCrZr heat sinks. Background mockup was fabricated using deep penetration electron beam welding process and foreground mockup was fabricated using low temperature HIP diffusion process.

Figure 18 - Photograph of tungsten brush armored mockup (PW-10) after 500 cycles of high heat flux testing at 30 MW/m^2. Rods were 3.2mm for this sample. Note the erosion of the rod tips due to thermal evaporation.

Another tungsten brush structure even survived an accidental melting of a small portion of the tungsten surface (~10 mm diameter circular melt region) when the electron beam rastering system malfunctioned and stalled (see Figure 19). This melting of the W surface actually simulated the off normal disruptions expected in a fusion energy reactor. Although there was some bridging of W from one rod to the next after resolidification, when cyclic loading was resumed no damage to either the brush-backing material joint or the backing material-heat sink joint was observed.

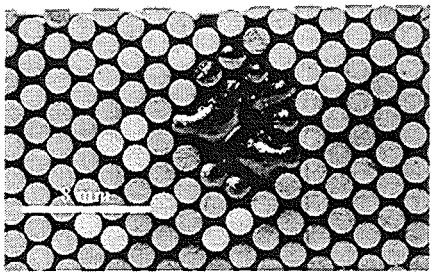

Figure 19 - Photograph (top view) of tungsten brush armor (1.5mm dia.) showing melted region that occurred when the electron beam rastering system stalled during high heat flux testing simulating a plasma disruption. Note the tungsten melted, but did not debond.

5. SUMMARY

The results of this investigation have shown the feasibility of fabricating revolutionary beryllium and tungsten brush structures for long pulse high heat flux PFC armor. Diffusion barrier and bond coat coatings have been investigated to enhance the bond between the brush and the matrix material. Pull-out tests have been performed to determine the effect of various coats on the bond strength. VPS parameters and techniques have been developed to insure a dense matrix material is deposited on the tips of the brush structure In addition, the ability to join matrix materials by deep penetration electron beam welding brazing has been demonstrated. Thermal fatigue testing has shown tungsten brush (12mm thick) can survive heat fluxes as high as 30 MW/m^2.

REFERENCES

1. R.D. Watson, et al., Fusion Engineering and Design, 37 (1997) 553-579.
2. R.D. Watson, et al., Technology of Fusion Energy, Vol. 34, No. 3 (1998) 443-453.
3. M. Roedig, et al., Technology of Fusion Energy, Vol. 34, No. 3 (1998) 464-468.
4. A.F. Rowcliffe, et al., Irradiation Testing of Copper Alloys and Copper/Stainless Steel Joints, Final Report (1998).
5. Unpublished work by personnel at Sandia National Laboratories (1996).

Comparative strength analysis and thermal fatigue testing of Be/CuCrZr and Be/GlidCop joints produced by fast brazing

A. Gervash[a], I.Mazul[a], N. Yablokov[a], V. Barabash[b], A. Ganenko[c]

[a]Efremov Institute, 189631 St. Petersburg, Russia

[b]ITER Joint Central Team, 85748 Garching, Germany

[c]CRISM "Prometey", 193167 St. Petersburg, Russia

Proposing beryllium as plasma facing armour this paper presents the recent results obtained in Russia in the frame of such activities. Last year testing of actively cooled mock-ups produced by fast brazing of Be onto Cu-alloy heat sink allows to consider mentioned Russian method as promising for Both PH-copper like CuCrZr and DS-copper like GlidCop. Summarizing recent experimental results with their previous data authors attempt to comparatively investigate a behaviour of Be/CuCrZr and Be/GlidCop joints in ITER relevant conditions. Mechanical properties, brazing zone microstructure and thermal response were taken for comparison. The shear strength for both types of joints was found as 150-200 MPa and did not depend on testing temperature. The brazing zone morphology and microhardness are presented, the thermal fatigue behaviour of investigated joints is described. All main results as well as the nearest future plans are discussed.

1. INTRODUCTION

Beryllium is one of the plasma facing materials (PFM) for using in the tokamaks like ITER. As plasma facing material beryllium must protect the actively cooled copper alloy heat sink of the first wall and some other components from sputtering erosion, transients events like disruption and successfully withstand the number of cycles under the expected heat and neutron fluxes [1]. One of the main requirements to use Be as a candidate for plasma facing component in ITER is providing a reliable joint between Be and Cu-alloy heat sink structure. The unique fast brazing technology, which combines the fast heating and new modification of amorphous brazing alloy, was developed in Russia [2]. The results of the high heat flux tests (HHF) obtained in Russia during the last couple of years [3] allow to consider the fast brazing technique as promising for joining Be to both PH-Cu like CuCrZr and DS-Cu like GlidCop heat sink candidates. Summarizing previous data with a recent experimental results this paper attempts to more deep understand the fast brazing phenomena and to comparatively investigate the Be/CuCrZr and Be/GlidCop joints after the different heat treatment history and in different testing conditions.

2. EXPERIMENT

The number of identical Be/CuCrZr and Be/GlidCop joints were produced by the fast brazing and by traditional brazing in resistive furnace as a reference. The amorphous Cu-Sn-In-Ni brazing composition was used for the brazing.

2.1 Heat treatment history

The Be/CuCrZr and Be/GlidCop joints were comparatively studied in the four heat treatment conditions:

- in initial state (just after the fast brazing procedure)
- after "annealing" 100 hrs at 300°C. Even in the longest performed thermal cycling experiments the summarized heating time of Be/Cu-alloy brazing zone is about 10 hours. In real ITER operation the summarized heating time is expected as 2.5 10^3

hours. Aiming to check a tendency the long heating time was simulated by annealing the joints during 100 hrs at 300°C.

- after the brazing in resistive furnace. To reveal advantages/disadvantages of the fast brazing method the number of Be/Cu-alloy joints were produced by traditional brazing in resistive furnace.

2.2 Analysis of the brazing zone structure

The comparative metallography of Be/CuCrZr and Be/GlidCop joints with different heat treatment history was carried out. The width of brazing zone, distribution of the brazing elements, presence of intermetallic layers and cross-section hardness were compared. To study the distribution of the elements in the brazing zone SEM analysis with back scattered electrons energy detector was used. To measure a hardness of the Be/Cu-alloy cross-section the microindentor with a 2μm moving step was used.

2.3 Mechanical properties

To comparatively estimate the brazing quality shear strength measurements of investigated joints were carried out at RT. and 300°C.

2.4. Thermal cyclic tests

To study the ability to withstand cyclic heat loads comparative thermal cycling of the joints was performed in TSEFEY e-beam test facility [4]. With that aim the number of identical actively cooled Be/CuCrZr and Be/GlidCop joints were prepared. The tests were performed in two modes – screening (to define a heat flux limit of the joints) and thermal cycling at 8 MW/m^2 (to define a number of cycles before detachment).

3. RESULTS AND DISCUSSIONS

3.1. Brazing zone structure

The general views of the cross-sections of investigated joints with different heat treatment history are given in the figures 1-8. One can say that the brazing zones of both Be/CuCrZr and Be/DS-Cu joints produced by the fast brazing look very similar. For both types of joints it can be also seen that there are no significant differences in the width and morphology of brazing zones after thermal cycling or annealing 100 hours at 300°C in

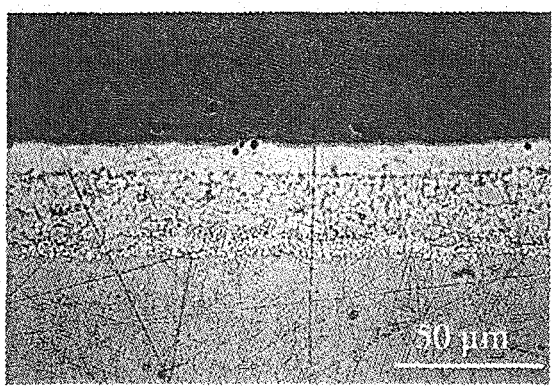

Fig. 1. Be/CuCrZr (fast brazing)

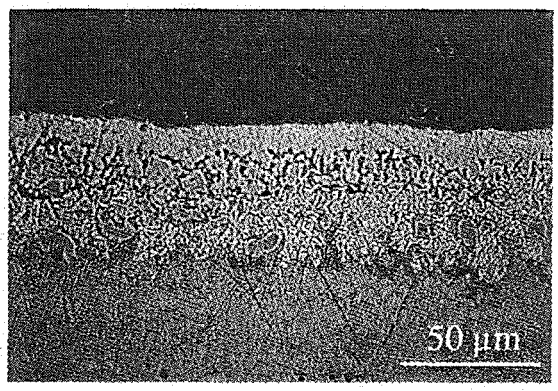

Fig. 2. Be/CuCrZr (annealed 100 hours at 300°C)

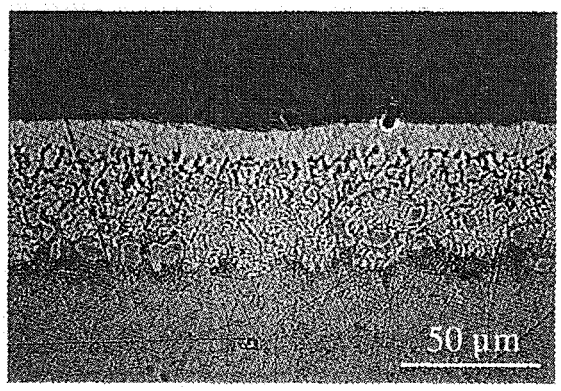

Fig. 3. Be/CuCrZr (after 1000 cycles at 5 MW/m^2)

comparison with the initial state. The brazing zone width is about 30-40 μm. But in case of brazing in traditional resistive furnace the width of the brazing zone was found at least twice wider (80-90μm).

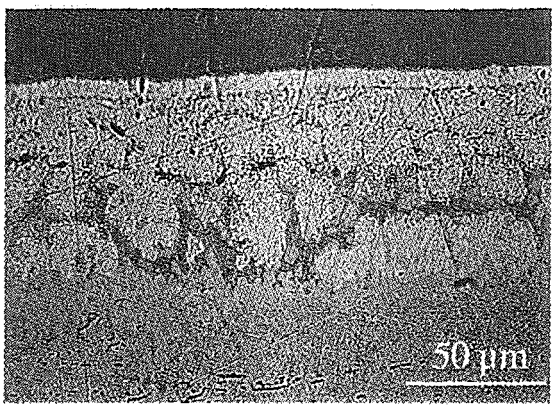

Fig. 4. Be/CuCrZr (brazed in resistive furnace)

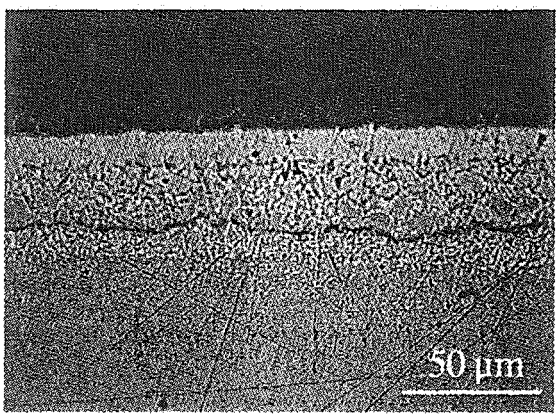

Fig. 5. Be/DS-Cu (fast brazing)

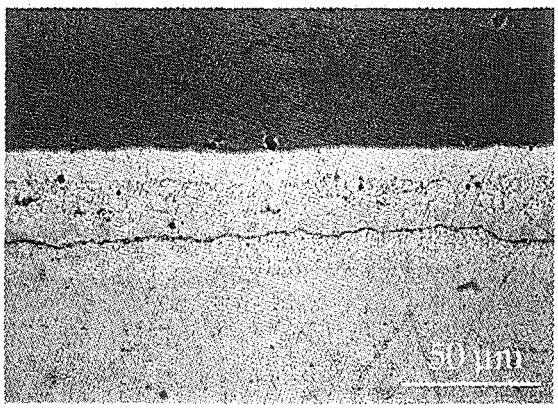

Fig. 6. Be/DS-Cu (annealed 100 hours at the temperature 300°C)

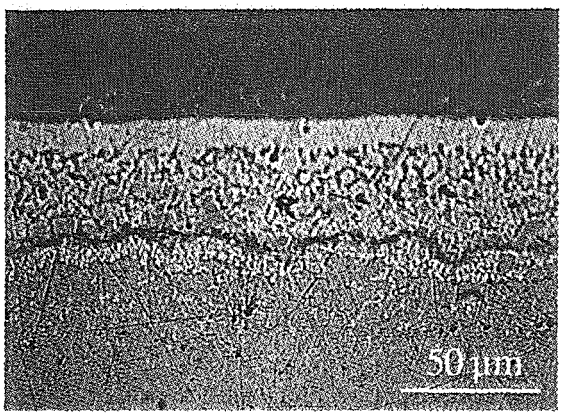

Fig. 7. Be/DS-Cu (after 1000 cycles at 8 MW/m^2)

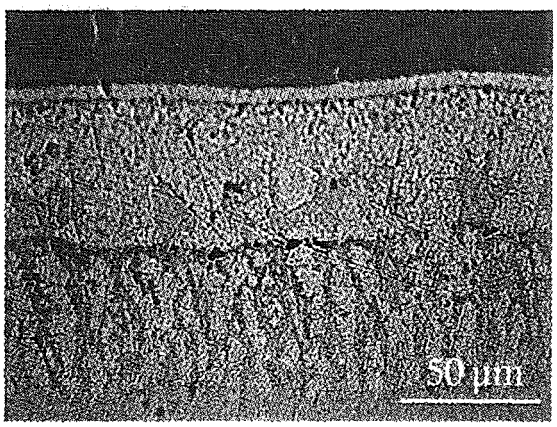

Fig. 8. Be/DS-Cu (brazed in resistive furnace)

3.2. Distribution of elements

To prepare Be/CuCrZr and Be/GlidCop joints Cu-Sn-In-Ni brazing alloy was used. The SEM image of Be/Cu-alloy joint produced by the fast brazing is presented in figure 9.

One can see that Ni forms about 10 µm layer close to Be boundary and more than less uniformly distributed through the rest of the brazing zone. It can be also seen the Cu-Sn-In eutectics and the Sn-In enriched areas close to the bulk Cu-alloy. It should be especially noted the presence of thin (1-1.5 µm) Be_2Cu layer just on the Be boundary. This brittle intermetallic can significantly influence on mechanical and thermal cyclic properties of joints. The elements distribution in Be/Cu-alloy joints that brazed in traditional resistive furnace is presented in figure 10.

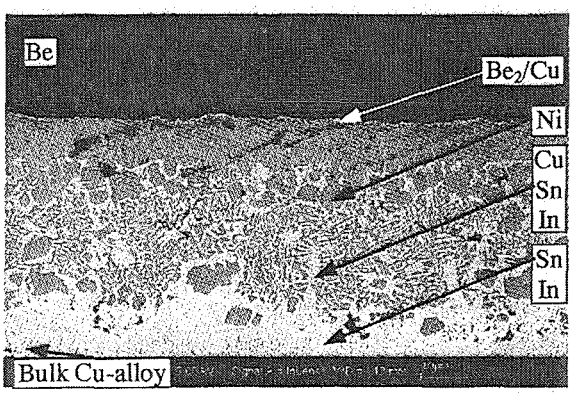

Fig. 9. Elements distribution (fast brazing)

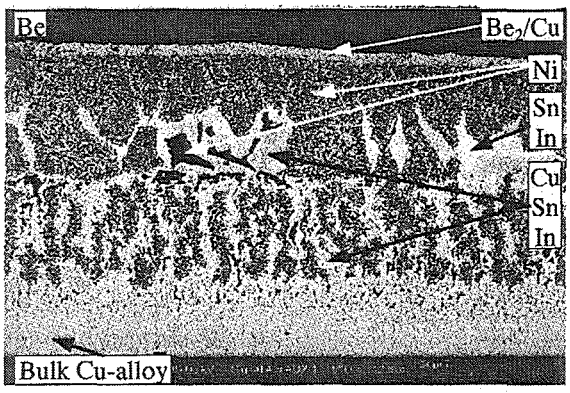

Fig. 10. Elements distribution (resistive furnace)

It was already noted that the thickness of the brazing zone is at least twice more in comparison with the fast brazing. It is very important to see that the width of the brittle intermetallic Be_2Cu is significantly increased up to 7-8 μm (1-1.5 μm after fast brazing).

3.3. Hardness measurements

The results of the hardness measurements of Be/CuCrZr joints are given in figure 11. It can be seen that all fast brazed Be/CuCrZr joints independently of their heat treatment history have practically the same hardness distribution. The maximum hardness is occurred on the Be boundary that corresponds to brittle intermetallic Be_2Cu (see fig. 9). After the brazing in resistive furnace the thickness of brazing zone is increased (see fig. 4). The maximum hardness is also occurred on the Be

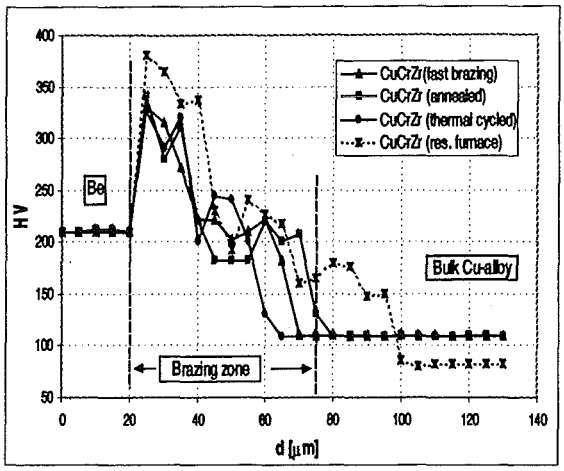

Fig. 11. Hardness of Be/CuCrZr joints

boundary but its absolute value and thickness is higher that is also in good correspondence with a Be_2Cu distribution (see fig. 10). It can be also noted that the hardness of CuCrZr after the brazing in resistive furnace decreased more significantly due to the CuCrZr overheating.

The results of the hardness measurements of Be/DS-Cu joints are given in figure 12. All fast brazed Be/DS-Cu joints independently of their heat treatment history have practically the same hardness distribution like it was with Be/CuCrZr joints. And again after the brazing in resistive furnace the maximum hardness and its thickness is higher.

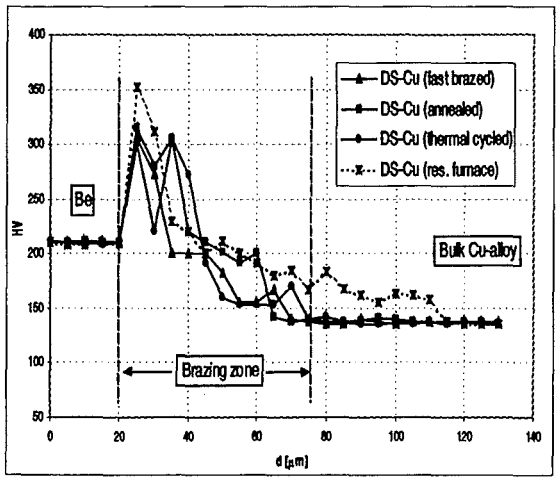

Fig. 12. Hardness of Be/DS-Cu joints

3.4. Mechanical properties

The results of the shear strength measured at RT. are presented in figure 13. The shear strength of the fast brazed Be/CuCrZr joint at room temperature was found as about 150 MPa. Annealing 100 hours at 300°C does not influence on the shear strength of the fast brazed Be/CuCrZr joints. The shear strength of Be/CuCrZr joints brazed in resistive furnace is significantly less (~ 70 MPa) probably due to the thick brittle intermetallic layer (see Fig. 10). The shear strength of the fast brazed Be/DS-Cu joint at room temperature was found as about 200 MPa. Annealing 100 hours at 300°C also does not influence on the shear strength of the fast brazed Be/DS-Cu joints. Again the shear strength of Be/DS-Cu joints brazed in resistive furnace is significantly less (~ 45 MPa) and again probably due to the thick brittle intermetallic layer.

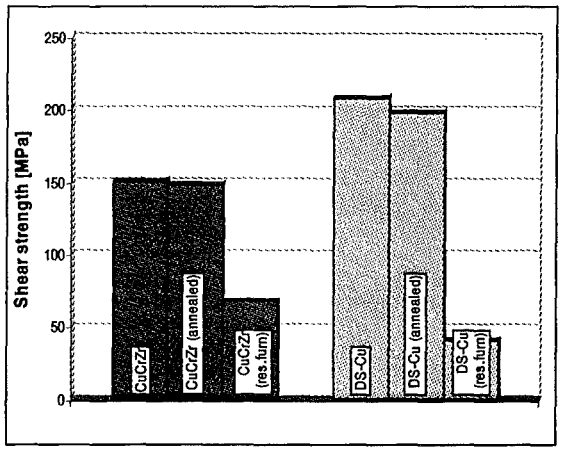

Fig. 13. Shear strength of Be/Cu-alloys (RT)

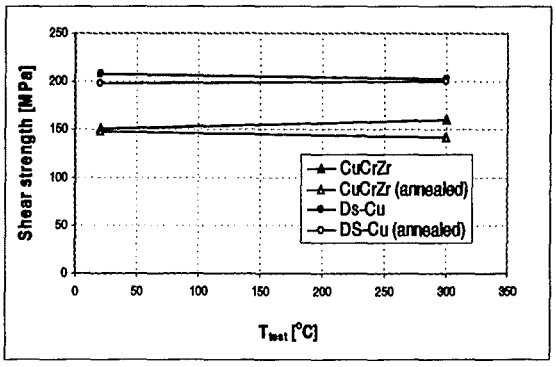

Fig. 14. Shear strength of Be/Cu-alloys at 300°C

Figure 14 presents the results of the shear strength measured at 300°C. One can see that the shear strength of the fast brazed Be/Cu-alloy joints does not depend on the testing temperature in the range RT.-300°C.

3.5. Thermal cyclic tests

The scheme of testing of actively cooled Be/Cu-alloy joints is given in figure 15.

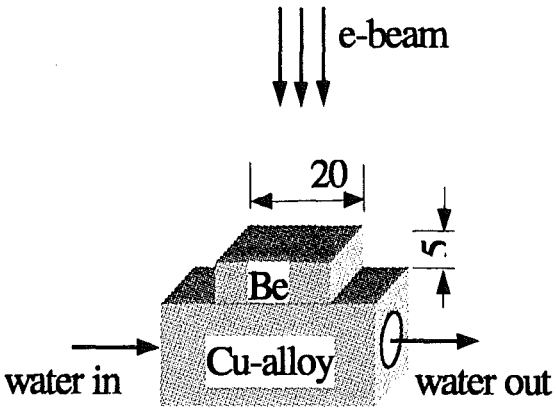

Fig. 15. Thermal cycling of Be/Cu-alloy (scheme)

Figure 16 presents the results of comparative screening test. Heat flux limit of the fast brazed Be/CuCrZr joint was found as 11.5 MW/m^2 independently of its heat treatment history. Screening of the fast brazed Be/DS-Cu joints revealed 10.5 MW/m^2 and also independently of its heat treatment history.

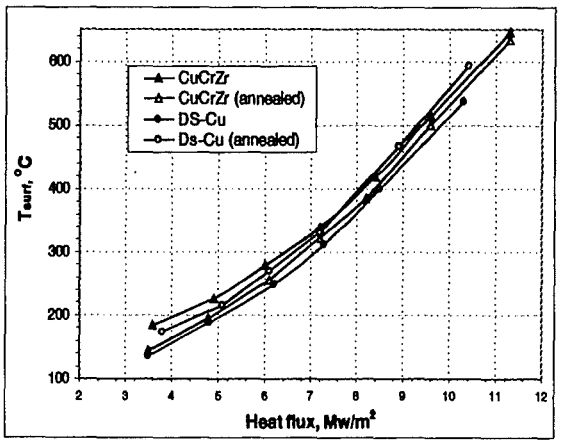

Fig. 16. Screening test of Be/Cu-alloy joints

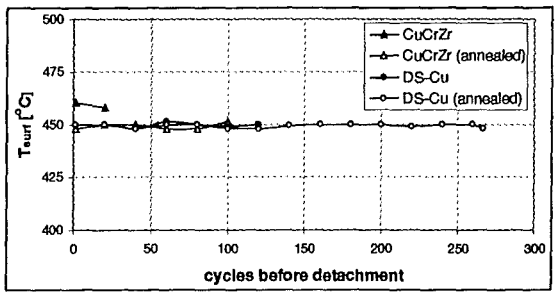

Fig. 17. Surface temperature of the samples during the thermal cycling

Figures 17 and 18 present the results of comparative thermal cycling. From the Fig. 17 it can be seen that the surface temperature of all tested samples remained constant from cycle to cycle and Be tiles were brittle rebounded through the brittle intermetallic Be_2Cu. To confirm this fact the results of the fracture analysis are on the way. We believe that unusually high surface temperature and the limited number of cycles before rebounding for the fast brazed Be/CuCrZr joint (see Fig. 17 and 18) were found due to the brazing defect (the results of the fracture analysis should confirm this fact). The main statistic of the comparative thermal cycling are presented in figure 18. It should be recognized that the heat power density (8 MW/m^2) was too high to make a clear comparison between Be/CuCrZr and Be/GlidCop. Summarizing this testing results with our previously obtained data [3] authors consider that both fast brazed Be/CuCrZr and Be/Ds-Cu joints have practically the same ability to withstand cyclic heat loads.

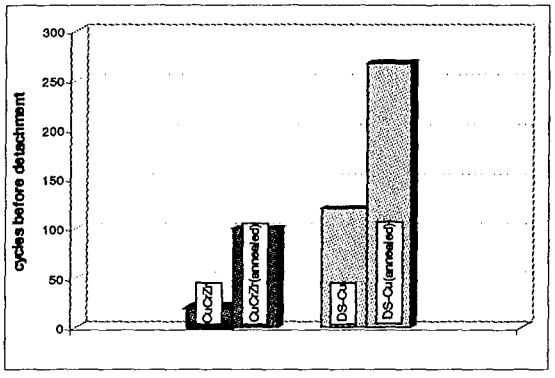

Fig. 18. Thermal cycling of Be/Cu-alloy joints

4. MAIN CONCLUSIONS

Joining Be to Cu-alloy fast brazing technique looks suitable for both PH-Cu(CuCrZr) and DS-Cu (GlidCop) heat sink candidates

Fast brazing method allows to minimize forming a brittle intermetallic layer close to Be boundary

Width and elements distribution in the brazing zone remain stable in the range RT – 300°C

Shear strength of the fast brazed Be/Cu-alloy joints does not depend on testing temperature in the interval RT – 300°C

Brazing in traditional resistive furnace forms wide brittle intermetallic layer that probably leads to significant decrease of shear strength

The results of fracture analysis are needed to confirm the influence of the brittle intermetallic layer on the mechanical and thermal fatigue properties.

6. AKNOWLEDGEMENTS

The authors wish to thank the colleagues from Forschungszentrum Juelich, Germany for their support in some part of the structural analysis.

REFERENCES

1. G. Janeshits et al, ITER Divertor and Pumping and Fuelling System Designs, presented at 16 IAEA Fusion Energy Conference, Montreal, Canada, 1996
2. A. Gervash et al, Comparative Thermal Cycling Testing and Strength Investigation of Different Be/Cu Joints, Fusion Engineering and Design, 39 (1998), pp. 543-549
3. A. Gervash et al, Beryllium Armoured Mock-Ups for Fusion High Heat Flux Application, in Proc. of the 20-th SOFT, Marseille, France, 1998, pp. 47-50
4. V. Gagen-Torn et al, Experimental Complex for High Heat Flux Materials Interaction Research, in Proc. of the 18-th SOFT, Karlsruhe, Germany, 1994, pp. 363-366

Steam chemical reactivity of Be pebbles and Be powder

R. A. Anderl[1], F. Scaffidi-Argentina[2], D. Davydov[3], R. J. Pawelko[1] and G. R. Smolik[1]

[1] *Idaho National Engineering and Environmental Laboratory*
PO Box 1625, Idaho Falls, ID 83415-7113

[2] *Forschungszentrum Karlsruhe, Institut für Neutronenphysik und Reaktortechnik*
Postfach 3640, D-76021 Karlsruhe, Germany

[3] *Bochvar All-Russian Research Institute of Inorganic Materials (VNIINM)*
Moscow, Russia

Abstract

This paper reports the results of chemical reactivity experiments for Be pebbles (2-mm and 0.2-mm diameter) and Be powder (14-31 μm diameter) exposed to steam at elevated temperatures, 350 to 900°C for pebbles and 400 to 500°C for powders. We measured BET specific surface areas of 0.12 m^2/g for 2-mm pebbles, 0.24 m^2/g for 0.2-mm pebbles and 0.66 to 1.21 m^2/g for Be powder samples. These experiments showed a complex reactivity behavior for the material, dependent primarily on the test temperature. Average H_2 generation rates for powder samples, based on measured BET surface areas, were in good agreement with previous measurements for fully-dense CPM-Be. Rates for the Be pebbles, based on measured BET surface areas, were systematically lower than the CPM-Be rates, possibly because of different surface and bulk features for the pebbles, especially surface-layer impurities, that contribute to the measured BET surface area and influence the oxidation process at the material surface.

1. INTRODUCTION

Evaluation of the safety hazards for advanced fusion devices and breeder-blanket concepts includes an assessment of the failures of plasma-facing-component (PFC) and tritium breeder blanket materials due to various accident scenarios. If beryllium is used as the first-wall PFC material or as the neutron multiplier material for the breeder blanket, accident scenarios that result in water or steam exposure of the Be are of particular concern because steam interacts exothermically with hot beryllium to produce hydrogen and BeO. Experimentally-derived, chemical reactivity data for various forms of Be are used in accident simulations to assess the consequences of such accident scenarios. In previous studies we have reported the results of steam chemical reactivity for several forms of Be, including: fully-dense, consolidated powder metallurgy (CPM) Be discs and cylinders [1,2], plasma-sprayed Be plates of variable density [3], and irradiated CPM Be cylinders [4,5].

In this paper we present the key results of materials characterization analyses and chemical reactivity experiments for Be pebbles and Be powder that are exposed to steam at elevated temperatures. Be pebbles are proposed as the neutron multiplier material for the European Helium Cooled Pebble Bed (HCPB) DEMO Blanket [6] and the reference breeding blanket for the International Thermonuclear Experimental Reactor (ITER) [7]. Reactivity of Be powder is of interest to evaluate the consequences of steam interaction with Be powder debris generated in plasma devices by mechanisms such as plasma-disruption-induced vaporization or sputtering of Be surfaces [8]. A detailed description of this work has been reported previously [9,10].

2. EXPERIMENTAL DETAILS

2.1 Specimen description

We tested Brush-Wellman Be pebbles with nominal 2-mm and 0.2-mm diameters. The larger size pebbles were obtained from an intermediate

Be-ore processing step in which beryllium fluoride is reduced by magnesium metal to molten beryllium and magnesium fluoride. These pebbles were recovered from a crushed solidified cake resulting from this process and subsequently sieved to provide "spherical" particles with nominal 2-mm diameters. The smaller Be pebbles were made by inert gas atomization and centrifugal atomization, yielding a product that is nearly spherical and with purity levels comparable to that for other commercial Be products. These particles were also sieved to provide the nominal 0.2-mm diameter material.

Microstructural and micro-chemical analyses have been reported previously for the pebble material [6]. The larger pebbles usually show indentations on the surface, a variability of coarse pores, with some pebbles having large voids, and a very small micro-porosity that is usually oriented along the crystal axis showing a very fine dendritic or cellular structure. In general, the porosity of the small pebbles is always smaller than that of the large pebbles. Metallographic structure of both small and large pebbles shows the presence of large grains, in some cases as large as the pebble diameter. Chemical analysis of the pebbles reveals much higher impurity concentration levels in the large pebbles compared to that in the small pebbles. In wt%, the principal impurity concentrations in the 2-mm pebbles are: BeO (0.078), F (0.0585), C (0.05), Mg (0.16), Fe (0.073), Al (0.025), Si (0.0205), Zr (0.0125), U (0.007), and Cr (0.015). Similarly, main impurity concentrations in wt% for the 0.2-mm pebbles are: BeO (0.34), C (0.07), Mg (<0.01), Fe (0.09), Al (0.04), and Si (0.03). Insoluble impurities in beryllium are usually observed at the grain boundaries, whereas iron and chrome are present in solid solution in the beryllium matrix. Principal precipitated phases are $Be_{13}Mg$, $Be_{13}(Mg, Zr, U)$, Mg_2Si and Al_2O_3. For the 2-mm pebbles, the external surface is usually covered by a 2-μm thick SiO_2 layer and/or a fluorine layer (probably BeF_2) having a thickness less than 2-μm.

Six different grades of Be powder were characterized and tested. These samples, with nominal diameters ranging from 14 to 31 μm, were produced by the technique of disc abrasion. A description of these powders, as reported by Davydov et al. [8], is summarized in Table 1. The specific surface area values given in the table were obtained in the prior work using N_2 as the adsorbent gas.

Table 1. Description of Be powders that were tested in this study.

Powder grade	CBP-56-1	CBP-56-2	CBP-56-3	CBP-30-1	CBP-30-2	DBP-30
Average particle size, (μm)	31.3	30.1	29.1	14.0	19.1	20.5
Bulk density (g/cm^3)	0.68	0.62	0.68	0.61	0.57	0.57
Specific surface area, N_2, (m^2/g)	0.43	0.65	0.46	0.90	1.0	1.03
Chemical composition	(wt %)	(wt %)	(wt %)	(wt %)	(wt %)	(wt %)
Be	99.13	99.00	98.81	98.61	97.73	98.9
Si	0.013	0.014	0.013	0.014	0.013	0.013
Fe	0.11	0.15	0.14	0.18	0.10	0.026
MN	0.0038	0.012	0.0043	0.0084	0.004	0.0026
Mg	0.008	0.011	0.008	0.0093	0.0004	0.002
Cr	0.026	0.036	0.028	0.064	0.028	0.0054
Ni	0.009	0.014	0.011	0.017	0.011	0.004
Al	0.014	0.017	0.015	0.024	0.013	0.004
Cu	0.004	0.004	0.005	0.0071	0.0043	0.0026
C	0.086	0.077	0.088	0.07	0.079	0.077
O	0.6	0.66	0.88	1.0	1.01	0.96

2.2 Measurement systems

Specific surface areas for the test specimens were measured as part of the present work using a Micromeritics Model ASAP 2010 Accelerated Surface Area and Porosimetry system with Kr as the adsorbent gas. The adsorbed gas data were analyzed by the method of Brunauer, Emmett and Teller [11], commonly referred to as the BET method.

Chemical reactivity experiments were conducted with a system developed to measure hydrogen generation rates for unirradiated and irradiated Be exposed to steam [1]. The system comprised a flow-through, integrated assembly with components set up in an inert-gas glovebox and in a laboratory hood. Argon carrier gas was used to sweep reaction gases from the hot sample reaction chamber through a process line equipped with condensers, a cryotrap, instrumentation for gas analyses and an ethylene-glycol trap at the end of the process line. Steam, introduced upstream from the sample furnace, reacted with the hot specimen inside the quartz reaction chamber and was condensed downstream from the sample furnace. Kinetic hydrogen generation rates and total quantities of H_2 generated were obtained from on-line mass-spectrometer measurements of the gas composition in the system process line. Mass peak signatures were mass-2 for H_2, mass-4 for ^4He and mass-40 for Ar.

A precision balance (0.1 mg sensitivity) was used to measure the specimen mass before and after testing. These weight-gain (WG) measurements of the oxygen uptake by Be provided a second means to obtain the total hydrogen generated during a chemical-reactivity test.

3. MEASUREMENTS AND RESULTS

Results of the Kr-gas, BET analyses for the test samples are summarized in Table 2, along with the previous N_2-gas measurements reported by Davydov et al. [8]. These results were obtained from multiple analyses for samples of each material. Uncertainties in the Kr-gas, specific surface area values are estimated to be between 5 and 10%, based on complementary Kr gas adsorption measurements with a surface area standard.

Table 2. BET specific surface area analyses.

Sample Type	Nominal Diameter	Specific Surface Area (m^2/g)	
		Kr	N_2
2-mm pebble	2-mm	0.12	
0.2-mm pebble	0.2-mm	0.24	
CBP-56-1 powder	31.3 μm	0.69	0.43
CBP-56-2 powder	30.1 μm	0.66	0.65
CBP-56-3 powder	29.1 μm	0.67	0.43
CBP-30-1 powder	14.1 μm	1.21	0.91
CBP-30-2 powder	19.1 μm	1.05	1.00
DBP-30 powder	20.5 μm	1.04	1.03

Steam-chemical reactivity experiments were performed at various temperatures for the pebbles and powders: at 10 temperatures between 350°C and 900°C for 2-mm Be pebbles; at 9 temperatures between 350°C and 800°C for 0.2-mm Be pebbles; and at 400°C and 500°C for the Be powder samples. Sample material was placed in 4-cm long by 3-cm wide by 0.5-cm deep ceramic (Al_2O_3) crucibles that were located at the center of the reaction-chamber hot zone for a test. Pebble and powder material was distributed uniformly over the bottom of the crucible. Be-pebble sample masses ranged from 0.5-2.6 g, with the largest samples tested at the lowest temperatures. Masses of Be powder samples were 0.3-0.5 g. Steam exposure times were 300-340 minutes for most experiments. Typical system parameters were: line pressure (~680 torr or 0.9 MPa), Ar carrier-gas flow rate (100 cm^3/min), steam flow rate (2500 cm^3/min for a water throughput of 2 cm^3/min), steam-generator temperature (350°C). For these conditions, the system response time was about 6 min and the H_2 detection sensitivity was about 3 ppm of H_2 in Ar. The on-line QMS was calibrated using Ar-H_2 standard gas mixtures in which the H_2 contents varied from 50 ppm to 50,000 ppm.

In Figures 1 and 2, we show the chemical reactivity kinetic behavior of 0.2-mm Be pebbles exposed to steam at 400°C and 550°C, respectively. Figure 1 shows parabolic H_2 generation kinetics, typical for all materials (pebbles and powders) tested at 400°C and below. Figure 2 shows paralinear H_2 generation kinetics, a sequential combination of parabolic and linear components, typical for 0.2-mm pebble samples tested between 450°C and 600°C, 2-mm-pebble samples tested between 450°C and

700°C, and powder samples tested at 500°C. Reactivity kinetics comprised a sequential combination of paralinear and accelerating components for 0.2-mm pebbles at 700°C and for 2-mm pebbles at 800°C. Autocatalytic behavior, for which the reaction chemical heat contributes to and enhances the reaction rate by raising the sample temperature, was observed for 2-mm pebbles tested at 900°C and 0.2-mm pebbles tested at 800°C. Mechanisms for these reactivity kinetics have been discussed by Petti et al. [12].

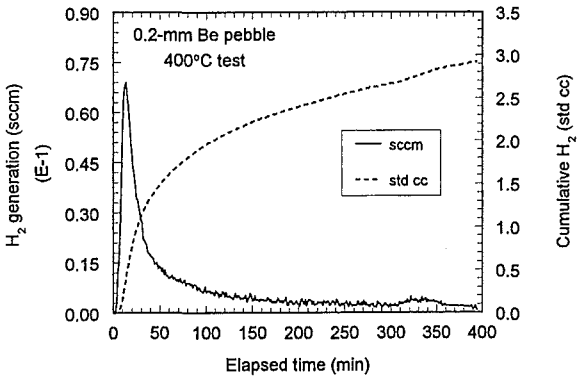

Figure 1. H_2 generation kinetics for 0.2-mm Be pebbles exposed to steam at 400°C.

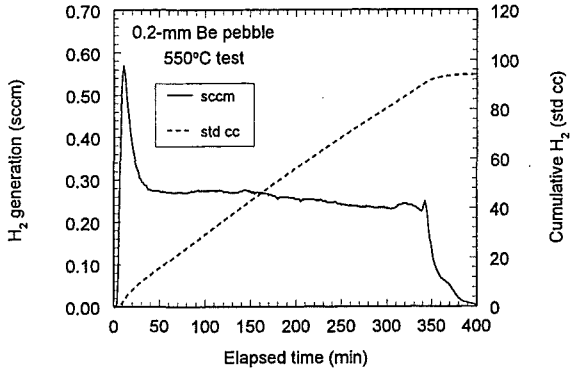

Figure 2. H_2 generation kinetics for 0.2-mm Be pebbles exposed to steam at 550°C.

A summary of average H_2 generation rates (liters/m^2-s) for the pebble and powder samples is presented in Figure 3, along with the results of previous measurements for fully-dense CPM Be discs and cylinders [1,2,13]. Pebble data are designated by *2.0-mm Be-WG, -G* and by *0.2-mm Be-WG, -G*. Powder data are designated by *R-Be PWDR-WG, -G*. Previous results for fully-dense CPM Be are designated by *INEL92-WG,-G*, [13], *INEL96-WG1, -G1, -WG2, and –G2*, [1,2]. In the legend labels, mass-spectrometer gas measurement results are identified with a G and values derived from weight-gain measurements are identified with WG. The results are presented as average values in that they correspond to the total quantities of H_2 generated during an experiment divided by the steam exposure time and the surface areas of the samples prior to the experiment. For the fully-dense CPM samples we used the geometric surface areas, as derived from specimen dimensional measurements. BET surface areas were used in the computation of the H_2 generation rates for the pebble and powder samples. Straight lines are drawn through the data for the different sample types to indicate the general trends in chemical reactivity for different temperature ranges. Values plotted for the powder data, *R-Be PWDR-WG,-G*, correspond to averages of the rates obtained from experiments at 400°C and 500°C for each of the six powder types identified in Table 1.

In Figure 4, we compare the pebble and powder chemical reactivity data with corresponding rates measured previously for fully-dense and low-density (porous) CPM Be. To demonstrate the influence of material specific surface area on chemical reactivity, the data are presented as average Be reaction rates (weight gain per unit time, per initial mass of the sample, mg/g-min). This figure permits the presentation of the results for experiments on each of the powder types, *CBP-30, CBP-56 and DBP-30*. Pebble data are designated by *2.0-mm Peb* and *0.2-mm Peb*. Previous results for fully-dense CPM Be discs and cylinders are designated by *INEL92-disc* [13] and by *INEL96-disc, -cyl* [1,2]. The results from previous experiments for low-density (85% theoretical density) porous Be, [14], are designated by *INEL92-Porous*. Straight lines are drawn through the data for the different sample types to indicate the general trends in chemical reactivity for different temperature ranges. In the figure, we also identify values for the specific surface areas that were determined for each material type.

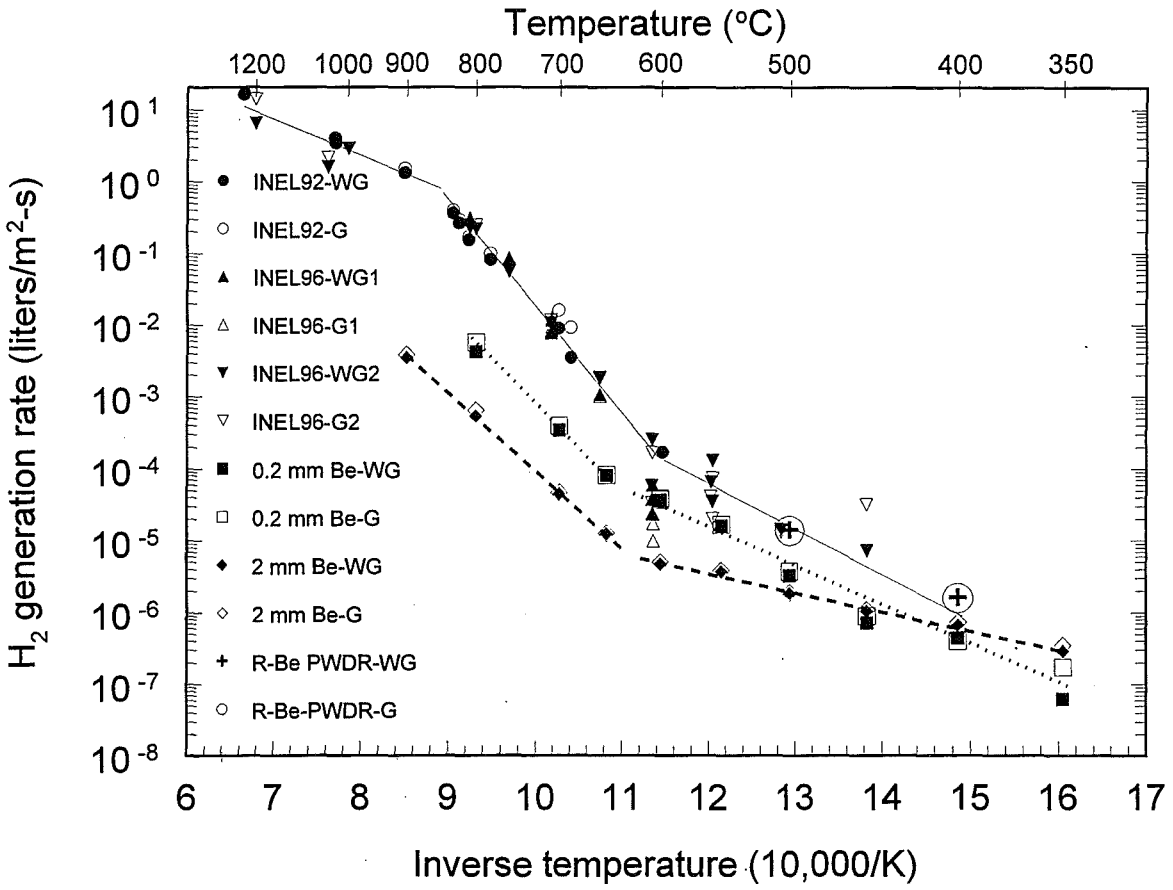

Figure 3. Comparison of average H_2 generation rates (liters/m^2-s) for Be pebble and powder material with those for fully-dense CPM Be.

In Figure 5, we plot average hydrogen generation rates as a function of nominal powder diameter for each of the six powder sample types that were tested in separate experiments. Note that the rate values have units of cc/min-g, in contrast to liters/m^2-s, as shown in Figure 3. This plot shows a systematic increase in the powder reactivity as the particle diameter decreases, indicating the increase in total surface area for a sample as the particle size becomes smaller.

Figure 6 presents parabolic rate constants for H_2 generation, as derived from the pebble-, powder- and CPM-Be kinetic H_2 generation data for temperatures of 600°C and below, the temperature region for which parabolic or paralinear behavior was observed. Parabolic rate constants, k_p, are defined by Equation 1,

$$(V_c/A)^2 = k_p * t, \quad (1)$$

where V_c is the cumulative quantity of hydrogen generated at an elapsed time "t" for a specimen with surface area "A". In the computation of the rate constants, geometric surface areas were used for the CPM-Be data and BET surface areas were used for the pebble and powder data. The constants were computed using a cumulative hydrogen value corresponding to an elapsed time of 35 minutes, an appropriate value in the region of parabolic kinetics before linear kinetics is operative. Straight lines are drawn through the data to guide the eye and indicate the trends for each data set.

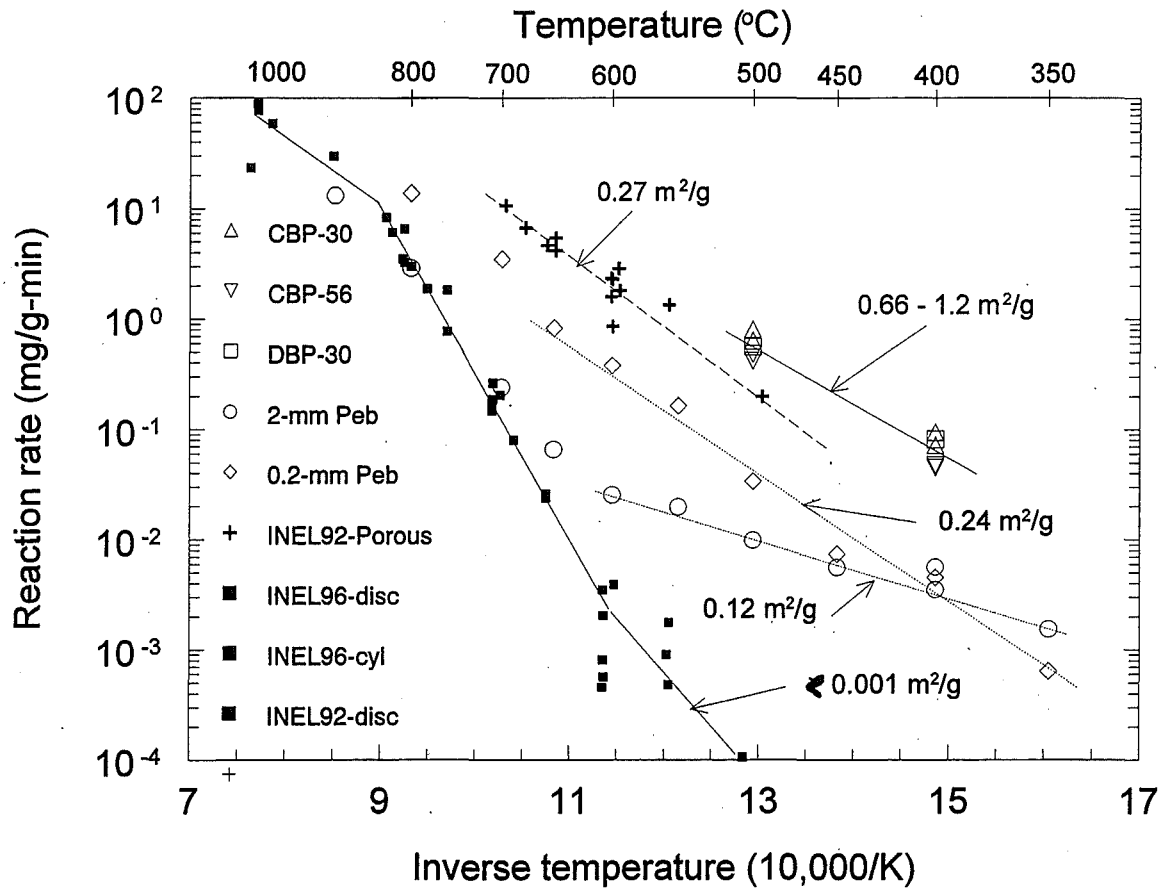

Figure 4. Comparison of average Be reaction rates (weight gain per unit time, per initial mass of sample) for different Be types: Be powder {CBP-30[1.0-1.2 m^2/g], CBP-56[0.66-0.69 m^2/g], DBP-30[1.0 m^2/g]}, Be pebbles {2-mm Peb[0.12 m^2/g], 0.2-mm Peb[0.24 m^2/g]}, low density, porous CPM Be {INEL92-Porous[0.27 m^2/g]}, and fully-dense CPM Be {INEL96-disc, INEL96-cyl, INEL92-disc;[<0.001 m^2/g]}. Specific surface areas are identified in square brackets for each material identification and in the figure for each data set.

4. DISCUSSION AND CONCLUSIONS

In this paper we have presented the results of steam-reactivity measurements for Be pebble and powder material, and we have compared those results to data for fully-dense, CPM-Be cylinder and disc samples. The results indicate, as shown in Figures 3 and 6, that H_2 generation rates for the powder material, based on BET surface area, are quite consistent with the CPM-Be data. In contrast, the rates for 2-mm and 0.2-mm diameter Be pebbles, based on BET surface area, are systematically lower than corresponding CPM-Be H_2 generation rates.

We believe that the observed H_2 generation rate differences for the pebble data can be attributed primarily to differences in the surface and microstructural features for the pebble material, as compared to the CPM-Be machined samples. As we noted in section 2, both the 2-mm and 0.2-mm pebble material have microstructural and surface topographical features that are substantially different for the pebbles. In addition, the bulk and surface impurity composition for the pebble material was substantially different from the CPM-Be material, especially for the 2-mm pebble material that had an ~2μm thick impurity surface layer of SiO_2 and/or BeF_2. The impact of such surface features and impurities could contribute to the BET surface area, as measured by gas adsorption techniques, but also affect the oxidation process at the material surface, resulting in some ambiguity between the BET

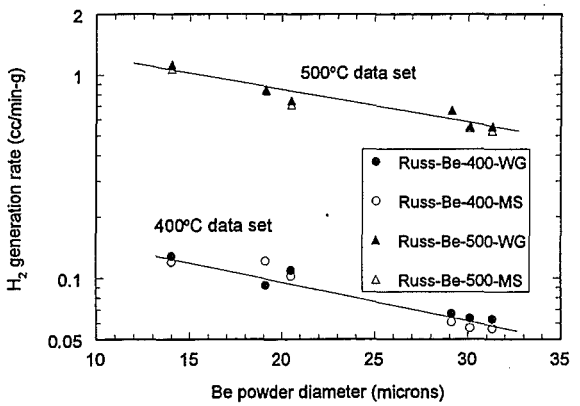

Figure 5. H_2 generation rates for Be powder as a function of nominal powder diameter.

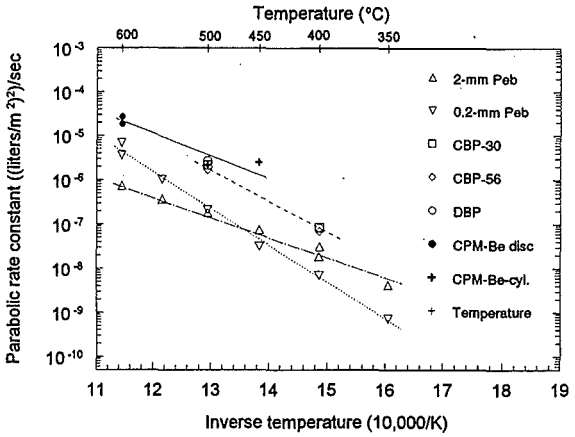

Figure 6. Comparison of H_2 generation, parabolic rate constants for Be pebble, Be powder and fully-dense CPM Be.

surface area and the reactive surface area. If the reactive surface area is less than the BET surface area, the derived H_2 generation rates for the pebble material, based on BET surface area, could be smaller than they should be.

The reaction rate results, presented in Figure 4 as weight-gain/(initial mass-min), demonstrate that specific surface area has a significant influence on the chemical reactivity of the various materials. Reactivity is directly proprotional to the specific surface area of the material, the larger the specific surface area, the larger the reaction rate. We note from Figure 4 that the slopes of the reaction-rate data for the 0.2-mm pebbles, the powders and the porous CPM Be are comparable, indicating that the mechanism controlling the reaction is similar for these materials and the magnitude of the reaction rate is governed by each materials' reactive surface area. In contrast, for temperatures below 650°C, the reaction-rate slope for the 2-mm pebbles is much less than that for the 0.2-mm pebbles, the powder and the porous Be, indicating that the reaction mechanism could be different. For temperatures above 650°C, the reaction-rate slope for the 2-mm pebbles is comparable to that for fully-dense CPM Be, indicating that the controlling mechanisms may be similar in this temperature range. We believe that these differences in reactivity mechanism for the 2-mm pebbles are due to the presence of the ~2μm thick impurity layer of SiO_2 and/or BeF_2, that can affect the oxidation process at the surface.

Table 2 provided a comparison of specific surface areas for the six types of Be powder, with values obtained by Kr gas adsorption analyses in the present work and values obtained from N_2 gas adsorption analyses in previous work [8]. Excellent agreement was noted for samples CBP-56-2, CBP-30-2 and DBP-30. Discrepancies for the other samples ranged from 30-60%. A possible reason for the discrepancy may be related to the use of different absorptive gases. The accuracy of BET analyses for materials with "low" specific surface area is typically improved when Kr is used rather than N_2. We note that the specific surface area values based on Kr adsorption correlate well to the variations in average diameters of the powder samples, whereas the values based on N_2 adsorption do not. Therefore, we believe that the BET results based on Kr are more accurate than the values based on N_2.

In conclusion, this work has contributed new experimental results of the reactivity of Be pebbles and powder exposed to steam at elevated temperatures. However, the work suggests the need for additional experiments, materials characterization and modeling analyses to better understand reactivity behavior for different forms of Be exposed to steam over a wide temperature range. In particular, experiments are required to elucidate the influence of bulk and surface impurities and other surface and microstructural features on both the BET surface area determinations and on oxidation behavior for materials exposed to steam.

ACKNOWLEDGEMENTS

This work is supported by the U. S. Department of Energy, Office of Fusion Energy Sciences, Idaho Operations Office, under Contract DE-AC07-94ID13223.

REFERENCES

1. R. A. Anderl et al., Fusion Technology 30 (1996) 1435-1441.
2. K. A. McCarthy et al., Fusion Engineering and Design 37 (1997) 543-552.
3. R. A. Anderl, R. J. Pawelko, G. R. Smolik and R. G. Castro, "Steam Chemical Reactivity of Plasma-Sprayed Beryllium," paper presented at the 13th Topical meeting on Fusion Energy, ANS Embedded Topical, Nashville, TN, June, 1998, accepted for publication in Fusion Technology.
4. R. A. Anderl et al., Journal of Fusion Energy 16 (1997) 101-108.
5. R. A. Anderl et al., Journal of Nuclear Materials 258-263 (1998) 750-756.
6. F. Scaffidi-Argentina et al., "Mechanical Performance of Irradiated Beryllium Pebbles," Proceedings of the Third IEA International Workshop on Beryllium Technology for Fusion, October 22-24, 1997, Mito City, Japan, JAERI-Conf 98-001.
7. K. Ioki, M. Ferrai, "ITER Final Design Report, Design Description Document WBS 1.6B, Tritium Breeding Blanket System," ITER Document G 16 DDD 2 98-06-10-W014.
8. D. A. Davydov et al., "Beryllium-Steam and Beryllium-Air Reaction Data, " A. A. Bochvar All-Russian Scientific Research Institute of Inorganic Materials (VNIINM), Moscow, Russia, ITER Russian Home Team Report: ITER-RF-96-B11M-SEH-1, July 16, 1996.
9. R. A. Anderl et al., "Steam Chemical Reactivity of Be Pebbles," Idaho National Engineering and Environmental Laboratory, INEEL/EXT-98-01149, December 9, 1998.
10. R. A. Anderl et al., "Steam Chemical Reactivity of Be Powder," Idaho National Engineering and Environmental Laboratory, INEEL/EXT-99-00338, April 30, 1999.
11. S. Brunauer, P H. Emmett and E. Teller, J. Amer. Chem. Soc. 60 (1938) 309.
12. D. A. Petti et al., "On the mechanisms associated with the chemical reactivity of beryllium in steam," Paper presented at the 9th International Symposium on Fusion reactor Materials, October 10-15, 1999, Colorado Springs, CO.
13. G. R. Smolik et al., Journal of Nuclear Materials 191-194 (1992) 153-157.
14. G. R. Smolik et al., "Reactions of porous Be in steam," EGG-FSP-10346, Idaho National Engineering Laboratory, July, 1992.

Determination of Beryllium Reactivities with Thermal Analysis

Frank Druyts

SCK•CEN
Boeretang 200, 2400 Mol, Belgium[+]

In the framework of the European Fusion Programme SEAL we performed TG/DTA tests on vacuum hot pressed S-200 beryllium with three different irradiation histories: (i) a reference "unirradiated dense" S-200 beryllium with a theoretical density of 99.9 %, (ii) "irradiated dense" beryllium, irradiated in BR2, the materials testing reactor of the Belgian nuclear research centre SCK•CEN, up to a fast neutron fluence of 1.6 10^{21} n/cm^2 (E>1MeV) or a helium content of 300 appm He and with a theoretical density of 99.9 %, and (iii) "irradiated porous" beryllium, irradiated in BR2 up to a fast neutron fluence of 4 10^{22} n/cm^2 (E>1MeV) or 21000 appm He and with a theoretical density of 97.2 %.

In air, all beryllium types exhibited parabolic oxidation kinetics at 600°C within the length of the experiments (six hours). At 800°C and 1000°C, the reaction accelerated and became linear until the specimen was depleted of unreacted beryllium. At 700°C the dense samples (unirradiated and irradiated) showed parabolic behaviour while the reaction accelerated for the irradiated porous samples. The irradiated samples showed a higher oxidation rate in air than the unirradiated specimens, except at 600°C. There was no pronounced influence of porosity on the reaction rate, but this is probably due to the relatively high theoretical density of the irradiated porous Be samples.

In steam, kinetics were parabolic for all tested beryllium types at 600°C. At 700°C, kinetics were parabolic for unirradiated Be and irradiated dense Be, and accelerating/linear for irradiated porous material. At 800°C, all samples showed accelerating/linear behaviour. There was no influence of porosity on the reaction rate of beryllium in steam, except at 700°C, where the reaction rate for the irradiated porous samples is an order of magnitude higher than for the irradiated dense material. This can be attributed to the different kinetic regimes for the two beryllium types at 700°C. No pronounced influence of irradiation on the reactivity of beryllium in steam was observed.

1. INTRODUCTION

In the design of future fusion reactors, beryllium is a prime candidate material for the plasma facing components (PFC). The use of beryllium in a fusion reactor contest however, entails the consideration of two accident scenarios. The first is a loss of coolant accident (LOCA). In the case where water is used as cooling fluid, a LOCA involves the beryllium/steam reaction:

$$Be + H_2O \rightarrow BeO + H_2 + 370\ kJ/mol \qquad (1)$$

The second major safety hazard is a loss of vacuum accident (LOVA) during which air intrudes the reaction chamber and oxygen reacts with PFC beryllium at high temperature according to the reaction:

$$Be + \tfrac{1}{2}\ O_2 \rightarrow BeO + 610\ kJ/mol \qquad (2)$$

To assess the consequences of a LOCA or LOVA, kinetic data on the beryllium/steam and beryllium/air reaction are necessary.

In the last decade, a worldwide effort was made to provide data on the beryllium chemical reactivity, using mass spectromery [1-3], weight gain measurements [4] and thermogravimmetry [5]. This paper presents results from a research programme on the chemical reactivity of irradiated beryllium [6] in

[+] This research programme was financially supported by the European Commission in the European fusion programme SEAL (Safety and Environmental Assessment of Fusion Power – Long-term Programme).

the framework of the European Fusion Programme SEAL. It was part of a larger programma focussing on the properties of irradiated beryllium [7]. Combined thermo-gravimetric analysis and differential thermal analysis (TG/DTA) was used to study the kinetics of the beryllium/steam reaction. In this paper, only the TG data are discussed.

2. EXPERIMENTAL DETAILS

2.1. TG/DTA system

The chemical reactivity of beryllium samples exposed to air or steam was determined with combined thermogravimetric analysis/differential thermal analysis (TG/DTA). A Setaram TG 92-12 type TG/DTA was adapted for performing thermal analysis on irradiated material in an inert atmosphere, air, or steam. To this purpose, the thermal analyser was connected to a steam generator and incorporated in a glove box. The complete laboratory setup is described elsewhere [8].

During the experiments the beryllium samples are heated in a vertical tubular furnace, heated by metallic resistors, in which the TG/DTA rod, connected to the microbalance, is placed. The microbalance has a sensitivity of 1 μg. Attached to the rod is the TG/DTA platform, with two crucibles, one for the reactive sample and one filled with thermally inert α-alumina, annealed at 1500°C prior to the tests. Two type S thermocouples are connected to the crucibles for the DTA measurement. The temperature of the furnace is also monitored with a type S thermocouple.

Steam is delivered to the furnace by a steam generator system consisting of the following parts:

- a piston-type micropump that injects a precise volume of water into the evaporator,
- an electronic mass-flow controller for the inert carrier gas, and
- an evaporator with programmable temperature, placed adjacent to the furnace.

Typical operating parameters for the experiments are a flow rate of 0.5 ml/min water to the evaporator that is held at 350°C. The specimens are heated in the furnace at 25°C/min to the desired test temperature between 600°C and 1000°C under Argon atmosphere. When the isotherm is reached, we introduce the reactive gas (air or steam) into the furnace.

The reaction rates as presented in this paper were determined from the TG curves. The DTA results will be analysed and discussed in a later phase. For the tests at low temperatures, where parabolic behaviour was observed, the total mass increase of the beryllium specimen after two hours of exposure was used to calculate the mean reaction rate in $g/m^2.s$. The geometric surface area was used for this calculation. For the tests at high temperatures showing accelerating/linear behaviour, the maximum reaction rate, corresponding to the linear part of the TG curve was used for the calculation. For the tests in steam, the corresponding hydrogen generation rate was calculated, expressed in $l/m^2.s$, according to reaction (1) and assuming standard conditions.

Table 1
Properties of the investigated beryllium samples

	UD	ID	IP
Fabrication characteristics			
Grade	S-200F	S-200F	S-200E
[BeO] (wt.%)	1.2	1.2	1.9
Other elements (wt.%)	0.36	0.36	0.36
Av.grain size (μm)	8.2	8.2	10-13
Theor. Density (g/cm^3)	1.856	1.856	1.862
Reported Density[1] (g/cm^3)	1.854 (99.9%)	1.854 (99.9%)	1.852 (99.5%)
Measured Density[2] (g/cm^3)	1.838 (99.0%)	1.838 (99.0%)	1.810 (97.2%)
Irradiation characteristics			
Neutron fluence (n/cm^2) (E>1MeV)	-	$1.6\ 10^{21}$	$4\ 10^{22}$
Helium content (appm)	-	300	21000

[1]Reported by the manufacturer
[2]Measured at SCK-CEN.

2.2. Beryllium samples

Three types of beryllium samples were used for the experiments: UD (unirradiated dense), ID (irradiated dense), and IP (irradiated porous). Table 1 summarises the main fabrication and irradiation chracteristics of these materials. Unirradiated dense and irradiated dense samples were cut from tensile rods of S-200F vacuum hot pressed material (Brush Wellman). The tensile specimens have a theoretical density of 99.9% and an average grain size of 8.2 μm [9]. UD samples were cut from reference tensile specimens. ID samples were prepared from tensile

specimens irradiated at 235°C in BR2, the Belgian materials testing reactor, up to a fast neutron (E>1MeV) fluence of 1.6 10^{21} n/cm^2, corresponding to a helium content of 300 appm He. The IP samples were cut from VHP S200E beryllium cylinders (manufactured by Kawecki Berylco Industries) irradiated in BR2 at 40-50°C up to a fast neutron fluence of 3.9 10^{22} n/cm^2, corresponding to a helium content of 21000 appm He [10]. Table 1 summarises the properties of the investigated beryllium samples. The helium generation and induced swelling of the irradiated samples are described elsewhere [9], as well as their microstructure [11]. The main 'other elements' were Al, C, Fe, Mg and Si.

For the initial measurements, no additional surface treatment such as mechanical polising or chemical etching was performed after slicing the discs.

3. RESULTS AND DISCUSSION

3.1. Beryllium/air

TG/DTA experiments were performed on beryllium samples exposed to air at 600°C, 700°C, 800°C and 1000°C. At 600°C and 700°C, the mass increase of the sample is small and the kinetics of the reaction are essentially parabolic during the length of the test (six hours), as can be seen on Figure 1 for unirradiated dense Be. Parabolic kinetics are associated with the growth of a protective oxide layer [12-14].

On Figure 1, the initial mass increase rate at 700°C is lower than at 600°C, which is an apparent contradiction and is due to the large scatter in results at these low temperatures. We observe a large scatter in the reactivity results for all tested beryllium types in both air and steam at 600°C and 700°C, except for irradiated porous Be at 700°C, where kinetics are accelerating/linear and the mass increase is higher. There are two possible explanations for this poor repeatability. First, the signal/noise ratio is rather low at 600°C and 700°C due to the relatively small variations in mass and the adverse effect of air and steam injection on the microbalance stability. Second, there is the uncertainty on the initial surface state of the samples, as they were not polished after sawing. Surface analysis of the reacted samples with Scanning Electron Microscopy [15] revealed that the oxide growth inititation preferentially took place at ridges produced by slicing of the tensile specimens into cylindrical samples. Reference tests with polished samples confirmed this: oxidation was more homogeneous over the beryllium surface, the scatter on chemical reactivity results was smaller, and the reaction rates were in general lower than for the samples that were not surface treated.

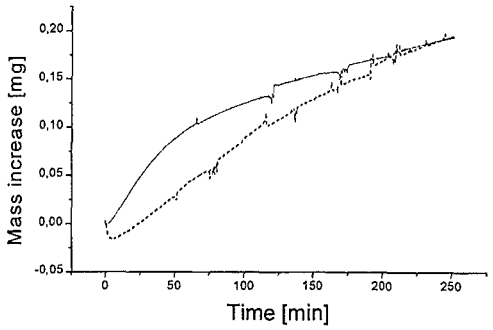

Figure 1. TG curves for unirradiated beryllium samples exposed to air at 600°C (solid line) and 700°C (dotted line).

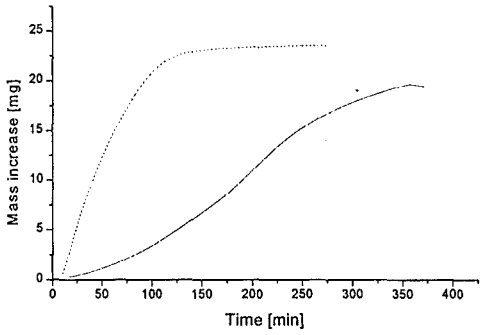

Figure 2. TG curves for unirradiated dense beryllium exposed to air at 800°C (solid line) and 1000°C (dotted line).

Figure 2 shows TG curves of unirradiated dense beryllium samples exposed to air at 800°C and 1000°C. At these temperatures, the protective oxide layer cracks almost immediately and oxidation is dominated by grain boundary diffusion of oxygen molecules. This increases the effective surface area available for oxidation, hence the increase in reaction rate. As the oxidation is accompanied by an increase in molar volume, the oxidised grain boundaries perform a wedge-like action and grains detach from the specimen, resulting in new

unreacted surface. After a while the increase in fresh reactive surface is counterbalanced by the slow mass transport through half-reacted particles and the overall reaction kinetics become linear. When the sample is almost depleted of unreacted metal, the reaction rate decreases and the sample mass remains constant.

This behaviour as a function of temperature was observed for all tested specimens in air. Kinetics are approximately parabolic at 600°C and 700°C for unirradiated dense and irradiated dense Be, and at 600°C for irradiated porous Be. At 800°C and 1000°C for the dense beryllium, and at 700°C and above for irradiated porous Be, kinetics are accelerating/linear.

Figure 3 summarises the oxidation rates of the investigated beryllium samples in air as a function of temperature. In general, the reaction rate is slightly higher for the irradiated samples than for the unirradiated but, in particular at low temperatures, this effect is not very pronounced. At 800°C and 1000°C, where the repeatability of the experiments is better, the influence of irradiation on reaction rate is more manifest.

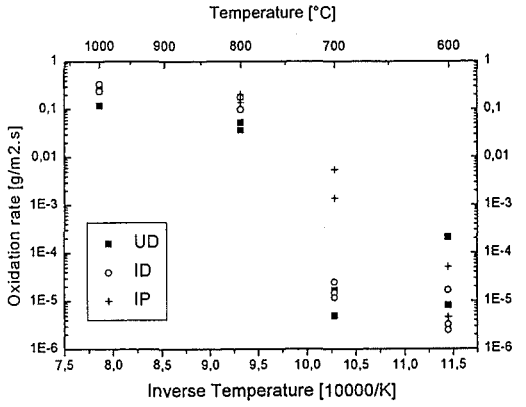

Figure 3. Oxidation rates of beryllium samples exposed to air at different temperatures, derived from TG data and based on the geometric surface area of the samples: unirradiated dense (UD), irradiated dense (ID) and irradiated porous (IP) beryllium.

We did not observe any significant influence of porosity on the reaction rate in air. The rates for the irradiated dense and irradiated porous samples are of the same order of magnitude and the influence of porosity is much less than the influence of irradiation. This is due to the low porosity of the 'porous' samples (approximately 3%) compared to, for example, the porous material used for steam chemical reactivity experiments at INEEL, that had a theoretical density of 88% [3]. Only at 700°C the reaction rate for irradiated porous Be was ten times higher than for irradiated dense Be. This can be explained by the difference in reaction kinetics of the two materials at this temperature: parabolic for the dense Be and accelerating/linear for the porous samples.

3.2. Beryllium/steam

TG/DTA experiments were performed on beryllium samples exposed to steam at 600°C, 700°C, and 800°C. Figure 4 summarises the TG results for the different types of beryllium. The reaction rates are expressed both in terms of mass increase (g/m².s) and hydrogen production (l/m².s). The hydrogen generation rate is based on the TG results and reaction (1), assuming standard conditions. Reaction rates are based on the geometric surface area of the samples.

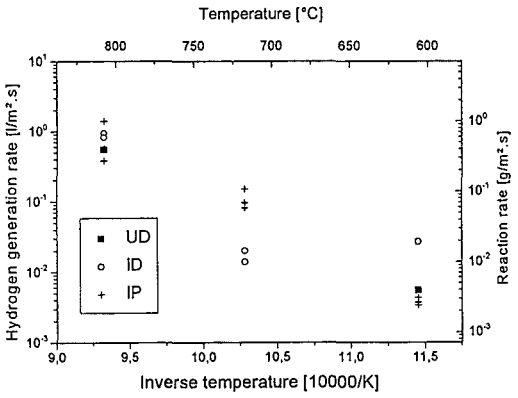

Figure 4. Oxidation rates of beryllium samples exposed to steam at different temperatures, derived from TG data and based on the geometric surface area of the samples: unirradiated dense (UD), irradiated dense (ID) and irradiated porous (IP) beryllium.

The reaction rate of the samples in steam increases with temperature. No pronounced effect of

porosity on the reaction rate is observed, but as explained above, this is probably due to the low porosity of the samples. Only at 700°C, the reaction rate for irradiated porous beryllium is one order of magnitude higher than for the irradiated dense beryllium. One should bear in mind however that, as was the case for Be/air, the kinetics of the reaction of the materials in steam at 700°C were different. The irradiated dense Be showed parabolic kinetics over the length of the experiment, while the irradiated porous Be initially exhibited parabolic kinetics but after approximately fifty minutes acceleration of the reaction occurred. The corresponding TG curves are shown in Figures 5 and 6 respectively.

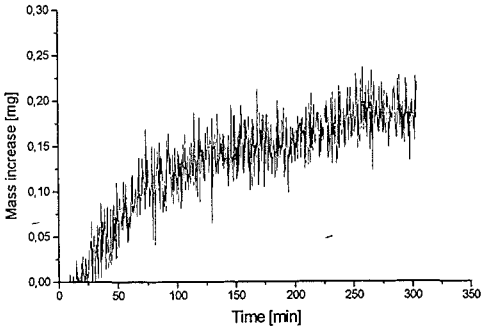

Figure 5. TG curve for irradiated dense beryllium exposed to steam at 700°C.

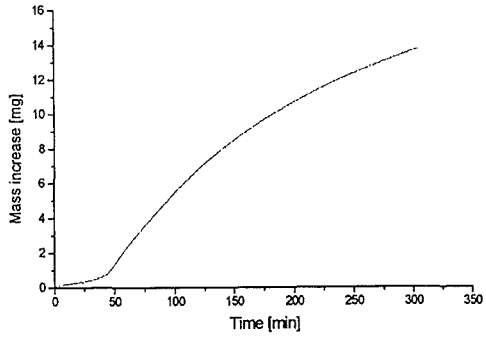

Figure 6. TG curve for irradiated porous beryllium exposed to steam at 700°C.

There is a slight tendency for the irradiated samples to react more rapidly than the unirradiated, although this effect is not very pronounced. The effect of irradiation is less important than for the beryllium/air reaction. At 600° the irradiated dense material reacted up to one order of a magnitude faster than the unirradiated dense beryllium. However, the reaction rate for irradiated dense Be at this temperature seems exceptionally high, as it is superior to the reaction rate found for the same material at 700°C. The causes of the large experimental scatter were already discussed in the previous section (beryllium/air experiments).

4. ONGOING WORK

Interpretation of the TG/DTA results continues. For the experiments showing parabolic behaviour, the parabolic rate constants are being determined. The DTA results will be used for determining the rate equations too. To enhance the repeatibility of the experiments at the low temperatures, the following measures will be taken: polish the samples, work in pure TG mode as this decreases the noise on the TG signal, and increase the length of the experiments up to a few days. Longer-term experiments at 600°C and 700°C are also useful in completing the database, as literature data suggest that after initial parabolic behaviour, the reaction in air/steam becomes accelerating/linear after a while.

5. CONCLUSIONS

In this paper results from thermal analysis of the beryllium/air and beryllium/steam reactions were discussed. Combined TG/DTA was used to determine the reactivity of three types of unirradiated and irradiated beryllium.

In air, parabolic behaviour was observed at 600°C and 700°C for the dense material and at 600°C for the porous material. At these temperatures, the scatter on reactivity results is large, probably due to the influence of the initial surface state on the oxidation kinetics. The beryllium did not receive any particular surface treatment. At 800°C and 1000°C, the reaction of beryllium in air accelerated and became linear until the specimen was depleted of unreacted beryllium. Except at 600°C, the reactivity of irradiated beryllium was always higher than for unirradiated

beryllium. There was no pronounced influence of porosity on the reaction rate, but this could be due to the relatively low porosity of the tested beryllium sample (97.2% theoretical density).

In steam, kinetics were parabolic for all tested beryllium types at 600°C. At 700°C, kinetics were parabolic for unirradiated Be and irradiated dense Be, but accelerating/linear for the 97.2% TD irradiated porous material. At 800°C, the reaction accelerated for all investigated beryllium types. Again, there was a large scatter on the experimental results at 600°C. There is no influence of porosity on the Be/steam reactivity, except at 700°C, where the reaction rate of irradiated porous Be is an order of magnitude higher than for irradiated dense Be. This can be attributed to the different kinetics of the reaction in steam for both materials at 700°C (parabolic for dense Be vs. accelerating/linear for porous Be). The irradiated samples had a higher chemical reactivity in steam than the reference unirradiated samples.

Thermogravimetry provides a powerful tool for determining beryllium reactivities in air and steam, but there are some drawbacks to the technique at low temperatures. In the near future therefore, we shall try to increase sensitivity and decrease microbalance noise in order to obtain a better repeatability of the results at 600°C. Action to enhance the performance of the thermobalance include: working in pure TG mode, increasing the lengths of the tests, and polishing the samples after slicing.

REFERENCES

1. R.A. Anderl, R.J. Pawelko, M.A. Oates, G.R. Smolik and K.A. McCarthy, Fusion Technology 30 (1996) 1435-1441.
2. K.A. McCarthy, G.R. Smolik, R.A. Anderl, R.J. Pawelko, M.A. Oates, R.S. Wallace, Fus. Eng. Des. 37 (1997) 543-552.
3. R.A. Anderl, K.A. McCarthy, M.A. Oates, D.A. Petti, R.J. Pawelko and G.R. Smolik, J. Nucl. Mater. 258-263 (1998), 750-756.
4. D.A. Davydov, Yu.V. Konovalov, V.A. Gorokhov et al., in: Proceedings of the Third IEA International Workshop on Beryllium for Fusion Technology. October 22-24, 1997, Mito, Japan. JAERI Conf. 98-001.
5. H. Yoshida, K. Ashibe, K. Ono and M. Enoeda: Measurements of Breakaway Reaction between Beryllium and Water Vapor for ITER Blanket Design, Report JAERI-M 92-083, 1992.
6. F. Druyts and P. Van Iseghem, Interaction of beryllium with air/steam: determination of chemical reactivities with thermal analysis, SEAL1.1 Final Report, SCK•CEN, BLG-806, 1999.
7. F. Druyts, F. Scaffidi-Argentina, R.A.H. Edwards et al.:Properties of Irradiated Beryllium, SEAL1 Summary Report. SCK•CEN, BLG-817, 1999.
8. F. Druyts, P. Van Iseghem, F. Moons, L. Coheur and P. Deboodt: Interaction of Beryllium with Air/Steam: Laboratory Setup, SEAL1.1 Technical Report, SCK•CEN, 1997.
9. F. Moons, L. Sannen, A. Rahn and J. Van De Velde, J. Nucl. Mater. 233-237 (1996), pp. 823-827.
10. L. Sannen and Ch. De Raedt, Fusion Technology, Proceedings of the 17th Symposium on Fusion Technology (1992) (Eds. C. Ferro, M. Gasparatto and H. Knoepfel), Vol. 2, 1474-1478.
11. M. Verwerft, Irradiation Effects in Beryllium: a Comparison of Powder Types and Consolidation Techniques, Progress Report for ITER Task T23, SCK•CEN, 1997.
12. D.W. Aylmore, S.J. Gregg and W.B. Jepson, J. Nucl. Mater. 2, 2 (1961) 160-175.
13. D.W. Aylmore, S.J. Gregg and W.B. Jepson, J. Nucl. Mater. 3,2 (1961) 190-200.
14. G. Ervin Jr. and T.L. MacKay, J. Nucl. Mat. 12, 1 (1964) 30-39.
15. A. Leenaers, M. Verwerft, Be/air and Be/steam reactions: microstructure of the beryllium samples, Final report for SEAL1, SCK•CEN, R-3329, 1999.

ACKNOWLEDGMENTS

The author gratefully acknowledges the financial support of the European Commission in the framework of SEAL.

The author also wishes to thank Mr. Kris Penasse for his invaluable technical assistance.

MICROMECHANICAL MODELING OF FRACTURE INITIATION IN BERYLLIUM

R. Chaouadi and M. Scibetta
SCK•CEN, Boeretang 200, 2400 Mol, Belgium.
Tel: +32 14 332231
Fax: +32 14 321529
email: rchaouad@sckcen.be

One of the major drawbacks of using beryllium in a neutron environment is its susceptibility to radiation-induced degradation resulting mainly from helium production. The degradation of the mechanical properties are clearly displayed by a drastic loss of ductility and fracture resistance.

This paper investigates the correlation between the tensile properties and fracture initiation toughness of beryllium. Micromechanical modeling associated to detailed finite element calculations allow to better understand the correlation between the flow and the fracture properties in the presence of helium bubbles.

4th IEA International Workshop on
Beryllium Technology for Fusion
15-17 September, 1999

Comparison of Elevated Temperature Properties of HIP'd Impact Ground Beryllium (S-65-H) and HIP'd Gas Atomized (GA) Beryllium

D.E. Dombrowski[1], W.J. Haws[1] and P. Mckeighan[2]

[1]Brush Wellman Inc., 17876 St. Clair Avenue, Cleveland, OH 44110, U.S.A.

[2]Southwest Research Institute , P.O. Drawer 28510, San Antonio, TX 78228-0510, U.S.A.

Abstract

Fusion designers have been limited to simple tensile properties and physical properties for modern beryllium grades. The work reported here expands the elevated temperature database to more complicated mechanical tests. The elevated temperature (ambient to 648°C) thermomechanical properties of two beryllium grades made by Hot Isostatic Pressing (HIP) are compared: S-65H (made from impact ground powder) and GA (made from Gas Atomized powder). Successful measurements of elevated temperature smooth and notched fatigue were made for the first time on modern beryllium grades. Valid beryllium K_{Ic} fracture toughness results were obtained for the first time at temperatures above room temperature. Elevated temperature creep, and tensile are also presented.

Keywords: Beryllium, elevated temperature, fatigue, creep, fracture toughness, tensile properties, ITER, plasma facing components, Hot Isostatic Pressing (HIP)

1.0 INTRODUCTION

Fusion designers have been limited to simple tensile properties and physical properties for modern beryllium grades. The work reported here expands the elevated temperature database to more complicated mechanical tests such as creep , fatigue and fracture toughness.

This work contrasts the elevated temperature mechanical properties of two beryllium grades made by Hot Isostatic Pressing (HIP): S-65-H and HIP'd Gas Atomized powder (GA). Gas atomized beryllium powder is a new beryllium grade which has shown indication of superior fracture toughness [1]. It has the lowest beryllium oxide (BeO) content of all Brush Wellman structural beryllium products. S-65-H is a commercial beryllium grade which has the best high temperature ductility of the conventional impact ground beryllium grades. It also has a lower metallic impurity level than all structural beryllium grades, including HIP'd gas atomized powder. The vacuum hot pressed version of S-65-H is S-65C. S-65C is the ITER reference grade for

beryllium in First Wall applications [2]. A comparison of these two grades over an extended mechanical property test matrix will not only determine which has superior properties, it will indicate which approach to beryllium manufacture has the most potential for improvement of critical elevated temperature properties.

1.1 Background

Both beryllium grades were consolidated by Hot Isostatic Pressing (HIP). The advantage of HIP is that it provides isotropic mechanical, physical and optical properties. It is also much more amenable than vacuum hot pressing to producing a shape close to the final machined shape of a component (near net shape processing).

2.0 Experimental Procedure

2.1 Test Materials

Two different nominally pure beryllium materials were used for this evaluation program. An impact ground powder (S-65-H) was used. A spherical powder (GA) produced by gas atomization was used. This section describes the powder production, blending, and consolidation processes.

2.1.1 Powder Production

2.1.1.1 S-65-H

Impact ground S-65 beryllium powder was obtained from a standard production of impact ground powder. Process details are described elsewhere [3]. The impact grinding process involves pneumatic acceleration of machining chips taken from a vacuum cast beryllium billet to a high velocity towards a solid beryllium target. The impact causes the particles to fracture into finer and more symmetric particles. Oversized particles are recycled through the grinding process until they reach the desired degree of fineness. Powders are blended to assure uniformity and then characterized by analysis of chemistry and particle size distribution.

2.1.1.2 Gas Atomized Spherical Be

The gas atomized spherical beryllium powder (GA) was produced by inert gas (nitrogen) atomization. Process details are described elsewhere [3]. The process includes the vacuum melting of solid stock and pouring through a fine nozzle. The molten stream is impinged with a high velocity gas stream breaking the stream into fine droplets which solidify into spherical particles. This material is screened to remove oversize material and blended to provide a uniform product. The powder is then characterized by chemical analysis and particle size distribution as determined by Coulter Counter.

2.1.2 Powder Consolidation

The two powders were consolidated by hot isostatic pressing (HIP) to produce a relatively isotropic solid material. The HIP process was the same for both materials. The basic process includes loading the powder into a mild steel container, high temperature vacuum degassing to remove adsorbed gases, hermetically sealing the can, and consolidating at a temperature (1050°C) and pressure to (103 MPa) achieve full density. The quality of the HIP'd billet is determined by density measurement, thermal induced porosity (T.I.P.) measurement, and room temperature tensile tests. The T.I.P. test measures the amount of inert gaseous contaminants which were trapped in the microstructure after HIP. These gases are present as a result of incomplete degassing or loss of hermeticity during

HIP. The test consists of a density measurement before and after a heat treatment procedure(788 °C for beryllium). The minimum bulk density after T.I.P. for S-65-H is 99.7% of theoretical density with a maximum decrease in density due to T.I.P. of 0.2% of theoretical density.

2.1.3 Heat Treatment

The HIP'd billets for both grades were given the proprietary S-65 heat treatment to maximize elevated temperature ductility. This heat treatment is how the GA material differs from the recently introduced O-30-H beryllium grade, which is based on the same spherical beryllium powder.

2.2 Test Matrix

The test matrix for the S-65-H beryllium and the gas atomized spherical beryllium is shown in Table 1. Two orientations of test specimen were tested, longitudinal and transverse. Longitudinal and transverse represent the orientation of the specimen gage length with regard to the axis of loading of the HIP billet with longitudinal being parallel to the axis of loading and transverse being perpendicular to the axis of loading. Schematic drawings of the test specimens are found in the Appendix.

2.3 Tensile

The tensile testing was performed in accordance with the specifications of ASTM E8, E4, and E21. In addition the special requirements for beryllium testing as recommended by the Materials Advisory Board [4] were also followed particularly the strain rate requirement of 8.3×10^{-5} s^{-1} up to 1% strain measurement, and 8.3×10^{-4} s^{-1} thereafter. Single specimens were tested at room temperature and at 150°C, 205°C, 260°C, 315°C, 370°C, 425°C, 480°C, 540°C, and 650°C. Specimens were tested in two orientations, longitudinal and transverse which represent the orientation of the specimen gage length with regard to the axis of loading of the HIP billet. The properties measured were ultimate strength, 0.2% yield strength, upper yield strength, lower yield strength, % elongation, and reduction in area.

2.4 Notched Tensile

The notched tensile testing was performed in accordance with the specifications of ASTM E602. Specimens were tested in two orientations, longitudinal and transverse. The stress concentration factor (K_t) for these tests was 3. The property measured was ultimate notch strength.

2.5 Creep

Creep testing was performed in accordance with the specifications of ASTM E139. Single specimens were tested at 90% of the yield strength at temperatures 150°C, 205°C, 260°C, 315°C, 370°C, 425°C, 480°C, 540°C, and 650°C. Single specimens were also tested at 70% of the yield strength at the same temperatures. Creep tests performed at temperatures higher than 205°C were performed in vacuum. The specimen orientation for these tests was transverse.

2.6 Fracture Toughness

Fracture Toughness Testing was performed in accordance with the specifications of ASTM E399-90 (K_{Ic}) and ASTM E813 (J_{Ic}). Based upon the fracture toughness pretesting performed at SWRI, it was determined that it was

Table 1 Test Matrix for S-65-H and Gas Atomized Spherical Be

TEST	ORIENTATION	LOAD	TEST TEMPERATURE									
			RT	150°C	205°C	260°C	315°C	370°C	425°C	480°C	540°C	650°C
TENSILE	LONGITUDINAL		1	1	1	1	1	1	1	1	1	1
	TRANSVERSE		1	1	1	1	1	1	1	1	1	1
NOTCHED TENSILE	LONGITUDINAL		1	1	1	1	1	1	1	1	1	1
	TRANSVERSE		1	1	1	1	1	1	1	1	1	1
FRACTURE TOUGHNESS	L-T		1	1	1	1	1	1	1	1	1	1
CREEP	TRANSVERSE	90% YS		1	1	1	1	1	1	1	1	1
		70% YS		1	1	1	1	1	1	1	1	1
FATIGUE	TRANSVERSE	90% YS	3	1	3	1	3	1	3	1	3	3
		70% YS	2		2		2		2			
NOTCHED FATIGUE	TRANSVERSE	90% YS	3	1	3	1	3	1	3	1	3	3

appropriate to measure K_{IC} between room temperature and 260°C and to measure J_{IC} between 315°C and 650°C. The specimen orientation for these tests was L-T.

2.7 Smooth Axial Fatigue

Axial Fatigue Testing was performed in accordance with the specifications of ASTM E466. The Run Out level is 10^6 cycles for all tests. The stress ratio ($_{max}$/ $_{min}$), R, for these tests was -1 which means that the stress on the specimen was cycled between tension and compression with the same stress level. Testing was performed at maximum stress levels of 90% and 70% of the yield strength. The test temperatures were room temperature, 150°C, 205°C, 260°C, 315°C, 370°C, 425°C, 480°C, 540°C, and 650°C. The test matrix is shown in Table 2. Specimen orientation for these tests was transverse. Axial fatigue tests performed at temperatures higher that 205°C were performed in vacuum. Nominal test frequency was 30 Hz. Test frequency at the start of each test was 2 Hz. The frequency was increased when the internal gage section is no longer present. The waveform was sinusoidal.

2.8 Notched Axial Fatigue

Notched Axial Fatigue Testing was performed in accordance with the specifications of ASTM E466 and ASTM E-468. The Run Out level is 10^6 cycles for all tests. The stress ratio ($_{max}$/ $_{min}$), R, for these tests was -1 which means that the stress on the specimen was cycled between tension and compression with the same stress level. The notch was made to result in a stress concentration factor K_t = 3. Testing was performed at maximum stress levels of 90% and 70% of the yield strength.

Table 2 Axial Fatigue Test Matrix

Test Temp.	Load % YS	Number of Tests
RT	90% YS	3
RT	70% YS	2
150°C	90% YS	1
205°C	90% YS	3
205°C	70% YS	2
260°C	90% YS	1
315°C	90% YS	3
315°C	70% YS	2
370°C	90% YS	1
425°C	90% YS	3
425°C	70% YS	2
480°C	90% YS	1
540°C	90% YS	3
650°C	90% YS	3

The test temperatures were room temperature, 150°C, 205°C, 260°C, 315°C, 370°C, 425°C, 480°C, 540°C, and 650°C. The test matrix for notched fatigue is the same as that of the smooth axial fatigue and is shown in Table 2. Specimen orientation for these tests was transverse. Notched axial fatigue tests performed at temperatures higher that 205°C were performed in vacuum. Nominal test frequency was 30 Hz. Test frequency at the start of each test was 2 Hz. The frequency was increased when the internal gage section is no longer present. The waveform was sinusoidal.

3.0 Results and Discussion

3.1 Qualification Of Consolidated Billet

After HIP consolidation the billet is leached in nitric acid to remove the mild steel HIP container. Several tests are performed to qualify the billet before further processing into components. These tests include thermal induced

porosity (TIP) test at 788°C, grain size measurement, room temperature tensile properties, microyield strength, linear coefficient of thermal expansion (CTE) and chemical analysis.

3.1.1 S-65-H Billet

The results of the chemical analysis performed on the solid billet and the powder used to produce the billet are presented in Table 3. The table shows that the billet meets the chemical composition specifications for S-65-H.

Based upon the chemical analysis of the solid billet which indicated a BeO content of 0.7 weight %, the theoretical density of the S-65-H billet is 1.8527 g/cc. The densities of the billet before T.I.P. test and after T.I.P. test at 788°C are presented in Table 4. The minimum bulk density for S-65-H is 99.7% of theoretical density with a maximum decrease in density due to T.I.P. of 0.2% of theoretical density. These measurements are well within the specification for theoretical density and well within the requirements for change in density due to the T.I.P. resistance test.

The microstructure of the HIP billet is uniform. The average grain size was measured in accordance with ASTM E-112 using the line intercept method at 500x magnification. The average grain size was found to be 6.6 μm with the maximum grain size of 36.0 μm. The specification for the grain size in S-65-H is that the average grain size not exceed 15 μm. The grain size is well within specification for S-65-H.

The linear coefficient of thermal expansion (CTE) was measured in three orthogonal directions (two transverse directions and longitudinal direction respectively) as 11.39 ppm/°C, 11.39 ppm/°C, and 11.34 ppm/°C for the temperature range of 5-65°C. There is no S-65-H specification for the value; the specification only requires that the values be reported.

3.1.2 Gas Atomized Spherical Be Billet

The results of the chemical analysis performed on the solid billet and the powder used to produce the billet are presented in Table 5. There are no chemical composition specifications for gas atomized powder but the billet meets the chemical composition specifications for S-65-H for all elements with the exception of the iron content, which is 900 ppm as opposed to the specification level of 800 ppm.

Based upon the chemical analysis of the solid billet (0.32% BeO), the theoretical density of the gas atomized spherical Be Billet is 1.8500 g/cc. The densities of the billet before T.I.P. and after T.I.P. at the two temperatures are presented in Table 5. There is no specification for gas atomized powder but these results are well within the specification for theoretical density and well within the requirements for change in density due to the T.I.P. resistance test for S-65-H.

The microstructure of the HIP billet is uniform. The average grain size was measured in accordance with ASTM E-112 using the intercept method at 500x magnification. The average grain size was found to be 9.5 μm with the maximum grain size of 57.0 μm. There is no specification for the grain size of HIP'd gas atomized spherical Be billets but this grain size is within the specification for S-65-H. It should be noted that the gas atomized spherical Be powder is considerably coarser than the S-65-H powder.

Table 3 **Chemical Analysis of HIP'd S-65-H Billet (Lot H0984) and Powder Lot Used to Produce S-65-H Billet.**

Element	Powder Lot 950810	HIP Lot H0984	S-65-H Specification
Be		99.89%	99.0% min.
BeO	0.72%	0.70%	1.0% max.
C	0.013%	0.012%	0.10% max.
Fe	615 ppm	695 ppm	800 ppm max.
Al	195 ppm	200 ppm	600 ppm max.
Si	135 ppm	135 ppm	600 ppm max.
Mg	15 ppm	30 ppm	600 ppm max.
Zn	<10 ppm	<10 ppm	
Ni	125 ppm	135 ppm	
Mn	20 ppm	20 ppm	
Sc	<5 ppm	<5 ppm	
Cu	60 ppm	75 ppm	
Ag	<3 ppm	<3 ppm	
Ti	20 ppm	15 ppm	
Co	5 ppm	6 ppm	
Pb	<20 ppm	<20 ppm	
Ca	<20 ppm	<20 ppm	
W	<100 ppm	<100 ppm	
U	45 ppm	35 ppm	
Mo	<20 ppm	<20 ppm	
Cr	15 ppm	15 ppm	
N	175 ppm	90 ppm	
Zr	20 ppm	30 ppm	

Note: Total of all other metallic impurities 400 ppm maximum

Table 4 T.I.P. Response of HIP'd S-65-H Billet H0984

Condition	Density (g/cc	% Theoretical Density
Pre-T.I.P.	1.8517	99.95
After 1450°F T.I.P.	1.8514	99.93

Table 5 Chemical Analysis of HIP'd Gas Atomized Spherical Be Billet (Lot H1001) and Powder Lot Used to Produce Gas Atomized Spherical Be Billet.

Element	Powder Lot 960117	HIP Lot H1001
Be		
BeO	0.32%	0.32%
C	0.066%	0.066%
Fe	895 ppm	900 ppm
Al	335 ppm	335 ppm
Si	225 ppm	245 ppm
Mg	105 ppm	105 ppm
Zn	<10 ppm	<10 ppm
Ni	135 ppm	135 ppm
Mn	50 ppm	45 ppm
Sc	<5 ppm	<5 ppm
Cu	80 ppm	75 ppm
Ag	<3 ppm	<3 ppm
Ti	40 ppm	40 ppm
Co	6 ppm	7 ppm
Pb	<20 ppm	<20 ppm
Ca	<20 ppm	<20 ppm
W	<100 ppm	<100 ppm
U	65 ppm	50 ppm
Mo	<20 ppm	<20 ppm
Cr	75 ppm	75 ppm
N	465 ppm	405 ppm
Zr	30 ppm	30 ppm

Table 6 T.I.P. Response of HIP'd Gas Atomized Spherical Be Billet H1001

Condition	Density (g/cc)	% Theoretical Density
Pre-T.I.P.	1.8510	100.05
After 1450°F T.I.P.	1.8510	100.05

The linear coefficient of thermal expansion (CTE) was measured in three orthogonal directions (two transverse directions and longitudinal direction respectively) as 11.49 ppm/°C, 11.44 ppm/°C, and 11.43 ppm/°C for the temperature range of 5-65°C.

3.2 Tensile Testing

3.2.1 S-65-H Billet

The results of tensile testing are presented in Table 7 and Figure 1. This data was collected without an extensometer at the high temperatures due to mechanical problems with the high temperature extensometer. The rate of crosshead movement was linked to the chart speed to collect a load vs. displacement curve. The values presented in Table 7, as measured without the use of an extensometer, are consistent with previous data for S-65-H. A yield point was not observed for any of the specimens.

The data showed little difference between the longitudinal and transverse testing direction. This was expected since the particle shape is somewhat isotropic and the consolidation method was isostatic.

3.2.2 Gas Atomized Spherical Be Billet

The results of tensile testing are presented in Table 8 and Figure 1. A yield point was not observed for any of the specimens. This data was collected without an extensometer at the high temperatures due to mechanical problems with the high temperature extensometer. This procedure was shown to be accurate based upon the S-65-H testing results.

The data showed little difference between the longitudinal and transverse testing direction. This was expected since the gas atomized powder is spherical and the consolidation method was isostatic.

Comparison of HIP'd GA with GA Made in 1990

Previous work [5] obtained the room temperature tensile and fracture toughness properties of a spherical beryllium powder produced by inert gas atomization of S-200F grade beryllium feedstock with argon gas. Properties were obtained for both HIP'd and VHP'd spherical beryllium powder.

A comparison of the properties obtained for the present gas atomized powder and those obtained previously are shown in Table 9. Properties of the HIP'd GA beryllium made for the present work are consistent with the previous work. Deviations from the other values can be explained based on known processing-property relationships. The present work HIP'd GA has higher strength than the other HIP'd GA (cases A and B) because it was HIP'd at lower temperature. It has lower percent elongation than case A because it was HIP'd at lower temperature and there is insignificant differences in grain size. Similarly, the difference between the present work and previous values is consistent with differences in grain size, consolidation temperature and input powder sieve fraction.

Table 7 **Tensile Properties of HIP'd S-65-H Be for Longitudinal and Transverse Specimen Orientations**

Specimen ID	Specimen Orientation	Test Temp. (°C)	Ultimate Tensile Strength (MPa)	0.2% Offset Yield Strength (MPa)	Elongation (%)	Reduction in Area (%)
A1	Longitudinal	23	462	288	4.8	4.8
A105	Longitudinal	150	431	292	25.9	18.8
A106	Longitudinal	205	390	276	34.4	27.6
A11	Longitudinal	260	352	248	56.4	57.2
A107	Longitudinal	315	308	232	62.2	70.1
A108	Longitudinal	370	272	207	65.0	75.0
A113	Longitudinal	425	248	190	50.2	74.8
A110	Longitudinal	480	225	174	38.6	68.9
A111	Longitudinal	540	201	156	36.3	58.1
A112	Longitudinal	650	120	92	19.5	16.8
A12	Transverse	23	464	302	5.5	6.0
A137	Transverse	150	428	290	14.5	12.4
A138	Transverse	205	390	274	26.2	21.2
A139	Transverse	260	348	258	53.6	55.0
A22	Transverse	315	312	228	64.0	73.7
A140	Transverse	370	277	209	58.5	74.8
A23	Transverse	425	248	195	53.1	73.9
A141	Transverse	480	224	174	41.1	69.1
A142	Transverse	540	201	157	37.8	59.0
A143	Transverse	650	116	92	18.4	16.5

3.2.3 Comparison of S-65-H and GA Tensile Properties

Figure 1 compares the tensile properties of S-65-H and GA beryllium. The mean of longitudinal and transverse properties are shown since there was no significant difference between the two orientations. The ultimate tensile strength and yield strength of S-65-H are greater than GA across most of the temperature range. These properties gradually become closer as temperature is increased. At 480°C and above, these properties are identical. As discussed in the previous section, the difference in room temperature strength is consistent with the grain size difference. At elevated temperatures a greater number of slip systems become active, and the difference in strength decreases. As noted in the metallography section, at some temperature both grades experience grain deformation during testing.

S-65-H has greater percent elongation and reduction in area than GA between room temperature and 650°C. The greater S-65-H room temperature elongation can be attributed to the finer grain size. The greater S-65-H elongation at elevated temperatures is usually attributed to lower impurity levels, a closely controlled Fe/Al ratio, and a

Table 8 **Tensile Properties of HIP'd Gas Atomized Spherical Be for Longitudinal and Transverse Specimen Orientations**

Specimen ID	Specimen Orientation	Test Temp. (°C)	Ultimate Tensile Strength (MPa)	0.2% Offset Yield Strength (MPa)	Elongation (%)	Reduction in Area (%)
A24	Longitudinal	23	388	245	3.2	2.5
A25	Longitudinal	150	345	241	10.7	9.3
A26	Longitudinal	205	321	220	17.8	15.7
A27	Longitudinal	260	296	202	27.5	28.1
A28	Longitudinal	315	274	197	40.8	54.8
A29	Longitudinal	370	252	181	49.4	63.0
A30	Longitudinal	425	233	176	34.9	60.6
A31	Longitudinal	480	221	168	27.9	56.5
A32	Longitudinal	540	205	154	27.8	49.4
A33	Longitudinal	650	130	91.0	16.8	14.9
A35	Transverse	23	380	244	4.2	3.4
A36	Transverse	150	338	233	10.5	9.0
A37	Transverse	205	318	220	15.7	16.7
A38	Transverse	260	296	204	32.7	32.5
A39	Transverse	315	272	187	48.4	54.2
A40	Transverse	370	250	185	47.8	64.1
A41	Transverse	425	232	177	40.0	62.2
A42	Transverse	480	220	173	25.8	55.5
A43	Transverse	540	205	153	28.5	47.9
A44	Transverse	650	128	84.1	13.4	18.7

unique heat treatment which maximizes conversion of all aluminum impurities from low melting point metallic aluminum to the higher melting point intermetallic compound $AlFeBe_4$.

Hall-Petch Relationship

Figure 2 shows room temperature UTS and YS of the present work and 1990 work [5] plotted as a function of the reciprocal square root of grain size. Note that the average of longitudinal and transverse measurements were plotted. The HIP'd GA from the present work is in general agreement with the relationships for UTS and YS derived in the earlier work.

Figure 2 also compares the present room temperature S-65-H data to 1989 data for I-70H. The I-70H shown there was a similar impact ground powder grade which was HIP'd at 827°C [6]. Ultimate tensile strength and yield strength of S-65-H from the present work follows the general Hall-Petch trend for HIP'd beryllium. There is considerable scatter for the impact ground powder data. This is partially attributed to the early manufacturing problems in loading HIP cans with the low symmetry impact

Table 9 Comparison of Room Temperature Mechanical Properties between HIP'd GA made in the present work and HIP'd or VHP'd GA made previously [5].

	Present Work	Previous Work (1990)					
		A	B	C	D	E	F
Sieve Fraction	**- 200 mesh**	- 200 mesh	-200/ +325	- 200 mesh	- 200 mesh	-200/ +325	-200/ +325
Consol. Method	**HIP**	HIP	HIP	VHP	VHP	VHP	VHP
Consol. Temp. (°C)	**1050**	1100	1100	1000	1050	1000	1050
Grain Size (μm)	**9.5**	10.3	12.8	6.9	7.4	9.8	8.6
UTS (MPa) -L	**388**	338	289	404	380	351	352
- T	**380**	348	298	398	381	345	350
0.2% YS (MPa) - L	**245**	212	182	301	245	247	241
- T	**244**	232	185	290	243	238	283
% Elong - L	**3.2**	3.7	2.8	3.0	3.3	2.9	2.2
- T	**4.2**	4.6	3.2	2.5	3.6	2.4	2.2

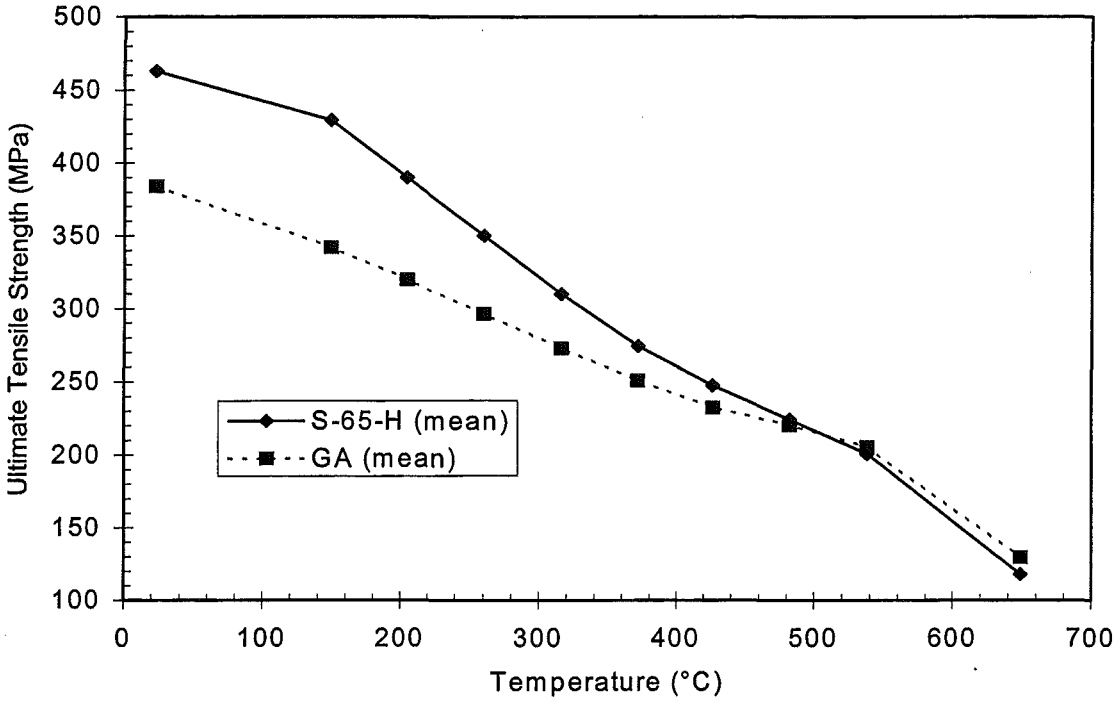

a.

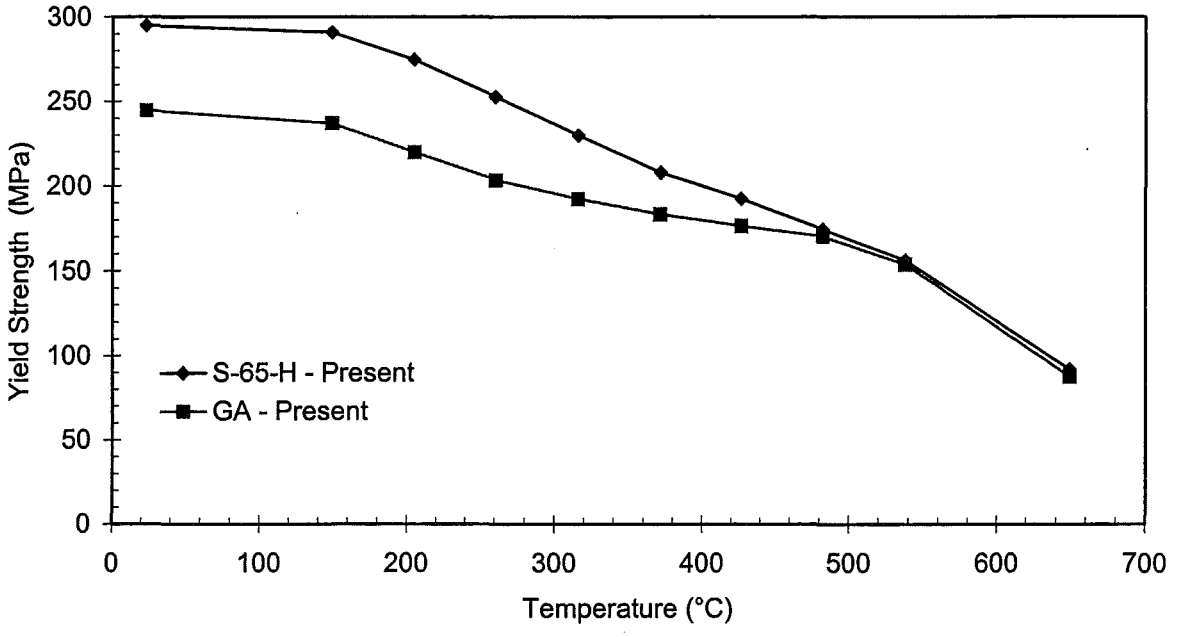

b.

Figure 1. Comparison of S-65-H and GA tensile properties. a. UTS b. YS c. Percent elongation d. Reduction in area

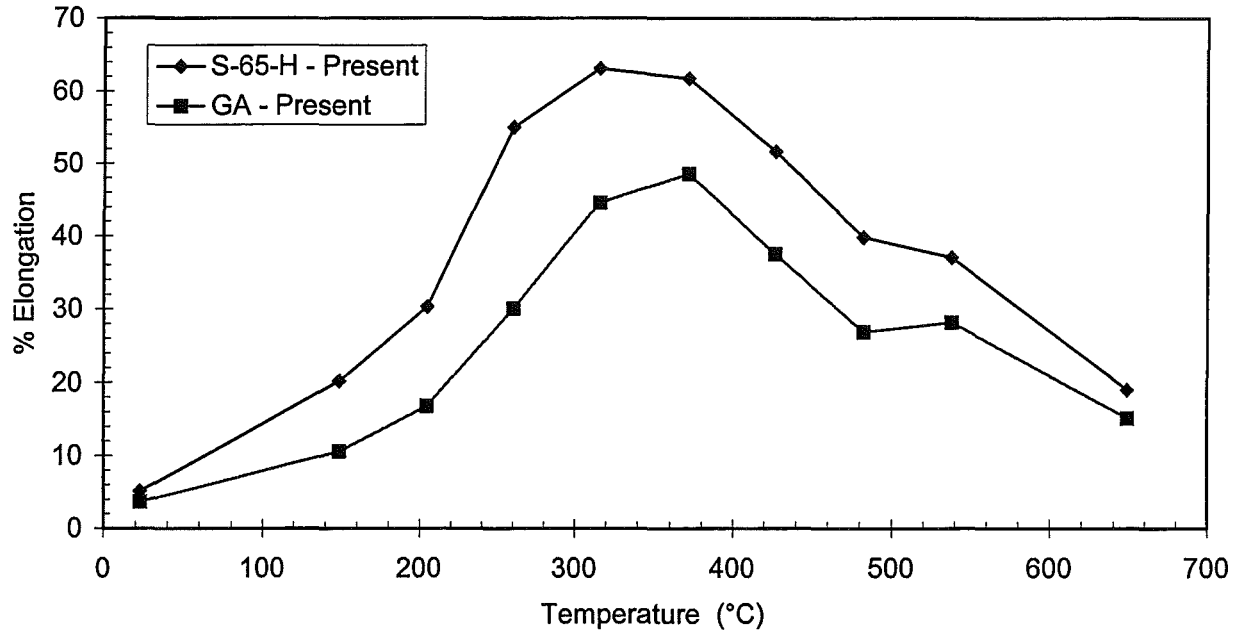

c.

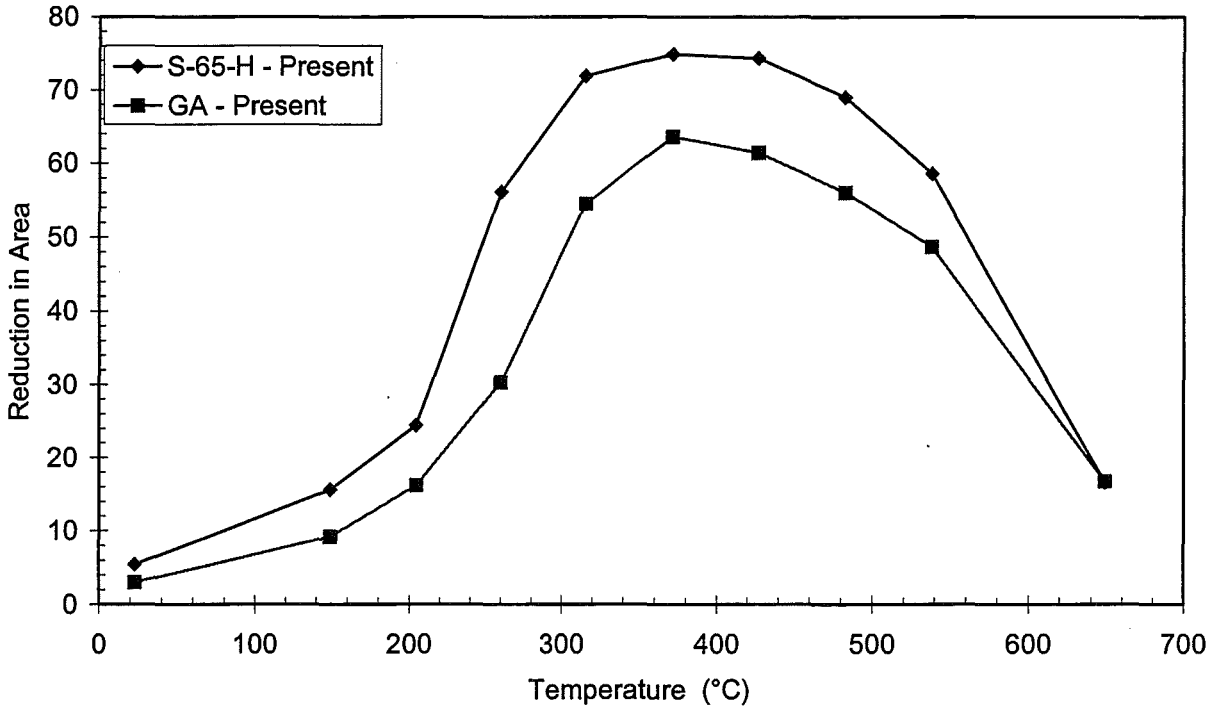

d.

Figure 1, cont.

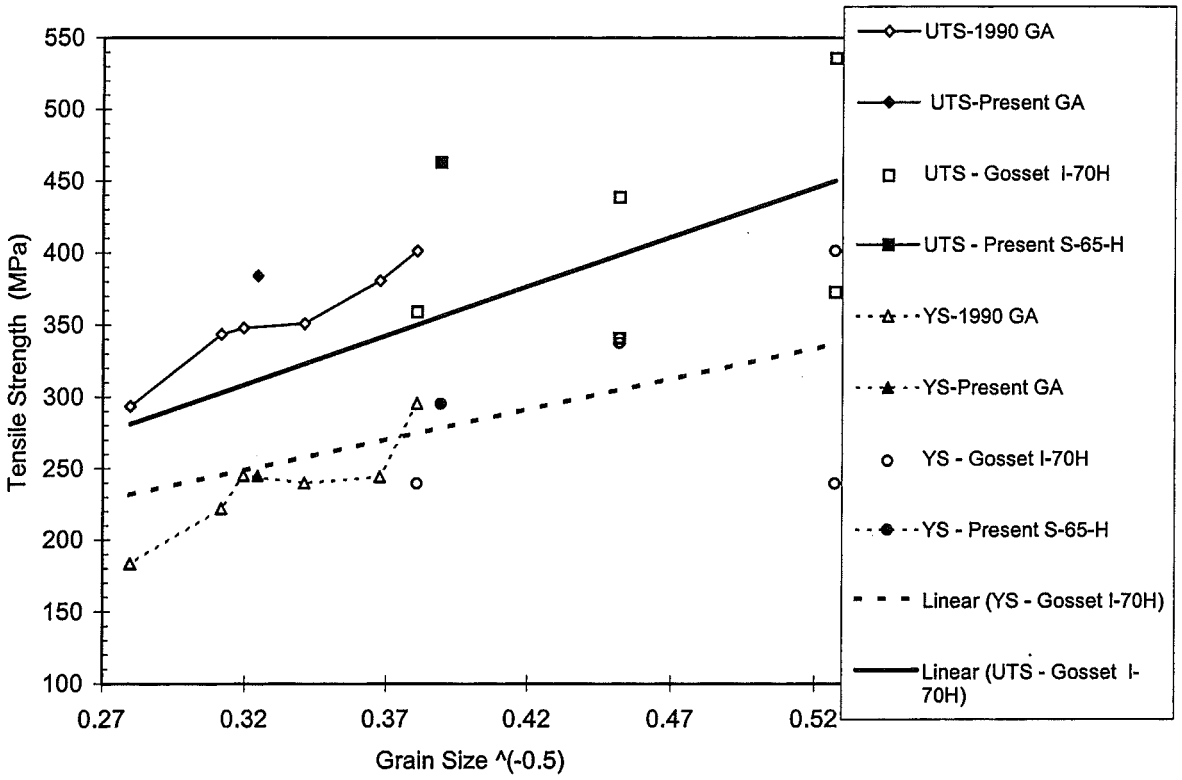

Figure 2 Hall-Petch Plot for HIP'd Gas Atomized Beryllium (GA) and HIP'd Impact Ground Beryllium (S-65-H and early form of I-70H)

ground powder. The material analyzed by Gosset et. al was loaded into HIP cans with continuous vibration and this greatly hindered achievement of random arrangement of the crystallographic directions needed for isotropic properties. Present day practice produces a very isotropic product.

The Hall- Petch plot shows that the differences between S-65-H and GA room temperature ultimate tensile strength and yield strength are consistent with the difference in grain size.

Comparison of S-65-H with VHP Be Grades

Figure 3 compares the tensile properties of S-65-H with the vacuum hot pressed grade S-65C, which is the ITER reference grade. Measurements by Goods et al. [7] , Smith et. al [8] and Chaouadi et. al [9] are shown. S-65-H UTS has close agreement with the measurements by Smith et. al., but the measurements by Goods are consistently lower. S-65-H has higher yield strength than S-65C, but this is consistent with the difference in grain size. The percent elongation measurements are in reasonable agreement between the two grades. The S-65-H reduction in area measurements are in good agreement with the values obtained by Goods up to about 315°C. S-65-H UTS as measured by Chaouadi et al [9] is greater than the S-65-H measured in this study. This may be due to the slightly higher HIP temperature used to produce the present S-65-H. The measurements of Goods et al. for S-65C agree in general with Chaouadi et. al. Similar trends are observed for yield strength.

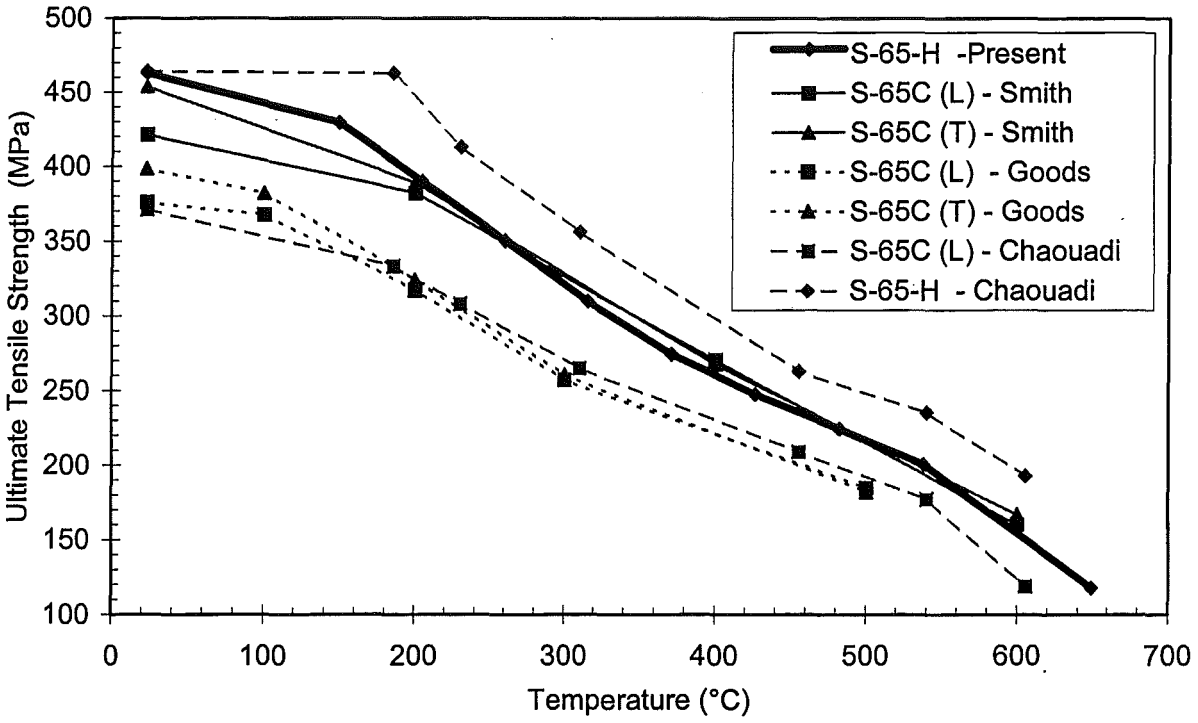

a.

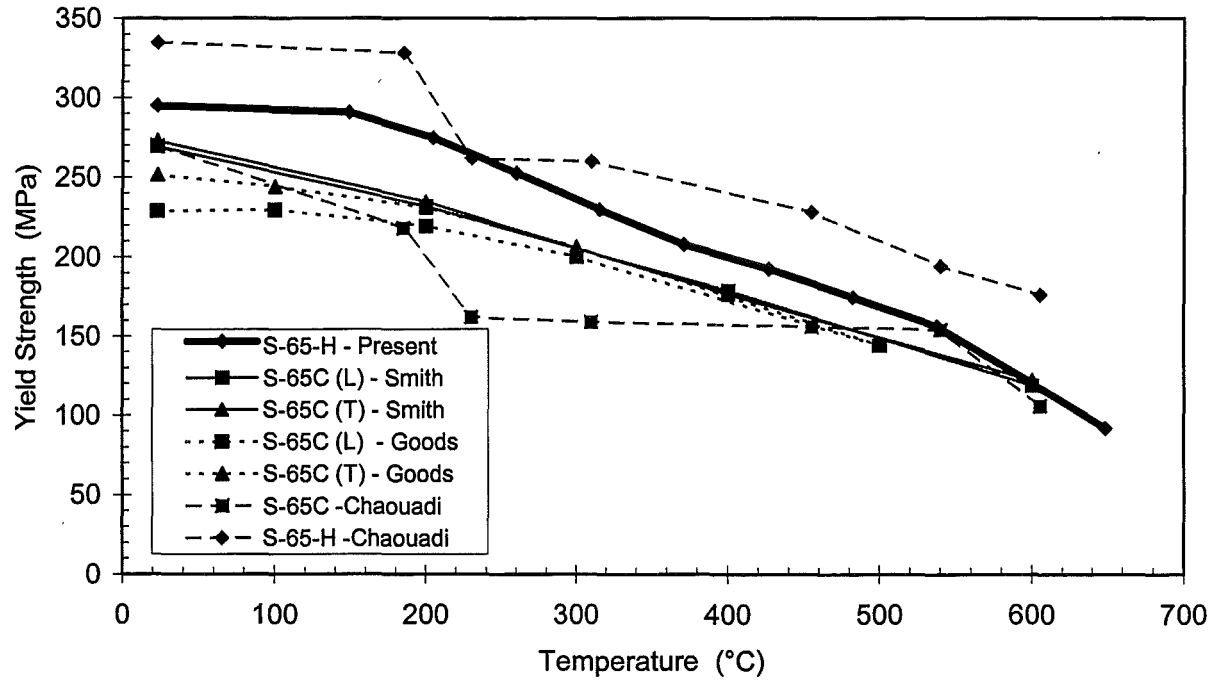

b.

Figure 3 Comparison of Tensile Properties versus Temperature of S-65-H and the Vacuum Hot Pressed Grade, S-65C. a. UTS. b. YS. c. % elongation. d. Reduction in Area

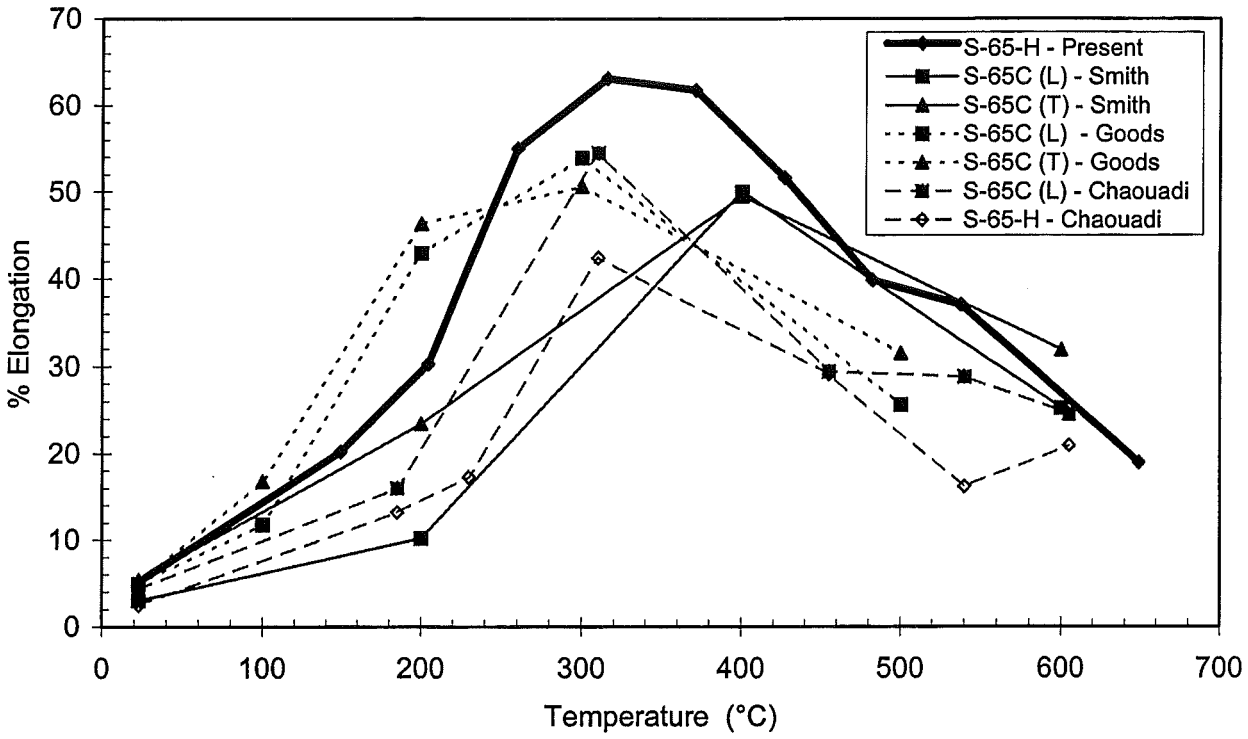

c.

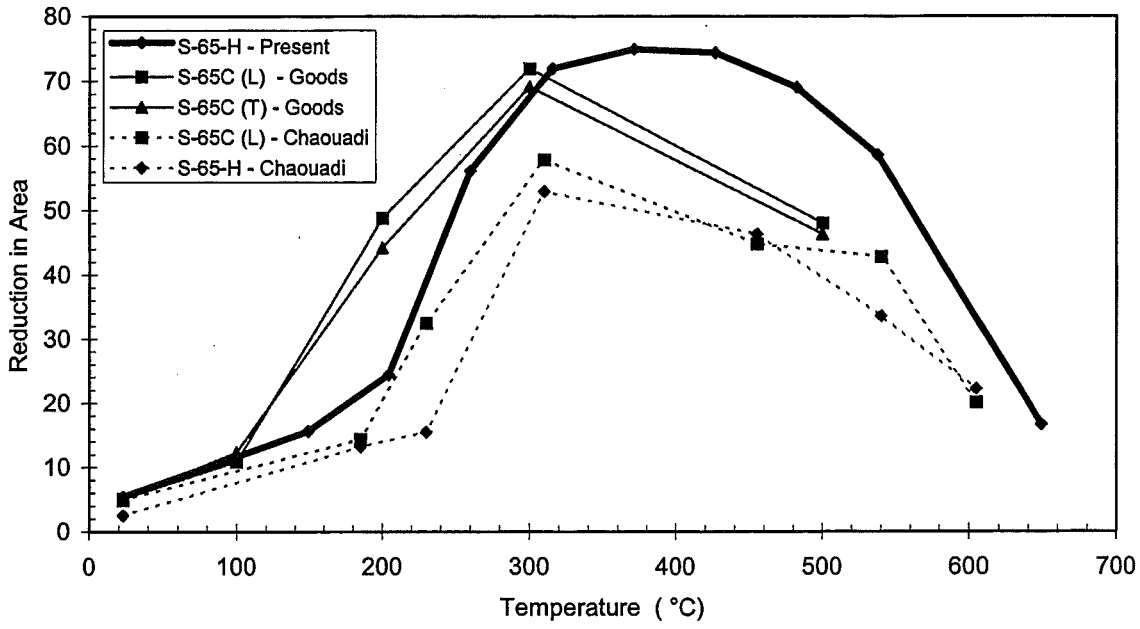

d.

Figure 3, cont.

The present S-65-H percent elongation measurements agree in general with the measurements by others for S-65C. There is a significant difference between the present measurements and those of Chaouadi et al.

The present S-65-H reduction in area measurements agree in general with the measurements by Goods et al. for S-65C. There is significant difference between the present measurements and those of Chaouadi et al in the 300 - 500°C range.

In general, the vacuum hot pressed grades seem to lose their anisotropy in tensile properties at elevated temperatures.

3.3 Notched Tensile

3.3.1 S-65-H Billet

The results of the notched tensile tests performed on both longitudinal and transverse specimens are presented in Table 10. The stress concentration factor for these tests was 3.0. The data shows a slight rise in value from room temperature at about 300°C and then a continuous decrease with increasing temperature. There is little difference between longitudinal and transverse orientations. The data is also shown graphically in Figure 4. The sharp notch strength ratio of S-65-H Be for the transverse orientation is shown in Figure 5. Two notch strength ratios are plotted, the notch strength/yield strength ratio and the notch strength/ultimate strength ratio. Since the Notched Strength/Ultimate Tensile Strength ratios are greater than one for all temperatures, S-65-H is not notch sensitive.

Table 10 Sharp Notch ($K_t = 3$) Tensile Strength of S-65-H Be

Temperature	Sharp Notch Tensile Strength (MPa)	
(°C)	Longitudinal	Transverse
23	461	452
150	449	461
205	476	496
260	469	498
315	460	459
370	415	411
425	374	370
480	339	336
540	284	287
650	153	141

Table 11. Sharp Notch ($K_t = 3$) Tensile Strength of HIP'd GA Be

Temperature	Sharp Notch Tensile Strength (MPa)	
(°C)	Longitudinal	Transverse
23	371	372
149	386	385
204	381	378
260	370	376
316	376	379
371	372	372
427	348	347
482	330	328
538	265	292
649	153	159

3.3.2 Gas Atomized Spherical Be Billet

The results of the notched tensile tests performed on both longitudinal and transverse specimens are presented in Table 11. The stress concentration factor for these tests was 3.0. The data shows a slight rise in value from room temperature at about 400°C and then a continuous decrease with increasing

temperature. There is little difference between longitudinal and transverse orientations. The data is also shown graphically in Figure 4. The sharp notch strength ratio of GA Be is shown in Figure 5 for the transverse specimen orientation. Two notch strength ratios were plotted, the notch strength/yield strength ratio and the notch strength/ultimate strength ratio. Since the Notched Strength/Ultimate Tensile Strength ratios are greater than one for all temperatures, GA is not notch sensitive.

3.3.3. Comparison of S-65-H and GA

Both S-65-H and HIP'd GA are not notch sensitive at all temperatures but room temperature. At room temperature these grades have notch strength ratios (NSR) of 0.97 and 0.96 respectively and are notch sensitive. However, it should be kept in mind that a notch with $K_t = 3$ is a very severe notch; i.e., there is a very steep stress gradient. Overall, the two beryllium grades performed well under this severe condition. The overall behavior is consistent with previous measurements done on S-200F [10]. Notch strength ratio (NSR) is used primarily as a binary measure of notch sensitivity; NSR> 1 means the material is not notch sensitive and NSR<1 means that the material is notch sensitive. Comparison of two NSR above 1 does not provide any further information. Figure 7 compares notch strength ratios of transverse S-65-H and GA specimens. The behavior with temperature is nearly identical. Since both materials exhibit a similar pattern of fracture surface morphology as a function of temperature, it is expected that there is no difference in overall notch behavior.

Sharp notch strength of S-65-H is greater than GA, which is consistent with the higher strength of S-65-H. Sharp notch strength of both materials starts to rapidly decrease with temperature at about 300°C. The sharp notch strength of GA starts that decrease at about 400°C.

3.4 Creep

3.4.1 S-65H Billet

The results of the creep tests are presented in Table 12. The loads are sometimes not exactly 70% YS and 90% YS. This is because the loads for the initial S-65H creep tests were calculated based on initial tensile tests which had a slight extensometer problem. These early tensile test results were discarded, but the creep tests had already been conducted. The creep tests are still valid and useful; the loads just vary from one to seven percentage points off the initially planned %YS.

Table 13 and Figure 6 presents creep rate as a function of loading stress and temperature. Increasing the load from 70% YS to 90% YS increases the creep rate by two orders of magnitude. Creep rate was calculated from the load versus time graphs. There is some fluctuation in values at lower temperatures, but this is expected because the creep rate is so low and often there is significant noise in the creep measurement. Note also that only one data point was taken for each set of conditions.

3.4.2 Gas Atomized Spherical Be Billet

The results of the creep tests are presented in Table 14.

Table 15 and Figure 7 presents creep rate as a function of loading stress and temperature. Increasing the load from.

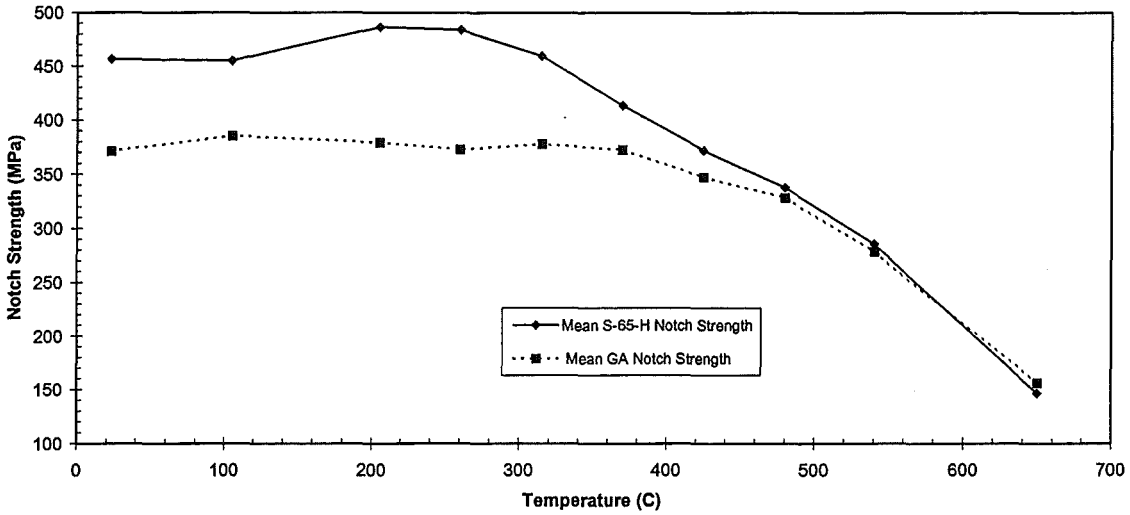

Figure 4 **Sharp Notch Strength ($K_t = 3$) of HIP'd S-65-H Be and GA . Mean of Longitudinal and Transverse Specimen Orientations.**

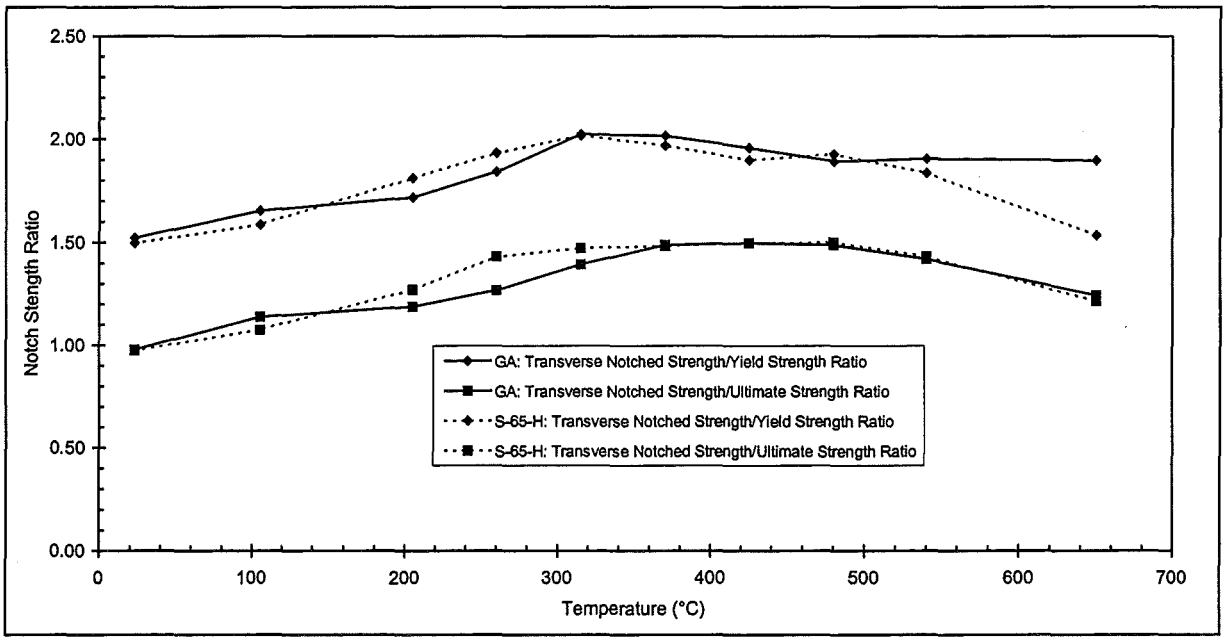

Figure 5. Comparison of Notch Strength Ratios ($K_t = 3$)for Transverse S-65-H and HIP'd GA Be.

Table 12 S-65-H Transverse Creep Test Data. Tests Using 90% Yield Strength Loads are in Clear Text. Tests Using 70% Yield Strength Loads Are Shaded.

Test Temp. (°C)	Stress (MPa)	Time to % Creep (hrs)					Duration (hrs)	Final Creep (%)	Status
		0.1	0.2	0.5	1.0	2.0			
150	245	6.60	10.2				23.3	0.47	Discontinued
150	191						403.6	0.20	Discontinued
205	233	0.86	1.20	1.90	60.0		137.8	1.08	Discontinued
205	181	308					407.7	0.11	Discontinued
260	214	0.04	0.09	0.26	0.81		169.3	1.82	Discontinued
260	167	0.09	0.17	0.53			426	0.78	Discontinued
315	200	0.05	0.09	0.25	0.75		74.6	1.68	Discontinued
315	156	0.05	0.11	0.31	254		472.8	1.05	Discontinued
370	190	0.04	0.07	0.24	0.70		311.7	1.62	Discontinued
370	148	0.06	0.12	0.32	13.0		404.6	1.10	Discontinued
425	170	0.00	0.01	0.07	0.30	7.70	20.6	2.24	Discontinued
425	132	0.03	0.09	0.25	1.20		622.6	1.11	Discontinued
480	153	0.02	0.06	0.22	0.90	6.60	19.2	4.68	Failed
480	119	0.16	0.50	191.			407.5	0.61	Discontinued
540	127	0.00	0.01	0.03	0.10	0.20	0.4	4.25	Failed
540	98	0.02	0.04	0.14	0.40	27.0	56.4	4.11	Failed
650	82	0.01	0.02	0.04	0.07	0.11	0.1	3.28	Failed
650	64	0.02	0.05	0.15	0.50	2.10	3.1	3.61	Failed

Table 13. S-65-H Creep Rate as a Function of Load and Temperature

Temp. (°C)	Creep Rate (percent/sec)	
	90% YS	70%YS
150	NA	4.92E-08
205	2.94E-07	NA
260	1.85E-07	4.49E-09
315	7.44E-07	6.51E-08
370	5.56E-08	5.59E-08
425	5.56E-06	7.41E-09
480	3.81E-05	1.74E-07
540	0.003254	5.2E-06
650	0.004348	0.000148

NA = not available

Table 14 HIP'd GA Be Transverse Creep Test Data. Tests Using 90% Yield Strength Loads are in Clear Text. Tests Using 70% Yield Strength Loads Are Shaded.

Test Temp. (°C)	Stress (MPa)	Time to % Creep (hrs)					Duration (hrs)	Final Creep (%)	Status
		0.1	0.2	0.5	1.0	2.0			
150	213	0.14	0.56	15.70			65.4	0.64	Discontinued
150	165	387.0					401.2	0.10	Discontinued
205	198	0.04	0.19				42.7	0.48	Discontinued
205	154	22.00					425.8	0.11	Discontinued
260	183	0.04	0.10	0.31	1.30		39.7	1.11	Discontinued
260	142	0.07	0.10	0.34			425.4	0.97	Discontinued
315	173	0.03	0.09	0.41			23.4	0.72	Discontinued
315	134	0.03	0.09	0.25	1.10		405.2	1.16	Discontinued
370	165	0.02	0.07	0.23	1.00		91.3	1.20	Discontinued
370	128	0.05	0.07	0.19	0.80		425.9	1.38	Discontinued
425	158	0.01	0.07	0.20	0.70		500	1.37	Discontinued
425	123	0.03	0.06	0.20	0.70		402.9	1.30	Discontinued
480	153	0.03	0.08	0.27	8.10	164.	413.3	2.71	Discontinued
480	119	0.03	0.07	0.19	0.60		157	1.84	Discontinued
540	138	0.02	0.05	0.15	0.40	3.00	94.8	11.01	Failed
540	108	0.01	0.04	0.15	0.50	29.00	175	6.61	Failed
650	79	0.01	0.04	0.09	0.20	0.60	2.4	9.07	Failed
650	61	0.03	0.06	0.17	0.50	3.00	11.5	6.38	Failed

Table 15. HIP'd GA Be Creep rate as a Function of Load and Temperature

Temp. (°C)	Creep Rate (percent/sec)	
	90% YS	70%YS
150	5.74E-07	2.34E-08
205	1.76E-07	1.77E-09
260	2.06E-07	5.09E-09
315	2.25E-07	1.32E-08
370	3.31E-06	1.11E-08
425	6.49E-08	2.37E-08
480	7.06E-07	3.71E-07
540	2E-05	5.66E-06
650	6.52 E-04	9.79E-05

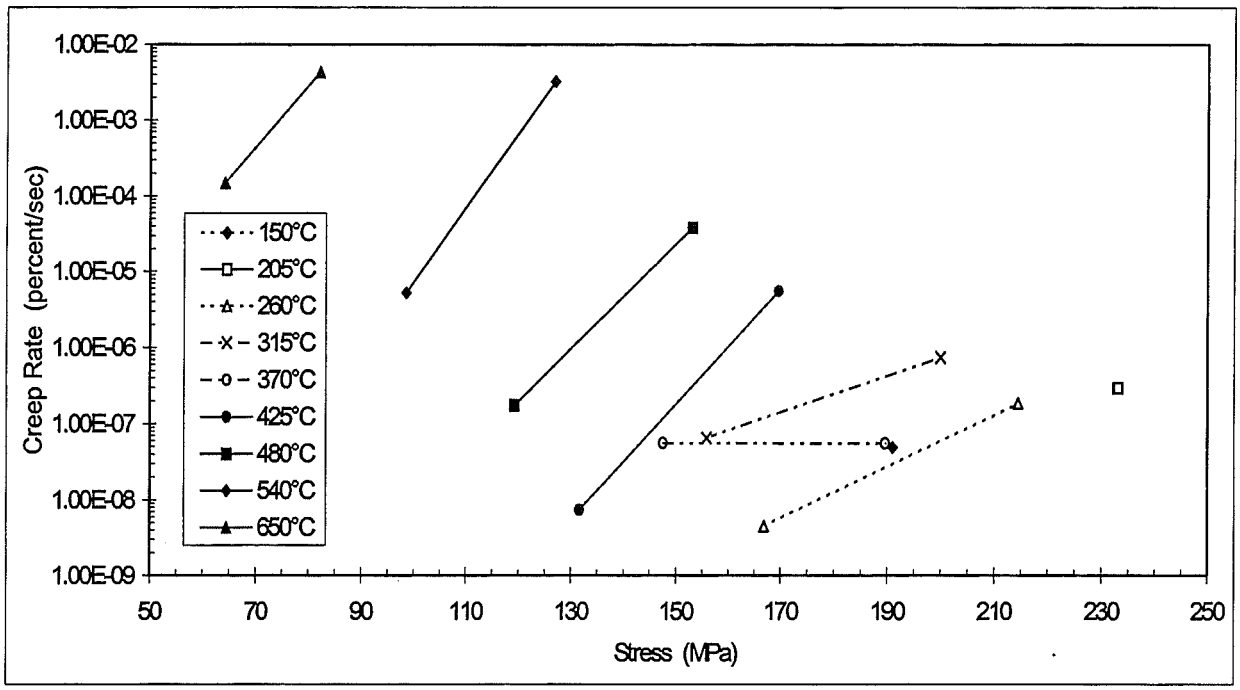

Figure 6 Stage II Creep Rate as a Function of Temperature and Load for S-65-H

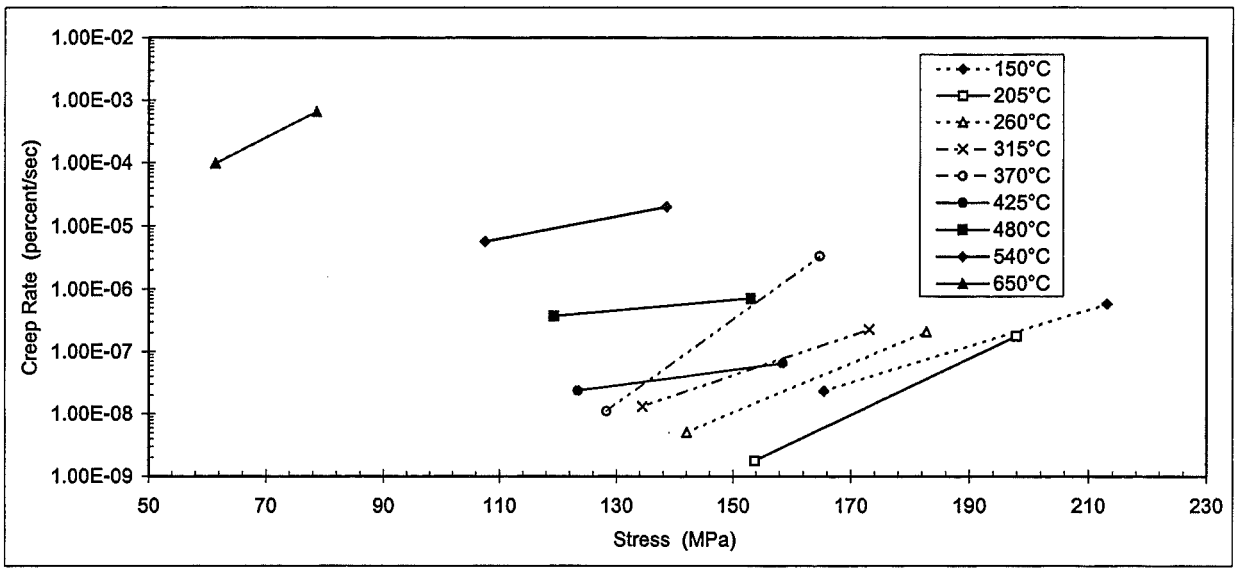

Figure 7 Stage II Creep Rate as a Function of Temperature and Load for GA

70% YS to 90% YS increases the creep rate by two orders of magnitude

3.4.3 Comparison of S-65-H and GA Creep

The stage II creep rates of the two beryllium grades are compared in Figure 8 for 480-650°C. GA clearly has the lower creep rate for this range of temperature and stresses.

Chawla and Meyers [11] note that creep typically becomes important in the range $0.5T_M < T < T_M$ (where T_M and T are in degrees Kelvin). This is because creep is dependent on diffusion. T_M for beryllium is 1562K and 0.5 T_M is 781K (508°C). Beryllium creep behavior is consistent with that. In the present work, the final change in length of the creep specimens is less than the tensile elongation up to the 480°C tensile temperature. At 480°C and above, creep rupture occurs. 480°C is reasonably close to $0.5T_M$.

The present program was not designed to determine creep mechanisms. However, the results of Webster and Crooks [12-13] can be used to discuss the relative behavior of the two beryllium grades. In their first paper, Webster and Crooks stated that the creep strength of beryllium is controlled by grain size, oxide distribution, initial dislocation density and concentration of certain impurity elements (Al + Si + Mg) in the 650-1150°C temperature range [12]. Coarser grain size, higher initial dislocation density, BeO at the grain boundaries and lower impurity content result in higher creep strength. In their second paper [13], Webster and Crooks noted that creep resistance was found to markedly decrease when BeO content was less than 1 wt%. Table 16 compares grain size ,impurity content, and BeO content for S-65H and GA. Oxide distribution and initial dislocation density have not been determined for these.
Given the significantly better stage II creep rate of GA, grain size appears to be important in this temperature and stress range. However, the difference in average grain size is actually quite small (3 μm) and the maximum grain size measurements indicate that there may be considerable overlap. Figure 6 in Webster and Crooks [12] shows almost no effect of grain size for a medium purity industrial grade beryllium at 650°C. The influence of impurity content appears to be small in the temperature and stress range used in the present program. Thisdoes not necessarily contradict Webster and Crooks [12]; they state that the effect of impurities begins at about 760°C.

It is hypothesized that the main difference between creep behavior of these two beryllium grades in the present temperature and stress regime may be oxide distribution. There may be tendency for the oxide to be distributed at the prior particle boundaries and grain boundaries for the gas atomized grade. This would have to be confirmed by transmission electron microscopy. Initial dislocation density could be measured with that technique also. The initial dislocation density of these two grades is unknown, but Webster and Crooks [12] state that it should be high for beryllium HIP'd at temperatures below 1093°C, which is the case here.

Comparison of Creep Behavior With Other Beryllium Grades

It is difficult to make a meaningful comparison with the creep rates measured for other beryllium grades.

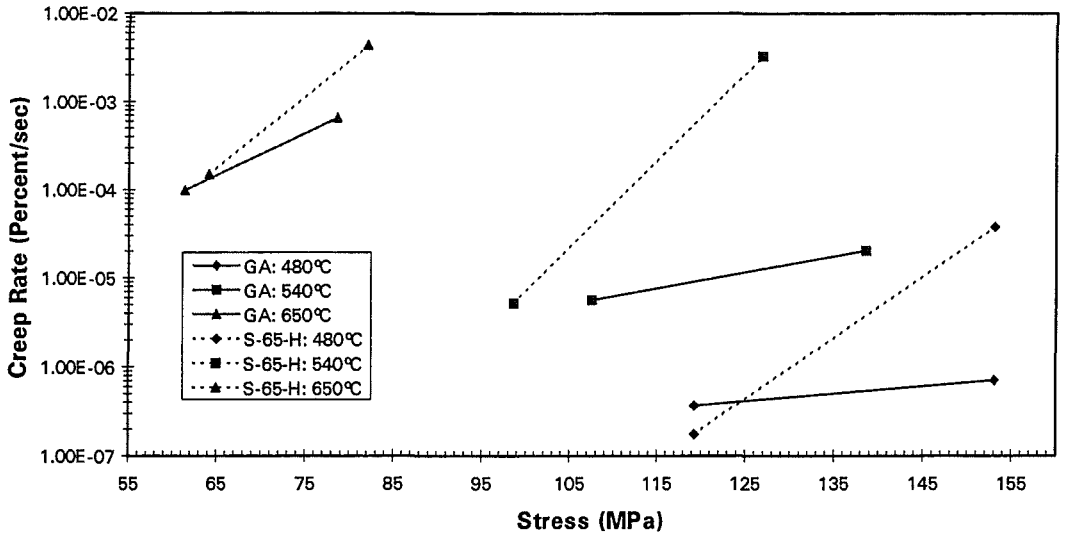

Figure 8 Comparison of Stage II Creep Rates for S-65-H and GA at 480, 540 and 650°C

Table 16 Comparison of Creep Prediction Parameters for S-65-H and HIP'd GA Be.

Parameter	Value		Grade With Better Creep Strength as Predicted by This Parameter
	S-65-H	HIP'd GA	
Average Grain Size (μm)	6.6	9.5	GA
Maximum Grain Size (μm)	36	57	GA
Impurity Content Al + Si + Mg (ppm)	365	685	S-65-H
BeO (wt%)	0.70	0.32	S-65-H

Creep of beryllium was studied in the early 1970s, and those studies used test temperatures (>760°C) well above the temperatures used in this program [14].

3.5 Smooth Axial Fatigue

3.5.1 S-65-H Billet

The results of the smooth axial fatigue testing with R=-1 are presented in Table 17. The loads are sometimes not exactly 70% YS and 90% YS. This is because the loads for the initial S-65H fatigue tests were calculated based on initial tensile tests which had a slight extensometer problem. These early tensile test results were discarded, but the fatigue tests had already been conducted. The fatigue tests are still valid and useful; the loads just vary from one to seven percentage points off the

initially planned %YS. Figure 9 is a plot of load stress versus number of cycles before failure (S/N plot). Note that all specimens which achieved one million cycles were run outs with the exception of the 425°C test specimen with highest number of cycles (1.2 million). 70% YS loads had run outs at all temperatures except possibly 425°C. Even at 425°C fracture occurred in only one of the million cycle samples.

The present results should only be used to identify general trends. There is wide variation in results for a given load and temperature; the number of cycles can be seen to differ by up to a factor of five at room temperature. Sufficient duplicate tests must be run at each temperature and sufficient loads must be represented to supply the needed statistical data base for design and for mechanistic studies.

3.5.2 Gas Atomized Spherical Be Billet

The results of the smooth axial fatigue testing with R=-1 are presented in Table 18. Figure 10 is an S/N plot of the data. Note that all specimens which achieved one million cycles were run outs with the exception of the two 425°C test specimens with highest number of cycles (1.1 and 1.4 million). 70% YS loads are apparently safe at all temperatures except possibly 425°C. Even 425°C may be safe using moderate criteria.

This study did not obtain either a fatigue limit or a fatigue strength for S-65-H and GA. Haws [26] conducted room temperature rotating beam fatigue tests at R= -1 for S-200F grade beryllium which suggested that beryllium, unlike other nonferrous metals, has a fatigue limit. He found 262 and 265 MPa for the fatigue limits of longitudinal and transverse directions respectively for a 10^7 cycles criterion. There is insufficient data in the present work to obtain a fatigue limit at each temperature. 70% YS consistently provides run outs at 10^6 cycles, but it is not known if this is the maximum stress which could produce run out or whether a stress intermediate between 70% YS and 90% YS could produce run out. S/N curves featuring fatigue limits usually have a discontinuity at the fatigue limit, so the present graphs showing straight lines between the two different loads at each temperature cannot be used to estimate a fatigue limit. Similarly, a fatigue strength (maximum strength to obtain a specified cycle life) cannot be estimated because there is insufficient data to indicate that 70% YS is the maximum stress at which 10^6 cycles could be obtained.

The present study was not designed to determine fatigue mechanisms in beryllium, so little can be stated about the fundamental reasons for differences in beryllium grades. Fatigue mechanisms are not well understood [15] in metals in general and in beryllium in particular. Much depends on the specific mechanics of slip band propagation in the beryllium, and there are a number of factors which influence this: inclusions, stacking fault energy, grain size, precipitates, interstitial elements and so on. Increasing homogeneity of slip deformation is thought to maximize fatigue life in general, and all these variables affect this. This is complicated at elevated temperatures (480°C and above) where there is creep and fatigue occurring during the same test. Optical microscopy and transmission electron microscopy of specimens which are only part way through their slip life are needed to further define homogeneity of slip deformation for these beryllium grades

Table 17 S-65-H Smooth Fatigue Test Data

Test Temp. (°C)	Actual Load (MPa)	Cycles	Comments
23	265	40984	Failure
23	265	191316	Failure
23	265	33766	Failure
23	207	191470	Run Out
23	207	229400	Run Out
150	245	25476	Failure
205	233	36419	Failure
205	233	29988	Failure
205	233	33201	Failure
205	181	145230	Run Out
205	181	233200	Run Out
260	214	163616	Failure
315	200	22056	Failure
315	200	34127	Failure
315	200	24546	Failure
315	156	108219	Run Out
315	156	136449	Run Out
370	190	6545	Failure
425	170	10302	Failure
425	170	16191	Failure
425	170	18048	Failure
425	132	124081	Failure
425	132	101804	Run Out
480	153	21851	Failure
540	127	314364	Failure
540	127	343075	Failure
540	127	251445	Failure
650	82	209639	Run Out
650	82	213130	Run Out
650	82	235609	Run Out

Table 18 HIP'd GA Be Smooth Fatigue Test Data

Test Temp. (°C)	Actual Load (MPa)	Cycles	Comments
23	221	956571	Failure
23	221	1119034	Failure
23	221	2538000	Failure
23	172	1005816	Run Out
23	172	2260000	Run Out
23	172	1830000	Failure
23	172	2432520	Failure
150	213	275317	Failure
205	199	152570	Failure
205	199	233055	Failure
205	199	312196	Failure
205	154	1920960	Run Out
205	154	2234160	Run Out
205	138	2070000	Run Out
205	138	2181960	Run Out
260	183	209081	Failure
315	173	36137	Failure
315	173	49616	Failure
315	173	58633	Failure
315	134	1670400	Run Out
315	134	1739046	Failure
315	121	2222222	Run Out
315	121	4477682	Failure
370	165	9384	Failure
425	158	2885	Failure
425	158	3012	Failure
425	158	3290	Failure
425	123	357159	Failure
425	123	433697	Failure
425	111	1060294	Failure
425	111	1423000	Failure
480	153	1803	Failure
540	138	1500	Failure
540	138	2249	Failure
540	138	2951	Failure
650	79	1331022	Run Out
650	79	1708010	Run Out
650	79	2161080	Run Out

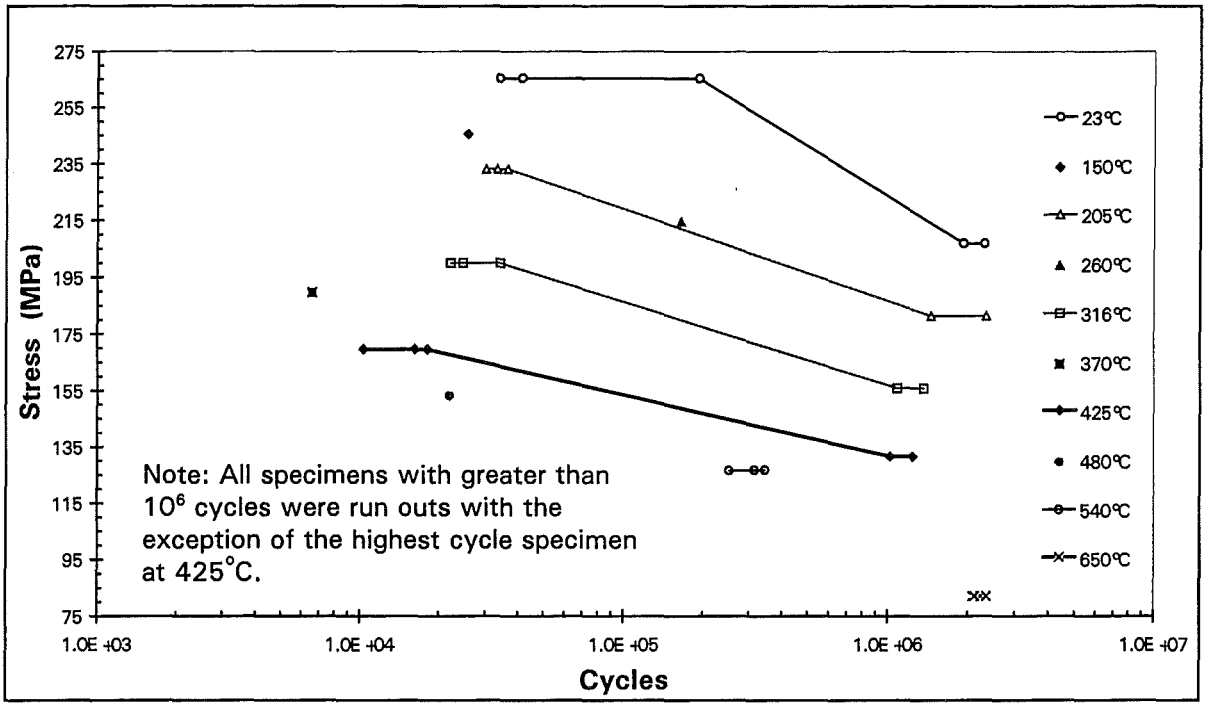

Figure 9 Smooth Fatigue Data for S-65-H with R= -1 for Specimens with Transverse Orientation. Two stress levels were tested at each temperature: 70% YS and 90% YS. 30 Hz nominal test frequency.

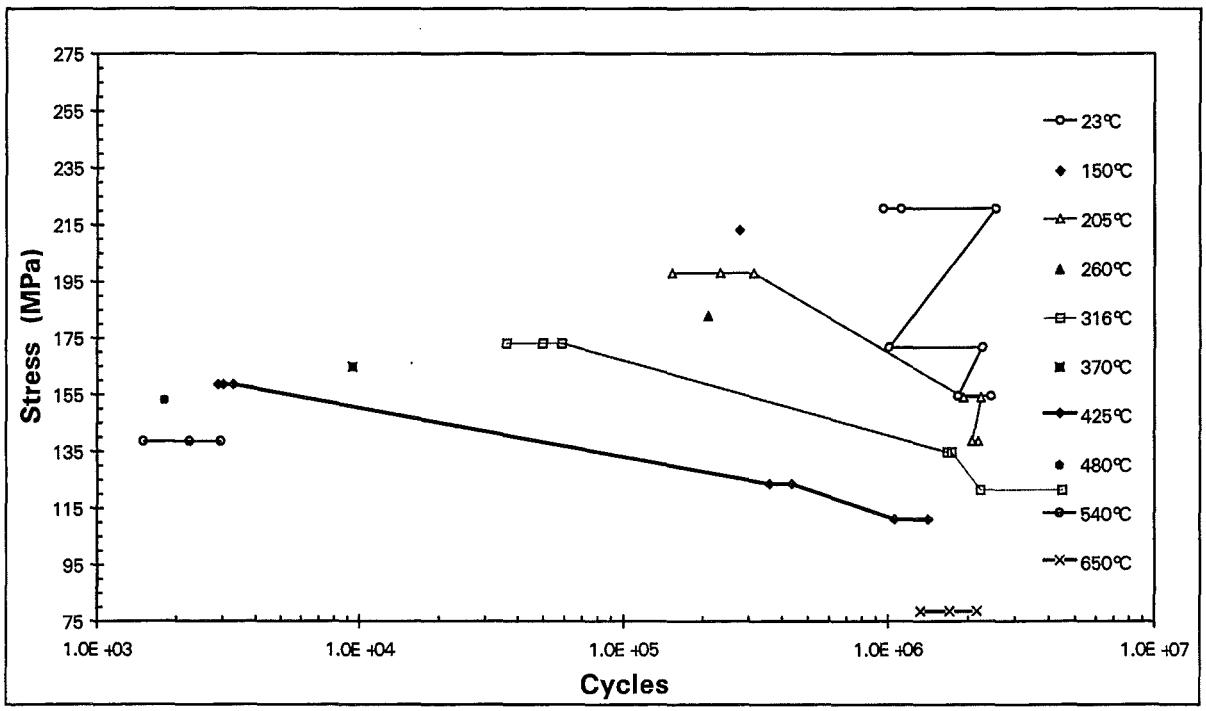

Figure 10 Smooth Fatigue Data for HIP'd GA Be with R= -1 for Specimens with Transverse Orientation. Two stress levels were tested at each temperature: 70% YS and 90% YS. 30 Hz nominal test frequency.

Comparison of S-65-H and GA

A comparison between S-65-H and GA smooth fatigue performance is shown in Figure 11. Two factors make this comparison difficult. The first is that although assigning loads based on a percentage of yield strength yields a handy rule of thumb for design, it does not allow comparison of S-65-H and GA for the same absolute load until the yield strengths converge at 650°C. The second factor is that there are too few loads represented at each to build up a curve which could be used to predict performances at other loads. There are only straight lines connecting the points and these straight lines do not represent the actual functional relationship. Ideally one would like to compare the two grades by drawing a horizontal line across at some constant load and pick off some estimate of fatigue life for each grade from their respective curves. With only two sets of data available, one can have small confidence in a semi-quantitative comparison made by drawing such a line across to the straight lines in the Figure. Given that, a comparison of the 90%YS data points indicates that GA and S-65-H roughly have the same behavior through 205°C. The GA data points at 23°C and 205°C are very near or on a line connecting the S-65-H points. From 315°C through 540°C, the 90% YS data points for GA generally fall far short of the lines connecting the S-65-H data points; there is some indication that S-65-H has better fatigue performance in this temperature range. One cannot distinguish between the two grades at 650°C because both grades have run out behavior. A comparison of the 70% YS points does not distinguish between the two grades because all the data points except 425°C are run outs. Again, all these comparisons are tentative because of insufficient data and the scatter in the existing data. A major recommendation of this study is to obtain a statistical amount of data at a range of loads so that a more valid comparison can be made.

3.5.3 Comparison of S-65-H and GA with Other Be Grades

There is no other smooth axial fatigue data at elevated temperatures for any remotely modern grade of beryllium. The only other smooth axial fatigue data for beryllium that has been found is a 1960 study done on QMV grade made by Brush Wellman [16]. QMV differs radically in terms of chemical composition, grain size and production process from any grade of beryllium now produced. In that work, two forms of QMV grade were tested: 1. vacuum hot pressed 2. vacuum hot pressed and extruded. Unfortunately, the R ratios which were used in that past study prevent comparison with the present work. The past study used R= 0.20 and R = ∞, and data with these ratios cannot be reasonably compared to the R = -1 data.

3.6 Notched Axial Fatigue

3.6.1 S-65-H Billet

The results of the notched axial fatigue testing with R=-1 and a stress concentration factor K_t = 3 are presented in Table 19. The loads are sometimes not exactly 70% YS and 90% YS. This is because the loads for the initial S-65-H fatigue tests were calculated based on initial tensile tests which had a slight extensometer problem. These early tensile test results were discarded, but the fatigue tests had already been conducted. The fatigue tests are still valid and useful; the loads just vary from one to seven percentage points off the

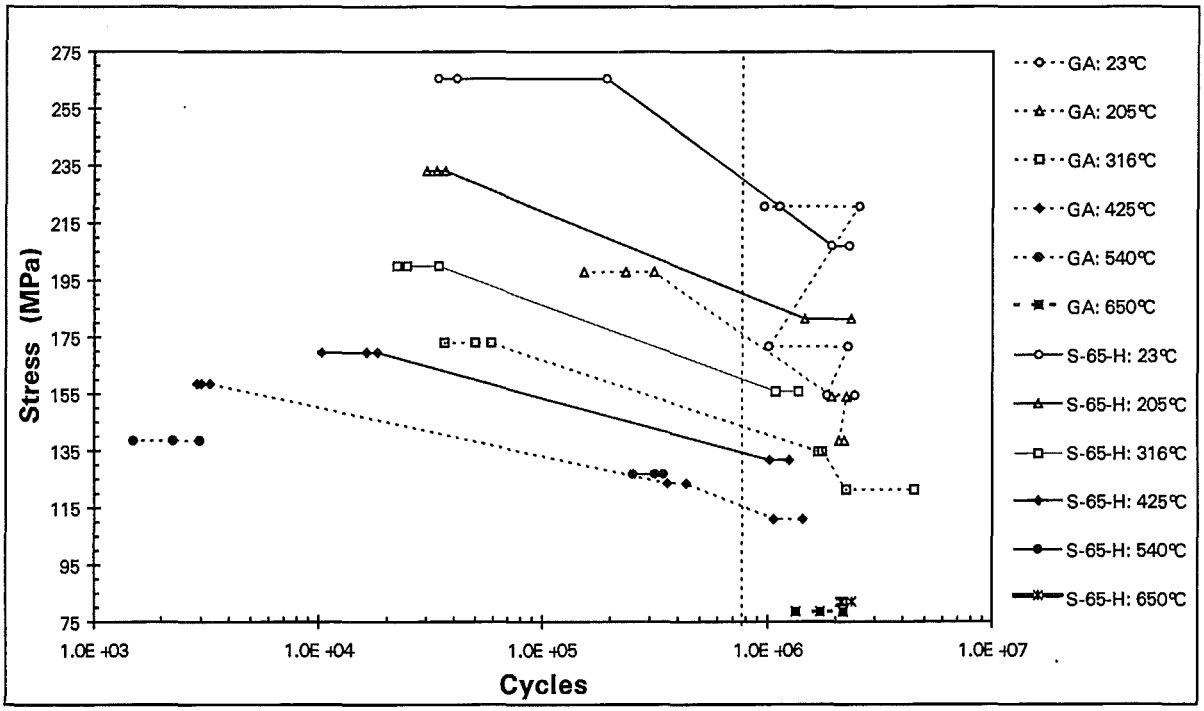

Figure 11 Comparison of S-65-H and GA Smooth Fatigue Behavior at Selected Temperatures in an S/N Plot. R = -1. 30 Hz nominal test frequency. Loads are nominally 70% YS and 90% YS.

initially planned %YS. Figure 12 is an S/N plot of the data. Note that three specimens achieved one million cycles, but only one was a run out. This is a contrast to the equivalent smooth fatigue tests, where nearly all 70% YS loads were run outs.

The present results should only be used to identify general trends. There is wide variation in results for a given load and temperature. Sufficient duplicate tests must be run at each temperature and sufficient loads must be represented to supply the needed statistical data base for design and for mechanistic studies.

3.6.2 Gas Atomized Spherical Be Billet

The results of the smooth axial fatigue testing with R=-1 and a stress concentration factor K_t = 3 are presented in Table 20. Figure 13 is an S/N plot of the data. Note that three specimens achieved over one million cycles but only one was a run out.

3.6.3 Comparison of S-65-H and GA

Notch sensitivity for fatigue of a material is usually measured by a notch sensitivity factor q [17]. This sensitivity factor is calculated as follows

$$q = \frac{K_f - 1}{K_t - 1}$$

where

K_t = the stress concentration factor = 3 for the present work

K_f = the ratio of fatigue limit (or fatigue strength) for smooth specimensto the fatigue limit (or fatigue strength) for notched specimens for the same number of cycles.

Table 19. Notched Axial Fatigue Data for S-65-H at K_t = 3, and R = -1. 30 Hz nominal test frequency.

Test Temp. (°C)	Actual Load (MPa)	Cycles	Comments
23	265	567	Failure
23	265	618	Failure
23	265	707	Failure
23	207	8492	Failure
23	207	17342	Failure
150	245	1602	Failure
205	233	1971	Failure
205	233	2085	Failure
205	233	3275	Failure
205	181	18919	Failure
205	181	34265	Failure
260	214	9369	Failure
315	200	22067	Failure
315	200	22160	Failure
315	200	22633	Failure
315	156	158103	Failure
315	156	163367	Failure
370	190	19683	Failure
425	170	49847	Failure
425	170	67008	Failure
425	170	71025	Failure
425	132	317793	Failure
425	132	501581	Failure
480	153	96559	Failure
540	127	248374	Failure
540	127	253275	Failure
540	127	254838	Failure
650	82	1406200	Run Out
650	82	1524947	Failure
650	82	1902596	Failure

Table 20. Notched Axial Fatigue Data at K_t = 3 and R = -1 for HIP'd GA Be. 30 Hz nominal test frequency.

Test Temp. (°C)	Actual Load (MPa)	Cycles	Comments
23	221	771	Failure
23	221	908	Failure
23	221	1156	Failure
23	154	64617	Failure
23	154	69570	Failure
150	213	1048	Failure
205	198	1587	Failure
205	198	2695	Failure
205	198	2939	Failure
205	154	40052	Failure
205	154	110212	Failure
260	183	7566	Failure
315	173	10366	Failure
315	173	10413	Failure
315	173	10921	Failure
315	134	286694	Failure
315	134	358205	Failure
370	165	17460	Failure
425	158	17293	Failure
425	158	17935	Failure
425	158	19430	Failure
425	123	256159	Failure
425	123	369912	Failure
480	153	24996	Failure
540	138	53457	Failure
540	138	53804	Failure
540	138	55088	Failure
650	79	1836415	Failure
650	79	2328787	Run Out
650	79	2475741	Failure

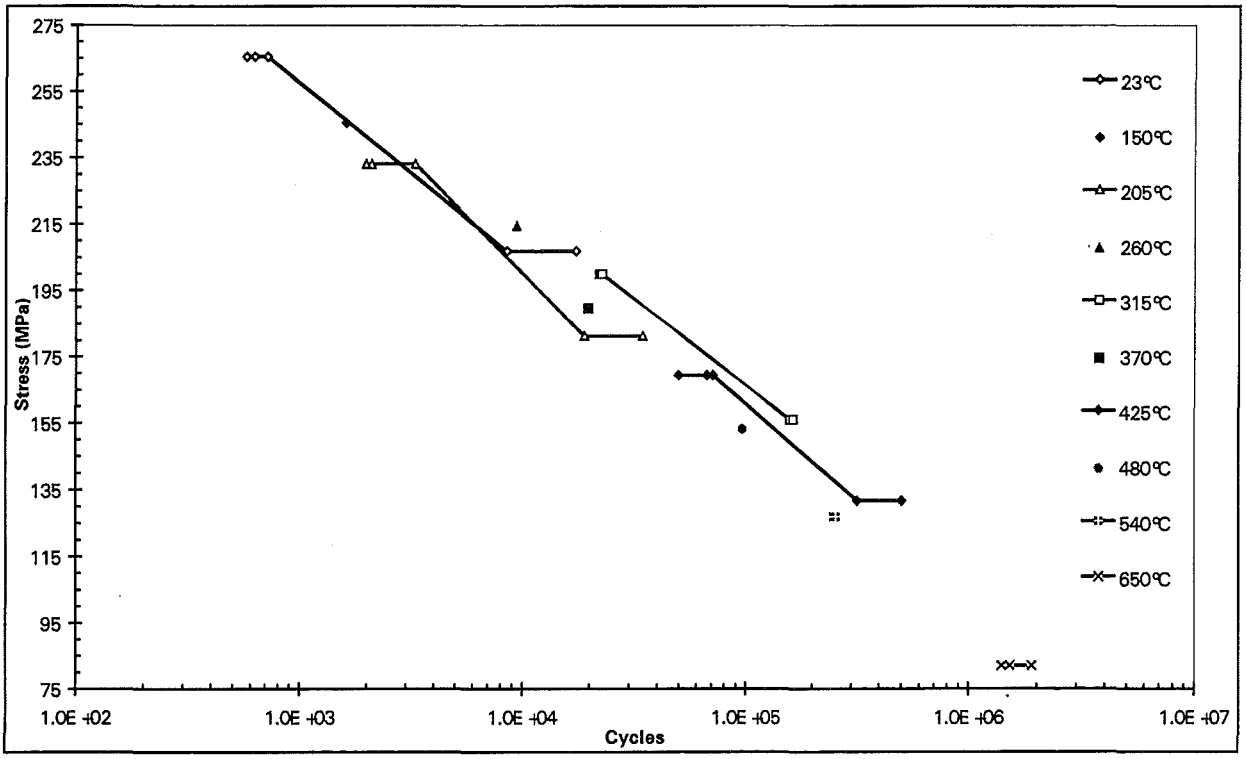

Figure 12 S-65-H Notched Fatigue at K_t = 3 and R = -1 as a Function of Temperature and Load. 30 Hz nominal test frequency.

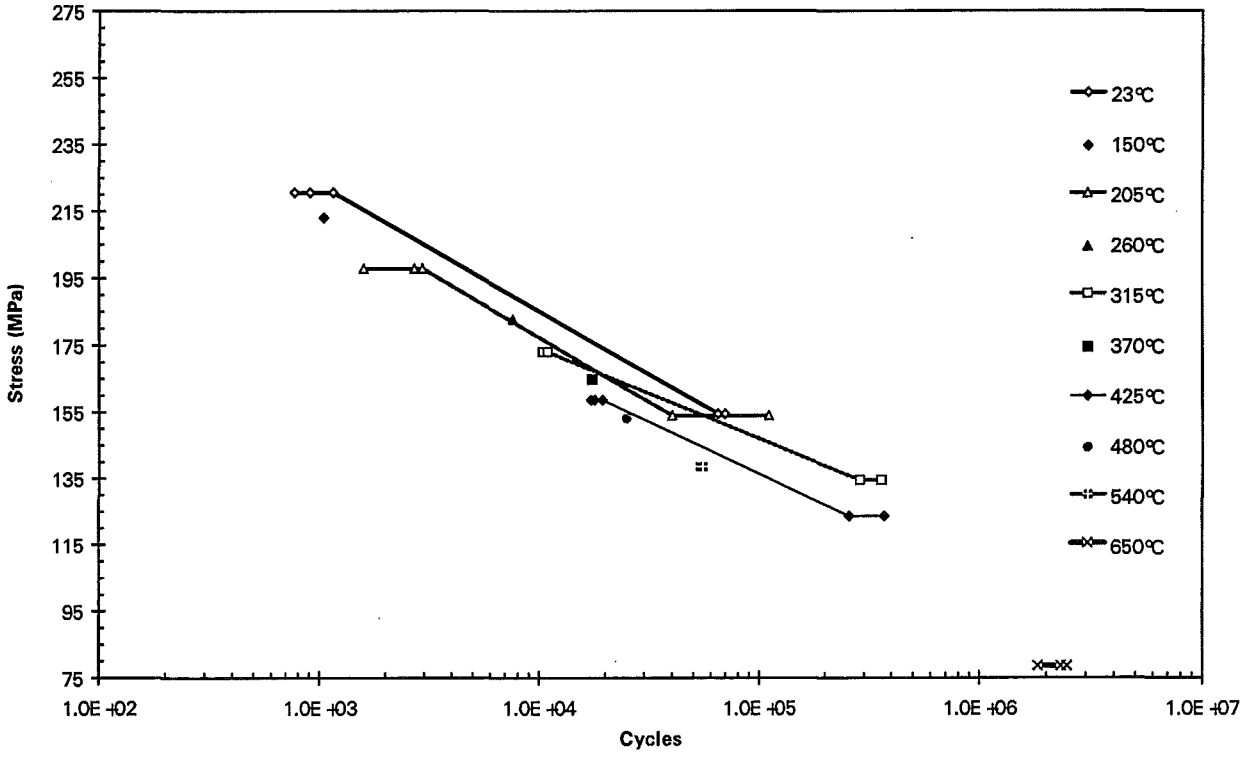

Figure 13 HIP'd GA Be Notched Fatigue at K_t = 3 and R = -1 as a Function of Temperature and Load. 30 Hz nominal test frequency.

As discussed in the previous section on smooth (smooth) fatigue, no fatigue limit or strength was obtained for smooth fatigue of S-65-H and GA. Neither notched fatigue strengths nor notched fatigue limits were obtained for identical reasons.

Although the notch sensitivity factor cannot be calculated from the present data, a comparison of notched and smooth values at each temperature indicates a transition from notch sensitivity to no notch sensitivity. Figure 14 compares these values for S-65-H and Figure 15 compares them for GA. For S-65-H, there is some overlap of smooth and notched lines at 315°C, much overlap at 425°C, and complete overlap at 540°C and 650°C. This indicates that S-65-H fatigue is fatigue notch sensitive below 315°C, is in a transition region to no fatigue notch sensitivity at 315-425°C, and is not fatigue notch sensitive at 540°C and above. Where there is clear notch sensitivity, there is a difference of two orders of magnitude in fatigue life for the same nominal load. A similar trend is observed for GA, except that the transition appears to occur at 425°C.

3.6.4 Comparison of S-65-H and GA with Other Be Grades

There is no other axial notched fatigue data at elevated temperatures for any remotely modern grade of beryllium. The only other notched axial fatigue data for beryllium that has been found is a 1960 study done on QMV grade from Brush Wellman [16]. QMV differs radically in terms of chemical composition, grain size and production process from any grade of beryllium now produced. In that work, two forms of QMV grade were tested: 1. vacuum hot pressed 2. vacuum hot pressed and extruded. Unfortunately, the R ratios which were used in that past study prevent comparison with the present work. The past study used R= 0.20 and R = ∞, and data with these ratios cannot be reasonably compared to the R = -1 data. Further, the value of the stress concentration factor K_t is not specified.

3.7 Fracture Toughness

Fracture toughness testing was performed and analyzed at Southwest Research Institute.

3.7.1 S-65-H Billet

The fracture toughness testing results are summarized in Table 21. All data were analyzed using E399 (linear-elastic) K_{Ic} procedures. This means that data from the J_{Ic} tests were stripped of the unload sequences. K_q and K_{max} values are listed. Those K_q values which met K_{Ic} validity requirements are also K_{Ic} values. As can be observed from these results, at temperatures below 260°C, valid K_{Ic} toughnesses were measured. All other tests yielded invalid results primarily as a consequence of insufficient thickness and crack length as well as excessive nonlinearity. Above 205°C, the fracture surface roughness, nonlinearity of the load-displacement curves and area under the curves all increased. The nonplanar fracture surface is taken to indicate that damage concentration is not strongly localized at the crack tip. Above 480°C, there is crack tearing, increased plasticity (indicated by increased hysteresis in the load-displacement curves) and time dependent deformation processes. There is currently no theoretical treatment for such complex behavior.

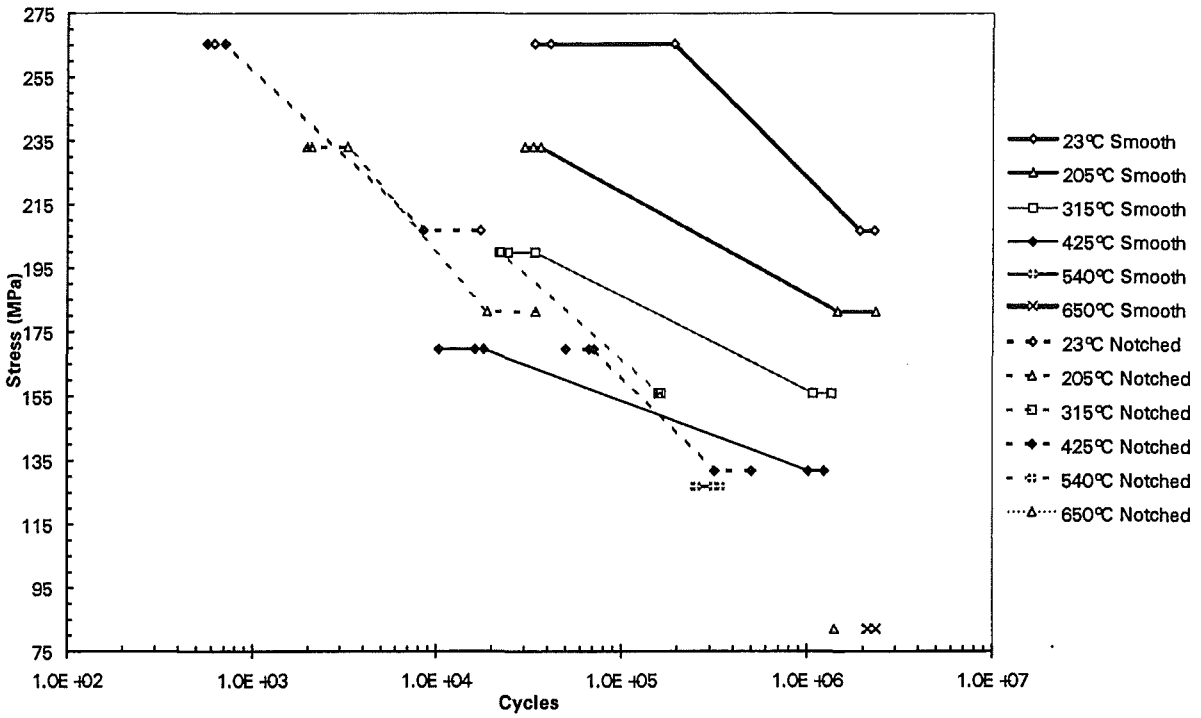

Figure 14 Comparison of Smooth and Notched (K_t = 3) Fatigue Behavior as a Function of Temperature and Load for S-65-H. R = -1. 30 Hz nominal test frequency.

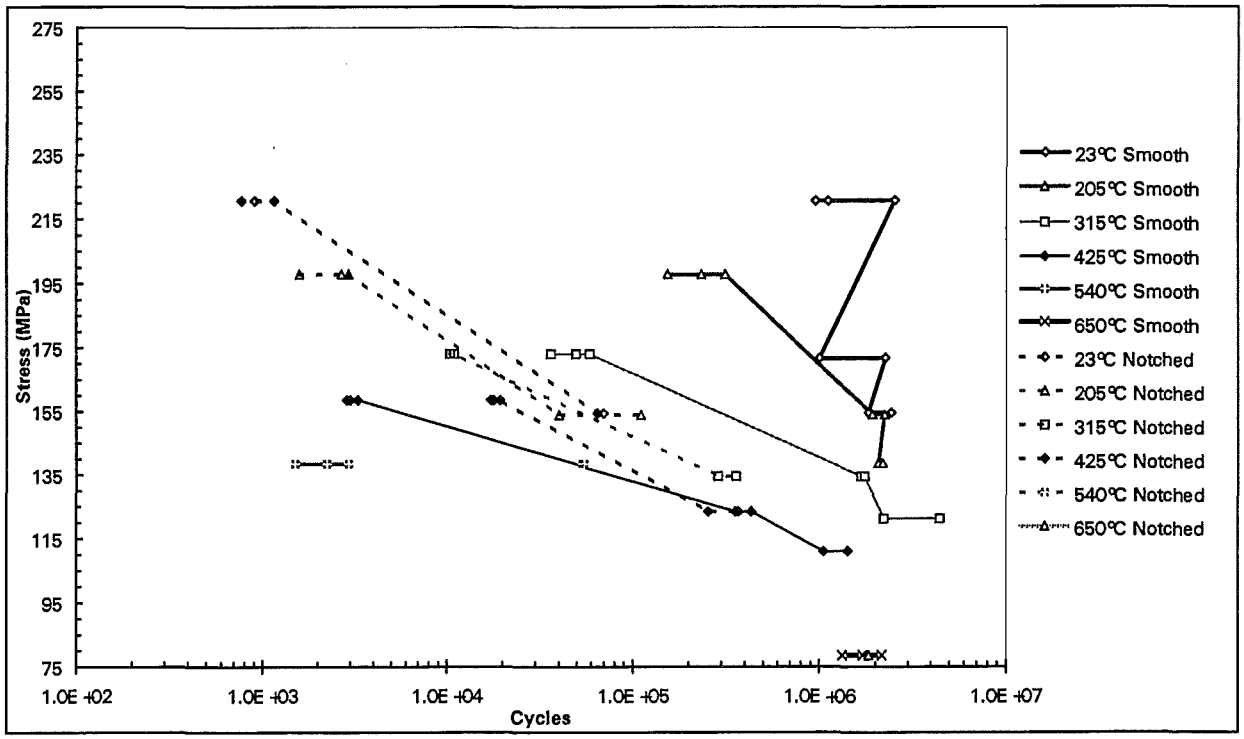

Figure 15 Comparison of Smooth and Notched (K_t = 3) Fatigue Behavior as a Function of Temperature and Load for GA. R = -1. 30 Hz nominal test frequency.

The tabulated results also provide a K_{max} measure which corresponds to the K value at the maximum load assuming the crack was stationary. Although all of the data in excess of 205°C are clearly invalid and not necessarily in the linear-elastic regime, the K_{max} parameter does provide a relative, albeit potentially geometry-dependent, measure of toughness.

Both K_q and K_{max} measurements are shown as a function of temperature in Figure 16. There is an apparent plateau in the 315-540°C range. However, this plateau may also mean that the assumptions of the K_{max} analysis are not valid.

J_{Ic} analytical techniques were not successful. Meaningful crack advance was only observed at temperatures of 480°F or higher. This is important because without any measurable crack advance, generating a J_{Ic} value is not possible. Furthermore, the degree of crack advance required to calculate a J_{Ic} value is approximately 1.52 mm. Based on this criteria, only the highest-temperature 650°C specimens could provide any data suitable for J_{Ic} toughness calculation. Less-than-optimum results were obtained for J_{Ic} evaluation of the highest-temperature fracture tests. These J_{Ic} evaluations yielded poor data for a variety of reasons including:

- lack of any significant physical crack extension or tearing during the fracture test (which is critical for calculation of a J_{Ic} toughness),

- hysteretic behavior consistent with a time-dependent phenomenon (e.g., a creep-dominated response) that caused significant nonlinearity in the load-displacement behavior,

- inconsistent and poorly repeatable unloading compliances implying either no crack extension or apparent crack shortening (so-called crack backup), and

- unreliable performance of the high-temperature clip gage.

3.7.2 Gas Atomized Spherical Be Billet

The fracture toughness testing results are summarized in Table 22. All data were analyzed using E399 (linear-elastic) K_{Ic} procedures. This means that data from the J_{Ic} tests were stripped of the unload sequences. K_q and K_{max} values are listed. Those K_q values which met K_{Ic} validity requirements are also K_{Ic} values. As can be observed from these results, at temperatures below 260°C, valid K_{Ic} toughnesses were measured. All other tests yielded invalid results primarily as a consequence of insufficient thickness and crack length as well as excessive nonlinearity.

The tabulated results also provide a K_{max} measure which corresponds to the K value at the maximum load assuming the crack was stationary. Although all of the data in excess of 205°C are clearly invalid and not necessarily in the linear-elastic regime, the K_{max} parameter does provide a relative, albeit potentially geometry-dependent, measure of toughness.

Figure 17 displays K_q and K_{max} values as a function of temperature. The peak suggested by the K_{max} data may be in error if the K_{max} calculation assumptions do not apply.

Table 21 Fracture toughness test results for S-65-H. The K_{max} calculation assumes that no crack advance occurred during the test.

Material Type	Temp. (°C)	K_q, (MPa-√m)	K_{max}, (MPa-√m)	Invalidity Criteria	Valid crack length and thickness (mm)
S-65-H	23	9.9	9.9	valid	-
	150	11.6	11.6	valid	-
(K_{Ic} evals)	205	15.2	15.2	valid	-
	260	24.6	24.6	a, b	> 28 mm
	315	30.3	44.4	a, b, c	> 48 mm
	315	25.6[1]	34.0	a, b, c	> 33 mm
(J_{Ic} evals)	370	23.8	42.8	a, b, c	> 33 mm
	425	26.1[1]	43.8	a, b, c	> 51 mm
	425	32.4	41.9[†]	a, b, c	> 79 mm
	480	-	40.3[†]	-	-
	540	-	37.8[2, †]	-	-
	650	-	12.6[†]	-	-

NOTES:
[†] tested at a higher rate
[1] graphically analyzed recorded data (ASTM valid method)
[2] unreliable and corrupt load-line displacement data

INVALIDITY CRITERIA:

a - crack length (a) shorter than allowed	*criteria: $a > 2.5\ (K_{Ic}/sys)^2$*
b - insufficient plane strain thickness (B)	*criteria: $B > 2.5\ (K_{Ic}/sys)^2$*
c - excessive load-displacement nonlinearity	*criteria: $P_q > 0.8\ P_{max}$*

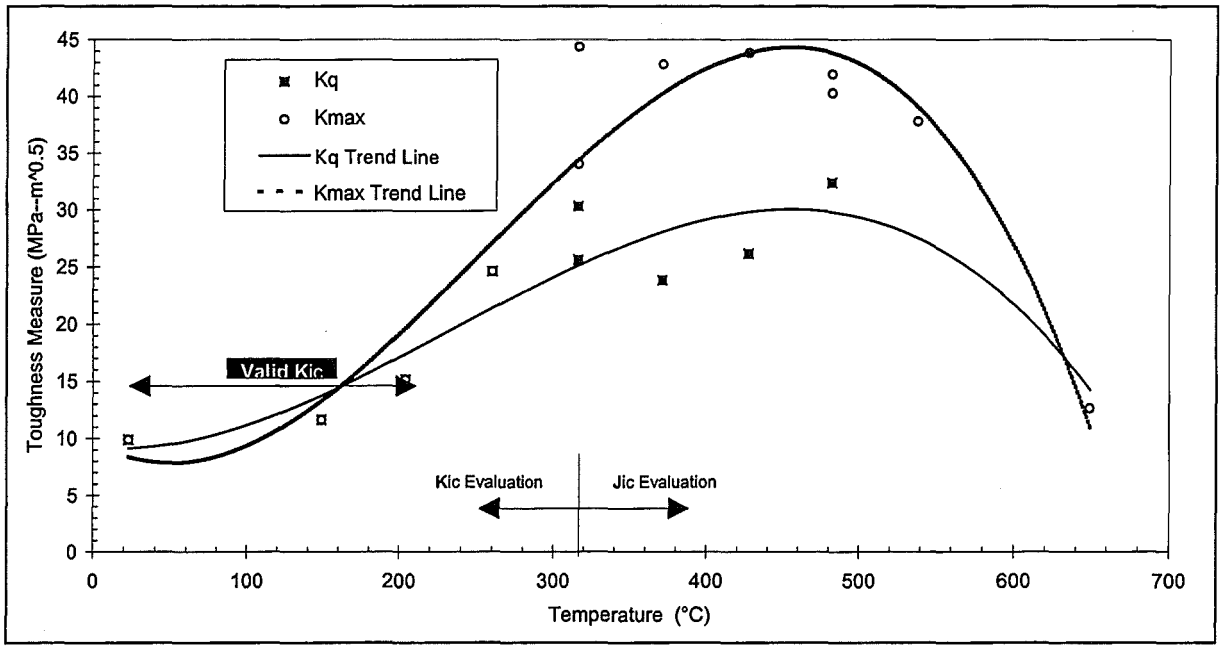

Figure 16 S-65-H Toughness as a Function of Temperature. Kq from room temperature through 205°C are valid K_{Ic}.'

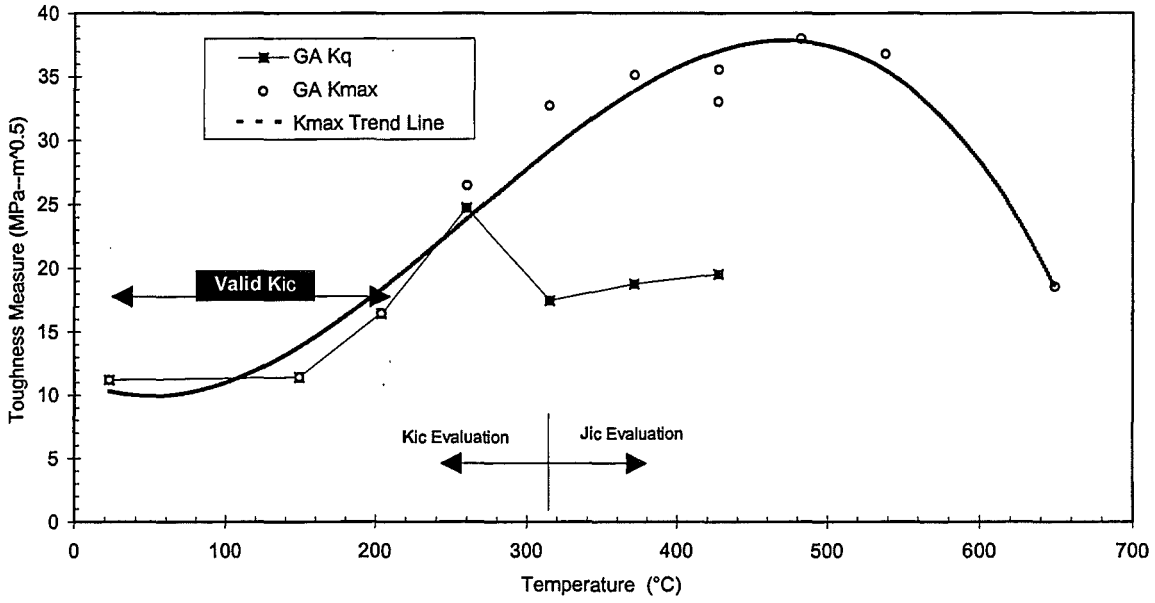

Figure 17 GA Toughness as a Function of Temperature. Kq from room temperature through 205°C are valid K_{Ic}.'

3.7.3 Discussion of S-65-H and GA Results

One of the characteristics of beryllium in this testing is that crack propagation tends to be rapid. It is difficult to conduct precracking in the tensile-tensile mode because once a crack starts it propagates very rapidly. This was true at elevated temperatures also, which was why the J_{Ic} analysis could not be successfully applied. Crack growth was too rapid and unstable. There is some indication in tests up to 425°C that the specimen could not freely rotate on the loading pins, and that this in turn caused problems measuring crack advance. Some innovation in loading pin design may help.

Figure 18 compares the trends in K_q and K_{max} for S-65-H and GA. Both materials have valid K_{Ic} values through 205°C. GA has slightly better performance than S-65-H in that range. Between 205 and 425°C, S-65-H K_q appears to be higher. However, the complicated morphology of the fracture surfaces and lack of stable crack growth in both materials in this temperature range indicate that the processes taking place are complex. SWRI recommends caution in use of the data because of this and because there is usually only a single data point at each condition. Increasing the sample dimensions and improving the loading pin motion may allow more reliable data to be obtained. The K_{max} values calculated above 425°C have even greater uncertainty associated with them. In addition to the uncertainties observed in the 205-425°C temperature range there are clearly creep-fatigue interactions occurring which are beyond the scope of current theory. SWRI also hypothesizes that rotation of the gage pin in the circular gage holes may have been impeded in a number of ways. Use of D-shaped holes may provide more well behaved experimental data, but advances in theory would still be needed.

Figure 19 compares the results obtained here and those obtained by Chaouadi et. al for S-65C and S-65-H [9]. No valid K_{Ic} data was obtained previous to these two programs for temperatures above room temperature.

Table 23 compares the room temperature results to previous work [1, 10, 18,19, 20]. S-65-H and GA results from the present work lie within the range of measurements made on previous grades. The vacuum hot pressed GA measurement still sticks out as unusual and is significantly different from the HIP'd GA value. There may be some advantage of vacuum hot pressing; the vacuum hot pressed S-65C grade has slightly higher K_{Ic} values than S-65-H measurements made here. D. Harries stated that SCK-CEN had found that HIP'd S-65 (S-65-H) and HIP'd S-200F (S-200F-H) required a lower precracking stress for miniature compact tension test specimens than did specimens made from the equivalent vacuum hot pressed grades (S-65C and S-200F) [21]. It is also clear that while there is consistent fracture toughness behavior within lots, there is significant variation between lots. The variation between lots encompasses the room temperature values for S-65-H and GA.

In summary, it can be said that GA has some advantage in fracture toughness over S-65-H through 205°C. These results are the first valid K_{Ic} results ever obtained above room temperature for any beryllium grade. There is some indication that S-65-H may offer better toughness

Table 22 Fracture toughness test results for HIP'd GA Be. The K_{max} calculation assumes that no crack advance occurred during the test.

Material Type	Temp, (°C)	Kq (MPa-√m)	Kmax (MPa-√m)	Invalidity Criteria	Valid crack length and thickness, B
Gas Atomized	23	**11.2**	**11.2**	valid	-
(K_{Ic} evals)	150	**11.4**	**11.4**	valid	-
	205	**16.5**	**16.5**	valid	-
	260	24.7	26.4	a, b	> 37 mm
(J_{Ic} evals)	315	17.4	32.7	c	-
	370	18.8	35.1	b, c	> 27 mm
	425	19.5	35.6	a, b, c	> 31 mm
		-	33.0†	-	-
	480	-	38.0	-	-
	540	-	36.8†	-	-
	650	-[1]	18.6†	-	-

NOTES:
Valid K_q tests provide K_{Ic} data.
† tested at a higher rate
[1] unreliable and corrupt load-line displacement data

INVALIDITY CRITERIA:

a - crack length (a) shorter than allowed	*criteria: $a > 2.5\ (K_{Ic}/sys)^2$*
b - insufficient plane strain thickness (B)	*criteria: $B > 2.5\ (K_{Ic}/sys)^2$*
c - excessive load-displacement nonlinearity	*criteria: $P_q > 0.8\ P_{max}$*

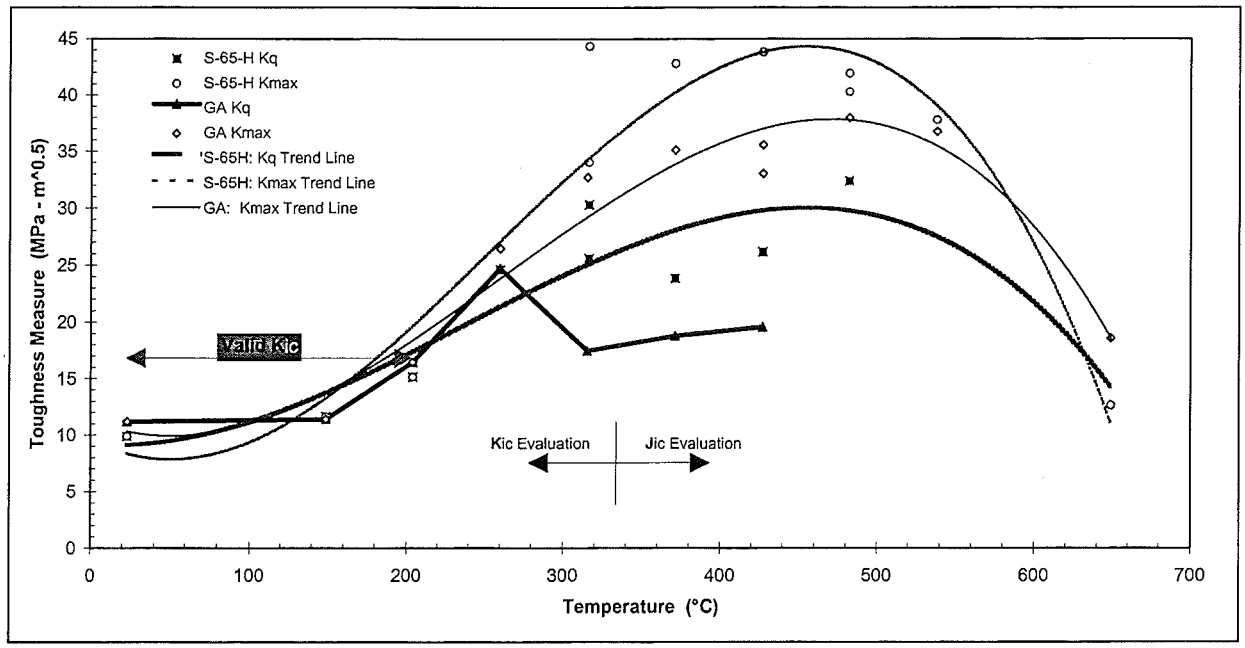

Figure 18 Comparison of S-65-H and HIP'd GA Be Toughness. K_q measurements through 205°C are valid K_{Ic} results.

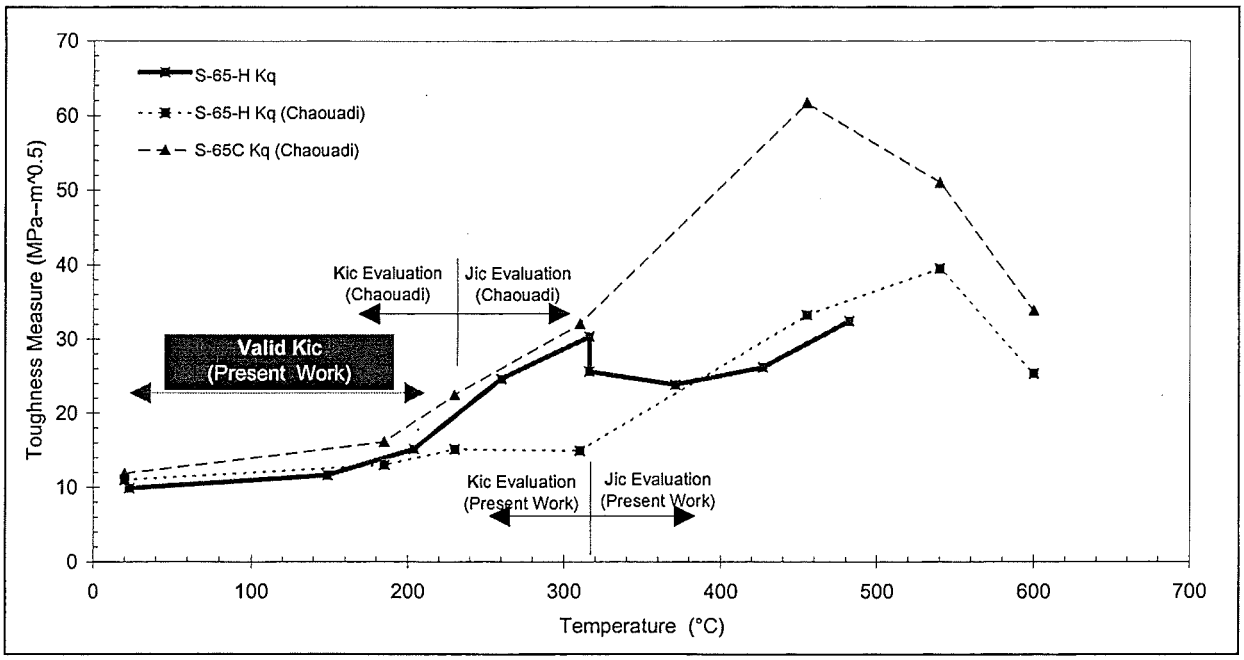

Figure 19 Comparison of Present S-65-H toughness results with other results for S-65-H and S-65-C.

Table 23 Comparison of Present Room Temperature Fracture Toughness Measurements with Vacuum Hot Pressed Grades (S-200E, S-200F, S-65C, VHP'd GA) and HIP Grades (S-65-H, S-200F-H, HIP'd GA)

Material	Specimen Orientation	K_{Ic}			wt% BeO	Grain Size	Reference
		Mean (MPa $\sqrt{m}$)	Std. Dev. (MPa $\sqrt{m}$)	n		(μm)	
S-65-H	L-T	9.9	-	1	0.70	6.6	Present Work
HIP'd GA	L-T	11.2	-	1	0.32	9.5	Present Work
VHP S-200E	L-T	10.3	0.466	5	1.1	NA	18
	T-L	12.3	0.229	3			
VHP S-200F	L-T	10.6	-	1	0.67	8.7	1
	T-L	12.3	-	1			
VHP S-200F	L-T	9.5	0.279	3	1.06	NA	10
	T-L	10.9	0.379	4			
VHP S-65	L-T	10.6	0.770	3	0.7	11.4	19
	T-L	10.9	0.719	3			
VHP GA Be	T-L	13.6	-	1	0.37	13.2	1
S-200F-H	L-T	9.0	0.409	3	0.78	7.0	20
	T-L	9.1	0.320	3			

L-T : Applied Load parallel to Longitudinal (L) direction in VHP billet, and crack propagation parallel to Transverse (T) direction

T-L : Applied Load parallel to Transverse (T) direction in VHP billet, and crack propagation parallel to Longitudinal (L) direction

than GA in the 205-425°C temperature range, but the present data indicate a need for additional testing. Above 425°C, the data at best indicates that beryllium can absorb significant energy without catastrophic failure.

4.0 Conclusions

Smooth Tensile Testing

1. The elevated temperature properties (UTS,YS, percent elongation, reduction in area) of S-65-H generally exceed those of HIP'd GA Be up to 650°C.

2. The elevated temperature tensile properties of S-65-H are consistent with the vacuum hot pressed version of S-65 (S-65C).

3. The elevated temperature tensile properties of HIP'd GA are comparable to a vacuum hot pressed grade with similar chemical composition (S-200F). HIP'd GA has equivalent ultimate tensile strength over the whole temperature range, lower yield strength over the whole temperature range, and superior percent elongation in the 315-425°F temperature range.

4. The room temperature tensile properties of HIP'd GA are consistent with properties of consolidated GA made in 1990 with argon atomization.

5. Low temperature tensile strength differences between S-65-H and HIP'd GA are consistent with grain size differences. Grain size is a less obvious contributor in the 205°C to 540°C temperature range since significant grain deformation occurs there. Failure is by grain boundary decohesion at 650°C.

Notched Tensile Testing

6. Both S-65-H and HIP'd GA are not notch sensitive in the 150-650°C temperature range. Both grades are notch sensitive at room temperature.

Creep

7. HIP'd GA clearly has significantly lower stage II creep rates for 480-650°C and the range of stresses considered. Stage II creep rates for both grades are only significant in this temperature range, which is consistent with contribution of diffusion to creep.

Fracture Toughness

8. Over the temperature range from ambient to 650°C, the fracture mode of beryllium transitions from brittle, plane-strain behavior, through a higher energy plasticity dominated mode to hysteretic, creep-influenced behavior at the highest temperature.

9. Valid linear-elastic K_{Ic} toughness values were obtained for temperatures in the range of ambient to 205°F. GA has a small but consistently higher values than S-65-H. Over this range, the toughness increases approximately 50% in magnitude from approximately 10-11 MPa $\sqrt{m}$ to 15-16 MPa $\sqrt{m}$

10. At temperatures of 260°C and higher, fracture nonlinearity as well as insufficient specimen thickness and crack length invalidate the K_{Ic} data. Specimen thicknesses on the order of 50 to 75 mm or more would be required at the higher temperatures to generate geometrically independent toughness values.

11. Fracture toughness, as measured by either K_q or K_{max}, continues to increase with temperature until it reaches a plateau at approximately 315-540°C. However, it should be noted that the validity of this observation as well as any of the toughness data in excess of 480°C is subject to debate since neither linear elastic or elastic plastic conditions no longer dominate.

12. Physical measurements of crack extension reveal that slow stable crack advance or tearing does not generally occur at temperatures less than 480°C. Minimal amounts of slow stable cracking were observed as temperature increased. At the highest 650°C condition, significant crack tearing and load relaxation (creep) was observed.

13. Meaningful J_{Ic} toughness results were not possible with the data recorded in this program. This is due to the low levels of slow stable cracking observed as well as the time-dependent fracture mode observed at the highest temperatures.

Smooth Fatigue Testing

14. 90% Yield Strength Load GA and S-65-H have roughly the same behavior for room temperature through 205°C. From 315°C through 540°C there is some indication that S-65-H has better fatigue performance. One cannot distinguish between the two grades at 650°C because both grades have run out behavior.

15. 70% Yield Strength Load Nearly all samples exceeded the run out level (10^6 cycles) for the entire temperature range.

16. A major recommendation of this study is to obtain a statistical amount of data at a range of loads so that a more extensive comparison can be made.

Notched Fatigue Testing

17. S-65-H fatigue is notch sensitive below 315°C, is in a transition region to no notch sensitivity at 315-425°C, and is not notch sensitive at 540°C and above. Where there is clear notch sensitivity, there is a difference of two orders of magnitude in fatigue life for the same nominal load.

18. HIP'd GA fatigue is notch sensitive below 425°C, and is not notch sensitive at 540°C and above.

19. A statistical amount of data for notched fatigue and smooth fatigue is needed for calculation of the notch sensitivity factor (q).

References

[1]. F. Grensing, D. Hashiguchi, and J. Marder, " Fracture Toughness of Vacuum Hot Pressed Beryllium Powder", in 1990 Advances in Powder Metallurgy, vol. 2, compiled by E.R. Andreotti and P.J. Mcgeehan, American Powder Metallurgy Institute, Princeton, NJ, pp. 27-30.

[2] K.J. Dietz, T. Ando, A. Antipenkov, S. Chiocchio, G. Federici, G. Janeschitz, E. Martin, R. Tivey, The ITER Divertor, in G.H. Miley and C. Elliott (ed.), Proceedings of 16th IEEE/NPSS

Symposium Fusion Engineering, IEEE Service Center, Piscataway, NJ, 1995, pp. 144-149

[3] D.E. Dombrowski, Fus. Eng. and Des., 37 (1997) 229-242

[4] Evaluation test methods for beryllium (Mechanical property test methods for beryllium) Materials Advisory Board, National Academy of Sciences, National Research Council, Washington, D.C., March 1966, Report No. :MAB-205 M, (Contract No.: ARPA SD-118)

[5]. D.H. Hashiguchi, J.M. Marder, "Property Evaluation of Spherical Beryllium Powder Billets", 1990 Advances in Powder Metallurgy, vol. 2, Metal Powder Industries Federation, Princeton, NJ, pp. 37-49.

[6] . E.W. Gossett Jr., J.Marder, R. Kendrick, O. Cross,"Evaluation of hot isostatic pressed beryllium for low scatter optics", SPIE vol. 1118 Space Optical Materials and Space Qualification of Optics, 1989, pp. 50-58

[7] S.H. Goods, D.E. Dombrowski, Mechanical Properties of S-65C Grade Beryllium at Elevated Temperatures, in Proceedings of the Third IEA International Workshop on Beryllium Technology for Fusion, H. Kawamura, M. Okamoto, eds., Japan Atomic Energy Research Institute, JAERI-Conf 98-001, 1998, pp. 129-1136

[8] M.F. Smith, R.D. Watson, J.B. Whitley, J.M. McDonald, "Thermomechanical Testing of Beryllium for Limiters in ISX-B and JET", Fusion technology, vol. 8, July 1985, pp. 1174-1183

[9] R. Chaouadi, F. Moons, J.L. Puzzolante,"Tensile and Fracture ToughnessTest Results of Neutron Irradiated Beryllium", in Proceedings of the Third IEA International Workshop on Beryllium Technology for Fusion, H. Kawamura, M. Okamoto, eds., Japan Atomic Energy Research Institute, JAERI-Conf 98-001, 1998, pp. 241-253

[10] W.J. Haws, Characterization of Beryllium Structural Grade S-200F, Internal Brush Wellman Technical Memorandum TM-778, May 27, 1985

[11]. M. A. Myers, K.K. Chawla,Mechanical Metallurgy: Principles and Applications, Prentice-Hall, Englewood Cliffs, New Jersey, 1984, pp. 659-683

[12]. D. Webster, D. Crooks, Met Trans. A., vol. 6A, 1975, pp. 2049-2054

[13] D. Webster, D. Crooks, Met Trans. A., vol. 7A, 1976, pp. 1307-1315

[14] N.R. Borch, Elevated Temperature Behavior, in Beryllium Science and Technology, vol. 1.eds., D. Webster, G.J. London, Plenum Press, New York, 1979, pp. 322-329

[15] G.E. Dieter, Mechanical Metallurgy, 3rd ed., McGraw-Hill Publishing Co., New York, 1986, p. 376

[16] A.E. Riesen, R.T. Ault, Mechanical Properties of Beryllium, Wright-Patterson Air Force Base, WADD technical report 60-425, September 1960

[17] ASM Handbook, vol. 8, Mechanical Testing, American Society of Metals, Metals Park, Ohio, 1985, pp. 363-375

[18]. W.O. Shabbits and W.A. Logsdon, J. Test. Eval., 1(2), 1973, p. 110-118

[19]. D.D. Lemon, W.F. Brown,Jr., Journal of Testing and Evaluation, 1985, pp. 152-161

[20] D. Barclay, Brush Wellman internal memo, June 8, 1993

[21] D.H. Harries, consultant to KfK (Karlsruhe, Germany) and SCK-CEN (Mol, Belgium),Private Communication, 1993

Appendix

APPENDIX E

TEST SPECIMEN MACHINING PRINTS & PROCEDURES

TENSILE TESTING PROCESS 01-5127

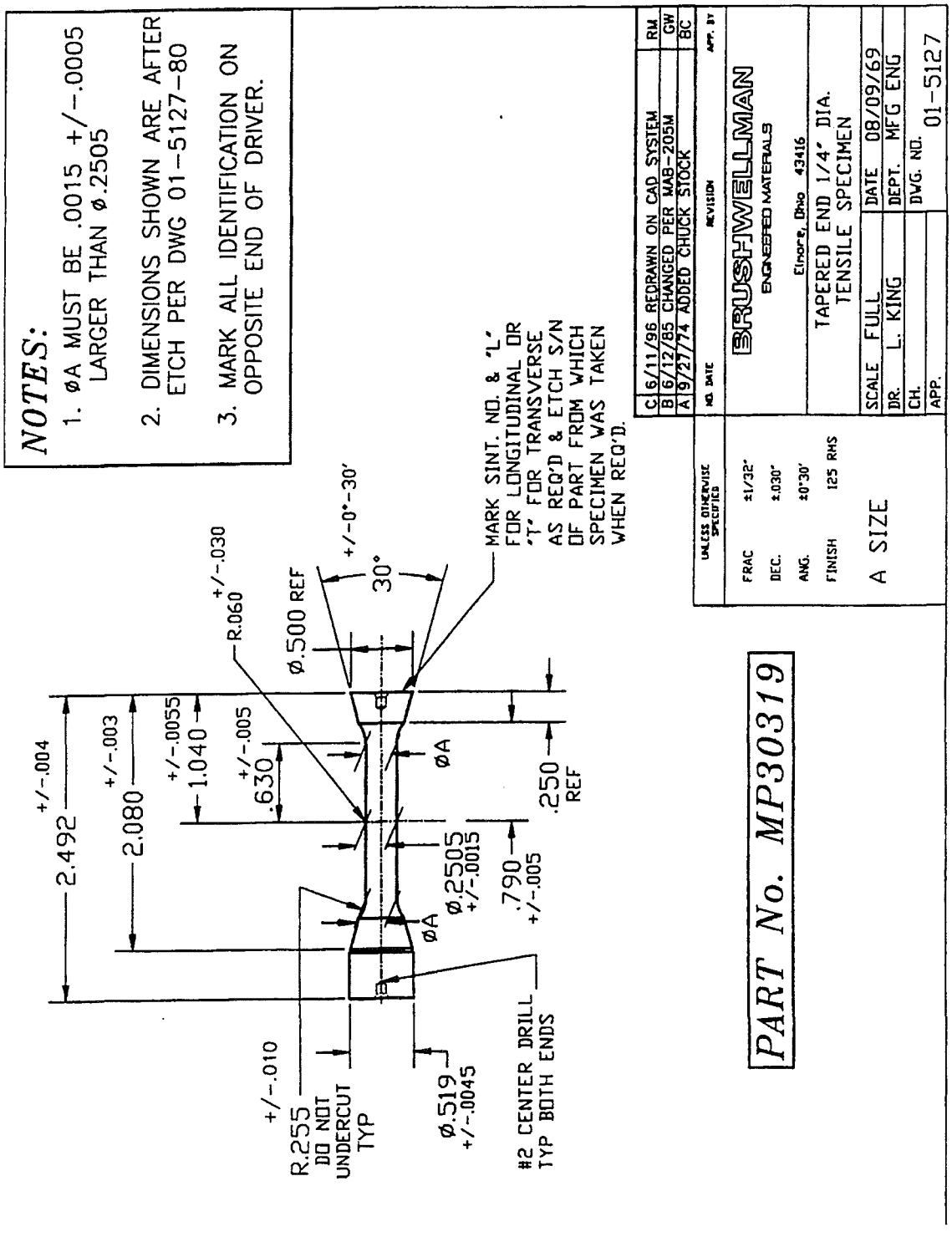

APPENDIX E

TEST SPECIMEN MACHINING PRINTS & PROCEDURES

NOTCHED TENSILE PROCESS 01-5195

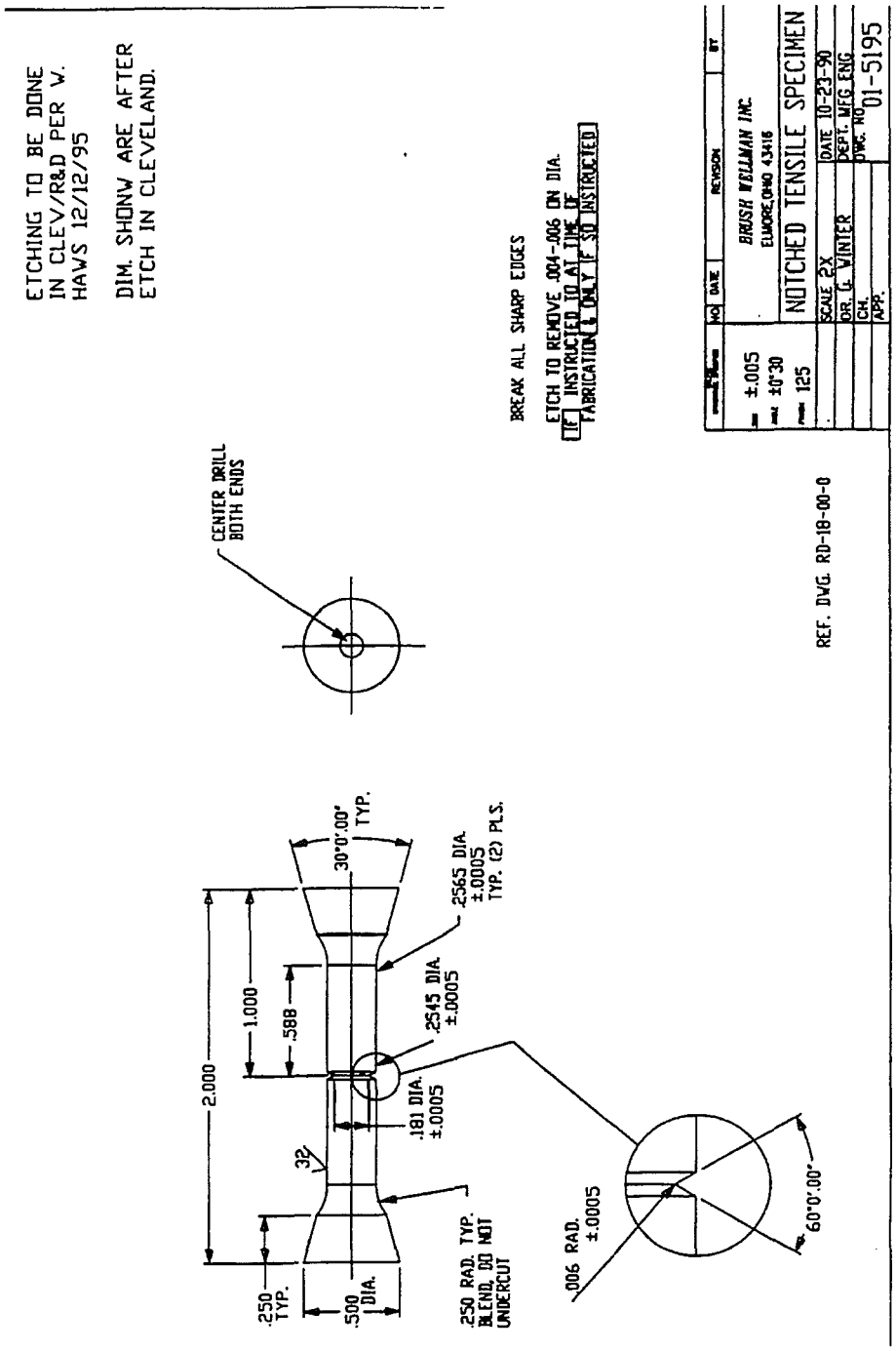

APPENDIX E

TEST SPECIMEN MACHINING PRINTS & PROCEDURES

NOTCHED AXIAL FATIGUE PROCESS 01-5236

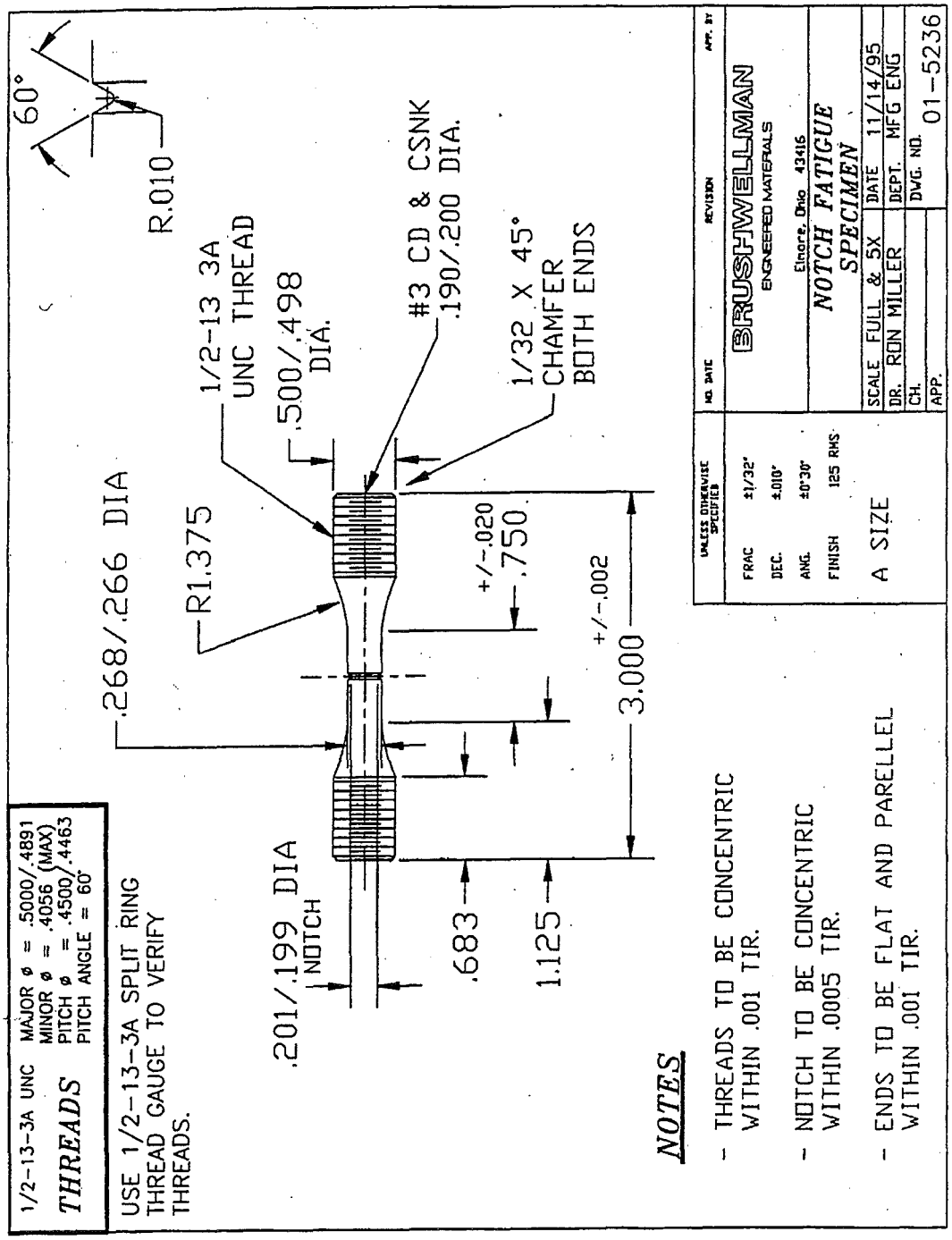

APPENDIX E

TEST SPECIMEN MACHINING PRINTS & PROCEDURES

FRACTURE TOUGHNESS PROCESS 01-5233 (K_{IC})

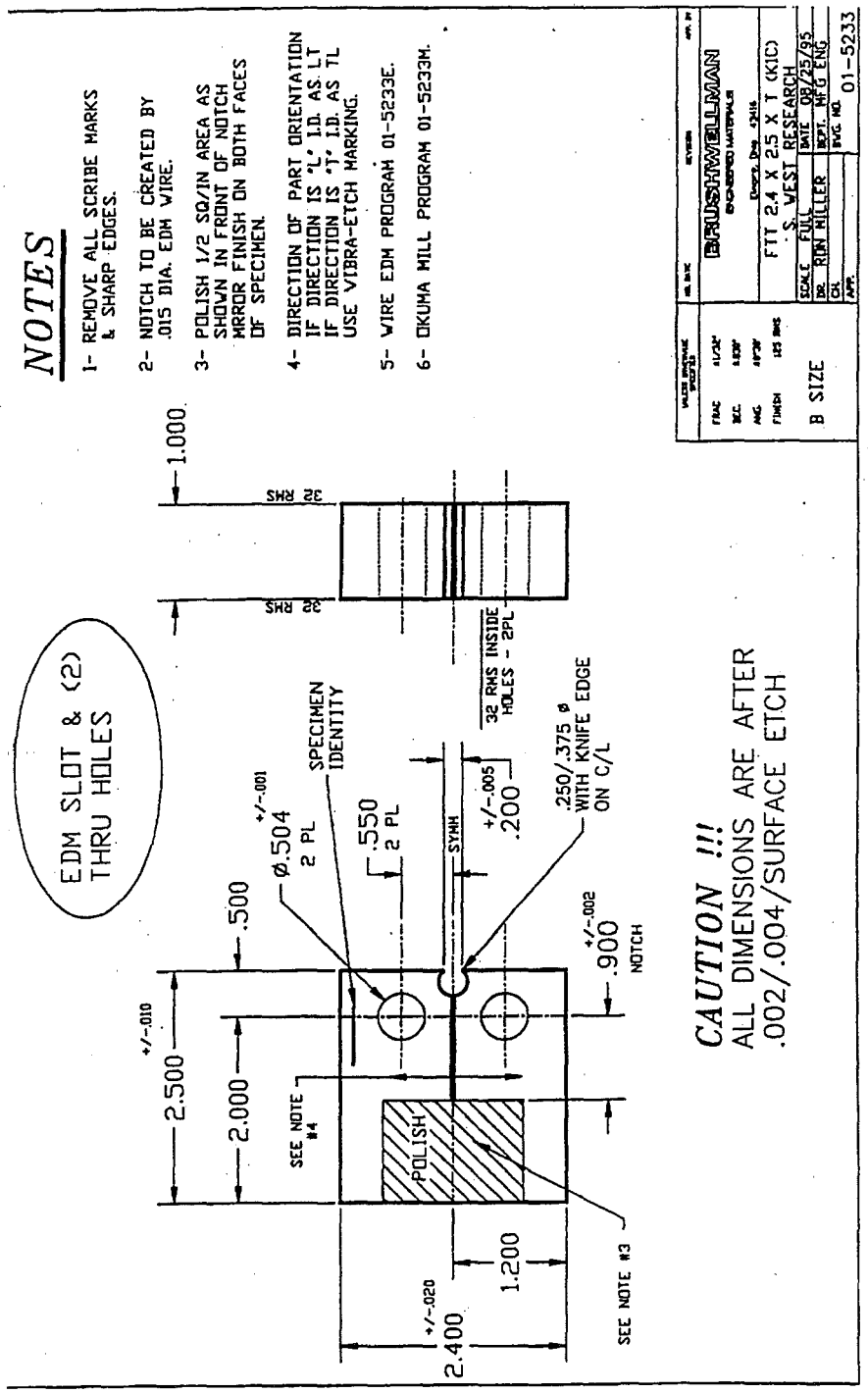

APPENDIX E

TEST SPECIMEN MACHINING PRINTS & PROCEDURES

FRACTURE TOUGHNESS PROCESS 01-5240 (J_{IC})

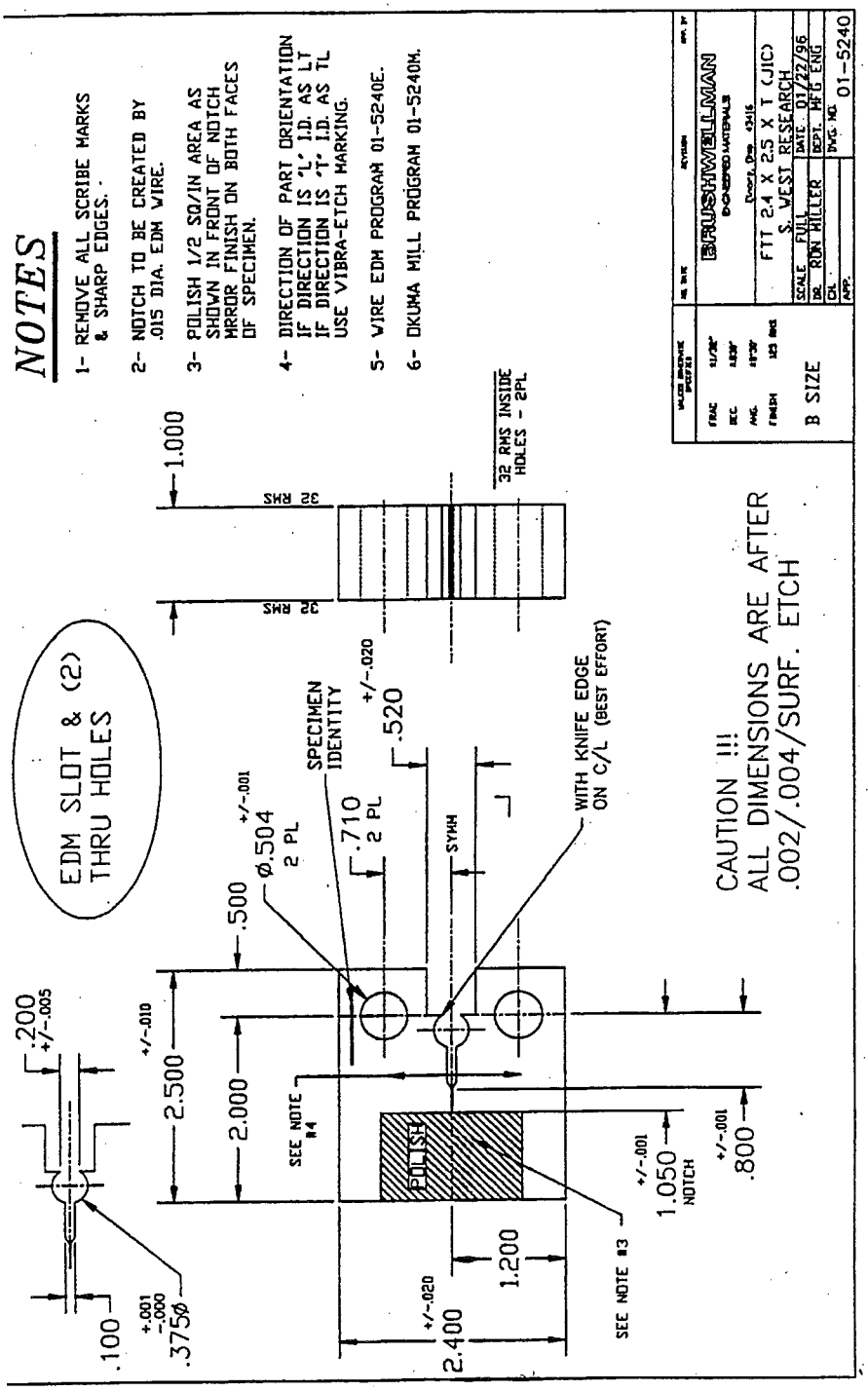

APPENDIX E

TEST SPECIMEN MACHINING PRINTS & PROCEDURES

CREEP PROCESS 01-523

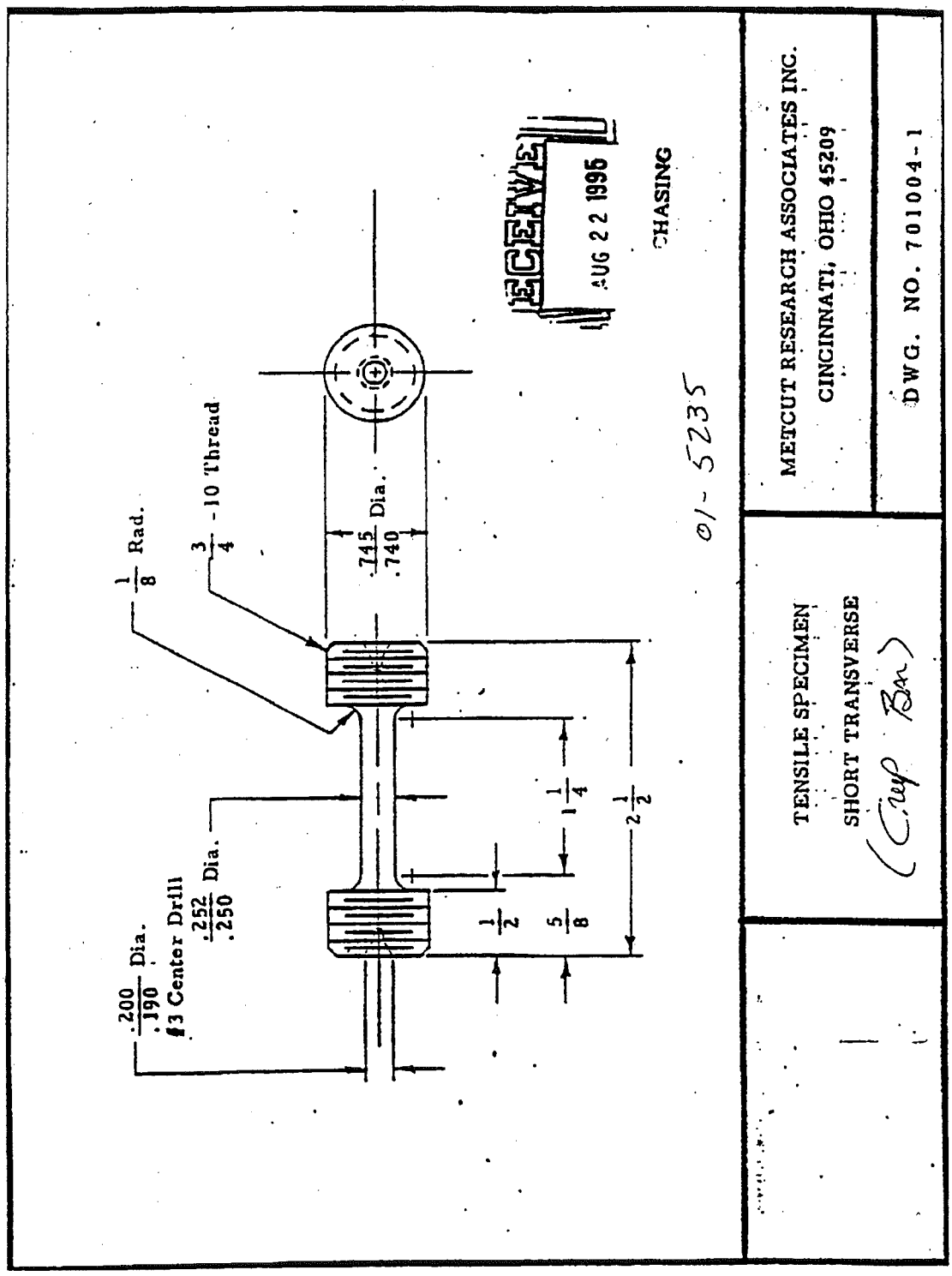

Temperature-strain rate dependence of mechanical properties of a beryllium of the DShG-200 brand

A.M. Khomutov, V.A. Gorokhov, V.S. Mikhailov, G.N. Nikolaev, R.Yu. Timofeev and V.M. Chernov

National Research Center of the RF – A.A. Bochvar Research Institute of Inorganic Materials (VNIINM)
123060, P.O. Box 369, VNIINM, Moscow, Russia.

Beryllium preforms of the DShG-200 brand of improved quality were manufactured by the method of a powder metallurgy and the mechanical tests on tension in longitudinal and transversal directions in temperature range 20-600°C and strain rates of 0,02 – 20 mm/min were held. It was shown, that at an alteration of strain rate within the indicated limits the values of stresses of flow and of the relative elongation can vary by several times.

Comparison testing for tension by the Russian and American procedures (GOST and ASTM) was made. The obtained results can be beneficial at calculations of thermal stresses originating in Fusion Reactors (FR).

1. INTRODUCTION

One of the basic demands made on beryllium as a shielding material of the first wall of the FR is the ability to withstand considerable and variable in time thermal loads originating both at normal conditions of maintenance, and at accidents. It is apparent, that the material will not fail at thermal effects, if the relaxational processes in it take place with the rate exceeding the rate of onset thermal stresses. Indirectly it is possible to access the relaxational ability of a material by responsivity of stresses of flow to a strain rate - the lower it is, the better relaxational ability is.

From model presentation [1] it follows, that beryllium of heightened purity with a relative coarse grain and low-level content of oxide inclusions along the grain boundaries has the best relaxational ability. Such metal is certain to have not high mechanical properties at a room temperature, however this circumstance is minor at use of beryllium as a liner of the first wall. Thermal resistance of beryllium depends also on the crystallographic texture. Beryllium with a texture of forging has the greatest stability to thermal shocks, then, in decreasing order follow extruded and hot-pressed metal. That is why, in the NRC of the RF VNIINM beryllium DShG-200 having feeble texture of forging and maximum relaxation rate of stresses was developed as one of materials promising for use as a shield of the first wall of ITER reactor. The tests held [2] proved the selected approach.

The rate of onset of thermal stresses is determined, with other things being equal, by the intensity of a heat flow effecting the first wall, or, in other words, by loading rate. In beryllium stresses of flow at heightened temperatures strongly depend on a strain rate [3] and, that is why, at computer simulation of fields of thermal stresses it is necessary to allow for this circumstance. Now for this purpose values of mechanical properties obtained at static tests are used, as a rule.

In this connection it should be noted that Russian and American standards of mechanical tests for tension presuppose different strain rates at loading to yield point, that is why, comparing results obtained by those two methods (especially at elevated temperatures) does not look quite correct.

From above-stated follows the significance of determination of temperature dependence of mechanical properties of beryllium supposed for use as a shielding material of the first wall at different strain rates, as well as holding of comparative mechanical tests under Russian (GOST) and American (ASTM) procedures. The experimental results for the DShG-200 brand, obtained by an improved technique, are given below.

2. EXPERIMENTAL PART

2.1. Host material

As a feed stock there was used beryllium after vacuum distillation, which after subdivision was exposed to pebbling in the ball mill. Further refinement was conducted in a grinder with subsequent air separation. Further followed merging in a mechanical mixer and certification (attestation) of the obtained batch of powder (not less than 5 kg) for chemical and granulometric compositions. The certified powder was exposed to a cold isostatic pressing. Then the cylindrical preform was loaded in a graphite mould with a clearance providing for its "conditional" strain at a subsequent hot pressing. The final manufacturing stage of DShG-200 brand beryllium is drop forging (settling) of the preform in an enclosed die. Before settling the preform was sealed hermetically in a steel envelope.

The results of chemical analysis of the initial powder and the compact metal are listed in the table, and in Figure 1 the typical microstructure of the obtained metal is presented.

Table
The content of basic impurities in the initial powder and compact metal (mass %).

Si	Fe	Al	C	O_2	
0,013	0,024	0,0045	0,077	0,52	initial powder
0,013	0,022	0,0043	0,079	0,79	compact metal

2.2. Mechanical tests

The mechanical tests for tension were conducted pursuant to the GOST 9651-61 on truncated samples with the diameter of the working section of 5 mm carved in bridge and perpendicularly to settling direction at three rates of migration of fissile capture: 0.02, 2.0 and 20 mm/min. The tests at heightened temperatures were conducted in vacuum. Before the tests the samples were exposed to electropolish for removal of a stratum injured at machining (operation) for the depth of 0.2 mm,

Figure 1. Microstructure of beryllium of DShG-200 brand. Polarized light.

since it is known, that surface defects, which emerge at machining, can essentially (up to 80%) bring down mechanical properties of beryllium.

The comparison testing by the Russian and American standards was made on hot-pressed beryllium of TGP-56 brand. At tests by ASTM procedure, before reaching yield point the strain rate was 0.05 mm/min, and then went up to 0.2 mm/min (the same samples were used, as at tests by the GOST). In all cases three samples per point were used.

For beryllium of DShG-200 brand values of Young's modulus were also measured. The measuring was conducted in an atmosphere of helium by an electrostatic method in temperature range 20-600°C. Cylindrical samples with diameter 5 and length 55 mm were used.

The observed data are presented in a graphic form in a Fig. 2-5.

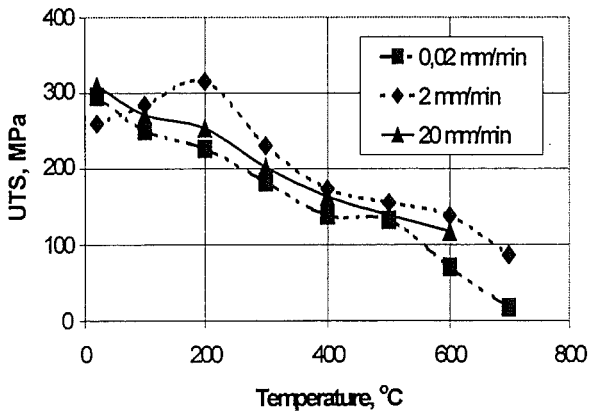

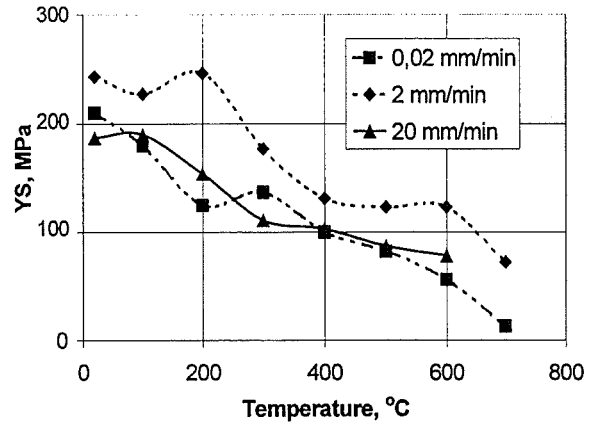

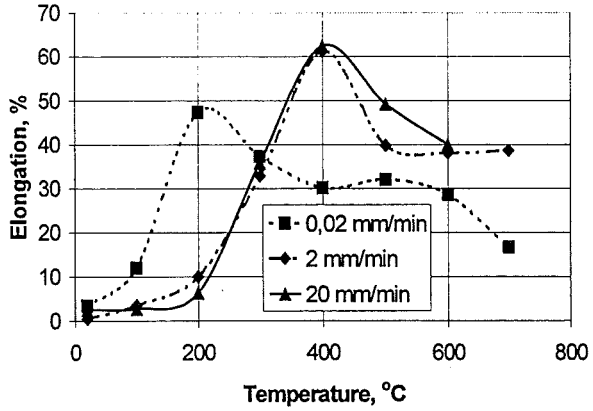

Figure 2. Temperature dependence of mechanical properties of DShG-200 brand for different strain rates. Transverse direction.

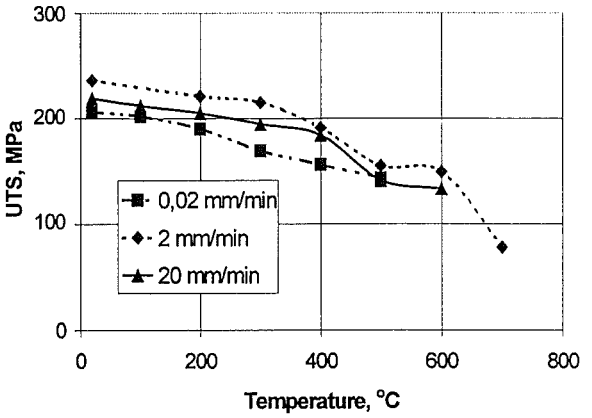

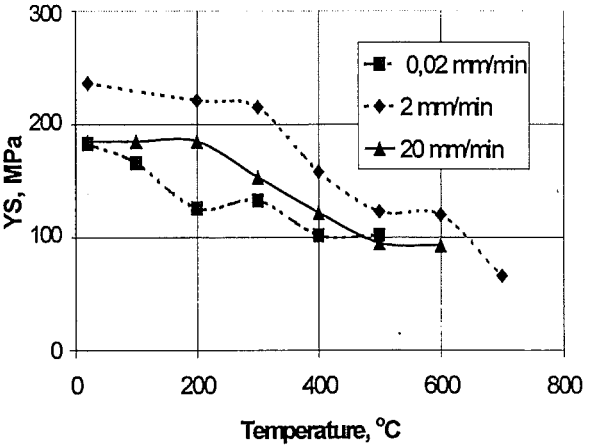

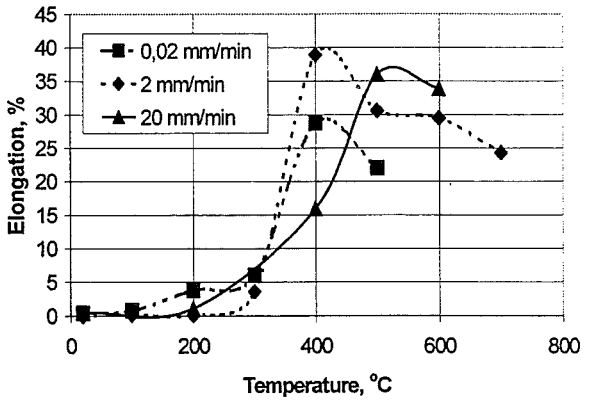

Figure 3. Temperature dependence of mechanical properties of DShG-200 brand for different strain rates. Longitudinal direction.

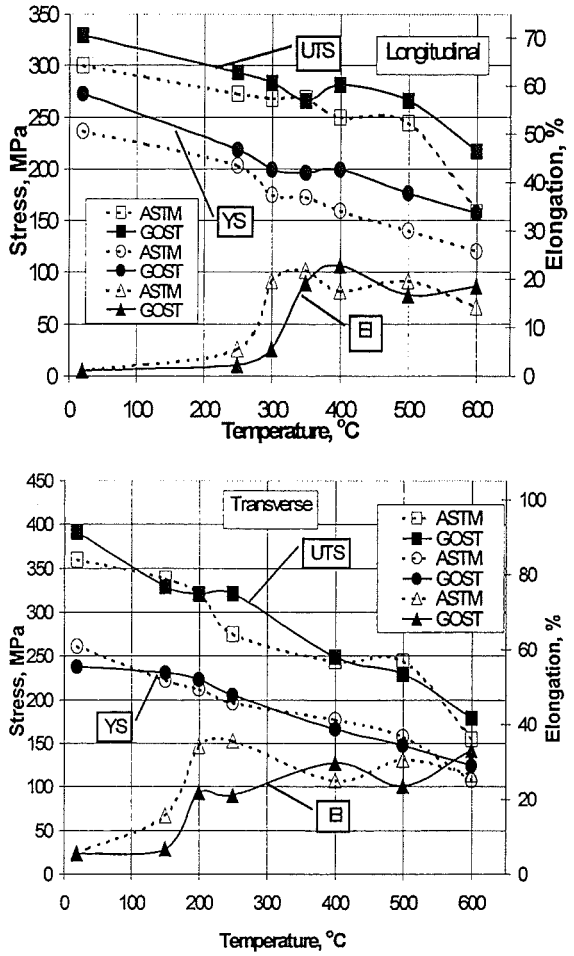

Figure 4. Comparison of mechanical properties of hot-pressed Be tested by using Russian and American standards.

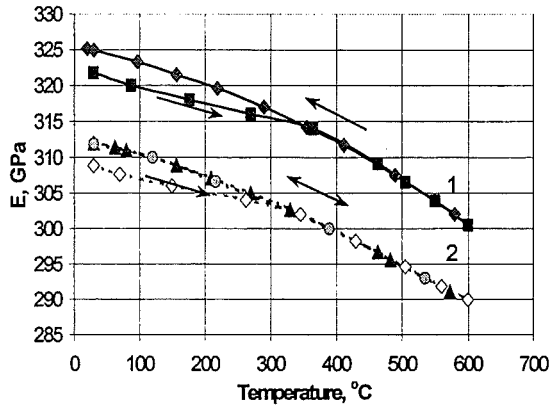

Figure 5. Temperature dependence of Young's modulus in two directions for DShG-200 brand.

3. CONCLUSION

The basic factor effecting beryllium in the composition of the first wall is the intensity of a heat flow, defining rate of thermal stresses ascending, maximum magnitude of which depends on the magnitude of stresses of flow in stated conditions. The obtained results on influence of a strain rate on the mechanical properties can be used as reference data at calculations of fields of thermal stresses in beryllium of DShG-200 brand.

The difference in result of mechanical tests, carried out in accordance with the Russian and American standards, is, mainly, in the overrated values of relative elongation of samples tested by ASTM, which is predetermined by the difference in loading rates at tests. Besides ASTM gives lower value of DBTT.

REFERENCE

1. A.M. Khomutov, V.S. Mikhailov, V.N. Pronin, Ya. D. Pakhomov. Inherent Structure Features of Beryllium and Their Influence on the Performance of Polycrystalline Metal under Different Conditions. In: Proc. of the Third IEA Int. Workshop on Beryllium Technology for Fusion. Oct. 22-24, 1997,Mito City, Japan.
2. M. Rodig, R. Duve, A. Gervash, A. Khomutov, J. Linke, A. Schuster. Thermal Shock Tests with Beryllium Coupons in the Electron Beam Facility JUDITH. In: Proc. of the 2nd IEA Int. Workshop on Beryllium Technology for Fusion. Sept. 6-8, 1995, pp 39-57.
3. Papirov I.I. and Tikhinskij G.F. Plastic Deformation of Beryllium. Atomizdat, Moscow, 1973. (in Russian)

Experimental Investigations on the Thermal and Mechanical Behaviour of Single Size Beryllium Pebble Beds

M. Dalle Donne[a], A. Goraieb[b], G. Piazza[a], F. Scaffidi-Argentina[a]

a) Forschungszentrum Karlsruhe, IKET, Postfach 36 40, D-76021 Karlsruhe, Germany
b) Goraieb Versuchstechnik, In der Tasch 4a, D-76227 Karlsruhe, Germany

For the next generation fusion reactors with a ceramic breeder blanket the use, as a neutron multiplier, of either a binary bed of large (≈ 2 mm) and small (≈ 0.1-0.2 mm) beryllium pebbles or a single size bed made of 1 mm or 2 mm pebbles is foreseen. The heat transfer parameters of such a binary pebble bed, namely the thermal conductivity and the heat transfer coefficient to the containing wall, have been investigated in the experimental devices PEHTRA and SUPERPEHTRA and have been reported in the companion paper at this workshop (Ref. [1]). In the present paper the results of analogous investigations for the single size beryllium pebble bed are shown and equations are given to correlate the heat transfer parameters.

1. INTRODUCTION

Originally the heat transfer work at FZK was concentrated on binary beryllium beds as they were proposed for the ITER breeder blanket and for the HCPB Demo Blanket design [2], because due to the higher pebble bed packing factor, they offer the possibility of having higher bed thermal conductivity and higher tritium breeding, although less space is available in the bed for the swelling and creep of the pebbles occurring during irradiation. Recently a study has shown that for an improved design of the HCPB blanket it is possible to have a sufficient breeding also by using a single size bed [3]. Thus heat transfer data for this bed was required. The experiments have been performed with the same devices, PEHTRA and SUPER-PEHTRA, and the same evaluation system used for the binary beds. These are dealt with in Ref. [1] and their description does not need to be repeated here.

2. EXPERIMENTS WITH THERMAL INSULATION

The types of experiments performed for the single size pebble bed were the same as for the binary bed (Ref. [1]). The pebbles used were the same as the 2 mm pebbles used for the binary bed. Furthermore the chosen packing factor was about 63 %, i.e. the same used for the 2 mm pebbles of the reference binary bed. Also the filling of the annulus test section was performed in the same way as for the binary bed, but of course without the final filling with the smaller pebbles.

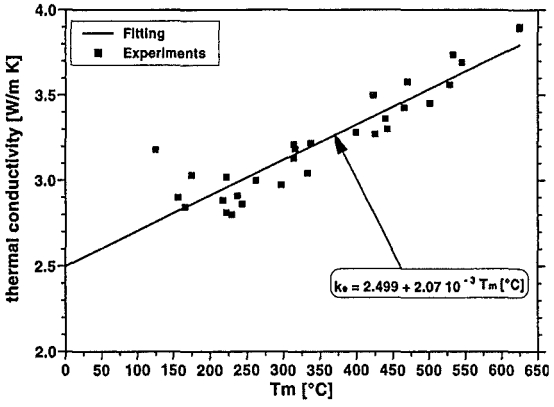

Fig. 1: PEHTRA: Thermal conductivity of the single size bed with 63 % packing factor, thermal insulation.

The first experiments were performed in the PEHTRA test rig. For these experiments the outer tube was surrounded by a thick and uniform thermal insulation to obtain values of the interference $\Delta\ell/\ell$ practically equal to zero.

This would not have been possible by the use of SUPER-PEHTRA due to the presence of the bulky pressure sensors at the measuring axial section of the test rig. Fig 1 shows the thermal conductivity data for the single size bed with the packing factor of ≈ 63 %, in the range $100 \leq T_m \leq 600$ °C, while Fig. 2 shows the heat transfer coefficient values for the temperature range $100 \leq T_W \leq 670$ °C.

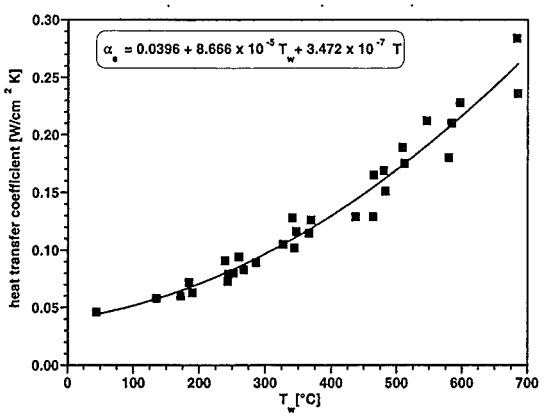

Fig. 2: PEHTRA: wall heat transfer coefficient of the single size bed with 63 %, packing factor, thermal insulation.

Further experiments with thermal insulation were performed for a single size bed with a packing factor of about 60 %. This kind of bed was used for the 2 mm pebbles in the intermediate binary bed (Ref. [1]). Fig. 3 and 4 show the thermal conductivity and heat transfer coefficient for the data with 60 % packing factor respectively.

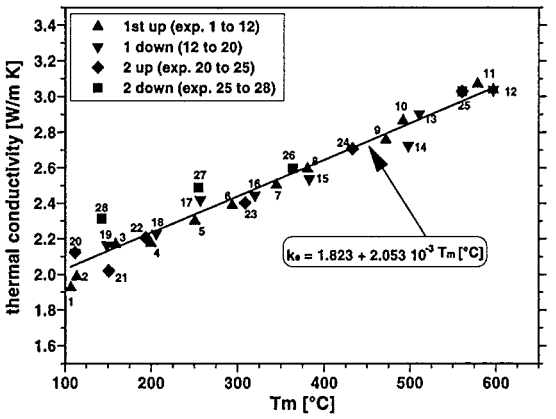

Fig. 3: PEHTRA: thermal conductivity of the single size bed with 60 % packing factor, thermal insulation.

The correlating equations are:

$$k_e\ [W/mK] = 2.50 + 2.07 \cdot 10^{-3}\ T_m \pm 10\ \% \qquad (1)$$

$$\alpha\ [W/cm^2K] = 0.0396 + 8.666 \cdot 10^{-5}\ T_w + + 3.472 \cdot 10^{-7}\ T_w^2 \pm 10\ \% \qquad (2)$$

for P.F ≈ 63 %; $100 \leq T_m \leq 600$ °C and $100 \leq T_w \leq 670$ °C;

$$k_e\ [W/mK] = 1.823 + 2.053 \cdot 10^{-3}\ T_m \pm 10\ \% \qquad (3)$$

$$\alpha\ [W/cm^2K] = 6.146\ 10^{-2} - 8.867 \cdot 10^{-5}\ T_W + + 7.899 \cdot 10^{-7}\ T_w^2 \pm 10\ \% \qquad (4)$$

for P.F. ≈ 60 %; $100 \leq T_m \leq 600$ °C and $100 \leq T_W \leq 670$ °C.

In both cases the thermal conductivity data present a small hysteresis which can be neglected as it lays within the scattering of the experimental points.

The heat transfer coefficients are plotted versus T_W (wall surface temperature of the inner rod) rather than T_m (average bed temperature), because they refer to a region in the immediate vicinity of the inner rod. T_m is used to correlate the thermal conductivity data because these refer essentially to the bulk of the pebble bed.

3. EXPERIMENTS WITH WATER COOLING

These experiments are performed with water cooling of the outer tube of the SUPER-PEHTRA experimental rig. This allows to make experiments only up to average bed temperatures in the range 25 – 200 °C. Furthermore the water cooling ensures a very uniform cooling of the casings containing the cylinders transmitting the pressure exerted by the bed to the pressure sensors, thus allowing a more precise measurement of the pressures than in the case of air cooling.

Fig. 5 shows the thermal conductivity values obtained with a single size pebble bed with a packing factor of 63.2 % and water cooling. The curve describing the first going-up phase (points 1-5) reaches up to a $\Delta\ell/\ell$ value of 0.66 %. The elastic-plastic deformations of the pebbles extend to the major part of the curve, the elastic region being probably limited to $\Delta\ell/\ell$ values lower than 0.1 %. During the first going down-phase (5-8) a fast decrease of the thermal conductivity is observed,

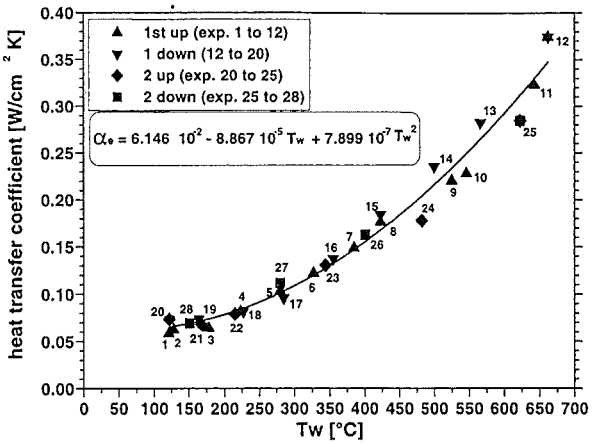

Fig. 4: PEHTRA: wall heat transfer coefficient of the single size bed with 60 % packing factor, thermal insulation.

showing that the constraint of the pebbles is released and the pebbles can detach from their contact surfaces. In the second part of the going down-phase (9 – 12), the thermal conductivity varies little, indicting that this is the phase where the pebbles locally relocate or rotate. The second going-up phase (13 – 18) shows a steep increase of the thermal conductivity, indicating the presence of large elastic-plastic deformations. The second going-down phase (19 – 22) is practically coincident with the first one. During the air cooling experiments also the second going-down phase has been repeated (Section 4), which shows that the cycling on the curves second going-up and going-

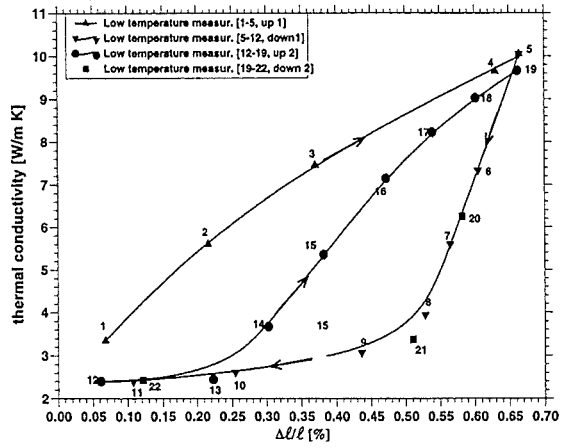

Fig. 5: SUPER-PEHTRA: thermal conductivity of the single size bed with 63 % packing factor, water cooling, first bed.

down is stable. The first going up is the locus of the apexes of the possible cycles. The hysteresis of the single size bed is very pronounced, showing very distinctly the different characteristics of the various phases.

Fig. 6 shows the thermal conductivity values obtained with a bed with single size pebbles, packing factor 63.2 % and water cooling. The thermal conductivity is similar to the one of the previous bed.

Fig. 7 shows the measured heat transfer coefficients. As in the case of the binary beds apart from the first going-up curve the hysteresis is quite small and probably within the scatter of the experimental points so that these data can be correlated by a single equation only.

Fig. 8 shows the measured pressures on the outer tube. The shape of the curves is quite similar to that of the relative thermal conductivity. The pressure data of Fig. 8 has been used by S. Hermsmeyer to calculate the contact surfaces of the pebbles and thus, with the help of the Schlünder model [4] calculate the thermal conductivity of the bed. The calculated values agree quite well with the experimental data of Fig. 6.

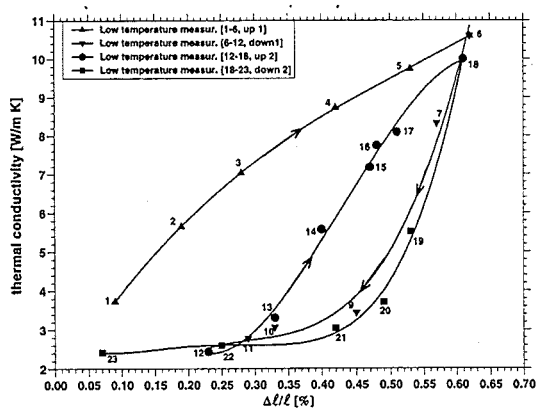

Fig. 6: SUPER-PEHTRA: thermal conductivity of the single size bed with 63 % packing factor, water cooling, second bed.

4. EXPERIMENTS WITH AIR COOLING

As in the case of the binary bed experiments, experiments with air cooling for the outer tube were performed in the SUPER-PEHTRA experimental device. This was done to obtain bed average temperatures of around 200 °C with $\Delta\ell/\ell$ values higher than zero. The use of water at temperatures above 100 °C was avoided to prevent too high steam pressures.

Fig. 9 shows the radial bed temperature distribution in a linear/logarithmic plot for the last test performed with air cooling (Test Nr. 34). As in the case of the binary bed experiments, the experimental points for all the runs performed in these experiments can be fitted well by a straight line (standard deviation 1.2 % - 2.8 %) indicating that the thermal conductivity is practically constant across the bed. Fig. 10 shows the measured

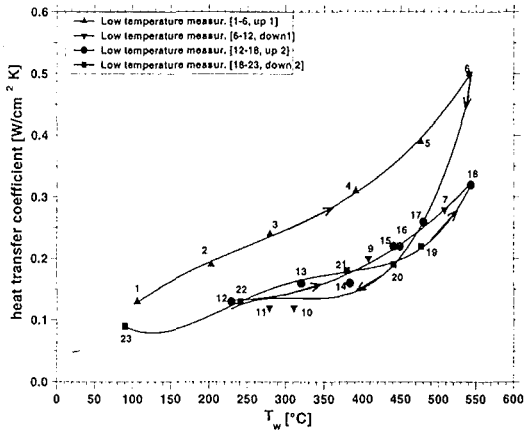

Fig. 7: SUPER-PEHTRA: wall heat transfer coefficient of single size bed with 63 % packing factor, water cooling, second bed.

temperature distribution on the walls of the outer and inner tube. The figure shows quite clearly that, even with the last performed experiment of this series, the heat moves essentially in the radial direction.

The thermal conductivity as a function of the interference $\Delta\ell/\ell$ is shown in Fig. 11. The first experimental runs (1 – 8) represent the heating up of the bed. The increasing values of $\Delta\ell/\ell$ are obtained by increasing the heat power and/or varying the cooling of the outer tube. The first cooling down phase (runs 8 – 14 and 23 – 30) and second going-up phase (runs 15 – 28 and 31 – 34) have been run twice, showing that they are repeatable. These two phases are the most important for design calculations as they are valid for the heating-up phase and the cooling down phase. The first going-up phase (runs 1 – 8) represents the upper locus of the apexes of the hysteresis cycles.

Fig. 12 shows the wall heat transfer coefficients at the inner rod surface. These account for the smaller packing factor at the inner rod wall which acts as a

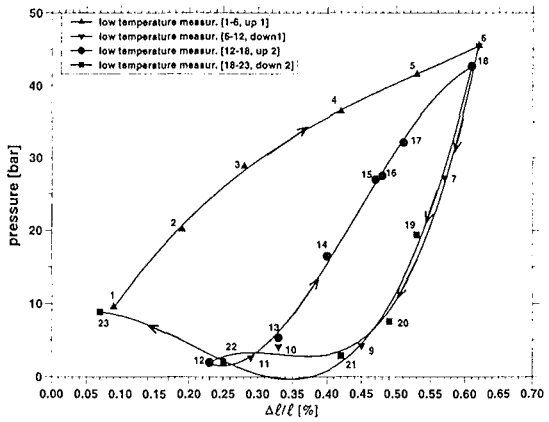

Fig. 8: SUPER-PEHTRA: average pressure at the four sensors as a function of $\Delta\ell/\ell$, water cooling, 63 % packing factor, second bed.

disturbance to the pebble causing locally a considerable decrease of the packing factor (from 63 % to about 48 %). The heat transfer coefficients are obtained by the heat flux at the wall divided by the difference between the measured temperature of the rod surface and the bed temperature

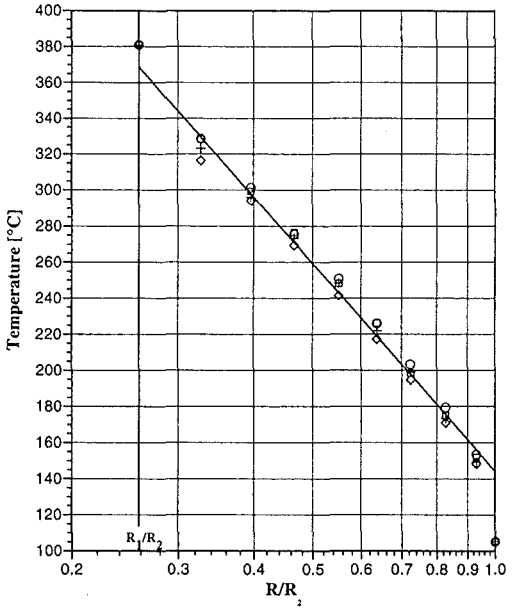

Fig. 9: SUPER-PEHTRA: radial temperature distribution in the bed: experiment 34, air cooling.

extrapolated to the rod surface. These temperature differences are relatively small, thus the data obtained for the inner rod are more reliable of those at the outer tube surface as the heat flux there is much smaller. The heat transfer data of Fig. 12 are thus those for the inner rod. The hysteresis between

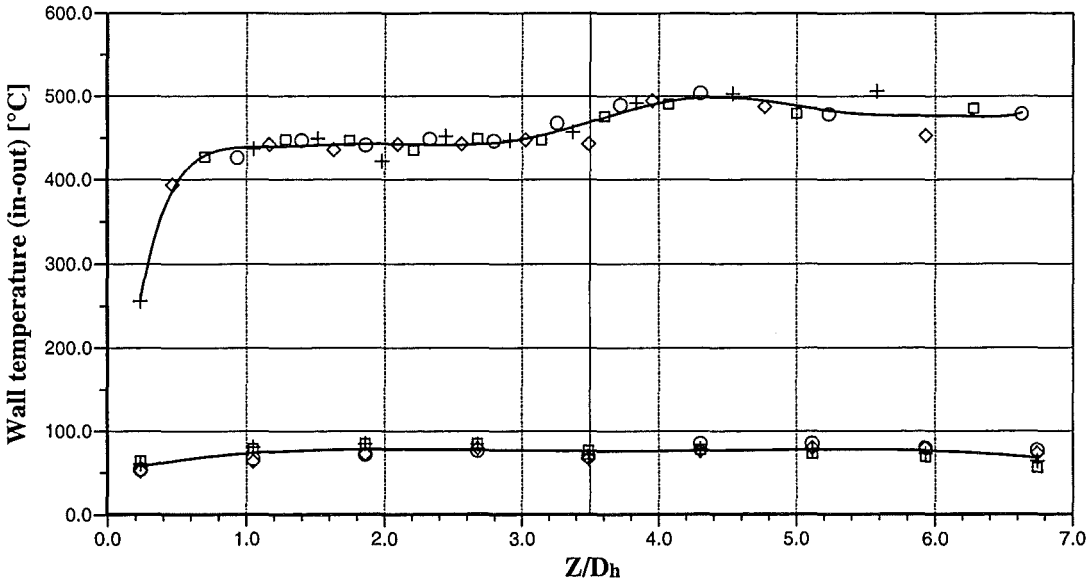

Fig. 10: SUPER-PEHTRA: axial temperature distribution at the inner and outer tube for experiment 34 ($\Delta\ell/\ell$ = 0.45 %, air cooling).

the first going-down phases (8 – 14 and 23 – 30) and second going-up (15 – 23 and 31 – 34) is more pronounced than in the case of the binary bed experiments and almost certainly greater than the scattering of the experimental points.

5. EXTRAPOLATION TO HIGHER TEMPERATURES OF THE SINGLE SIZE BED THERMAL CONDUCTIVITY EXPERIMENTAL DATA WITH THE HELP OF THE SCHLÜNDER MODEL

The present experiments have been performed for average bed temperatures up to 200 °C, while for the HCPB DEMO blanket maximum temperatures of up to 640 °C at BOL and of up to 500 °C at EOL are foreseen [2]. The temperature limitation in the present experiments is due to the fact that to reach high values of the interference $\Delta\ell/\ell$ we have to increase the temperature difference between the inner rod and the outer tube of the test section. However we have to avoid local temperatures above 500 °C near the inner rod as, in presence high values of $\Delta\ell/\ell$, we would have the creep of the pebbles producing a local increase of the bed thermal conductivity [6]. Creep and beryllium swelling under irradiation are governed by different phenomena than those relevant in the present experiments and are and shall be investigated separately with the computer model ANFIBE [7, 8].

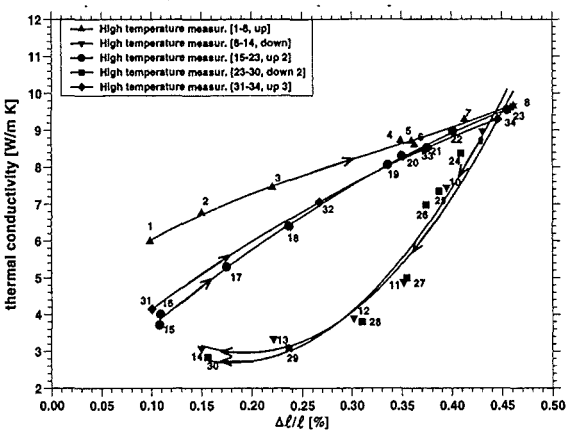

Fig. 11: SUPER-PEHTRA: thermal conductivity of the single size bed with 63 % packing factor, air cooling.

Furthermore an extrapolation to higher temperature experiments obtained at 200 °C would produce too high thermal conductivity values as the thermal conductivity of beryllium at 200 °C is about 25 % higher than at 400 °C.A reliable extrapolation of our experiments can however be performed with the

help of the Schlünder model [4]. This model accounts for practically all the parameters which determine the thermal conductivity of the bed. The model has been successfully tested with many experiments and works well especially with single size beds. Most of these parameters can be obtained by the input data. For instance the thermal conductivity of the solid and fluid is given at the proper bed temperature as an input. A parameter which, however should be determined with specific experiments is the one accounting for the heat transfer between the solid pebbles, which is given by the square of the ratio between the diameter of the contact surface of the pebbles d_K and the average diameter of the pebble $\bar{d}$

$$\rho_K^2 = \left(\frac{d_K}{\bar{d}} \right)^2 \qquad (5)$$

Schlünder and Bauer suggest that the parameter ρ_K^2 should be determined by an experiment [4]. We have determined experimentally the parameter ρ_K^2 for a pebble bed at an average temperature of 200 °C, i.e. at a beryllium pebble temperature of 200 °C. To obtain bed thermal conductivity data at

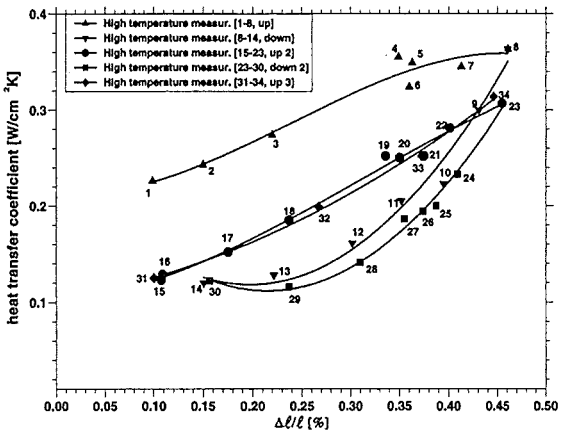

Fig. 12: SUPER-PEHTRA: wall heat transfer coefficient of single size bed with 63% packing factor, air cooling.

higher temperatures we have simply to replace as an input in the Schlünder model the beryllium thermal conductivity at the chosen higher temperature in place of the one at 200 °C.

The parameter ρ_K^2 is a microscopic variable. To be able to produce a correlation, we should correlate ρ_K^2 with a related macroscopic parameter which we have measured. The best suited experimental variable appears to be $\Delta\ell/\ell$, which is also related to the contact surface of the pebble. Indeed it can be shown by simple geometrical considerations that in case of a bed formed by pebbles arranged as in a radial chain,. ρ_K^2 is equal to 0.5 $\Delta\ell/\ell$[a].

To facilitate the work of the designer we have calculated the following equation which is a fitting of the Schlünder model:

$$k(T,\rho_k^2) = a(T_m) + b(T_m)\,(\rho_k^2) + c(T_m)(\rho_k^2)^2$$

$$a(T_m) = 2.372 + 2.957\ 10^{-3}\ T_m - 17.67\ 10^{-7}\ T_m^2 \qquad (6)$$

$$b(T_m) = 25.3809 - 31.7344\ 10^{-3}\ T_m + 2.2049\ 10^{-5}\ T_m^2$$

$$c(T_m) = -10.6289 + 12.022\ 10^{-3}\ T_m - 9.23\ 10^{-6}\ T_m^2$$

with T_m [°C] and k[W/m°C].

Fig. 13 shows a plot of equation (6), i.e. the bed thermal conductivity as a function of the bed average temperature and ρ_K^2. For each experimental point of Fig. 11 we have obtained the value of ρ_K^2 which allows to have the best agreement of the experimental k value with the Schlünder model prediction. This allows us to find the relationship:

$$\rho_K^2 = f\left(\frac{\Delta\ell}{\ell} \right) \qquad (7)$$

Of course this relationship varies for the various phases i.e. for the first go-up phase, the following go-down phases or go-up phases.
By the fitting of the experimental points we obtain:

[a] It should be noticed that a radial chain arrangement of the pebbles certainly does not occur in the beds we have investigated in the present experiments. It could only be present in a pebble bed confined by two parallel plates and in presence of a simple cubic arrangement of the pebbles which implies a relatively low packing factor (52.4%)

for the first going up phase

$$\rho_k^2[\%]=1.547\left(\frac{\Delta\ell}{\ell}[\%]\right)-1.346\left(\frac{\Delta\ell}{\ell}[\%]\right)^2 \quad (8)$$

$$for\ 0\le\frac{\Delta\ell}{\ell}[\%]\le 0.46$$

for the first going down phase

$$\rho_k^2[\%]=-1.091\left(\frac{\Delta\ell}{\ell}[\%]\right)+4.474\left(\frac{\Delta\ell}{\ell}[\%]\right)^2 \quad (9)$$

$$for\ 0.46\ge\frac{\Delta\ell}{\ell}[\%]\ge 0.25$$

$$\rho_k^2[\%]=0 \quad for\ 0\le\frac{\Delta\ell}{\ell}[\%]\le 0.25$$

for the second going up phase

$$\rho_k^2[\%]= 0.9205\left(\frac{\Delta\ell}{\ell}[\%]\right) \quad (10)$$

$$for\ 0\le\frac{\Delta\ell}{\ell}[\%]\le 0.46$$

With equations (6), (7), (8), (9), (10) we are able to

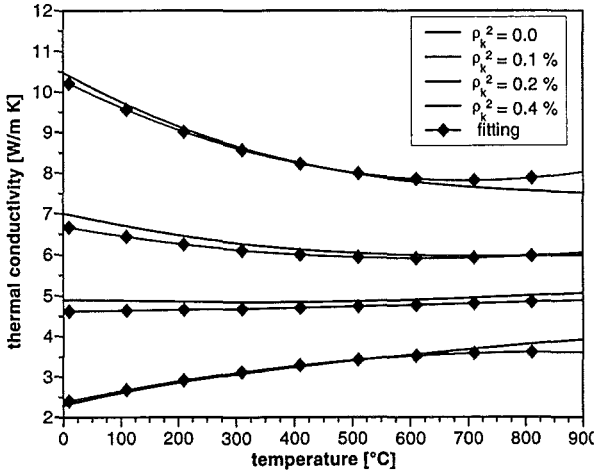

Fig. 13: thermal conductivity of the single size bed with 63 % packing factor according to the Schlünder model and fitting of our experimental values.

predict the thermal conductivity of the single size bed with 2 mm beryllium pebbles, and a packing factor of 63 % for temperatures up to the limitation caused by the occurring of other phenomena such as creep and volume swelling under irradiation. It should be stressed that these equations should be used only in the ranges of $\Delta\ell/\ell$ [%] indicated.

6. ALTERNATIVE DATA CORRELATION METHODS

6.1 Correlation with thermal conductivity versus pressure

The correlation method used in Chapter 5 offers the advantage that it accounts for the hysteresis which is present with our thermal conductivity data. This hysteresis implies that irreversible phenomena associated with the plastic deformations and local displacements of the pebbles occur in the bed. However reversible phenomena occur as well, such as elastic deformations and local relocations of the pebbles. These reversible phenomena are related to changes of the pressure exerted on the containment walls.

The plots of the thermal conductivity (Fig. 6) and pressure (Fig. 8) are rather similar, so we decided to use the correlation k versus p to see if it were possible to eliminate the hysteresis which could sometimes make the application of our correlation rather difficult.

Fig. 14 shows the thermal conductivity of the single size bed with 63 % p.f. , in the case of the second bed with water cooling. The scatter of the experimental points is slightly higher than in Fig. 6 and 8. In the experiment 23, the measured pressure is probably too high (see Fig. 8). The data are correlated by the equation:

$$k\ [W/m\ K] = 2.2 + 0.184\ p\ [bar] \pm 10\ \% \quad (11)$$

for $2.2 \le p[bar] \le 46$.

The pressure of 46 bar corresponds to a deformation of $\Delta\ell/\ell$ [%] = 0.65 (see Fig. 8). The elastic deformation of solid beryllium is limited to about 0.1%. This means that the reversible deformation caused by pebble relocation is preponderant.

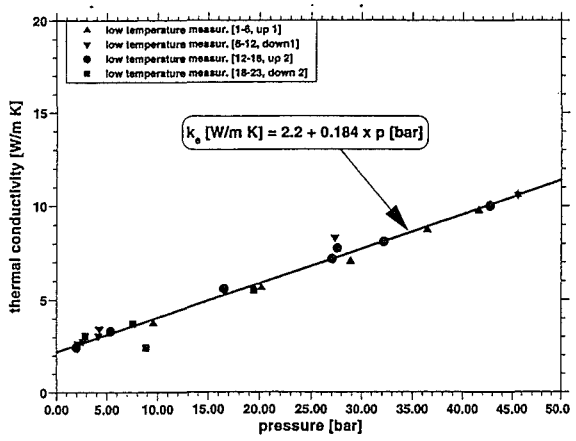

Fig. 14: thermal conductivity of the single size bed with 63% packing factor versus pressure. Water cooling, second bed.

Although in our experimental arrangement we have a bed subjected to a triaxial constraint (radial, circumferencial, axial), we can measure the thermal conductivity of the bed assuring that at the axial middle of the test section, it is well defined because the constraint and the heat flux are both in the radial direction. Thus our thermal conductivity data are valid for situations where the heat flux and the constraint are both in the same direction.

In the application of our data this clearly defined situation is sometime not possible to realize. In the praxis there are often situations where the heat flux does not go in the direction of the main constraint. To reduce the errors connected with this situation, it would be probably convenient to correlate our thermal conductivity data versus the volumetric interference in the pebble bed investigated.

The volumetric interference has been calculated for each experiment (see Appendix I).

The data can be thus correlated with a procedure analogous to the case for the correlation with $\Delta\ell/\ell$.

As in case of $\Delta\ell/\ell$ we use the fitting of the Schlünder model given by Eq. (6). For each experimental value of ΔV/V we obtain the value of ρ_k^2 which allows to have the best agreement of the experimental k value with the Schlünder model prediction. This allows us to find the relationship

$$\rho_K^2 = f\left(\frac{\Delta V}{V}\right) \qquad (12)$$

As in the case of $\Delta\ell/\ell$ this relationship varies with various phases, i.e. the first going up phase and the following going down or going up phases.

By the fitting of the experimental points we obtain

for the first going up phase

$$\rho_k^2[\%]=0.139+0.609\left(\frac{\Delta V}{V}[\%]\right)-0.184\left(\frac{\Delta V}{V}[\%]\right)^2 \qquad (13)$$

$$for\ 0\le\frac{\Delta V}{V}[\%]\le 0.6$$

for the two going down phases

$$\rho_k^2[\%]=0.078-0.96\left(\frac{\Delta V}{V}[\%]\right)+2.65\left(\frac{\Delta V}{V}[\%]\right)^2 \qquad (14)$$

$$for\ 0.25 \le \frac{\Delta V}{V}[\%]\le 0.6$$

$$\rho_k^2[\%]=0 \quad for\ \ 0\le\frac{\Delta V}{V}[\%]\le 0.25$$

for the second and third going up phase

$$\rho_k^2[\%]=0.0056+0.85\left(\frac{\Delta V}{V}[\%]\right)-0.26\left(\frac{\Delta V}{V}[\%]\right)^2 \qquad (15)$$

$$for\ 0\le\frac{\Delta V}{V}[\%]\le 0.6$$

Also here, like in the case of correlation based on $\Delta\ell/\ell$, it should be stressed that these equations should be used only in the ranges of ΔV/V[%] indicated.

7. CONCLUSIONS

The heat transfer parameters and pressures exerted on the containment walls of two single size beryllium pebble bed with 63 % and 60 % packing factors have been obtained by investigations performed in the PEHTRA and SUPER-PEHTRA experimental devices.

The experiments with thermal insulation were performed in PEHTRA and allowed to measure the heat transfer parameters for an interference $\Delta\ell/\ell$ [%] = 0. These data are given by Equation (1), (2) and (3), (4) for the two packing factors respectively.

The experiments with $\Delta\ell/\ell$ [%] > 0 were performed in SUPER-PEHTRA. Two series of experiments were performed with $\Delta\ell/\ell$ [%] > 0. The first was with water cooling, which allowed to have pebble bed average temperatures of 25 – 200 °C. The second was with air cooling and bed average temperatures of about 200 °C. As the data of the single size bed were needed for the design of the

bed average temperatures of 25 – 200 °C. The second was with air cooling and bed average temperatures of about 200 °C. As the data of the single size bed were needed for the design of the DEMO HCPB blanket and for high temperature irradiation tests, the experimental data were extrapolated to higher temperatures with the help of the Schlünder model. The extrapolated correlation is not valid for temperatures above 500 °C, because at these temperatures and in presence of a strong constraint ($p \geq 60$ bar) of the bed the pebbles start to creep. To give the possibility to the designers to use in various cases the present experimental data on the measured parameters of the single size beryllium pebble bed investigated, these data have been correlated in terms of $\Delta\ell/\ell$ (linear interference) and $\Delta V/V$ (volumetric interference) and with the pressure exerted on the outer containment wall.
The equations (6), (7), (8), (9), (10) and (6), (13), (14) and (15) give the correlation equation in terms of $\Delta\ell/\ell$ and $\Delta V/V$ respectively.
Equation (11) gives the relationship between the thermal conductivity and the pressure for a single size pebble bed for a packing factor of 63 %.

ACKNOWLEDGEMENT

This work has been performed in the framework of the nuclear Fusion Project of the Forschungszentrum Karlsruhe and is supported by the European Communities within the European Fusion Technology Program. The authors wish to thank R. Aymar, L.V. Boccaccini, W. Dänner, S. Hermsmeyer, K. Schleisiek, G. Sordon and R. Toschi for their support and the many useful discussions

REFERENCES

[1] M. Dalle Donne, A. Goraieb, G. Piazza, F. Scaffidi-Argentina: "Measurements of the heat transfer parameters in infiltrated binary beryllium beds. Comparison between the results with PEHTRA and SUPER-PEHTRA", 4th Int. Workshop on Beryllium Technology for Fusion, Forschungszentrum Karlsruhe, Karlsruhe, Germany, Sept. 15 – 17, 1999.

[2] M. Dalle Donne (compiler), "European DEMO BOT solid breeder blanket", Kernforschungszentrum Karlsruhe report KfK 5429, November 1994.

[3] S. Hermsmeyer, "Improved Helium Cooled Pebble Bed blanket", Executive Summary, Forschungszentrum Karlsruhe, July 1999.

[4] E.V. Schlünder, "Particle Heat Transfer", Proc. 7th Int. Heat Transfer Conf., Munich, Germany, 1982, Vol. 1, RK10, 195 – 212.
See also: VDI-Wärmeatlas, Berechnungsblätter für den Wärmeübergang, VDI-Verlag GmbH, Verlag des Vereins Deutscher Ingenieure, Düsseldorf, 4. Auflage 1984, De10 Ersatz 1985.

[5] S. Hermsmeyer, Forschungszentrum Karlsruhe, October 1999, private communication.

[6] J. Reimann and M Behnke, Forschungszentrum Karlsruhe, 1999, private communication.

[7] F. Scaffidi-Argentina, M. Dalle Donne, C. Ronchi and C. Ferrero, "ANFIBE a comprehensive model for swelling and tritium release from neutron irradiated beryllium, I: Theory and model capabilities", Fus. Technol. 32, 179 – 195, September 1997.

[8] F. Scaffidi-Argentina, M. Dalle Donne, C. Ronchi and C. Ferrero, "ANFIBE a comprehensive model for swelling and tritium release from neutron irradiated beryllium, II: Comparison of model predictions with experimental results", Fus. Technol. 33, 146 – 163, March 1998.

List of Symbols

E_{ss} = elasticity module of stainless-steel [MPa]

k = $k_e = \dfrac{Q_0 R_1 \ln \dfrac{R_2}{R_1}}{T_1 - T_2}$

T_1 = bed temperature extrapolated at the rod surface [°C]

T_2 = bed temperature extrapolated at the outer tube surface [°C]

ℓ = thickness of the bed in the direction of the heat flow = R_2 - R_1 [cm]

p = pressure on the outer tube [MPa]

Q_o = heat flux at the inner wall [W/cm^2]

R_1 = outer radius of the inner heating tube [cm]

R_2 = inner radius of the outer containing tube [cm]

S = outer tube thickness [cm]

$T=T_m$= average temperature of the bed calculated over the total surface of the annulus containing the bed [°C]

T_{w1}= temperature of the outer surface of the inner tube [°C]

T_{w2}= temperature of the inner surface of the outer tube [°C]

T_o = room temperature = 20 °C

α= heat transfer coefficient between bed and containing wall at the outer surface of the inner tube [W/cm^2°C]

α_{Be} = thermal expansion coefficient of beryllium at T_{Be} [K^{-1}]

α_{St} = thermal expansion coefficient of the containing walls of stainless steel [K^{-1}]

σ = standard deviation

$\Delta\ell/\ell$ [%] = percental difference between the thermal expansion of the bed and of the confinement walls referred to the thickness of the bed =

$$= 100x \left[\frac{\int_{R_1}^{R_2} \alpha_{Be}(T_{Be})(T_{Be} - T_0)dr}{R_2 - R_1} + \frac{\alpha_{St2}R_2 - \alpha_{St1}R_1}{R_2 - R_1} T_o - \frac{\alpha_{St2}R_2T_{w2} - \alpha_{St1}R_1T_{w1}}{R_2 - R_1} - \frac{pR_2}{SE_{ss}} \right]$$

Subscripts:

m = mean value
w = wall
1 = inner wall (r = R_1)
2 = outer wall (r = R_2)
o = at room temperature
Be = beryllium
St = stainless steel
exp = expanded
bed = pebble bed

APPENDIX I: CALCULATION OF ΔV/V

$$\Delta V/V = (V_{bed} - V_w) / V_0$$

$$V_{bed} = \sum h\, 2\pi\, r_i\, \Delta r\, (1+\alpha_{Be}(T)\Delta T(r_i))^3$$

$$V_w = \pi\, h_{exp}\, (R_2^2{}_{exp} - R_1^2{}_{exp})$$

$$V_0 = \pi\, h_0\, (R_2^2 - R_1^2)$$

$$h_{exp} = h_0\, (1+ \alpha_{st}(T_{w2})\, \Delta T_2)^a$$

$$R_{2exp} = R_2\, (1+ \alpha_{st}(T_{w2})\, \Delta T_2)$$

$$R_{1exp} = R_1\, (1+ \alpha_{st}(T_{w1})\, \Delta T_1)$$

$$\Delta T_1 = T_{w1} - 20\ °C$$

$$\Delta T_2 = T_{w2} - 20\ °C$$

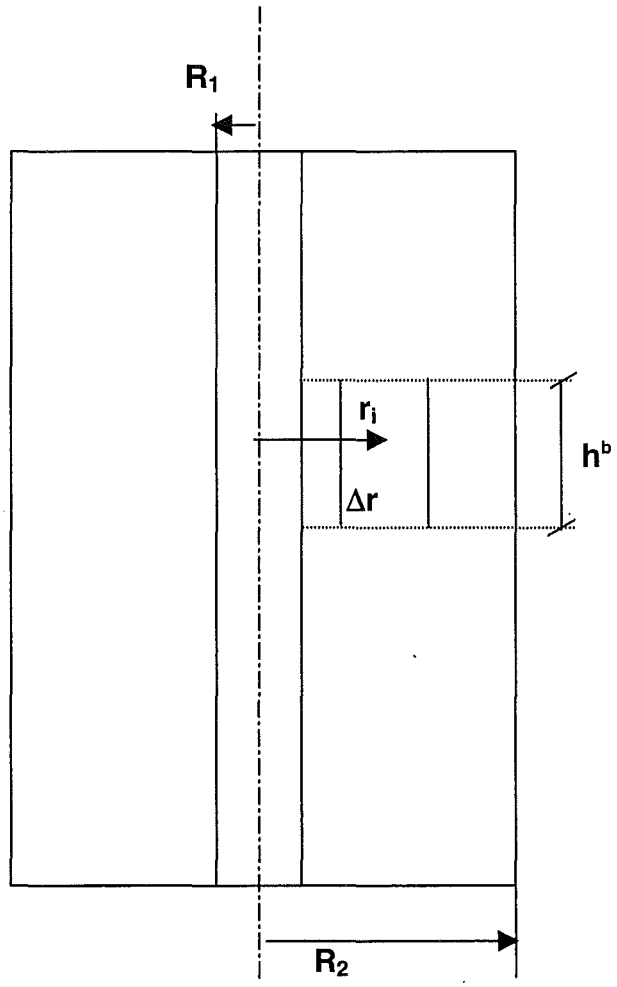

The meaning of the symbols can be obtained from the list of symbols and from the sketch shown above.

---

[a] the constraint in axial direction is given by the expansion of the outer tube only, as the inner heating rod is free to expand in the axial direction

[b] h is the height of a short axial section around the middle cross axial cross section where the experimental measurements are performed

Mechanical behaviour of monosized and binary beryllium pebble beds

J. Reimann, M. Behnke

Association FZK-EURATOM, Forschungszentrum Karlsruhe,
Postfach 3640, D-76021 Karlsruhe, Germany

Uniaxial compression tests with monosized and binary beryllium pebble beds were performed in a temperature range between ambient temperature and 480 °C and pressures up to 8 MPa. Empirical correlations for the moduli of deformation are given for the different bed types and first measurements for thermal creep are presented. Stress-strain relations depend sensitively on the initial state of the bed and with this on the filling procedure. This is of special importance for binary beds where it must be ensured that a homogeneous distribution of small pebbles in the bed is obtained.

First results for triaxial compression tests for monosized and binary beds are reported. The internal friction of these beds is significantly larger than that of beds with particles with smooth surfaces.

1. INTRODUCTION

Ceramic breeder blankets consist of ceramic breeder and beryllium pebble beds; the latter are needed for neutron multiplication. For the ITER breeding blanket [1] binary beryllium pebble beds are foreseen, consisting of large pebbles of about 2 mm diameter and small pebbles between 0.15 and 0.25 mm. During operation, stresses arise due to different thermal expansions of the structural and the pebble bed materials, pebble bed swelling and thermal creep. These stresses cause deformations of the pebble beds because of pebble rearrangements into a denser configuration, pebble failure, and elastic and plastic deformations of pebbles which increase the contact areas between pebbles. The latter is of importance for the heat removal by conduction in the pebble bed.

This stress build-up jeopardises the safe blanket operation if the mechanical integrity of the blanket element is endangered or if heat and tritium removal are significantly deteriorated due to pebble breakage or melting.

In order to describe the thermomechanical behaviour of a blanket element, finite element codes are used with appropriate models for the description of pebble beds. As input, these models require data on characteristic pebble bed properties determined in standard-type tests currently used in soil mechanics.

Of prime importance are uniaxial compression tests (UCTs). In these tests, an axial force is exerted on the top of a pebble bed contained in a cylindrical cavity (details given in Section 2.1) and the relationship between the axial stress within the pebble bed (identical to the axial pressure) and the axial strain is determined. Keeping the pressure constant at elevated temperatures, such an apparatus is also used to measure thermal creep strains.

For the description of the macroscopic movement (flow) of pebbles, triaxial compression tests (TCTs) are additionally required which provide information on the inner friction angle of the pebble bed. In these tests, cylindrical pebble beds are subjected to an increasing vertical pressure (resulting in a vertical strain), while at the same time the horizontal pressure is kept constant and the bed is allowed to deform in the horizontal direction, for details, see Section 2.2.

Prior to the present investigations, no relevant data from UCTs and TCTs existed for beryllium pebble beds. There is a considerable amount of UCT data for different ceramic breeder materials [2-3], an overview is given in [4]. The original aim of the present

investigations was to generate data for binary beds for temperature and pressure ranges characteristic for the ITER breeding blanket. However, results from measurements with monosized beds are also presented which might become of interest for future blanket concepts. This paper presents a summary of the results, for more details, see [5].

2. EXPERIMENTAL

2.1. Uniaxial compression test (UCT) apparatus

The handling of Be pebble beds required the construction a new test facility installed in a glove box. This glove box consisted of 3 parts: the lock, the storage area and the experimental area. Storage and experimental areas were connected with a rail system to transport more easily components from one side to the other. The helium gas (pressure: slightly subatmospheric) in the glove-box was circulated to a cooling system in order to limit the temperature increase during operation at the top of the glove box to about 60°C.

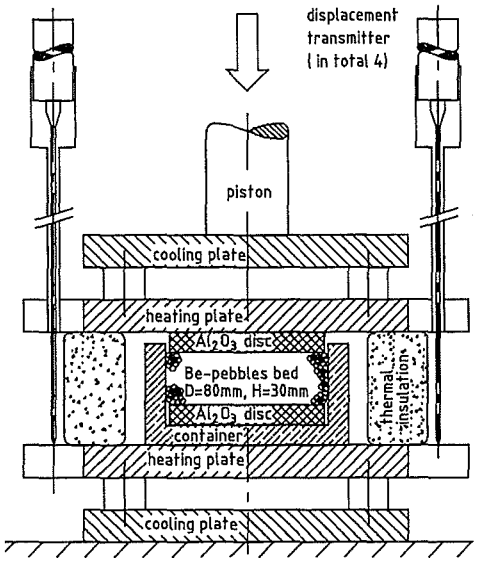

Figure 1. Set-up for UCT

Figure 1 shows schematically the press (Fa Weber, Germany) with the most relevant parts of the UTC: The granular material was filled in a circular stainless steel cavity with an inner diameter of 80 mm and an inner height of 45 mm, see Fig. 2. Al_2O_3 discs were used at the top and the bottom (as in previous experiments [2-3]) because of the good compatibility with the granular material (no fritting together) and the large surface hardness. Bed heights up to 43 mm were investigated. The small ratio of bed height to diameter ensured that the wall friction does not affect remarkably the results.

The pebble bed was heated from the top and the bottom to constant temperature levels by temperature controlled heating plates; the adjacent cooling plates were required to avoid the heating-up of other parts of the facility.

The bed temperature was determined by three thermocouples installed in the container wall. The bed strains were measured by four inductive displacement transducers positioned outside the high temperature zone by using quartz rods and tubes, see Fig. 1. The use of 4 transducers proved to be very beneficial for the control of the parallelisms of the top Al_2O_3 disc during operation.

The pressure exerted axially on the pebble bed was measured via a pressure transducer in the hydraulic system.

The measured signals were processed by a data acquisition system (MEMESS) and stored in a PC.

2.2. Triaxial compression test (TCT) apparatus

The TCT-apparatus developed for the present experiments is schematically shown in Fig. 2. The pebble bed is filled in a cylindrical cavity of 60 mm diameter where the cylindrical wall consists of solid polyethylenglycol (PEG) separated by a rubber membrane from the pebble bed. This PEG annulus is connected via a sight glass to a gas system. After filling-in the pebble bed, a controlled gas pressure p_2 is applied and the PEG is melted (melting point ≈ 40°C) by heating up the container with the heating plates of the press. During axial compression, PEG is displaced into the sight glass. Originally, it was anticipated to use the measurement of the PEG height in the sight glass for the determination of the change of the bed volume during compression. However, operational tests proved that the measurement accuracy was not satisfactory and the sight

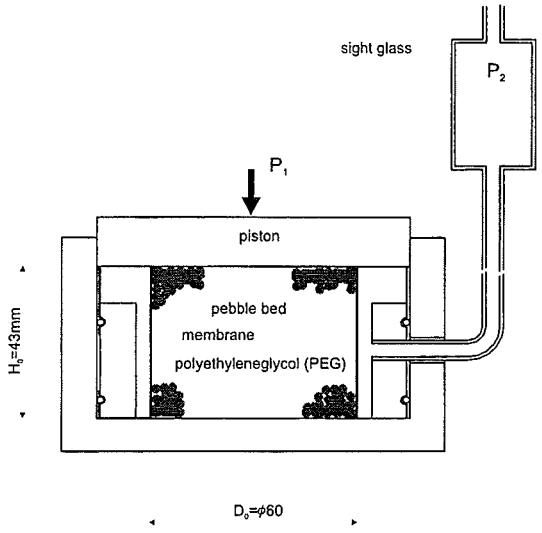

Figure 2. Schematic of TCT apparatus

glass was replaced by a small steel container. After termination of the TCT, the system was cooled down in order to freeze the PEG such that the shape of the pebble bed surface at the end of the TCT could be visualised.

2.3. Characteristics of investigated materials

The beryllium pebbles, fabricated by Brush Wellman, consisted of pebbles with diameters of about 2 mm and 0.1 - 0.2 mm. The large pebbles are approximately of spherical shape with indentations on the surface and a variety of coarse pores, as shown in Fig. 3.

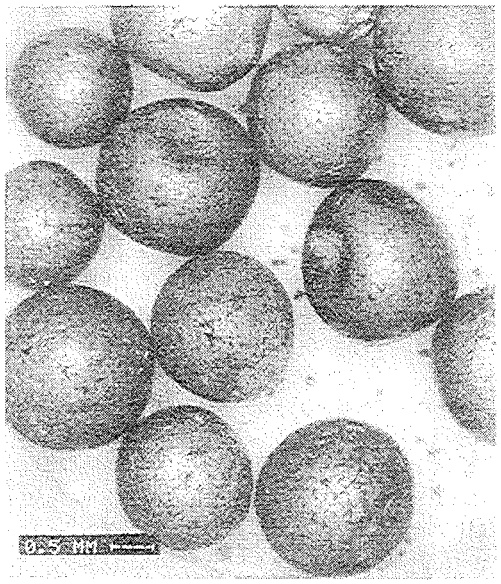

Figure 3. Large beryllium pebbles

The small (0.1 - 0.2 mm) beryllium pebbles were made by inert gas atomization and centrifugal atomization. These processes involve break-up and rapid cooling of a molten metal stream to form a powder with impurity levels comparable to that for other commercial beryllium products. Figure 4 shows that the small pebbles are by far less regular than the large ones. A detailed characterisation of the pebbles is given in [6,7].

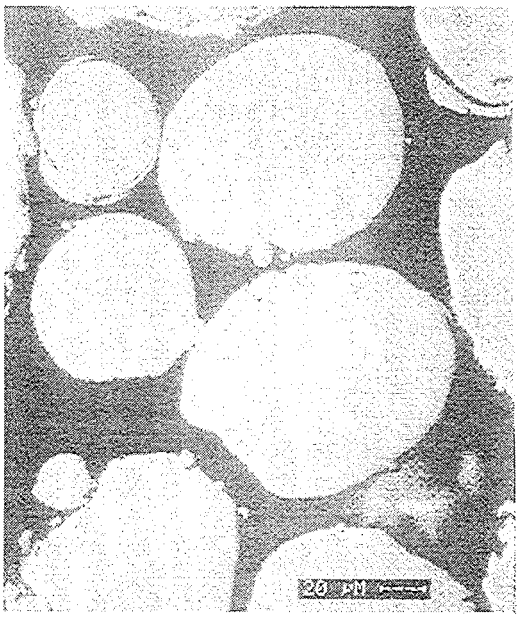

Figure 4. Small beryllium pebbles

2.4 Experimental procedure

First, the large pebbles were filled in the container by knocking simultaneously with a small hammer or a screwdriver at the container wall in order to obtain a dense packing. After putting the lid on the top, the container was positioned in the press and the piston was moved towards the lid until a pressure increase of about 0.2 MPa was reached. In this position the initial bed height H_0' was determined and the UCT was started. With this procedure, filling factors γ_L between 59 and 60 % were obtained for MBs.

For the generation of binary beds (BBs) the container filled with the large pebbles was removed from the press and the small pebbles were filled in. Due to the roughness of small and large pebbles again some slight knocking was needed to reach high filling factors. Great attention was directed to avoid that the large pebbles changed their position because in this case the small pebbles slipped easily between the large ones and the large pebbles did swim up. In practice, this swimming-up could not be totally avoided: for small pebble packing factors of $\gamma_s \approx 18\%$, a bed swimming-up of ≈ 1-1.5 % occurred. The initial bed height for binary beds H_o was determined after this filling procedure.

An interesting observation was made during these filling procedures by pressing excentrically by hand on the upper Al_2O_3 disc on the bed: the MBs behaved much stiffer than the BBs where the bed yielded more easily. It appeared that the small pebbles behaved like ball bearings between the large pebbles. A strong movement of particles has to be avoided during filling because of unfavourable dilatance effects, see Section 4. Therefore, no initial pressure was exerted on the bed before starting the experiment.

At the end of the experimental campaign additional experiments were performed with glass pebbles with much smoother surfaces. These experiments are presented separately in Section 3.3.

3. RESULTS FROM UNIAXIAL COMPRESSION TESTS (UCTs)

Figure 5 shows a characteristic result of an UCT at elevated temperatures: the axial compressive stress (identical with the vertical pressure exerted on the bed) is shown as a function of the axial compressive strain (ratio of axial displacement (mean value from the four displacement transmitters) to initial bed height). After having reached steady-state temperature conditions, the pressure was increased during a time period of about 30 min to the selected maximum value. Then, the pressure was decreased to zero during a time period of about 15 min, increased again to the maximum value, and kept constant for a given time period for the

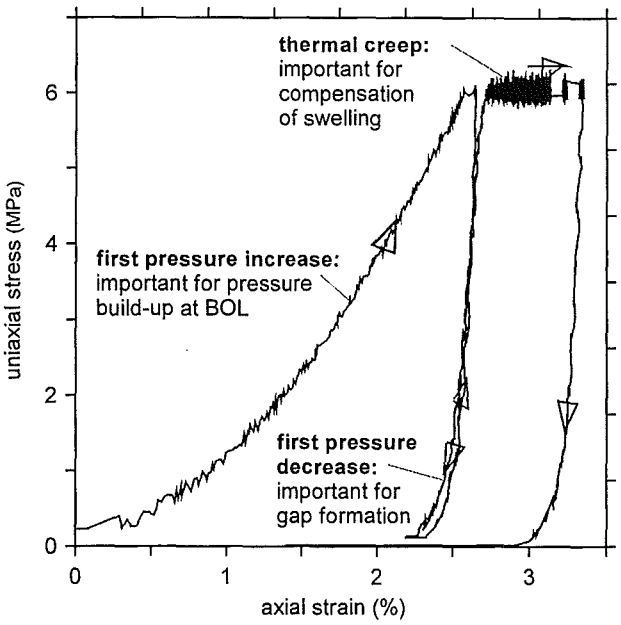

Figure 5. Characteristic UCT at elevated temperature (binary bed, T=480°C)

measurement of thermal creep. At the end of the experiment, the pressure was decreased to zero again. The characteristic parts of an UTC are:

- *The first pressure increase , (curve "1st pi"):* this curve is caused by the irreversible displacement of particles forming a denser configuration and plus some elastic and plastic deformation of particles.
  For the description of the thermomechanical interaction between pebble beds and structural material the knowledge of this curve is of prime importance because it determines the pressure build-up during the first blanket operation.
- *The first pressure decrease (curve "1st pd"),* and *second pressure increase (curve "2nd pi"),:* the slopes of the curve "1st pd", and the subsequent stress increase are much steeper than the slope of curve "1st pi" because these curves are caused mainly by elastic deformations. The hysteresis is characteristic for the influence of internal friction. For further cycles, these curves do not differ significantly.
  The difference between the curves *"1st pi "* and "1st pd" is relevant for the formation of

gaps which might form during blanket operation.

- Creep strain: keeping the stress constant at a given value, the strain increases with time due to thermal creep. The knowledge of thermal creep is important for the relaxation of stresses during the first days of blanket operation and for the compensation of swelling due to irradiation which occurs during long operational time periods.
- Cycling at the end of the creep period might show that the bed stiffness has increased slightly due to the enlarged contact areas between individual particles because of creep. This effect is not expressed in the present experiments due to the small creep rates experienced.

3.1. Stress-strain relationships for 1st pressure increase

In the following, results are presented on the relationships between uniaxial stress, σ, and strain, ε, for the 1st pressure increase. From these relationships the moduli of deformation E are determined, see Section 3.4.

3.1.1. Monosized pebble beds (MBs)

Figure 6 shows the stress-strain dependence for all experiments performed with MBs. For

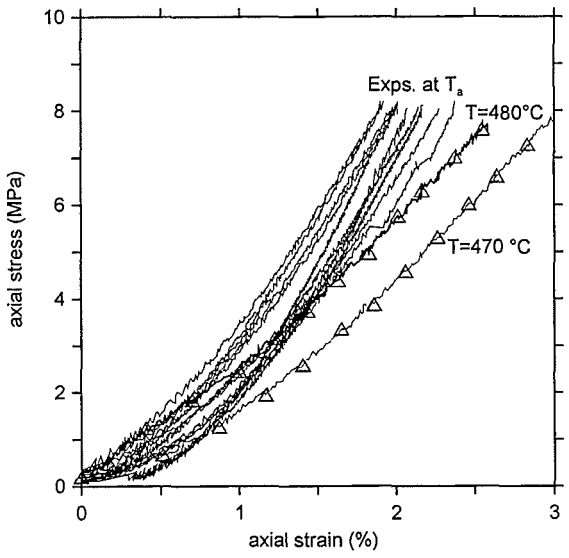

Figure 6. Monosized bed: first pressure increase

ambient temperature, there is a certain data scattering which is caused by an initially non-perfect horizontal bed surface (it should be kept in mind that already bed height differences of 0.2 mm correspond to 0.5% strain difference) or by the influence of small differences in the filling factor.

Figure 6 contains also data from two experiments at high temperatures. From these data it might be concluded that with increasing temperature the beds become "softer" (larger strains for a given stress). Such a tendency was observed for ceramic breeder materials [2-5], however, at temperatures above 600 °C. More experiments at elevated temperatures are required in order to decide if a real temperature effect exists or if the data are within the scattering range which is, at least for binary beds, significantly larger at elevated temperatures than at ambient temperature, see below.

Due to the lack of data, a temperature effect is not elaborated in the present stage. A relationship of the type

$$\sigma(\text{MPa}) = A\,\varepsilon(\%)^n \qquad (1)$$

is used to fit the data. The following values were obtained: $A_{MB,i} = 1.89$; $n_{MB,i} = 1.89$.

3.1.2. Binary beds (BBs)

Figure 7 presents results for the 1st pressure increase for BBs at ambient temperature. The data scattering is similar to that of the corresponding tests with MBs, however, the beds are distinctively softer. This softer behaviour is characteristic for the experiments with filling factors γ_l between 59 and 60 %. This effect might be explained by the "ball bearing" effect of the small pebbles, mentioned above, which enables the bed to rearrange more easily into a denser configuration. For larger filling factors, the differences between MBs and BBs disappears, as outlined in the next section.

The data scatter of the experiments at elevated temperatures is much more expressed, for details, see [5]. Again, a distinct temperature effect was not observed and the following values are recommended to be used until more detailed data will be available: $A_{BB,i} = 0.80$ and $n_{BB,i} = 2.08$.

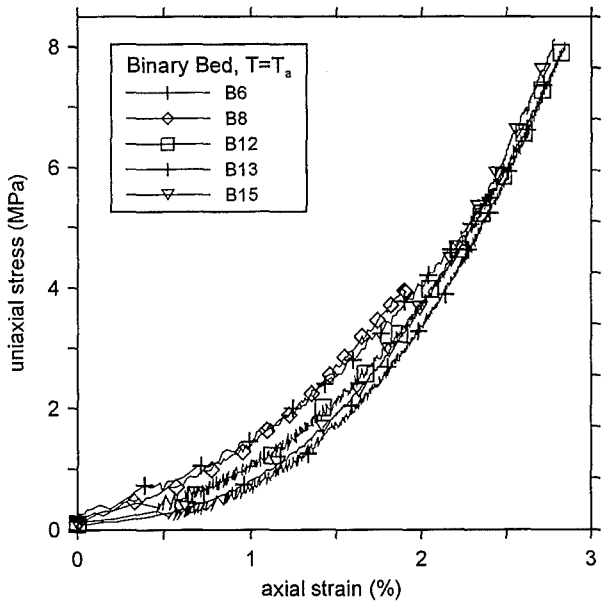

Figure 7. Binary beds; first pressure increase

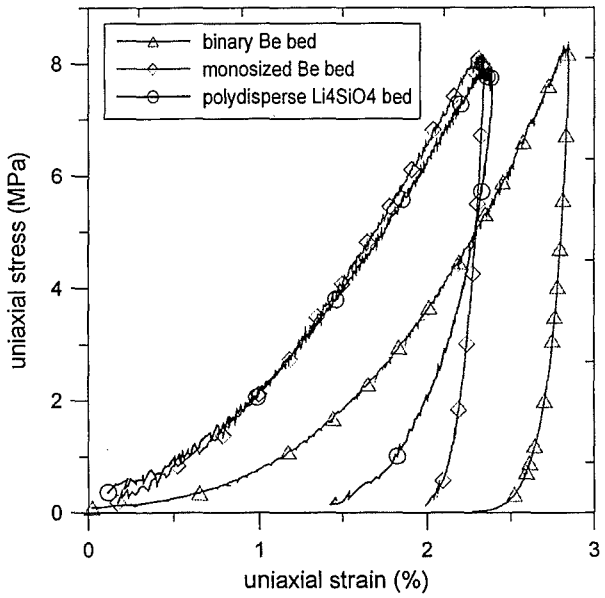

Figure 8. UCTs of a monosized and a binary Be bed and a polydisperse Li_4SiO_4 bed

Figure 8 shows a comparison of UCTs with a monosized and a binary beryllium bed, and a polydisperse Li_4SiO_4 bed [3] (pebble diameters between 0.25 and 0.6mm). The stress-strain dependences of the 1st pressure increase are quite similar for the monosized Be bed and the Li_4SiO_4 bed. The slope of the curve for the pressure decrease is steeper for the Be bed than for the Li_4SiO_4 bed which might indicate that for the beryllium beds the pebbles are plastically deformed during the pressure increase (for Li_4SiO_4 a plastic deformation can be excluded for $T = T_a$).

3.2. Influence of the initial state of pebble beds

For a given granular material the filling factor γ is an important parameter. For polydisperse Li_4SiO_4 pebble beds, the stress-strain dependences differed significantly for different filling factors [9].

For MBs, maximum filling factors for an ideal face-centered cubic array of spherical particles are $\approx$ 74%. Real beds are not of this array and for small bed dimensions the larger local porosity close to the walls decreases the averaged value. It is generally assumed that the wall influence starts to become remarkable at bed dimensions less than $\approx$ 10 pebble diameters. In practice, values of $\gamma \approx 66$ % are reached by moderate vibration during filling for large bed dimensions with smooth particles. For rough particles, the attainable values decrease often to values of less than 60%, see e.g. [2]. In the present experiments the values between 60 and 62 % were obtained for MBs.

For BBs, filling factors of up to 20 % for small pebbles are obtained for smooth particles. Again, these values can become significantly smaller for rough pebble surfaces.

In order to investigate the influence of higher filling factors on the stress-strain relation, first, some screening tests with monosized and binary beds consisting of glass pebbles were performed. The larger pebbles (equivalent diameter about 2 mm) consisted of rounded cylindrical particles with a diameter to height ratio of about 1. The small pebbles were spherical with diameters between 0.1 and 0.2 mm. Compared to the beryllium pebbles, the pebble surfaces were very smooth.

The UTCs were performed either with large pebbles loosely poured in the cylindrical container (nonvibrated bed) or with beds afterwards vibrated. The small pebbles were poured in both cases on the surface of the MB without any remarkable vibration. No attempt was made to obtain maximum filling factors but

to avoid a swim-up effect. Table 1 shows that high filling factors for the vibrated MB were obtained.

Table 1. Characteristics of glass pebble experiments

diameter (mm)		density (g/cm^3)
large pebbles	≈ 2	2.44
small pebbles	0.1-0.2	2.5
	filling factor (%) nonvibrated bed	vibrated bed
monosized bed	63.1	67.4
binary bed	63.1+16.8 = 79.9	67.4+13.5 = 80.9

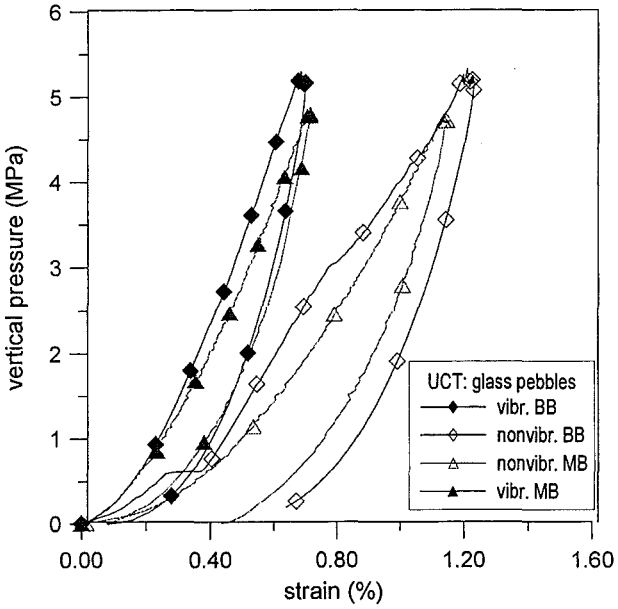

Figure 9. UTCs with vibrated and nonvibrated glass pebble beds

Figure 9 shows the results: compared to the beryllium beds the curves of the pressure increase are much stiffer and the elasticity during the pressure decrease is much more expressed. As expected, the stress-strain dependence is softer for the smaller filling factor of the monosized bed. This difference is quite expressed for a constant strain value. There is no significant difference between monosized and binary beds in contrast to the previous results with beryllium beds. As already mentioned, the extrapolation of these results to beryllium beds is probably very limited; the TCTs also showed significant differences between binary glass pebble beds and beryllium pebble beds.

When preparing dense binary beds consisting of rough pebbles the swim-up effect can occur. There are procedures to limit or to undo this effect. However, these procedures can give rise to a significant internal stress build-up. This effect, was recently also observed for beryllium beds in long cylindrical cavities [8]. This internal stress build-up represents a preconsolidation of the bed and has a strong impact on the results of a subsequent UCT.

3.3. Stress-strain relationships for 1st pressure decrease

The slope of the 1st pressure decrease is much steeper than the slope of the 1st pressure increase as already demonstrated in several figures. Characteristic results for both MBs and BBs are shown in Fig. 10. For a better comparison, all curves were shifted to a common starting point of 0.4 % for σ_{max} = 8 MPa. There is no distinct difference between MBs and BBs. Using again relationship (1) for an average curve through σ = 0 at ε = 0, the values $A_{BB,i}$ = 68.9 and $n_{BB,i}$ = 2.86 are obtained.

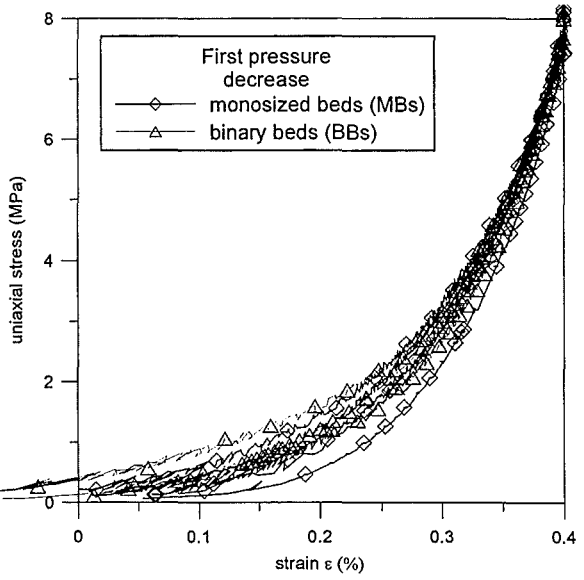

Figure 10. First pressure decrease for MBs and BBs (starting with σ = 8 MPa at ε = 0.4)

The relationship for the 2nd pressure increase differs negligibly from that for the 1st pressure decrease, see Fig. 6. As already mentioned, there is a small hysteresis effect due to the different directions of the influence of friction between pebbles.

3.4. Moduli of deformation

The aim of the experiments is to provide computer codes for the description of the thermomechanical interaction between pebble beds and structural materials with empirical correlations for the stress-strain relations presented above.

In soil mechanics, often the ***uniaxial modulus of deformation*** is used, defined by the ratio of stress to strain, $E(MPa) = \sigma(MPa)/\varepsilon(1)$, or with the corresponding incremental values, $E^* = \Delta\sigma/\Delta\varepsilon$.

Characteristic for granular materials is a power law dependence of the type:

$$E = C\sigma^m \quad (2).$$

Then, the modulus E^* only differs from E by the factor 1/(1-m):

$$E^* = C(1-m)^{-1}\sigma^m \quad (2a).$$

These moduli of deformation are determined directly from the stress-strain relationship (1) by

$$C = 100A^{1/n}\ ,\ m = 1-1/n \quad (3).$$

Figure 11 shows results for the modulus of deformation, E, for the 1st pressure increase for the MB and BB reference curves obtained in Section 3.1. The agreement between fit and experimental data is quite well except at very low stresses which are not of large practical importance. The proposed correlation for MBs is recommended generally for dense beds, whereas the correlation for BBs is more relevant for total filling factors of ≈ 78 %. For remarkably higher values (≈ 82 %) the same correlation as for MBs is recommended as discussed in Section 3.2.

Table II summarises the values of the fit parameters. As already mentioned, these values are recommended to be used in a

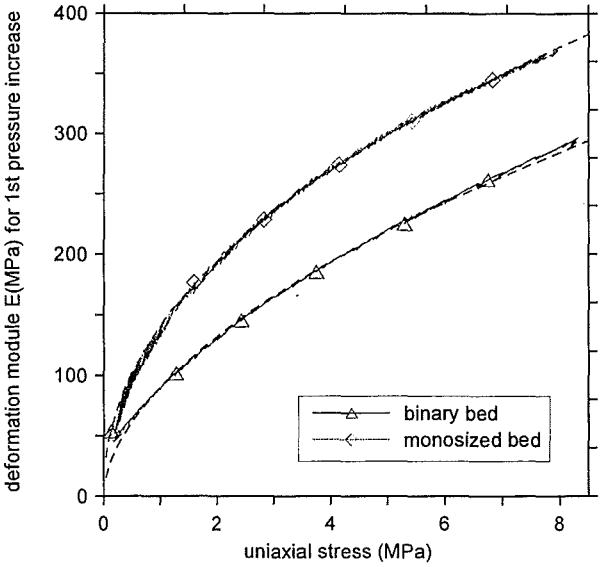

Figure 11. Moduli of deformation for 1st pressure increase for MB and BB

temperature range between ambient and about 500°C where a distinct temperature effect was not found experimentally. At higher temperatures, the modulus of deformation for the 1st pressure increase should become smaller, similar to the tendency observed for ceramic pebble beds [4].

Table II: Moduli of deformation, E

	MB		BB*	
	m	C	m	C
1st pressure increase	0.47	140	0.52	90
1st pressure decrease	0.65	440	0.65	440

*for filling factors ≥ 82%, the same values as for MBs are recommended

3.5. Thermal Creep

Keeping the pressure constant at elevated temperatures, the strain increases with time. Modelling of thermal creep strain rates of pebble beds is different from that of homogeneous materials because the contact zones between pebbles change with time. Therefore, the creep rate

$$d\varepsilon_{creep}/dt = f(\text{material properties, T, p, t}).$$

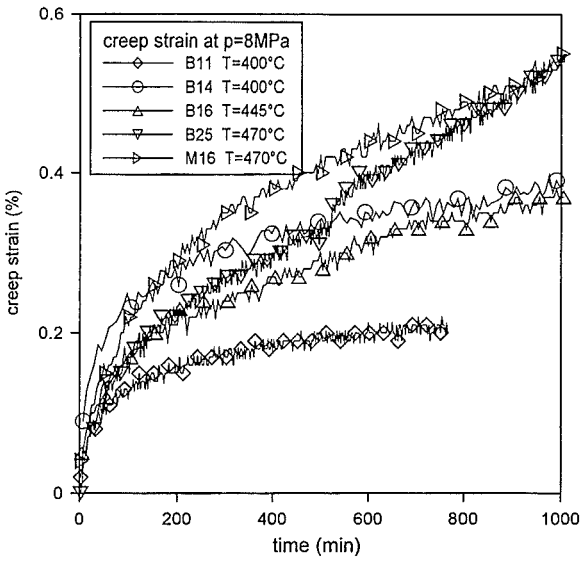

Figure 12. Thermal creep strain at p = 8 MPa

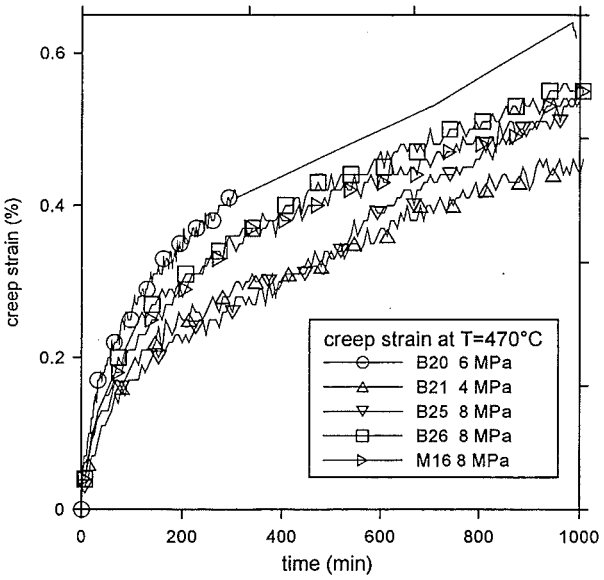

Figure 13. Thermal creep strain at T= 480°C

Creep strain results are summarised in Figs. 12 and 13. The main result is that for the investigated parameter range creep strains are very small. Due to these small values measurement inaccuracies are large and the data are not always consistent with respect to the expected influences of temperature and pressure. Creep should increase both with pressure and temperature. Most of the data are relevant for BBs. From the few MB data, no distinct differences can be seen.

The investigated parameter range is characteristic for the ITER breeding blanket. For this case the effect of thermal creep might be neglected in evaluations of the thermomechanical behaviour of blanket elements. For a DEMO reactor significantly higher temperatures are also of interest. Therefore, the present data might be considered as a valuable first step but experiments are required at higher temperatures.

3.6. Characterisation of pebble beds after UCTs

After demounting the upper Al_2O_3 disc it was observed that the upper small pebbles close to the bed surface had moved downwards by ≈ 1mm indicating that small pebbles had filled some voids in the pebble bed during the experiment. In order to visualise the bed structure a portion of the pebble bed was fixed by glue. It proved that many large pebbles were separated by small pebbles, as also seen in Fig.14. There was a significant hooking of small and large pebbles due to the large surface roughness, see Fig.15.

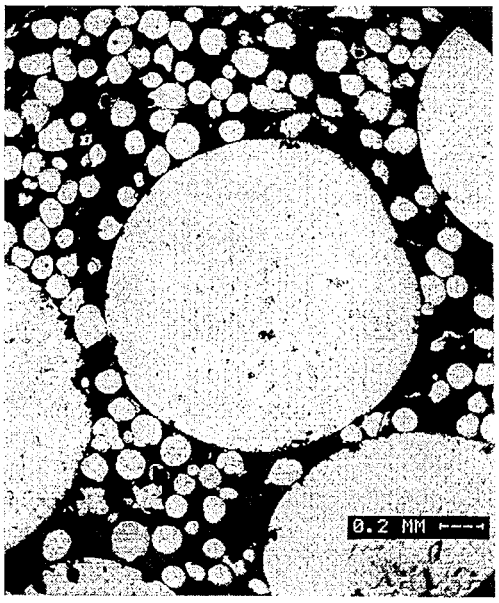

Figure 14. Binary pebble bed after UTC

For BBs it was difficult to detect visually any pebble deformation. For the MBs, a very small portion of the pebbles showed cracks, preferably those pebbles with significant initial surface indentations or inner voids.

The elastic deformation of the pebbles was reduced due to strength hardening.

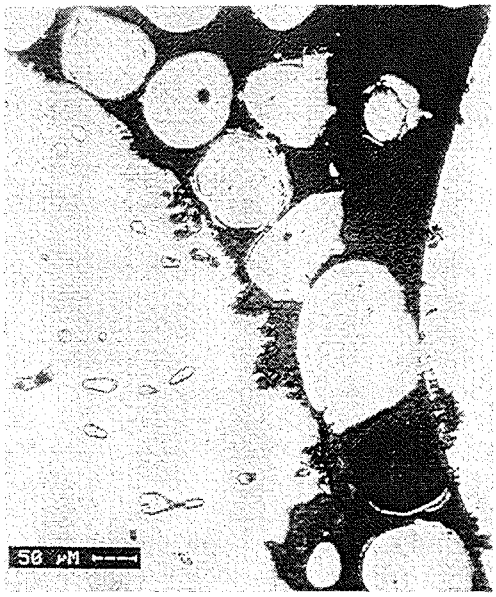

Figure 15. Binary pebble bed (detail of Fig.14) after UTC

4. RESULTS FROM TRIAXIAL COMPRESSION TESTS (TCTs)

Figure 16 shows a characteristic result of a TCT. Because of the isotropic initial compression of the pebble bed to the value of the selected horizontal pressure p_2, the bed is more compressed at the beginning than that of a UCT. The axial deformations are quite small when the axial stress σ_1 exceeds the horizontal stresses $\sigma_2 = \sigma_3$ (corresponding to the horizontal pressure p_2 = 0.25 MPa). In contrast to UCTs, the axial strain becomes increasingly larger with increasing axial stress due to the ability of the pebble bed to deform in the radial direction. The maximum of the curve is reached when no further stress increase is required to generate further strain. This maximum is characteristic for "the state of perfect plasticity" and the internal friction angle α, defined by sin $\alpha = (\sigma_1-\sigma_2)/(\sigma_1+\sigma_2)$, at this position is of prime importance.

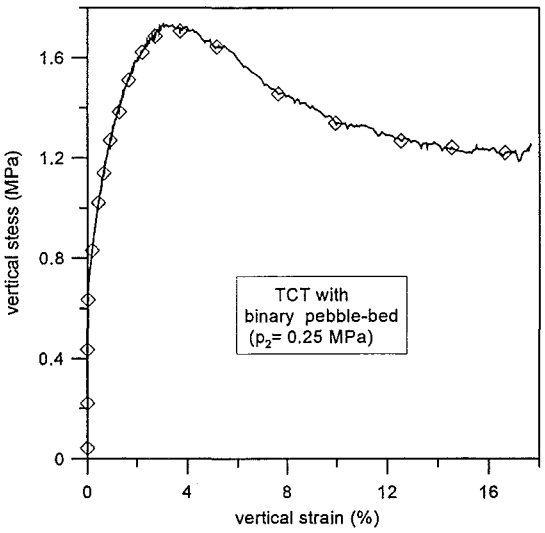

Figure 16. Characteristic result of a TCT

Depending on the initial consolidation of pebble beds, the minimum required stress for further strain increase can be fairly constant or it can become smaller. The latter tendency is clearly observed for the beryllium pebble beds, see also Fig 17.

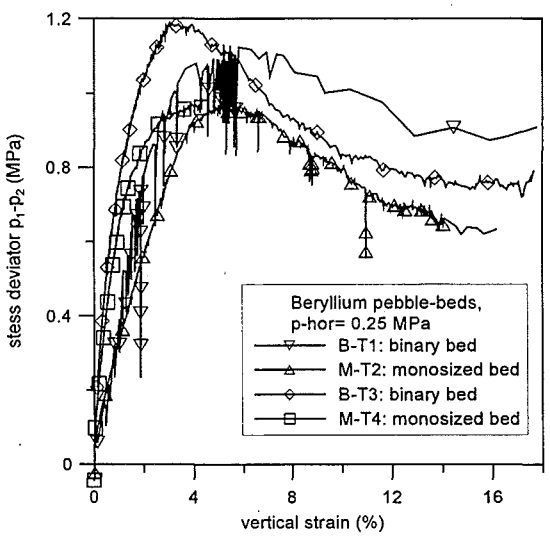

Figure 17. TCTs for MBs and BBs at p_2 = 0.25 MPa

Figure 17 contains results for p_2 = 0.25 MPa for both MBs and BBs. As ordinate, the deviator (σ_1-σ_2) is used. The results for BBs are somewhat higher than those for MBs; differences in the curves might be due to slightly differing filling factors. Because of the few data points, the influence of the filling factor cannot be separated.

An important result is shown in Fig. 18 where the data at the stress maximum are presented and are compared with results from Li_4SiO_4 and glass pebble beds: The data for the beryllium beds are distinctively higher than those for the other granular materials

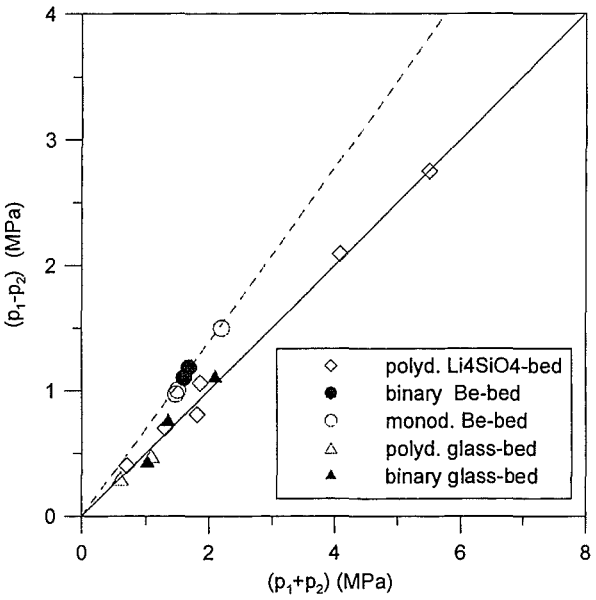

Figure 18. State of perfect plasticity of different granular materials

which consist of fairly spherical pebbles with much smoother smooth surfaces. The slopes of the curves are representative for the inner friction; the higher inner friction of the beryllium beds might be explained by the more irregular pebble shapes and the rougher surfaces.

The inner friction angle is an important quantity for the description of the flow of particles. For blanket relevant shallow Li_4SiO_4 beds (bed height ≈ 10 mm) it was shown experimentally and theoretically [9] that the particle flow becomes negligible at already quite low side stresses (perpendicular to the direction of the axial stress). This facilitates the computation and reduces considerably the experimental effort to characterise pebble beds (UTCs would be sufficient). A higher friction factor of beryllium pebbles compared to Li_4SiO_4 pebbles favours the tendency that a flow of particles is suppressed. Calculations will be performed in the near future if for larger beryllium bed heights (≈ 40 mm) the particle flow is of concern.

5. CONCLUSIONS

Uniaxial compression tests with monosized and binary beryllium pebble beds were performed in a temperature range between ambient temperature and 480 °C and pressures up to 8 MPa. Empirical correlations for the modulus' of deformation are presented for the different bed types and first measurements for thermal creep are presented.

Additionally, results for triaxial compression tests for monosized and binary beds are reported. The internal friction of these beds is significantly larger than that of spherical particles with relatively smooth surfaces (ceramic breeder pebbles) indicating that the ability of beryllium pebbles to flow is more suppressed.

The experiments showed that the initial state of consolidation of the pebble bed is very important for the stress-strain dependence. Therefore, pebble bed characterisation tests (UCTs, TCTs, etc.) and related experiments (e.g. heat conductance investigations) are to be performed with the same initial bed conditions as existing in the blanket. The latter depend on blanket relevant filling procedures which are presently not sufficiently defined and require corresponding investigations. The filling issues are much less expressed for monosized (or polydisperse) beds than for binary beds.

ACKNOWLEGDEMENTS

This work was supported by the European Communities within the European Fusion Technology Programme, V60/1 (BL 16.5-1).

REFERENCES

1. K. Ioki and M. Ferrari (Eds.), ITER Final Design Report, Design Description Document WBS 1.6B, Tritium Breeding Blanket System, ITER Document G 16 DDD 2 98-06-10 W0.4, 1999.
2. J. Reimann, E. Arbogast, S. Müller and K. Thomauske, Thermomechanical behaviour of ceramic breeder pebble beds, 7th Int. Workshop on Ceramic Breeder Blanket Interaction, Petten, The Netherlands, Sept.14-16, 1998.
3. J. Reimann, E. Arbogast, M. Behnke, S. Müller, K. Thomauske, Thermomechanical behaviour of ceramic breeder and beryllium pebble beds, 5th Int. Symp Fusion Nuclear Techn, Roma, Italy, Sept.19-24, 1999.
4. A. Y. Ying, M. A. Abdou, L. Bühler, M. Enoeda, S. Malang, Y.Ohara, J. Reimann, Summary of laboratory experiments and modelling for thermomechanical properties and interactions of solid breeder pebble bed materials, dito.
5. J. Reimann, M. Behnke, Experimental investigation of basic properties of monosized and binary beryllium pebble beds, FZKA 6337, 1999.
6. R. A. Anderl, R. J. Pawelko, G. R. Smolik, F. Scaffidi-Argentina, "Steam Chemical Reactivity of Beryllium Pebbles", INEEL Report INEEL/EXT-98-01149, Idaho National Engineering and Environmental Laboratory, Idaho Falls, USA, December 1998.
7. F. Scaffidi-Argentina, G. R. Longhurst, V. Shestakov, H. Kawamura, Beryllium R&D for fusion applications, 5th Int. Symp Fusion Nuclear Techn, Roma, Italy, Sept.19-24, 1999
8. M. Dalle Donne, A. Goraieb, G. Piazza, F. Scaffidi-Argentina, Experimental Investigation on the Thermal and Mechanical Behaviour of a Binary Beryllium Pebble Bed, dito.
9. L. Bühler, J. Reimann, E. Arbogast, K. Thomauske, Mechanical behaviour of Li_4SiO_4 pebble beds in a blanket typical geometry, dito.

Measurement of the Heat Transfer Parameters in Infiltrated Binary Beryllium Beds. Comparison between the Results with PEHTRA and SUPER-PEHTRA

M. Dalle Donne[a], A. Goraieb[b], G. Piazza[a], F. Scaffidi-Argentina[a]

[a] Forschungszentrum Karlsruhe, IKET, Postfach 36 40, D-76021 Karlsruhe, Germany

[b] Goraieb Versuchstechnik, In der Tasch 4a, D-76227 Karlsruhe, Germany

For the next generation fusion reactors with a ceramic breeder blanket the use, as a neutron multiplier, of either a binary bed of large (≈ 2 mm) and small (≈ 0.1-0.2 mm) beryllium pebbles or a single size bed made of 1 mm or 2 mm pebbles is foreseen. The heat transfer parameters of such a binary pebble bed, namely the thermal conductivity and the heat transfer coefficient to the containing wall, have been investigated previously in the experimental device PEHTRA available at FZK. The experiments allowed to measure the effect of the bed temperature and of constraint exerted by the containing walls. The constraint is defined by the bed interference, i.e. the difference in the radial expansion between bed and the constraining walls related to the bed thickness ($\Delta\ell/\ell$). However, with the PEHTRA experiments, it was only possible to achieve a $\Delta\ell/\ell$ value of 0.1 % [1]. A new experimental rig (SUPER-PEHTRA) has been constructed at FZK, which allows to achieve $\Delta\ell/\ell$ values of 0.3 % and to measure the pressure of the expanding bed on the containing walls. First experiments with a binary bed have been performed [2]. The present paper reports on further experiments with binary beds and the establishing of equations correlating the data obtained for the present binary beds and for the binary bed experiments described in ref [2].

1. INTRODUCTION

The Forschungszentrum Karlsruhe has accumulated a considerable experience in the field of the heat transfer in pebble beds [1-4]. The Helium Cooled Pebble Bed (HCPB) DEMO relevant blanket, which is being developed within the European Community, is based on the use of ceramic breeder pebble beds and of beryllium pebble beds as neutron multiplier and the study of the heat transfer in these beds is essential for the assessment of the blanket temperature during the operation of the blanket. The ITER team has adopted a blanket arrangement quite similar to that of the HCPB and has requested FZK to perform experiments capable to establish the correlation for the binary beryllium pebble bed up to the end–of-life operation of the blanket. This means an interference value of ≈ 0.3 % to cover the maximum beryllium swelling estimated with the code ANFIBE [5,6] at 1%. Furthermore, also data on the pressure exerted by the bed on the containing walls should be provided. This required the construction of a new rig (SUPER-PEHTRA). The paper presents and discusses the results obtained with this test rig for a binary bed of beryllium pebbles.

2. THE HEAT TRANSFER EXPERIMENTS

The binary bed of beryllium pebbles is formed by pebbles of two different sizes, namely:

- Pebbles of 2mm ± 0.3 mm in diameter, made by the firm Brush Wellman as an intermediate product in the production of beryllium with the method of Mg reduction of BeF_2 (average density of the pebble material = 1.831 g/cm^3);
- pebbles of 0.1-0.2 mm in diameter made by the firm Brush Wellman with the atomisation method (melting and spraying with an inert gas). The average density of these pebbles is 1.806 g/cm^3.

2.1. Experimental Apparatus

Fig. 1 shows schematically the experimental apparatus to measure the heat transfer parameters of the bed. The pebble bed is contained between two vertical concentric tubes (annulus). The inner tube contains an electrically heated rod. Helium can flow in the axial direction through the bed. The

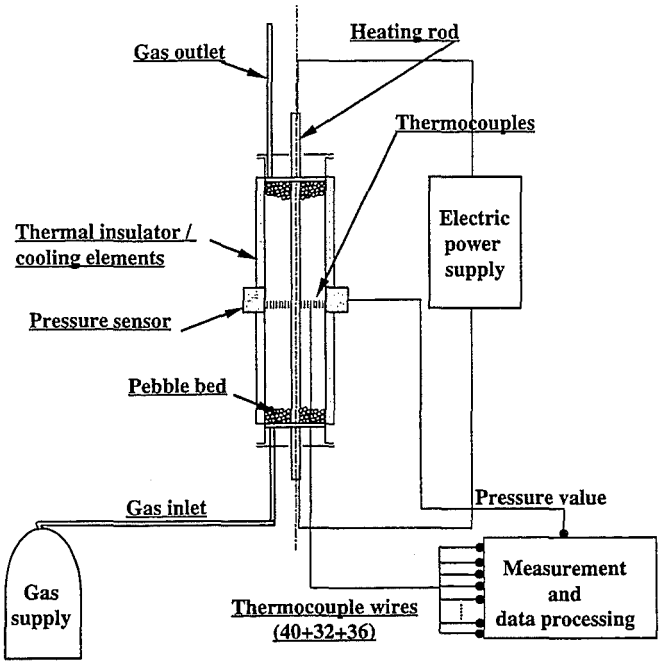

Fig. 1: Experimental apparatus to measure the heat transfer parameters of a pebble bed.

necessity to obtain $\Delta\ell/\ell$ values up to 0.3 % required to increase the heating power of the device to 16 kW in comparison to 3.5 kW for the previous rig PEHTRA [3]. This required an increase of the heater rod diameter from 16 mm [3] to 30 mm. The thickness of the bed was, however, maintained at 43 mm as in PEHTRA resulting in an outer tube inner diameter of 116 mm. Furthermore, four pressure sensors were placed at the walls of the outer tube in the axial section where the measurements of the bed temperature were performed (Fig. 2). The radial temperature distribution in the bed was measured by a bank of 32 thermocouples placed at various radii at four different azimuthal angles, in the middle axial section of the annulus, where the axial temperature gradients in the annulus walls were expected to be negligible in comparison with the radial ones, thus ensuring that the heat produced in the inner rod moves in the radial direction only. The temperatures on the inner and outer tube surface were measured by 40 and 36 thermocouples respectively, placed in the walls to control the axial temperature distribution in the tubes. A porous steel plate was placed just in contact with the pebble bed upper surface and kept in place by a piston pressed on its surface by maintaining a pressure of 2 bar on the piston. A sensor measures continuously the level of the bed during the filling operation and the experiments. This arrangement allows to avoid any demixing of the bed and to know at any time the bed packing factors. This is important because a constancy of the bed level during the filling of the small pebbles ensures that the small pebbles flow between the larger ones (infiltrated bed). Only in this case it is possible to obtain high heat transfer parameters and packing factors of the beds. If a stochastic distribution of the pebbles were obtained, this would imply only a marginal gain in comparison to single size beds.

The filling of the test section with the pebbles was made in the following way:

- filling of the annulus between the two concentric tubes (outer radius of inner tube = 15 mm, inner radius of the outer tube 58 mm) with the 2mm pebbles; strong vibration of the pebble bed by means of a compression hammer applied to the outer tube through a wood plate ; this allowed to achieve a packing factor of the 2 mm pebbles of 63.2 % for an height of the bed of 680 mm.
- afterwards , filling of the annulus with 0.1-0.22 mm pebbles and vibrating while keeping the bed upper surface pressed by the piston with an overpressure of 2 bar. The final packing factor reached was 19.3 %. The small pebbles flowed in between the bigger ones as shown by the constancy of the bed level.

The resulting packing factor of the binary bed was 82.5 %.

Besides the measurements with a total of 108 thermocouples, the mass flow of the helium flowing through the bed, the helium pressure at the inlet and outlet of the test section and the pressure exerted by the bed onto the outer tube were measured. The measurements were performed with helium flowing at very low velocity so that the heat transfer parameters are not affected by the helium

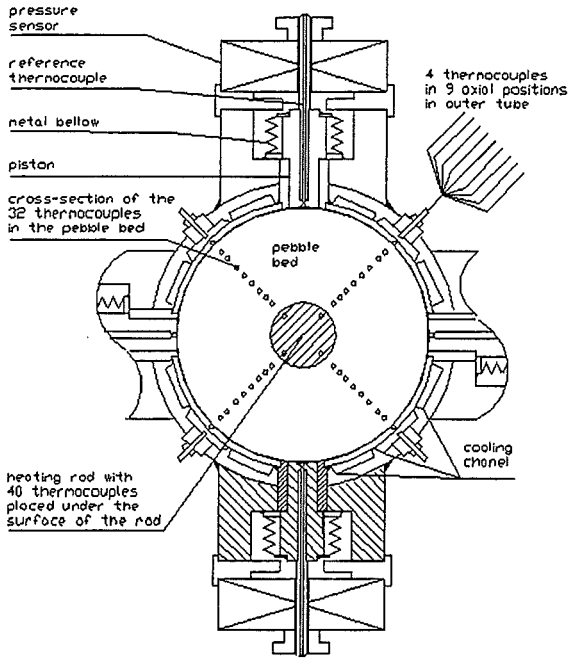

Fig. 2: Cross section of the outer tube test section of SUPER-PEHTRA showing the arrangement of the four pressure sensors and of the thermocouples bank to measure the temperature distribution in the bed.

convection. This is also the case for the pebble bed in the blanket, where the velocity of the purge helium flow is very small (≈ 10 cm/s).

2.2. Experimental Results

2.2.1 Preliminary experiments

Before performing the experiments with the reference binary bed two kind of preliminary experiments were performed:

1. Experiments with the binary bed of Ref. [1] with the nominal packing factor of 80.8 %. However the real packing factor in the axial measurement cross section was probably even higher than that of the present reference binary bed, due to the use of too small pebbles which were going down during the experiment. These experiments were performed in PEHTRA with a thermal insulation ($\Delta\ell/\ell = 0$) in a temperature range of 100-600 °C. Fig. 3 shows the bed thermal conductivity data obtained in two series of runs. The data show clearly that the thermal conductivity is more or less constant above 200 °C, while it is higher at temperatures below 200 °C. This is clearly explained by the fact that the ratio beryllium/helium thermal conductivity is higher in the range $20 \leq T_m \leq 200$ °C than for $T_m > 200$ °C.

2. Experiments with the reference binary bed with PEHTRA and SUPER-PEHTRA to check if the experimental data between the two experimental apparatus were consistent. Due to the limitations of the two rigs this comparison could be made only for the case $\Delta\ell/\ell > 0$ obtained with water cooling. Fig. 4 shows the results of these experiments. The agreement of the data is excellent. Of course the data with SUPER-PEHTRA extend to considerably higher values of $\Delta\ell/\ell$.

The conclusions from these preliminary experiments are:

1) Experiments with average bed temperature above 200 °C are more important for the objectives of the present experiment as the constancy of the thermal conductivity makes for an easier application of the data to the blanket case. Furthermore, data for temperatures above 200°C are more relevant for the application to fusion blankets.
2) Experiments with PEHTRA and SUPER-PEHTRA are consistent.

2.2.2 Experiments with the reference binary bed

Contrary to the case of the PEHTRA experiments [1], with SUPER-PEHTRA only experiments with $\Delta\ell/\ell > 0$ can be performed as the presence of the pressure sensors makes the use of a thick and uniform thermal insulation on the outer tube impossible. Experiments with the thermal insulation in PEHTRA with $\Delta\ell/\ell \approx 0$ for the same binary bed used in SUPER-PEHTRA have been performed in the frame of the present work.
The small beryllium pebbles used in the PEHTRA experiments [1] could not be used for the SUPER-PEHTRA experiments, as, due to the bigger annulus volume of SUPER-PEHTRA, the available amount of the pebbles was not enough. Furthermore, these pebbles were too small (0.034 – 0.156 mm) and during the experiments they went partially down towards the lower part of the

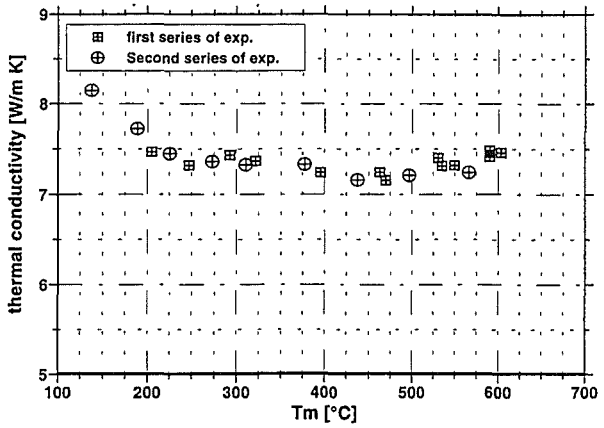

Fig. 3: PEHTRA: thermal conductivity of the binary bed of Ref. [1] as a function of average bed temperature.

annulus, however still above the axial annulus cross section, where the temperature measurements are performed. This effect was much stronger in the regions near the bed walls, where the packing factor of the bigger pebbles is only about 50 %. This explains the very large values of the wall heat transfer coefficient obtained in the previous PEHTRA experiments [1]. The heat transfer coefficients depend essentially on the number of pebble contact points per unit surface of the containing walls.

Thus, new lots of small pebbles were purchased by Brush Wellman. Two types of smaller pebbles were used: the first did not give satisfactory results as the pebbles were in a too large diameter range (0.02-0.5 mm, this distribution was known to the authors only 5 months after the beginning of the

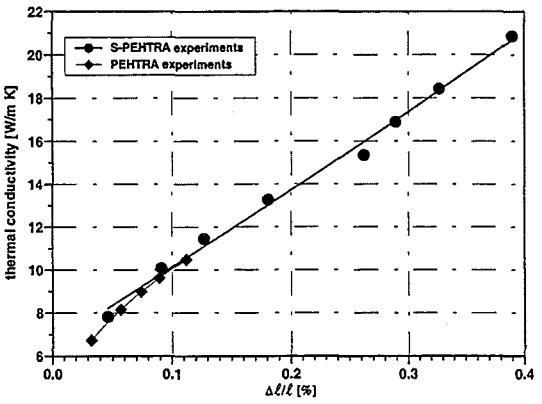

Fig. 4: Comparison of the thermal conductivity data of PEHTRA and SUPER-PEHTRA. Water cooling: T_m<200 °C

experiments) and contained too many not-spherical particles. Again during the experiments the smaller of the small particles went down towards the lower part of the annulus. This situation was confirmed during emptying of the test section: the upper part of the section was emptied layer by layer and showed quite clearly the not homogeneous axial distribution of the smaller pebbles.

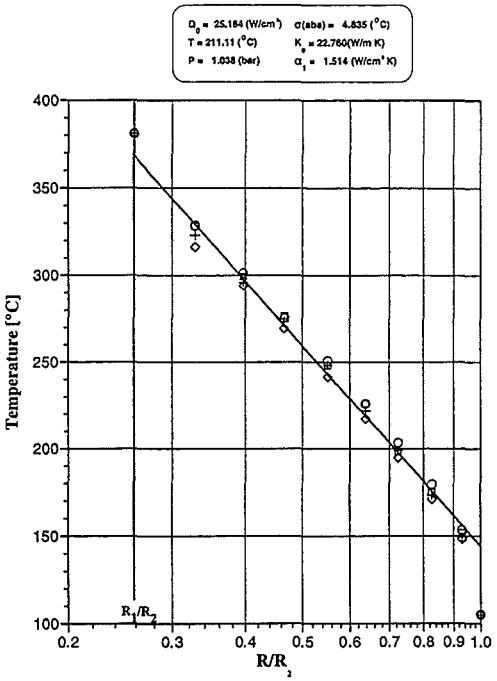

Fig. 5: SUPER-PEHTRA: Radial temperature distribution in the bed : experiment 21 (stable beryllium pebble bed) with $\Delta\ell/\ell$ = 0.3 % performed with air cooling at the outer tube.

To have a well defined and stable bed structure it was decided to use the smaller beryllium pebbles received later. These contained a smaller number of not-spherical pebbles and were originally in a diameter range 0.03-0.22 mm. This range was further restricted by sieving to 0.1-0.22 mm. The filling of the bed was performed in successive steps increasing the total amount of small pebbles at every step. The axial homogeneity of the bed was controlled at the end of the filling operation by the axial temperature distribution of the surface of the inner heating rod. The stable and homogeneous structure was achieved with a packing factor of the

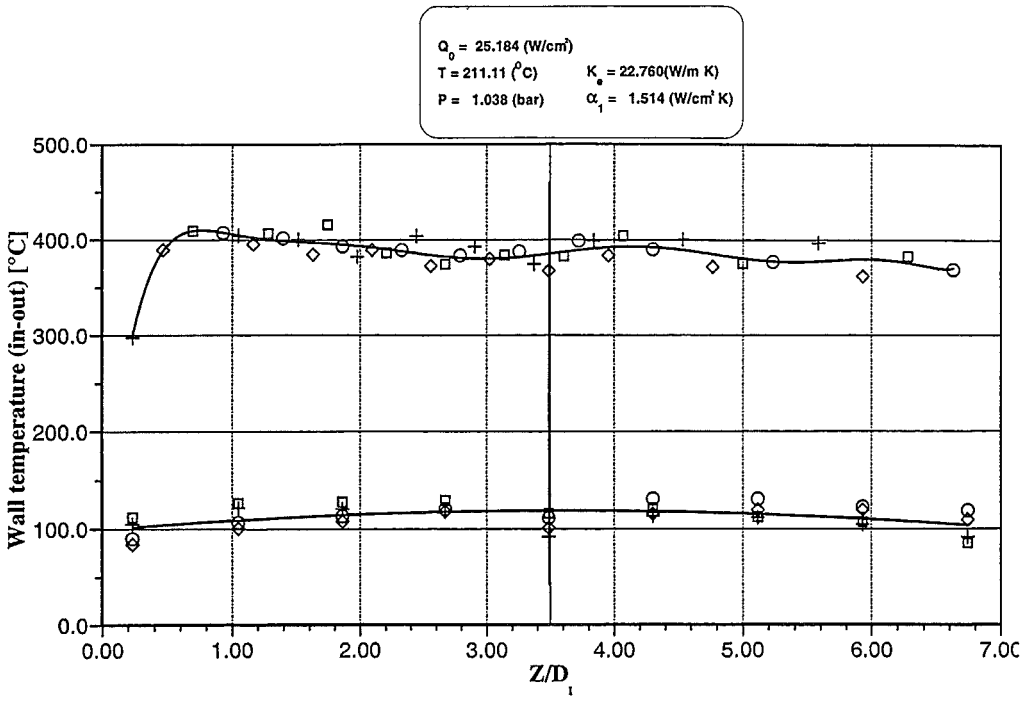

Fig. 6: SUPER-PEHTRA axial temperature distribution in the inner and outer tube surface for the experiment 21 ($\Delta\ell/\ell$ = 0.3 %, air cooling)

small pebbles of about 19.3% giving a total packing factor of the binary bed of 82.5%.

The results of the stable binary bed with the packing factor 82.5% (reference binary bed) in terms of pebble bed heat transfer parameters and wall contact pressure are described down below.

Fig.5 shows the radial bed temperature distribution in a linear/logarithmic plot for the last test performed with air cooling (Test Nr.21). The thermal conductivity is determined only by thermocouples placed in the bed. The scattering of the measured temperatures is small, considering the large temperature differences. The points can be fitted well by a straight line (standard deviation 1.5% -3%) indicating that the thermal conductivity is practically constant across the bed. This was always the case for all tests performed during the experiments. The good accuracy of the thermocouples measurements is probably mainly due to the fact that they lay on isothermal surfaces in the bed. Furthermore the disturbances the thermocouples cause to the bed are quite small, as the hydraulic resistance of the bed is very high anyhow and the pressure drop of beds containing similar banks of thermocouples agree quite well with those predicted by the Schlünder correlation for undisturbed beds [7]. Fig 6 shows the measured temperature distribution on the walls of the outer and inner tube. The figure shows quite clearly that, even in the last performed experiment with the stable bed, the heat moves essentially in the radial direction.

The thermal conductivity as a function of the interference $\Delta\ell/\ell$ is shown in Fig. 7. The first experimental runs (1-7) represent the heating-up of the bed. In the initial phase (1-4) the thermal conductivity values are even higher than those of the second series of upwards runs. The reason for this is given by the fact that, in order to achieve the

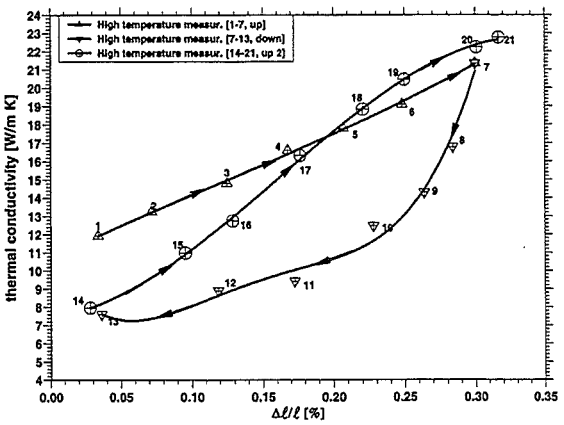

Fig. 7: SUPER-PEHTRA thermal conductivity of the stable binary bed as a function of $\Delta\ell/\ell$ (air cooling)

high packing factor necessary to make the bed stable, it was necessary, before initiating the measurement runs, to vibrate the bed quite strongly and to add in successive steps a relatively large amount of small pebbles. Of course, the curves to be used for design calculations are the 14-21 during the heating up phase and the 7-13 ones for the

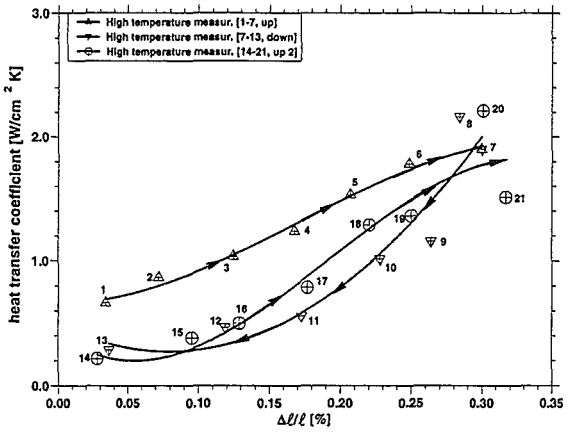

Fig. 8: SUPER-PEHTRA: Heat transfer coefficient at the inner tube wall as a function of $\Delta\ell/\ell$ (air cooling)

cooling down phase. The increasing values of $\Delta\ell/\ell$ are obtained by increasing the constraint of the bed by increasing the heating power of the inner rod which causes an increase of the bed average temperature. A further increase can be obtained by a stronger cooling of the outer tube. This further degree of freedom allows to vary independently $\Delta\ell/\ell$ and the average temperature of the bed.
The thermal conductivity of the reference binary bed (Fig. 7) can be correlated by the following equations:

first going up phase:

$$k\ [W/m\ K]=10.64+34.87\cdot(\Delta\ell/\ell\ [\%])\ \pm 10\% \qquad (1)$$

first going down phase:

$$k\ [W/m\ K]=10.8-149.1\ (\Delta\ell/\ell\ [\%])+ +2036\cdot(\Delta\ell/\ell\ [\%])^2-9904\ (\Delta\ell/\ell\ [\%])^3+ +1.716\cdot 10^4\ (\Delta\ell/\ell\ [\%])^4\ \pm 10\% \qquad (2)$$

second going up phase:

$$k\ [W/m\ K]=6.318+53.83\ (\Delta\ell/\ell\ [\%])\ \pm 10\ \% \qquad (3)$$

for $T_m \approx 200$ °C and $0 \le \Delta\ell/\ell \le 0.3\%$

Fig. 8 shows the wall heat transfer coefficients at the inner rod surface. These account for the smaller packing factor at the inner rod wall, which acts as a disturbance to the pebble bed. They are obtained by the known heat flux at the wall and the difference between the measured temperature of rod surface and the bed temperature extrapolated to the rod surface. The heat transfer coefficients have a similar behaviour to that of the thermal conductivity. However the hysteresis of the curves 7-13 and 14-21 is much less pronounced and possibly within the accuracy of the experiments.
The equation correlating the heat transfer coefficient for the second going-up and the first going down phases is:

$$\alpha\ [W/cm^2\ K]=0.2194-0.174\cdot\Delta\ell/\ell\ [\%]+ +18.66\cdot\Delta\ell/\ell\ [\%])^2\ \pm 20\% \qquad (4)$$

for Tm ≈ 200 °C and $0 \le \Delta\ell/\ell \le 0.3\%$
Fig. 9 shows the average pressure exerted by the bed on the four pressure sensors. The initial curve 1-7 shows quite clearly that the compression occurred essentially during the filling of the bed. Up to $\Delta\ell/\ell = 0.2$ % the pressure remains essentially constant, indicating that during this period, only

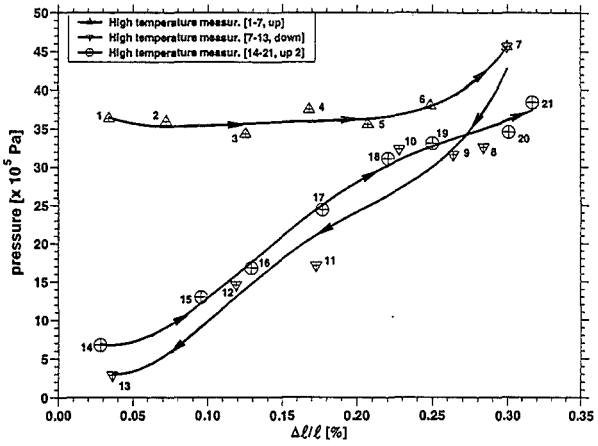

Fig. 9: SUPER-PEHTRA: Average pressure at the four sensors as a function of $\Delta\ell/\ell$ (air cooling)

local movements of the pebbles occur. However, for $\Delta\ell/\ell > 0.2$ % the pressure increases considerably, indicating that elastic-plastic deformations occur, which increase the contact surface of the pebbles, thus strongly increasing the bed thermal conductivity, due to the large thermal conductivity difference between beryllium and helium. As in the case of the wall heat transfer coefficient the hysteresis of the curves 7-13 and 14-21 is less pronounced than in the case of the thermal conductivity data. This hysteresis behaviour is quite similar to that described in [8] for a bed of single size Li_4SiO_4 pebbles. Of course the large ratio of thermal conductivity

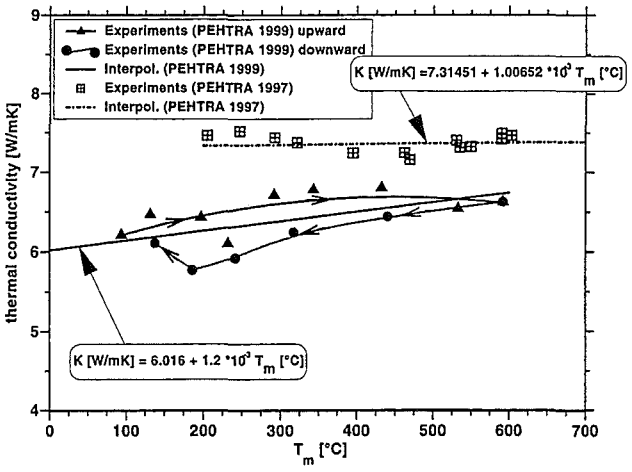

Fig. 10: PEHTRA: thermal conductivity of the reference binary bed (p.f.=82.5%) as a function of the average bed temperature. (The thermal conductivity of the bed of Ref. [1] is given for comparison).

beryllium/helium explains also the fact that the hysteresis in the thermal conductivity data is much higher than the one in the pressure data shown in Ref. [8].

The correlation for the pressure given by the experimental data of Fig. 9 can be obtained by neglecting the narrow hysteresis between the second upward curve and the downward curve. Thus the equation resulting from the data of Fig. 9 is

$$p[\text{bar}] = 125.3\ (\Delta\ell/\ell\ [\%])\ \pm 20\% \qquad (5)$$

for $T_m \approx 200$ °C and $0 \leq \Delta\ell/\ell \leq 0.3\%$

Fig. 10 and 11 show the results of the experiments which have been performed for the reference binary bed in PEHTRA with $\Delta\ell/\ell$ (%) = 0 (thermal insulation). These data refer to the thermal conductivity and the heat transfer coefficient to the wall respectively. In the first case the data are plotted versus the bed average temperature, in the second they are plotted versus the wall temperature T_w of the inner rod surface as they refer to the region near the inner rod. Plotted in the graphs are also the data for the binary bed of Ref. [1]. The data from Ref. [1] are higher indicating that the smaller pebbles did not go down in the annulus below the measurement cross section of the annulus, thus increasing the local packing factor rather than decrease it.

The binary bed thermal conductivity for $\Delta\ell/\ell(\%) = 0$ shows a relatively narrow hysteresis, so that the data can be correlated by a straight line (Fig. 10). The heat transfer data practically do not show any appreciable hysteresis and can be correlated by an exponential curve (Fig. 11).

2.2.3 Experiments with a binary bed with intermediate values of thermal conductivity

The best data for the blanket designer would be the ones with the highest thermal conductivity and the lowest pressure against the containing wall. Unfortunately, generally the highest thermal conductivity implies high pressure. In the present paper we have investigated a binary bed with relatively high thermal conductivity and pressures. In the companion paper to be presented at this workshop, we show the experimental results obtained for a single size bed with a packing factor of 63.2 % [10], which has thermal conductivities about half of those of the present reference binary bed. It was therefore decided to perform an experiment for a stable binary bed with a thermal conductivity between the two.

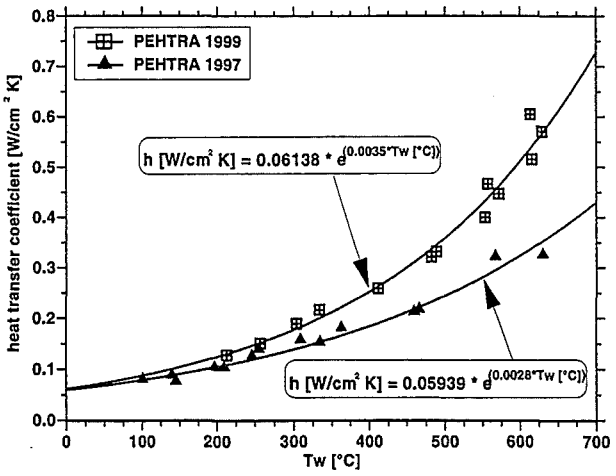

Fig. 11: PEHTRA: heat transfer coefficient for the reference binary bed (p.f.=82.5%) as a function of the average bed temperature. (The heat transfer coefficient for the bed of Ref. [1] is given for comparison).

The bed was also chosen with the objective of having relatively low pressures against the constraining walls. To do so the large pebbles were poured in SUPER-PEHTRA up to the level of 680 mm without exerting the pressure of 2 bar on the

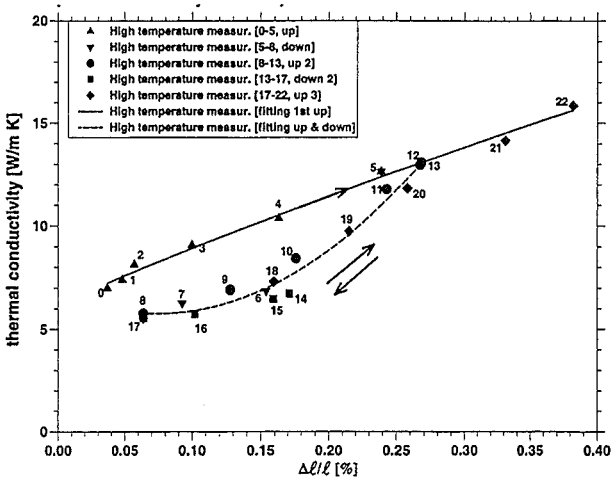

Fig. 12: SUPER-PEHTRA: thermal conductivity of the intermediate binary bed as a function of $\Delta\ell/\ell$, air cooling.

upper free surface of the bed. The resulting packing factor was 60%. Later on, the 0.1 – 0.22 mm small pebbles were poured in with great caution to avoid as much as possible a precompression. The resulting packing factor of small pebbles was 20%, without any appreciable increase of the pebble bed level.

Fig. 12 shows the thermal conductivity of the intermediate binary bed. The experimental runs 0 to 5, 12 to 13, 13 to 22 represent the first heating up of the bed. Starting from the run 5 a going down phase (5-8) is initiated similar to that of the reference binary bed. However, in this case the second going up phase (8-13) is practically coincident with the going down curve 5-8. The same can be said for the following cycles. Thus, one has a situation with only two curves: the first going up line and a cycling curve without hysteresis. This behaviour is similar to that of the experiments of Ref. [8] for Li_4SiO_4 pebble beds.

The results of the pressure measurements are depicted in Fig. 13. These results are analogous to the thermal conductivity ones. However, a relatively narrow hysteresis is present in the cycling region (going up and down).

The upwards curves are correlated by the following equations:

$$k_e\ [W/m°C] = 6.6\ (1+3.64\ \Delta\ell/\ell\ (\%)\ ) \pm 5\% \qquad (6)$$

$$p\ [b] = 6.837 + 19.12\ \Delta\ell/\ell\ (\%)\ ) \pm 20\% \qquad (7)$$

for $T_m = 200°C$ and $0 \leq \Delta\ell/\ell \leq 0.38\%$

3. DISCUSSION OF THE RESULTS

The present experiment with SUPER-PEHTRA and the previous with PEHTRA [3] have helped considerably to understand the behaviour of infiltrated binary beryllium beds. The thermal-mechanical behaviour of the beds is very complex, mainly for two reasons:

i. the thermal conductivity of beryllium is almost 3 orders of magnitude greater of that of helium;
ii. the coordination number (number of contact points of a pebble with the surrounding ones) of an infiltrated binary bed is higher than in a single size pebble bed.

Hysteresis effects have been observed to occur during pebble bed thermal conductivity experiments in the past [9]. However the effects are rather strong in the present experimental data relating to the thermal conductivity, so that an explanation of these effects could be helpful for the application of the present data. The most plausible explanation appear to be the following.

During the first increase of constraint the bed experiences a sequence of phenomena caused by the increasing pressure:

- first a local relocation of the pebbles toward a small increase of their packing factor and of the coordination number;
- second, an elastic deformation of the pebbles causing a reversible increase of their contact surface,
- third, a plastic deformation of the pebbles causing an irreversible increase of their contact surface.

All these three phenomena tend to increase the bed thermal conductivity, especially because the beryllium thermal conductivity is so much higher than that of helium. The second and third phenomena are overlapping.

During the constraint decrease the bed goes through the same sequence, however in the inverse order:

- first, the plastic deformed pebbles detach from each other due to the relaxation of the elastic stress;

- second, during the detachment phase the pebbles relocate or rotate, so that the flattened opened-up surfaces of contiguous pebbles are not parallel anymore, and when the constraint increase begins again the pebbles go through the same process as in the first constrainment phase, however starting from a different initial condition, which requires relocations and elastic-plastic deformations again. This of course means that the second constraint increase can be quite different from the first, producing a thermal conductivity which lays inbetween the first increase and the first decrease of the constraint.

However, infiltrated binary beds are very useful for the blanket application as they have higher packing factors and higher thermal conductivity of single size beds. Thus they give the possibility of having higher tritium breeding ratios and lower beryllium temperatures. For this reason they are often been proposed for fusion blankets.
Following the example of ITER most of the presently proposed TOKAMAK designs have a single divertor. This implies that vertical pebble beds are unavoidable, at least in a large portion of the blanket. This fact introduces a further complication. If the small particles are too small they can go down during the blanket operation causing considerable temperature increases in the upper part of the blanket. This was avoided in the present experiment by the use of small pebbles in the range 0.1-0.2 mm and forcing in the bed the maximum amount of small pebbles possible. This method can be successfully applied to the case of the actual blanket, as the thickness (43 mm) and the length (680 mm) used in the present experiment are typical of the current blanket designs.

4. CONCLUSIONS AND RECOMMENDATIONS

The heat transfer parameters and the pressures exerted on the containment walls of two binary beryllium pebble beds have been obtained by investigations performed in the PEHTRA and SUPER-PEHTRA experimental devices.
The reference binary pebble bed was investigated with the objective of obtaining high values of the bed thermal conductivity. This required a high packing factor with 63.2% of large pebbles (2 mm) and 19.3% of small pebbles (0.1 – 0.22 mm). The measured thermal conductivity data, the heat transfer coefficient and the pressure exerted on the constraining walls are given by the equations (1),

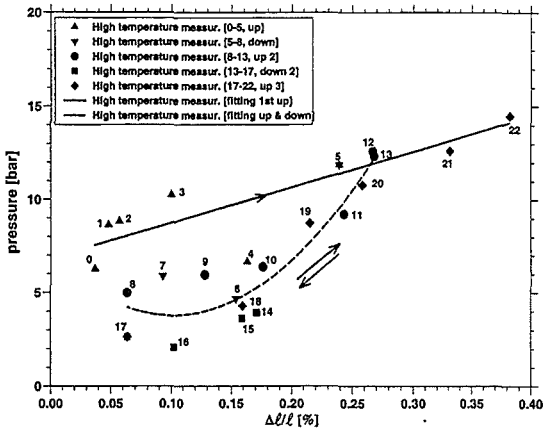

Fig. 13: SUPER-PEHTRA: average pressure at the four sensors placed at the outer tube, air cooling, intermediate binary bed.

(2), (3), for the thermal conductivity, by the equation (4) for the heat transfer coefficient, and by equation (5) for the pressure exerted on the constraining wall, respectively. The data are correlated as a function of the interference in the radial expansion between bed and constraining walls related to the bed thickness. The bed interference is the difference between the free radial expansion of the bed and the actual expansion under consideration of the constraining walls. The interference is determining the elasto-plastic deformations of the pebbles and the extent of their contact surfaces. Due to the very large ratio between the beryllium and helium thermal conductivities (almost three order of magnitude), the extent of the pebbles contact surfaces is the most important factor in determining the bed heat transfer parameters, thus in the correlations these parameters are given as a function of $\Delta\ell/\ell$.
Besides the reference binary bed also an intermediate binary bed was investigated to have conductivity values between those of the reference

and of the single size beryllium pebble beds which are reported in a companion paper presented at this workshop [10]. Again, the data for the intermediate binary bed are correlated in terms of the interference $\Delta\ell/\ell$ and are shown by equations (6) (thermal conductivity) and (7) (pressure on the constraining wall).

The equations showing the thermal conductivity and the heat transfer coefficient for the reference binary bed for $\Delta\ell/\ell$ (%) = 0 are shown in Fig. 10 and 11 respectively.

Of course there are upper temperature limits for the application of the present correlation. Probably the lowest limit is given by the creep of the pebbles by higher temperatures coupled with high pressures exerted by the wall. The effect of an initiating creep was observed in the PEHTRA device by the testing of a single size beryllium pebble bed: at temperatures of about 450 - 500°C near the inner heating rod, it was observed a decrease of the slope of the bed temperature gradient, corresponding an increase of thermal conductivity of about 30% [11]

Nevertheless the correlations provided in this paper are probably sufficient for the ITER breeder blanket. Indeed, due to the use of water rather than helium as coolant of the ITER blanket, the average temperatures of the beryllium bed are 310 °C at BOL and 255 °C at EOL. Thus, the extrapolation from a temperature of 200 °C to these temperatures would be sufficiently small and could be compensated by correcting the bed thermal conductivity proportionally to the solid beryllium thermal conductivities at the temperatures of 310 °C and 255 °C [12]. This means a decrease of the bed thermal conductivities of 14 % and of 6 % at BOL and EOL respectively.

Finally, we would like to stress that care should be taken, in the application of the present correlation, of the fact that $\Delta\ell/\ell$ is a function of the thermal expansion coefficient of the containing walls. Indeed, the values of $\Delta\ell/\ell$ given in this paper are those related to stainless steel, because the experiments were performed with stainless steel tubes. In case of materials with lower expansion coefficients such as martensitic steels or silicon carbide the $\Delta\ell/\ell$ values would be higher.

ACKNOWLEDGEMENTS

This work has been performed in the framework of the nuclear Fusion Project of the Forschungszentrum Karlsruhe and is supported by the European Communities within the European Fusion Technology Program. The authors wish to thank R. Aymar, L.V. Boccaccini, W. Dänner, S. Hermsmeyer, K. Schleisiek, G. Sordon and R. Toschi for their support and the many useful discussions

REFERENCES

[1] M. Dalle Donne, G. Piazza, A. Goraieb, G. Sordon, "Measurement of the thermal conductivity and heat transfer coefficients of a binary bed of Beryllium Pebbles", 3rd Int. Workshop on Beryllium Technology for Fusion, Mito, Oct. 22-24, 1997. JAERI-Conf. 98-001.

[2] M. Dalle Donne, A. Goraieb, G. Piazza, F. Scaffidi-Argentina, "Experimental Investigations on the thermal and Mechanical Behaviour of Binary Beryllium Pebble Bed", presented at the ISFNT-5, Rome, Sept. 19-24, 1999.

[3] M. Dalle Donne and G. Sordon, "Heat transfer in Pebble Beds for Fusion Blankets", Fus. Technol., 17, 597-635, July 1990.

[4] M. Dalle Donne, A. Goraieb and G. Sordon, "Measurements of the Heat Transfer Parameters of Mixed Beds of Beryllium and Lithium Orthosilicate Pebbles", in Proc. of Workshop on Beryllium for Fusion Applications, Karlsruhe, 4-5 Oct. 1993, KFK 5271, Dec. 1993.

[5] F. Scaffidi-Argentina, M. Dalle Donne, C. Ronchi and C. Ferrero, " ANFIBE a comprehensive model for swelling and tritium release from neutron irradiated beryllium, I: Theory and model capabilities", Fus. Technol. 32, 179-195, Sept. 1997.

[6] F. Scaffidi-Argentina, M. Dalle Donne, C. Ronchi and C. Ferrero, " ANFIBE a comprehensive model for swelling and tritium release from neutron irradiated beryllium, II: Comparison of model predictions with

experimental results", Fus. Technol. 33, 146-163, March 1998.

[7] A. Goraieb "Dipl-Ingenieur Abschlußarbeit", unpublished.

[8] J. Reimann and S. Müller "First experiments on the thermomechanical behaviour of Li_4SiO_4 pebble beds", Proc. 20th Int. Symp. on Fusion Technology (SOFT), Marseille, France, Sept. 7-11, 1998, Vol. 2, 1337-1340.

[9] R. O. A. Hall and D. G. Martin, " The evaluation of the Temperature Jump Distances and Thermal Accomodation Coefficients from Measurements of the Thermal Conductivity of UO_2 Packed Sphere Beds", Nucl. Eng. Design 101 (1987) 249-258.

[10] M. Dalle Donne, A. Goraieb, G. Piazza, , F. Scaffidi-Argentina, "Experimental Investigation on the Thermal and Mechanical Behaviour of Single Size Beryllium Pebble Bed", this workshop.

[11] M. Dalle Donne et al., J. Nucl. Mat. 212-215 (1994) 872-876.

[12] ITER Design Description Document: WBS 1.6 B "Tritium Breeding Blanket System", G.166 DDD 2 97-12-03.

LIST OF SYMBOLS

E_{ss} = elasticity module of stainless-steel [MPa]

$$k = k_e = \frac{Q_0 R_1 \ln \frac{R_2}{R_1}}{T_1 - T_2}$$

T_1 = bed temperature extrapolated at the rod surface [°C]

T_2 = bed temperature extrapolated at the outer tube surface [°C]

ℓ = thickness of the bed in the direction of the heat flow = R_2 - R_1 [cm]

p = pressure on the outer tube [MPa]

Q_o = heat flux at the inner wall [W/cm^2]

R_1 = outer radius of the inner heating tube [cm]

R_2 = inner radius of the outer containing tube [cm]

S = outer tube thickness [cm]

$T=T_m$=average temperature of the bed calculated over the total surface of the annulus containing the bed [°C]

T_{w1}= temperature of the outer surface of the inner tube [°C]

T_{w2}= temperature of the inner surface of the outer tube [°C]

T_o = room temperature = 20 °C

α= heat transfer coefficient between bed and containing wall at the outer surface of the inner tube [W/cm^2°C]

α_{Be} = thermal expansion coefficient of beryllium at T_{Be} [K^{-1}]

α_{St} = thermal expansion coefficient of the containing walls of stainless steel [K^{-1}]

σ = standard deviation

$\Delta\ell/\ell$ [%] =percental difference between the thermal expansion of the bed and of the confinement walls referred to the thickness of the bed =

$$= 100x \left[\frac{\int_{R1}^{R2} \alpha_{Be}(T_{Be})(T_{Be} - T_0)dr}{R_2 - R_1} + \frac{\alpha_{St2}R_2 - \alpha_{St1}R_1}{R_2 - R_1} T_o - \frac{\alpha_{St2}R_2T_{w2} - \alpha_{St1}R_1T_{w1}}{R_2 - R_1} - \frac{pR_2}{SE_{ss}} \right]$$

SUBSCRIPTS:

m = mean value
w = wall
1 = inner wall (r = R_1)
2 = outer wall (r = R_2)
o = at room temperature
Be = beryllium
St = Stainless steel

Influence of Temperature and Pressure on the Beryllium Pebbles Bed Electrical Resitivity

E. Alves [1,2], L.C. Alves [1,2], F. Scaffidi-Argentina[3], M.F da Silva[1,2], A.A.Melo[1,2], J.C.Soares[1,2]

1- Instituto Tecnológico e Nuclear, EN. 10, P-2686-953 Sacavém, Portugal
2- Centro de Fisica Nuclear da Univ. de Lisboa, Avenida Prof. Gama Pinto 2, P-1699 Lisboa Codex, Portugal
3- Forschungszentrum Karlsruhe - IKET, Postfach 3640, D-76021, Karslsruhe, Germany

Abstract

The electrical resistivity behaviour of a beryllium pebble bed has been studied as a function of the temperature and pressure. At room temperature the resistivity of a single size 2 mm pebble bed decreases drastically from $2 \cdot 10^{-2}$ Ωm to 10^{-4} Ωm by applying an external pressure. After this first drop, the resistivity shows an almost linear decrease with the applied pressure. The same trend appears for a single size 0.1-0.2 mm pebble bed, but the resistivity values are about one order of magnitude higher than in the case of the 2 mm pebbles. At room temperature, the lowest resistivity values were found for the case of a binary pebble bed.

After a mechanical cycling the electrical resistivity of the bed never reaches its initial value for zero pressure but it remains about one order of magnitude below the original value. After the first loading cycle the following loading/unloading resistivity curves do not show any significant change.

The temperature dependence of the mixed pebble bed was investigated in air at 300 °C, 450 °C and 550 °C. The resistivity behaviour of the pebble bed with the applied pressure is, at high temperature, qualitatively the same as that observed at room temperature. For the same applied load the pebble bed electrical resistivity increases almost linearly with the temperature.

Measurements of the oxyde content of the pebbles before and after the heating show a higher beryllium oxide content for the heated pebbles than for the not heated ones.

I- Introduction

The International Experimental Thermonuclear Reactor (ITER) breeding blanket should use beryllium in the form of a binary pebble bed as neutron multiplier [1]. Solid breeder blankets with lithium ceramics as breeder and stainless steel as structural material require beryllium to increase the tritium breeding ratio (TBR) performance. Since under neutron irradiation beryllium becomes brittle and swells its use in the form of small pebbles offers various advantages [2]. In fact, within small pebbles the temperature differences are small, thus the stresses caused by thermal gradients and by different swelling rates (swelling is temperature dependent) are considerably reduced. Because it is important to achieve a high beryllium density in the blanket a binary bed of larger and smaller beryllium pebbles is used, which allows the bed to achieve a packing factor of about 80%. The larger pebbles (diameter $\Phi = 2 \pm 0.2$ mm) considered so far are a relatively inexpensive intermediate product of the beryllium fabrication route, called Fluoride Reduction Process (FRP). An alternative production method called Shot Process (SP) - which would result in substantial cost savings - is under development. On the other hand the smaller pebbles can be produced either by Inert Gas Atomization (IGA) or by the Rotating Electrode Process (REP).

Although beryllium has no structural function in the blanket, microstructural and electrical properties are important, as they might influence the material behavior during both normal and off-normal reactor operating conditions like plasma disruptions. To confirm the conservative assumptions about the electrical resistivity of the beryllium pebble bed made in the course of the electromagnetic analyses for the Reference ITER Breeding Blanket, this property has been measured as a function of temperature and applied load. The microstructural changes were analysed by means of both optical microscopy and Rutherford backscatering spectrometry.

II- Experimental details

II.1 Material

The material used for the analyses consists of two types of beryllium pebbles (pebble diameter Φ= 0.1-0.2 mm and Φ= 2 mm) produced by the Brush Wellman company. The 2 mm pebbles were produced by Fluoride Reduction Process, which is an intermediate step in the process of winning beryllium from ore [3]. In that intermediate step beryllium fluoride is reduced with magnesium metal to molten beryllium and magnesium fluoride. Upon cooling, a solidified cake of beryllium spherical pebbles, magnesium fluoride and unreacted beryllium fluoride is formed. The solid cake is crushed in a hammer mill and leached with water to remove the beryllium fluoride and most of the magnesium fluoride. A density separation step is used to separate the beryllium from the residual magnesium fluoride. Size distribution of the pebble ranges from approximately one millimeter to above sixty millimeter. For normal beryllium production, the pebble proceeds to the next processing step (vacuum melting) without any size separation step. For fusion research, the pebble is separated into the required sizes (2 mm) using industrial screens (sieves). Although some perfect spheres are found, the shape is generally not perfectly spherical. Since they are an intermediate product, these pebbles contain significant amounts of impurities, notably fluorine and magnesium.

On the other hand, the 0.1-0.2 mm pebbles were made by Inert Gas Atomization (IGA). This process involves break up and rapid cooling of a molten metal stream to form pebbles [3]. This pebbles are very close to spherical in shape and have the purity level of other commercial beryllium products.

II.2 Experimental techniques

The 2 mm beryllium pebbles were analyzed by the Rutherford backscattering spectrometry (RBS) using a 1.6 MeV He^+ beam collimated to 0.8 mm. The backscattered particles were detected with two surface barrier detectors placed at 140° and 180° and with an energy resolution of 12 keV and 15 keV respectively. The detectors and the ion beam were placed in the same horizontal plane and the pressure inside the measuring chamber was about 10^{-4} Pa. Some 0.1-0.2 mm pebbles were studied using a He^+ microbeam of 6 μm. In this way we can avoid the effects of the surface shape on the RBS spectra. The metallographic characterization of both the 2 mm FRP and 0.1-0.2 mm IGA pebbles was carried out by means of optical microscopy.

Resistivity measurements have been performed for both a single size pebble bed (pebble diameter Φ= 0.1-0.2 mm or Φ= 2 mm) and a binary pebble bed (pebble diameter Φ= 0.1-0.2 mm and Φ= 2 mm). The pebble bed column with a lengh l=21 mm is enclosed in an insulating alumina tube with a radius r=5 mm. The ends of the tube are closed by two pieces of steel which are used to apply the force (measured with a balance) and make the electrical contacts. A constant current of 250 mA was applied and the voltage drop along the Be pebble bed column was measured. For the temperature measurements the alumina tube was placed inside a tubular furnace. The temperature was monitored with a thermocouple in contact with the metallic piece on the top of the pebble bed. In order to avoid the bending of the column containing the pebble bed due to the applied force the column was placed inside a steel tube isolated by sapphire balls. The possible influence of the l/r ratio on the resistivity was checked in a pebble bed column with a length of 11.5 mm and a radius of 19.5 mm at room temperature. All the measurements were carried out at ambient atmosphere.

III- Results

III.1 Structural characterization

Fig. 1 shows a typical metallographic structure of the 2 mm FRP beryllium pebbles.

Macroscopically, the pebbles show a relatively large number of surface indentations probably due to the fact that during the fabrication process, very hot (or still partially molten) beryllium pebbles come in contact with cold and already solidified ones. The optical microscopy revealed both large pores of various size (a pore size of 0.1-0.2 mm has been often observed and a microporosity usually oriented along the crystal axis perpendicular to the basal plane. Furthermore, a large number of pebbles presents, near the external surface, a dense region the depth of which usually reaches 0.2-0.3 mm. In this region, the pebbles usually shows a metallographic structure characterized by the presence of large grains

(average grain size 100-300 μm). On the other hand, the remaining part of the pebbles shows a metallographic structure characterized by relatively small grains the average size of which is 50-100 μm. This kind of pebble structure (which has been already observed in other types of pebbles subjected to fast thermal treatments) is typically generated during the cooling phase of the fabrication process.

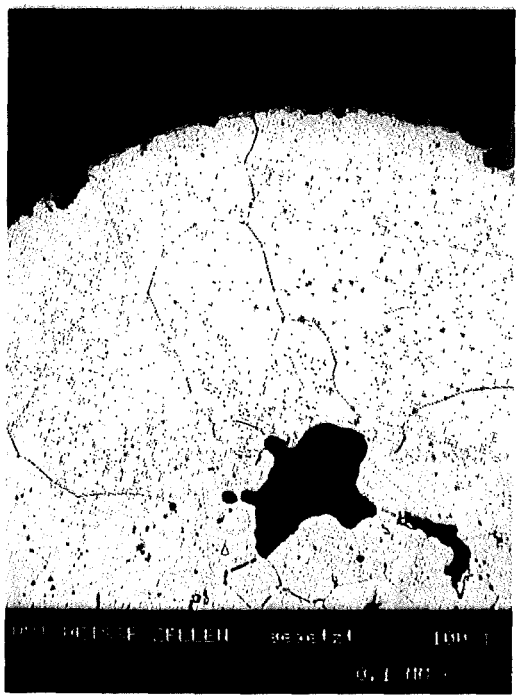

Fig. 1: Typical metallographic structure of the 2 mm FRP beryllium pebbles (etched).

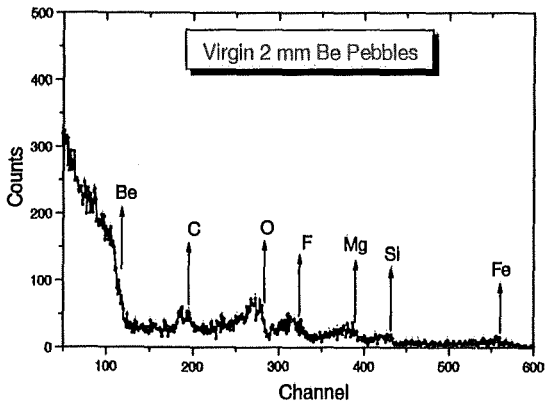

Fig. 2a: RBS spectrum of a 2 mm Be pebble (as received) revealing the presence of a large number of impurities.

The Rutherford backscattering (RBS) spectrum of a 2mm Be pebble is shown in figure 2a. The results indicate the presence of most of the impurities reported by the producer [3]. The oxygen concentration profile, shown in figure 2b, is below the value corresponding to the existence of a pure BeO layer at the surface.

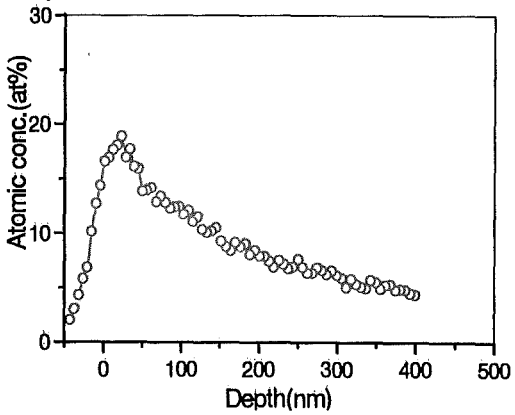

Fig 2b: Depth profile of the oxygen obtained from the spectrum of figure 2a.

These result can be interpreted assuming the presence of BeO regions surrounded by metallic Be. The BeO, is therefore probably distributed along the grain boundaries as revealed by the optical microscopy.

When the pebbles are submited to load/unloading cycles at high temperatures a large increase in the amount of oxygen has been observed as shown in figure 3. On the other hand the signal of the other impurities do not show any significant change.

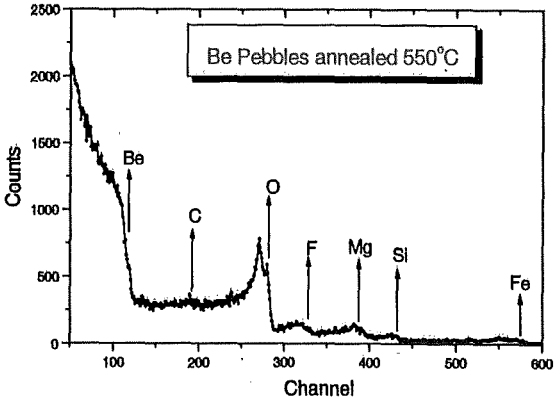

Fig.3: RBS spectrum of a 2mm pebble after heating at 550°C in open air.

With reference to the smaller IGA pebbles (0.1-0.2 mm) it has been observed that their porosity is always smaller than that of the 2 mm FRP pebbles, which clearly confirms that coarse porosity is generated during the cooling phase of the fabrication process. Only in isolated cases a big pore in the center of the pebbles has been observed. The metallographic structure of the IGA pebbles always shows the presence of large grains, in some of the smaller pebbles as large as the pebble diameter as is clearly indicated in figure 4. The RBS results obtained for these pebbles were similar to ones found for the 2 mm pebbles.

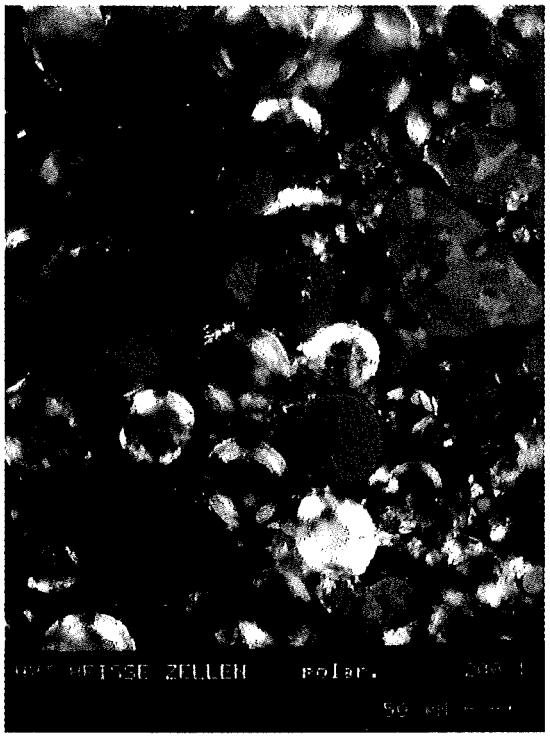

Fig. 4: Typical metallographic structure of the 0.1-0.2 mm IGA beryllium pebble (polar. light).

III.2 Electrical Characterization

The resistivity measurements performed at room temperature are shown in figure 5. In the case of the single size 2 mm pebble bed, the resistivity of the bed decreases drastically to about 10^{-4} Ωm by applying an external pressure. After this first drop, the resistivity shows an almost linear decrease with the applied pressure. The same trend appears for the single size 0.1-0.2 mm pebble bed, but the resistivity values are about one order of magnitude higher than in the case of 2 mm pebbles because of its larger BeO content. The lowest resistivity values were found for the case of a binary pebble bed. The initial drastic drop in the electrical resistivity is probably due to the formation of electrical contacts promoted by the mechanical arrangement of the pebbles due to the applied load. After that, the resistivity of the bed decreases almost linearly with the applied pressure.

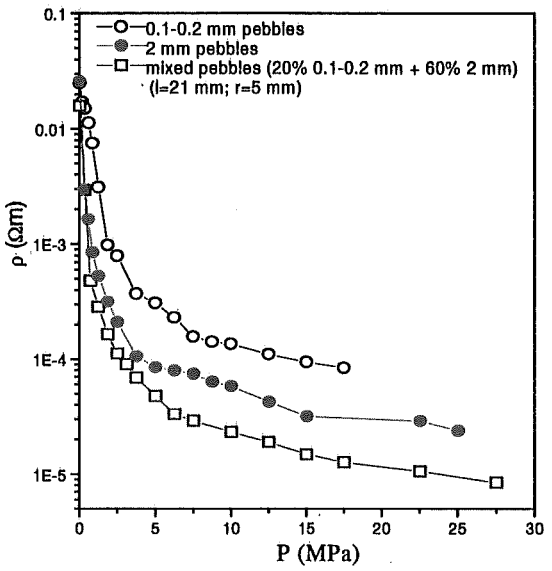

Fig. 5: Electrical resistivity as a function of pressure at room temperature.

As expected, the effect of the pressure is linear, as the increase of the ratio of the contact surface to the cross section of the pebbles is also linear. Because this increase is quite small in comparison to the pebble diameter, it is proportional to the external pressure (if one neglects a second order contribution). For low external pressure values the resistivity of the binary bed is coincident with that of the single size 2 mm pebble bed. This is due to the fact that in the mixed pebble bed the small pebbles just fill the empty spaces, but they result in additional paths for the current flow only after the electrical contact between small and large pebbles has formed. The increase in the number of paths explain the lower value of the resistivity found at higher pressure.

After a mechanical cycling the electrical resistivity of the bed never reaches its initial value for zero

pressure but it remains about one order of magnitude below the original value, as shown in figure 6. These measurements were done in a pebble bed with a radius higher then the length in order to see the influence of the pressure distribution inside the pebble bed. It can be noticed that one obtain the same results as in figure 5 (note that due to the large value of r, the final pressure is much lower), which leads to the conclusion that the value of the l/r ratio has no influence on the electrical resistivity results. This is true as long as the radius of the bed were much higher then the pebbles dimensions. The irreversible behavior of the pebble bed could be due to both pebbles relocation and pebbles plastic deformation.

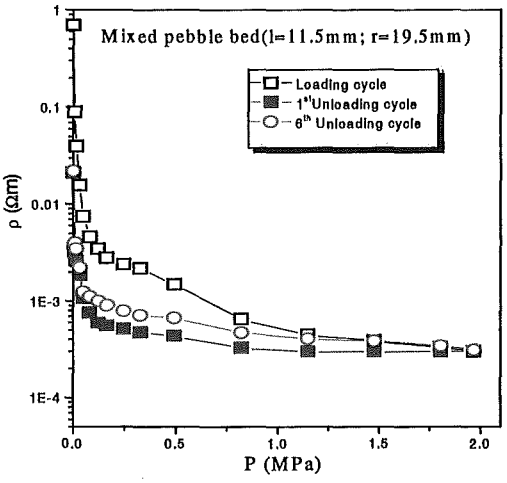

Fig. 6: Loading/unloading cycling behavior of the electrical resistivity at room temperature.

After several load/unload cycles the resistivity curves do show any significant change with respect to the first unloading curve, thus indicating that a stable condition has been reached. This behavior is essentially the same as that observed in the case of the mechanical behavior of a pebble bed.

When the pebble bed is heated during the loading cycle the resistivity increases. The results obtained for two loading values are shown in figure 7.

It can be noticed that the resistivity follows a linear dependence with the temperature in the pressure and temperature range studied. The increase of the resistivity becomes less pronounced for the highest values of the temperature reached in the experimental setup

After the cooling of the pebble bed the resistivity measurements has been repeated and the results were compared with the curves obtained at the beginning (see Fig. 8). Although the curves were similar there was a shift of the resistivity to higher values after the heating cycle. These increase of the resistivity can be related with an increase of the BeO layer of the pebbles during the measurements at high temperature. In fact RBS measurements show an increase on the oxide content of the pebbles during the heating.

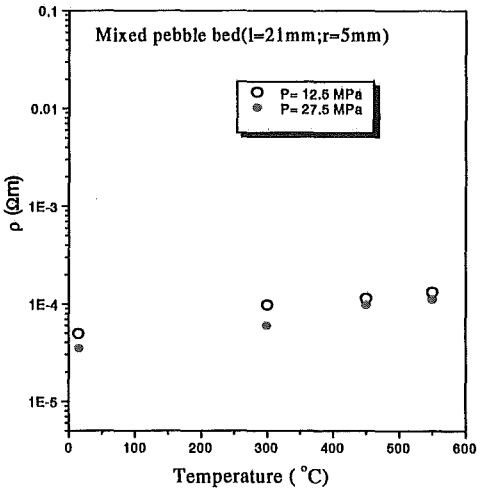

Fig. 7: Temperature dependence of the resistivity for two applied pressures.

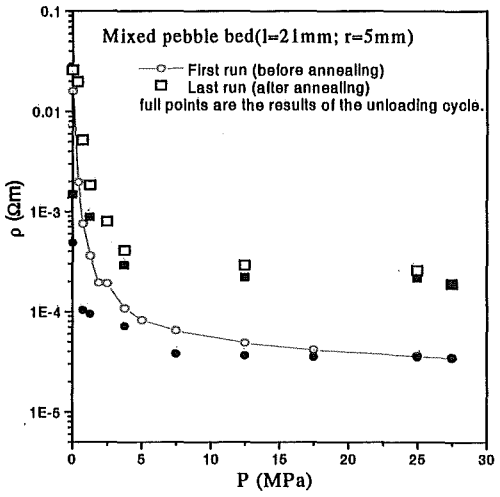

Fig. 8: Resistivity curves obtained before and after the measurements at 550°C.

IV- Conclusion

The metallographic characterization of the pebbles indicates the presence of a certain amount of BeO distributed on the pebble external surface as well as along the grain boundaries, which contributes in increasing the effective electrical resistivity of the pebble bed. At room temperature the electrical resistivity measurements indicate the presence of two regimes for the electrical resistivity of the Be pebble bed. The first one correspond to the mechanical arrangement of the pebble bed and results in a drastic decrease in the pebble bed resistivity. The second regime is linear with the pressure and is probably related with the increase in the contact area between the pebbles under the effect of the external pressure. After a mechanical cycling the bed shows an irreversible behavior and the electrical resistivity never reaches its initial value for zero pressure. The resistivity increases linearly with the temperature up to 550 °C. After cooling the pebble bed heated at 550 °C the resistivity curve shifts to values one order of magnitude higher due to the increase oxyde content of the pebbles.

Acknowledgement

Part of this work has been performed in the framework of the nuclear fusion programme of the Forschungszentrum Karlsruhe and is supported by the European Union within the European Fusion Technology Programme.

References

[1] K. Ioki, M. Ferrari, ITER Final Design Report, Design Description Document WBS 1.6B, Tritium Breeding Blanket System. To be published.

[2] M. Dalle Donne, G.R. Longhurst, H. Kawamura, F. Scaffidi-Argentina, "Beryllium R&D for Blanket Application", in Proceedings of the 8th International Conference on Fusion Reactor Materials. Sendai, October 26-31, 1997. To be published.

[3] D. E. Dombrowski, Personal Communication, 1997.

THERMAL-MECHANICAL TESTING OF BERYLLIUM PEBBLE BED IN REACTOR RELEVANT CONDITIONS

G. Dell'Orco, I.Alessandrini, F. Desideri, L.F. Moreschi, A. Pizzuto, G. Polazzi, M. Simoncini
ENEA Brasimone, P.O. BOX 1 – 40032 CAMUGNANO (BO), Italy
Tel.: +39-0534-801129, Fax: +39-0534-801244 - E-mail:DELLORCO@BRASIMONE.ENEA.IT

ABSTRACT

At beginning 1998, ENEA launched an experimental activity planned in the EU R&D Task Programme for the ITER Breeding Blanket. This activity aims at investigating the out-of-pile thermal-mechanical behaviour (thermal conductivity, wall heat transfer coefficient and interaction pebbles-walls) of Beryllium, in form of binary pebble bed. Two mock-ups, called SMARTS 1-2 (SMALL RECTANGULAR TEST SECTIONS), were manufactured for the reproduction of a rectangular portion a Be cell. The Be pebbles will be filled between two water-cooled lateral plates. A flat electrical heater, dividing the Be bed in two radial-poloidal cells, will impose the thermal loads with a radial toroidal pattern. The heat transfer phenomenon will be evaluated as a function of the differential thermal expansion between the pebbles and the surrounding steel walls; the measurements of the variation of the overall electric resistivity of the pebbles will be also performed. The temperature distribution will be measured by thermocouples located in the pebble bed, on the heater surfaces and on the lateral cooling plates. The differential thermal expansion between the Be pebbles and the steel walls will be controlled by varying the inlet water flow temperature in the range 20-120 °C. The lateral mechanical constrain will simulate either a rigid containment of the pebbles by stiffening the lateral cooling plates (SMARTS 1) or, in alternative, a flexible containment without stiffening (SMARTS 2). The measurements of the forces or deformations of the cooling plates will be also carried-out respectively by load cells and LVDT's. The tests will be performed at the reference thermal chemical conditions in the blanket. In fact the pebbles will be swept by a Helium purge flow at the reference pressure and flowrate. The paper presents the detailed design of the mock-ups, the preliminary thermal-mechanical calculations, the filling procedure of the Be pebbles and the status of the testing activity.

1. INTRODUCTION

The ENEA experimental programme aims to investigate the thermomechanical interactions between the Beryllium binary pebble bed and the surrounding Cooling Plate (CP) steel structure by using two different small-scale mock-ups. These mock-ups will reproduce a small rectangular cell of the Beryllium binary pebble bed layer in between two cooling plates. The heating of these pebbles will be performed by a flat electrical heater immersed in the bed. As far as the mechanical interaction is concerned, two different boundary conditions will be adopted: i) a rigid containment of the Beryllium bed, simulating the reference central cell; ii) a flexible containment of the Beryllium bed, simulating the reference lateral cell. The tests will be performed at the reference thermal chemical conditions in the pebbles, and the heat transfer phenomenon will be evaluated as a function of the differential thermal expansion between the pebbles and the surrounding steel walls. In fact, the mock-up steel frame temperature and the pebble temperature will be independently controlled by regulating both the CP inlet water temperature and the electrical supply to the heater. As a consequence, the pebble thermal expansion will be regulated by the lateral CP mechanical constraints on the bed. More particularly, the test programme includes the following experimental activities: i) measurement of the Beryllium pebble bed thermal conductivity and the pebble bed-wall heat transfer coefficient; ii) measurement of the pressure loads or displacements between the pebble bed and the surrounding structure; iii) measurement of the overall electrical resistivity of the Beryllium pebble bed.

2. MOCK-UP DESIGN AND FABRICATION

The SMARTS 1-2 mock-ups reproduce two rectangular portions of the ITER Breeding Blanket cells with the Beryllium pebble beds in between two CP's, Fig. 1-2 [1].

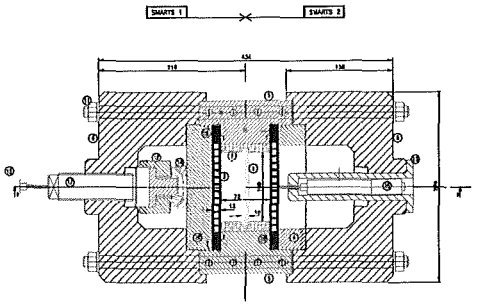

Fig. 1 – SMARTS 1-2 toroidal section

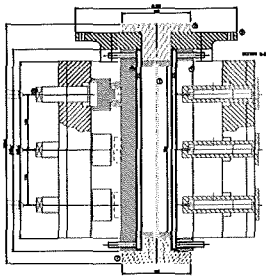

Fig. 2 - SMARTS 1-2 poloidal section

In the SMARTS 1, the rigid containment of the reference central cell is reproduced by using very stiff lateral plates. In the SMARTS 2, the flexible containment of the reference lateral cell is reproduced by using the original CP stiffness. The single mock-up Beryllium cell dimensions are 400 mm in poloidal height, 100 mm in radial length and 33.5 mm in toroidal net width. The total net volume of the two cells is 2680 cm^3. The final mock-up design was completed in May '98, whilst the procurement of the materials and components was launched in mid-'98. The mock-up steel structure manufacturing started in July '98, with the machining of the AISI 316 austenitic steel structure, and was completed in December '99, Fig. 3. The Beryllium pebble production was performed by BRUSH WELLMAN using two different technologies: i) Mg reduction of BeF_2 for the pebbles of 1.6-2.4 mm in diameter (Batch n° MS-1, MS-2 and MS-3; ii) atomisation and screening method for the pebbles of 0.1-0.2 mm in diameter (Batch n° 981103).

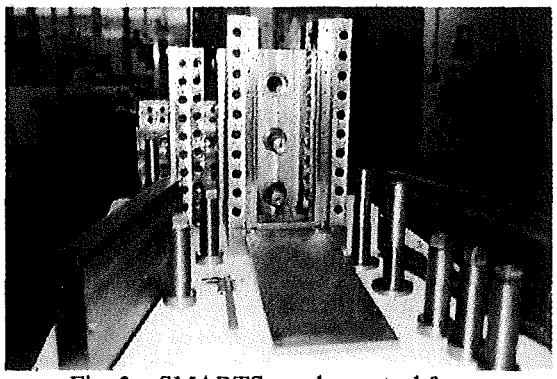

Fig. 3 – SMARTS mock-up steel frame

The CP's were built by brazing tubes of 10x10x1 mm between two 2 mm thick steel sheets. The brazing was carried-out in a furnace under vacuum at 1030 °C with a Cu 70%-Ni 0.9% alloy paste. A flat electrical heater immersed in the axial plane of the beds will perform the heating of the pebbles. The heat flux will be regulated by a special DC power supply up to a maximum value of 14 W/cm^2. This heater was constructed with KANTHAL A-1 flat strips and two INCONEL 718 cladding sheets with thickness of 1.5 and 1.6 mm respectively, Fig. 4.

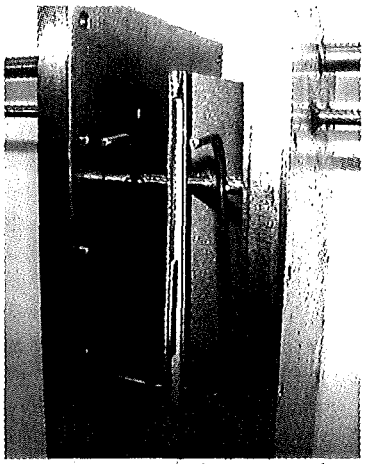

Fig. 4 – CP, Heater and thermocouple supporting rods

The resistor and the internal surfaces of the cladding sheets were coated by 0.15 mm of plasma sprayed

alumina acting as the electrical insulation, the total thickness of the heater being 5.0 mm. The mock-up temperature distribution will be measured by 12 thermocouples per cell positioned in the Beryllium pebble bed at different heights by a supporting rod, Fig. 4. The heater surfaces and the corresponding facing CP's will be also monitored by 9 thermocouples on each surface. In the SMARTS 1 assembly, the thermal interaction, and the related pressure loads of the pebble bed on the lateral CP walls will be measured by 3 load cells each per side. For SMARTS 2, the thermal expansion of the bed and its CP will be measured by 3 LVDT gauges each per side at the same locations as before. The Beryllium pebbles will be swept by a Helium purge flow at reference pressure and flowrate. The thermohydraulic testing, both at steady state and thermal cycling conditions, will be carried-out in the THESIS apparatus of the CEF 1-2 thermal-hydraulic facility in Brasimone [2].

3. THEORETICAL CALCULATION

Some thermal-hydraulic and thermal-mechanical preliminary calculations were performed by means of ANSYS 5.4 FEM code in order to verify the mock-up design [2]. The criterion used for these calculations was the modelling of an equivalent homogeneous material instead of considering each single pebble. This means that the material properties are the overall result of the interactions among the pebbles and the voids. The equivalent thermal-physical properties of the pebble bed were interpolated from the available results of the experiments performed by FZK [3]. The temperature and the equivalent Von Mises stress maps are shown in Figs. 5-6. Further calculations were performed by ABACUS FEM code [4]. For the thermal-hydraulic calculations, both steady state, start-up and LOFA transient were examined. In the Tab. I a summary of the steady state main results is reported.

Tab. I - Results of the thermal-hydraulic calculations in SMARTS 1

Case	Water inlet temp [°C]	Heater flux (W/cm2)	Max temp. in Be pebbles [°C]	Min temp. in Be pebbles [°C]	Max temp. in steel structure [°C]
A1	100	14.0	487	157	172
A2	100	10.0	377	141	152
A3	100	5.0	239	121	126
B1	50	14.0	430	109	123
B2	50	10.0	330	93	103
B3	50	5.0	191	72	76
C1	20	14.0	413	91	94
C2	20	10.0	302	64	73
C3	20	5.0	161	43	47

Tab. II - Results of the thermal-mechanical calculations in SMARTS 1

Case	Water inlet temp [°C]	Heater flux (W/cm2)	Max stress in steel [MPa]	3Sm in steel structure [MPa]	Max plastic strain in Be [10-3]	Max pressure in Be pebbles [MPa]
A1	100	14.0	372	450	7.47	0.327
A2	100	10.0	359		5.33	0.193
A3	100	5.0	352		2.8	0.081
B1	50	14.0	240	477	7.66	0.306
B2	50	10.0	173		5.42	0.183
B3	50	5.0	132		2.59	0.076
C1	20	14.0	311	496	7.82	0.298
C2	20	10.0	222		5.56	0.174
C3	20	5.0	112		2.7	0.072

At the maximum heat flux and water inlet temperature, for both mock-ups, the calculated time constants are in range of 4.5-5.5 minutes. In a very severe LOFA simulation the temperature in the resistor has reached the maximum operating value (1100 -1340 °C) in 30 minutes; correspondingly the steel structure has reached 800-1000°C. For the thermal-mechanical calculations, the Drucker-Prager model, developed for non-homogeneous materials such as concrete and available in the code, was adopted. In the Tab. II are reported the main results of the stress and strain calculations. The secondary stress in the AISI 316L steel are within the ASME limits; the equivalent plastic deformation and the equivalent pressure in the Be pebbles have reached respectively 0.8 % and 0.3 MPa.

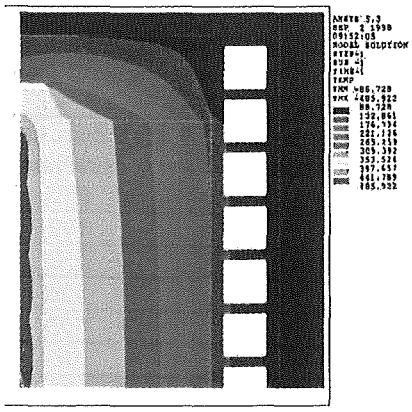

Fig. 5 - Temperature distribution

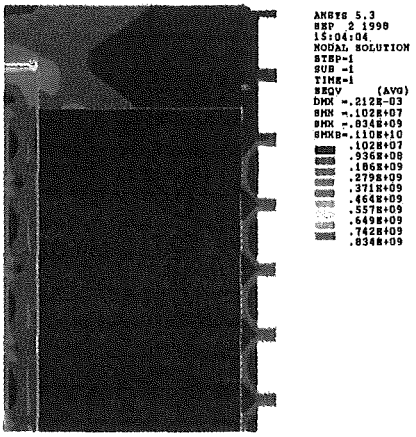

Fig. 6 – Von-Mises Stress distribution

4. PRELIMINARY MEASUREMENTS

The large and small Beryllium pebbles were both examined by optical and electronic microscopy. A mixed binary bed picture, obtained by electronic microscopy, is shown in the Fig. 7.

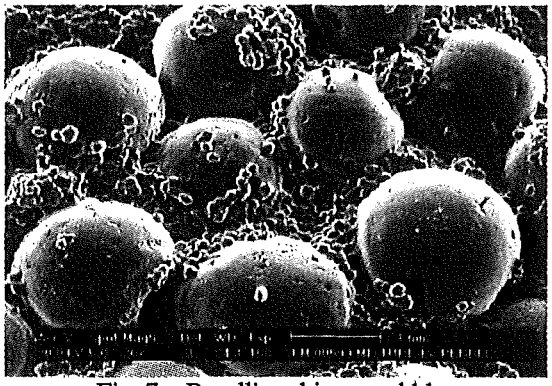

Fig. 7 – Beryllium binary pebbles

The small pebbles contain minute quantities of residual manufacturing products with dimensions in the range of tenths of μm; therefore filtration at 100 μm was performed in order to maintain their reference size distribution. The mock-up assembly and its mechanical characterization were performed in spring 1999. The stiffness of the steel structural containment was investigated by means of the insertion of an oil-dynamic piston system inside the frame. The tests simulated the pressure loads against the CP due to the differential pebble thermal expansion, assuming an overall equivalent Young's modulus of the Beryllium pebbles in the range of few GPa. The results demonstrated that at 2.5 MPa of simulated internal pressure of the pebbles against the CP, and a corresponding total load of 10 tons, the average strain of each side reached 16-17 μm, Fig. 8. The difference between the strain measurements at the two sides was better than 1 μm. The actual filling of the pebbles into the SMARTS mock-ups will be performed using an appropriate glove box from the Brasimone Beryllium Lab., Fig. 9. The procedure used to fill the SMARTS mock up was preliminarily investigated and optimised by means of tests carried out with glass pebbles reproducing the reference Beryllium pebble dimensions. The tests aimed at finding the more

efficient way to accomplish the pebble filling up to the reference packing factor of 82 %.

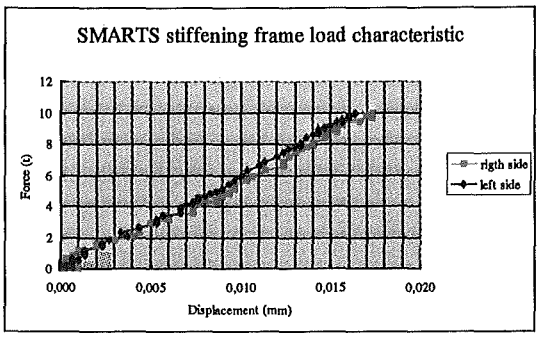

Fig. 8 –SMARTS stiffening frame load characteristic

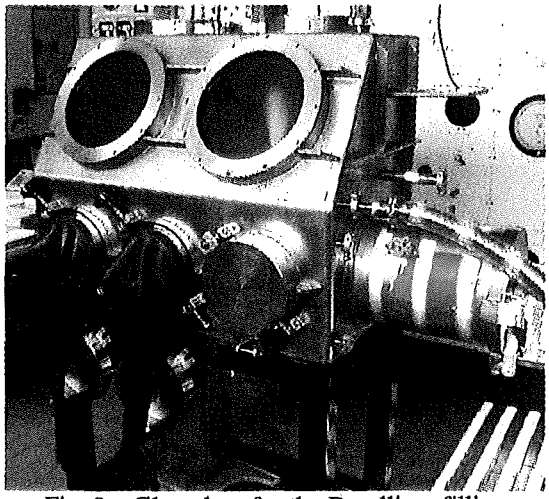

Fig. 9 – Glove box for the Beryllium filling

The visual inspection of the procedure was performed by replacing one of the CP's with a Plexiglas window, Fig. 10, recording the whole sequence by a camcorder.

The procedure began with the filling of 2 mm glass pebble up to the higher level of the mock-up. A little vibration, induced by a pneumatic hammer, completed this first step, Fig. 11. The second step was the filling of the 100-200 μm small pebbles induced by the mechanical vibrations of the steel frame. Two accelerometers, located on the steel lateral wall, recorded the vibration signal spectrum in the vertical and lateral directions.. The optimisation of the vibrations was reached exciting the steel frame at a resonance of 5640 Hz in the lateral direction, Fig. 12. This value, higher than the mechanical resonance of the steel frame and the glove box (15-24 Hz), was selected in order to excite only the small pebbles

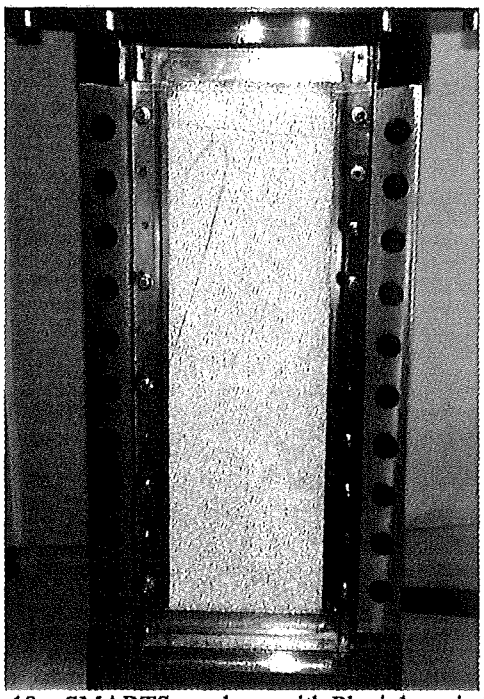

Fig. 10 – SMARTS mock-up with Plexiglas window

Fig. 11 – Simulation of SMARTS filling by glass binary pebbles

The dropping down of the small pebbles was evident and no movement of the larger ones was observed

(Fig. 13). No any de-mixing phenomenon was observed when the vibration prosecuted after the filling completion. The time duration of the filling sequence, evaluated for later reproduction in the actual conditions, was within one hour for each volume to be filled.

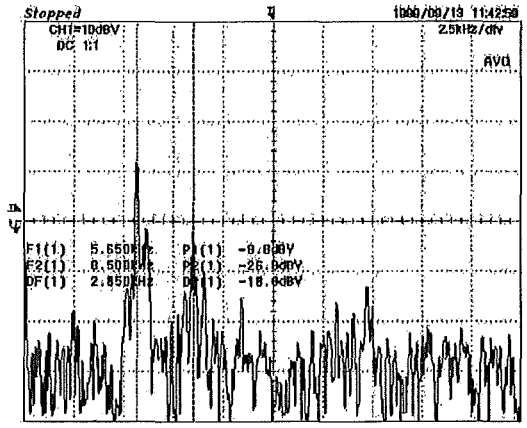

Fig. 12 – FFT spectrum of vibrations

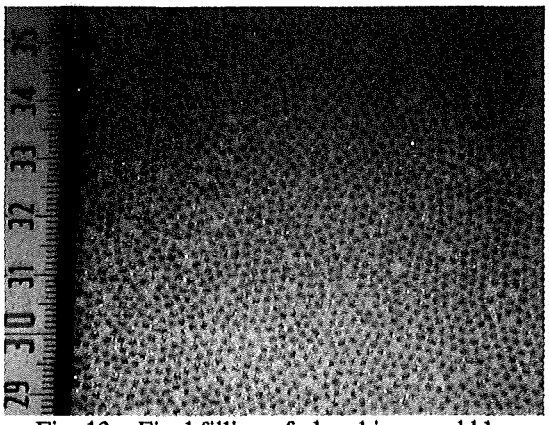

Fig. 13 – Final filling of glass binary pebbles

5. TEST PROGRAMME

The test activity on the first SMARTS 1 assembly will start next September 1999 and will finish by the end of 1999 when the SMARTS 2 characterization will start. The experimental campaigns will be carried out in the THESIS apparatus of the CEF 1-2 thermal-hydraulic facility at Brasimone. The tests on the SMARTS 1-2 mock-ups will be performed measuring the thermomechanical loads (force or displacements) using the following thermal-hydraulic scenarios: i) Steady State Isothermal tests, carried-out at different cooling plate temperatures in the range 20-100 °C; ii) Steady State Heat Flux tests, carried-out at different cooling plate temperatures in the range 20-100 °C and regulating the electrical heater heat flux in the range 5-14 W/cm^2; iii) Thermal Cycling tests, carried-out controlling the cooling plate temperature at constant values and regulating the heater heat flux with pulsating cycles.

6. CONCLUSIONS

The SMARTS mock-up fabrication was completed at the end of 1998. The theoretical calculations for the thermal-hydraulic and thermal-mechanical characterization were completed too both for steady state and transient conditions. The mock-up assembly, the qualification of the Beryllium pebbles, the preliminary tests on the mock-up stiffening frame and the simulation of the pebble bed filling procedure using glass spheres, were carried out during mid-'99.

REFERENCES

[1] G. Dell'Orco et al., Preliminary design of the experiments on the Beryllium pebble bed-wall interactions of the ITER Breeding Blanket, ENEA Internal Report BB-G-N-001, 27 Feb. 1998.

[2] G. Dell'Orco et al.: 'Interaction Tests between Beryllium Pebble Bed and adjacent steel structure in ITER Breeding Blanket relevant conditions ', Proc. 20th SOFT, Marseille 7th-11th September, 1998, pp. 1309-1312.

[3] Dalle Donne M., Goraieb A., Piazza G., Sordon G., 'Measurement of the thermal conductivity and of the heat transfer coefficient of a binary bed of Beryllium pebbles', 3rd IEA Int. Workshop on Beryllium for Fusion Application, Mito (Japan), 22-24 Oct, 1997.

[4] D. Zito, G. Mercadante: 'Verifica di fattibilità dei modelli sperimentali dei mantelli triziogeni a letti di sfere previsti nei progetti dei Reattori nucleari a fusione ITER eDEMO refrigerati ad elio', Tesi di Lurea, Università di Palermo, July 1999.

Thermomechanical analyses of the DEMO-HCPB TBM medium scale mock-up to be tested in the HE-FUS3 facility

E. Oliveri, G. Vella, P. Di Maio, G. Mercadante, D. Zito

Dipartimento di Ingegneria Nucleare, Università di Palermo, Viale delle Scienze 90128 Palermo, +39-091 232215, vella@din.din.unipa.it

1. ABSTRACT

Within the framework of the European Fusion Technology Programme intense research activities are being carried out on the Helium Cooled Pebble Bed (HCPB) blanket concept of the DEMO reactor. Among them a particular attention is being paid to those concerning the HCPB Test Blanket Module (TBM) to be tested in the ITER reactor. The activity programme foresees the performing of out of pile experiments with small and medium TBM mock-ups to be tested in facilities capable of reproducing the thermal loads foreseen during ITER working cycle.

In this paper the attention will be focused on a HCPB-TBM medium scale mock-up jointly designed by ENEA and FZK and to be tested in the HE-FUS3 facility (ENEA, Brasimone), whose main aim is to investigate the thermo-mechanical behaviour of both the Beryllium and Lithium OrthoSilicate (Li_4SiO_4) pebble beds.

Analyses have been performed in order to investigate the mock-up thermal and mechanical behaviour both in steady state and in transient conditions, using a three dimensional finite element model representing a portion of its poloido-radial middle section extending for 10 mm in the toroidal direction. In order to model the pebble beds mechanical behaviour there have been used particular constitutive models, adopted in preliminary analyses, capable to well reproduce the experimental results of the FZK oedometric tests. The analyses have been performed taking into account both the heat flux on the FW and the space dependent heat generation in the pebble beds as thermal loads and the helium pressure in the cooling channels as mechanical load.

The results obtained up till now seem to show that the mock-up is able to withstand the loads it will undergo during the HE-FUS3 working cycle and they can be also used to suggest possible hints for a further mock-up design optimization.

2. INTRODUCTION

Within the framework of the European Fusion Technology Programme 1999-2002 (EFTP), intense research activities are being carried out on the DEMO-HCPB blanket concept. Among these activities the EFTP foresees the design and validation of a Test Blanket Module reproducing a smaller poloidal portion of the DEMO-HCPB breeding blanket module, that is intended to be tested and validated in the ITER reactor in order to verify and demonstrate the functionality of the module system in the fusion environment [1].

The HCPB-TBM is a box-shaped helium cooled system containing both the neutron multiplier and the tritium breeder arranged in toroido-radial layers alternating in poloidal direction. The reference structural material is low activation EUROFER martensitic steel, while the neutron multiplier and the tritium breeder reference materials are, respectively, Beryllium and Lithium OrthoSilicate (Li_4SiO_4) both in form of pebble beds [1].

The EFTP foresees, as intermediate steps before the TBM implementation, the performing of intense Out of Pile testing activities of appropriate small and medium scale TBM mock-ups in order to investigate its thermal and mechanical behaviour both in steady state and in operational or accidental transient conditions [2].

In particular the research programme foresees two medium scale HCPB-TBM mock-ups to be designed and assembled by the ENEA and FZK and to be subsequently tested in the HE-FUS3 facility available at the ENEA laboratories of Brasimone.

The first mock-up, called HEXCALIBER, is at the moment being designed and it should be assembled by the end of 1999 allowing the starting of testing activities. The test programme foresees the performing of hydraulic tests at steady state isothermal conditions, thermo-mechanical tests at different heat fluxes, thermal cyclic fatigue tests and

Loss Of Flow Accident (LOFA) and Loss Of Coolant Accident (LOCA) tests [2].

The Department of Nuclear Engineering (DIN) of the University of Palermo is at the present involved in the research activities on the mock-up feasibility with a particular reference to the thermal-hydraulic and thermo-mechanical design aspects.

3. THE HEXCALIBER MOCK-UP

The HEXCALIBER mock-up was conceived with the specific aim of investigating the thermal and mechanical behaviour of the HCPB-TBM neutron multiplier and tritium breeder pebble beds. It is, consequently, designed to closely reproduce the HCPB-TBM pebble beds thermo-mechanical conditions, presenting some simplifications as far as First Wall (FW) and Cooling Plates (CPs) are concerned, that are only intended to provide the correct mechanical pebble beds boundary conditions [2].

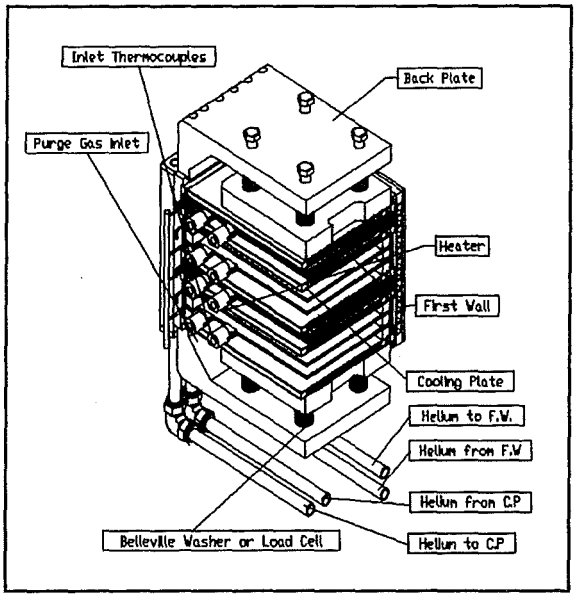

Figure 1. The HEXCALIBER mock-up.

The HEXCALIBER mock-up (fig.1) is a box-shaped system with an overall poloidal height of 280 mm, a toroidal length of 700 mm and a radial depth of 300 mm. It is mainly composed of a First Wall, five toroido-radial Cooling Plates, an electric heating system and four cells delimited by the CPs.

The FW has an extension of 29*280*700 mm respectively in radial, poloidal and toroidal directions, and T91 ferritic martensitic steel as reference material. It houses 12 rectangular-shaped toroidal cooling channels of 12*17 mm respectively in radial and poloidal direction, poloidally arranged with a pitch of 20 mm [3].

The CPs, directly TIG-welded to the FW, have toroido-radial dimensions of approximately 700*200 mm, a poloidal thickness of 14 mm and T91 ferritic martensitic steel as reference material. Every CP houses 18 rectangular-shaped toroidal cooling channels of 8*8 mm both in radial and poloidal direction, toroidally arranged with a pitch of 10 mm.

Helium at a pressure of 8 MPa and at a temperature radially increasing from 300 to 430 °C flows at high velocity inside FW and CPs cooling channels as coolant fluid.

The electric heating system is devoted to simulate the TBM pebble beds nuclear heating, being designed to closely reproduce the TBM pebble beds thermal field with a particular reference to its poloido-radial profile. It is mainly composed off 8 toroido-radial Heating Plates (HPs) poloidally arranged in such a way to subdivide each cell in three equal parts. Each HP has a poloidally layered structure composed off a central 1mm thick KANTHAL electric heater, two AL23 electrical insulators and two INCOLOY 800H sheet-steel heater jackets, for an overall HP poloidal thickness of 5 mm. The heater is composed off conductive strips having radially increasing poloido-radial section in order to close simulate the TBM pebble beds thermal field profile [4].

The cells, delimited by two following CPs, contain the neutron multiplier or the tritium breeder pebble beds alternatively arranged in poloidal direction. The reference neutron multiplier material is Beryllium in the form of binary mixed pebbles of 2 mm and 0.1-0.2 mm in diameter, while the reference tritium breeder material is Lithium OrthoSilicate in the form of pebbles of 0.25-0.63 mm in diameter. Both Beryllium and Lithium OrthoSilicate pebble beds are subdivided by the HPs in three layers with a poloidal thickness of respectively 15 and 5 mm.

Helium at a pressure of 0.1 MPa and at a temperature of approximately 450 °C, flowing through the pebble beds, is also provided to take into account the effects of the TBM purge gas on the pebble beds thermal behaviour.

4. THERMO-MECHANICAL ANALYSES

Thermo-mechanical studies have been performed at the DIN in order to investigate the mock-up thermal and mechanical behaviour, with a particular reference to the pebble beds constitutive model, both in steady state and in operational or accidental transient conditions.

A set of numerical non linear fully coupled thermo-mechanical analyses of the HEXCALIBER mock-up has been, consequently, performed

adopting the Finite Element Method by the means of quoted numerical codes.

4.1. The Finite Element Model

For the mock-up thermo-mechanical analyses it has been used a three dimensional finite element model built using I-DEAS code [5] that consists of a geometrical, a thermal-hydraulic and a mechanical model.

The geometrical model

The geometrical model taken into account for the analyses (fig.2) represents a portion of the mock-up poloido-radial middle section extending for 10 mm in the toroidal direction.

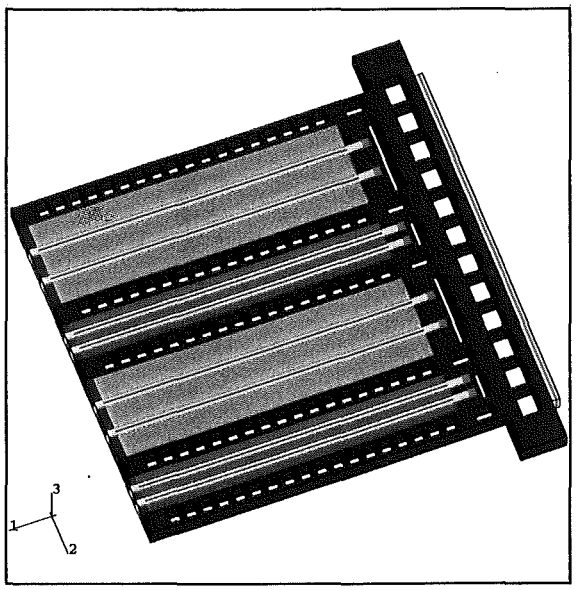

Figure 2. The Mock-up geometrical model.

Particular attention has been paid to the simulation of the HPs-FW bonding regions as well as of the HPs structure. It consists of 78987 nodes and 49320 linear quadrilateral brick elements.

The thermal-hydraulic model

The thermal-hydraulic model takes into account the mock-up forced convection heat transfer with both high pressure helium coolant and low pressure helium purge gas, the mock-up natural convection heat transfer with air and the HPs heat generation.

The forced convection with high pressure helium coolant has been simulated applying to the cooling channels heat transfer coefficients and coolant bulk temperatures evaluated by a preliminary thermal-hydraulic analysis in such a way to maintain as flattest as possible the CPs temperature radial profile. For the CPs cooling channels the values of the heat transfer coefficient and of the coolant bulk temperature vary with the channel radial position, respectively, from about 3170 down to 1070 W/m^2K and from about 432 to 427 °C, while for the FW cooling channels they are respectively 2985 W/m^2K and 306 °C.

The forced convection with the purge gas has been simulated applying a constant heat transfer coefficient of 300 W/m^2K with a purge gas bulk temperature of 450°C on to the rear part of the mock-up and on to the HPs supports hollows.

With regard to the mock-up natural convection with air, it has been simulated applying a small convection coefficient of 5 W/m^2K and an air bulk temperature of the 20 °C to the mock-up external surfaces.

The HPs heaters electric heat generation has been taken into account applying a power density distribution given by:

$$q'''(r,T) = \rho(T) J^2(r)$$

where J(r) is the density of current, that has been assumed depending on the radial position according to the particular heater structure, and ρ(T) is the KANTAL temperature-dependent electric resistivity. Maximum power density values have been applied to the heaters in order to achieve a maximum temperature of 865 °C and 550 °C respectively in the Lithium OrthoSilicate and Beryllium pebble beds, and an average FW radial heat flux of about 0.24 MW/m^2 [3].

The mechanical model

The mechanical model consists of the mechanical loads, the constrains and the constitutive models.

The mock-up mechanical loads have been simulated taking into account the helium coolant pressure of 8 MPa on both the FW and the CPs cooling channels, the purge gas pressure of 0.1 MPa on the HPs supports hollows and the thermal loads due to the mock-up thermal field.

The model was constrained applying a poloido-radial plane symmetry to its lower face, an equal toroidal displacement to the nodes of the upper one and an equal radial displacement to the nodes of its rear part.

Different constitutive models have been adopted in order to close simulate the mock-up mechanical behaviour. All the materials have been simulated with a linear elastic constitutive model except for the T91 and the Beryllium and Lythium OrthoSilicate pebble beds.

With regard to the T91 ferritic-martensitic steel, it has been assumed an elastic plastic model with an isotropic hardening rule.

Concerning the pebble beds, a particular attention has been paid to the study of their mechanical constitutive model as it has a pivotal role in the HCPB blanket design.

As it is well known, during operation, the blanket structure restrains the pebble beds and, therefore, causes significant stresses arising from the different thermal expansion coefficient of the structural and pebble beds materials and from the pebble beds swelling. The amount of these contributions strictly depends on temperature and hence on the local position in the blanket.

The pebble beds are particular granular systems composed off a very large amount of small particles whose mechanical behaviour is quite different from that of a solid sample of the same size and material being very highly load-dependent.

When such a kind of system undergoes a mechanical cycle composed off a monotonic compressive loading and a subsequent relaxation, it shows a highly non-linear elastic behaviour characterised by an elastic modulus strictly depending on the pressure system, and a residual permanent deformation. This is probably due to the bed compaction during the compression phase, to the fracture of a number of particles or to their plastic deformation [6].

The knowledge of the pebble beds behaviour during their first cycle of loading and relaxation seems to have a pivotal role because it determines the pressure build-up during the first operation of the structural device to whom they belong possibly causing its failure.

The present knowledge of the pebble beds mechanical properties is quite limited and their observed mechanical behaviour can be simulated by adapting two mechanical constitutive models known as the Porous Elasticity and the extended Drucker-Prager models [7].

The Porous Elasticity is a non-linear elastic constitutive model apt to simulate the granular systems elastic behaviour [8].

It is based on the experimental assumption of a linear dependency between the elastic void ratio e and the logarithm of the system pressure p. It foresees a functional dependency of the pressure from the volumetric elastic strain ε_{vol}^{el} given by:

$$p_{PE}\left(\varepsilon_{vol}^{el}\right) = -p_t^{el} + \left(p_0 + p_t^{el}\right)\exp\left[\frac{1+e_0}{k}\left(1-\exp\left(\varepsilon_{vol}^{el}\right)\right)\right]$$

where p_t^{el} is the tensile strength of the pebble bed and p_0 is the pressure value corresponding to a null volumetric elastic strain.

The extended Drucker Prager [9] is a plasticity model able to provide a yielding surface and a flow potential apt to well simulate the bed compaction behaviour whereas as plastic strain it is intended the pebble bed compaction irreversible deformation under a loading cycle.

It is based on the assumption that the elastic domain is delimited in the deviatoric and pressure stress plane by a pressure depending curve composed off a linear part called Drucker Prager shear failure surface and a Cap elliptic curve. The first curve delimits yielding by shear stress while the second delimits yielding by hydrostatic pressure.

These two models have been successfully used to numerically reproduce the experimental results of the oedometric tests performed in FZK laboratories [6,10] both on Beryllium and Lythium OrthoSilicate as it is shown in fig. 3 [11].

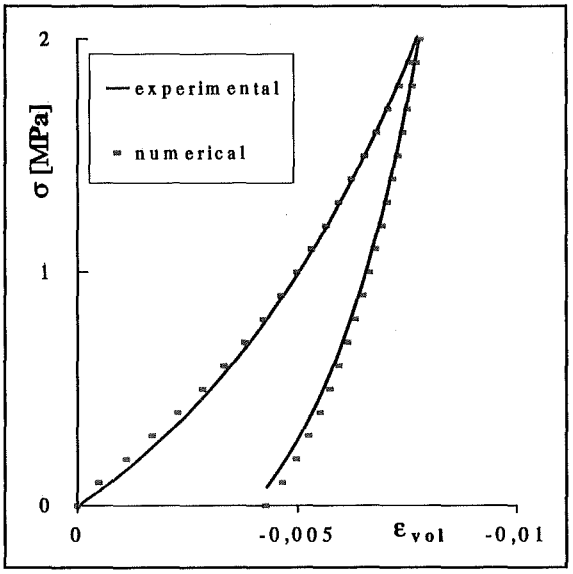

Figure 3. Comparison between experimental and numerical results of the Li_4SiO_4 oedometric test.

The requested parameters for the use of these two models, adopted in these preliminary analyses, have been subsequently used in the HEXCALIBER thermo-mechanical studies.

The analyses have been performed using the ABAQUS finite element code [12] that contains the above mentioned constitutive models.

5. RESULTS AND DISCUSSION

There have been performed steady state analyses to investigate the mock-up behaviour and transient analyses to evaluate also the mock-up thermal time constants during the start-up and the LOFA transients.

5.1. The steady state analysis

Concerning the thermal results of the steady state analysis, the obtained thermal field (fig. 4) matches very well the prefixed goals. In fact it presents in every pebble bed the expected trapezoidal poloidal profile with the flat portion located in the pebble bed layer between the HPs. At the same time it shows in every pebble bed a decreasing radial profile from the center to the extremity of the bed.

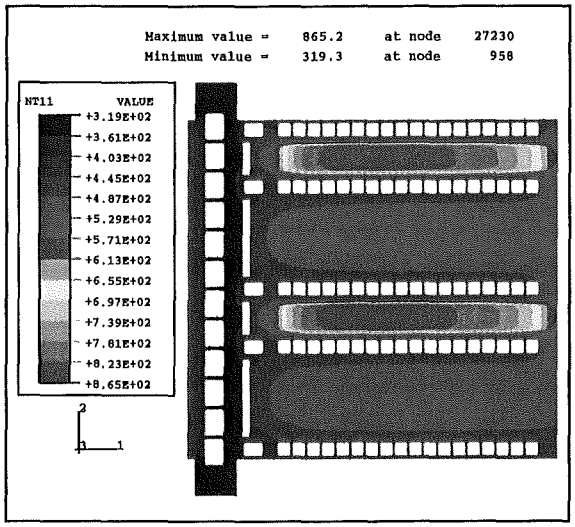

Figure 4. The mock-up thermal field [°C].

It shows, moreover, the required maximum temperatures of 865 and 550 °C in, respectively, Lythium OrthoSilicate and Beryllium pebble beds, together with the desired flat CPs thermal radial profile.

It is also possible to observe that the rear part of the mock-up has an average temperature of about 520 °C probably due to the low convective heat transfer with the purge gas.

Moreover it is to remark that the steel box has wide regions, as the HPs support area, where a 500 °C exceeding temperature is reached and where it may occur the drop of the yield strength and a subsequent plastic strain.

The heat flux field matches too the fixed goals, showing an average FW value of 0.24 MW/m^2.

With regard to the mechanical results of the steady state analysis, the attention is to be focused on to the box equivalent Von Mises (VM) stress field, on to the pebble beds equivalent plastic strain and on to the deformed shape of the model.

The obtained equivalent Von Mises stress field (fig.5) in the box shows that the most critical areas are the HPs supports where both for the high temperature reached and for the form discontinuity yield occurs. Except for these very small regions the equivalent Von Mises stress seems to satisfy the ASME $3S_m$ criterion [13] allowing the mechanical feasibility of the mock-up.

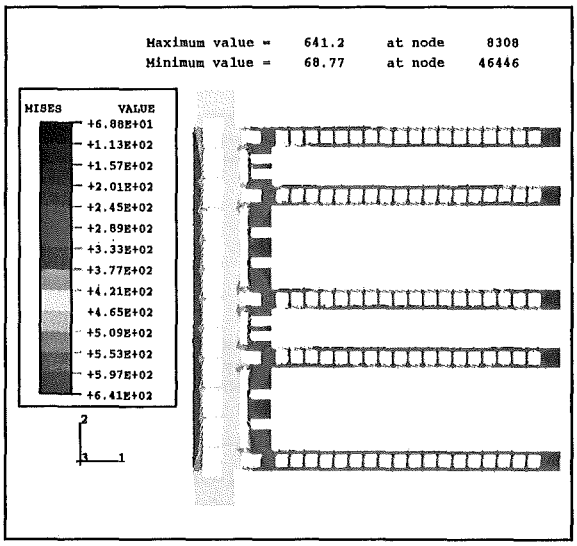

Figure 5. The mock-up box VM stress field [MPa].

The obtained equivalent plastic strain field in the bulk of the pebble beds (fig.6,7), that has to be intended as a measure of their compaction deformation, highlights that the most critical areas of both the pebble beds are the interface regions between the same beds and both the CPs or the HPs, especially the ones near to the HPs supports, where are reached equivalent plastic strain of 2.98 % and 16.71 %, respectively for Beryllium and Lythium OrthoSilicate.

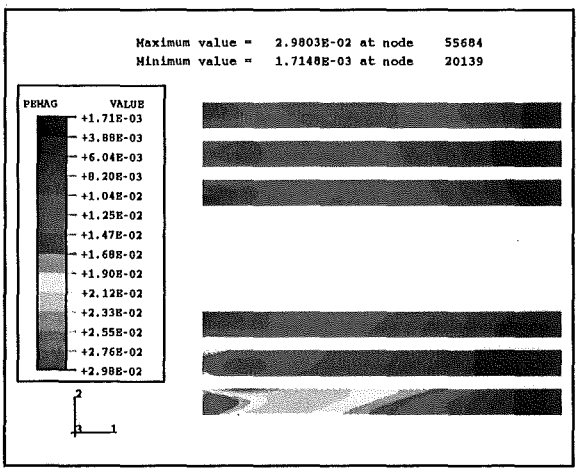

Figure 6. The mock-up Beryllium bulk pebble beds equivalent plastic strain field.

Very high compaction deformation of about 58.8% and 110%, respectively for the Beryllium and Lythium OrthoSilicate pebble beds are reached in the box interface regions, probably due both to the

lack of a contact model for the simulation of these regions behaviour and to the high local heat flux.

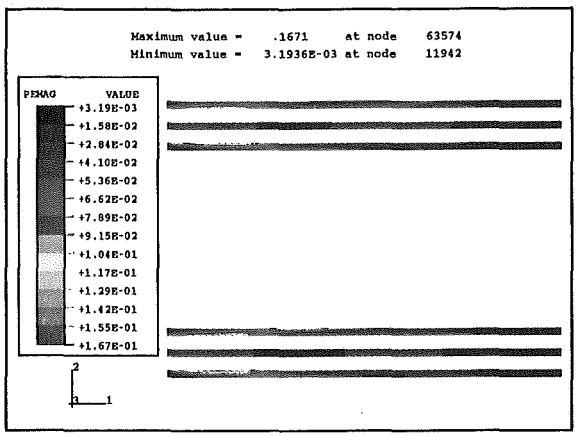

Figure 7. The mock-up Lythium OrthoSilicate bulk pebble beds equivalent plastic strain field.

The deformed shape (fig.8) shows a reasonably field of mock-up displacements.

The obtained maximum poloidal displacements of the external CPs, that will be directly monitored during the testing activities, are 1.4E-3 and –6.5E-4 m, respectively for the upper and lower CPs.

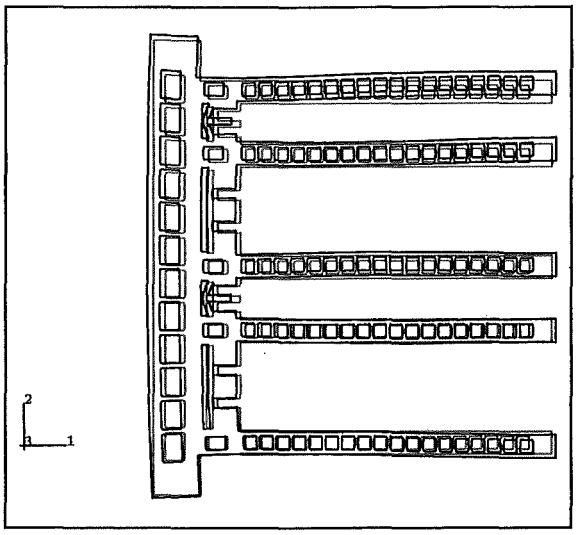

Figure 8. The mock-up box deformed shape (magnification factor = 4).

5.2. The start-up transient analysis

In order to simulate the start-up transient, it has been assumed that during this phase the mock-up is firstly warmed by the circulation of the Helium coolant and of the Helium purge gas and then it is loaded by supplying electric power to the HPs. It has been, then, assumed as thermal initial condition, the thermal field that arises in the mock-up due to the circulation of both cooling and purge Helium and as thermal load the HP power density.

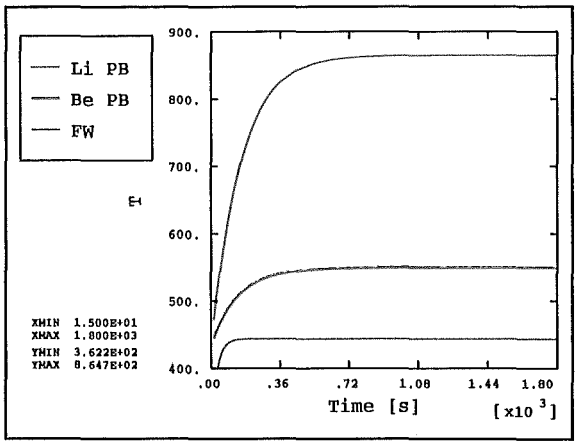

Figure 9. The mock-up main components start-up thermal time evolution.

The obtained results relevant to the time evolution of the mock-up thermal field showed in fig.9 for the three most critical nodes of, respectively, FW and Beryllium and Lythium OrthoSilicate pebble beds, seem to indicate that the thermal time constants τ of these components are the ones showed in Table 1.

Table 1
Mock-up start-up time constants τ [s]

Component	τ
FW	75
Beryllium pebble bed	115
Lythium OrthoSilicate pebble bed	145

The obtained mechanical results show that the mock-up does not encounter during this transient a stress field more severe than the steady state one.

5.3. The LOFA transient analysis

In the LOFA analysis a particular attention has been paid to the determination of the minimum time within whom it is necessary to stop electric power supply to prevent the mock-up failure. It has been assumed, in a conservative way, that, at the beginning of the LOFA transient, the heat transfer coefficient relevant to the cooling channels and to the purge gas hollows falls to zero, giving rise to the mock-up overheating.

From the thermal point of view the obtained results relevant to the mock-up LOFA transient for the three most critical nodes of, respectively, FW and Beryllium and Lythium OrthoSilicate pebble

beds, showed in Table 2, seem to indicate that the maximum intervention time to prevent mock-up failure is about 120 s, when the pebble beds and the FW reach critical temperatures.

Table 2
Mock-up LOFA temperature time evolution [°C]

Component	60 s	120 s
FW	723	936
Beryllium pebble bed	794	958
Lythium OrthoSilicate pebble bed	945	1070

The obtained mechanical results show, obviously, the necessity to further reduce the intervention time to a value of about 20 s because of the box mechanical crisis due to the wide plastic deformation produced by the decreasing of the yield stress with the increasing of temperature.

This intervention time seems to be still reasonably for the automatic control system to operate stopping electric power supply and to start the emergency mock-up cooling.

6. CONCLUSIONS

The HEXCALIBER medium-scale HCPB-TBM mock-up thermo-mechanical study in both steady state and operational (start-up) and accidental (LOFA) transient conditions has been presented in this work.

A detailed 3D finite element model of the mock-up has been developed, with a particular reference to the Beryllium and Lythium OrthoSilicate pebble beds mechanical constitutive.

The obtained results seem to show that the mock-up, in its actual lay out, is able to withstand the thermal and mechanical loads it undergoes during its regime condition, even if the HPs supports could yield in some restricted areas. Moreover, the results show that the mock-up has an overall start-up thermal time constant of about 150 s and it is able to withstand to the thermal loads it undergoes during a LOFA transient for a time of about 20 s which is still reasonably for the intervention of the emergency safety system.

The knowledge of the pebble beds thermo-mechanical properties is still incomplete, therefore several aspects have to be addressed with precaution. This concerns, in particular, the thermo-mechanical behaviour of the contact regions between pebble beds and structural materials. A further improvement should be obtained with the set up of specific contact models able to well reproduce the behaviour of these regions.

REFERENCES

1. Design Description Document, European Helium Cooled Pebble Bed (HCPB) Test Blanket. Status: 5.12.97.
2. G. Dell'Orco, G. Bertacci, F. Cecchini, S. Cevolani, F. Franchini, S. Goordeev, S.Malang, P. Neri, L. Sansone, K. Schleisiek, M. Serra, M. Simoncini, B. Spadoni, Design of the HCPB Test Blanket Module mock-ups for the HE-fus3 Facility. Fusion Technology, 20th SOFT (7-11 September 1998), volume 2, 1305-1308.
3. G. Dell'Orco, Personal communications. 1999.
4. H. Lehning, P. Norajitra, G. Reimann, R. Ruprecht, Design of high-power heating plates with simulation of the ITER medium-scale test mockup in HE-FUS3. Institut fur Materialforschung III-Forschungszentrum Karlsruhe. June 1998.
5. SDRC,1996-I-DEAS Master Series™ 4.0.
6. J. Reimann and S. Muller, First Experiments on Thermomechanical Behaviuor of Li_4SiO_4 Pebble Beds. Fusion Technology, 20th SOFT (7-11 September 1998), volume 2, 1337-1340.
7. Buhler, Personal communication. 1998.
8. ABAQUS version 5.8, Theory Manual, Porous Elasticity,. 4.4.1-1, 4.4.1-2.
9. D. C. Drucker and W. Prager, Soil Mechanics and Plastic Analysis or Limit Design. Quarterly of Applied Mathematics, vol.10, pp.157-165, 1952.
10. F. Scaffidi Argentina, Personal communications. 1998.
11. G. Mercadante and D. Zito, Verifica di fattibilità dei modelli sperimentali dei mantelli triziogeni a letti di sfere previsti nei progetti dei reattori nucleari a fusione ITER e DEMO refrigerato ad Elio. Tesi di laurea, Facoltà di Ingegneria, A.A. 1998/1999.
12. Hibbit, Karlsson & Sorensen INC., ABAQUS version 5.8. 1998.
13. ASME III, Rules for Construction of Nuclear Power Plant Components, Division 1, Subsection NB, Class 1 Components. ASME. 1992 edn.

Status of Blanket Design for RTO/RC ITER

M. Yamada, K. Ioki, A. Cardella, F. Elio and N. Miki

ITER Garching JCT, Boltzmannstraße 2, 85748 Garching, Germany

Abstract

Design has progressed on the FW/blanket for the RTO/RC (Reduced Technical Objective/ Reduced Cost) ITER. The basic functions and structures are the same as for the 1998 ITER design. However, design and fabrication methods of the FW/blanket have been improved to achieve ~ 50 % reduction of the construction cost compared to that for the 1998 ITER design. Detailed blanket module designs with flat separable FW panels have been developed to reduce the fabrication cost and the future radioactive waste. Most of the R&D performed so far during the EDA (Engineering Design Activity) is still applicable. Further cost reduction methods are also being investigated and additional R&D is being performed.

Introduction

The performance specifications for RTO/RC ITER [1] are as follows,
(i) to achieve energy multiplication Q>~10, not precluding ignition, with an inductive burn duration between 300s and 500s, (ii) to aim at demonstrating steady state operation using non-inductive current drive with Q>~5, (iii) to use as far as possible technical solutions and concepts developed and qualified earlier during the EDA, (iv) to reach a target of about 50% of the direct capital cost of the 1998 ITER design.
To carry out nuclear and high heat flux component testing relevant to a future fusion reactor, the engineering requirements are (i) average neutron flux ≥0.5 MW/m^2, and (ii) average fluence ≥0.3 MWa/m^2.
It is assumed that there will be an adequate supply of tritium fuel from external sources throughout the operational life.
However, the option for later installation of a tritium-breeding blanket on the outboard of the device is not precluded.
The device includes test tritium breeding modules that would lead in a future reactor to tritium self-sufficiency, the extraction of high-grade heat, and electricity generation.
Two distinct example layouts and specific sets of parameters have been prepared for preliminary study:

- IAM: With an aspect ratio of ~3.3, single null divertor, asymmetric magnetic configuration.
- LAM: With an aspect ratio of ~2.8, with a symmetric configuration and able to support (if proven useful) a double null divertor.

The main parameters of these machines are shown in Table 1. These examples of RTO/RC ITER are used in the following sections to evaluate blanket performance, to analyse specific engineering solutions and to quantity costs.

Table 1
Main Parameters of RTO/RC-ITER

	IAM	LAM		IAM	LAM
R[m]	6.20	6.45	Aspect Ratio	3.26	2.77
a[m]	1.90	2.33	Peak TF[T]	12.4	10
Ip [MA]	13.3	17	Elongation k @95	1.68	1.74
Bo [T]	5.51	4.23	Number of coils	18	20

2. Blanket System [1], [2], [3]

The basic concept of the blanket system has also stayed the same as that for 1998 ITER design maintaining a modular configuration with a mechanical attachment system. The blanket system (**Fig. 1**) is composed of blanket modules with a FW (First Wall) and a shield, and blanket attachments including electrical and hydraulic connectors and module supports. The most important changes proposed to occur to the blanket result from efforts to reach a 50% cost reduction target. A summary of the proposed changes is as follows:

(i) The inlet temperature and pressure of the blanket cooling water would be reduced from 140 to 100 °C and from 3.8 to 1.8 MPa, respectively.

(ii) The blanket shielding modules could contain a separable first wall. They could have a straight poloidal profile which eliminates the double curvature of the first wall, apart from in the case of the baffle. These features reduce the fabrication cost and the future volume of radioactive waste.

(iii) The back plate could be eliminated completely and its previous functions could transferred to the vacuum vessel. The blanket module thickness would be increased from 400 mm to 450 mm in this case. The thicker module is required to accommodate the thermal stress limits of the VV inner shell and to provide adequate neutron shielding for the VV.

Table 2
RTO/RC ITER Shield Blanket Parameter

		1998 ITER design	LAM	IAM
Fusion power (nominal+excursions) (1)	GW	1.5+0.3	0.525+0.21	0.5+0.20
Pulse duration	s	1000	650	410
Total blanket thermal power	GW	2.1	0.735	0.7
Heat flux on FW, average/max.	MW/m^2	0.25/0.5	0.15/0.5	0.2/0.5
Heat flux on limiter, average/max.	MW/m^2	~3/~8	~3/~8	~3/~8
Heat flux on baffle, average/max.	MW/m^2	~1.5/~3	~1.5/~3	~1.5/~3
Neutron wall loading, average/max.	MW/m^2	0.92/1.2	0.51/0.71	0.63/0.82
Number of modules		739	526	391
First wall surface area	m^2	~1200	753	626
Total weight of modules	t	2900	1780	1534
Max. weight of module	t/mod.	4.0	4.5	4.5
Typical blanket module dimension (Inboard midplane)	mm	1573x 1000x395	1065x 1266x450	1250x 1070x450
Coolant pressure during plasma op.	MPa	3.8	1.8	1.8
Coolant temperature, inlet/outlet	°C	140/190	100/150	100/150

Note (1): Values in this row include both nominal and excursions. All other values in this table are based on the nominal fusion power only.

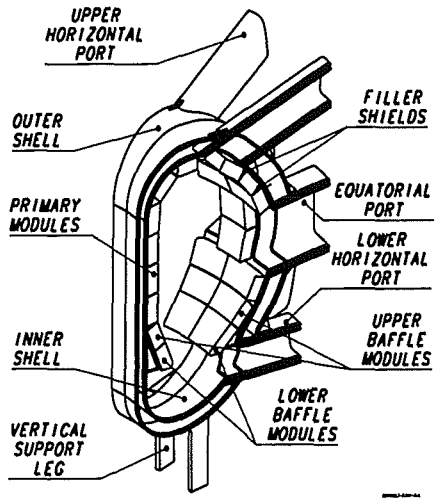

Fig. 1 Blanket and VV System

(1) First Wall [4]

The basic structure and materials of the plasma facing armour and the heat sink remain the same as in the 1998 ITER design. Beryllium (S65C) is used as the plasma facing armour material at the primary FW, the limiter, and in the upper regions of the baffle. It is expected to have lower retained tritium inventory when compared with CFC and also offers the prospect of repair by plasma spray. W is used in the lower baffle near the divertor, due to that higher heat loads there and also ensure tritium inventory.

The primary FW heat sink is made of an array of 10 mm diameter by 1 mm wall thick 316 L (N)-IG stainless steel tubes. The tubes are embedded in sections of a dispersion strengthened copper alloy Al25-IG or CuCrZr-IG. Due to the higher heat fluxes, the baffle FW uses copper alloy tubes instead of tubes of stainless steel. A stainless steel liner, ~0.2 mm thick, will be used inside the copper tube to avoid corrosion problems.

The decision to set a minimum operating temperature > ~ 150-180 °C for the Cu alloys was taken earlier in the EDA.

As a consequence of further R&D there is now additional data available on the material behaviour under irradiation that allow a reassessment of the effect of low temperature operation on Cu alloys. The effects on the material behaviour of decreasing the inlet water coolant temperature from 140 to 100 °C are as follows,

- The irradiation dose at which the reduction of Cu alloy ductility saturates will be reached in both cases, and elongation will be < 2% both at 100 °C and 140 °C.
- The fracture toughness and mechanical strength of Cu alloys are higher at lower temperatures.
- The probability of corrosion cracking and IASCC (irradiation-assisted stress corrosion cracking) of SS is lower in the temperature range 100-150 °C compared with 150-200 °C.
- For Be, the main concern is low temperature embrittlement. The level of embrittlement depends on the fluence. For S-65C VHP irradiated (up to 2-2.45 dpa) and tested at 185 °C, brittle fracture of Be has been observed [F.Moons,1995], while recently has been observed that for the same material irradiated at 110 – 275 °C up to 0.65 dpa [L. Snead,1998] the ductility of irradiated samples was still at a reasonable level of a few %. Change of irradiation temperature range 220 – 280 to 170 – 230 °C generally increases the level of embrittlement, but for the RTO/RC ITER fluence (~ 1 dpa) it seems that the total elongation could still be at the level ~ 1%.

(2) Blanket Segmentation

The segmentation of the shield modules is dictated by the weight limit of 4.5 t per module imposed by the performance of the remote maintenance equipment (see **Fig. 2**), and the desire to minimize the number of modules for cost reduction. The LAM could have a toroidal segmentation of 20 modules on the inboard and 40 modules on the outboard. The IAM, blanket modules have a toroidal segmentation of 18 modules on the inboard, 36 modules on the outboard and 27 modules on the top. The module toroidal length varies from 1.1 to 1.9 m relative to 0.8 to 1.3 m for the poloidal length. The total number of modules for IAM and LAM is 391 and 526 respectively,

instead of 739 for the 1998 ITER design.

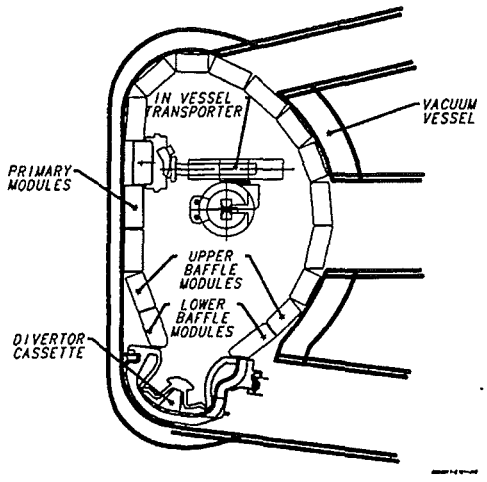

Fig.2 Blanket Segmentation and In-vessel Transporter

(3) Blanket Module Design

The RTO/RC ITER blanket module design has also been improved from the1998 ITER design, (1) to reduce the module unit cost for manufacturing, and (2) to reduce EM loads on blanket modules due to disruptions/VDEs.

The separable first wall has facet geometry consisting of multiple flat panels, where 3-D machining will be not required. The resulting configuration simplifies the design and manufacturing of the main components thus reducing the associated costs. The separation of the shield body allows the application of less expensive manufacturing processes reducing its cost, and solid HIP will be used only for the FW panel fabrication. The use of multiple panels also makes possible the replacement of individual damaged units reducing the replacement time and volume of nuclear waste, and simplifies the repair and replacement methods. A deeply slitted shield block configuration minimises the induced eddy currents and EM loads. This EM load reduction is required especially for the concept without the back plate and the direct application of the modules to the vessel.

Two options are under consideration for the new module design (**Fig. 3a and Fig. 3b**). In both options, the module design consists of one shield block and individual, ~100 mm thick, flat FW panels. As in the earlier design, the FW is a Cu-alloy heat sink panel cooled by internal circular SS tubes. The Cu-alloy panel is attached by HIP to a supporting SS plate. In Option B, the FW panel is slotted poloidally, forming a comb-type structure in order to reduce to a minimum the electromagnetic loads. The FW panel support structure consists of a central rectangular beam, which penetrates inside, and is bolted to the back of the shield block. In Option A, serpentine cooling pipes are used and the FW panel is bolted to the shield block by access from the plasma side. In Option B, the shield is formed from four forged blocks, which are welded together at the rear section. A 2 mm gap is left between the blocks in the front part and each block has two additional slots made by cutting, in order to reduce the electromagnetic loads. The shield is cooled inside by drilled poloidal cooling channels. On the top and bottom part of the blocks the main headers are made by machining, and closure plates are welded on afterwards. In Option A, two half blocks with radial cooling channels are stacked and welded around the perimeter. In both options the shield block is provided with front access penetrations for the mechanical, hydraulic and electrical connections of the module to its supporting structure.

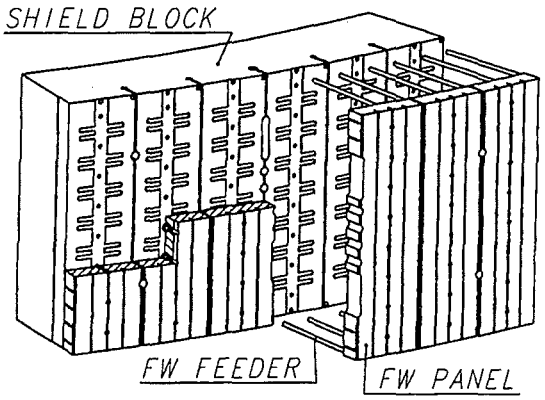

Fig. 3(a) Blanket Module Design (Option A)

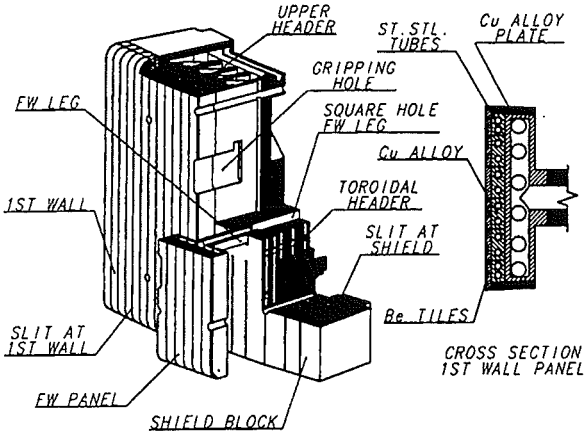

Fig. 3(b) Blanket Module Design (Option B)

(4) Module attachments

The module installation and replacement is performed from the plasma side. Each module has access holes of 30 mm diameter. Considering the reaction scheme of the radial torque and the toroidal and poloidal forces, two module attachment concepts are used.

- Type 1 used in the outboard region of the blanket, is the 1998 ITER design concept utilized in between the ports, but with the supports inverted and mounted on the VV instead of the module. A "stub key" with flat contact pads is integrated into the flexible support housing. The two hydraulic connections and electrical straps have been combined into a single unit with a co-axial interface, located in the center of the module.
- Type 2 used in the VV inboard region where the electromagnetic forces are large, is the basic 1998 ITER design scheme again with the flexible support inverted and mounted into the VV instead of the module. The attachment design still utilizes a center pin, two branch pipes, two electrical straps, and a key between the modules.

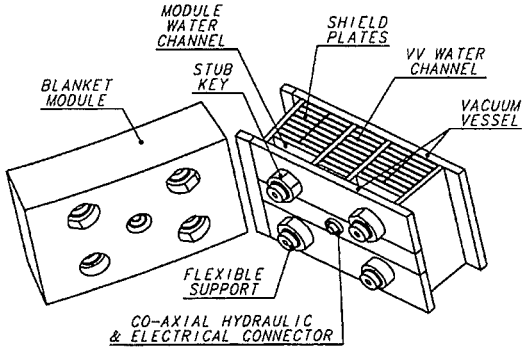

Fig. 4(a) Blanket module attachment (Type1)

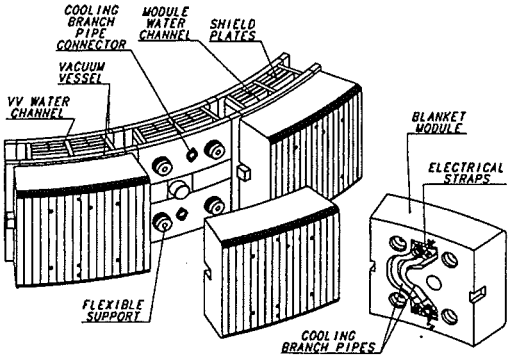

Fig. 4(b) Blanket module attachment (Type 2)

(5) Back Plate

Back plate elimination has been considered for the RTO/RC ITER concept for the following reasons;

(1) minimization of the total thickness of the VV and blanket, by eliminating a gap of ~70 mm between VV and back plate,
(2) elimination of the fabrication and assembly cost of the back plate and BP supports,
(3) reduction in the VV/ blanket assembly time and complexity,
(4) elimination of the complicated operations to be done remotely in case of removal of a segment of VV and TF coil.

For this concept the support housings for the modules are structurally integrated into the vacuum vessel. The blanket cooling channels are structurally part of the VV double wall structure.

Given that work on the 1998 ITER design with back plate and the work performed on the RTO/RC-ITER machine without a back plate, both options seem feasible.

(6) Stress Analysis and EM Loads

The major changes in the design loads on the modules of RTO/RC-ITER are due to:

- shorter current quench time, the plasma disruption data base, as used for 1998 ITER design indicates that the current quench for RTO/RC ITER will be faster due to higher plasma current densities (see **Table 3**);
- relatively smaller toroidal magnetic field on inboard modules;
- slitted configurations of the blanket module to reduce the eddy current;
- changes of module toroidal length related to the smaller machine size;

A representative 2-dimensional section of the typical inboard module has been modelled to investigate the temperature and stress distributions.

Stresses due to the normal operating loads are below the $3S_m$ limit in the FW panel and the shield block. Thermal deflection of the FW panel is 2.2 mm in the poloidal and 0.6mm in the toroidal direction and these are small enough from a gap control viewpoint.

Thermal deflection of the SS shield block is 1.2mm radial, 1.6mm toroidal and bowing of the SS block is approximately 0.5 mrad, which is accommodated by the flexible supports.

The shorter current quench time for RTO/RC ITER leads to higher EM loads. However, the slitted configuration is effective of reducing the EM loads. I_{halo}/I_{plasma} and the toroidal peaking factor (TPF) of halo current are assumed to be similar to that for the 1998 ITER design. The FW-normal halo current density is assumed to be 0.18 MA/m^2. The consequence is that there are small reductions in the loads due to relatively lower toroidal magnetic field and lower halo current per module.

The first wall panel is attached to the shield block by its leg. Structural analyses of the separable first wall panel under EM loads have been performed to assess the stresses in the panel and the leg. These stresses g are within allowables,

Table 3 Current quench time and magnetic field

		1998 ITER design	LAM	IAM
Current quench time during CD	ms	50.0	40.0	25.0
Equivalent quench time during VDE	ms	35.7	27.3	17.6
B_{pmax} in inboard module	T	-1.7	-1.7	-1.7
B_{rmax} in inboard module	T	-0.18	-0.22	-0.22
B_{tor} in inboard module	T	9.35	7.40	8.82

Note: "Equivalent quench time during fast VDE" is assumed, considering the additional magnetic field change due to plasma movement.

References

[1] K. Ioki et al., Journal of Nuclear Materials 258-263 (1998) 74-84

[2] K. Ioki et al., Fusion Engineering and Design 39-40 (1998) 585-591

[3] F. Elio et al., "Engineering Design of the ITER Blanket and Relevant R&D Results," 20th Symposium on Fusion Technology, Marseille (Sept. 1998).

[4] A. Cardella et al.," Application of beryllium as first wall armour for ITER primary Baffle and limiter modules" this workshop

Application of beryllium as first wall armour for ITER primary, baffle and limiter modules

A.Cardella[1], V. Barabash[1], K. Ioki[1], M. Yamada[1], T. Hatano[2], P. Lorenzetto[3], I. Mazul[4], M. Merola[3], Y. Ohara[2], Y. Strebkov[5]

[1]ITER Garching JWS, Boltzmannstr. 2, D-85748 Garching, Germany
[2]Japan Atomic Energy Research Institute, Naka-machi, Naka-gun, Ibaraki-ken, 311-01 Japan
[2]The EFDA Close Support Unit Garching, Boltzmannstr. 2, D-85748 Garching, Germany
[3]D.V.Efremov Institute of Electrophysical Apparatus, 189631 St.Petersburg, Russia
[5]ENTEK, R.D.I.P.E., P.O.B. 788, Moscow 101000, Russia

During the engineering design activities of the ITER project, beryllium has been selected as the armour material for the first wall of the primary, baffle and limiter blanket modules. These components have different requirements according to their function, so the armour design and its joining technology has been developed in order to withstand different operating and loading conditions. Extensive R&D has been performed to develop, select and characterise the beryllium material and the joining techniques. In parallel, beryllium plasma spray coating has been developed, mainly as a possible in situ repair method for locally damaged areas. For the reduced technical objectives / reduced cost (RTO/RC) ITER project, it is proposed to maintain Be as the reference armour material and to optimise the manufacturing technologies in order to minimise costs. The paper presents the rationale of the design choices for the application of beryllium to the blanket first wall and gives an overview of the R&D performed and the results achieved.

1. INTRODUCTION

During the engineering design activities of the ITER project (ITER EDA), beryllium has been selected as the armour material for the first wall (FW) of the primary, limiter and baffle blanket modules [1]. The main reasons of this choice are:

- low Z materials are advantageous for tokamaks which operate with high temperature, low to medium density plasmas in order to reduce the impurity content and avoid large plasma radiation losses;
- there is experimental evidence that plasma performances are best with a Be armoured FW.

The first reason restricts practically the choice to Be and C. Carbon in the form of carbon fibre composites has some attractive advantages such as its robustness, non-toxicity and the absence of melting. However Be has been preferred because of the better plasma performances. These are not only due to the lower Z_{eff} achievable with Be, but also because of the resulting low main plasma pollution, the absence of chemical sputtering, and its oxygen gettering capability.

Furthermore the use of a large C coverage of the FW has some important disadvantages:

1. C erosion, transport and redeposition on neighbouring surfaces of the first wall and divertor which may:
   - aggravate the tritium co-deposition problem in the divertor,
   - worsen plasma contamination, and
   - degrade performance by altering the gettering and wall recycling properties of a Be armoured FW;
2. the requirement of high-temperature baking and periodical wall conditioning for C and C-contaminated walls;
3. the experimental evidence that in JET high runaway electron (RE) loads have been experienced with C walls; these have not occurred with Be, but this advantage needs to be confirmed in ITER where the dominant RE mechanism may be an avalanche effect which is not important in present tokamaks.

In ITER, Be has therefore been applied to the FW design of all the components of the blanket system with the exception of the lower baffle where tungsten has been selected in order to withstand enhanced erosion caused by the high neutral particle density in this region. In parallel, extensive R&D has been launched to characterise Be properties in irradiated and unirradiated conditions and to develop suitable joining techniques to the copper alloy FW structures.

Table 1 are summarises the main design data for the blanket system.

The Be choice is kept presently for the RTO/RC ITER design and new R&D is planned to improve and possibly reduce the costs of the manufacturing technologies. For the RTO/RC ITER, the main requirements are expected to be less stringent than those of the 1998 ITER design, see Table 2.

Carbon, operating at high temperature, has been alternatively proposed for limited surfaces (e.g. for guard limiters). A recent assessment indicates that, if C is kept in hot conditions (>1000 C), the C-erosion and the T-retention are increased ~1% with respect to those caused by CFC on the divertor [3]. On the other hand there are concerns that, due to a low sticking probability, particles may travel long distances and be deposited in large areas where cleaning is extremely difficult. For this reason a proposed solution is to eliminate carbon from the reactor.

The plasma facing surfaces of the FW are subjected to different conditions according to their position along the last closed magnetic surface and the system to which they belong. This has resulted in different armour designs and technological solutions.

2. BE APPLICATION TO FW COMPONENTS

The structure surrounding the plasma, identified as FW, can be subdivided into:

I. a primary FW, covering most of the plasma chamber surface and providing a generic protection to the structures located behind it,
II. a limiter FW located in selected equatorial ports (two in the 1998 ITER design) which limits the plasma during the start-up and shut-down plasma phases and,
III. a baffle FW located in the lower region near the divertor system, which maintains a higher neutral particle pressure in the divertor region than in the main plasma chamber.

2.1 Primary First Wall

The primary FW will be subjected to a relatively low heat flux (maximum 0.5 MW/m^2) but has to withstand the highest neutron load. during normal operation and an intense heat shock during plasma off-normal conditions such as a plasma vertical displacement event or runaway electron impact (30 – 60 MJ/m^2 for 0.3 – 1 sec).

These heat loads allow the use of Be in the form of large tiles (typically 50x100 mm). In order to give enough protection against off-normal events, while still limiting the material and manufacturing costs, the tile thickness has been specified at 10mm. This thickness should give an adequate armour lifetime and protect underlying materials and coolant channels from serious damage following hard disruption events [3, 4].

Table 1 - ITER 1998 Design - Main Data for the Shielding Blanket Components

Specifications	Units	Primary Wall	Limiter	Baffle	
		Max.	Port	Lower	Upper
Peak heat flux	MW/m^2	0.5	~8	3	1
Average heat flux	MW/m^2	0.2	2.6	1.8	0.5
Neutron wall load	MW/m^2	1.19	1.17	0.77	0.90
BPP radiation damage*)	dpa	~1	~1	~0.4	~0.5
BPP He production	appm	~1000	~1000	~400	~500
Irradiation temperature	°C	230-280	230-280	200-500	200-500
Number of cycles	--	13000	26000	13000	13000
Water temp. inlet	°C	140			
Water press. Inlet	MPa	4			
Central disruption energy	MJ/m^2	1			
No. of central disruption	--	500			
VDE peak H.Load \ dur.	MJ/m^2-s	60 \ 0.3	--	60 \ 0.3	60 \ 0.3
No. of VDE's	--	10	--	10	10
Runaway electrons \ dur.	MJ/m^2	50 \ 0.3	--	50 \ 0.3	50 \ 0.3
Bakimg	°C	240			

[D]Large Vertical Displacement Events are assumed not to strike the limiter. The thermal quench load for limiters in the limiter regime has not been determined yet but is expected to be low because plasma energy is low.
*) BPP = Basic Performance phase

2.2 Limiter First Wall

The FW of the limiter is instead subjected to high heat fluxes (up to ~8 MW/m^2 in the 1998 ITER design) during the start-up and shut-down phases of each reactor pulse. In this case small (typically 6x6 mm) and relatively thin (4-5 mm) tiles or similarly a frequent castellation are used to assure high thermal-mechanical performace and to limit the maximum tile operating temperature.

Table 2 Expected main data for RTO/RC ITER	
Max. Heat Flux P.FW [MW/m^2]	0.5
Peak Heat Flux Limiter [MW/m^2]	5 or 6 [1])
Max. Heat Flux Baffle [MW/m^2]	2 - 3
Max. Fluence [MWy/m^2]	~0.5
Max. Wall Loading [MW/m^2]	~0.8
Average Wall Loading [MW/m^2]	~0.6
Inlet Water Temperature [°C]	100
Nominal Operating Pressure [Mpa]	1.8
Baking Temperature [°C]	240

[1]) for 2 or 3 limiter modules respectively.

2.3 Baffle First Wall

In the 1998 ITER design the baffle was subdivided into a lower and an upper baffle module. The FW of the lower baffle was armoured with tungsten in order to be able to withstand the high erosion due to impinging high energetic neutrals. The FW of the upper baffle was instead amoured with Be. and has somewhat intermediate requirements between the limiter and the primary FW (up to 1 MW/m^2) and armour dimensions closer to those of the primary FW.

3. R&D ON BERYLLIUM

Extensive R&D has been performed to develop, select and characterise the beryllium material and the joining techniques. In parallel, beryllium plasma spray coating has been developed, mainly as a possible repair method for locally damaged areas.

3.1 Beryllium Grades

Be S-65C has been selected as reference armour material for all the components because of its better thermal fatigue and thermal shock resistance (also in irradiated conditions) than other grades, its availability, and the previous experience in JET. S-65C is produced by vacuum hot pressing (VHP) from impact ground beryllium powder. This is usually made by chipping vacuum-cast ingots, followed by milling or grinding. During these processes, a thin oxide layer forms around the particles resulting in a high oxide content, typically greater than 0.5 wt % BeO. Ingot grade beryllium (that is made by induction melting scrap or pebble, casting, and then directionally solidifying) contains about 0.05 wt % oxide. The amount of other impurities can vary depending on their content in the feed stock. The impact ground powder is vacuum hot pressed at 1050-1150°C. The use of the impact ground powder gives good mechanical properties and reduces anisotropy. A final treatment at 870°C forces aluminium impurities to form $AlFeBe_4$ intermetallic compounds.

The grade DShG-200 is considered as a second option. It is produced from distilled ~200 µm Be Powder, hot pressed to partial density and then punched to full density.

S-65C and DShG-200 Be are produced typically in the form of blocks with a wide range of thickness and diameter.

Be plasma spray coating is considered mainly as a possible repair method of low heat flux, locally damaged FW areas and alternatively as bulk protection material. Low Pressure Plasma Spray (LPPS) is the reference technique. It results in high density coatings, approaching the theoretical density of beryllium and the thermal conductivity of bulk beryllium in the temperature range room temperature to 600°C. Coating thickness of the order of 10 mm can be obtained.

More detailed data on these materials together with the main results of the R&D are reported in [4].

Table 3 reports the main chemical composition of these grades.

Table 3 S-65C - DShG-200 chemical composition		
Element, wt.%	S-65C	DShG-200
Be (min)	99	99.34
BeO (max)	1.0	0.79
Al (max)	0.06	0.0045
C (max)	0.1	0.077
Fe (max)	0.08	0.024
Mg (max)	0.06	-
Si (max)	0.06	0.013
Others , (max)	0.04	0.04
Average grain size µm	8-10	33-37

The superior thermal fatigue resistance of the selected materials can be seen in Fig. 1, produced by SANDIA N.L. in USA [3].

The selected grades have good mechanical properties. As an example Fig. 2 and 3 show the ultimate tensile and the yield strength of S-65C VHP as a function of temperature.

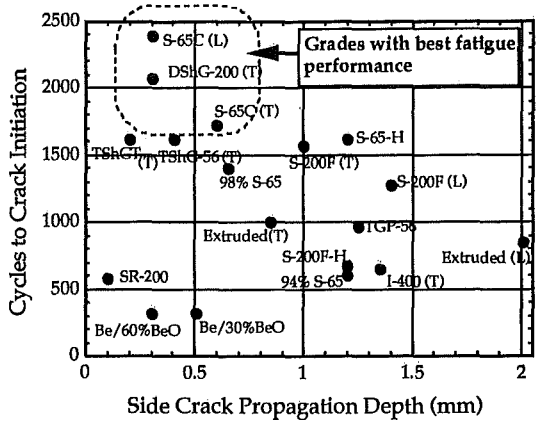

Fig.1 No. of cycles to crack initiation vs. crack propagation depth

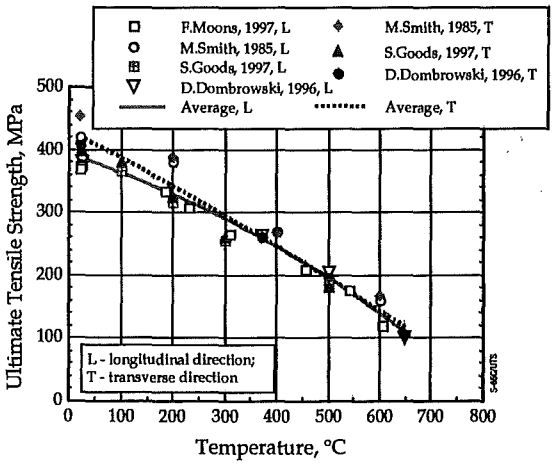

Fig. 2 Ultimate tensile strength of S-65C VHP vs. temperature [4]

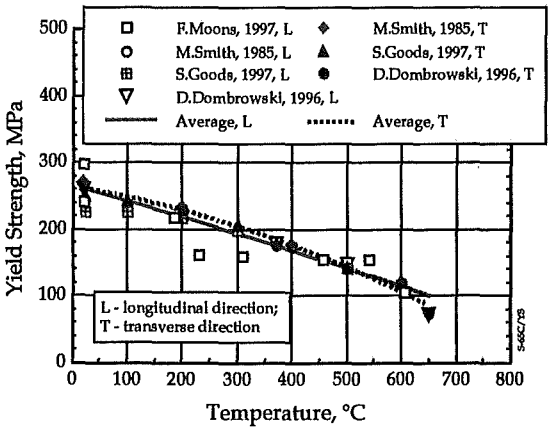

Fig. 3 Yield strength of S-65C VHP vs. temperature, [4]

Beryllium maintains acceptable tensile and yield strength properties under irradiation in the range of the relevant fluences, but the total elongation drops to low values already at less than 1 dpa. A decrease in the irradiation temperature range 220-280 to 170 - 230°C increases the level of embrittlement. However, for the RTO/RC ITER fluence (~ < 1 dpa) it seems that the total elongation could be still at the level ~ 1%. However, the embrittlement of Be at low temperature could lead to brittle destruction of the tiles and enhanced erosion. It is recommended to avoid any stress concentrating design feature (e.g. partial castellations etc.) in Be tiles in cold areas.

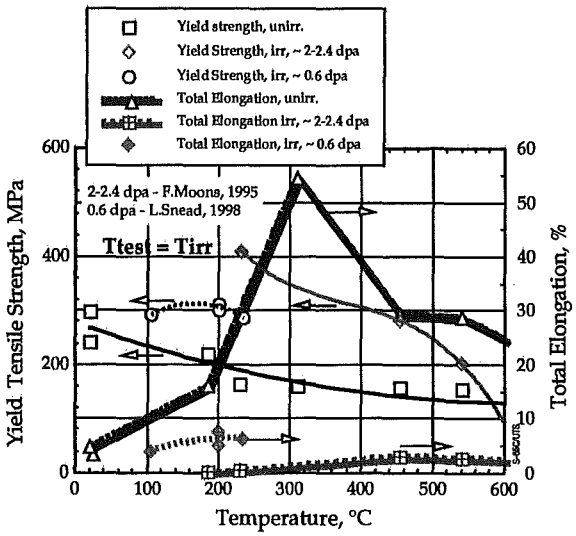

Fig. 4 Influence of irradiation T on Be yield strength and total elongation, [5,6].

3.2 Be/Cu alloys joining technologies and results of HHF testing

R&D on the technology of Be/Cu-alloys joints for application in ITER PFCs has been carried out in the ITER Home Teams. Different technologies have been proposed and studied:

- low and high temperature HIP with or without interlayers,
- brazing (CuMnSnCe, Cu-Mn, CuInSnNi, Ti-Zr),
- low and high temperature diffusion bonding,
- plasma spray,
- explosion bonding,
- joint rolling etc.

Braze materials containing silver e.g TiCuSil braze are not permitted due to nuclear transmutation of silver to cadmium, which is not compatible with the high vacuum requirements and cause high activation.

More than 40 mock-ups have been fabricated and have already been tested. The detailed results are included in [4]. As a result of this R&D the technologies which have given the best results in terms of reliability and performance have been

selected and are now considered as reference for the components.

Low and medium heat flux and large surfaces: such as the Be Primary First Wall:

- High temperature HIPing, Hot Isostatic Pressing, (800-850°C, 2h, 120 MPa, Ti interlayer) was identified as the most promising method [7]. A Be/DS-copper/SS mock-up was manufactured with this technology by CEA Grenoble (F). Overall dimensions are 96x86x59.4 mm, with a tile thickness of 9.4 mm, see Fig. 5. This has survived 1000 cycles at 2.5 MW/m^2. Test data: 11s on / 11s off for 100 cycles and then 31s on / 31 s off for up to 1000 cycle with an inlet water temperature of 25 °C and a pressure of 3.5 Mpa. Destructive examination indicated small cracks at the edge of the mock up in the Be/Cu joint. This could suggest that the dimensions of this single Be tile are close to the limit acceptable for such an incident heat flux. Based on other preliminary tests, the failure limit for this technology seems to be ~5 MW/m^2.
- A HIP technology with different bonding materials and interlayers is also being developed by JAERI (JA), using Glidcop AL-25 ITER grade as basic DS Cu alloy. Strong bonding have been obtained (e.g up to ~260 Mpa in 4 point bending tests [8]) so far using two methods:
  1. Coating the DS Cu base material with Cu (PVD, 10μm) and then HIP Be tiles at 620 °C, 140 Mpa for 2 h;
  2. Vacuum plasma spray Aluminum (0.7 mm) on Be, plus coating layers of Al+Ti+Cu on the DS Cu base material (PVD, 10μm), and finally HIP using an additional intermediate Al layer (0.1 mm thick at 555 °C 140 Mpa for 2 h).
- As alternative method Be plasma spray is considered (both for bulk material and joint), [9]. Mock-ups with and without special preparation of the Cu alloy substrate have been manufactured by SANDIA/Los Alamos (US) (Fig. 6) and tested. They survived 3000 cycles at 1 MW/m^2, with failure limit ~ 2.5 MW/m^2, [10].

For higher heat flux components:

- the joining methods with best results were obtained by the Efremov Institute (RF), [11, 12]. They have developed a CuInSnNi fast brazing technique (~ 800°C, for a few minutes), which results in a reliable and robust joint. Several mock-ups have been tested. A mock-up with tiles 5x5x5 mm did not fail after 4500 cycles at 12 MW/m^2, see Fig. 7. For this technology the effect of the tile size on the durability of the joint has also been determined (see Fig. 8). Tiles with size 20x20x5 mm detached at 12 MW/m^2, while tiles with size 5x5x5, 7x7x5 and 10x10x5 mm did not detach in this condition. Curved mock-ups also have been tested (fig. 9): no damage has been observed after 1000 cycles at 11 MW/m^2, [13]. This technology seems the best developed up to now. It is the reference for the manufacturing of the port limiter, and its the application could be extended to the primary FW in the future.
- Alternatively HIP at 625°C with AlBeMet™ or with Al interlayers and different diffusion barriers onto Be and Cu alloy have been developed by SANDIA (USA) [14]. A mock-up (Fig. 10) withstood 1000 cycles at 5 and 10 MW/m^2 without any damage to joints. Mock-ups have also been tested simulating plasma disruption events (VDE): although the Be tiles were severely melted, the joints did not fail.
- The EU HT is also developing brazing with CuMnSnCe alloy (~720°C, few min). No damage has been observed after testing a sample at 5.4 MW/m^2, 1000 cycles, [15]

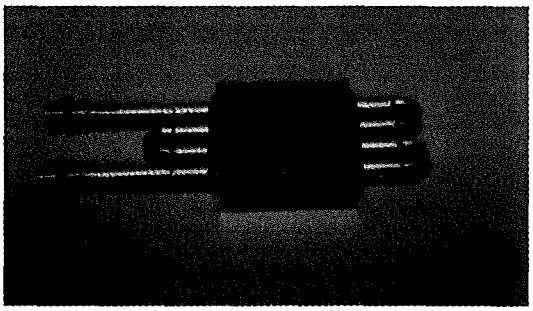

Fig. 5 FW Mock-up with Large Be Tile (EUHT), [7].

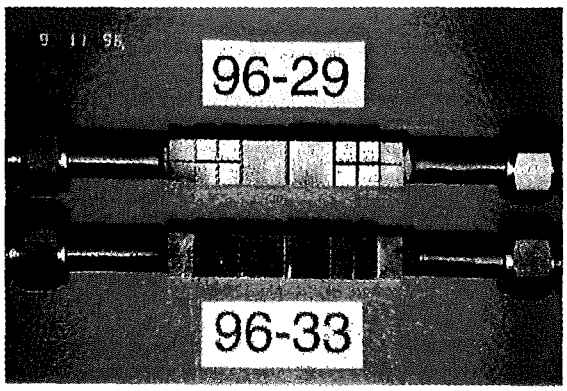

Fig. 6 Plasma sprayed Be/Cu First Wall mock-ups (US HT), [10].

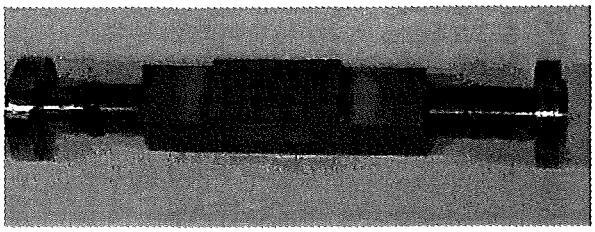

Fig. 7 Mock-up with 5x5x5 mm Be tiles brazed with fast amorphous brazing (RFHT), [11].

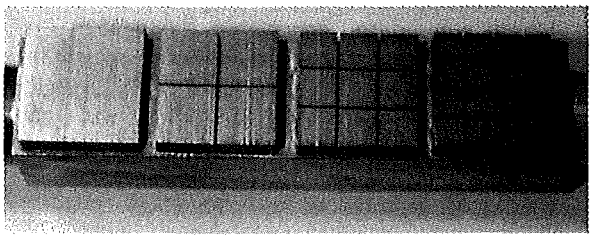

Fig. 8 Mock-up with 5x5x5, 7x7x5, 10x10x5, 20x20x5 mm Be tiles brazed with fast amorphous brazing (RFHT), [13].

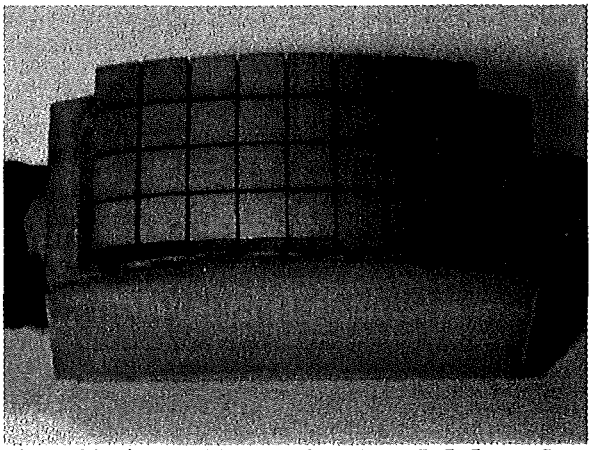

Fig. 9 Mock-up with curved surface, 5x5x5 mm Be tiles brazed with fast amorphous brazing (RFHT), [13].

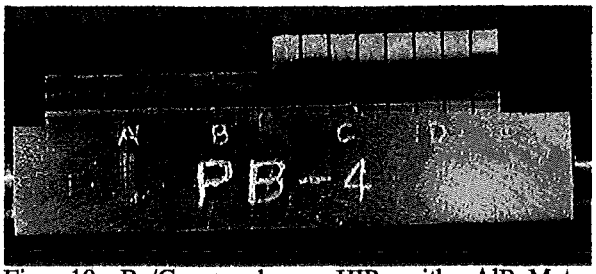

Fig. 10 Be/Cu mock-up, HIP with AlBeMet interlayer (US HT), [B14].

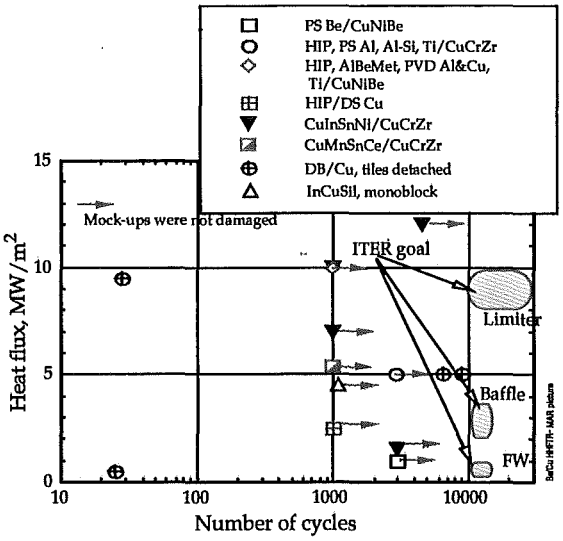

Fig. 11 Summary of HHF testing results of the actively cooled Be-Cu mock-ups in comparison with ITER requirements, [4].

- Other innovative techiques (macrobrush, monoblock, etc.) may also be considered in a new R&D plan to enhance the performance

Experiments have also been performed to investigate the effect of neutron irradiation on Be and on the durability of the Be/Cu alloy joints [16]. The FZ Juelich research centre has tested Be samples and Be/Cu actively cooled mock-ups of different geometries and joining techniques, irradiated at 350°C up to a dose of 0.3 dpa. The mock-ups have been high heat flux tested and all the mock-ups survived 1000 cycles at 5-7 MW/m^2 without any degradation of joints. This experiment indicates that neutron irradiation should not be critical for the performance of joints (at least for the assumed conditions).

A in-pile high heat flux testing was also carried out with Be/Cu mock-ups by the Efremov institute (joining technology - Ag braze), [17]. The experiment was performed with a heat flux of ~ 3 MW/m^2 and a neutron fluence up to ~0.25 x $1021n/m^2$ (~0.2 dpa), and ~100 cycles. No visible damage was observed in the Be and Be/Cu joints.

4. CONCLUSIONS

- Beryllium has been selected as the FW armour for the primary wall, limiter and baffle blanket modules because this choice results in the best plasma performance.

- This choice is confirmed for the RTO/RC ITER design.
- Extensive R&D has been performed to characterise the material in un-irradiated and irradiated conditions and to develop suitable joining technologies. The main results are:
  - Be S-65C and DShG-200 have been chosen as the best grades;
  - solid HIP of relatively large tiles (typ. 50x100x10) with Ti interlayer is presently the preferred manufacturing solution for the low to medium heat flux components (primary FW and Baffle);
  - fast amorphous brazing of small tiles (typ. 5x5x5) is the preferred solution for high heat flux components (limiter);
  - plasma spray coating has been developed as a repair method for locally damaged surfaces, and it is being considered for further development.

References

1. ITER Technical Basis for the ITER Final Design Report, Cost Review and Safety Analysis, Iter EDA Documentation Series No. 16, IAEA, Vienna, 1998.
2. C.H Wu: "Erosion and T-retention in EU-I", June 99, private communication.
3. R. Watson, D.L. Youchison, D.E. Dombrowski et al., "Low Cyclic fatigue of Beryllium", Proc. 2nd IEA International Workshop on Beryllium Technology for Fusion, Wyoming, Sep.6-8, 1995. p. 7-38
4. V.Barabash, S.Tanaka, R.Matera, "Beryllium Assessment and Recommendation for Application in ITER Plasma facing Components", Proc. of the 3d IEA International Workshop on Beryllium Technology for Fusion, Oct. 22-24, 1997, Mito City, Japan, JAERI-Conf 98-001, p.1-13, and references therein.
5. Chaouadi, R., Moons, F. and Puzzolante, J.L., "Tensile and Fracture Toughness Test Results of Neutron Irradiated Bryllium", Proc. 3d IEA Int. Workshop on Berylium Technology for Fusion, Mito, Japan, Oct. 22-24, 1997, p.241.
6. Snead, L., "Low-temperature low-dose neutron irradiation effects on Brush Wellman S65-C and Kawecki Berylco P0 beryllium", to be publ. in J.Nucl. Mater.
7. F. Saint Antonin, G. Bangeois, G. Le Marouis et al., "Small scale testing of FW/BS modules", Note Technique D.E.M/S.G.M N 64/96, CEA, CEREM, Dec 1996.
8. T.Hatano, JAERI, private communication, Sept. 1999.
9. R.G. Castro, A. H. Bartlett, K.E. Elliott and K.J. Hollis, "The structure and thermal properties of plasma-sprayed beryllium for ITER", 9th Nat. Thermal Spray Conf., Cincinnati, Ohio, 1996
10. R.G. Castro, P.W. Stanek, K.E. Elliot, et al., Phys. Scripta T64 (1996) 77-83.
11. R. Giniatulin, I. Mazul, A. Gervash et al., "Investigation of the Be/Cu joints via HHF tests of small-scale mock-ups", Proc. of the 3rd IAE Workshop on Beryllium Technology for Fusion, Oct. 1997, Mito, Japan, 113-122.
12. A.Gervash, R. Giniatulin, V.Komarov et al., Fusion Eng. and Design, 39-40 (1998) 543-550.
13. A.Gervash, R.Giniatulin, I.V.Mazul, R.Watson, Beryllium armoured mock-ups for fusion heat flux application, ", Proc. of the 20th Symp. on Fusion Technology, Marseille, Sept. 1998, v.1, 47-50.
14. B.C. Odegard, C.H. Cadden, " Solid State bonding of Beryllium Copper for an ITER First Wall Application", Proc. of 3rd IEA Workshop on Beryllium Technology for Fusion, Mito, Japan, Oct. 1997, 123-128.
15. J.H.Vincent et al., Development of procedure for attaching Beryllium tiles onto CuCrZr testpieces and divertor mock-ups plates", GEC-Marconi Materials technology, report MS/20416, Nov 1995
16. M.Roedig, R.Duwe, J.linke, A.Lodato, SOFT20, Marseille, 1998, p. 193.
17. Mazul, R. Giniatulin, R. Melder, "Post Irradiation Examination of Be-Cu Divertor Mock-up After In-pile Thermocycling Experiment with Active Cooling Proc. of 3rd IEA Workshop on Beryllium Technology for Fusion, Mito, Japan, Oct. 1997, p.221-228.

Acknowledgements

This report was prepared as an account of work undertaken within the framework of the ITER EDA Agreement. The views and opinions expressed herein do not necessarily reflect those of the parties to the ITER Agreement, the IAEA or any agency thereof. Dissemination of the information in this paper is governed by the applicable terms of the ITER EDA Agreement.

SOME ASPECTS OF USING Be AS HIGH HEAT FLUX PROTECTIVE ARMOUR MATERIAL

A. Gervash[1], I. Mazul[1], N. Yablokov[1], J. Linke[2]

1 Efremov Institute, 189631 St. Petersburg, Russia

2 Forschungszentrum Juelich GmbH, EURATOM Association, D-52425 Juelich, Germany

The beryllium as plasma facing armour material must protect the actively cooled copper alloy heat sink of the First Wall and Divertor components from sputtering erosion, disruption and VDE transients and withstand the number of cycles under expected heat and neutron fluxes. The presented paper discusses some topical questions and presents recent results obtained in Russia in the frame of such consideration.

In real operation beryllium as plasma facing component will be subjected to sequence of normal (cyclic heat fluxes) and off-normal (disruption, VDE) heat loads. Aiming to investigate the results of mentioned events the experiments with the number of Russian Be grades (DShG-200, TGP-56, TShG-56, TR-30, Condensed Be) as well as S-65C (ITER reference grade) at simulated disruption loads (~5 MJ/m^2) and subsequent thermal cycling (~5 MW/m^2, 1000 cycles) were carried out. Experiments have revealed no macroscopic damage of the tested grades, although significant differences in crack formation and propagation were observed. The main statistics of performed experiments is presented and discussed.

One of the main requirements to use Be as a candidate for plasma facing component is providing a reliable joint between Be and Cu-alloy heat sink structure. The unique Russian fast brazing process of joining beryllium to Cu-alloy that allows to survive high heat fluxes $\geq$10 MW/m^2 during thousand heating/cooling cycles without serious damaging in the armour material and its joint was described in previous works. The main goal of experiments presented in this paper was to study the high heat flux durability limit for joints as function of the pulse duration (i.e. investigation of creep/fatigue interaction). Authors present a description of the testing procedure and discuss the first results of mentioned experiments.

Results of HHF tests and metallographic investigation of beryllium HHF mockups

R. Giniaytulin[a], V. Komarov[a], I. Mazul[a], N. Yablokov[a], R. Watson[b], C. Cadden[b], N. Yang[b]

[a] Efremov Research Institute, St. Petersburg, Russia
[b] Sandia National Laboratories, Albuquerque, Livermore, US

The reliability of the beryllium-armoured elements for any fusion facilities strongly depends from the armour tile geometry and determines by the armour thickness and how it is castellated in the planar dimensions. The mockup with the tile dimensions of 5x5x5 mm demonstrated best results during the HHF tests at EBTS facility (SNLA). Thermal response test demonstrated the ultimate heat flux level of 16.6 MW/m2 without failure of the joint, melting of the beryllium surface limited the level of the heat flux. During thousand cycles by heat flux density of 13.5 MW/m^2 no damages in the Be/CuCrZr joint occurred that was approved by metallographic investigation of the tested and non-tested cross-sections. This paper presents the results of HHF testing with Be-armoured mockup that has optimized armour geometry, 2-D temperature analysis for testing conditions and the results of metallographic analysis. The results are discussed and the recommendations for armour dimensions are also made.

1. INTRODUCTION

During the investigation of the Be/Cu joining several bonding techniques such as diffusion bonding, traditional furnace brazing and fast brazing were used [1, 2, 3]. The best results were obtained for mockups fabricated with using of fast brazing technique [2]. All previous investigations were aimed for the selection of optimal armour geometry and examination of the mockup reliability with different geometry under the ITER relevant conditions that correspond to different divertor element [2]. The promising results were obtained for the mockup with the tiles in dimensions of 5x5x5 mm^3: the mockup survived 4500 thermal cycles under the heat flux density of 12 MW/m^2 [4]. Another mockup with this armour geometry also demonstrated highest reliability in screening experiment: no debonding during few cycles at 15 MW/m^2 [5]. So, these dimensions of the beryllium tiles were accepted as an optimal for high heat flux components.

The main goal of the present work was to examine the joint reliability under the highest heat cyclic loading for the mockup with tile dimensions of 5x5x5 mm^3. The criterion of the mockup reliability was absence of the surface melting, armour delamination and drastic beryllium degradation.

2. EXPERIMENT

The mock-up (figure 1) is manufactured from isotropic grade beryllium TGP-56 brazed to the CuCrZr heat sink block. The mechanical and physical properties of used armour and heat sink materials are presented in reference [6]. The precipitation hardened copper alloy CuCrZr was considered as heat sink due to its good resistance to neutron damage, better weldability and ductility in comparison with other alloys. CuInSnNi-alloy (STEMET® 1108 from AMETO, Moscow) was used as brazing alloy in the form of a 50-μ-thick foil [7].

The mock-up has 32 beryllium tiles of 5x5x5 mm^3 in dimensions brazed to the flat CuCrZr surface. To manufacture the mockup 6-mm thick block of TGP-56 isotropic beryllium was castellated with the depth of 5 mm, the maintaining surfaces between the beryllium, brazing foil and copper alloy heat sink block were chemically etched. The beryllium block, brazing foil and heat sink block were then mechanically clamped by molybdenum jigs and brazed by electron-beam heating [2]. The 1-mm top layer of beryllium block was then cut off to get thirty-two 5x5x5 mm^3 tiles. The heat sink block has cooling channel with diameter of 12 mm and holes for bulk thermocouples. The drawing of cross-section and view of the mockup are presented in figure1. To demonstrate power-handling capability under different heat loads thermal response test was perform. Cyclic thermal fatigue tests under the highest heat flux density were performed to examine the reliability of the brazing zone and any degradation of the beryllium armour. The tests were performed at the EBTS facility (SNLA, US) [1].

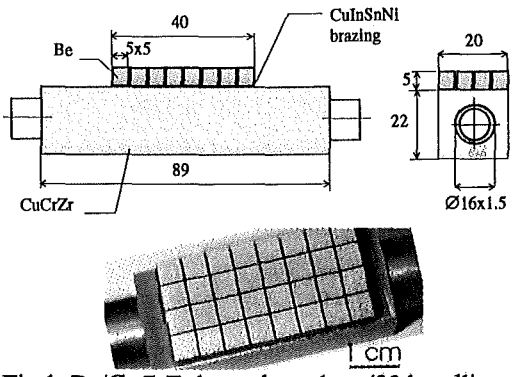

Fig.1. Be/CuCrZr brazed mockup (32 beryllium tiles, 5x5x5 mm).

3. RESULTS OF THE HHF TESTING

3.1. Thermal response testing

The goal of the thermal response testing is to check the reliability of the joint and measure the steady-state temperature response of the mockup to applied steady heat flux. Two armour rows (eight tiles) were subjected to the thermal-response test (see figure 2) by incrementally increasing heat fluxes in the range of 5÷16 MW/m^2. The conditions and measured parameters during the thermal response test are presented in table 1.

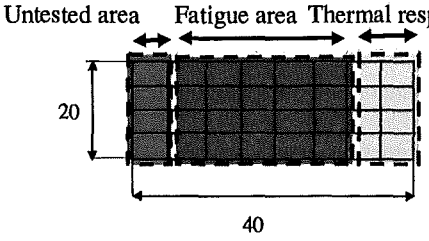

Fig. 2. The scheme of thermal-response and fatigue tests.

The performed test did not damage the joint. Last shot of this testing set lead to a melting of the beryllium surface. The plot of measured surface and joint temperatures are presented in Fig. 3.

3.2. Thermal fatigue testing

Thermal fatigue testing was performed with five rows (20 tiles) of armour (Fig.2) to check joint reliability under the heat loading conditions close to melting. One row (4 tiles) was saved untested for further metallographic investigation. The conditions and measured parameters of fatigue tests are presented in Table 2. The average heat flux density during the fatigue test

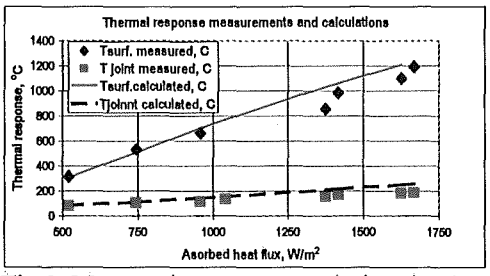

Fig.3. Measured temperatures during the thermal response test.

was about 13500 MW/m2, one thousand thermal cycles were performed. The inlet temperature of coolant was set as RT in order to decrease surface temperature of the armour at the highest heat flux density. The plot of measured surface/joint temperatures and absorbed heat fluxes are presented in figure 4. The measured maximum steady state joint temperature remained constant during all cycles. Figure 5 presents the example of IR-image during testing. The surface temperature has a tendency of slight increasing during the fatigue tests. This fact is explained by the changing of beryllium emissivity [1]. The side view of the joint was observed visually few times during the tests using an in situ optical borescope. No visible cracks in the joint were observed. The view of the mockup after the tests is presented in figure 6.

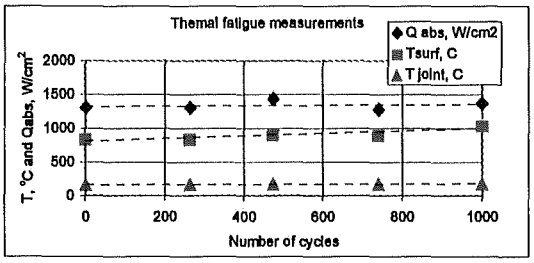

Fig.4. Measured temperatures during the thermal fatigue test.

4. THERMAL ANALYSIS

Two-dimensional finite element analysis of the thermal response was performed using the QuickField code. Temperature depended material properties were used for TGP-56 beryllium and CuCrZr alloy. The value of the heat transfer coefficient was used as 80000 W/K·m^2 on the base of the previous experimental results with the same cooling conditions [1]. Good agreement between calculation and experimental results was found (Fig.3). Figure 7

demonstrates the example of temperature distribution across the mockup at the heat flux

Table 1. The conditions and measured parameters during the thermal response test.

shot #	Q abs, W/cm2	Pulse length, s	Number of the shots	Heated area, cm2	Tsurf, C	T joint, C	Tin, C	Pin, MPa	w, m/s
1(169645)	521	30	1	2.4	312	79			
2(169647)	875	30	1	2.4	530	100			
3(169648)	958	30	1	2.4	660	110			
4(169649)	1042	30	1	2.4	750	130	11	1	15
5(169657)	1375	30	1	2.4	853	150			
6(169658)	1417	30	1	2.4	980	165			
7(169659)	1625	30	1	2.4	1096	175			
8(169660)	1667	30	1	2.4	1190	180			

Table 2. The conditions and measured parameters during the thermal fatigue test.

shot #	Q abs, W/cm^2	Pulse length, s	Accumu-lated shots	Pause length, s	Tsurf, C	T joint, C	Tin, C	Pin, MPa	w, m/s
1(169688)	1308	5	1	5	840	167	11	1	15
2(170055)	1308		264		840	171			
3(170072)	1431		474		904	175			
4(170459)	1277		740		900	175			
5(170723)	1369		1000		1040	180			

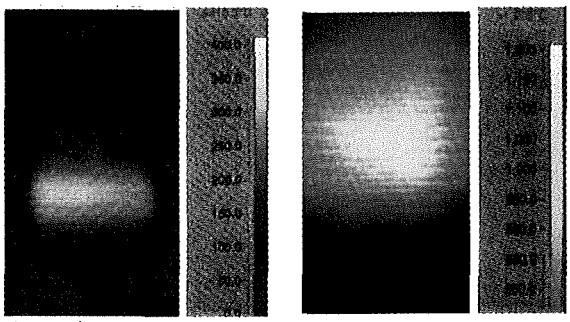

Screening test on two rows, Q=5 MW/m^2 | Fatigue tests on five rows, Q=13.5MW/m^2

Fig. 5. The examples of IR-images at thermal response and fatigue tests

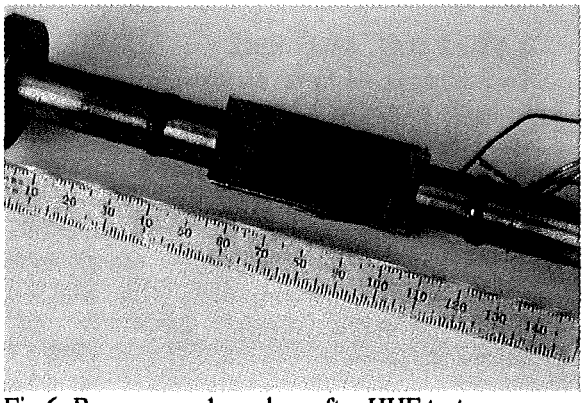

Fig.6. Be-armoured mockup after HHF tests.

density level of 13.5 MW/m^2. The calculation and experimental measurement (fatigue tests) give the surface temperature level of 1030 °C and 1040 °C correspondingly for this heat flux level.

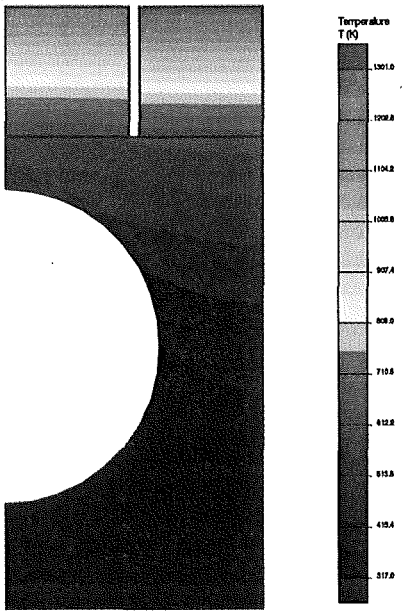

Fig.7. Temperature distribution across the mockup at Q_{abs}=13.5 MW/m^2.

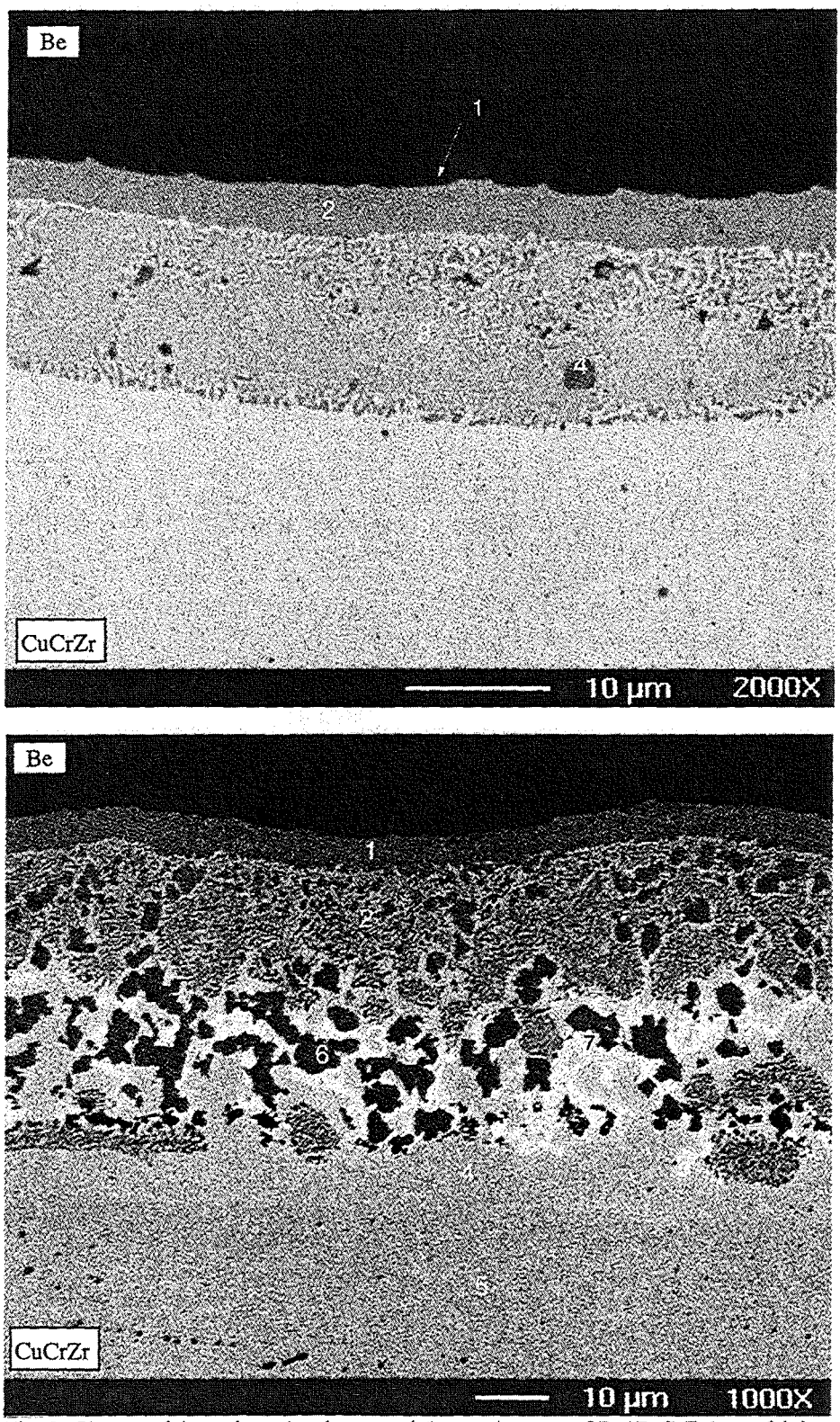

Fig. 8. The tested (top picture)and untested (bottom) zones of Be/CuCrZr brazed joint.

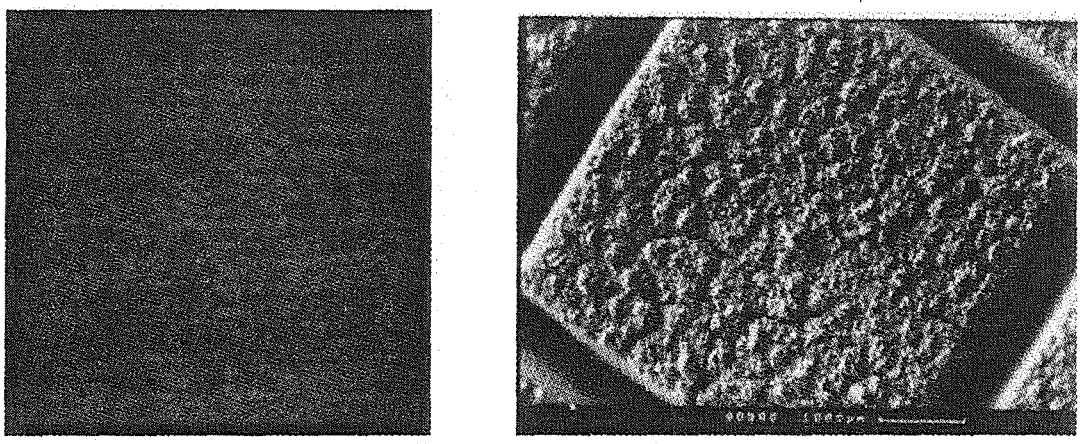

Fig.9. The view of the Be-surface before (left view) and after (right view) fatigue test on EBTS facility (mockup#56, Q=13.5 MW/m^2, N=1000)

5. POST-TEST ANALYSIS

After the HHF testing the mockup was wire cut and cross-section of tested and untested parts were prepared for metallographic investigation. The tested and untested zones were inspected to detect the cracks or delamination before and after the fatigue tests. No defects were found. The SEM micrographs of the tested and untested zones are presented in figure 8.

.Untested brazing zone consist from layers 1 and 2 – Be_2Cu, BeCu and copper phases; layer 3 – solution of Cu, Cr, Sn, In and Ni; area 4 – CuCrZr; layer5 – CuCrZr.

Tested brazing zone has the same content with the difference in the width of layers. The thickness of layers 1,2 and 3 are increased and the grains dimensions are increased also. The joint is changed from thin and uniform multi-layers to layers mixed with different concentrated phases (with Ni and Sn) during the fatigue testing. This effect can be explained by prolonged holding of the joint at a temperature about 200 °C. A change in the zone width is not significant. The total width of the brazing zone increased during the fatigue testing from ~20 μm up to ~60 μm. The Be/CuCrZr zone remained reliable at fatigue test. No damages were observed in the joint.

The beryllium surface was covered by cracks about 0.5 mm in depth, smooth surface changed to rough, fig. 9. This change in the armour surface did not influence on joint and armour reliability.

6. CONCLUSIONS

The performed thermal response and thermal fatigue tests of the mockup with optimized armour geometry have demonstrated an excellent joint reliability under the highest heat flux level. The level of the heat flux density in the thermal response testing was limited only by melting of beryllium surface. The level of the heat flux during the fatigue test was very close to the melting level. The results of Be/CuCrZr-joint analysis after the fatigue testing did not show the cracks and delamination. The surface of the beryllium tiles was covered by mesh of microkracks, but this changing did not affect on mockup reliability.

The beryllium armoured elements that have armour tiles with dimensions of 5x5x5 mm^3 and brazed to Cu-alloy heat sink structure with using of described technique could be recommended as plasma facing components that works under high heat load cyclic conditions.

7. REFERENCES

1. D.L.Youchison et al, Thermal fatigue testing of a diffusion-bonded beryllium divertor mockup under ITER relevant conditions, Journal Fusion Technology of American Nuclear Society, v.29, number 4, July 1996, pp.599-613.
2. Final Report on ITER Task T222 "Manufacturing and testing of permanent components", RF Home Team, 1998, pp.1-14.
3. R. Giniyatulin et al, "Investigation of Be/Cu Joints via HHF Tests of Small-scale Mock-ups",in Proc. of the 3rd IEA International Workshop on Beryllium Technology for Fusion, 1997, pp. 113-122. R. Giniyatulin,

A. Gervash et al, "Investigation of Be/Cu Joints via HHF Tests of Small-scale Mock-ups",in Proc. of the 3rd IEA International Workshop on Beryllium Technology for Fusion, 1997, pp. 113-122

4. A. Gervash et al, Comparative thermal cyclic test of different beryllium grades previously subjected to simulated disruption loads, Fusion Engineering and Design 00, 1999, 1-7.
5. A. Gervash et al, Beryllium armor mockups for fusion high heat flux application, in Proc. of 20-th SOFT,7-11 September, Marseille, France, v.1, pp.47-50.
6. Material Assessment Report. Armour/Heat Sink Joints, ITER, G A1 DDD 1 97-12-08 W 0.2.
7. Final Report on ITER Task T221, RF Home Team, "Development of Be and other armour materials", pp.1-31.

High Heat Flux Performance of Beryllium Before and After Neutron Irradiation

Lodato[a-b], M. Rödig[a], R. Duwe[a], H. Derz[a], J. Linke[a], R. Castro[b], A. Gervash[c]

[a]Forschungszentrum Jülich GmbH, EURATOM Association, D-52425 Jülich, Germany

[b]Vacuum Vessel and Blanket Division, Garching JWS, ITER JCT

[c]Los Alamos National Laboratory, P.O. Box 1663, Los Alamos, NM 87545, USA

[d]D.V. Efremov Scientific Research Institute, St. Petersburg, 189 631, Russia

Beside carbon materials and tungsten, beryllium will play an important role as Plasma Facing Material (PFM) in the International Thermonuclear Experimental Reactor (ITER). It will mainly be used for the primary wall, the limiter and the upper baffle. During off normal operation the surface of Be may be loaded by severe thermal shocks, caused by plasma disruptions with energies of several ten MJ/m^2 within a few milliseconds.
The influence of high heat fluxes on several un-irradiated Be grade have been investigated before. During the operation of ITER the material will suffer irradiation with 14 MeV neutrons generated in the fusion process. In order to study the material degradation caused by fast neutrons, different samples have been neutron irradiated in the High Flux Reactor (HFR) at Petten. The thermal shock behaviour of the different beryllium grade before and after neutron irradiation is now compared.

1. INTRODUCTION

Plasma facing components in ITER are protected by sacrificial armour material that can be replaced in case of damage. The working conditions of the PFM are very complex. During normal operation they are stressed by thermal fatigue loads and simultaneously influenced by high heat flux and neutron or ion fluxes. During off normal operations, the PFM may suffer severe thermal shocks caused by plasma disruptions, with energies up to several ten MJ/m^2 within a few milliseconds and by vertical displacement events (VDE), with energy densities of 20-60 MJ/m^2 within 0.3 to 1 s.
Beside carbon materials and tungsten, beryllium will play an important role as a plasma facing material because of good plasma compatibility, low activation, and the possibility of in-situ repair (e.g. by plasma spraying) [1].
The neutrons generated in the fusion process will affect the thermal and mechanical properties of beryllium. To investigate the materials degradation processes, a neutron irradiation campaign has been carried out in HFR at Petten, The Netherlands. Actively cooled Be/CuCrZr mock-ups, mechanical test samples and thermal shock samples from different beryllium grades have been irradiated up to 0.35 dpa at 350 °C and 700 °C.
These grades include beryllium S65C manufactured by Brush Welman Inc., (USA), and the Russian beryllium grades TR30, DShG200, and TShG56. Besides these, powder-metallurgically produced materials, plasma sprayed beryllium (Los Alamos National Laboratory) and condensed beryllium (D.V. Efremov Institute, St.Petersburg) were investigated.

2. EXPERIMENTAL DETAILS

The behaviour of several Be grades when subjected at High Heat Flux (HHF) loads, before and after neutron irradiation, was investigated using an electron beam. Pre- and post-irradiation electron beam tests have been carried out in the 60 kW Electron Beam (EB) test facility JUDITH located in the Hot Cells of Forschungszentrum Jülich, Germany [2]. The facility was upgraded with respect to the handling of the irradiated samples by means of a mechanical manipulator.

The mounting of samples in a remote-controlled holder and the remote-controlled weighting of samples before and after the high heat flux test was performed by the mechanical manipulator.
It was clear from previous experiments that the test conditions were not always reproducible. A change of some characteristics of the beam may occur between different testing campaigns. To achieve the most accurate comparison of the material behaviour before and after nuclear irradiation, beryllium samples un-irradiated, irradiated at 350 °C and at 700 °C have been tested in sequence without any break of vacuum.
For a given incident power the fraction of that power deposited in the material has been monitored by current measurements. In fact not all of the incident electrons deposit their energy in the material being influenced by effects of emission and reflection of electrons, material ablation, erosion, etc.
During the electron beam loading the test samples were electrically isolated and grounded by a resistor of ~100 Ω. The electrical current absorbed by the test samples was determined from the voltage drop on this resistor (Fig. 1).

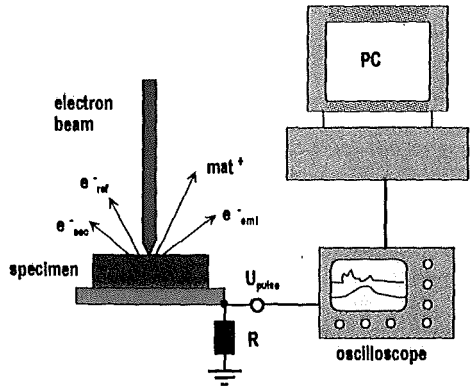

Figure 1. Measurement of the beam current flowing into the sample.

3. LOADING CONDITIONS

A list of the investigated grades together with the applied loading condition is reported in table 1.
Sample dimensions were 12x12x5 mm^3 for most grades. Samples of dimension 12x12x10 mm^3 have been also used in case of PS-Be.
All tests have been carried out at room temperature.
Due to a possible pollution of the deflection system of the electron gun, the distributions of the electrical current on the samples wasn't very accurate. Sometime a more circular crater shape has been observed after testing. This has an influence on the energy density. If e.g. the energy is deposited on a circular area of 4 mm diameter, the energy density increases by ~27 % compared to a square shaped area of 4x4 mm^2. For this reason a directly comparison of the results has been carried out only for samples showing the same crater shape.

Table 1
HHF Test on irradiated Be samples

Be grades:	S65C, DShG200, TShG56, TR30, Condensed Be, PS Be
Beam current:	~ 360 mA
Acceleration voltage:	120 kV
Loaded area:	~ 4x4 mm^2
Number of spot:	5
Pulse duration:	5 ms
Power density:	~ 2700 MW/m^2

4. TEST RESULTS

For each Be sample the current absorbed during the first and the fifth electron beam shot has been recorded. In fig. 2 the absorbed current behaviour in case of S65-C un-irradiated is shown.
An interesting phenomenon has been observed. About during the first 2 ms from the beginning of the shot, the absorbed current is approximately 90% of the incident value. Then it drops to 50% of the initial value.
This is common for all samples and a small difference in the amount of the drop has been observed between the first and the fifth shot.
Similar behaviour has been monitored in case of irradiated samples.
Fig. 3 shows the comparison between the absorbed current monitored during the fifth shot on S65C un-irradiated, irradiated at 350 °C and at 700 °C.
In table 2 the values of the significant points of fig. 3 are reported.
In case of samples irradiated at 700 °C the drop is ~10 % bigger with respect to the un-irradiated sample and appears ~0.34 ms earlier.
Several effects could originate this drop.

The high incident power density could lead to a very fast ablation of the material so that the incoming electrons could be shielded from the mass of the evaporated material. On the other hand due to the elevated temperature of the sample the electron thermal emission could have a significant effect [3].

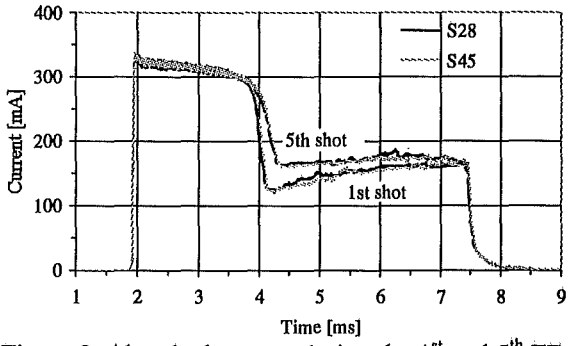

Figure 2. Absorbed current during the 1st and 5th EB shot on Be S65C un-irradiated samples.

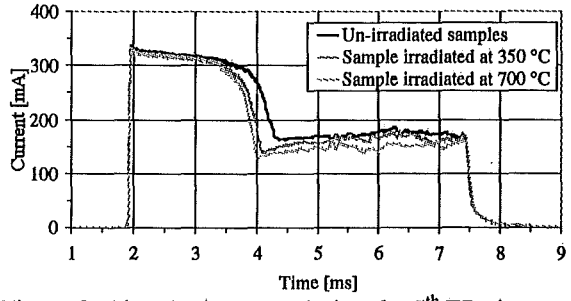

Figure 3. Absorbed current during the 5th EB shot on Be S65C for un-irradiated and irradiated samples.

Unfortunately it was not possible to measure the surface temperature during the test. A computational simulation of the experiment based on a sophisticated finite element analysis methodology has been carried out [4]. The comparison between experimental and analytical results is in progress and should clarify the origin of the absorbed current drop.

All Be grades tested showed a similar absorbed current behaviours.

After the thermal shock loading the material erosion has been quantified by two independent methods: weight loss measurements and 3D surface profile determined by a laser micro-profilometer.

Fig. 4 shows the weight loss comparison between four Be grades.

For the reason explicated in par. 3, a directly comparison with the other two grade wasn't possible therefore their results weren't included.

All materials shown bigger erosion (50%÷150%) after neutron irradiation but little differences are observed for the two irradiation temperatures.

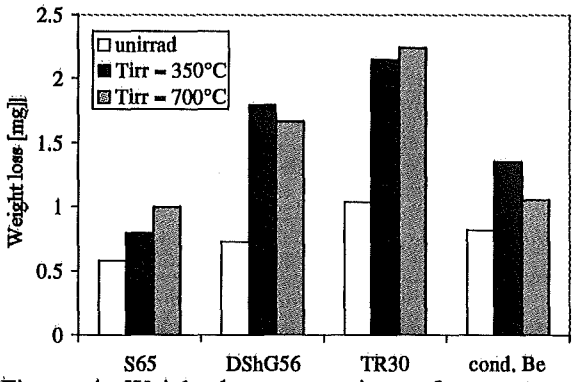

Figure 4. Weight loss comparison after neutron irradiation.

In similar direction seem to evolve the results from laser profilometry. The maximum crater depth before and after neutron irradiation has been measured for all Be grade. Deeper craters have been observed after neutron irradiation.

Metallography investigations are in progress for a more accurate analysis and in order to study the cracking behaviour.

Table 2.
Time and absorbed current values during the 5th EB shot on Be S65C.

Sample un-irradiated		Sample irradiated at 350 °C		Sample irradiated at 700 °C	
Time [ms]	I_{abs} [mA]	Time [ms]	I_{abs} [mA]	Time [ms]	I_{abs} [mA]
0	323	0	323	0	323
1.56	300	1.36	300	1.28	300
2.22	165	1.97	139	1.88	130
5	175	5	165	5	150

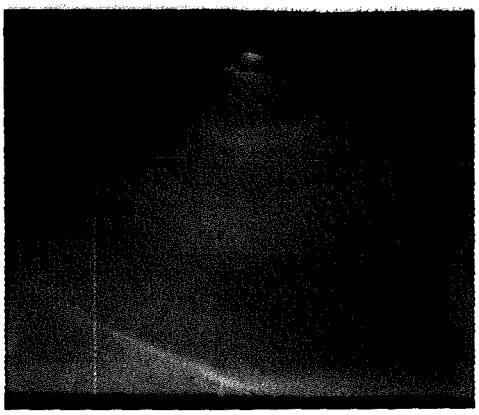

a)

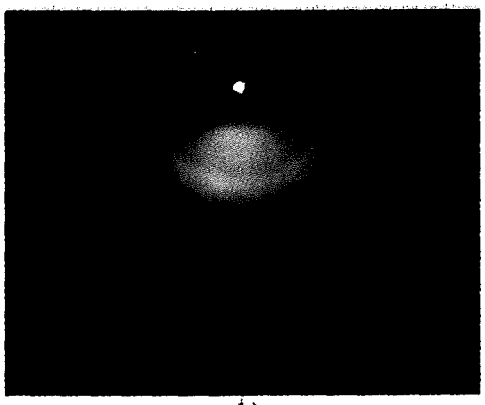

b)

Figure 7. The electron diffraction patterns of the target M3: a) sputtering zone, b) re-deposition zone.

The results of studying the phase composition in the sputtering zone of the sample M2 by the X-ray crystal analysis technique are given in Figure 8. The surface layer in the sputtering zone under deuterium ion bombardment consists mainly of α- and β-beryllium. Along with them, an insignificant amount of BeO, predominantly of α-modification, is observed.

The beryllium microstructure in various zones essentially differs also. The original structure is shown in Figure 9a. In the sputtering zones of the targets M1 and M2 the blister production is observed (Figure 9b). The growth of cones is observed in the sputtering zone of the target M3 irradiated with essentially higher proton dose (Figure 9c). The microstructure of this zone is different for the differently oriented faces, the borders of which are displayed as a result of ion etching. The structure of one of such areas in the sputtering zone is given in Figure 9d. The formation of columnar structures is observed in the re-deposition zone of the target M3 (Figure 9e).

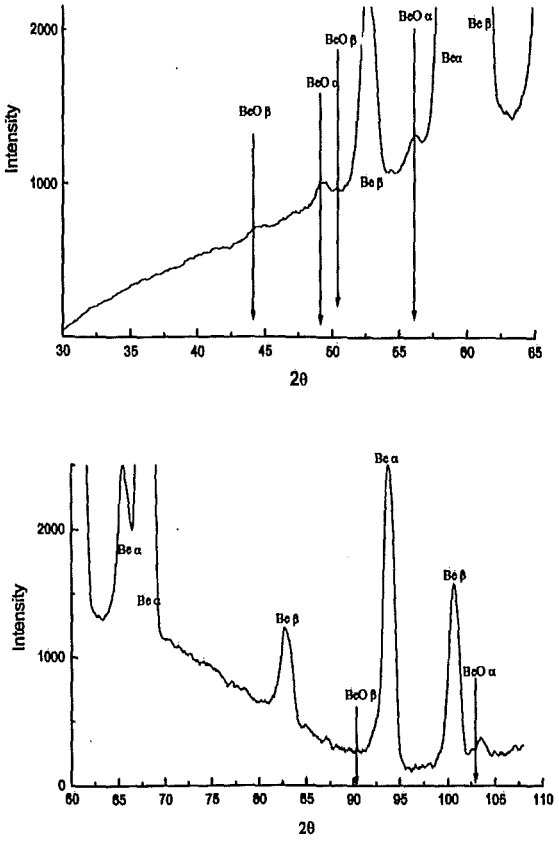

Figure 8. X-ray diffraction spectra of reflection for the sputtering zone of the target M2.

Profiles of hydrogen isotope atoms distribution in re-deposited target layers are presented in Figure 10. Deuterium (targets M1 and M2, Figure 10a) and hydrogen (target M3, Figure 10b) are distributed in re-deposited beryllium layers practically uniformly. Only thickness of layers containing hydrogen isotopes is different depending on different irradiation doses. For the target M3, a 500 nm thick re-deposited beryllium layer was analysed since the helium ion energy equal to 1.8 MeV turned out to be insufficient for studying the whole film thickness.

In fig. 5 is shown the metallography section of PS-Be irradiated at 350 °C after test. Cracks are generated not only perpendicular to the surface but also in parallel direction. The origin of the latter is ascribed to the fabrication method. This crack behaviour would suggest that a total detachment of a piece of Be could take place if the tile is subjected to thermal fatigue after a disruption.

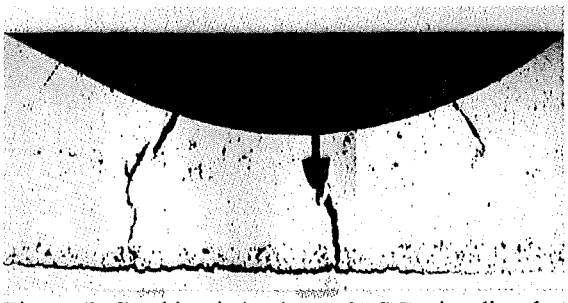

Figure 5. Cracking behaviour of PS-Be irradiated at 350 °C. Initial value of absorbed power density ~ 2850 MW/m^2.

The surface status of the samples has been investigated by optical microphotography.
Microphotographs of the craters have been taken through an image scanner. Fig. 6 shows the surface area scans of Be S65C un-irradiated and irradiated at 350 °C, after test.

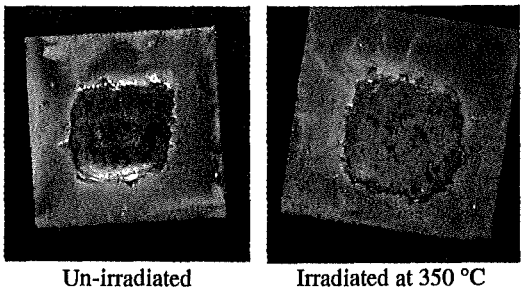

Un-irradiated Irradiated at 350 °C

Figure 6. Be S65C microphotography after test. Initial value of absorbed power density ~2700 MW/m^2.

Cracks on the surface samples are present both in case of un-irradiated and irradiated samples. Nevertheless a bigger damage of the sample surface is evident in case of irradiated samples. Similar performance has been detected for all Be grade.
Measurements of the thermal conductivity of Be after neutron irradiation and tensile tests have been carried out [5]. No thermal degradation has been detected after neutron irradiation but a loss of ductility is found. Therefore the erosion and crack behaviour should be attributed to a changes in mechanical properties.

5. CONCLUSION

Thermal shock tests on several Be grade samples have been carried out in the electron beam facility JUDITH at Forschungszentrum Jülich, Germany. The behaviour of the different Be grades before and after neutron irradiation has been compared.
The electrical current absorbed by the test sample during the electron beam shot has been monitored. A drop after ~ 2ms from the applied load has been detected. The origin of this drop could be ascribed both to a shielding of incoming electrons from the mass of the evaporated material and to the thermal emission of electrons from the metal. Further investigations are necessary to clarify this behaviour.
All materials show higher erosion after neutron irradiation. The effect could be ascribed to decreased ductility after irradiation. No large differences are observed for the two irradiation temperatures.
The comparison of the different beryllium grades indicates the ITER grade S65C and the condensed Be as the material with lowest erosion after neutron irradiation.

REFERENCES

1. V. Barabash et al., Proceedings of 3th IEA International Workshop on Be Technology for Fusion, Japan, 22-24 Oct., 1997, p. 2-13.
2. R. Duwe, W. Kühnlein, H. Münstermann, Proceedings of the 18th Symposium on Fusion Technology (SOFT), Karlsruhe (Germany), Oct. 22.-26, 1994, p. 355-358.
3. J. Linke, H. Bolt, R. Duwe, W. Kühnlein, A. Lodato, M. Rödig, K. Schöpflin, B. Wiechers, Proceedings of ICFRM-9, Colorado Springs, 10-15 Oct., 1999, to be published in Fusion Technology.
4. A. Cardella, H. Gorenflo, A. Lodato, K. Ioki, R. Raffray, Proceedings of ICFRM - 9, Colorado Springs, 10-15 Oct., 1999, to be published in Fusion Technology.
5 ITER Material Assessment Report, ITER Document no. G A1 DDD 1 98-05-28 W 0.3.

An Assessment of the Tensile and Fracture Toughness Data Generated in the Beryllium Irradiation Embrittlement Test (BSBE) Programme

D.R. Harries[a], M. Dalle Donne[b] and F. Scaffidi-Argentina[c]

[a] Consultant, Oxford, England
[b] University of Karlsruhe
[c] IKET, Forschungszentrum Karlsruhe, Postfach 3640, D-76021, Karlsruhe, Germany

Experimental data on the ambient and elevated temperature tensile and fracture toughness properties of unirradiated (reference), thermally aged and neutron irradiated hot isostatic (HIP) and vacuum hot (VHP) pressed S-65 and S-200F beryllium grades are assessed with respect to the effects of material, test and irradiation variables. The limitations of the existing data are acknowledged and the additional investigations required to clarify some of the present uncertainties are summarised.

1. INTRODUCTION

The effects of thermal ageing and neutron irradiation in the Mol BR2 reactor on the room and elevated temperature tensile and fracture toughness properties and microstructures of S-65 and S-200F beryllium, produced by direct hot isostatic (HIP) and axial vacuum hot (VHP) pressing of impact ground powders [1], have been reported previously [2][3]; the BeO contents, total minor impurity concentrations and grain sizes of the respective beryllium grades are reproduced in Table 1.

An independent analysis and assessment of the tensile and fracture toughness data at test temperatures in the range ambient to 605 C for the beryllium grades in the unirradiated (reference), thermally aged (2203 h at temperatures from 185 to 605 C) and irradiated (atom displacement doses and helium concentrations of 0.8 - 2.6 dpa and 240 - 750 appm respectively at temperatures within the range 185 to 610 C) conditions are summarised in this paper; additional details are provided in a report due for publication [4]. The primary aim of the exercise is to further the development of composition - structure - property relationships for the unirradiated and irradiated beryllium.

2. TENSILE PROPERTIES

The effects of ageing, irradiation and test temperature on the tensile strengths and ductilities of the beryllium are exemplified by the data for the S-65. HIP grade presented in Fig. 1.

2.1 Unirradiated (reference) and aged materials

Prior thermal ageing does not have a statistically significant influence on the proof and ultimate tensile strengths of the unirradiated (reference) beryllium. However, the strength values decline progressively with increasing test temperature, the magnitudes of the reductions decreasing in the order S-65. HIP, S-200F. HIP, S-200F. VHP and S-65. VHP.

The uniform and total elongations and reductions of area of the unirradiated (reference) beryllium are all relatively small at ambient temperature, increase to maxima at about 300 C and then decrease at temperatures up to 605 C; the deformation at the higher test temperatures occurs predominantly in a non - uniform manner. The highest ductilities at temperatures in the range 300 to 605 C are shown by the S-65. VHP material followed by the S-65. and S-200F. HIP

Table 1
Oxide and Impurity Concentrations and Grain Sizes of the Beryllium Grades

Grade	BeO Content (wt. %)	Total Impurity* Conc. (wt. %)	Average Grain Diameter (μm)
S-65. HIP	0.5	0.16	6.6
S-65. VHP	0.6	0.17	8.4
S-200F. HIP	0.9	0.29	7.1
S-200F. VHP	1.2	0.34	8.2

* Fe, C, Al, Mg, Si, etc.

grades. The total elongations and reductions of area of the S-200F. VHP beryllium are considerably lower than those of the other materials at all temperatures, being ≤ 3.5 and $\sim 2\%$ at 540 and 605 C respectively; the corresponding total elongation and reduction of area values for the other grades are ≥ 10 and 15%. Ageing does not significantly affect the uniform elongations of the unirradiated beryllium but increases the total elongations and reductions of area of the S-200F. HIP and VHP beryllium at 455, 540 and 605 C and of the S-65. VHP grade at intermediate temperatures (230 - 455 C). It follows that ageing enhances the non - uniform ductilities of these materials by modifying the ductile fracture process. The ductilities of the S-65. HIP beryllium (Fig.1) are not influenced by the prior thermal ageing at all temperatures.

The proof and ultimate tensile strengths of the S-65. VHP beryllium at ambient and elevated temperatures are in good agreement with published data for this grade [5 - 8]. All the data show maximum ductilities at 300 - 400 C. However, the ductilities (reduction of area values) for the BSBE S - 65. VHP beryllium grade in the reference condition are considerably lower than those for the other lots at temperatures in the range 200 - 500 C (Fig. 2) but, prior thermal ageing enhances the ductilities such that the values approach or coincide with those of the other batches.

The 0.2% proof stresses of the S - 200F. VHP beryllium tested in the BSBE Programme and in other investigations [8 - 10] are in reasonably good agreement at all test temperatures. However, the ductilities (total elongations) for the BSBE material in the reference condition are much lower at the higher test temperatures due to reduced non - uniform (necking) deformation (Fig. 3); thermal ageing again increases the high temperature elongations so that all the values become comparable. The differences in the tensile ductilities recorded here are tentatively ascribed to the differences in the BeO and impurity concentrations and distributions. SEM examinations of the fracture surfaces have revealed a high density of small BeO particles with which small pores are associated in the S - 200F. VHP BSBE lot [3]. In addition, the low ductility values at the high temperatures may be attributed to the high aluminium content (0.05 wt.%) as it is reported that this elemental impurity at the grain boundaries liquates and nucleates intergranular cracking at temperatures above 500 C [11]. This detrimental influence of the aluminium on the high temperature ductility may be negated by the formation of the higher melting point $AlFeBe_4$ intermetallic compound during the thermal ageing; it is often the practice to initially heat treat the beryllium at a temperature of about 870 C followed by step cooling to promote the formation of this phase [6].

The absolute values and temperature dependences of the tensile 0.2% proof and ultimate strengths and ductilities (uniform and total elongations and reductions of area) for the unirradiated (reference) and thermally aged materials are also in good agreement, allowing for the disparities in the BeO and impurity contents (and, possibly, distributions) and the different test temperatures employed in the respective studies, with the reported data [11] for impact ground S - 65B. VHP (1.0% BeO), S - 200F. VHP (1.5% BeO) and S - 200F. HIP (1.5% BeO) beryllium.

The SEM examinations of the fracture surfaces show transgranular cleavage failure of the S-65. HIP specimens in the tests at ambient temperature [3]; ductile crack initiation precedes transgranular cleavage crack propagation at 230 C whilst ductile dimple fracture predominates at the higher test temperatures. These observations are generally consistent with those reported in the literature [5][11]; failure at temperatures up to 200 C occurs

by cleavage, ductile/ fibrous fracture takes place at 200 - 500 C, and some beryllium grades exhibit an increasing tendency to fracture intergranularly at higher temperatures.

The hexagonal close packed (hcp) beryllium crystal deforms by slip on the basal (0001) and prismatic ($10\bar{1}0$) planes at ambient and elevated temperatures. At temperatures below about 200 C the shear stress for the activation of prismatic slip is relatively high and slip on the basal planes is favoured. Dislocations are piled up against a grain boundary as a result of coarse slip within the grain, resulting in an intense tensile stress field on one side of the slip band and compressive on the other side (Fig. 4). The tensile stress concentration may be alleviated by slip in the adjacent grain if it is suitably oriented, otherwise the combined tensile stress from the slip and the externally imposed stress can result in the initiation of a crack; the crack propagates rapidly to produce cleavage or pseudo - cleavage transgranular failure along the (0001) basal planes or is arrested following a reduction of the stress concentration at the crack tip by plastic flow. The critical stress for prismatic slip approaches that for basal slip with increasing temperature above 200 C and both slip systems become operative (Fig. 5); the critical stress for cleavage fracture increases, the beryllium thus becomes more ductile and fails by fibrous fracture at temperatures up to 500 or 600 C.

It has been noted previously [12 - 14] that the tensile strengths of S-200F and other beryllium grades are dependent on $d^{-\frac{1}{2}}$, where d is the grain diameter. The tensile strengths of the present beryllium grades at the respective test temperatures increase with decreasing grain size and can also be correlated with $d^{-\frac{1}{2}}$ as exemplified in Fig. 6.

The Hall - Petch relationships between the tensile lower yield (σ_y) and brittle fracture (σ_f) stresses and d are as follows [15][16]:

$$\sigma_y = \sigma_i + k\, d^{-\frac{1}{2}} \qquad (1)$$

where σ_i is a measure of the resistance of the lattice itself and impurities, precipitates, other dislocations, clusters of point defects, helium bubbles, etc. to dislocation movement, and

k is a measure of the tensile stress required to initiate plastic yielding in the grains ahead of the plastic front and, hence, the dislocation locking stress which is usually sensitive to both the test temperature and rate of straining.

$$\sigma_f = \sigma_i + k_f\, d^{-\frac{1}{2}} \qquad . (2)$$

where k_f is a measure of the tensile stress needed to crack the metal at the tip of a slip band or pile up of dislocations and is normally independent of temperature and rate of straining.

The unirradiated (reference) and thermally aged S-200F. HIP samples differ from those of the other grades in showing upper and lower yield points in the load - displacement curves at ambient temperature and 310 C whilst serrated yielding is often observed on testing at higher temperatures. Both "normal purity" and high BeO content beryllium are reported to exhibit yield points [12]. The yield point behaviour has also been observed in tensile tests on S - 65C. VHP beryllium at an initial strain rate of 1.1×10^{-4} s^{-1} and temperatures up to 500 C [6]. The yield point behaviour is attributed to the locking of the dislocations by the impurity atoms or precipitates of $AlFeBe_4$ or $FeBe_{11}$, as discussed in refs. [6][12]; in addition, the serrated yielding shown by the S-200F. HIP in tests at the higher temperatures is probably due to dynamic strain ageing as a result of the transient locking of the glissile dislocations. An analysis of the stress - strain curves for the S-200F. HIP beryllium samples exhibiting the yield point phenomenon shows that the lower yield stresses are determined primarily by σ_i [4], the dislocation locking term being relatively independent of test temperature and prior history.

Ductile fracture in tension occurs by the nucleation of voids as a result of the cracking or decohesion of hard particles in a soft matrix. The voids grow in three dimensions under the triaxial stress system established during the non - uniform (necking) deformation or at the root of a notch in tension. The voids eventually touch and the ligaments of matrix material extend so that each particle on the fracture surface lies in a dimple surrounded by edges and points. The rate of

increase of void size is dependent on the plastic strain, stress and stress state [17][18].

There is no systematic correlation between the ductilities of the unirradiated (reference) and thermally aged beryllium grades and their BeO contents in the tests at ambient temperature, 185 and 230 C; the beryllium specimens deform uniformly and fracture occurs in a relatively brittle manner without necking and the establishment of a triaxial stress system. However, the non - uniform ductilities at test temperatures of 310 to 605 C decrease with increasing BeO content in the range 0.6 - 1.2% (Fig. 7); this effect is tentatively attributed to the progressively increasing influence of the BeO inclusions acting as cavity nucleation sites and thereby facilitating ductile fracture. The behaviour of the S-65. HIP grade, with a BeO content of 0.5%, does not appear to be entirely consistent with this hypothesis as the ductilities are generally lower than those of the S-65. VHP containing 0.6% BeO. However, the strengths of the S-65. HIP grade at the relevant test temperatures are considerably greater than those of the S-65. VHP and the other beryllium grades, particularly at 540 and 605 C, thereby promoting ductile fracture with reduced ductilities. Furthermore, since the tensile strengths are proportional to $d^{-\frac{1}{2}}$, a fine grain size has an indirect effect in promoting ductile failure and lower ductilities at the higher test temperatures.

The enhancement of the non - uniform deformation and the associated improvements in ductilities produced by prior ageing are also evident in Fig. 7, particularly for the grades with the higher BeO and impurity concentrations tested at 455, 540 and 605 C; these beneficial effects of ageing are tentatively attributed to the reduced segregation of the impurity atoms at the BeO - matrix and other interfaces as a result of their precipitation as $AlFeBe_4$ and / or $FeBe_{11}$ intermetallic compounds, thereby inhibiting micro - void growth and coalescence and increasing the resistance to ductile fracture.

Intergranular failures of metals and alloys at elevated temperatures generally occur by wedge or cavitation fracture. Wedge cracks are formed at grain boundary triple junctions as a result of the stress concentrations produced by grain boundary sliding. However, wedge cracking is unlikely in the fine grained (6.6 to 8.4 μm) beryllium as it is computed that stresses in excess of the ultimate tensile strengths at temperatures of $\geq$ 500 C would be required to initiate this type of cracking [4]. There are several possible nucleation sites for grain boundary cavitation failures during testing at elevated temperatures, the favoured being non - wetting particles. The cavities on grain boundaries normal to the applied tensile stress direction grow by grain boundary vacancy diffusion and eventually coalesce to form intergranular cracks if the stress (σ_t) exceeds a value given by [19]:

$$\sigma_t = 2\gamma/r \qquad (3)$$

where γ is the effective surface for grain boundary fracture and r is the radius of the cavity.

$$2\gamma = 2\gamma_s - \gamma_{gb} \qquad (4)$$

where γ_s and γ_{gb} are the surface and grain boundary energies respectively.

Taking $\gamma = 1\ N.m^{-1}$, it follows that cavities with radii of $\geq$ 20 nm lying on the transverse boundaries will grow at temperatures at which grain boundary vacancy diffusion is sufficiently rapid at applied tensile stresses of 100 MPa. Thus, small non - wetting BeO particles and pores, high densities of which have been detected in the S-200F. VHP beryllium [3], may act as cavity nuclei for grain boundary fracture during the high temperature tensile testing.

2.2 Irradiation effects

All the beryllium grades exhibit significant radiation hardening (as evidenced by the increases in proof and ultimate tensile stresses) at irradiation / test temperatures of 185 to 485 or 540 C and severe embrittlement (decreases in the uniform and total elongations and reductions of area) over the whole irradiation / test temperature range investigated (Fig. 1). The hardening is most pronounced at temperatures of 230 and 310 C; progressive recovery of the radiation damage occurs with increasing irradiation / test temperature so that the proof and ultimate stresses are either

unaffected or reduced at 540 and about 600 C. Partial recovery of the ductilities also occurs at 485 and/or 540 C. but the total elongations and reduction of area values are again reduced on testing at the higher temperatures of 540 and/or 600 C. The maximum radiation hardening and embrittlement are generally produced at ~ 310 C. even though the displacement dose (0.8 dpa) and helium concentration (240 appm) induced during the irradiation at this temperature are minimal.

Fracture generally occurs within the elastic range of the stress - strain curves for irradiation / test temperatures up to 310 C The specimens irradiated and tested at the higher temperatures of 485, 540 and 600 C show plastic instability and fracture after limited uniform but significant non - uniform deformation.

The specimens irradiated and tested at temperatures up to 485 C fail primarily by brittle cleavage fracture but with some intergranular decohesion in the S-200F. VHP beryllium [3]; pronounced intergranular cracking and isolated regions of ductile dimple (micro void coalescence) are evident in the fracture surfaces of the samples following reactor exposure and testing at higher temperatures.

There is little to choose between the various grades with respect to radiation damage resistance at the lower temperatures (310 C) as they are all very brittle. However, the ductilities of the S-65. HIP beryllium are marginally superior at 485 C whilst the S-65. VHP and S-200F. HIP grades are slightly more ductile at 540 and ~ 600 C.

The radiation hardening and embrittlement at the lower irradiation / test temperatures result from the formation of vacancy and interstitial point defects, defect clusters, dislocation loops and intragranular helium bubbles. Theoretical considerations based on the cutting of the irradiation - induced obstacles by dislocations have shown that the lattice hardening is initially proportional to the square root of the neutron fluence (ϕt) or displacement dose (dpa) [20][21]:

$$\Delta\sigma_c = A(\phi t)^{\frac{1}{2}} \text{ or } B(\text{dpa})^{\frac{1}{2}} \qquad (5)$$

where A and B are constants.

However, the number of new obstacles formed during a given increment of fluence (or displacement dose) decreases as the fluence increases so that a saturation effect is obtained.

It has also been proposed [22] that the increased yield stress due to the pinning of the glissile dislocations by intragranular helium bubbles is given by the following relationship:

$$\sigma_{ib} = \sigma_u + Gb(N_b r_b)^{\frac{1}{2}} \qquad (6)$$

where σ_{ib} is the yield strength of the irradiated beryllium, σ_u is the unirradiated yield strength, N_b is the number of bubbles per unit volume and r_b is the radius of the intragranular bubbles.

This relationship has been applied successfully to predict the effects of irradiation on the yield strengths in earlier studies on hot pressed and extruded beryllium [23].

The 0.2% proof stresses for the unirradiated beryllium and for the irradiated beryllium grades exhibiting measurable plastic deformation prior to failure, together with the fracture stresses for cleavage, are shown as a function of irradiation and/or test temperature in Fig. 8. The cleavage fracture stress is reached before general yielding for most of the beryllium specimens at the lower temperatures as shown schematically in Fig. 5; the radiation damage enhances the shear stresses for basic and prismatic slip without significantly affecting the cleavage fracture stress so that the temperature at which some plasticity is restored is increased relative to that for the unirradiated beryllium. Furthermore, the data plotted in Fig. 9 demonstrate that the cleavage fracture stresses are proportional to $d^{-\frac{1}{2}}$, in accordance with the Hall - Petch relationship [equation 2].

Recovery of the strengths and, to a limited extent, the ductilities occurs at the higher irradiation / test temperatures as a consequence of the annealing and annihilation of the point defects and clusters and coarsening of the intragranular helium bubbles. However, the ductilities may be further reduced at the high temperatures as the helium bubbles nucleated on the grain boundaries orthogonal to the applied tensile stress can grow

continuously by the grain boundary vacancy diffusion process if the stress exceeds a critical value, assuming ideal gas behaviour, given by [24]:

$$\sigma_{crit} = 0.76\gamma/r_o \qquad (7)$$

where r_o is the initial radius of the grain boundary gas bubble.

It again follows, assuming $\gamma = 1$ N.m^{-1}, that helium bubbles with radii equal to or in excess of 7.6 nm lying on transverse grain boundaries will grow by this process at a stress of 100 MPa. The bubbles nucleate cavities which enlarge and coalesce to form cracks, resulting in premature intergranular failure with low ductilities in beryllium irradiated and tested at temperatures sufficiently high for the vacancies to be mobile. It is the fracture and not the deformation mode which is modified in this high temperature irradiation (helium) embrittlement process so that the ultimate tensile and proof stresses are not, in general, significantly affected.

3. FRACTURE TOUGHNESS

The fracture toughness of the unirradiated, aged and irradiated beryllium was determined according to: (a) The recommended LEFM procedures and the K_Q (or K_{1c} if all the ASTM validity requirements are satisfied) values quoted, or (b) EPFM J - integral procedures; the equivalent stress intensity factor K_{Jc} (= $\sqrt{JE(1 - \nu^2)}$), where J is the J - integral, E is Young's modulus and ν is Poisson's ratio, represents the fracture toughness when the fracture occurs in an unstable manner. However, it was difficult to define the point at which the crack initiated when the fracture occurred in a stable manner and the fracture toughness (K_{JcFmax}) was therefore determined at the maximum load.

The effects of thermal ageing, irradiation and test temperatures on the fracture toughness of the unirradiated (reference) beryllium are illustrated by the data for the S-65. HIP and VHP grades in Fig. 10. The principal observations may be summarised as follows:

(i) The fracture toughness of the unirradiated (reference) beryllium grades increases with increasing test temperature up to a maximum at 455 or 540 C and then decreases at higher temperatures.
(ii) Thermal ageing at 455 C increases the fracture toughness of all the beryllium grades in the tests at this temperature; however, the prior ageing has relatively little effect at the other test temperatures.
(iii) Irradiation has an extremely detrimental influence on the fracture toughness of the beryllium grades at all irradiation/test temperatures, the irradiation - induced reductions being most pronounced at about 450 or 540 C; the toughness at temperatures of $\leq$ 230 C is often reduced to below the fatigue pre - cracking level of about 9 MPa but some recovery is evident above about 435 C.
(iv) The differences in the fracture toughness of the respective beryllium grades in the irradiated condition are relatively small, with the exception that the S-200F. HIP beryllium is much tougher at irradiation / test temperatures of 435 and 600 C.

The fracture toughness values decrease progressively with increasing tensile proof and ultimate stresses for the unirradiated (reference) beryllium grades at test temperatures in the range 185 to 455 C [Fig. 11 (a) and (c)] and for the thermally aged materials at 185, 230 and 310 C [Fig. 11 (b)]. These inverse dependences of the fracture toughness on the tensile strengths imply that an increased grain size within the range 6.6 to 8.4 μm and reduced lattice hardening enhance the toughness at the low and intermediate test temperatures investigated in the BSBE Programme. However, the fracture toughness of the beryllium in the unirradiated (reference) condition at test temperatures of 540 and 605 C and of the thermally aged grades at 455 C increase with increasing reduction of area values in the tensile tests at the same temperature [Fig. 11 (d)]]. It follows that the fracture toughness of the beryllium at these higher test temperatures are reduced with increasing concentrations of BeO, other coarse inclusions and precipitates, and / or impurity elements; these features may restrict the non - uniform deformation in the tensile tests by promoting intragranular microvoid nucleation and coalescence and intergranular cavitation failures.

Although the irradiation and test temperatures, displacement doses and helium concentrations are

not precisely the same, the data in Fig. 12 illustrate that the tensile proof stresses and reductions of area and the fracture toughness exhibit similar dependences on the BeO (and / or impurity) contents of the beryllium. The superior toughness of the S-200F. HIP grade and the inferior toughness of the S-200F. VHP material in the post - irradiation tensile and fracture toughness tests at 485 and 435 C respectively are again apparent.

4. CONCLUSIONS

The main conclusions of this assessment are as follows:

(i) The tensile proof and ultimate strengths of the HIP and VHP S-65 and S-200F beryllium grades in the unirradiated (reference) and thermally aged conditions decrease progressively with increasing temperature from ambient to 605 C and, at a given temperature, increase with the inverse square root of the grain size (d) in accordance with the Hall - Petch relationship.

(ii) The results of an analysis of the tensile stress - strain curves for the S-200F. HIP beryllium suggest that the yield stresses are determined principally by the impurities, precipitates, etc. which increase the lattice friction stress opposing the movement of free dislocations..

(iii) The tensile ductilities of the unirradiated beryllium increase to a maximum at 230 - 310 C and then decrease at higher temperatures; thermal ageing increases the non - uniform ductilities of the S-200F grades in tests at 455 - 600 C, possibly as a result of the redistribution and/ or precipitation of the impurity atoms.

(iv) The non - uniform tensile ductilities generally decrease with increasing BeO and / or impurity content on testing at temperatures in the range 310 to 605 C.

(v) The present observations on the unirradiated (reference) and aged tensile tested beryllium samples are consistent with a change in primary fracture mode from brittle transgranular cleavage to ductile (dimple) fibrous and, possibly, intergranular with increasing temperature.

(vi) Irradiation produces marked embrittlement at irradiation/test temperatures of 185, 235 and 310 C but there is some recovery of the ductility at the higher temperatures of 485, 540 and 600 C. The enhanced tendency to cleavage fracture at the lower temperatures is associated with a larger irradiation - induced increase in the yield than in the fracture stress; the cleavage fracture stress is dependent on $d^{-\frac{1}{2}}$, again in agreement with the Hall - Petch relation. The irradiated samples show intergranular and/or ductile dimple fracture at the higher temperatures; the intergranular cracking probably results from the stress - induced growth and coalescence of adjacent grain boundary helium bubbles.

(vii) There is little to choose between the beryllium grades in respect of their resistance to radiation hardening and embrittlement at the lower irradiation/ tensile test temperatures ($\leq$ 310 C) as they are all brittle; however, the S-65 VHP and especially the S-200F HIP grades are more ductile at 435 to 600 C.

(viii) The fracture toughness values for the unirradiated (reference) and aged beryllium are broadly in agreement with the tensile data in that they increase up to a maximum at intermediate temperatures and decrease again at higher temperatures. The fracture toughness decreases with increasing tensile strengths at the low and intermediate temperatures and increases with increasing tensile reductions of area at the higher test temperatures.

(ix) Irradiation markedly reduces the fracture toughness at all temperatures but there is some recovery at an irradiation/test temperature of about 600 C; there are only small differences in the fracture toughness of the irradiated beryllium grades. Limited data suggest that there is a reasonable correlation between the fracture toughness and the tensile proof stress and / or reduction of area values for the irradiated beryllium.

5. LIMITATIONS OF THE EXISTING DATA AND FUTURE REQUIREMENTS

The BSBE Programme was initiated to provide data in support of the proposed application of beryllium as a neutron multiplier in a DEMO fusion power reactor blanket design based on the use of a solid lithium ceramic for the tritium breeding and helium as the coolant. However, this

initial concept, in which the beryllium is in the form of plates, has now been abandoned in favour of a design utilising small beryllium pebbles and, as a consequence, many of the original material and design data requirements are no longer applicable. Nevertheless, it is considered that the following additional investigations are necessary to validate some of the conclusions of the present assessment with respect to the factors determining the tensile and fracture toughness properties and behaviour of the unirradiated and irradiated beryllium, to advance our understanding of the effects of irradiation and, thereby, enable further progress to be made in establishing material composition - structure - property relationships:

(i) Detailed analytical TEM examinations of the (a) microstructures (BeO particles, precipitates, dislocations, etc.) of the unirradiated (reference) and thermally aged beryllium, and (b) radiation damage structure (point defect clusters, dislocation loops, inter - and intra - granular helium bubble sizes and densities, interfacial segregation and precipitation) for each of the beryllium grades as a function of the irradiation temperature, displacement dose and helium concentration.
(ii) Further SEM examinations of the existing specimens to elucidate the effect of temperature on crack nucleation and propagation modes for both the unirradiated and irradiated beryllium samples.
(iii) Additional irradiations of specimens, ideally to a number of equivalent displacement damage and helium concentrations at several irradiation temperatures in the range up to 600 C, followed by tensile and fracture toughness testing at the same temperatures, so as to allow a more precise evaluation of the effects of the irradiation variables to be made for a limited number of modern beryllium grades.
(iv) Development of an isotropic commercial beryllium product with a sub - micron grain size and low BeO and elemental impurity contents in an attempt to increase the cleavage fracture stress and the ductility and toughness at the lower temperatures. (It is probable that this objective can never be fully realised because of the inherent characteristics of the beryllium crystals [11]).

REFERENCES

1. D.R. Harries and M. Dalle Donne, "Beryllium Irradiation Embrittlement Test Programme: Material and Specimen Specification, Manufacture and Qualification", FZKA Report 5778, June 1996.
2. R. Chaouadi, F. Moons and J.L. Puzzolante, Proc. Third Int. Workshop on Beryllium Technology for Fusion, Mito City, Japan, October 1997, H. Kawamura and M. Okamoto (Eds.), JAERI - Conf. 98-001, January 1998, p. 241.
3. M. Verwerft, "Irradiation Effects in Beryllium: a Comparison of Powder Types and Consolidation Techniques", SCK/CEN Report TEC96/51. F040005/7/MV/mv, February 1997.
4. D.R. Harries, M. Dalle Donne and F. Scaffidi - Argentina, FZKA Report to be published.
5. L.L. Snead, "Fusion Materials Semiannual Progress Report for Period Ending June 30, 1998", U.S. Dept. of Energy, DOE/ER - 0313/24, September 1998, p. 215.
6. S.H. Goods and D.E. Dombrowski, as ref. 2, p. 39.
7. I.B. Kupriyanov et al, as ref. 2, p. 267.
8. D.E. Dombrowski, Brush - Wellman Inc., private communication, October 1996.
9. W. Haws, "Characterisation of Beryllium Structural Grade S - 200F", Brush Wellman Technical Memo. TM - 778, May 1985.
10. G.A. Henshall, S.G. Torres and J.E. Hanafee, "The Elevated Temperature Tensile Properties of S - 200E Commercially Pure Beryllium", Proc. 2nd. IEA Workshop on "Beryllium Technology for Fusion Applications", Jackson Lake, Wyoming, U.S.A., November 1995.
11. D.E. Dombrowski, E. Deksnis and M.A. Pick, "Thermomechanical Properties of Beryllium", Brush Wellman Engineered Materials Report TR - 1182, February 1995.
12. T.J. McCarville et al, "Technical Issues for Beryllium Use in Fusion Blanket Applications", Lawrence Livermore National Laboratory Report UCID - 20319, January 1985.
13. D.H. Hashiguchi, T.P. Clement and J.M. Marder, Modern Developments in Powder Met., 18 - 21 (1988) 627.
14. A.M. Khomutov et al, as ref. 2, p. 25.
15. N.J. Petch, J. Iron Steel Inst., 174 (1953) 25.

16. N.J. Petch, Prog. in Metal Phys., 5 (1954) 52.
17. F.A. McClintock, J. Appl. Mech., June 1968, p. 363.
18. J.R. Rice and D.M. Tracey, J. Mech. Phys. Sol., 17 (1969) 201.
19. R.W. Balluffi and L.L. Seigle, Acta Met., 5 (1957) 449.
20. A.D. Whapham and M.J. Makin, Philosophical Mag., 5 (1960) 237.
21. M.J. Makin and F.J. Minter, Acta Met., 8 (1960) 691.
22. R.S. Barnes, Proc. Int. Conf. on "The Metallurgy of Beryllium", London, October 1961, Chapman and Hall, London, 1963, p. 372.
23. G.P. Walters, Proc. Conf. on "The Physical Metallurgy of Beryllium", Gatlinburg, April/ May 1963, USAEC Report CONF-170, p. 138.
24. E.D. Hyam and G. Sumner, Proc. Symp. on "Radiation Damage in Solids and Reactor Materials", Venice, May 1962, IAEA, Vienna, p. 323.

Figure Captions

Fig.

1. Effects of ageing, irradiation and test temperature on the tensile properties of the S - 65. HIP beryllium.
2. Comparison of the BSBE and published data on the ambient and elevated temperature ultimate tensile strength and reduction of area values for S-65. VHP beryllium.
3. Comparison of the BSBE, BWI and LLNL data on the total elongations at ambient and elevated temperatures for S-200F. VHP beryllium.
4. Illustration of slip and cracking at the tips of slip bands.
5. Schematic illustration of the critical stresses for slip and fracture in unirradiated and irradiated beryllium.
6. Correlation of the tensile 0.2% proof stresses at test temperatures in the range ambient to 605 C with the grain sizes of the respective beryllium grades
7. Effect of BeO content on the tensile reduction of area values of the beryllium in the unirradiated (reference) and thermally aged conditions at temperatures in the range 310 to 605 C.
8. Effects of irradiation and/or test temperature on the tensile 0.2% proof and cleavage fracture stresses of the beryllium grades.
9. Effect of grain size on the cleavage fracture stress for the irradiated beryllium.
10. Effects of ageing, irradiation and test temperature on the fracture toughness of the S - 65. HIP and VHP beryllium.
11. Correlations of the fracture toughness with the tensile proof and ultimate strengths and reductions of area at elevated temperatures for the unirradiated (reference) and thermally aged beryllium grades.
12. Dependences of the tensile proof stresses and reductions of area and fracture toughness on the BeO contents of the beryllium grades irradiated and tested at 485/435 C.

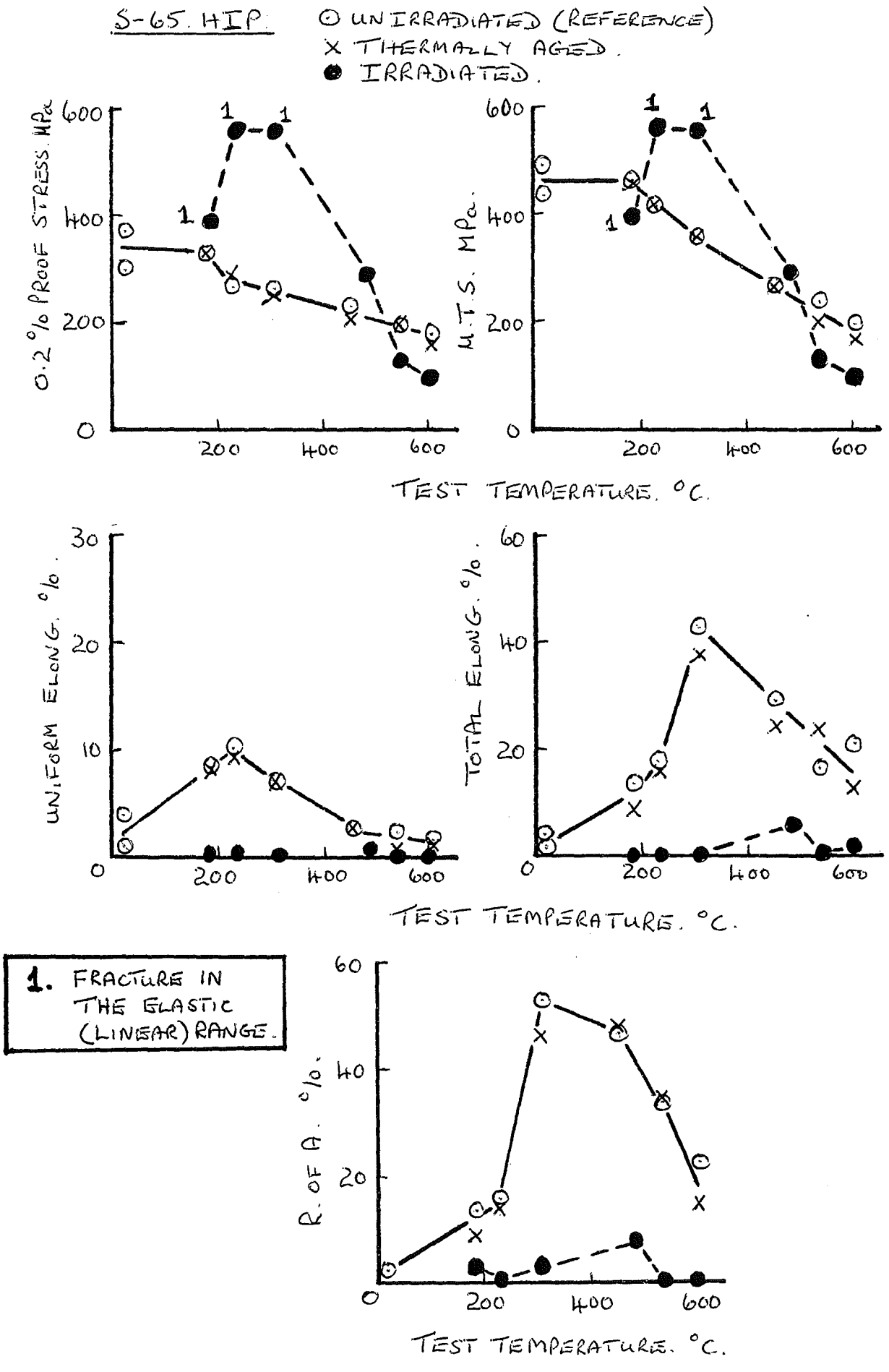
S-65. HIP
⊙ UNIRRADIATED (REFERENCE)
X THERMALLY AGED.
● IRRADIATED.
0.2 % PROOF STRESS. MPa
U.T.S. MPa.
TEST TEMPERATURE. °C.
UNIFORM ELONG. %.
TOTAL ELONG. %.
TEST TEMPERATURE. °C.
1. FRACTURE IN THE ELASTIC (LINEAR) RANGE.
R. OF A. %.
TEST TEMPERATURE. °C.

FIG. 1

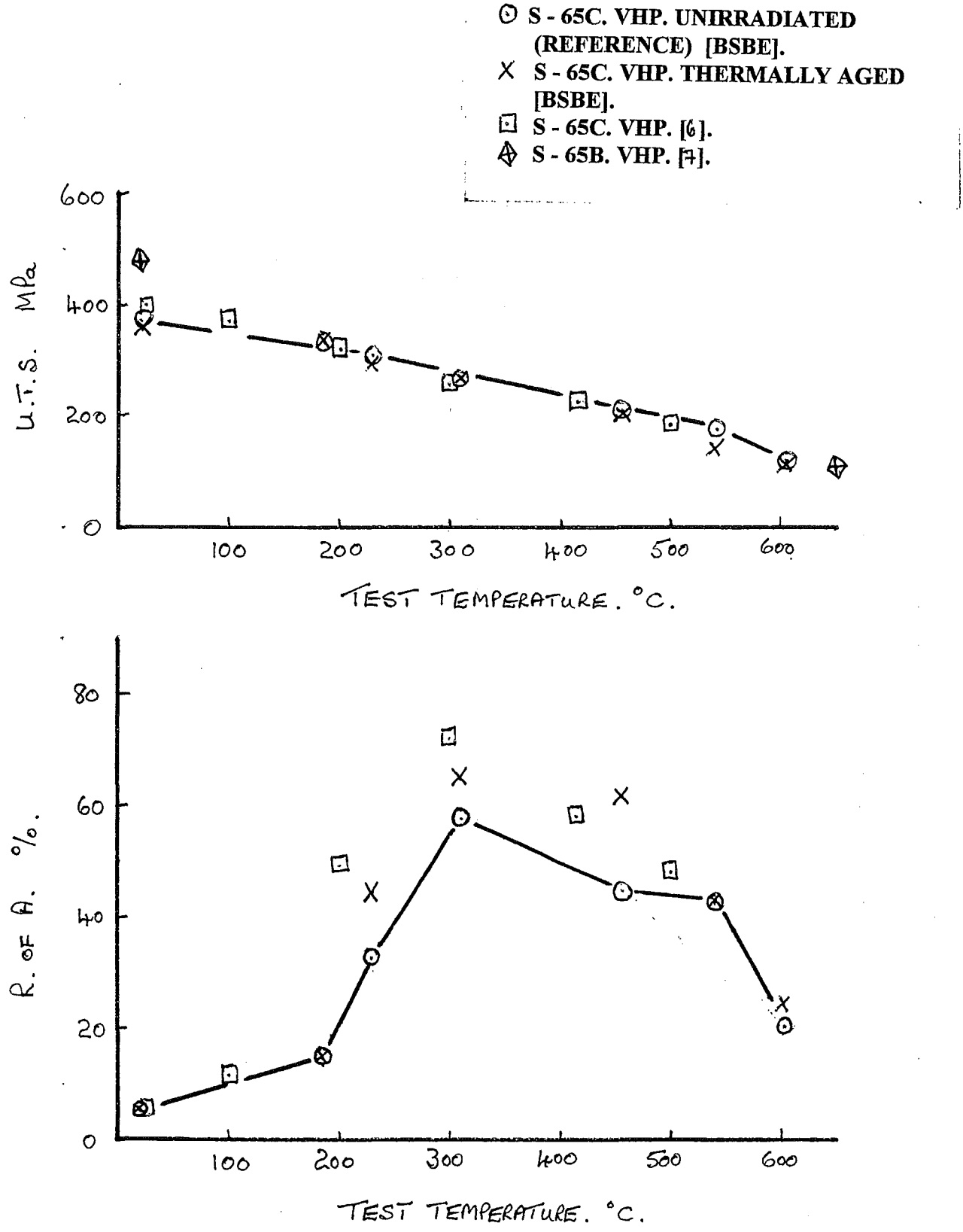
S - 65C. VHP. UNIRRADIATED (REFERENCE) [BSBE].
S - 65C. VHP. THERMALLY AGED [BSBE].
S - 65C. VHP. [6].
S - 65B. VHP. [7].
U.T.S. MPa
600
400
200
0
100
200
300
400
500
600
TEST TEMPERATURE. °C.
R. OF A. %.
80
60
40
20
0
100
200
300
400
500
600
TEST TEMPERATURE. °C.

FIG. 2.

S - 200F. VHP.

⊙ **UNIRRADIATED (REFERENCE) [BSBE].**

× **THERMALLY AGED {BSBE}.**

▽ **BWI DATA [8].**

⊡ **LLNL DATA [8].**

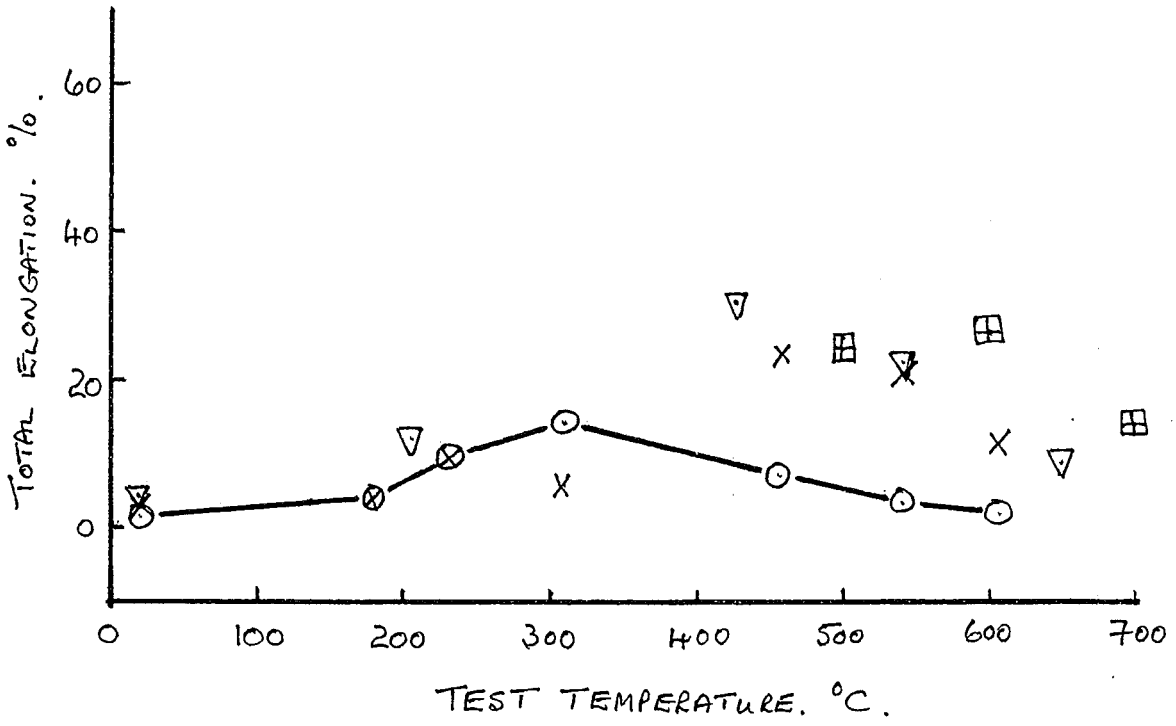

FIG. 3

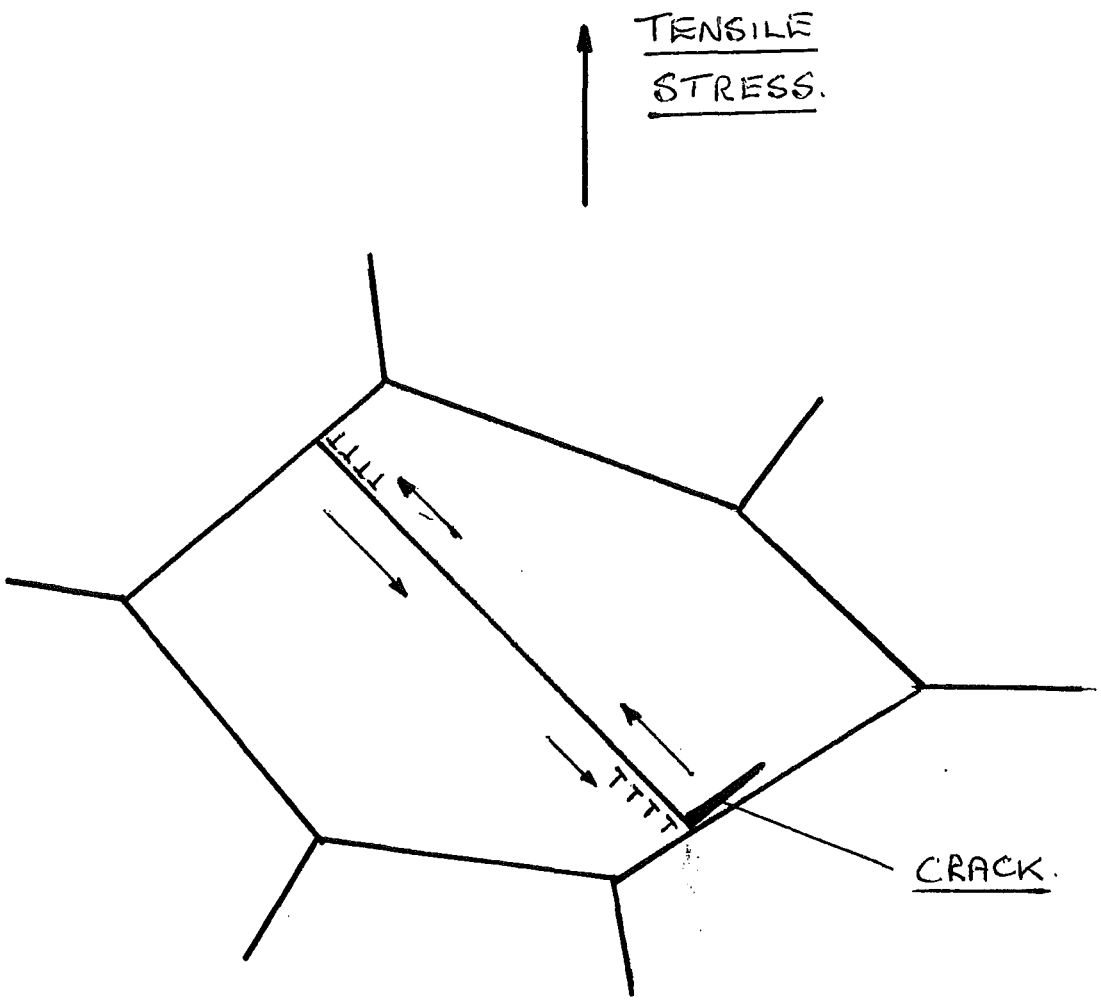

FIG. 4.

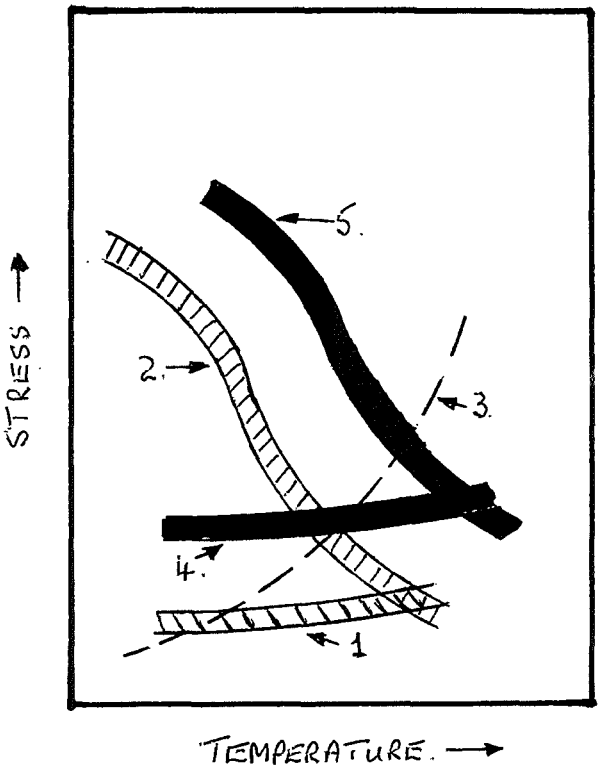

CRITICAL STRESSES FOR SLIP ON BASAL (1) AND PRISM (2) PLANES – UNIRRADIATED.

CLEAVAGE FRACTURE STRESS – UNIRRADIATED AND IRRADIATED (3).

CRITICAL STRESSES FOR SLIP ON BASAL (4) AND PRISM (5) PLANES – IRRADIATED.

FIG. 5.

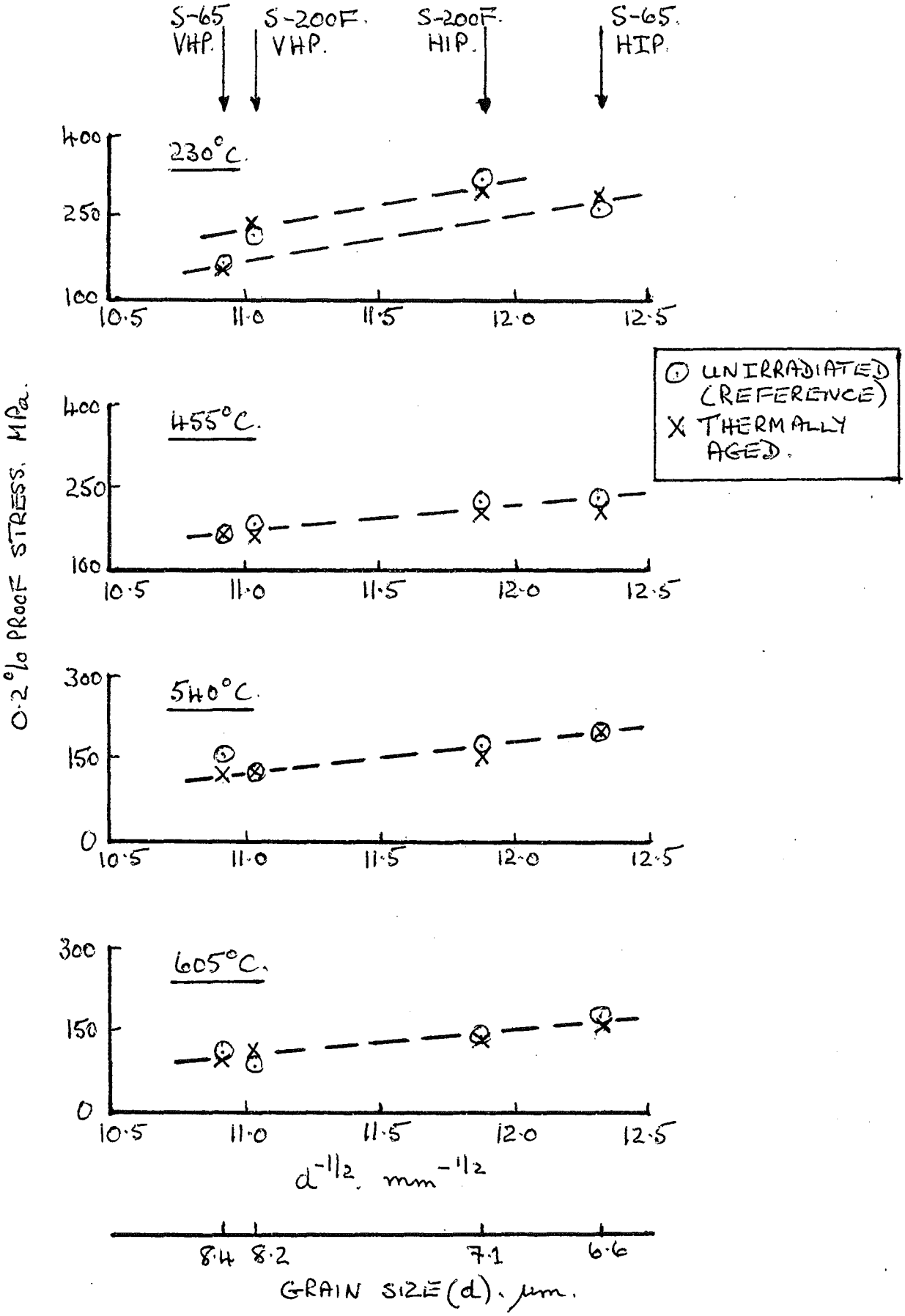
S-65 VHP.
S-200F. VHP.
S-200F. HIP.
S-65. HIP.
230°C.
455°C.
540°C.
605°C.
400
250
100
300
150
0
10·5
11·0
11·5
12·0
12·5
○ UNIRRADIATED (REFERENCE)
X THERMALLY AGED.
0·2% PROOF STRESS. MPa.
d^-1/2. mm^-1/2
8·4
8·2
7·1
6·6
GRAIN SIZE (d). μm.

FIG. 6.

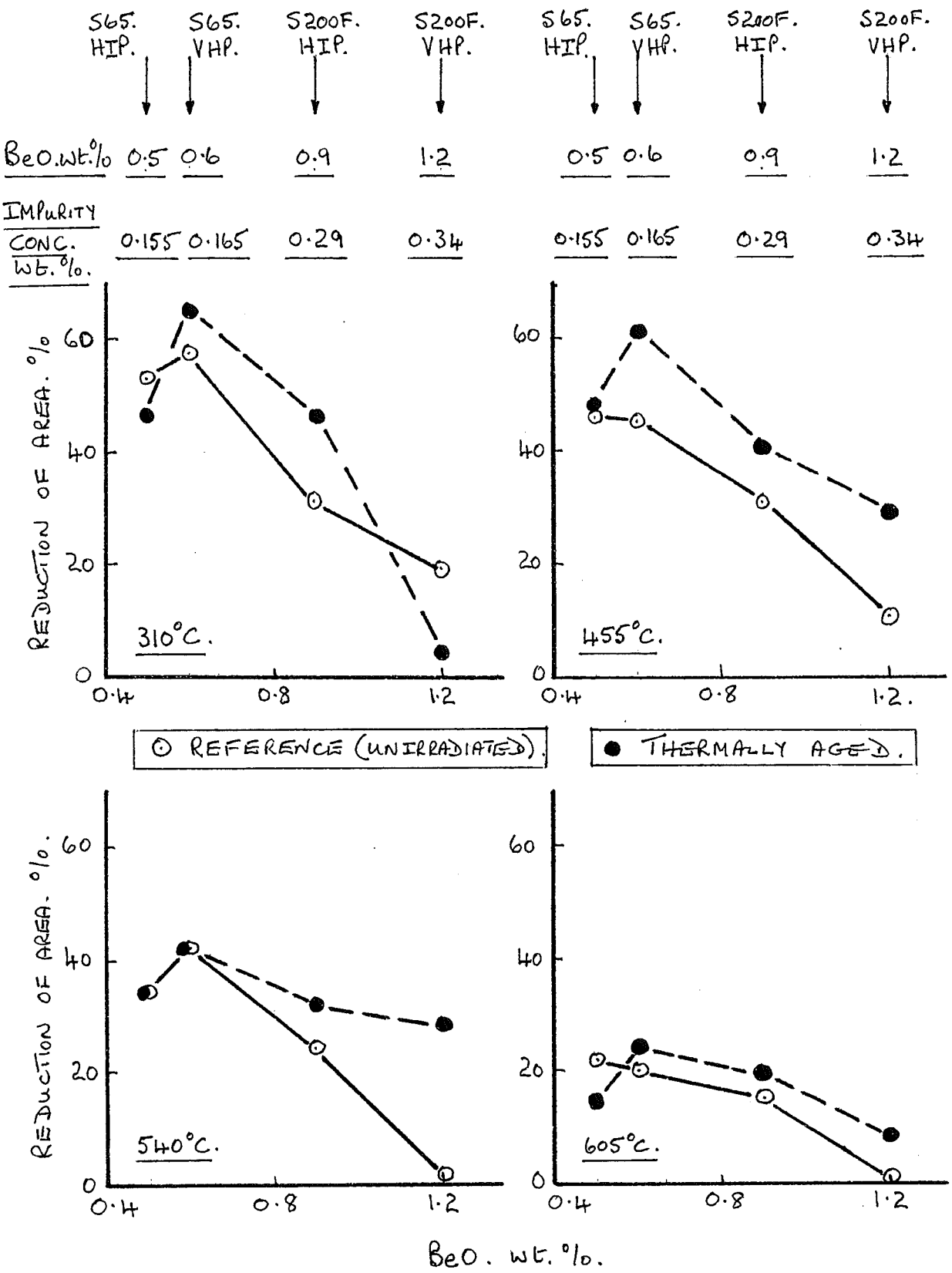
S65. HIP.
S65. VHP.
S200F. HIP.
S200F. VHP.
S65. HIP.
S65. VHP.
S200F. HIP.
S200F. VHP.
BeO. wt.%
0·5
0·6
0·9
1·2
0·5
0·6
0·9
1·2
IMPURITY CONC. wt.%.
0·155
0·165
0·29
0·34
0·155
0·165
0·29
0·34
REDUCTION OF AREA. %
60
40
20
0
0·4
0·8
1·2
310°C.
455°C.
540°C.
605°C.
⊙ REFERENCE (UNIRRADIATED).
● THERMALLY AGED.
BeO. wt.%.

FIG. 7.

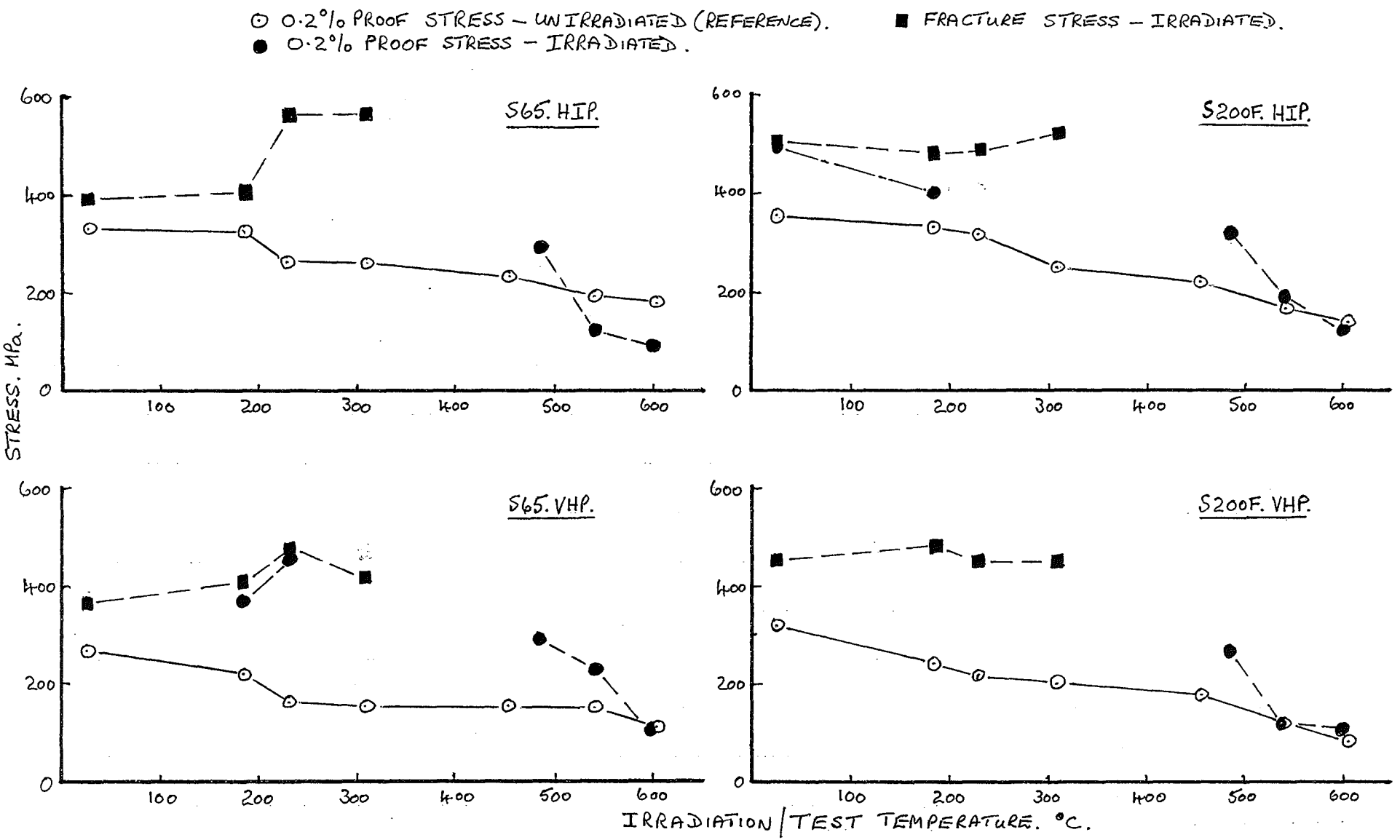
⊙ 0·2% PROOF STRESS – UNIRRADIATED (REFERENCE).
■ FRACTURE STRESS – IRRADIATED.
● 0·2% PROOF STRESS – IRRADIATED.
S65. HIP.
S200F. HIP.
S65. VHP.
S200F. VHP.
STRESS. MPa.
IRRADIATION / TEST TEMPERATURE. °C.
0
200
400
600
100
200
300
400
500
600

FIG. 8.

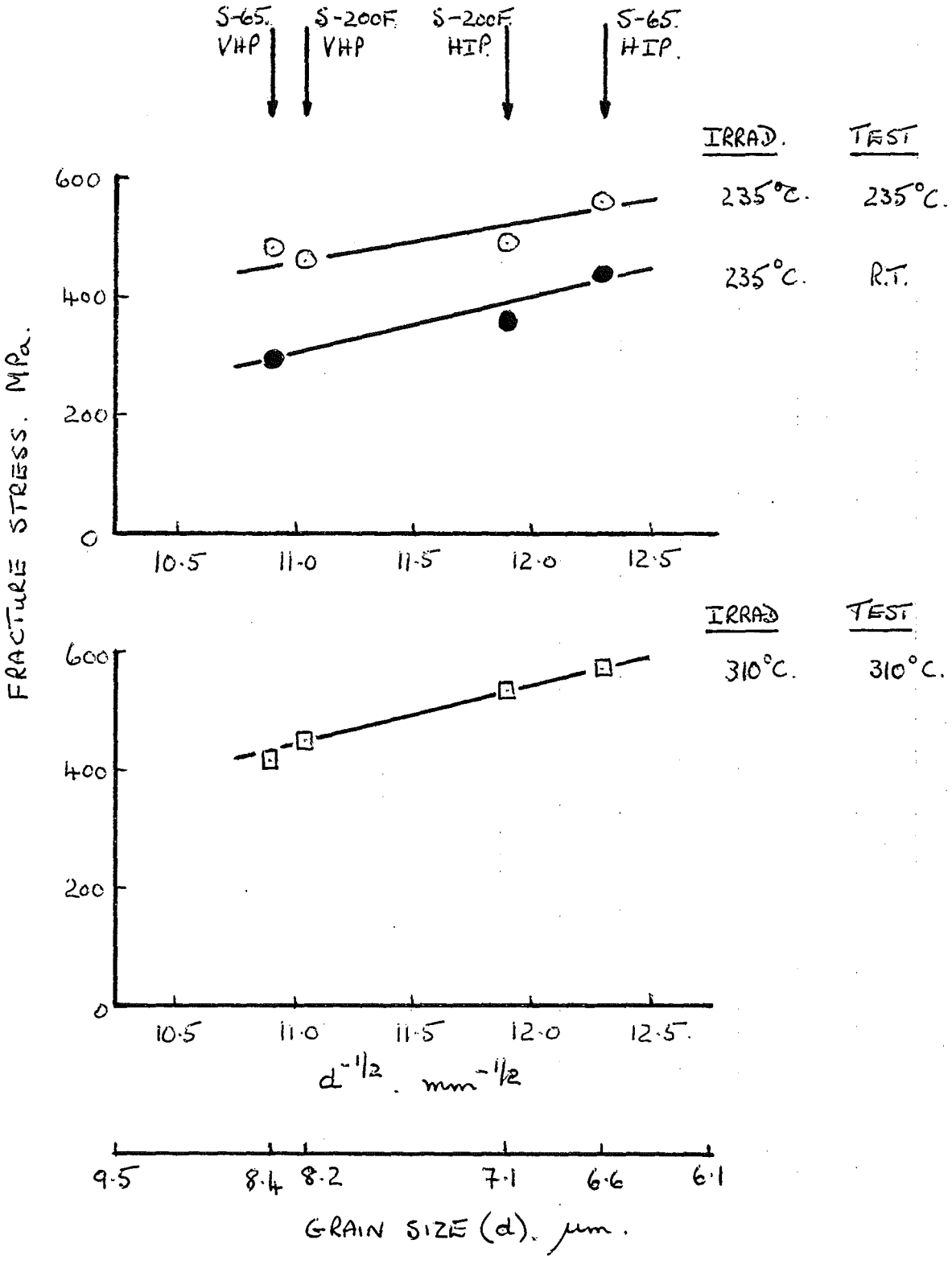
S-65. VHP
S-200F VHP
S-200F HIP
S-65. HIP
IRRAD. TEST
235°C. 235°C.
235°C. R.T.
600
400
200
0
10·5
11·0
11·5
12·0
12·5
IRRAD TEST
310°C. 310°C.
FRACTURE STRESS. MPa.
d^-1/2. mm^-1/2
9·5
8·4
8·2
7·1
6·6
6·1
GRAIN SIZE (d). μm.

FIG. 9.

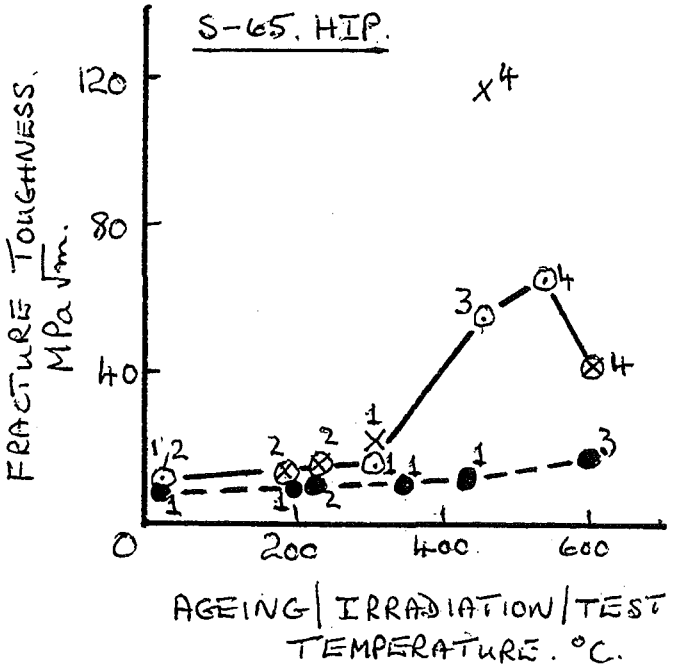

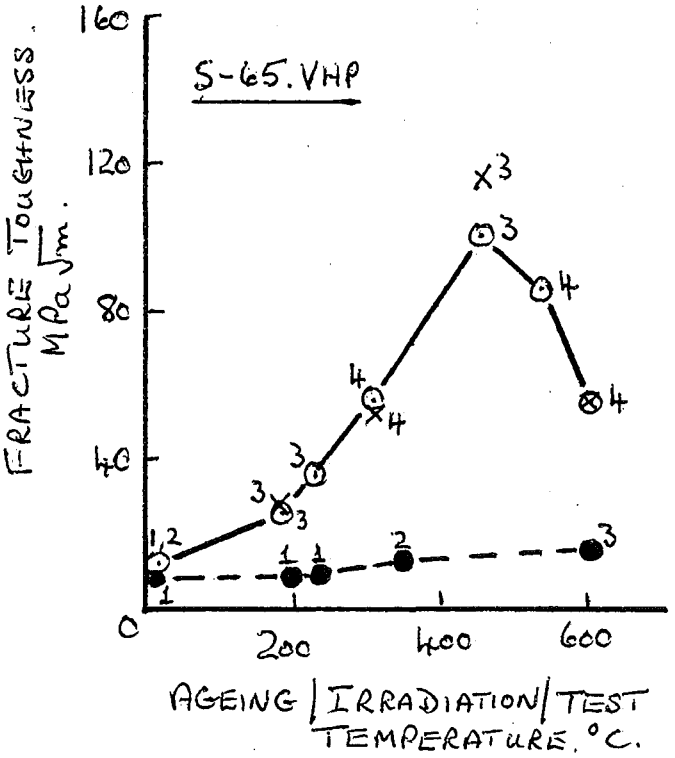

⊙ UNIRRADIATED (REFERENCE).
X THERMALLY AGED.
● IRRADIATED.
1. K_Q. 2. K_{Ic}
3 K_{Jc}. 4. K_{JcFMAX}.

FIG. 10.

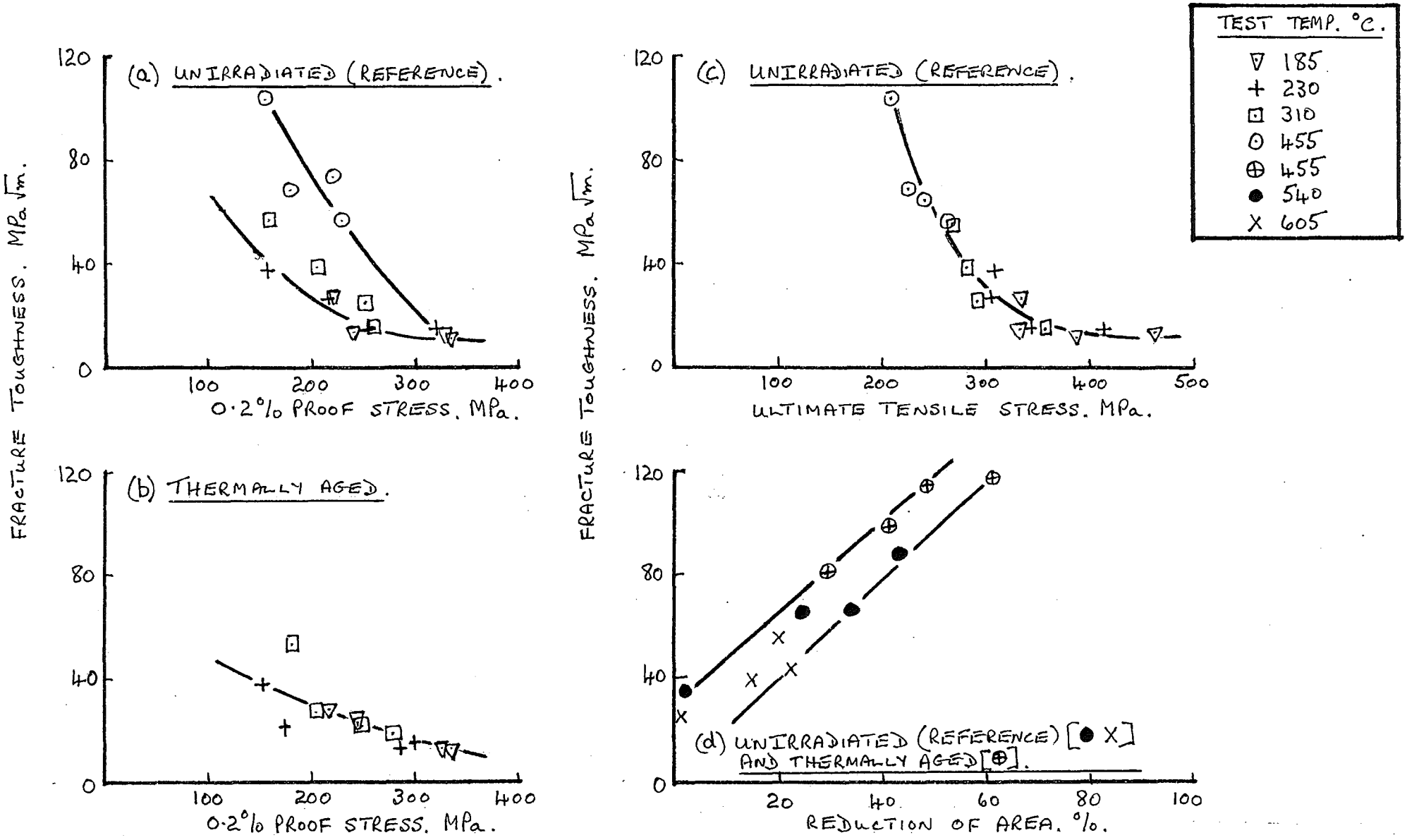
(a) UNIRRADIATED (REFERENCE).
(b) THERMALLY AGED.
(c) UNIRRADIATED (REFERENCE).
(d) UNIRRADIATED (REFERENCE) [● X] AND THERMALLY AGED [⊕].
FRACTURE TOUGHNESS. MPa √m.
0·2% PROOF STRESS. MPa.
ULTIMATE TENSILE STRESS. MPa.
REDUCTION OF AREA. %.
TEST TEMP. °C.
185
230
310
455
455
540
605

FIG. 11.

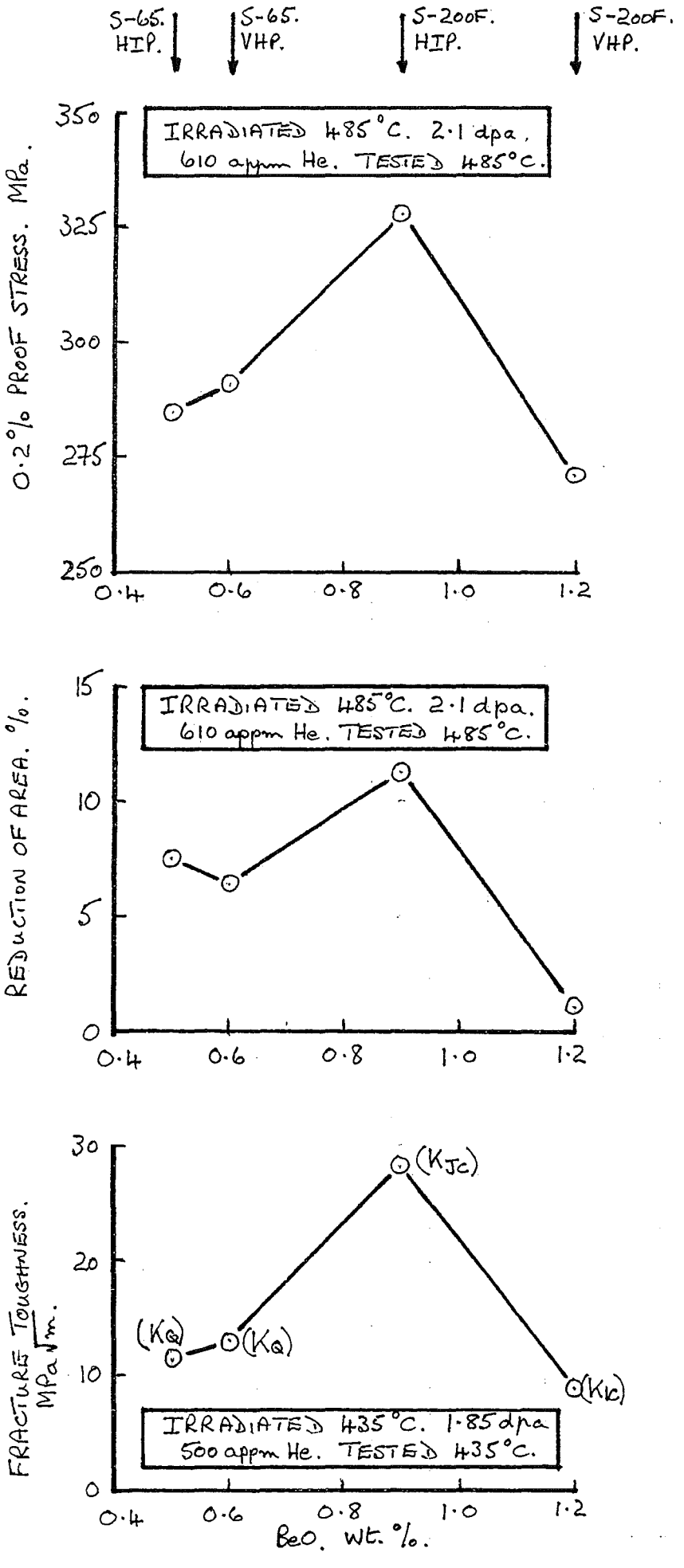
S-65. HIP.
S-65. VHP.
S-200F. HIP.
S-200F. VHP.
IRRADIATED 485°C. 2·1 dpa, 610 appm He. TESTED 485°C.
0·2% PROOF STRESS. MPa.
350
325
300
275
250
0·4
0·6
0·8
1·0
1·2
IRRADIATED 485°C. 2·1 dpa. 610 appm He. TESTED 485°C.
REDUCTION OF AREA. %.
15
10
5
0
IRRADIATED 435°C. 1·85 dpa 500 appm He. TESTED 435°C.
FRACTURE TOUGHNESS. MPa√m.
30
20
10
(KJC)
(KQ)
(KQ)
(KIC)
BeO. wt. %.

FIG. 12.

Radiation Effects on the Mechanical Properties of Irradiated Beryllium

R. Chaouadi [a], A. Leenaerts [a], J.L. Puzzolante [a] and M. Scibetta [a]

[a] SCK•CEN, Reactor Materials Research
Boeretang 200, 2400 Mol, Belgium

This paper aims to critically analyze the tensile and fracture toughness test results obtained on Beryllium irradiated in various conditions. Four ITER grade beryllium alloys (S65 and S200 powder, VHP and HIP consolidation) were tested in the reference condition, thermal aged condition and irradiated condition (fluence ~ 0.5 to 2.5 10^{21} n/cm, E>1 MeV; irradiation temperatures ~ 200 to 600°C). This data bank was systematically evaluated in terms of effect of material grade, effect of thermal ageing, effect of irradiation temperature and neutron fluence.

It is found that the four grades are quite similar and no thermal ageing effect could be evidenced. VHP materials exhibit lower strength than HIP samples but fracture toughness is significantly higher. Irradiation drastically reduces the ductility and fracture toughness. Scanning electron microscopic investigations revealed that irradiation at 600°C promotes intergranular fracture due to bubbles formed at grain boundaries.

1. INTRODUCTION

Beryllium is a material that has received at lot of attention within the fusion community. However, little is known on its mechanical integrity upon irradiation. More specifically, there is an obvious lack of experimental data on fracture toughness behavior of beryllium, in particular in the irradiated condition at high test temperatures. This is not only due to the inherent nature of beryllium (toxicity) but also the high costs of such tests. Furthermore, the parameters involved in the embrittlement mechanisms are so numerous that usually a large number of specimens is needed before being able to reliably understand and evaluate the effects of irradiation on the mechanical properties of beryllium. Indeed, the material (chemical composition, powder size, fabrication route, ...) as well as the environmental and testing conditions (temperature, fluence) play an important role. Most of published data concern the tensile or compression properties. Unfortunately, the materials grades, the irradiation and testing conditions are quite disparate that it is difficult to separate the importance and contribution of each parameter to the damage.

Within the European Long Term Fusion Technology Programme related to the ITER blanket design, a task T23 was performed at SCK•CEN on generating experimental data on tensile and fracture toughness of four ITER grade beryllium alloys [1,2]. Although large, this data bank suffers from the large number of involved parameters. However, it should be noted that originally, the aim of this investigation is to characterize beryllium manufactured by Brush Wellman using modern powder production and consolidation techniques irradiated and tested at high temperatures. Indeed, most of the experimental data available on the irradiation effects on beryllium were from

the 50's while the beryllium tested here was produced in the 90's.

The results of the T23 task were reported in [1] and presented at the 3rd IEA Workshop on Beryllium Technology for Fusion [2]. However, the fracture toughness test results were re-evaluated and both tensile and fracture toughness data were systematically analyzed in order to:

- Compare the SCK•CEN test results to literature data;
- Compare the four beryllium grades in the un-irradiated (baseline) condition;
- Evaluate the effect of thermal ageing if any;
- Investigate the effect of irradiation in terms of irradiation as well as testing temperatures and neutron damage (dose).

2. MATERIALS

All specimens were manufactured by Brush Wellman [3] using two powder grades, i.e., S65 and S200. The impact grinded powder was either axially vacuum hot pressed (VHP) S-200-F and S-65 or direct hot isostatically pressed (HIP) S-200-FH and S-65-H. The nominal chemical composition and tensile properties are reported in Tables 1 and 2. The four materials differ mainly by their Be- and BeO-contents. The HIP process results in higher strength (yield and ultimate stress).

Table 1.
Chemical analysis of the four beryllium grades (in wt. %) [3].

grade	Be	BeO	Fe	C	Al	Mg	Si	others
S65 VHP	99.4	0.6	0.06	0.03	0.02	<0.01	0.03	<0.04
S65-H HIP	99.5	0.5	0.06	0.03	0.02	<0.01	0.02	<0.04
S200-F VHP	98.9	1.2	0.10	0.12	0.05	0.02	0.03	<0.04
S200-FH HIP	99.1	0.9	0.10	0.08	0.04	0.02	0.03	<0.04

Table 2.
Density, average grain size and tensile properties at ambient of the four beryllium grades [3].

material grade	theoretical density (%)	average grain size (μm)	yield stress (MPa)	UTS (MPa)	total elongation (%)
S65 VHP	99.8	6.6	242	377	3.7
S65-H HIP	99.9	8.4	340	492	3.6
S200-F VHP	99.9	8.2	262	377	2.1
S200-FH HIP	99.9	7.1	352	441	5.0

3. ANALYSIS OF THE FRACTURE TOUGHNESS TEST RESULTS

Details on the test procedures and evaluation can be found in [1] and [2]. The fracture toughness test data evaluated in the elastic plastic fracture mechanics approach (K_{Jc}) given in [1] and [2] are not correct. Indeed, the test records being available in hard copy only (no digitized data), the area under the load displacement curves was evaluated using a planimeter device. However, the size reduction of the test records and the

planimeter calibration factor to accurately determine the actual area were not taken into account. This resulted in a small bias in K_{Jc} values when fracture occurs after a limited amount of plastic deformation but becomes significant for larger non linear displacements. Another correction was also considered here for the unirradiated samples for which the displacement should be corrected (reduced) to accommodate the difference between the load line displacement and the location of the extensometer. Finally, finite element simulation of the round compact tension specimen allowed us to verify the experimental measurements and therefore to confidently support the new data. It is important to notice that the discussion and conclusions given in [1] and [2] are not affected by these changes, the trends of fracture toughness evolution remain applicable. The corrected fracture toughness data are given in Tables 3 and 4 for the baseline and irradiated conditions, respectively. These data are obtained with precracked round compact tension specimens of 8 mm thickness and 16 mm width [1,2].

Table 3.
Fracture toughness data in the un-irradiated condition.

test T	ageing T	S65 VHP		S65 HIP		S200 VHP		S200 HIP	
20	-	11.8	a	10.8	a	11.5	♀♀♀♀	10.7	♀♀♀♀
	-	11.9	♀	11.2	♀	11.6		10.5	
	185	12.5	a	9.9	a	11.6		10.3	
	230	11.5	a	9.4	a	12.9		9.5	a
185	-	26.4	b	13.0	♀♀	14.4	a	11.3	♀♀
	185	28.0	b	13.6	♀	21.7	b	13.9	♀
230	-	37.5	b	15.1	♀♀	26.6	b	14.7	♀♀
	230	--		14.1	♀	20.2	b	15.1	♀
250	310	32.4	b	14.8	♀	30.2	b	14.8	♀
	455	--		--		11.3	a	15.3	a
	540	41.3	b	15.0	♀	48.9	b	17.9	a
	605	47.5	b	17.8	a	24.3	b	16.7	a
310	-	56.8	c	14.9	a	38.3	b	25.1	a
	310	53.1	c	21.2	a	26.1	b	18.6	a
455	-	104.4	c	73.3	c	68.5	c	74.1	c
	455	117.7	c	115.8	c	81.4	c	97.9	c
540	-	87.3	c	65.7	c	34.7	c	64.5	c
605	-	55.9	c	42.4	c	24.1	c	38.3	c
	605	55.9	c	40.9	c	43.5	c	38.5	c
	605	--		42.4	c	39.8	c	37.9	c

legend: (♀) ≡K_{IC} ; (a) ≡ K_Q ; (b) ≡ K_{Jc} and (c) ≡ $K_{J\,Fmax}$.

Table 4.
Fracture toughness data for the various testing and irradiation conditions.

test T	irrad. T	fluence	appm He	dpa	S65 VHP	S65 HIP	S200 VHP	S200 HIP
25	200 230	1.4 2.0	420 600	1.6 2.3	9.1 7.4	7.2 7.4	7.7 6.8	7.7 --
200	200	1.4	420	1.6	8.2	7.3	7.5	7.8
230	230	2.0	600	2.3	8.5	**10.1**	8.5	7.6
250	350 435 600 610	1.1 1.65 2.25 2.2	330 500 700 680	1.2 1.8 2.6 2.5	8.4 **10.8** **13.9** **11.2**	8.1 10.8 **12.6** **11.7**	9.0 7.6 **11.8** **13.4**	**11.4** -- **11.7** 11.4
350	350	1.1	330	1.2	**13.2**	9.7	--	**10.7**
435	435	1.65	500	1.8	--	11.6	**8.9**	*28.2*
600 610	600 610	2.25 2.2	700 680	2.6 2.5	-- *15.5*	*17.2* --	*14.3* *18.1*	*22.1* --

legend: K_Q in regular, **K_{Ic}** in **bold**, *K_{Jc}* in *italic*

4. DATA ANALYSIS AND DISCUSSION

4.1. Tensile test data:

The tensile test results performed at SCK•CEN were published in [1] and [2]. Three parameters are examined to investigate the effect of material grade, thermal ageing and irradiation: the strength (measured by the yield or ultimate stress), the ductility (reduction of area or total elongation) and the fracture stress.

The load –displacement curve of a tensile test of beryllium can be illustrated as shown in Figure 1. The effect of increasing test temperature and irradiation are also indicated. Five types of load-displacement behaviors can be differentiated (see Figure 1):

(a) premature fracture in the linear region;
(b) fracture occurs close to the yield strength;
(c) fracture occurs after plastic deformation but without necking;
(d) fracture occurs after significant necking;
(e) plastic instability: necking develops just after the yield strength is reached.

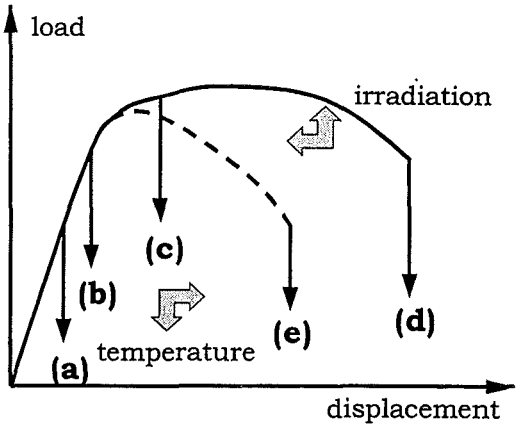

Figure 1. Typical load-displacement tensile behavior as a function of test temperature and irradiation

In the low temperature range, all specimens exhibit no necking: fracture occurs at or close to the maximum load (curve type 'c'). As the test temperature increases, the strength decreases (yield and UTS) while ductility improves (curve type 'd'). The maximum ductility is found

in the range of 300 to 500 °C. Above 500°C, the ductility starts to decrease but is still much higher than at ambient. The various Be-grades do not differ much except that the HIP process results in higher strength in comparison to the VHP process and that the ductility of the S200 VHP grade is significantly lower than the other grades.

Figures 2 and 3 show the evolution of the yield strength and ultimate stress as a function of test temperature. Comparison to published data [4-6] are also incorporated in these figures. A correlation was proposed by Billone [7,8] to estimate the yield strength and ultimate tensile stress of beryllium as a function of test temperature and porosity. Figures 1 and 2 show that the relations proposed by Billone overestimate the actual yield strength and ultimate tensile stress by about 20 and 50 MPa, respectively.

As mentioned before, in order to separate possible thermal ageing effects from radiation effects, a number of specimens were heat treated in the same temperature condition as experienced into the reactor, namely 2340 h at temperatures ranging from 185°C to 600°C. Figures 2 and 3 do not indicate any effect of the thermal ageing treatments. This is better illustrated in Figure 4, which shows at a single test temperature (250°C), no obvious effect of heat treatment could be evidenced. This is supported by Figures 5 and 6, which compare all tensile parameters in the reference condition and after thermal ageing treatment. This is also confirmed by transmission electron microscopy examination [9].

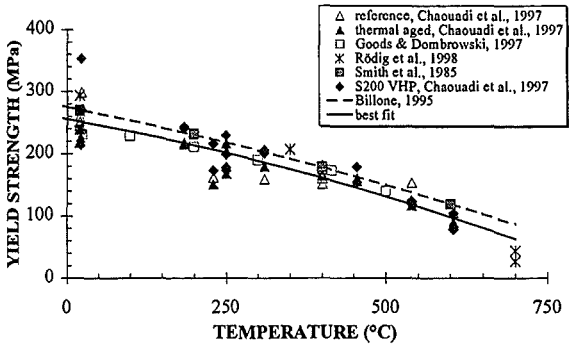

Figure 2. Yield stress as a function of temperature (S65 VHP).

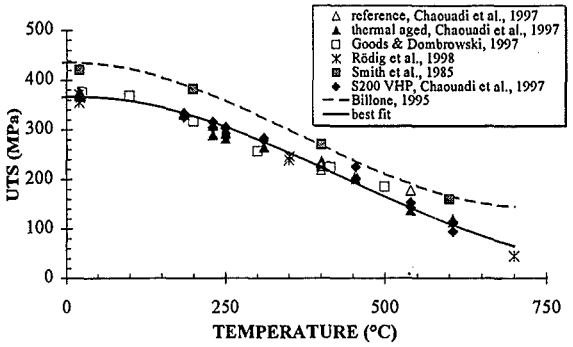

Figure 3. Ultimate tensile strength versus temperature (S65 VHP). The ultimate tensile strength (UTS) was chosen as it exhibits the lowest scatter in comparison to other parameters.

It is known that the main consequences of irradiation on the tensile properties are the increase of the strength (both yield and ultimate stresses) and the decrease of ductility (elongation, reduction of area).

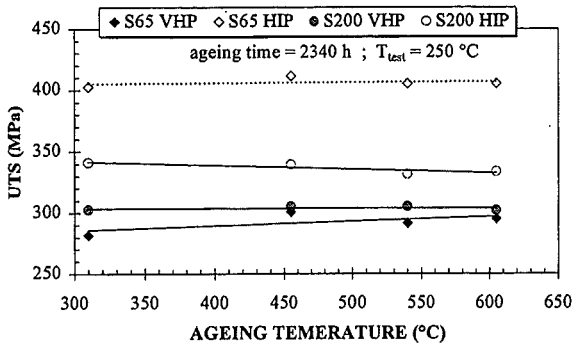

Figure 4. Effect of thermal ageing on the UTS.

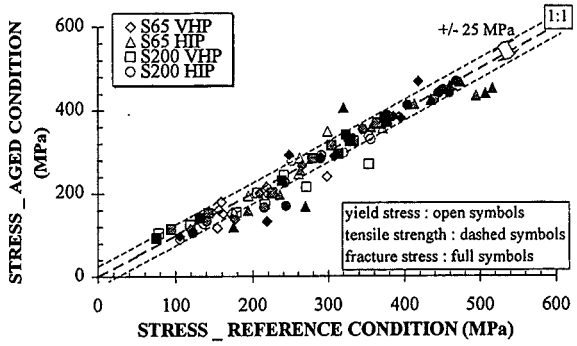

Figure 5. Within the experimental uncertainties, no effect of thermal ageing on the stresses.

As illustrated in Figure 1, up to 310°C, fracture occurs mostly within the elastic domain (curve type 'a' and 'b'). It should be emphasized that when fracture occurs in such a manner, the significance of yield stress and UTS loose their meaning, the fracture stress is more appropriate. At higher test temperature (485 to 600°C), fracture occurs after some non linear deformation but necking appears just after the yield strength is reached (curve type 'e'). This results in a plastic instability leading to fracture. It is important to note that in this temperature range, the hardening is modest compared to the low temperature range.

Billone [8] proposed also an empirical relation to estimate the yield strength increase. The main parameter in this relation is the helium concentration. However, as already mentioned, most of specimens do not exhibit a yielding behavior. Nevertheless, despite the high scatter, the yield strength increase is underestimated (see Figure 7).

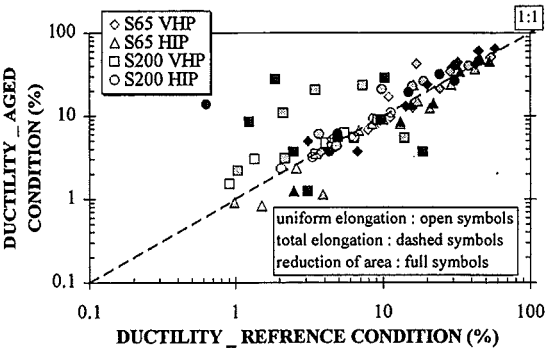

Figure 6. Ageing does not affect the ductility of the un-irradiated beryllium.

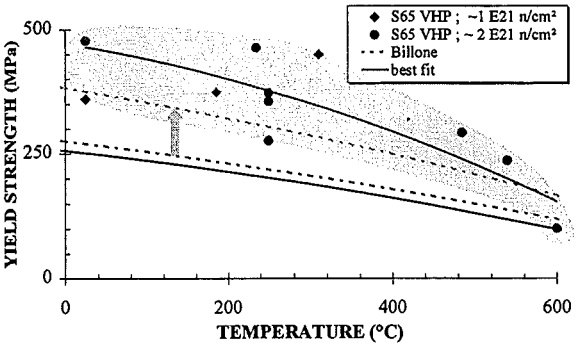

Figure 7. Yield increase as predicted with Billone relation: poor agreement with experimental data.

The effects of irradiation on both strength and ductility are illustrated in Figures 8 and 9. For most specimens, the stresses are increased while in some cases premature fracture occurs at stresses below the initial condition. On the other hand, ductility is drastically affected by a factor of about one order of magnitude upon irradiation. At higher test temperatures, the radiation effect becomes

modest in terms of strengthening mainly due to the irradiation temperature but the ductility is degraded.

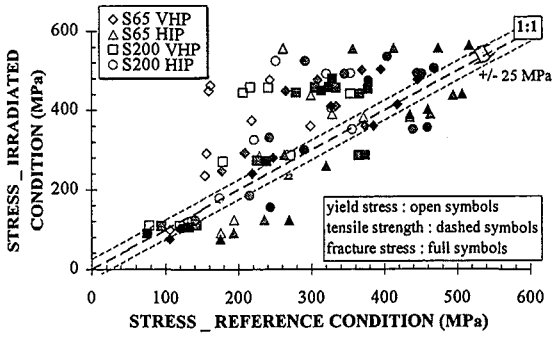

Figure 8. Radiation effects on the stresses. Stresses are much higher after irradiation except when premature fracture occurs.

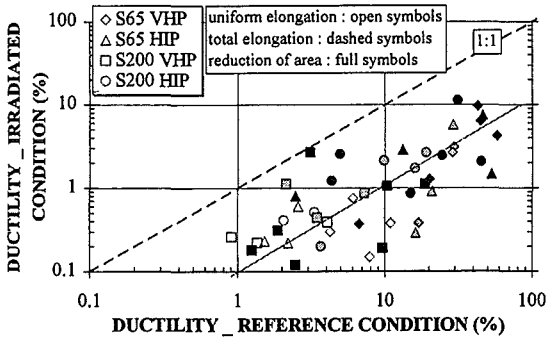

Figure 9. Radiation decreases ductility by one order of magnitude.

4.2. Fracture toughness data

Fracture toughness test results are summarized in Table 3 and 4 for un-irradiated and irradiated materials, respectively. The load –displacement curve of a fracture toughness test of beryllium can be illustrated as shown in Figure 10. The effect of increasing test temperature and irradiation are also indicated. Three types of load-displacement behaviors can be differentiated (see Figure 9):

(a) unstable fracture occurs in the linear elastic region (K_Q or K_{IC});
(b) unstable fracture occurs after non linear deformation but without ductile crack extension (K_{Jc});
(c) fracture occurs by a stable crack growth process (ductile fracture): initiation is assumed to occur at the maximum load ($K_{Jc\ Fmax}$).

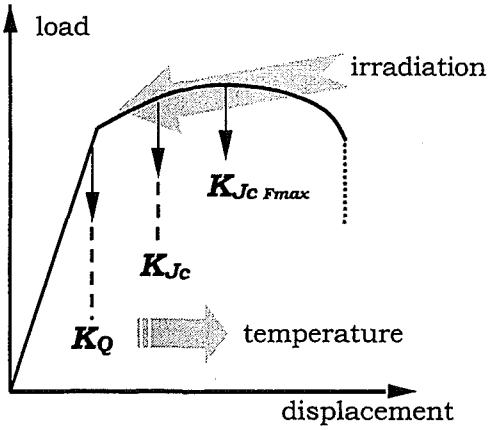

Figure 10. Typical load-displacement behavior as a function of test temperature and irradiation.

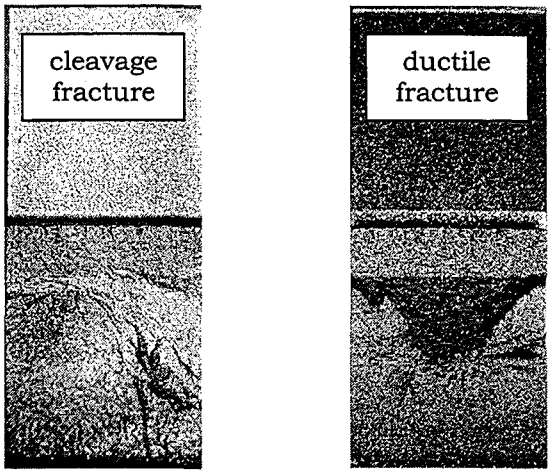

Figure 11. Fracture surface of broken compact tension specimen: cleavage versus ductile fracture.

The fracture surfaces of two round compact tension specimens tested at 310

and 455°C are shown in Figure 11. The fracture mode, cleavage versus ductile, can easily be identified.

As for tensile data, examination of fracture toughness data does not reveal any obvious thermal ageing effect. This is illustrated in Figure 12 where fracture toughness test data at the reference condition are compared to the thermally aged data. Within the experimental uncertainties, a one-to-one correlation can be observed. This is also supported by Figure 13 which compares the fracture toughness test results performed at 250°C. A slight increase of fracture toughness with increasing ageing temperature is observed with the S65 VHP grade. This does not seem to be the result of heat treatments but most probably this can be attributed to experimental scatter. On the other hand, comparison of the fabrication route, VHP versus HIP, clearly shows the superiority of VHP process (see Figure 14). Table 3 clearly shows that VHP grades fail within the LEFM (linear elastic fracture mechanics) domain only at 20°C while HIP grades fail in the LEFM in a large test temperature range (20 to 310°C). This is in agreement with the tensile data, which exhibit large flow stresses of the HIP grades in comparison to VHP grades. This can probably be associated with the different yield strengths of the two types of materials. Indeed, the stresses in the HIP grades are about 100 MPa higher than in the VHP grades. However, it should also be noticed that a size effect can be concerned. Both elements could support the possibility of loss of constraint with low yield strength materials tested with small fracture test specimens. Note also that the fracture mode may change by modifying the specimen size. Finally, the S200 VHP grade shows similar pattern as for the tensile data, i.e., a large scatter that may be attributed to material inhomogeneity.

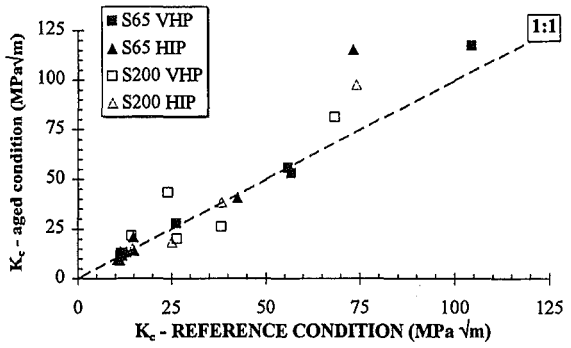

Figure 12. Thermal ageing effect of fracture toughness.

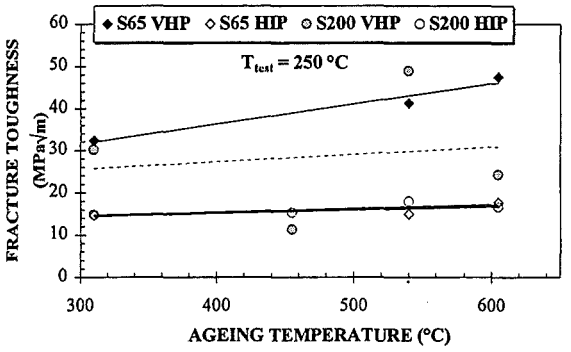

Figure 13. Effect of ageing temperature on fracture toughness: test temperature = 250°C.

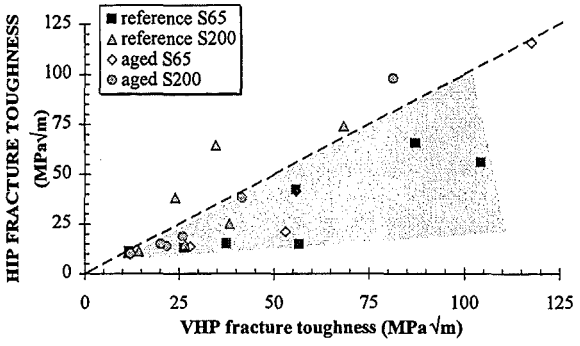

Figure 14. Fracture toughness of VHP beryllium is higher than HIP.

It is interesting to compare the fracture toughness results of Table 3 to literature data [10-14]. This comparison is depicted in Figure 15. At 20°C, a reasonable agreement is found despite the material variability. Most of these materials were fabricated by Brush Wellman but at different periods. Note also that Harrod et al. [7] used notched WOL (wedge opening loading) specimens. Their notch acuity is probably not as severe as a crack tip. At higher temperatures, i.e., 250 to 300°C, the disagreement between the various data sets on S200 VHP grade is obvious. However, not only the material batches are different, but also specimen size and configuration are different.

The 250°C to 310°C data comparison shown in Figure 15 are summarized in Table 5. As can be seen, the materials are not exactly similar, in particular the material of Perra and Finnie [12] exhibits a much higher tensile strength. The number of specimens is also limited. Therefore, it is difficult to actually address the size effect issue without performing detailed finite element calculations and probably some tests to support the calculations. This is out of the scope of the present paper.

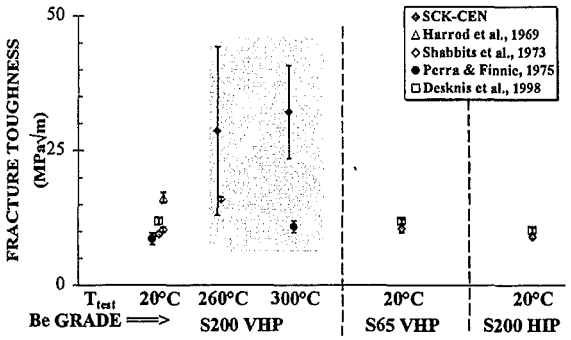

Figure 15. Reasonable agreement is found with literature although the material batches are quite different.

Table 5.
Specimen size effect of fracture toughness of S200 VHP grade.

T °C	N	specimen configuration	σ_y (MPa)	W (mm)	B (mm)	B_n (mm)	K_c (MPa√m)	reference
260	2	DCB	250	47	8.92	7.7	16.0 ± 0.4	Shabbits and Logsdon [11]
250	4	RCT	270	16	8	--	28.7 ± 15.6	this paper (Table 3)
300	6	CT	338	101.6	50.8	--	10.9 ± 1.1	Perra and Finnie [12]
310	2	RCT	270	16	8	--	32.2 ± 8.6	this paper (Table 3)

Legend: DCB=double cantilever-beam; RCT=round compact tension; CT=compact tension (ASTM E399); σ_y is the yield strength at 20°C; W is the width, B is the thickness, B_n is the net thickness (side grooved specimens), N is the number of tested specimens, T is the test temperature.

Upon irradiation, fracture toughness is drastically reduced at all test temperatures. This is illustrated in Figure 16 that clearly shows the high degree of degradation of fracture toughness. No ductile stable crack growth is observed with irradiated samples. Test temperature does almost not play any role. With reference to Figure 16 and Table 4, all samples fail in the LEFM regime except at 600°C where a small non linear deformation precede brittle fracture.

The brittle fracture can be associated with the high degree of radiation-induced hardening. Indeed, in the baseline condition, fracture occurs in cleavage up to 310°C and becomes ductile

for test temperatures ranging from 455 to 600°C. This means that the fracture mode changes around 400°C from cleavage to ductile. The yield stress at this temperature is close to 170 MPa. After irradiation, all specimens exhibit higher yield strengths at all temperatures except at 600°C.

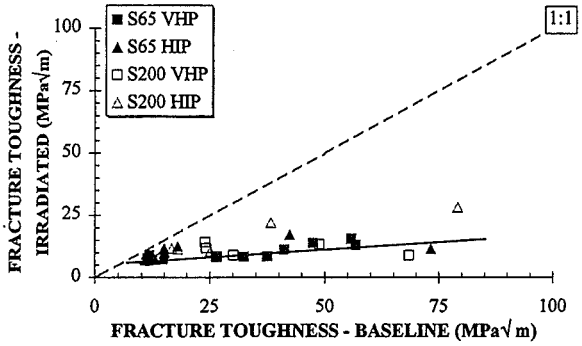

Figure 16. Drastic reduction of fracture toughness upon irradiation.

Extensive scanning electron microscopy (SEM) examination was carried out on the broken compact tension samples of S65 VHP grade. In the un-irradiated condition, from room temperature to 310°C, fracture is transgranular cleavage without any ductile crack extension (Figure 18-a). Between 455 and 600°C, the fracture mode is ductile. Figure 18-b shows the typical dimple fracture aspect as a result of the microvoid coalescence process.

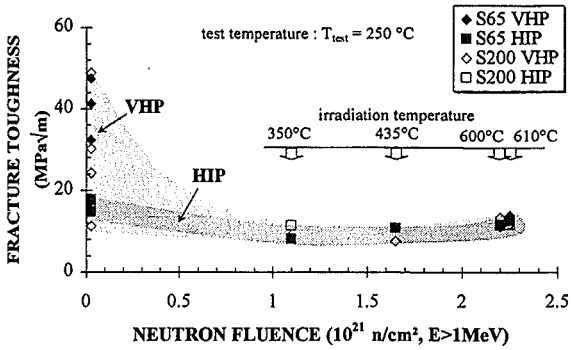

Figure 17: Comparison of irradiation effects on fracture toughness of VHP and HIP beryllium grades.

It is interesting to see that although VHP to HIP grades are different in the baseline condition from the fracture toughness point of view, upon irradiation no difference between the grades can be made (see Figure 17). This clearly indicates that improving the mechanical properties in the baseline condition does not guarantee a better resistance to irradiation.

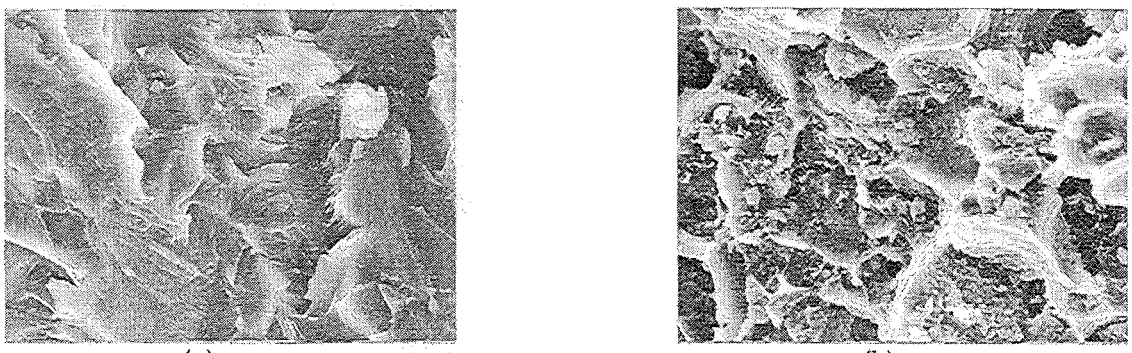

(a) (b)

Figure 18. SEM fractographic of unirradiated compact tension specimens: cleavage (a) and ductile (b).

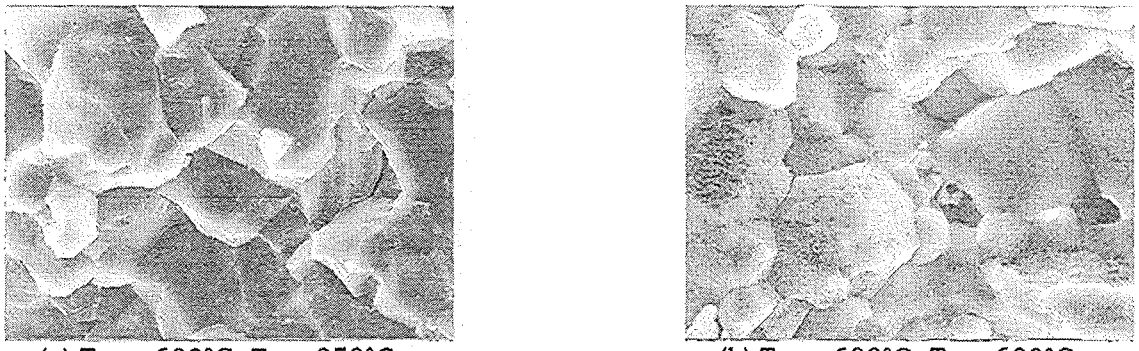

(a) T_{irrad}=600°C; T_{test}=250°C (b) T_{irrad}=600°C; T_{test}=600°C

Figure 19. SEM fractographic of irradiated compact tension specimens showing intergranular fracture.

Upon irradiation, test temperature is less important but irradiation temperature seems to promote intergranular fracture at 600°C. Indeed, all samples exhibit cleavage fracture except specimens irradiated at 600°C and tested at 250°C and 600°C. Figure 19-a and 19-b show the fracture surface for both test temperature. In Figure 19-b, a large number of small bubbles can be seen. This was also observed on the tensile specimens irradiated and tested at 600°C [15].

All fracture toughness test results data are shown in Figure 20. In the baseline condition, cleavage initiation toughness increases with testing temperature. Above 310°C, ductile fracture dominates. Ductile initiation toughness is maximum around 400°C and start to decrease with increasing test temperature. Irradiation suppresses the possibility of ductile stable crack growth. Within the experimental conditions considered here, there is no significant effect of neutron dose or test temperature.

Irradiation temperature equal or above 600°C promotes intergranular fracture, whatever the test temperature. The helium bubbles at grain boundaries were identified as the main source of embrittlement. Indeed, at 600°C, all point defects induced by irradiation are annealed. As a result, the yield strength remain almost unchanged. On the other hand, ductility is decreased by one order of magnitude. The weak grain boundaries provide privileged sites for premature fracture initiation.

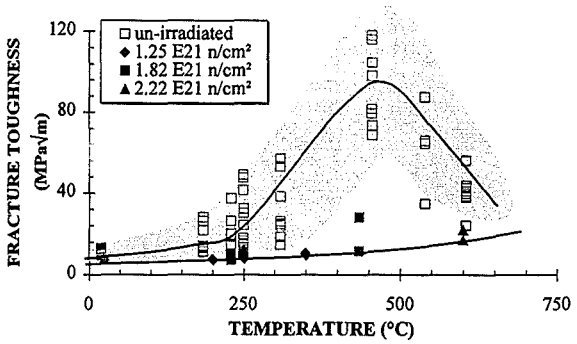

Figure 20. Radiation effect of the fracture toughness. No distinction can be made between the beryllium grades before and after irradiation.

Two embrittlement mechanisms were identified for irradiated beryllium [16,17]:

1. displacement damage: point defects that can cluster to form obstacles to dislocation motion;
2. helium production by transmutation (n-α reaction): formation of gas bubbles that act as obstacles to

dislocation motion but also that provide initiation sites for fracture.

The displacement damage is temperature sensitive. A recovery occurs for temperatures close to or above 600°C. On the other hand, helium bubbles are promoted by high temperature irradiation. This second embrittlement mechanism is the most problematic. With higher doses and helium production as will be experienced by a fusion machine, it is not known how beryllium will behave.

In the irradiated condition, only very limited experimental fracture toughness data were found [18,19]. On the other hand, materials, irradiation and experimental conditions are so different that it is extremely difficult to derive how fracture toughness varies with increasing neutron dose. Nevertheless, with the available data, the effect of neutron fluence on fracture toughness is represented in Figure 21. Irradiation temperatures are also indicated. All specimens are tested at 20°C. Neglecting the effect of material and the irradiation temperature (65 to 230°C), fracture toughness decreases with neutron fluence but saturates quite rapidly. However, extrapolation to very high neutron doses representative of a fusion machine is unknown, as long as the kinetics of damage accumulation is not available.

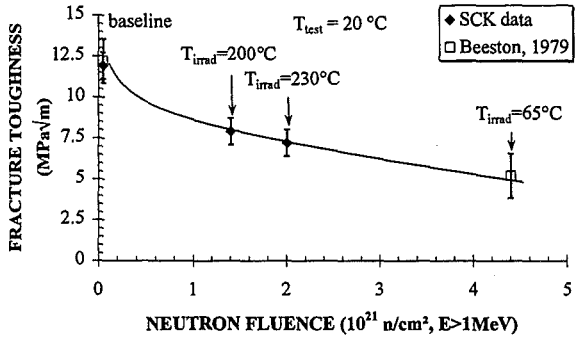

Figure 21. Radiation dose effect on fracture toughness.

5. CONCLUSIONS

The fracture toughness test results were re-evaluated in this paper. A systematic analysis of the data allowed to address the effect of material grade, thermal ageing and irradiation on the tensile and fracture toughness properties. Extensive scanning electron microscopic examination was conducted to better understand the fracture behavior of beryllium.

Systematic analysis of these data leads to the following outcomes:

1) In the baseline condition, the ageing treatment does not seem to significantly affect the tensile and the fracture toughness properties.
2) Irradiation results in strengthening of the material, loss of ductility and decrease of the fracture toughness. However, irradiation damage is much affected by the irradiation temperature.
3) The mechanisms of fracture are also affected by irradiation.

In the baseline condition, the transition from cleavage to ductile fracture mode of fracture toughness specimens occurs in the neighborhood of 400°C. Upon irradiation, ductile stable crack growth is suppressed. The material hardening resulting from defect points and helium production promote unstable fracture. Irradiation at higher temperature does not induce significant increase of yield strength, but a severe degradation of grain boundaries by bubble formation result in intergranular fracture.

Additional work is needed to address the possible specimen size effect in the baseline condition. This can also affect the ductile-to-brittle transition temperature. After irradiation, the 8 mm-thick round

compact specimens are adequate for measuring fracture toughness.

Note that in service, beryllium of the first wall will be exposed to energetic neutron bombardment resulting in the production of atom displacement damage of more than 70 dpa and the formation of helium will be about 1.6 10^4 appm at temperatures up to about 600°C. The helium embrittlement should be investigated with such levels, in particular the consequences on the mechanical properties, including thermal fatigue behavior.

ACKNOWLEDGMENTS

This work was supported by the European Commission Fusion Program. The authors gratefully acknowledge Marc Decreton for his strong support and interest.

REFERENCES

1. R. Chaouadi, F. Moons and J.L. Puzzolante, Tensile and fracture toughness test results of neutron irradiated beryllium, Final report ITER task T23, SCK•CEN report BLG-757, Mol, Belgium, Dec. 1997.
2. R. Chaouadi, F. Moons and J.L. Puzzolante, Tensile and fracture toughness test results of neutron irradiated beryllium, Proceedings of the 3nd IEA International Workshop on Beryllium Technology for Fusion, October 22-24, 1997, Mito City, Japan, pp. 241-253.
3. D.R. Harries and M. Dalle Donne, Beryllium irradiation embrittlement test programme – Material and specimen specification – Manufacture and qualification, Forschungszentrum Kalsruhe, FZKA-5778, June 1996.
4. S.H. Goods and D.E. Dombrowski, Mechanical properties of S-65C grade beryllium at elevated temperatures, Proceedings of the 3nd IEA International Workshop on Beryllium Technology for Fusion, October 22-24, 1997, Mito City, Japan, pp. 39-52.
5. M. Rödig, H. Derz, R. Duwe and J. Linke, Pre-irradiation characterization of beryllium and beryllium-copper joints, Final report ITER-task T1/3, Forschungszentrum Jülich, IWE-TN 1/98, 1998.
6. M.F. Smith, R.D. Watson, J.B. Whitley and J.M McDonald, Thermomechanical testing of beryllium for limiters in ISX-B and JET, Fusion Technology, Vol. 8, July, 1985, pp. 1174-1183.
7. M.C. Billone, M. Dalle Donne, R.G. Macaulay-Newcombe, Status of beryllium development for fusion applications, Fusion Engineering and Design, 27, 1995, pp. 179-190.
8. M.C. Billone, Recommended design correlations for S-65 beryllium, Proceedings of the 2nd IEA International Workshop on Beryllium Technology for Fusion, Sept. 6-8, 1995, Jackson Lake Lodge, Wyoming, pp. 348-363.
9. L. Coheur, J.M. Cayphas, M. Hou and P. Delavignette, Microstructural effects on neutron irradiation on beryllium, presented at the 4nd IEA International Workshop on Beryllium Technology for Fusion, September 15-17, 1999, Kalsruhe, Germany.
10. D.L. Harrod, T.L. Hengstenberg and M.J. Manjoine, Fracture toughness of beryllium, Journal of Materials, JMLSA, Vol. 4, No. 3, Sept. 1969, pp. 618-632.
11. W.O. Shabbits and W.A. Logsdon, S-200 grade beryllium fracture toughness properties, Journal of Testing and Evaluation, JTEVA, Vol. 1, N°. 2, 1973, pp. 110-118.
12. M.W. Perra and I. Finnie, Fracture toughness of a high-strength beryllium at room temperature and 300°C, Journal of Materials Science, 12, 1977, pp. 1519-1526.
13. M.W. Perra and I. Finnie, Fracture toughness tests of a high-strength beryllium from room temperature to

300°C, UCRL-51774, Lawrence Livermore Laboratory, March, 1975.
14. E.B. Deksnis, M.A. Pick and D.E. Dombrowski, Thermomechanical properties of beryllium, JET-IR(94)07, December 1994.
15. M. Verwerft, Irradiation effects in beryllium: a comparison of powder types and consolidation techniques, Progress report ITER task T23, SCK•CEN report BLG-735, Mol, Belgium, Feb. 1997.
16. D.S. Gelles, G.A. Sernyaev, M. Dalle Donne and H. Kawamura, Radiation effects in beryllium used for plasma protection, Journal of Nuclear Materials, 212-215, 1994, pp. 29-38.
17. D.S. Gelles, G.A. Sernyaev, M. Dalle Donne and H. Kawamura, Radiation effects in beryllium used for plasma protection, Proceedings of the 1st IEA Workshop on Beryllium for Fusion Applications, October 4-5, 1993, Kalsruhe, Germany, pp. 37-56.
18. J.M. Beeston, Fracture toughness of irradiated beryllium, Effects of Radiation on Structural Materials, ASTM STP 683, J.A. Sprague and D. Kramer, Eds., American Society for Testing and Materials, 1979, pp. 309-325.
19. J.M. Beeston, J.R. Longhurst, R.S. Wallace and S.P. Abeln, Mechanical properties of irradiated beryllium, Journal of Nuclear Materials, 195, 1992, pp. 102-108.

Microstructural effects of neutron irradiation in beryllium

L.Coheur*, J.-M. Cayphas, P. Delavignette, M. Hou,
Physique des Solides Irradiés, CP 234,Université Libre de Bruxelles, Bld du Triomphe B-1050 Brussels, Belgium

Abstract :Four various samples of beryllium have been irradiated in the BR2 reactor at three different temperatures: 200,400 and 600°C and at fluences between 2 and 3 dpa. These samples were examined before and after irradiation by TEM. This paper describes the results obtained and discussed them in correlation with theoretical calculations by molecular dynamics concerning the stability of various kinds of defects, such as dislocation loops, susceptible to occur in Be.
The formation of helium during irradiation seems to have an influence on the microstructure only for the samples irradiated at 400°C and 600°C. For these samples, helium bubbles are clearly observed at grain boundaries. Inside the grains some peculiar features are detected, the nature of which is still uncertain and is discussed in the paper.
At 200°C, there is only a small change with respect to the unirradiated samples. Dislocation loops are observed lying on the prismatic-type 2 planes of Be but such dislocation loops are already present in the unirradiated samples. Irradiation seems to increase their density but this observation is to be taken with care because of the heterogeneous distribution of the loops and the limited number of grains that could be observed under suitable conditions.
The differences in the fabrication schemes seem to have only a small influence, if any, on the microstructure after irradiation.

1.Introduction

The first examinations of the microstructure of irradiated Be date back to the beginning of the 60's when Be was envisaged as a potential canning material for fuel elements[1-6]. The main concern at this time was the production of He by the transmutation reactions and the investigations were directed to see how this He will behave in function of its concentration and of the irradiation temperature. Sometimes annealing experiments were performed on Be samples irradiated at low temperature, in order to simulate the Be behaviour during irradiation at elevated temperature or in order to study the thermal stability of the features observed in the low temperature irradiated samples. In these early times, replicas and TEM were both used for characterising the samples. The TEM imaging conditions are unfortunately not or insufficiently documented for checking now the validity of the conclusions drawn from these early observations. Roughly it can be summarised that no bubbles or irradiation defect clusters are found at temperatures less than 120°C [4]. Loops (not characterised) are observed after irradiation at 350°C [2, 3] but no bubbles. Bubbles are seen after irradiation at temperature >400°C [1, 4, 5]. Works by French scientists indicate that the He bubbles take the shape of thin hexagonal prisms lying on the basal plane [6].
A limited amount of studies occurred in the 70's [7-13]. They confirmed that at low temperature (~80°C) no effects of irradiation are detected [13] but that annealing of these samples at higher temperature (400-900°C) leads to the formation of bubbles on grain boundaries and at inclusions interfaces [7, 8]. In one examination of Be irradiated at a temperature < 130°C, scientists have noted the presence of black clumps and loops [9].

* The experimental part of this work has been carried out at the LHMA department of CEN/SCK where this author was an employee until last year

Irradiated at temperatures of 550°C, Be samples show bubbles at grain boundaries and in the grains, mainly on dislocations [11]. However at 750°C, no bubbles of a detectable size were observed after irradiation. Annealing of the samples at 800°C gives rise to a precipitation of fine bubbles in the matrix and of relatively larger bubbles at dislocation networks and grain boundaries.

Due to the regain of interest in the irradiation behaviour of Be motivated by its possible use in fusion reactors, new examinations have recently been carried out [14-17]. For the first time, Gelles and Heinisch [14] detected small c-type loops in samples irradiated at 400°C but not at 500°C. He bubbles were present at both temperatures in low angle grain boundaries and dislocations appear as a necklace of dark pearls. The largest bubbles presented facets and sharp corners. This was interpreted as the onset of swelling. Very recent Russian works on various kinds of commercial and experimental Be confirmed that at 150°C no bubbles or irradiation defect clusters are present. In the samples irradiated at 650-700°C, bubbles are observed at grain boundaries, inside the grains and at the interfaces with a second phase. The matrix bubbles are generally thin discs lying on the basal plane. This plate like shape is also observed by [16] in samples irradiated at 400°C, no radiation complexes were detected at this temperature. Irradiation at 790°C were also carried out in this work. In addition to a great density of pores located at the grain boundaries it was observed that the matrix contained parallelepipeds on dislocations or subgrain boundaries. Examinations of small Be pebbles irradiated at 390°C were recently reported [17]. They reveal the presence of many small features tentatively identified as bubbles lying as plate like features on the basal plane. The authors compared these features with the micrographs of Gelles and Heinisch [4] and found a contrast similar to that of the c-type loops. They assume that c-type loops can accumulate gases such as He or ^{3}H, eventually becoming highly anisotropic bubbles. These previous works can be summarised as follows. The fine microstructure is not modified by neutron irradiation at temperatures lower than 200°C. It is believed that all the He atoms are in solid solution in the Be. After irradiation at temperatures higher than 200°C, bubbles are detected at grain boundaries and in the matrix. At 400°C, but not at 500°C, c-type dislocation loops are detected by Gelles and Heinisch [4] and also by Dalle Donne [17]. There is a marked interaction between these bubbles or cavities and the dislocations. Some faceting of the bubbles has been reported.

2. Experimental

Samples of Be fabricated by Brush-Wellman (BW) following four different methods have been irradiated in a special rig in the BR2 reactor during five cycles in 1993 and 1994. The design of the rig has been extensively described and the progress of the experiment has been reported by A. Rahn in [18]. A full characterization of the starting material can be found in [19]. Table 1 gives a summary of the main material parameters. As far as TEM is concerned, the material which has been irradiated and examined had the shape of thin discs: 0.2 mm thick and 3 mm diameter. The discs were prepared by BW by grinding slices cut from Be pieces. For control, discs from the same fabrication and prepared following the same way were annealed at the same temperature as the irradiated temperature in a similar rig outside the reactor. The discs were arranged horizontally between two small meshed metallic nets, in direct contact with the NaK filling the capsule. Two discs per designation were irradiated at each temperature and examined. The fluence experienced by these discs is the same for all the discs at the same location. It is deduced from the fluence profile established for the rig by measurement of the different dosimeters. The irradiation data were analyzed by De Raedt in [19]. Table 2 sums up the main irradiation parameters concerning the TEM samples

Table 1: Material parameters.
HIP: hot isostatic pressing, VHP: vacuum hot pressing

Designation	Type of powder	Oxygen contents (BeO) (wt%)	Consolidation method
S-65 HIP	S65	0.5	HIP
S-65 VHP	S65	0.6	VHP
S-200 HIP	S200	0.9	HIP
S-200 VHP	S200	1.2	VHP

Table 2:Irradiation parameters

Temperature (°C)	Fast fluence (>1MeV) 10^{21} n/cm^2	He concentration (appm)	dpa
216	1.7	560	2.12
473	1.7	580	2.02
607	2.0	690	2.55

After irradiation, or control thermal treatment, the discs were covered by a dark adherent layer, which likely results from a reaction with the NaK. This layer was removed by gentle mechanically polishing up to a thickness of 150 µm. The control samples were electrolytically thinned with an electrolyte consisting of 5 percent nitric acid, 1 percent hydrochloric acid, 1 percent sulfuric acid, 31 percent ethylene glycol and 62 percent ethyl alcohol at 5°C and 35V.
The samples were not very satisfactory (deposit, small electron transparent areas, pitting) but useful locations were however found and suitable examinations carried out. Preparing the irradiated samples following the same way was found unsuccessful. The same difficulty as those encountered before were found but to such an extend that no part of the sample could be examined. Other conditions have been used, namely an electrolyte consisting of 25 percent nitric acid in methanol at -20 °C and 10V.
Better results, although not yet very good, were obtained. TEM examination of both kinds of samples (unirradiated and irradiated) was carried out with a Philips EM300 electron microscope operating at 100 keV and equipped with a single tilt goniometer

3. Observations

The results concerning the unirradiated samples and the influence of a thermal annealing at the same temperature as the irradiation temperature are first presented. After that and because all the four kinds of specimens were found to behave similarly, the only marked differences being the fact of the temperature, the observations of the irradiated samples are presented following this parameter

3.1 Unirradiated and annealed samples.

The results of these examinations were already presented in a progress report [21]. No differences concerning the fine microstructure (due to the limited size of the examined area in our TEM samples, nothing can be said about grain size) has been observed which could be related to the differences between oxide content or consolidation method. Some striking features emerge from these observations and two of them are particularly

relevant. The first one is the large proportion of low angle grain boundaries. This is illustrated in the progress report referenced above. The second one is the occurrence in some grains of a large density of dislocation loops. These loops have an elliptical shape and are located on the prismatic planes of type 2. The Burger vector was found to be 1/3 $<1\bar{1}20>$. No influence of the temperature of the thermal treatment has been detected.

3.2 Irradiation at 216 °C

At first sight, the fine microstructure is unchanged compared to the control samples. Some grains are displaying a high concentration of elliptical dislocation loops, which have the same characteristics as that observed in the unirradiated condition, i.e. they lie on the prismatic-type 2 planes and have a Burgers vector equal to 1/3 $<1\bar{1}20>$. Such dislocation loops are illustrated in figure 1. Because of the limited extension of good areas for observation, nothing can be concluded concerning the dislocation density or the abundance of small angle grain boundaries. Careful examination of the thinnest areas reveal however the presence of very small features (3-5 nm) in the matrix, too small to be characterized but which are believed to be defect clusters by similarity with the observations at 473 °C and 607 °C

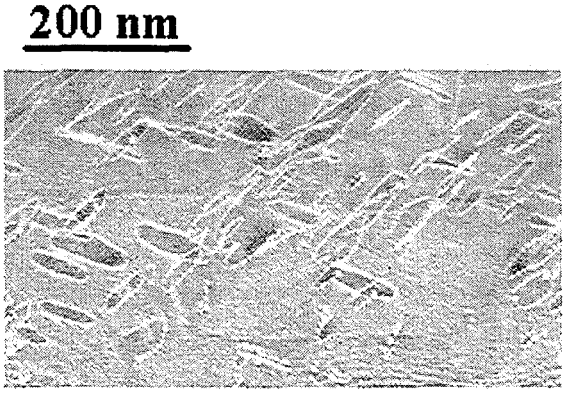

Figure 1: *S200 HIP after irradiation at 200 °C. A grain with a high density of loops lying on prismatic planes*

3.3 Irradiation at 473 °C

All the samples have revealed the presence of stacking faults. They were found to lie on the basal plane. Their density is around 10^{15} cm^{-3} and their dimensions are between 8 and 20 nm. The biggest of them were found to have an hexagonal shape., The sides of the hexagons correspond to the traces of the $(10\bar{1}0)$ planes. When view with the 0002 reflection these features are clearly appearing as plates. Their thickness is however difficult to measure because of strain contrast effects. Under some diffraction conditions, they clearly show interference fringes, an argument in favor of their two-dimensional characteristics.
A large number of these features were found to be arranged in rows, which could correspond to dislocations. However in most cases, the dislocations could not be brought into contrast.

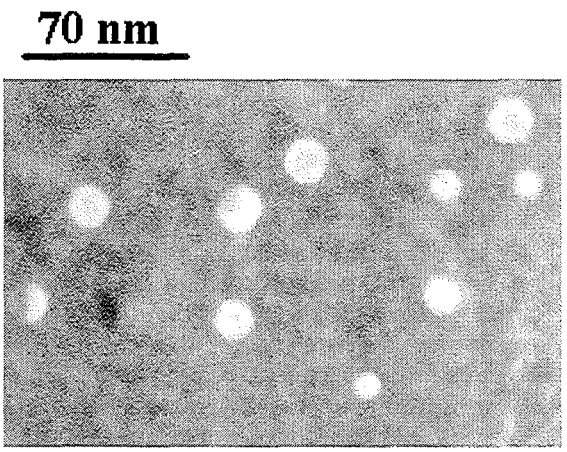

Figure 2:*S200 HIP after irradiation at 473 °C. Stacking faults in a grain near a grain boundary. Some of the stacking faults have hexagonal shapes.*

Figure 2 illustrates these observations. It has also been observed that a small zone along the grain boundary is free of stacking faults and that the number of them is lower and their size larger in the vicinity of the grain boundary.
Another important microstructural effect of the neutron irradiation is to be seen at the grain boundary illustrated in figure 3. It is covered with bubbles of approximately 5 nm diameter. It is to be noted that no small features like that found at 216 °C are observed in these specimens.

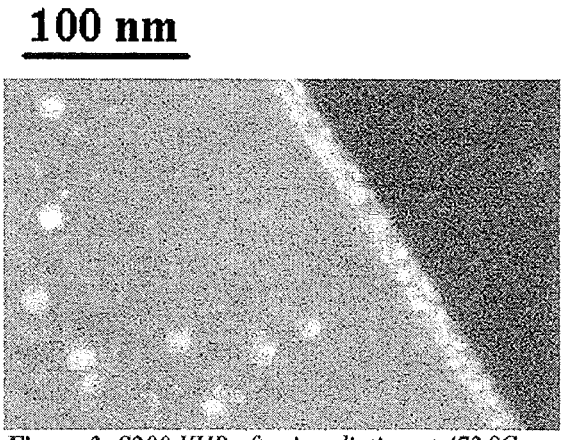

Figure 3: S200 VHP after irradiation at 473 °C. Staking faults in the grain and bubbles at the grain boundary.

3.4 Irradiation at 607 °C

The samples irradiated at this temperature show the same features as at 473 °C with a somewhat enlarged size. The stacking faults have now a size ranging from 10 to 50 nm. Their density is lower: 3 to 4 10^{14} cm^{-3}. The bubbles or cavities at the grain boundaries are some 10 nm in size. A rough estimate of the coverage proportion gives a value of 40 percent of the grain boundary surface. Figure 4 is an illustration of such a grain boundary.

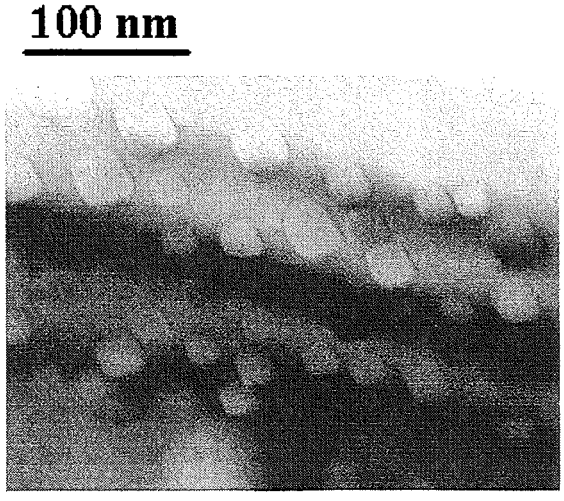

Figure 4: S200 HIP after irradiation at 607 °C. Polyhedral bubbles at a grain boundary.

Comparatively to the samples irradiated at 473 °C, a much lower proportion of stacking faults or dislocation loops are present in the form of rows. However, figure 5 is a particularly spectacular illustration of the interaction of these features with the dislocation network of a small angle grain boundary. The contrast of the dislocations is no longer apparent and they are materialized by a necklace of dislocation loops or stacking faults. This study did not allow to decide whether the small features are loops or stacking faults.

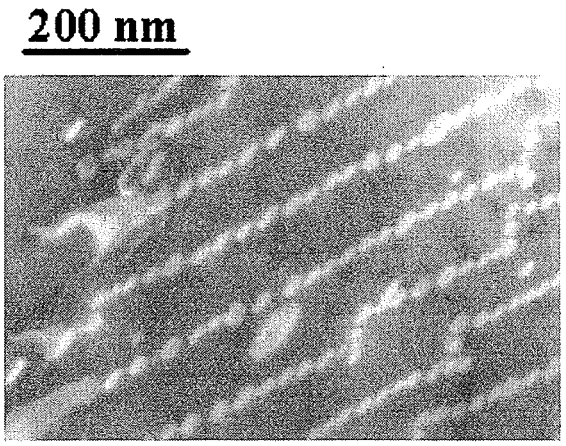

Figure 5:S65 VHP after irradiation at 607 °C. A small angle boundary showing rows of dislocation loops (or stacking faults) aligned along the dislocation constituting the grain boundary.

4 Discussion

4.1 Stacking faults and dislocation loops

It is the first time that the presence of stacking faults is reported in neutron irradiated Be. The most recent publications have detected the occurrence of planar defect clusters after irradiation at 400°C [14,17] but not at 500°C. These clusters were identified by Gelles and Heinisch [14] as small c-type loops lying in the basal plane. There is

no doubt that in our samples, stacking faults lying on the basal plane are present. The fact that some of them are showing a different contrast could be ascribed to a process of unfaulting which could leave finally c-type loops. Further observations are needed to check this hypothesis. This unfaulting process is believed to have occurred in the sample illustrated in figure 5 may be as a result of the interaction of the stacking faults with the dislocation network of the small angle grain boundary. Rows of stacking faults are in many instance clearly observable as in figure 6. Many references mention the occurrence of rows of bubbles or cavities. Such patterns are not observed in our samples. Could it be that the bubbles or cavities previously observed are in fact stacking faults or dislocation loops, or that what we are thinking to be stacking faults in our samples are in fact plate shape cavities? Some facts plead in favour of the first hypothesis. In figure 6 it is found that rows of stacking faults can be present. Further a comparison of the contrast in bright field between the features inside the matrix and the bubbles or cavities at the grain boundary clearly indicate a marked difference. On the other hand, on physical grounds, it is very difficult to explain the stability of very thin gas platelets. So it is believed that some of the previous observations of bubbles in the matrix are in fact related to stacking faults or dislocation loops

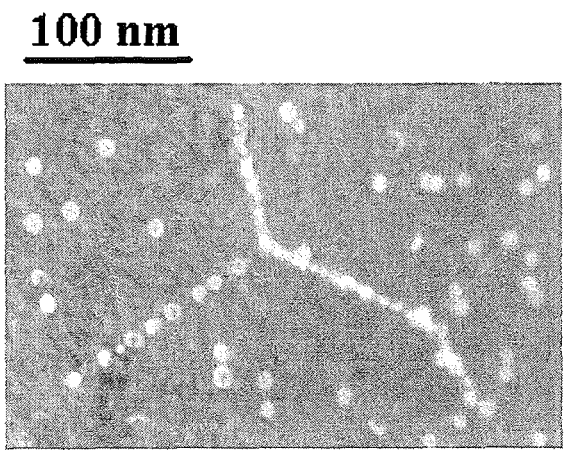

Figure 6: *S65 HIP after irradiation at 473 °C. Stacking faults, some of them are aligned.*

Whereas the stacking faults or loops have attracted a lot of He atoms remains to be further investigated. This is discussed in the paragraph concerning the numerical simulations. The comparison of the observations at 473 °C and 607 °C shows that the mean size of the stacking faults increases with the temperature and that their density decreases. The observation of small features at 216 °C, too small to be fully characterised and ascribed to bubbles or defects, is however in the trends detected in function of the temperature and on this basis it is believed that these small features are also small stacking faults and not bubbles. The evolution of the size and density of the stacking faults is given in table 3.

Table 3: *Size and density of stacking faults as a function of the irradiation temperature.*
** with the hypothesis that the small features observed at this temperature are stacking faults,*
*** a proportion of the stacking faults can be unfaulted and converted in dislocation loops. These loops are counted together.*

Irradiation temperature (°C)	Size (nm)	Density (cm^{-3}) **
216 *	2	-
473	8-20	10^{15}
607	10-50	3-4 10^{14}

4.2 Grain boundary bubbles

Bubbles or cavities were observed at the grain boundaries of the samples irradiated at 473 °C and 607 °C but not in the samples irradiated at 216 °C. This is consistent with the SEM observations of these specimens [27]. These bubbles or cavities tend to have a polyhedral shape. Due to preferential pitting at grain boundary the images with the grain boundary vertical are of very poor quality and we were unable to measure the dimension of the bubbles in a direction perpendicular to the grain boundary.

4.3 Numerical simulations

4.3.1 Introduction

In a previous paper and as a first step, we presented an atomic scale study of the trapping of He atoms by vacancies and di-vacancies in Be [22]. Constraint molecular dynamics was used to estimate formation energies and the stability of defect complexes was discussed on the basis of Helmoltz free energy calculations at the atomic scale. It was found that, in a temperature range from 0K to 600K, up to ten He atoms can be bound to one single vacancy and up to fourteen to one di-vacancy. The trapped He configurations were identified and the stability of such He vacancy clusters was found to be only little dependent on the vibrational entropy. With regard to the experimental observation of Be, it is obvious that larger defects also have to be considered, in order to learn about the possibility of He trapping which cannot be detected by TEM.

In this work, we present a first discussion of the stability of small dislocation loops and stacking faults

4.3.2 The Be potential

The potential used in [22] (named IKV in what follows) was neither designed for the study of extended defects, nor for the study of point defect mobility. Therefore, it had to be revised in depth and a new set of parameters can be suggested which is better adapted to our concern. A detailed discussion will be given elsewhere [23]. Here, we limit ourselves to the comparison of some computed material properties with experimental values. The results are given in table 4.

4.3.3 Dislocations loops and stacking faults

We computed the 0K excess energy of small edge vacancy dislocation loops lying in the basal plane and in the two prismatic planes. Their diameter range from 1.1 to 4.1 nm. For simplicity, they are assumed to be circular. Depending upon the size of the loops the simulation boxes contained from 30000 up to 150000 atoms. The three stacking faults considered were I2 type, constructed by inserting a FCC stack which produce a ABABCACA sequence, and those produced by removing a $(10\bar{1}0)$ (prismatic of type 1) or a $(1\bar{1}20)$ plane (prismatic of type 2). For all the cases the energies were obtained after a full relaxation of the crystals. The table 5 shows that the loop excess energies in the basal planes and in the type 2 prismatic plane differ by no more than 10 % and are systematically lower than excess energy of loops in the type 1 prismatic plane. This suggests that a majority of small loops may be prismatic of type 2. Dislocation loops in the basal plane cannot be excluded to take place. The table 6 compares the excess energies associated to stacking faults. The excess energy associated to I2 stacking fault is lower than those associated to prismatic 1 and 2. I2 stacking faults are thus more probable than the others, which is consistent with experiment

***Table 4** : comparison between experimental and calculated data using IKV potential and Improved Potential (IP). E_v^m is the activation energy for vacancy migration, E^{surf} the surface formation energy, C_1 and C_{66}, are elastic constants. (*) This estimate takes inner elastic contributions into account.*

	E_v^m (eV)	E^{surf} (J/m^2)	C_{12}(Mbar)	C_{66}(Mbar)
IKV	2.9 ;3.1	-0.06	0.494(*)	1.193(*)
IP	1.5 ;1.9	0.93	0.284	1.325
Experimental	1.63 ;1.71 [24]	1.3 [25]	0.276 [26]	1.359

***Table 5**: Excess energies of dislocation loops lying in a basal plane and in prismatic planes of types 1 and 2. Energies are expressed in eV.*

Dislocation loops diameter (nm)	Basal	Prismatic of type1	Prismatic of type 2
1.1	15.7	17.2	14.5
1.6	23.0	31.2	24.1
2.28	48.9	62.7	45.8
4.1	156	193.2	141

***Table 6**: Stacking fault excess energies for three types of defects. The energies are computed for the full-relaxed crystals*

	Basal (I2)	Prismatic of type 1	Prismatic of type 2
Stacking fault formation energies (J/m^2)	0.237	2.35	0.68

5.Conclusions

The most important results of this investigation are:

$\Rightarrow$ No influence of fabrication method is observed

$\Rightarrow$ No influence of temperature without irradiation has been detected

$\Rightarrow$ Nothing or may be very small features are present after irradiation at 216°C

$\Rightarrow$ Stacking faults are present after irradiation at 473 °C and 607 °C. They are hexagonal, lie on the basal plane and their sides are parallel to the traces of the $\{10\bar{1}0\}$ planes.

$\Rightarrow$ There is, an interaction between stacking faults and dislocations.

$\Rightarrow$ Bubbles are covering a large part of the surface of the grain boundary after irradiation at 607 °C (40 percent).

$\Rightarrow$ There is an increase of the size of the stacking faults and of the bubbles with the irradiation temperature.

$\Rightarrow$ Classical atomic scale modelling allowed to discuss the stability of the clusters trapped by vacancies and di-vacancies. On the expense of redesigning the Be EAM potential, it is shown that extended defects similar to those observed by TEM can be modelled. The modelling of the interaction between He and extended defects like stacking faults and dislocation loops is in progress.

Acknowledgments

This work has been carried out in the framework of the association ULB-CEN/SCK. A substantial part of the activities was supported by the EC in the framework of the fusion program under the task BSBE1. One of us (LC) is particularly grateful to the CEN/SCK for having permitted to use and publish the results of the TEM examinations notwithstanding his recent retirement

References

[1] J.B. Rich,G.P. Walters, R.S. Barnes, J.Nucl.Mater. 4(3) (1961), 287

[2] J.B. Rich,G.P. Walters, Proc. Int. Conf. on the Metallurgy of Beryllium, London 1961,362

[3] R.S. Barnes, Proc. Int. Conf. on the Metallurgy of Beryllium, London 1961, 372

[4] R.Summerling, E.D. Hyam, Proc. Int. Conf. on the Metallurgy of Beryllium, London 1961, 381

[5] J.R. Weir, Proc. Int. Conf. on the Metallurgy of Beryllium, London 1961,395

[6] CEA-R-2639(1964)

[7] R.Nagasaki et al, J.Nucl.Sc.Tech. 8(10) (1971) 546

[8] J.-M.Beeston, TREE-1063 (1976)

[9] J.-M.Beeston,M.R.Martin,C.R.Brinkman, CONF-730801 (1973) 59

[10] S.Morozumi,S.Goto M.Kinno, J. Nucl. Mat. 68 (1977) 82

[11] Y.Mishima,S.Hishimo,Shiozawa, Proc. 4th Int. Conf. on Beryllium, London 1977, paper 25

[12] G.JC Carpenter,R.G Fleck, Proc. 4th Int. Conf. on Beryllium, London 1977, paper 26

[13] R.G Fleck ASTM-STP 782 (1982) 735

[14] D.S Gelles,H.L Heinish, J.Nucl.Mater 191/194 (1992) 194

[15] I.B Kuprianov et al, JAERI-CONF-98-001 (1998) 267

[16] S.A Fabritsiev,A.S Pokrovsky, JAERI-CONF-98-001 (1998) 284

[17] M.Dalle Donne et al, JAERI-CONF-98-001 (1998) 296

[18] A.Rahn, F.Mons, Irradiation Report Mol F-BSBE1 AG-MOL Note n° 30/93, 38/93, 2/94, 10/94, 17/94, 04/95

[19] D.Harries, M.Dalle Donne, FZKA-5778

[20] C. De Raedt, FT/Mol/96-01

[21] F.Moons, BLG724 (1997) 27

[22] J.MCayphas, M.Hou, L.Coheur, J.Nucl. Mater. **246** (1997) 171

[23] ibid. to be published

[24] N.L. Peterson, J. Nucl. Mater. **69&70** (1978) 3

[25] W.R. Tyson, W.A. Miller, Surf. Sci. **62** (1977) 267

[26] H.J.P. van Midden, A.G.B.M. Sasse, Phys.Rev. **B46** (1992)

[27] M.Verwerft, BLG735 (1997)

MECHANICAL PROPERITES AND TRITIUM RELEASE BEHAVIOR OF NEUTRON IRRADIATED BERYLLIUM PEBBLES

E. Ishitsuka [1], H. Kawamura [1], T. Terai [2] and S. Tanaka [2]

[1] Japan Atomic Energy Research Institute, Oarai Research Establishment, Oarai-Machi, Higashi Ibaraki-Gun, Ibaraki-Ken 311-1394 Japan.
[2] University of Tokyo, 7-3-1 Hongo, Bunkyo-Ku, Tokyo 113-8656 Japan.
TEL : +81-29-264-8368, FAX : +81-29-264-8480, E-mail : ishi@oarai.jaeri.go.jp

Beryllium pebbles are expected as a neutron multiplier of a fusion reactor blanket. Mechanical properties and tritium release behaviors of the neutron irradiated beryllium pebbles were tested as a Post Irradiation Examination (PIE).

Two kinds of beryllium specimens (diameter:1mm, grain size: about 0.5mm), which were fabricated by the Rotating Electrode Method (REM) and by the Mg Reduction Method (MRM), were irradiated with a total fast neutron fluence of 1.6×10^{22} n/cm^2 (E>0.1 MeV) at 673, 773 and 873 K. The estimated helium concentration and dpa value were about 1×10^3 appmHe and 10dpa, respectively.

Compression tests were carried out at the room temperature in the Beryllium PIE Facility of JMTR (Japan Materials Testing Reactor) hot laboratory. Compression speed was 0.2 mm/min in ten tests for each specimen.

From the results of compression test, no significant difference in the compression strength was observed between two kinds of beryllium pebbles. Additionally, it was clear that not only helium concentration but also dpa value was an important factor on the mechanical properties, because the compression strength of the high dpa specimens (10 dpa) was smaller than that of the low dpa specimens (6 dpa) with similar helium concentration (about 1×10^3 appmHe).

Also, the tritium release experiment will be carried out for these specimens, and results will be presented in this workshop.

Swelling and mechanical properties of beryllium irradiated in the SM reactor at low temperature

V.P.Chakin[a], I.B.Kupriyanov[b], V.A.Tsykanov[a], V.A.Kazakov[a] and R.R.Melder[a]

[a]SSC RF RIAR, 433510, Dimitrovgrad, Ulyanovsk region, Russia
[b]SSC RF VNIINM, 123060, Rogova 5, Moscow, Russia

Results of the investigation of beryllium irradiated in the SM reactor in water at 60-75°C up to (0.61-2.37)·$10^{22}$$sm^{-2}$ (E>0.1 MeV) are presented in the paper. Beryllium of four grades (TE-56, TE-30, TIP, DIP) was studied. Early two grades of beryllium fabricated by vacuum hot pressing are defined by a considerable anisotropy relative to the direction of extrusion. The latest two grades of beryllium fabricated by hot isostatic pressing were isotropic in practice. The corrosion rate in water under irradiation was 0.1-5.4 g/m^2 (during time period of 2700 h) or 1.3-10.8 μm/y. Swelling was 0.07-0.91%. The volume of some samples was observed to decrease, in particular, the DIP grade of beryllium. The irradiation resulted to strong embrittlement of all studied beryllium grades and to decrease of ultimate fracture stress by 55-74% (24-42% for the DIP grade) under tensile tests and by 39-68% under compression tests.

1. INTRODUCTION

The efficiency of using of beryllium in nuclear and fusion reactors is defined by changing its properties under neutron irradiation. Swelling and mechanical properties are one of the main controlled parameters. At low irradiation temperature the diffusion of forming gas atoms is low and therefore a crystal lattice is in a very stressed state. This fact defines the values of dimensional changes and degradation in mechanical properties of irradiated beryllium samples [1,2].

The paper deals with investigation results of corrosion in water, swelling and mechanical properties for four beryllium grades by low temperature neutron irradiation. The data have been obtained in the frame of RIAR-VNIIIM joint program to study the post-irradiation damage of beryllium at temperatures 60-200°C within a wide range of neutron fluences.

2. MATERIAL AND EXPERIMENT

Four grades of beryllium manufactured by VNIINM has been investigated. Its mean grain size and chemical composition are given in Table 1.

Beryllium of TE-56 and TE-30 grades was fabricated by vacuum hot pressing (VHP), beryllium of TIP and DIP grades was fabricated by hot isostatic pressing (HIP).

Table 1
Mean grain size and chemical composition of beryllium grades

Material	Cutting direction	Mean grain size, μm	Content of element, mass %					
			O_2 (BeO)	Fe	Al	Σ(Cu+Ni+Mn+Mg)	Si	C
TE-56	axial	25	0.98	0.17	0.026	0.04	0.016	0.08
	cross	22	(1.48)					
TE-30	axial	23	1.66	0.11	0.015	0.025	0.013	0.088
	cross	16	(2.5)					
TIP	axial	12	0.89	0.13	0.013	0.032	0.013	0.07
	cross	12	(1.3)					
DIP	axial	13	1.3	0.028	0.005	0.012	0.013	0.067
	cross	13	(2.0)					

The VHP grades are characteristic of the high anisotropic structure in the axial and cross direction to extrusion. The HIP grades are characteristic of a negligible anisotropy. The samples of two types were used for mechanical tests: tensile (Fig.1) and compression (cylinder 5.9-6.0 mm diameter and 7.1-9.0 mm height).

Leaky capsules with samples were irradiated in the channels of the SM reactor. During irradiation the samples were washed with distilled water of the primary circuit. The rate of water flow was 67 m^3/h.

Irradiation temperature was in the range 60-75°C and fluence was of $(0.61\text{-}2.37)\cdot10^{22}cm^{-2}$ (E>0.1 MeV). The irradiation parameters are presented in more detail in Table 2.

Table 2
Irradiation parameters of beryllium grades

Material	Irradiation temperature, °C	Neutron flux, $x10^{-14}$ $sm^{-2}c^{-1}$			Neutron fluence, $x10^{-22}sm^{-2}$			Damage dose, dpa	Helium content, appm
		<1 eV	>0.1 MeV	>1MeV	<1 eV	>0.1 MeV	>1 MeV		
TE-56	60-75	2.2-4.1	9.9-24.4	4.9-11.5	0.21-0.40	0.96-2.37	0.48-1.12	5.1-12.8	2110-4970
TE-30		1.7-3.6	6.3-23.3	3.4-11.7	0.16-0.35	0.61-2.26	0.33-1.13	3.3-12.0	1520-5020
TIP		1.6-3.1	8.8-18.8	4.6-9.5	0.16-0.30	0.85-1.82	0.45-0.92	3.2-9.7	1340-4120
DIP		1.9-3.1	10.4-19.7	5.0-9.9	0.18-0.30	1.00-1.91	0.49-0.96	3.0-10.1	1320-4220

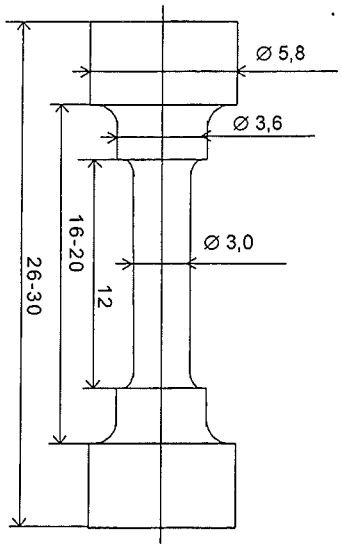

Figure 1. Sample for mechanical tensile tests.

Dimensions of cylindrical samples before and after irradiation was measured. The error of measurement did not exceed ±0.005 mm. The weight was measured with samples of tensile test. The error in measurement was ±0.0001 g. The mechanical tensile tests were carried out at room temperature in air and at 200°C - under vacuum of $1\cdot10^{-2}$Tor. The compression tests were carried out in air only. The strain rate in both types of tests was 1 mm/min. In determining strength and plastic characteristics the errors were 5 and 10%, respectively.

3. EXPERIMENT

3.1. Corrosion in water

Data of weight of samples measured before and after irradiation are presented in Table 3. The weight of all irradiated samples was observed to lower by 0.01-0.54%. This effect seems to be due to the corrosion of beryllium in the water coolant by which samples were washed under irradiation. The corrosion rate is estimated by 0.1-5.4 g/m^2 (during time irradiation period of 2700 h) or 1.3-10.8 μm/y. The calculated relative reduction of linear dimensions makes up 0.0043-0.0423%.

Table 3
Corrosion of beryllium grades in water under irradiation

Material	Cutting direction	F, $\times 10^{-22}$ sm^{-2} (E>0.1 MeV)	Weight P, g		Weight change, %	Corrosion rate		Relative decrease of linear size, %
			P_{init}	P_{irr}	$\frac{P_{irr}-P_{init}}{P_{init}} \times 100\%$	g/m^2 (2700 h)	μm/y	
TE-56	axial	0.96-1.81	0.8064	0.8042	-0.27	3.2	7.9	0.0282
			0.8060	0.8033	-0.33	4.0	7.9	0.0288
			0.7473	0.7460	-0.17	1.9	3.8	0.0138
	cross	1.26-2.31	0.84835	0.8483	-0.01	0.1	1.3	0.0045
			0.8183	0.8165	-0.22	2.7	5.4	0.0190
			0.80625	0.8032	-0.38	4.7	9.2	0.0345
TE-30	axial	1.19-2.16	0.7245	0.7227	-0.25	2.7	5.1	0.0186
			0.70975	0.7075	-0.32	3.4	6.6	0.0249
			0.71345	0.7100	-0.48	5.4	10.8	0.0423
	cross	0.80-2.01	0.7075	0.7059	-0.23	2.3	4.4	0.0154
			0.7048	0.7021	-0.38	4.0	7.6	0.0273
			0.7174	0.7147	-0.38	4.0	7.9	0.0290
TIP	axial	1.07-1.60	0,7316	0.7277	-0.53	5.4	10.5	0.0366
			0.7103	0.7086	-0.24	2.5	4.8	0.0170
			0.71705	0.7153	-0.24	2.6	5.1	0.0186
DIP	axial	1.01-1.78	0.6871	0.6859	-0.17	1.9	3.8	0.0149
			0.6928	0.6917	-0.16	1.8	3.5	0.0140
			0.6730	0.6715	-0.22	2.6	5.1	0.0222

3.2. Swelling

Data of dimensions of samples measured before and after irradiation are presented in Table 4. Diameter and height were measured and value of the cylindrical volume was calculated. The calculated values of volumes before and after irradiation were compared between them. Further analysis does not take account of decreasing the linear dimensions of irradiated samples caused by corrosion in water because, as a rule, the value of decrease by an order of magnitude or by several times less than increase of dimensions caused by swelling. Swelling of all studied samples is in the range of 0.07-0.91%. Five from eighteen investigated samples were observed to lower the volume. Four samples have the volume decreased by 0.03-0.14% and one - by 0.47%.

Comparison between the grades of beryllium demonstrated that the TE-56 grade has maximum swelling (0.34-0.91) % and all three investigated samples of the DIP grade have the decrease of volume.

Of two grades fabricated by VHP the TE-30 grade having less grain size, lower content of metallic impurities and greater amount of beryllium oxide has lower swelling. Comparison between diameter and height demonstrates that samples cut along the extrusion axis are changed in height to a greater degree than samples cut transversely to the axis. No difference was observed in change of diameters in this case.

Compared to the grades prepared by HIP and having rather isotropic structure, the DIP grade fabricated from the powder of distilled beryllium and involving higher content of beryllium oxide is superior to the TIP grade in the dimensional stability. The TIP grade is prepared from the powder of technical beryllium and its swelling is identical with the anisotropic type.

Table 4
Swelling of beryllium grades

Material	Cutting direction	F, $\times 10^{-22}$ sm^{-2} (E>0.1 MeV)	Diameter D, mm		Diameter change, %	Height h, mm		Height change , %	Swelling, %
			D_{init}	D_{irr}	$\frac{D_{irr}-D_{init}}{D_{init}}\times 100\%$	H_{init}	H_{irr}	$\frac{h_{irr}-h_{init}}{h_{init}}\times 100\%$	
TE-56	axial	2.24-2.35	5.945	5.953	0.13	8.982	9.004	0.22	0.51
			5.943	5.960	0.29	8.825	8.840	0.15	0.74
			5.953	5.973	0.34	8.635	8.655	0.21	0.91
	cross	2.37	5.953	5.963	0.17	8.845	8.845	0	0.34
			5.953	5.962	0.15	8.550	8.558	0.09	0.40
			5.968	5.986	0.30	8.400	8.398	-0.02	0.58
TE-30	axial	2.21-2.26	6.013	6.019	0.10	8.618	8.622	0.05	0.25
			6.013	6.023	0.17	8.417	8.444	0.04	0.52
			6.035	6.023	-0.20	8.040	8.063	0.29	-0.11
	cross	2.13-2.25	5.988	5.999	0.18	9.035	9.032	-0.03	0.33
			6.020	6.021	0.02	8.778	8.734	-0.50	-0.47
			6.025	6.023	-0.03	8.620	8.632	0.14	0.07
TIP	axial	1.68-1,82	6.010	6.013	0.05	9.006	9.026	0.22	0.32
			6.008	6.015	0.12	8.805	8.814	0.10	0.34
			6.013	6.021	0.13	8.595	8.611	0.19	0.45
DIP	axial	1.85-1.90	5.900	5.898	-0.03	8.030	8.025	-0.06	-0.13
			5.903	5.897	-0.10	7.830	7.835	0.06	-0.14
			5.903	5.901	-0.03	7.195	7.198	0.04	-0,03

3.3 MECHANICAL PROPERTIES

3.3.1. Tensile test results

Results of mechanical tensile tests of beryllium before and after irradiation are presented in Table 5. The tests were carried out at room temperature and 200°C. Irradiation resulted in a considerable worsening of mechanical properties of studied beryllium grades. All the irradiated samples showed the brittle fracture at essential decrease of stress. The value of decrease was 55-74%. The DIP grade only demonstrated that stress decreased to a lesser degree (by 24-42%).

3.3.2. Compression test results

Results of mechanical compression tests are given in Table 6. Before irradiation beryllium had a fine combination of strength and plastic properties. At above room temperature the non-cracking strain of samples occurred until the loading was stopped at 5000 kg. After irradiation all samples were found to have brittle fracture with the exception of the TV-30 grade in samples cut transverse to axis, as well as the TIP and DIP-grades at 200°C. In testing the level of failure stress decreased to 39-68% at room temperature.

Table 5
Tensile test results of beryllium samples

Material	Cutting direction	F, $\times 10^{-22}$ sm^{-2} (E>0.1 MeV)	T_{test}, ^0C	$\sigma_{0,2}$, MPa		σ_B, MPa		δ_0, %	
				init.	irr.	init.	irr.	init.	irr.
TE-56	axial	1.81	20	280	-	510	228	6	0
	cross	2.31	20	240	-	300	126	0	0
TE-30	axial	1.20	20	350	-	600	206	7	0
		1.67	200	280	-	420	150	25	0
	cross	2.01	20	330	-	330	283	0	0
		1.78	200	260	-	350	144	2	0
TIP	axial	1.60	20	450	-	530	137	4	0
		1.46	200	370	-	460	135	10	0
DIP	axial	1.78	20	400	-	520	300	4	0
		1.31	200	300	-	420	318	20	0

Table 6
Compression test results of beryllium samples

Material	Cutting direction	F, $\times 10^{-22}$ sm^{-2} (E>0.1MeV)	$T_{test.}$, ^0C	$\sigma_{0,2}$, MPa		σ_B, MPa		δ_0, %	
				init.	irr.	init.	irr.	init.	irr.
TE-56	axial	2.35	20	514	-	2044	663	37,5	0
		2.28	200	481	-	1786*	585	49**	0
	cross	2.37	20	478	-	1363	828	24,4	0
		2.37	200	413	-	1775*	1032	36**	0
TE-30	axial	2.26	20	522	-	1872	646	36,1	0
		2.26	100	510	-	1787*	767	39**	0
		2.26	200	438	-	1784*	1093	44**	0
	cross	2.25	20	552	-	1268	624	18,9	0
		2.23	100	540	-	1361	950	26,6	0
		2.21	200	515	1286	1784*	1424	39**	1,5
TIP	axial	1.83	20	522	-	1832	707	34	0
		1.78	100	597	-	1745*	762	32**	0
		1.75	200	466	977	1796*	1049	32**	1,0
DIP	axial	1.85	20	576	-	1946	652	34,6	0
		1.88	100	568	-	1817*	740	34**	0
		1.90	200	453	690	1790*	745	39**	11.6

* - maximum stress during sample loading
** - strain under maximum stress.

4. DISCUSSION

The use of beryllium as neutron moderator and reflector materials in nuclear reactors as well as its future application in fusion reactors as material for the first wall and blanket are based on the precise knowledge of irradiation influence on its main physical-mechanical properties within a wide range of temperature and dose. A number of works covering the irradiation temperature range from 300 to 800°C has appeared for recent years [3-6]. There are a few works dealt with irradiation influence on the beryllium properties at low temperatures

especially at high damage doses. G..A.Sernyaev in his earlier papers presented the investigation results of coarse-grained beryllium of dated grades [7-9]. The author found main laws of beryllium behavior under low temperature irradiation. But concerning the new grades of beryllium they are needed in some improvements and additions.

According to the results of the paper the mean corrosion rate of beryllium defined by weight decrease of samples does not present a considerable value. Beryllium is known to show a tendency to local pitting corrosion on the carboxide particles [10]. Beryllium is classified as very surface-sensitive material. Therefore the dimensional growth of local sites for corrosion damage serving the effectively concentrated surface stresses can lead to initiation of premature destruction of a sample under mechanical test.

According to the obtained results the swelling does not achieve 1% that is in agreement with other data [7,9]. Under irradiation some samples demonstrated the radiation-induced decrease of volume, as it has been reported elsewhere [11]. The DIP grade was found to indicate the similar decrease in the present paper. This beryllium grade is different from others by low content of metal impurities that probably indicate the relation of swelling value with a degree of beryllium matrix purification. Until the mechanism of the radiation-induced decrease of beryllium volume is unknown. It is possible in the change of dimensions (as well as the value of swelling, respectively) may be influenced by radiation growth, which (similarly to zirconium) can be observed under the low-temperature irradiation of beryllium as a representative of metals with HCP crystal lattice. Another reason of the effect can be the irradiation-induced shrinkage of beryllium. All investigated grades were obtained by powder metallurgy. The accommodation of separate crystals with one another can be different in the various grades. The shrinkage of beryllium prepared from the distilled powder is likely more significant.

The results of tensile and compression tests are indicative of the considerable worsening in mechanical properties of beryllium irradiated at low temperature. The strong embrittlement of samples is followed by a considerable decrease the level of fracture stresses. Such degradation of mechanical properties is due to the effect of swelling anisotropy, i.e. the anisotropy of separate crystallite swelling in the various crystallographic directions [7]. The internal stresses and lack of relaxation for them caused by low irradiation temperature resulted in relaxation of grain boundaries and boundary fracture under mechanical loading. From the point of view of degradation in mechanical properties there was no considerable difference between anisotropic and isotropic grades of beryllium under study.

5. CONCLUSION

Corrosion damage, swelling and mechanical properties of four beryllium grades irradiated in the SM reactor at 60-75°C up to $(0.62\text{-}2.37)\cdot10^{22}$ sm^{-2} (E>0.1 MeV) were investigated. It is shown that all beryllium grades irradiated in water of the primary circuit have the corrosion rate from 0.1 to 5.4 g/cm^2 (irradiation time period of 2700 h) or within 1.3 to 10.8 μm/y. The value of swelling is 0.07-0.91%. In some cases the volume of irradiated samples lowered, in particular, in the DIP grade of distilled beryllium fabricated by HIP. The low-temperature irradiation resulted in the strong embrittlement of beryllium in all studied grades and reduction of fracture stress by 55-74% (and only by 24-42% for the DIP grade) under tensile tests and by 39-68% under compression tests.

REFERENCIES

1. V.P.Goltsev, G.A.Sernyaev, Z.I.Chechetkina, Radiation material science of beryllium, Nauka and technika, Minsk, 1977.
2. G.A.Sernyaev, V.P.Goltsev, Z.I.Chechetkina. Origin and growth of gas-bubbles in mono- and polycrystals, RIAR's preprint P-223, Dimitrovgrad, 1974.
3. I.B. Kupriyanov, V.A. Gorokhov, G.N. Nikolaev, V.N. Burmistrov. Development of radiation resistant grades of Beryllium for nuclear and fusion facilities, Proc. 2nd IEA Int. Workshop on Beryllium Technology for Fusion, Jackson Lake Lodge, Wyoming, Sept. 6-8 (1995) 249-260.

4. I.B Kupriyanov, V.A.Gorokhov, R.R.Melder, Z.E.Ostrovsky, A.A.Gervash, J. Nucl. Mater. 258-263 (1998) 808-813.
5. A.S.Pokrovsky, S.A.Fabritsiev, R.M.Bagautdinov, Yu.D.Goncharenko, J. Nucl. Mater 233-237 (1996) 841-846.
6. F.Moons, L.Sannen, A.Rahn, J.Van De Velde, J. Nucl. Mater 233-237 (1996) 823-827.
7. G.A.Sernyaev. Swelling and spontaneous cracking of beryllium under low temperature irradiation, VANT, Ser. Yadernaja technika i technologija, 1992, vyp.2, 35-43.
8. G.A.Sernyaev. Dishardening and embrittlement of beryllium under low temperature irradiation, VANT, Ser. Yadernaja technika i technologija, 1992, vyp.2, 48- of linear size, %56.
9. V.P.Goltsev, G.A.Sernyaev, Z.I.Chechetkina, P.G.Averyanov. Svelling of beryllium under low temperature irradiation, RIAR's preprint P-264, Dimitrovgrad, 1975.
10. D.Webster and D.Floyd, ed., Beryllium Science and Technology (Plenum Press, New York, 1979).
11. I.B. Kupriyanov, V.A. Gorokhov, R.R. Melder, Z.E. Ostrovsky, G.N. Nikolaev. Neutron irradiation behaviour of ITER candidate beryllium grades, Proc. 3th IEA Int. Workshop on Beryllium Technology for Fusion. Oct. 21-23, 1997.

Helium and tritium behavior in neutron irradiated beryllium

I.B. Kupriyanov[a*], V.V. Vlasov[b]

[a] SSC A.A.Bochvar All-Russia Research Institute of Inorganic Materials (VNIINM), Box 369, 123060, Moscow, Russia

[b] NRC Kurchatov Institute, 123181, Moscow, Russia

The efficiency of the beryllium application as a plasma-facing material and a neutron multiplier in a solid breeder blanket will depend on helium-induced swelling and tritium and helium release from this metal. The effect of a neutron irradiation on helium and tritium mobility and swelling for three beryllium grades fabricated by VNIINM is described in this paper. The beryllium blocks were irradiated with a neutron fluence (E >0.1 MeV) (2.6 - 3.4) · 10^{21} cm^{-2} (1.3 - 1.8 dpa) at 550°C, 620°C and 790°C. Mass-spectrometry techniques was used to simultaneously monitoring of gas release during isothermal multi-stage annealing over 500 - 1300°C temperature range.

It is shown that the first signs of the helium release have been detected at temperature about 700°C, while the intense tritium release has occurred at all stages of annealing. Based on the data obtained, the diffusion parameters (D_o, E) for both the gases in beryllium were calculated. The total amount of helium accumulated in irradiated beryllium varied from 240 appm to 620 appm. The tritium mobility increases significantly when swelling increases, while that for helium changes very slightly. With swelling increase from 0.5 to 1.8 % the ratio of helium to tritium retentions alternates approximately from 4 : 1 to 10 : 1. The tritium and helium retentions and beryllium swelling are presented as a functions of a distance from the irradiated surface. The experimental data are also discussed in comparison with calculations.

1. INTRODUCTION

Beryllium is a leading candidate as a plasma facing material and neutron multiplier of tritium blanket. The efficiency of the beryllium application will strongly depend on its behavior under a neutron irradiation. In terms of fusion application the most important consequences of neutron irradiation are helium induced swelling, embrittlement and tritium inventory and mobility. Although a rich variety of experimental data on effect of neutron irradiation on beryllium were reported, not much is known on release and retention parameters of tritium and helium in irradiated beryllium[1-10], in particular after a high temperature irradiation.

This paper presents some results on investigation of tritium and helium retention and mobility in beryllium subjected to irradiation at high temperature and also several silent features of Be swelling.

2. MATERIALS AND EXPERIMENTAL PROCEDURE

Three grades of beryllium (TIP-30, TRR and DRR) produced by VNIINM, Russia were studied in this work. Chemical composition and some initial characteristics of the materials are presented in Table 1 and Table 2. All the materials were irradiated in high flux channels of CM-3 reactor in leaktight capsules. The beryllium blocks with 50-53

* Tel.: + 7-95-1908015.
Fax: +7-95-925 5972/925 2896
e-mail: vniinm.400@g23.relkom.ru

Table 1
Chemical composition of beryllium grades, wt. %

Material	Be	BeO	Fe	Al	Si	C	Mg
TIP-30	98.27	2.1	0.11	0.014	0.013	0.075	0.006
TRR	97.64	3.2	0.12	0.015	0.013	0.05	0.006
DRR	97.24	3.9	0.03	0.0061	0.013	0.05	0.0016

Table 2
Characteristics of beryllium

Material	Average grain size, μm	Direction	UTS, MPa	YS, MPa	TE, %	Compactiong method
TIP-30	18	trans.	487	416	1.8	HIP
		long.	482	463	0.8	
TRR	8-9	trans.	691		0	HIP
		long.	589		0	
DRR	8-9	trans.	633		0	HIP
		long.	602		0	

[a] Hot isostatic pressing

Table 3
Irradiation parameters of beryllium

Parameter	Material		
	TIP-30	TRR	DRR
Φ_s(E > 0.1 MeV), $cm^{-2}\cdot c^{-1}$	$3.2 \cdot 10^{14}$	$3.6 \cdot 10^{14}$	$3.6 \cdot 10^{14}$
Φ_{th}(E <0.68 eV), $cm^{-2}c^{-1}$	$3.0 \cdot 10^{14}$	$5.1 \cdot 10^{14}$	$5.1 \cdot 10^{14}$
F_s (E >0.1 MeV), cm^{-2}	$2.7 \cdot 10^{21}$	$(2.6; 3.4) \cdot 10^{21}$	$3.0 \cdot 10^{21}$
F_{th}(E <0.68 eV), cm^{-2}	$2.6 \cdot 10^{21}$	$(3.7; 5.0) \cdot 10^{21}$	$4.1 \cdot 10^{21}$
Radiation damage, dpa	1.4	1.3; 1.8	1.6
Irradiation temperature, °C	790	550, 620	780

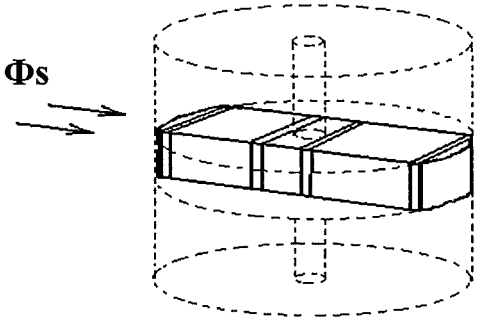

Figure 1. Cutting of the beryllium blocks

mm in diameter and 42 mm in height were irradiated up to fluence (2.6-3.5)· 10^{21} cm^{-2} (E >0.1 MeV) at temperature range 550- 790°C. Irradiation parameters are presented in Table 3.

Flat samples with 10×5×0.5 mm in dimensions were cut out from three different places of beryllium block perpendicular to the direction of a neutron flux at the depths of 3 mm, 20 or 30 mm and 47 or 50 mm from the irradiated surface. An error when cutting did not exceed ± 1 mm. The sampling is illustrated schematically in Figure 1. The measurements of weight and density were performed for all the samples.

Helium and tritium release kinetics was analyzed in a stepped isothermal annealing mode. Gases liberated under sample heating were collected in a closed volume equipped with omegatron mass-spectrometer (OMS)[5]. The OMS was calibrated against H_2, D_2 and ^4He standard leaks. A sensitivity to T_2 (mass 6) molecules was evaluated by

interpolating the H_2 (mass 2) and D_2 (mass 4) sensitivities. Released amounts of ^4He were calculated from reading the OMS signal at mass 4. For evaluation of tritium released amounts of the mass 6 alone was used because the fraction of tritium released in form of HT molecules was found to be negligible in our experimental conditions.

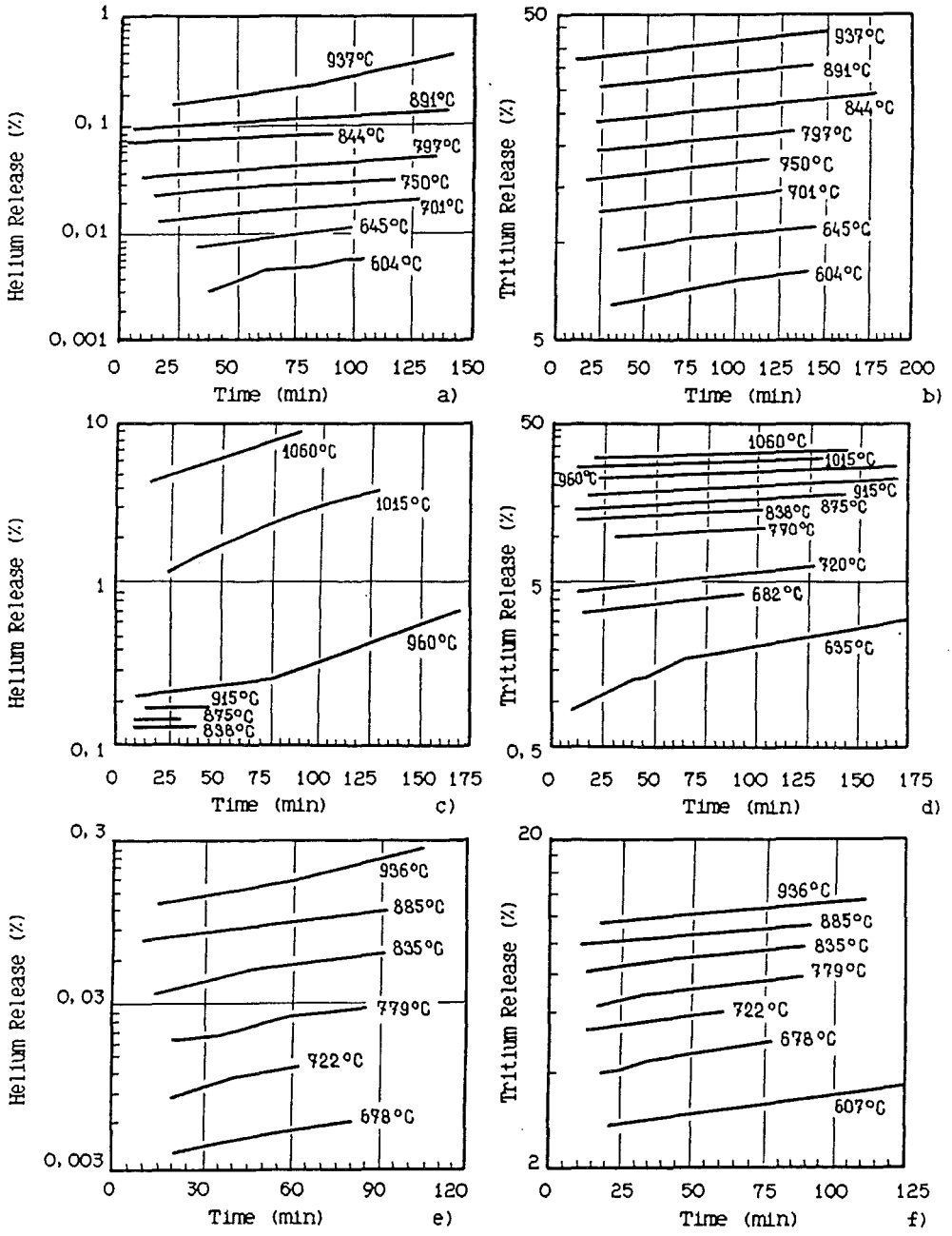

Figure 2. Helium and tritium release from TIP-30 beryllium:
a,b - sample at 3 mm depth; c,d - sample at 20 mm depth; e,f - sample at 47 mm depth.

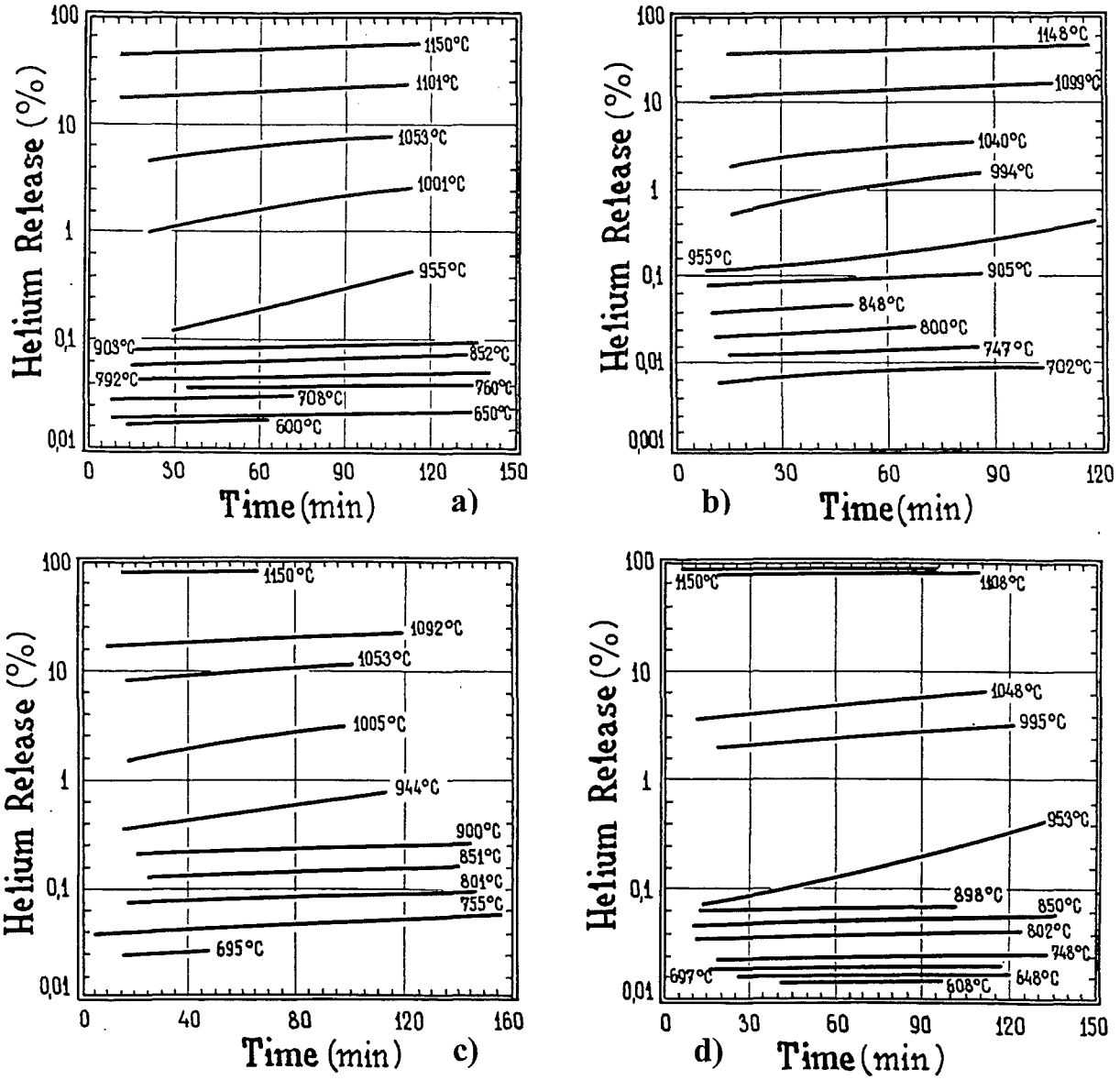

Figure 3. Helium release from TRR beryllium:
a,c,d - $F_s = 3.4 \cdot 10^{21}$ cm^{-2}(E >0.1 MeV), $T_{irr.}$=620°C, b - $F_s = 2.6 \cdot 10^{21}$ cm^{-2}(E >0.1 MeV), $T_{irr.}$=550°C; a - sample at 50 mm depth; b,c - sample at 30 mm depth; d - sample at 3 mm depth.

A temperature was elevated by 40-60°C with every step of multi-stage annealing. A heating duration averaged between 0.5 and 2.0 hours, and a temperature ranged within 500-1300°C. At the final step of multi-stage annealing the samples were managed to melting and the total amount of helium and tritium was measured.

3. EXPERIMENTAL RESULTS AND DISCUSSION

The data on released fraction of helium as a function of annealing time are shown in Figure 2, a, c, e (TIP-30 grade), . Figure 3 (TRR grade) and

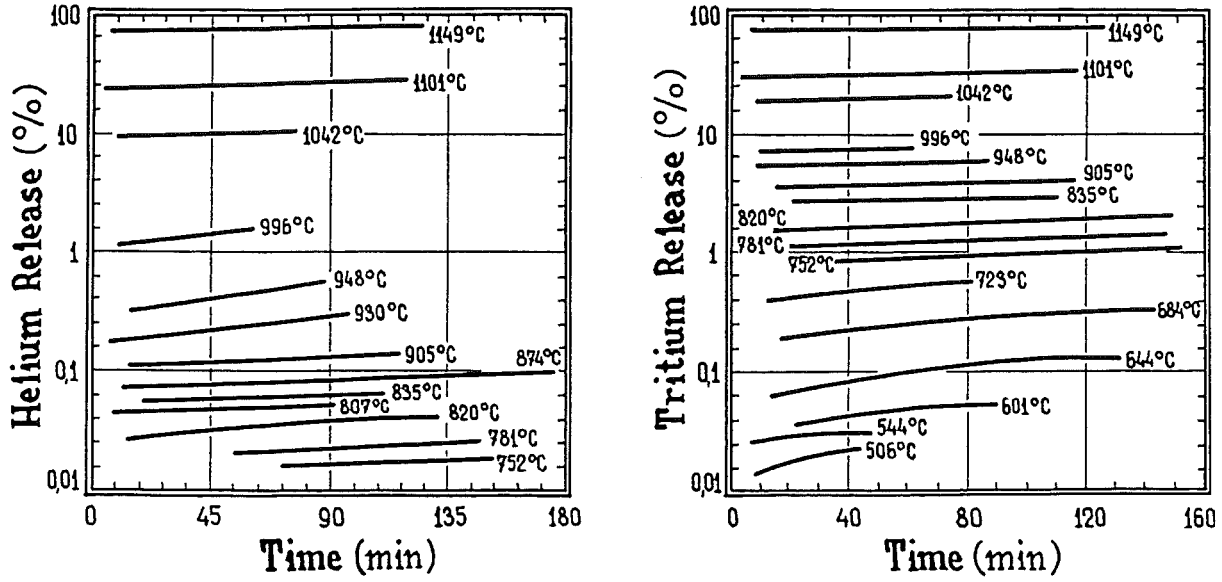

Figure 4. Helium and tritium release from DRR beryllium.

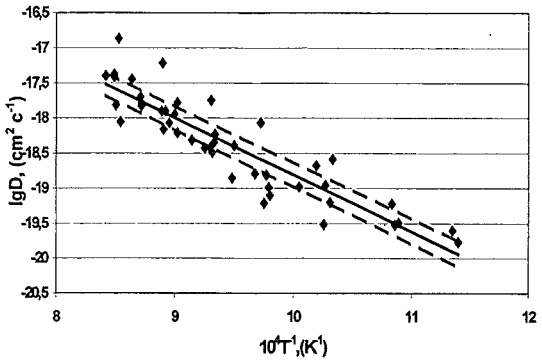

Figure 5. Helium diffusion coefficients.

Figure 4 (DRR grade). For all the samples helium release commences at 650 °C. Below 700 °C, only 0.02 % at total helium amount is released during annealing for 2 hours. At temperature below 700°C the He release is negligible(< 0.02 %). At temperature of annealing up to 950°C the integrated He release does not exceed 0.8 % for all the materials. The bulk of the He (80-95 %) has been released at the temperature range from 1050°C to 1200°C.

The results of the tritium release measurements from the samples of Be grades TIP-30 and DRR are presented in Figure 2, b, d, f and Figure 4, b, correspondingly. For all the samples the intense tritium release was detected at all the steps of annealing. At temperatures below 700°C the tritium release from TIP-30 samples averaged between 5 % and 14 %, depending on the place where the sample was cut out. For DRR grade the tritium release at temperature up to 700°C did not exceed 0.6 %. At annealing temperatures up to 950°C the integrated tritium release achieved 48 %, 18 % and 14 % for the samples cut out from the TIP-30 block at the depths of 3 mm, 20 mm and 47 mm, accordingly. For the DRR samples the integrated tritium release did not exceed 8 %.

The comparison studies of data on tritium release show that the extent to which tritium is kept during the multi-stage anneleang increases with distance from the irradiated surface within the thickness of the material and also with an increase the beryllium oxide content. The most part of the tritium releases from beryllium samples at temperatures above 950 - 1000°C

Using kinetic curves of gas release, diffusion coefficients of helium and tritium for all stages of annealing were calculated on the base of solution of differential equation for thin

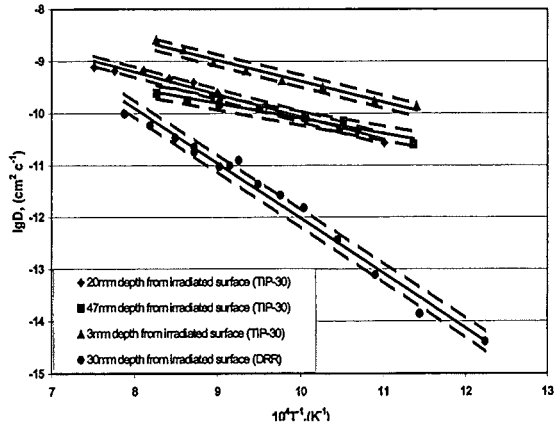

Figure 6. Tritium diffusion coefficients.

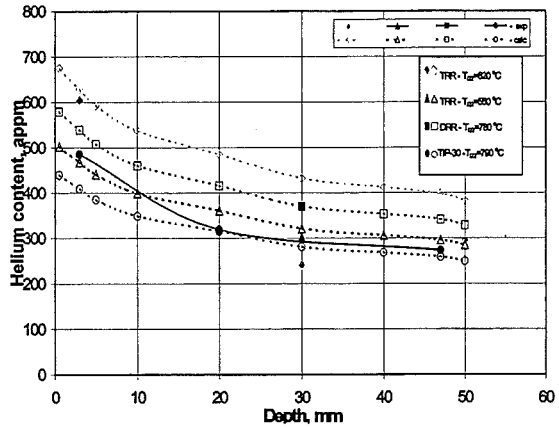

Figure 7. Helium content versus depth from irradiated surface

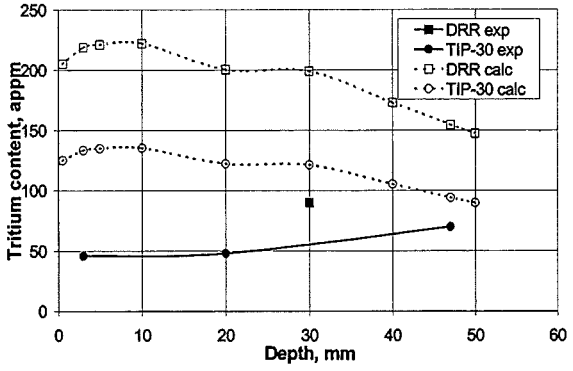

Figure 8. Tritium content versus depth from irradiated surface

plate (Figure 5,6). Statistical treatment of experimental data was performed for the temperatures up to 900°C. At higher temperatures an activation energy of helium release from beryllium was several times larger. That seems to be connected with an open porosity formation near the surface, resulting in an alternation of gas release mechanism [10]. By statistical treatment of experimental data, the empirical dependences for helium and tritium diffusion coefficients in berylluim were calculated:

For helium: $\ln D = -(24.6 \pm 2.2) - (155.3 \pm 2.6)/RT$

For tritium:

$\ln D = -(13.3 \pm 1.1) - (82.4 \pm 9.6)/RT$ (TIP-30, 3 mm depth)

$\ln D = -(12.3 \pm 1.4) - (77.2 \pm 11.6)/RT$ (TIP-30, 20 mm depth)

$\ln D = -(16.5 \pm 1.5) - (55.99 \pm 13.2)/RT$ (TIP-30, 47 mm depth)

$\ln D = -(3.3 \pm 1.8) - (202.5 \pm 15.3)/RT$ (DRR, 30 mm depth),

where activation energy is in kJ / mol · grades and diffusion coefficient - in cm^2/s.

Data presented show that when swelling of beryllium increases tritium mobility and release increase significantly, while helium mobility change negligibly.

The experimental data on helium and tritium contents obtained from the measurements of gases release at multi-stages annealing up to melting are shown in Figure 7 and 8. In addition to experimental data the results of neutron-physics calculations based on dependency of gases inventory in the beryllium block along the neutron flux direction are presented for various depths from the irradiated surface. One can see the good similarity of experimental data for helium retention and data of neutron-physics calculations (Figure 7). With one exception ($TRR_{620}{}^{o}C$, the depth=30 mm) the difference in value between experimental data and calculations ranged from 0 % to 20 %. For TRR sample ($TRR_{620}{}^{o}C$, the depth=30 mm) a significant discrepancy (~ 40 %) the values was noted. The reason of this discrepancy is not clear. According to data presented in Figure 7 almost all helium generated under irradiation remains in beryllium. Thas associates with both low diffusion mobility of beryllium and minor (less than 2 %) swelling of the samples investigated and also suggests that the initial technological porosity of 2-3 % is in sufficient to prevent swelling of the beryllium under high temperature irradiation.

Table 4
The extent of tritium release for TIP-30 grade

Depth from irradiated surface, mm	Swelling, %	(1- H^3exp./H^3 calc.) ·100, %	C_{BeO}, wt. %	C_{helium}, exp., appm
3	1.81	65	2.1	485
20	1.36	61	2.1	319
47	0.5	25	2.1	273

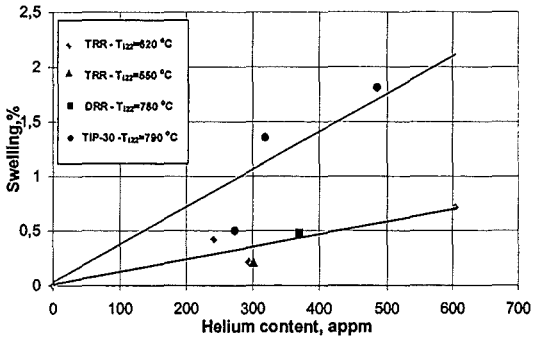

Figure 9. Beryllium swelling vs helium content

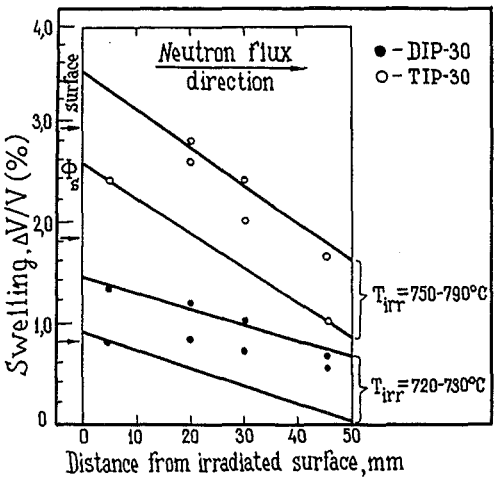

Figure. 10. Swelling inhomogeneity versus distance from a surface of irradiated beryllium

Much different results were obtained for tritium (Figure 8). Data on tritium content show that after irradiation the amount of tritium in beryllium is significantly lower than a calculated value. This distinction is greatest within the surface layers and decreases with distance from surface into a center of material. It follows that during a high temperature irradiation a significant part of tritium releases from beryllium. The extent to which tritium releases under irradiation will increase with both a rise of irradiation temperature and an increase of beryllium susceptibility to swelling and also decreases with distance from irradiated surface (Table 4). The data presented show that when gas-induced swelling rise from 0.5 % to 1.8 % it leads to alteration of helium to tritium retained amounts ratio approximately from 4 : 1 to 10 : 1.

The results obtained show, that:

1. Under high temperature irradiation in contrast to low temperature irradiation a significant part of tritium, generated by nuclear reactions, releases from beryllium. The extent of tritium release will increase with a rise of irradiation temperature, an increase of susceptibility to swelling and also as a sample is approached to irradiated surface.
2. After high temperature irradiation tritium retent presents in Be in more stable thermo-dynamic condition than after low temperature irradiation [6]. The extent to which tritium retents at post-irradiation annealing is higher for the samples with lesser swelling and higher content of oxide.

Figure 9 presents the dependencies of swelling against helium content for the samples irradiated. By statistical treatment of experimental data it was shown that they could be described by linear relationships.

Figure 10 presents some data on swelling inhomogeneity versus distance from a surface of irradiated beryllium. The higher a temperature of irradiation and beryllium grade susceptibility to swelling, the higher swelling inhomogeneity. For the TIP-30 grade (Table 4) swelling in near-surface layers is by a factor of 2.7 higher than that at the

depth of 20 mm from irradiated surface and by a factor of 3.6 higher than that at the depth of 47 mm. Swelling inhomogeneity is associated with the properties of beryllium to scatter and to slow down neutrons, resulting in production of transmutant-elements along the direction of neutron flux. Swelling inhomogeneity is a natural characteristic property of Be and it should be taken into account when designing beryllium elements of construction, because this phenomenon may result in additional alternate stresses, which can lead to inhomogeneous deformation of beryllium elements and even to their failure.

4. SUMMARY

The studies were conducted on swelling and helium and tritium retention in three beryllium grades irradiated at high temperature. It was shown that a significant part (from 25 to 65 %) of tritium generated during high temperature irradiation (T = 790°C) releases from Be, while almost all amount of helium retains in beryllium.

The extent, to which tritium releases, increases with a rise of irradiation temperature, an increase of swelling and also with approach to irradiated surface.

After high temperature irradiation tritium retent presents in Be in more stable thermo-dynamic condition than after low temperature irradiation. The extent to which tritium retents at post-irradiation annealing is higher for the samples with lesser swelling and higher BeO content.

The empirical dependences for helium and tritium diffusion coefficients in berylluim were calculated:

For helium: $\ln D = -(24.6 \pm 2.2) - (155.3 \pm 2.6)$ kJ/mol · grad /RT

For tritium: $\ln D = -(13.3 \pm 1.1) - (82.4 \pm 9.6)$ kJ/mol · grad /RT (TIP-30, 3 mm depth)

$\ln D = -(12.3 \pm 1.4) - (77.2 \pm 11.6)$ kJ/mol · grad /RT (TIP-30, 20 mm depth)

$\ln D = -(16.5 \pm 1.5) - (55.99 \pm 13.2)$ kJ/mol · grad /RT (TIP-30, 47 mm depth)

$\ln D = -(3.3 \pm 1.8) - (202.5 \pm 15.3)$ kJ/mol · grad /RT (DRR, 30 mm depth)

With increase in swelling induced by irradiation tritium mobility rises significantly, while mobility of helium varies very slightly. Increase in swelling from 0.5 to 1.8 % results in alternation of helium/tritium amounts ratio in irradiated beryllium approximately from 4:1 to 10:1.

It was shown that the inhomogeneity of swelling is a silent feature of beryllium. The higher a temperature of irradiation and susceptibility of Be grade to swelling, the higher swelling inhomogeneity. For the TIP-30 grade swelling in near-surface layers is by a factor of 2.7 and 3.6 higher than at depths of 20 and 47 mm, correspondingly.

REFERENCES

1. M.C. Billone, M. Dalle Donne and R.G. Macaulay-Newcombe, Status of Beryllium Development for Fusion Applications, Fus. Eng. Design 27 (1995) 179-190.
2. J.B Rich and G.P. Walters, Metallurgy of Beryllium (Chapman and Hall, London, 1963) p. 362.
3. B.G. Hickman, Nucleation and Growth of Gas Bubbles in Irradiated Metals, J. of the Austral. Inst. Met. Vol. 5 (1960) 173.
4. A.G. Bespalov et al., Dffusivity of the He in Irradiated Berylluim, Transactions of Phys. Energ. Inst. (1974) 443.
5. V.V. Vlasov and Y.G. Degaltsev, Migration of the Helium in Berylluim Irradiated by Alha-particals, preprint IAE, 3430/11, 1981.
6. D.L. Baldwin and M.C. Billone, Diffusion/Desorption of Tritium from Irradiated Beryllium, J. Nucl. Mater. 212-215 (1994) 948-953.
7. M.C. Billone, C.C. Lin and D.L. Baldwin, Tritium and Helium Behaviour in Irradiated Beryllium, Fusion Technology 19 (1991) 1707-1714.
8. H. Kawamura and E. Ishituka, Proc. Int. Workshop on Ceramic Breeder Blanket Interactions, Cleawater, FL (November 1991) pp 164-168.
9. I.B. Kupriyanov, V.V. Vlasov and V.A. Gorokhov, Helium and Tritium Retention and Migration in Beryllium, Proc. 16th IEEE/NPSS SOFE, Sept. 30- Oct. 5 (1995) pp. 948-951.
10. V.V. Vlasov and Y.G. Degaltsev, The Investigations of Helium Migration Processes at Annealings of Berylluim, VANT 3/57 (1991) 46-49.

ESR INVESTIGATIONS OF GAMMA IRRADIATED BERYLLIUM CERAMICS

Yu.A.Ryabikin, A.I.Polyakov, Yu.V.Petukhov, M.I.Bitenbaev, O.V.Zashkvara
Physical-Technical Institute MS&HE, 480082, Almaty 82, Kazakhstan,

In this report the result of ESR- investigation of kinetics of radiation paramagnetic defects accumulated in beryllium ceramics under gamma irradiation are presented. The data on quantum yield and destruction rate constants of these defects under ionizing irradiation are obtained.

I. INTRODUCTION

Beryllium and beryllium ceramics on beryllium oxide basis are one of construction materials which are widely used as heat-resistant protective coating in nuclear energetics, cosmic technique and various technologic processes. In this connection the problem of radiation stability of beryllium materials to affect of significant doses of ionizing irradiation is very urgent.

II. EXPERIMENTAL

The samples for the experiments with the dimensions of 2.5 × 6.0 × 1.0 mm were cut from one ceramic plate prepared in factory conditions and possessed of chemical-physical characteristics given below in Table I.

TABLE I. Physical-chemical characteristic of beryllium ceramic

1	Content,not less,%	
	BeO	99.5
	Fe	0.1
	Ti	0.05
	Y	0.03
	other impurities	0.12
2	Density, kg/sm^3	2.86-2.92
3	Mechanical strength for static bending, kg/sm^2, not less	1800-2200
4	Specific volume resistivity, ohm/sm, not less	$4.7 \cdot 10^{15}$
5	Tangency of dielectric losses angle at frequence,$1.0 \cdot 10^{10}$ Hz, not more	$2.0\ 10^{-4}$
6	Dielectric penetration at frequency, $1.0 \cdot 10^{10}$ Hz	5.8
7	Head conduction in vacuum, cal/sm·grad	0.62
8	Temperature coefficient of linear extension in temperature range 100-900^{0}C, 1/grad C	6-10

The samples irradiation was carried out by Co^{60}-source in the dose range 0÷100 Mrad. All following measurements were performed at the room temperature. For ESR-spectra registration the calibration standard samples were used; measurement geometry and registration conditions were such that exclude spectra distortion due to fast passage of resonance conditions or saturation effects [1,2]. As a result, relative error of paramagnetic defect concentration measurement in ceramics irradiated samples did not exceed 3-5%, at the irradiation dose definition error 5-10%.

III. RESULTS AND DISCUSSION

In fig.1 ESR- spectrum of initial non-irradiated sample of beryllium ceramics is given. Basing on g-factor, line width between maximal slope points ΔH_{pp} and line shape, the observed ESR-spectrum was attributed by us with trivalent iron ions Fe^{3+} presenting in the ceramics in oxide form with concentrations ~ 0.1%. This line intensity was observed to change significantly at transition from a sample of investigated ceramics to another one in spite of the fact that all samples were synthesized by means of the same technologic regulations.

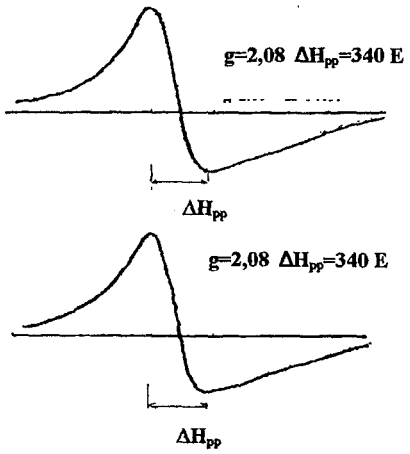

Fig. 1. EPR spectra of dopant three valent iron in ceramic on BeO basis:
a) Initial nonirradiated sample
b) γ-irradiated sample (D=24 MRad)

This fact signifies that iron in the ceramics obtained by powder metallurgy procedure is

distributed non-homogeneously on material bulk and that the use of iron impurity "as paramagnetic mark" permits with help of ESR to evaluate homogeneity of beryllium ceramics and articles of it.

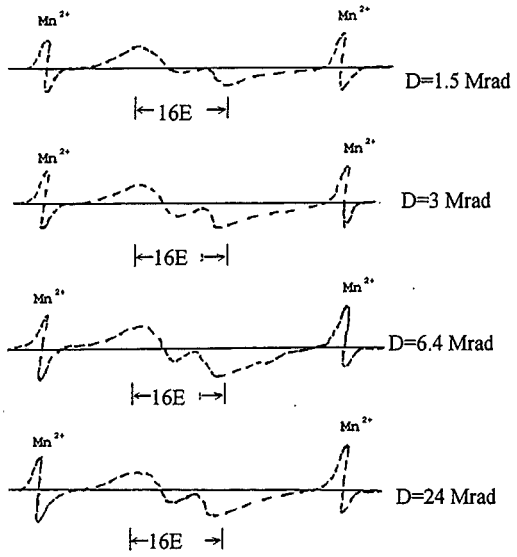

Fig.2. EPR spectrum of radiation paramagnetic defects in gamma-irradiated berillium ceramic (double line with g = 2.008 and splitting δ = 16 E).

Irradiation of beryllium ceramics by γ-rays leads to an appearance in ESR-spectrum a poor -resoluted

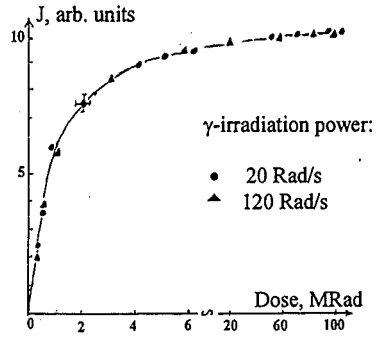

Fig. 3. Experimental dependence of ESR spectrum intensity of beryllium ceramic on γ -irradiation dose.

doublet (fig.2) with splitting Δ~16Oe between maxima and g –factor equal to 2.008. That is, paramagnetic centres responsible for this doublet are formed only under influence of ionizing radiation and therefore can be attributed with radiation paramagnetic defects.

It can be noted that γ- irradiation did not significantly affect on the intensity and other ESR-spectrum characteristics of impurity iron in all investigated dose interval. For a comparison, one of the spectra is given in fig.1b. At the same time the irradiation dose change influenced on doublet line intensity (fig.2). Since the intensity is a value proportional to radiation paramagnetic defect concentration, given in fig.3 curve reflects dose dependence of paramagnetic defect concentration (denomination well-known in literature: accumulation curve). As one can see in the figure, this dependence have a form of accumulation curve with saturation what is characteristic of many solid state systems (crystals, various polymers, organic substances and others) in which under radiation not only appearance of radiation paramagnetic centres occurs but their destruction owing to recombination or interaction with radiation field. Such a kind accumulation processes are described by following equation of general form [3-5]:

$$\frac{dR}{dt} = GP - k_1 PR - k_2 R^2 - \sum_i k_i B_i R \quad (1)$$

with initial condition [R]=0 at t=0.
In the equation (1) such designations are taken:

P - irradiation power;
G - quantum yield of defects;
k_1 - destruction rate constant of radiation defects directly by ionizing radiation;
k_2 - destruction rate constant of radiation defects because of their pair recombination;
k_i - destruction (or transformation) rate constants of the defects because of other possible mechanisms;
Bi(R) - term, accounting for concrete concentration dependence of radiation defect destruction rate because of other possible i-mechanisms.

In our experiments both ESR-spectra intensity and shape of irradiated ceramics did not practically depend on radiation power and exposure time of irradiated samples at room temperature (although this time is in appreciably excess of irradiation duration). This says that processes of paramagnetic defects transformation to other structures or their destruction because of recombination as well as other mechanisms do not significantly affect on kinetics of radiation paramagnetic defect accumulation and, consequently, in beryllium ceramics, at least in temperature range T<100^0 C, defect destruction occurs mainly because of their interaction with radiation field. In this case in right-hand side of the equation (1) one can neglect by all terms besides two first terms. Then, solution of obtained equation is:

$$R = R_{\lim}[1 - \exp(-k_1 D)] \quad (2)$$

$R_{lim}=G/k_1$ – limit value of radiation paramagnetic defect concentration.
For initial linear section of accumulation curve the

$$G=\frac{R_l}{D_l} \qquad (3)$$

ratio $k_1D<1$ holds and then
D_l and R_l - irradiation dose and corresponded defect concentration, respectively, on linear section of the accumulation curve.

Thus if the limit concentration value of radiation paramagnetic defects is known (in our case it is ($6.4\pm0.8)\cdot10^{14}$ defects per a sample), one can easily determine G and k_1 values for beryllium ceramics and confront them with similar data for other radiation-resistant materials.

However it should be remembered that G and k_1 values determined by means of above method will hold only in those case when experimental accumulation curve of radiation paramagnetic defects (fig. 3) is described by the equation (2) in a whole diapason of irradiation doses used in the experiment. Such a situation is known [3] to be possible if only one type of the defects is formed under irradiation and G and k_1 values, in turn, do not change in dependence on irradiation dose (or power).

To make more exact these circumstances the shape of the experimental accumulation curve presented in fig. 3 was analysed.

The accumulation curve rebuilt in corresponding coordinates is given in fig.4. The

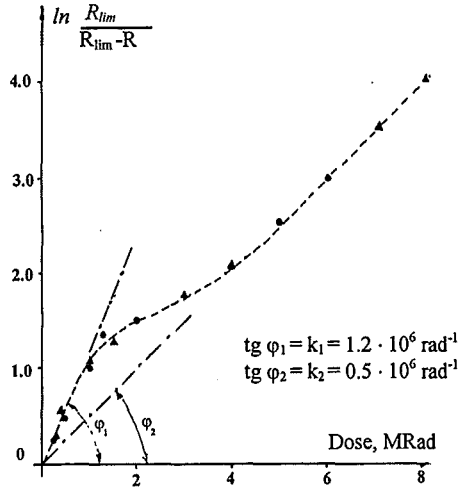

Fig. 4. Linear anamorphose of radiation damage storage curve in beryllium ceramic.

presence of two linear section with slope angles, differed more than two times, mean that in beryllium ceramics, most likely, an accumulation of some radical states occurs, one type of defects predominating at small doses (< 2Mrad) of irradiation, and other type of defects predominating at greater ones (> 3Mrad).

Performed by us an expansion of experimental dependence $R\sim R_{lim}\cdot f(D)$ by long range asymptote method [6] permitted to choose from summation dependence the contributions of various defect types and to get two analytical curves presented in fig. 5 as

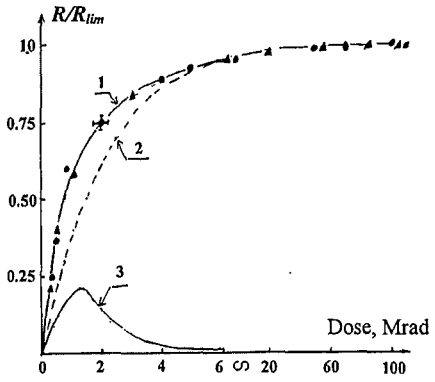

Fig..5. Kinetics of paramagnetic radiation damage of I and II-types storage in berillium ceramic.
1 - experimental function
2 - calculation by distant asymptotic method;
3 - difference between 1-st and 2-nd curves.

dotted lines. These curves are seen to differ significantly. One dependence R~ f(D) have got a view of traditional curve with a saturation and is characterized by single value of the G_1 and k_1 constants which do not depend on radiation power and integral irradiation dose.
The second dependence R~ f(D) have got a view with distinct maximum at D=1.2 Mrad. Previously we have show [7] that such an anomalous shape of accumulation curves of paramagnetic centres in γ-irradiated polymetacrylats is bound up with dependence of quantum yield on irradiation dose. In according to [7] a generalized equation for description of accumulation curve with a maximum (the second type of radiation paramagnetic defects in beryllium ceramics) can be written as:

$$\frac{dR_2}{dt}=G_0P\exp(-k_{3,2}D)-k_{1,2}PR_2 \qquad (4)$$

Where, R_2 -concentration of the radiation paramagnetic defects of the second type;
G_0 - quantum yield of defects of the second type on "linear part of accumulate curve initial section;
$k_{1,2}$ - rate constant of their destruction by ionizing radiation;
$k_{3,2}$ - rate concentration of quantum yield value change in dependence on irradiation dose.
The following analytical equation is the solution of the equation (4):

$$R_2=\frac{G_0}{k_{1,2}-k_{3,2}}\exp(-k_{3,2}D)\{1-\exp[-(k_{1,2}-k_{3,2})D]\} \qquad (5)$$

Quantum yield G_0 is defined from following expression:

$$G_0 = \frac{R_{2l}}{D_l} \qquad (6)$$

And the analysis of falling section of the accumulation curve, i.e. $k_{3.2}D>1$, have show that it is described by an exponential function and, consequently slop of its linear anamorphose,

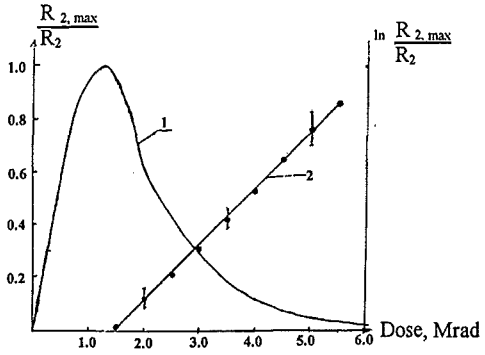

Fig.6. Storage curve of radiation defects of 2-nd type and linear anamorphose of decreasing part of this curve.

presented in fig.6, defines the constant $k_{3.2}$, i.e.

$$k_{3.2} = tg\alpha \qquad (7)$$

Now one can determine the constant $k_{1.2}$ value by using the circumstance that in range of maximum of the second type radiation paramagnetic defects, that is when D_{max}=1.2Mrad, the derivative in the equation (4) $dR_2/dt = 0$.
Then, for $k_{1.2}$ we get:

$$k_{1.2} = G_0 \cdot \exp(-k_{3.2} \cdot D_{max}) \qquad (8)$$

So, we have obtained the expressions for determination of all characterized constant for accumulation process of both types of radiation paramagnetic defects in γ-irradiated beryllium ceramics. Numerical values of these constants are listed in Table II.

IV. CONCLUSION

From obtained data it results that the differences in accumulation kinetics of radiation paramagnetic defects of the first and the second types in γ-irradiated beryllium ceramics is due to more than two times differed values of their quantum yield and the destruction rate constants and ionizing radiation effect. Upon that the summation paramagnetic characteristics of the ceramics in investigated dose range change weakly and is defined, mainly, by the first type of radiation paramagnetic defects.

The first type defects can be supposed to form in ceramics bulk and the second one – on the sample surface, therefore the influence of radiation-stimulated oxidizing processes proves to be important for them already at small irradiation doses.

Table II. Constants values of storage kinetic of radiation paramagnetic centers (pmc) in γ-irradiated beryllium ceramic.

Radiation paramagnetic defects	R_{lim}, 10^{14}, pmc/sp.	R_{max}., 10^{14}, pmc/sp.	G, 10^8, pmc/rad	k_1, 10^{-7}, rad^{-1}	k_3, 10^{-7},rad^{-1}
Type I	(6.4 ± 0.8)	-	3.2 ± 0.4	4.7 ± 0.5	-
Type II		1.4± 0.1	1.5 ± 0.2	2.4 ±0.2	2.2 ±0.2

Let us also note that for beryllium ceramics the defect quantum yield is by 2-3 orders lower than for heat-resistance polymer systems. This say about its heightened radiation stability and probable prospects for use in nuclear energetics plants.

REFERENCES

1. S. Lebedev, V.I. Muromtsev, ESR and relaxation of stabilized radicals, Moskow Chemistry, 1972.
2. M.I. Bittenbaev, A.I. Poljakov Saturation of non-uniformly extended ESR lines at quick modulation conditions Izv. AN Kaz.SSR, N4 (1982) 30-33.
3. L.A.Tihomirov, V.A. Beljaev, N.Ja. Buben Kinetic of free radicals accumulation at solid state radiolize, Izv. AN SSSR, N4 (1965) 594-598.
4. S.P. Pivovarov, A.I. Polyakov, Investigation of the accumulation of free radicals under irradiation of some polymethacrylate co-polymers in the 270-400 K temperature range, Rad.Eff., 59 (1982) 179-182.
5. N. Emmanuel, D. Knorre Chemical kinetics course, Moskow Vys. Shol., 1974.
6. A.I. Polyakov, Non linear relaxation spectroscopy of radiation defects in solids, Jnt. Conf Nucl. and Rad. Phys.Almaty, 1997, pp.97.
7. M.I. Bittenbaev, A.I. Poljakov, Anomalous dependence accumulation of radiation defects in polymers at high temperature irradiation, Izv. AN Kaz.SSR, N6 (1983) 16-20.

SURFACE REACTIONS AND LAYER FORMATION ON BERYLLIUM THROUGH CARBON AND OXYGEN BOMBARDMENT AND CARBON VAPOUR DEPOSITION

P. Goldstrass, W. Eckstein, and Ch. Linsmeier*

Max-Planck-Institut für Plasmaphysik, EURATOM Association, Boltzmannstr. 2, D-85748 Garching, Germany

Layers are formed by the bombardment of clean polycrystalline metallic beryllium with carbon, the co-bombardment with carbon and oxygen, and the evaporation of carbon on a clean metallic beryllium single crystal (0001). The bombarded samples are investigated experimentally by Rutherford backscattering spectrometry and by computer simulation using the Monte Carlo code TRIDYN. The experiments use C^+ and CO^+ ions with energies between 3 and 12 keV at normal incidence. The results of carbon bombardment from experiment and simulation agree well and show the buildup of a carbon layer on the metal surface. After the carbon layer formation, no more beryllium is eroded. For C and O co-bomardment, carried out by CO^+ ion bombardment, simulation and experiment agree for low fluences. At higher fluences a deposition/erosion equilibrium establishes, which is not predicted by the kinematic TRIDYN code. Weight loss measurements during 3 keV CO^+ ion bombardment show that a ternary mixture layer formed on the beryllium target leads to a continuous beryllium erosion. The vapour deposition took place at room temperature. The resulting films are investigated in situ by means of X-ray photoelectron spectroscopy (XPS) and Rutherford backscattering spectrometry (RBS). They are successively heated to temperatures between 473 K and 873 K in steps of 100 K and analyzed after each step. The as-deposited films consist of Be_2C at the beryllium/carbon interface and of a mixture of graphitic and disordered carbon on top. At elevated temperatures carbidization takes place between 473 K and 673 K and leads to a homogeneous layer of Be_2C on top of the beryllium. The Be_2C bulk photoelectron energies are found to be 282.7 eV for C 1s and 113.0 eV for Be 1s, respectively.

1. Introduction

Considering beryllium as a first wall material for magnetic confinement fusion devices [1], the formation of multi-component layers and compounds on the beryllium surface by (re-) deposition and erosion is of great interest. Elements like carbon and tungsten are under discussion for certain parts of the first wall while oxygen is present in the plasma as an impurity. The investigation of mixed materials formed by these constituents is essential to determine the physical and chemical properties of the first wall, e.g. important for erosion and hydrogen retention processes. Therfore, in this paper the effects of two different ways of layer formation are studied: The bombardment of Be with C^+ and CO^+ (simultaneous C and O bombardment) ions to study the effects of energetic particle bombardment and the deposition of carbon by evaporation to study the surface reactions of thin and very clean carbon films growing at room temperature without the influence of energetic particles.

2. Experiment

A polished polycrystalline Be target is irradiated at normal incidence with 3 keV and 5 keV C^+ and 3 keV, 5 keV and 12 keV CO^+ ions. The ions are produced by an electron impact source from CO gas (Linde 3.7) and subsequently mass-separated by a 80° magnetic deflection. The base pressure in the target chamber and during in situ RBS analysis was in the low 10^{-11} hPa range. During implantation the pressure did not exceed 5×10^{-11} hPa. The target was cleaned by periodic 5 keV Ar^+ bombardment and annealing to 673 K. The only impurities detectable by RBS were Ta (~ 6.0×10^{13} cm^{-2}),

* Corresponding author. Tel.: +49 89 3299 2285; fax: +49 89 3299 2279; e-mail: linsmeier@ipp.mpg.de

caused by sputter deposition from an aperture used in early steps of the cleaning procedure, and Ar (~ 2 × 10^{16} cm^{-2}) from the ion bombardment during the cleaning process. Rutherford backscattering analysis was performed using 0.6 MeV $^4He^+$ at normal incidence. Implantation and subsequent analysis were all carried with the sample at room temperature.

The weight loss measurements were carried out with a high-current ion source described in [2] using the same target as above. The Be target was cleaned by polishing leading to an oxygen and carbon impurity concentration in the range of (5 – 10) × 10^{16} cm^{-2}. An ion energy of 3 keV was used. The ions were mass-separated by magnetic deflection between the ion source and the target chamber. After certain ion fluences the weight of the sample was determined in vakuo using a Mettler 22 vacuum microbalance with a sensitivity better than ±1 μg. The weight loss is then calculated using the original sample weight measured before the ion bombardment in the same vacuum chamber. The base pressure in the target chamber is about 1 × 10^{-9} hPa, it increases during bombardment to 1 × 10^{-6} hPa.

A beryllium single crystal (0001) is cleaned by periodic 1 keV Ar^+ bombardment and heating to 673 K. The only impurities detectable by XPS and RBS are O (< 0.1%) and Ar (< 2%). Carbon films with thicknesses between 0.1 and 3.7 nm are deposited on the sample by electron beam evaporation of graphite (Goodfellow, 99.999%) at room temperature. Each film is heated in steps of 100 K from 373 K up to 873 K. The sample is left at each temperature for 10 min. and is allowed to cool below 373 K for XPS and RBS analysis. After the thermal treatment the oxygen contamination does not exceed 2.5 %. RBS analysis is performed using 1.0 MeV $^4He^+$ ions at normal incidence. The XPS probe is Mg K_α (1253.6 eV). The photoelectrons are detected at 90° relative to the sample surface. The electrostatic hemispherical analyzer (PHI, Ø 279.4 mm), equipped with an entrance lens system, is operated at a constant pass energy of 23.5 eV. The Au $4f_{7/2}$ core level line (84.0 eV) of a clean gold sample is used for energy calibration. The base pressure in the new UHV chamber ARTOSS during in situ RBS and XPS is in the 8 × 10^{-11} hPa range. The maximum pressure during evaporation did not exceed 5 × 10^{-10} hPa. The maximum pressure during the heating process is 1.5 × 10^{-9} hPa at 873 K.

3. Simulation

The calculations are performed with the Monte Carlo program TRIDYN (version 40.3) [3,4]. This program takes into account all collisional effects as implantation, reflection, and sputtering. Target composition changes due to the bombardment are regarded as well, so that effects like sputter yields, reflection coefficients and composition profiles can be determined as a function of the bombarding fluence. The program allows also simultaneous bombardment with several species of fixed energy or with a Maxwellian incident energy distribution. Surface binding energies, important for sputtering, are based on the elemental heats of sublimation and are interpolated due to the surface composition of the target [5]. Chemical erosion, diffusion and segregation are neglected. The sample is divided in thin layers of 0.25 nm thickness which may have different compositions. The output step is usually 1% of the total fluence applied. The composition of each layer is adjusted after processing every collision cascade. Thus, compositional changes due to the incoming ions are taken into account.

4. Results and Discussion

4.1. C^+ implantation

The Be target is bombarded after cleaning with C^+ ions up to a fluence of 5.5 × 10^{17} cm^{-2}. The maximum fluence is determined by the lifetime of the ion source filament. Figure 1 shows the calculated depth distribution of 5 keV C^+ implanted in Be for several fluences which correspond to the experimentally applied values. Beginning with 5 × 10^{16} cm^{-2}, carbon is deposited in a depth of roughly 20 nm with almost no carbon at the sample surface. For higher fluences, the carbon concentration on the target surface increases up to almost unity and the buildup of a carbon layer with increasing thickness is predicted. The further steps resulting in this layer formation are the erosion of the beryllium on the target surface above the implantation zone. During extended C^+ bombardment, the deposition zone with implanted carbon is finally reached. Since the self

sputtering yield of C^+ on pure carbon is below unity [2], a carbon layer starts to form on the Be substrate. This carbon surface layer grows steadily upon further C^+ ion bombardment.

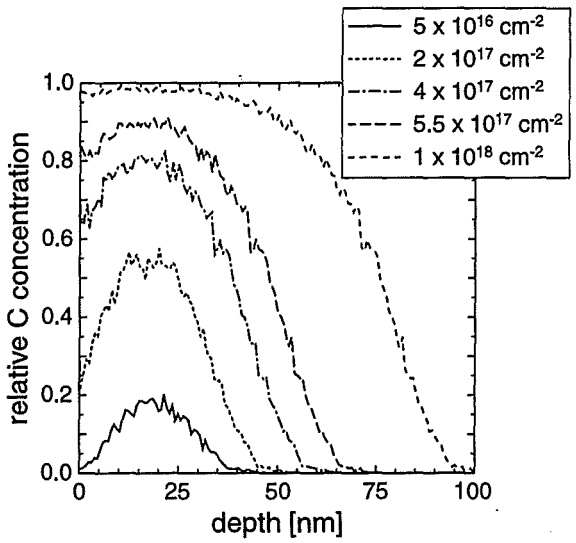

Fig. 1. Calculated depth distributions of C in Be. Be is bombarded with 5 keV C^+ at normal incidence (TRIDYN). The calculated fluences correspond to the values of the experiments.

The experimental results confirm the predictions from the TRIDYN simulation. Figure 2 shows the deposited amount of carbon on the target as a function of the C^+ fluence. The lines represent the TRIDYN calculations for a primary energy of the C^+ ions of 3 and 5 keV. Simulations are carried out both with KrC [6] and ZBL [7] interaction potentials. The difference between them is negligible and not visible in the diagram. The data points are the measured carbon concentrations in the Be target after the C^+ bombardment. Each experiment consists of one or more series, each starting with a clean Be surface containing no carbon and oxygen. The amount of deposited carbon after ion bombardment is calculated from the carbon peak area in the RBS spectra after background subtraction. For 5 keV C^+ the agreement between simulation and experiment is excellent. For 3 keV a deviation between the Monte Carlo calculation and the data points from RBS analysis can be recognized. However, the shape of the calculated line fits very well to the data points if these are scaled by a factor of 1.3. The scaling can be done either on the C^+ fluence or on the intensity axis to achieve this agreement. Since the deposited fluence is determined experimentally by integrating the current collected on the target and the surrounding Faraday cup during implantation, an error in the current measurement leads to an error in the C^+ fluence determination. Therefore, the agreement between the TRIDYN simulation and the RBS measurement can be regarded satisfying for both primary energies. The error bars at the experimental data points in Fig. 2 account only for the statistical error in the RBS spectra and do not reflect uncertainties in the current measurement.

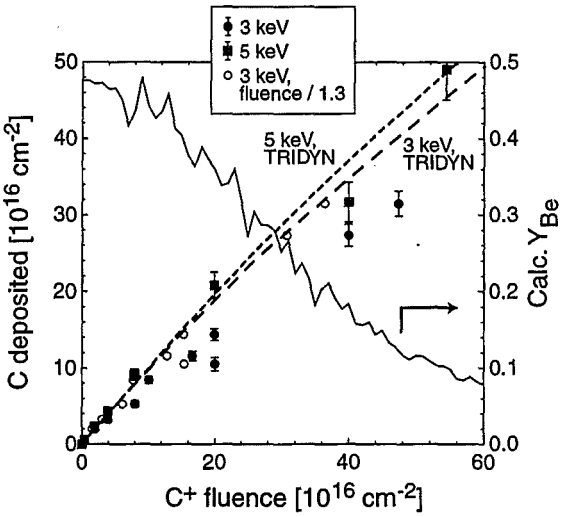

Fig. 2. Deposited C on the Be target versus the C^+ fluence due to the bombardment with 3 and 5 keV C^+ at normal incidence. Also shown is the calculated souttering yield of Be considering the compositional changes due to the C^+ bombardment.

As predicted by the simulation, the experiments show the buildup of a carbon layer on the sample surface. In the studied fluence range no saturation in the deposited amount of carbon is found. The carbon layer thickness at the maximum experimental C^+ fluence of 5.48×10^{17} cm^{-2} is 48.3 nm, calculated for a graphite density of 2.26 gcm^{-3}. This is in good agreement with the result from the calculation (Fig. 1), where the carbon concentration starts to decrease at a depth of about 50 nm. The maximum carbon concentration in the calculation is only 98 %, but the additional carbon in deeper layers leads to a total amount of carbon comparable to that detected in the

RBS experiments. The carbon layer at the maximum fluence after 3 keV C^+ bombardment (4.73×10^{17} cm^{-2}) reaches a thickness of 41.7 nm.

Both experiment and TRIDYN simulation in Fig. 2 show a change in the slope of the C amount with increasing fluence. This can be attributed to a compositional change in the surface layer during C^+ implantation. The carbon peak deposition zone is in a depth of approximately 20 nm. The sputtering process due to the collision cascades takes place at the outermost layers. This leads to an erosion of the mixed Be-C layer at the surface above the C implantation zone. This process continues until the surface layer consists predominantly of carbon. The gradual change in the composition results in an increase of the C^+ reflection. However, the reflected fraction of primary ions stays well below 0.2 % for both primary energies. For high C concentrations after greater fluences, the erosion of the Be-C mixed layer decreases and the C layer formation continues. This leads finally to a surface layer consisting almost exclusively of carbon, and as a consequence to the continuous build-up of a carbon layer on the beryllium substrate.

4.2. CO^+ implantation

Since the CO^+ currents from the ion source are much larger than for C^+, implantation fluences up to 2×10^{18} cm^{-2} are accessible in the experiment. Compared to the C^+ beams, the carbon and oxygen atoms impinging on the surface from CO^+ beams have lower energies. The kinetic energy is split between the atoms in the CO^+ molecule according to their mass ratio of C (3/7) and O (4/7). Therefore, carbon possesses energies around 1.286, 2.143 and 5.145 keV for the 3, 5 and 12 keV primary beams, whereas oxygen has energies of 1.714, 2.857 and 6.855 keV, respectively.

At low fluences below approximately 10^{17} cm^{-2}, the experimentally measured amounts of deposited carbon and oxygen in the sample increase according to the calculations by the TRIDYN program, see Fig. 3. This behaviour is similar to that of the C^+ bombardment and can be explained by the implantation of both C and O in the Be matrix. The ion bombardment also leads to a simultaneous sputtering of beryllium. Both carbon and oxygen are deposited in an implantation zone below the surface. The depth and width of this zone depend on the primary energy of the CO^+ ions. Since the kinetic energy splits asymmetrically between C and O upon CO^+ impact on the surface and these two species exhibit different stopping cross-sections on their paths through the target, their depth distribution is not identical. TRIM.SP calculations show that oxygen is implanted slightly deeper than carbon for ion energies of 3 and 5 keV [8]. The difference in implantation depth between C and O vanishes for a primary CO^+ ion energy of 12 keV. It can also be noted that the width of the implantation zones increases strongly with increasing CO^+ primary energy. The maxima of the implantation profiles given by TRIM.SP are located at a depth of about 5, 9 and 20 nm for 3, 5 and 12 keV, respectively.

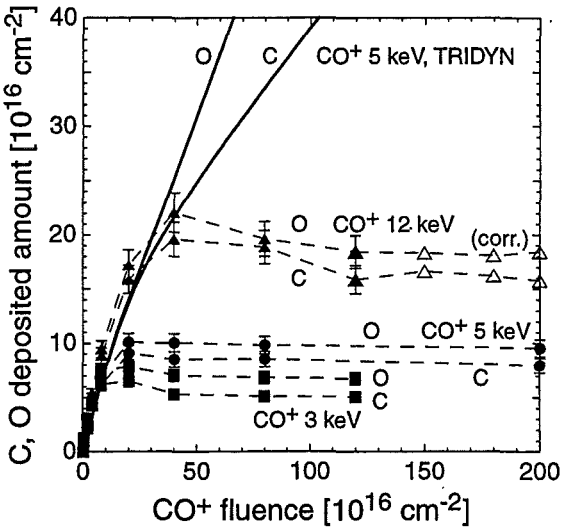

Fig. 3. Deposited C and O in the Be target versus the fluence due to the bombardment with 3, 5 and 12 keV CO^+ at normal incidence. Lines between the experimental data points are drawn to guide the eye. (The 12 keV CO^+ data points at fluences > 1.3×10^{18} cm^{-2} (open symbols) are corrected due to an error in the current measurement.)

During the continuing bombardment, the beryllium above the C and O deposition zones is eroded by sputtering. The actual sample surface recesses and subsequently C and O are deposited accordingly in greater depths. This will lead eventually to the formation of a mixed layer consisting of the three elements C, O and Be which starts at the surface and extends into the sample. In contrast to the C^+ implantation scenario, the ternary system of C, O

and Be is expected to show a more complex behaviour, which is demonstrated in the experimental results.

The C and O concentrations start to saturate at a fluence which depends on the CO^+ primary energy. Figure 3 shows a deviation of the RBS results from the TRIDYN calculations at fluences between 4×10^{16} cm^{-2} and 3×10^{17} cm^{-2}, depending on the CO^+ energies. Only shown is the TRIDYN calculation for 5 keV CO^+ ions, since the difference for 3 and 12 keV in the valid fluence regime below approx. 1.5×10^{17} cm^{-2} is negligible. The C and O concentrations start to saturate and reach an energy-dependent, constant value. The measurements also suggest that the amounts of deposited C and O pass through a maximum before reaching their saturation value. This saturation effect cannot be explained by mere atomic collisions and is therefore not predicted by the TRIDYN calculations. The experiments demonstrate that after a certain transition fluence an erosion mechanism other than collisional sputtering sets in. It leads to a constant C/O ratio and to a constant C and O inventory in the ternary compound formed on the beryllium target. This erosion mechanism releases C and O in equal amounts and is presumably of chemical nature. In experiments dealing with carbon erosion by oxygen, an erosion yield of about unity is found [2]. The formation of CO and CO_2 by chemical erosion of graphite and beryllium was observed under O^+ irradiation [9,10]. As observed in the O^+ ion experiments [10], this process may also be effective here only after an appreciable C concentration has been accumulated on the surface and after this layer is saturated in oxygen.

The reason for the initial increase in deposited carbon and oxygen, as predicted by the kinematic simulations, is the implantation of C and O in deeper layers. For the erosion mechanism via the formation of CO molecules and their subsequent desorption, a sufficiently high density of both C and O in the Be matrix is necessary. Moreover, the loss of CO by desorption is only possible at the outermost surface. Therefore, two criteria have to be fulfilled before CO erosion can take place and the observed deposition/erosion equilibrium sets in: (1) accumulation of C and O in a sufficiently high density for the formation of the CO molecules. This implies also that the substrate temperature (always room temperature in these experiments) may play an important role, since elevated temperatures will increase the mobility of implanted C and O species. Criterion (2) is the possibility for formed CO to desorb. This can only take place for CO reaching the target surface, either by the formation of CO molecules at the very surface or by diffusion of CO molecules from their formation location to the outermost surface. The increasing onset fluence, the increasing overall C and O inventories and the observed increasing C/O ratios for increasing CO^+ ion energies support this interpretation, as will be discussed in the following paragraphs.

The onset fluence for CO desorption reflects the depth of the implantation zone for C and O. For greater CO^+ primary energies this depth is larger and therefore a greater fluence is necessary to erode the overlying Be layer. Only after the implantation zone is sputtered, C- and O-containing material reaches the surface (CO formation at the surface) or the CO diffusion path length is long enough for CO to reach the surface (CO formation in deeper layers).

The increasing overall C and O inventory for increasing CO^+ primary energies is a consequence of the broader depth distribution for CO^+ ions with higher energies. This broader distribution leads to a greater thickness of the C-O-Be ternary mixture layer on the Be target and consequently to a greater C and O equilibrium concentration. Experimentally, the thickness of the ternary layer on the Be substrate is reflected in the shift of the Be edge in the RBS spectra. However, the edge shift compared to the edge of the clean Be sample is at the limit of the experimental resolution and may only be taken as a supportive argument.

The different C/O equilibrium ratios for the examined primary energies result from the difference in ion ranges and stopping cross-sections for C^+ and O^+ at their respective energies. For low primary energies, oxygen is implanted at slightly greater depths than carbon. After extended bombardment (after erosion of the Be layer above the implantation zone), the oxygen zone extends further into the sample than the carbon zone. This difference vanishes with increasing CO^+ primary energy. The different thicknesses of the C- and O-containing layers at equilibrium lead to different average C/O ratios of 0.75, 0.85 and 0.90 for the three respective CO^+ primary energies of 3, 5 and 12 keV. For higher ion energies, the C/O ratio appraches 1, since the implantation depths of C and O become equal.

The consequence of the equilibrium concentrations in the case of a C and O co-bombardment is an equilibrium composition of a ternary layer of finite thickness. This implies a continuous erosion of Be in addition to the CO desorption. Therefore, the chemical CO formation process, accompanied by kinematic sputtering, results in a continuous Be target erosion.

A continuous Be target erosion is also supported by the results of the weight loss experiments. A beryllium sample bombarded with 3 keV CO^+ ions shows an ongoing weight loss up to the maximum fluence applied (2×10^{19} cm^{-2}). Although the contamination of the sample used for the weight loss measurements was higher, RBS analysis shows that the bombardment results in the same equilibrium amount of C and O in the target. The weight loss depends linearily on the fluence indicating a constant erosion yield. Taking into account the measured constant C and O amounts in the target, the weight loss is explained by a constant erosion yield of beryllium, once the deposition/erosion equilibrium is reached.

4.3 Evaporated carbon films

To separate the effects of surface reactions of carbon with beryllium from the influence of the ion energy, thin carbon films have been deposited at room temperature on a beryllium single crystal (0001) by electron beam vapour deposition. Figure 4 shows the C 1s XPS signals for different amounts of carbon on Be after deposition. For the smallest coverage only one peak at a binding energy of 282.0 eV is observed. With increasing C layer thickness, another peak evolves. The signal around 284.2 eV dominates above a carbon coverage of 0.6 nm. A similar behaviour has been observed for carbon films on molybdenum [11] and tungsten [12]. This second peak can be attributed to an overlap of the peaks for graphitic and disordered carbon. The positions of these two peaks were determined on the inert gold surface to be 283.9 eV for graphitic carbon and 284.9 eV for disordered carbon [12]. The first peak is present at all coverages and shifts 0.5-0.7 eV to higher binding energies with rising coverage. The energies of this peak are well within the metal carbide range [13]. Therefore it is attributed to the only stable compound of beryllium and carbon [14]: Be_2C. The amount of Be_2C obtained from the XPS measurements first increases with rising coverage, reaches saturation at a thickness equivalent to two monolayers of carbon and decreases for the three highest coverages. This implies a carbidization at the interface. The observerd amount of Be_2C increases until the interface formation is complete and starts to decrease with rising coverage because of the attenuation of the interface signal in the carbon layer on top.

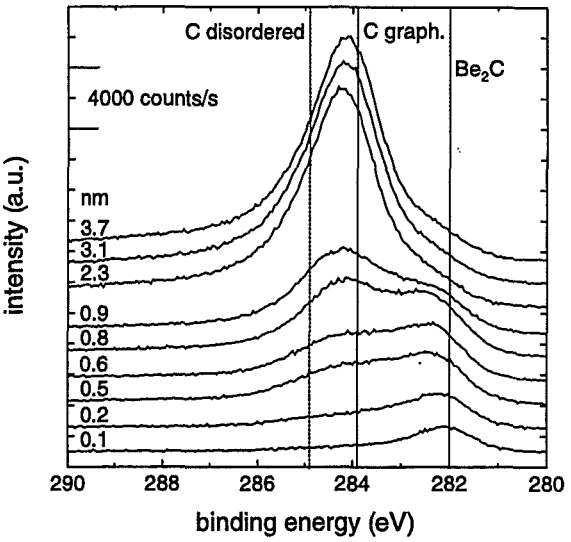

Fig. 4. XPS spectra of the C 1s region for different coverages. The thickness of each layer, obtained from the RBS analysis, is given in nm above each spectrum. The dotted lines show the peak positions for graphitic and disordered carbon for the carbon/gold system [12] and the measured Be_2C position for the lowest coverage.

During the thermal treatment of the films a complete carbidization takes place. The coverage-dependent Be_2C peak shift reported above is still observed after exposure to elevated temperatures. We believe that this is probably due to the incomplete interface formation and/or to beryllium surface effects not yet fully understood. Figure 5 shows the C 1s signals for a carbon amount of $4.2 \cdot 10^{16}$ cm^{-2} (3.7 nm) after each heating cycle. Up to 473 K almost no change is noticed in the spectra. Between 473 K and 673 K carbide formation takes place and proceeds with increasing substrate temperature until the carbon layer has completely reacted to Be_2C. At 573 K the

amounts of carbon and carbide are almost balanced. Above 673 K there is again no major change in the C 1s signal. The Be 1s signal shows similar but smaller shift due to the reaction compared to the C 1s signal. The difference to the Be_2C formation temperature of 873 K reported by Ashida et al. may be due to a high impurity contamination (about 20% Zn and 35% O as-deposited) of this layer [15]. Figure 6 shows the change in the surface atomic composition of the same sample with temperature according to the XPS analysis, calculated using the MultiPak software package [16]. After the carbidization of the layer the atomic composition Be:C is 7:3, in good agreement with the theoretical 67:33 for Be_2C.

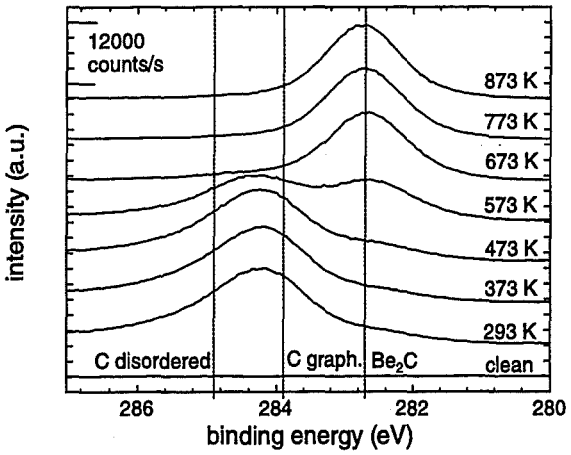

Fig. 5. XPS spectra of the C 1s region for 3.7 nm deposited carbon (after deposition at room temperature). The given temperatures describe the successive treatment applied in addition to the previous step. The dotted lines show the peak positions for graphitic and disordered carbon for the carbon/gold system [12] and the measured Be_2C position for the lowest coverage.

During the exposure to elevated temperatures up to 873 K carbon neither desorbs from the surface nor diffuses to a large extent into the bulk beryllium. RBS analysis shows that the total amount of carbon decreases only slightly (from $4.7 \cdot 10^{16}$ cm^{-2} at 673 K to $4.0 \cdot 10^{16}$ cm^{-2} at 873 K). The RBS carbon peak does not show the significant broadening one would expect in case of a carbon diffusion into the bulk. We conclude from the absence of carbon and metal

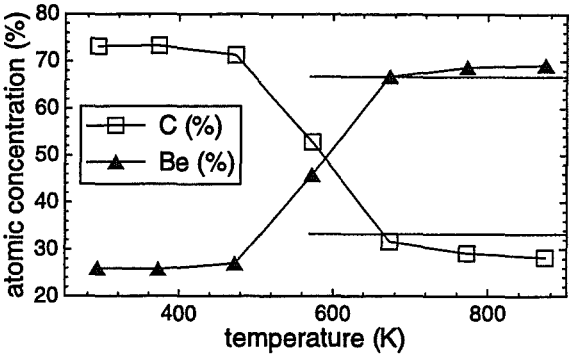

Fig. 6. XPS atomic composition of an as-deposited 3.7 nm thick carbon film on beryllium versus temperature during the thermal treatment. The dotted lines show the Be_2C stoichiometry.

beryllium peaks in the XPS spectra that a homogenous Be_2C layer forms on top of the beryllium substrate. Therefore, the XPS photoelectron energies observed after the temperature treatment for coverages above 1 nm are the Be_2C bulk energies. They are 282.7 eV for C 1s and 113.0 eV for Be 1s, respectively. The difference to the reported bulk peak energy of 282.0 eV for Be_2C reported by Ashida et al. [15] may be explained again by the high impurity contamination of their sample used to determine this energy.

5. Conclusions

It is shown that the experimental data are in good agreement with results calculated by the kinematic Monte Carlo code TRIDYN for 3 and 5 keV C^+ ions bombarding a clean beryllium target under perpendicular incidence. The interaction of the incoming ions with the target is fully explained by kinematic processes like implantation, reflection and sputtering. A carbon layer of increasing thickness is formed on top of the beryllium metal. After a fluence of approximately 1×10^{18} cm^{-2} no more Be is eroded.

Co-bombardment of beryllium with carbon and oxygen, simulated by the implantation of CO^+ ions in Be, shows a different behaviour. For low fluences, depending on the CO^+ primary energy, a kinematic description of the ion-target interaction is sufficient.

TRIDYN simulation and experiment both agree in the accumulation of carbon and oxygen in the Be target. However, after an energy-dependent fluence, anothe presumably chemical erosion mechanism dominates the ion-target interaction. This leads to a constant composition in the target surface layer. Both the composition and the thickness of the formed layer depend on the energy of the incoming CO^+ ions. The absolute amounts of C and O reach constant values for extended CO^+ implantation which in combination with the continuing weight loss of the target during borbardment means that the Be target surface is continuously eroded. The underlying chemical processes for this behaviour, which may imply the formation of BeO, Be_2C and additional compounds in the ternary layer, and the formation and transport of CO molecules as the desorbing species in the erosion process, are not yet identified and subject to further studies.

Carbon films vapour-deposited on beryllium at room temperature consist of Be_2C at the carbon/beryllium interface and a mixture of graphitic and disordered carbon on top. Between 473 K and 673 K a reaction takes place resulting in a homogeneous Be_2C layer on top of the sample. The Be_2C bulk photoelectron energies are 282.7 eV for C 1s and 113.0 eV for Be 1s. The erosion behaviour of such modified beryllium compound surfaces and their behaviour in hydrogen retention and reemission processes is subject of ongoing projects.

REFERENCES

[1] R.W. Conn, R.P. Doerner, J. Won, Fusion Engineering and Design 37 (1997) 481

[2] W. Eckstein, C. Garcia-Rosales, J. Roth, W. Ottenberger, IPP-Report 9/82, (1993)

[3] W. Eckstein, Computer Simulation of Ion-Solid Interaction, Springer, Berlin, 1991

[4] W. Möller, W. Eckstein, J.P. Biersack, Comput. Phys. Commun. 51 (1988) 355

[5] W. Eckstein, M. Hou, V.I. Shulga, Nucl. Instr. and Meth. B 119 (1996) 477

[6] W.D. Wilson, L.G. Haggmark, J.P. Biersack, Phys. Rev. B 15 (1977) 2458

[7] J.F. Ziegler, J.P. Biersack, U. Littmark, in: J.F. Ziegler (Ed.), The stopping and Range of Ions in Matter, vol. 1, Pergamon, New York, 1985

[8] P. Goldstrass, W. Eckstein, Ch. Linsmeier, J. Nucl. Mater. 266-269 (1999) 581

[9] V. Vietzke, A. Refke, V. Phillips, M. Hennes, J. Nucl. Mater. 220-222 (1995) 249

[10] A. Refke, V.Phillips, E. Vietzke, M. Erdweg, J. von Seggern, J. Nucl. Mater. 212-215 (1994) 1255

[11] P. Reinke, P. Oelhafen, Diamond and Related Materials 8 (1999) 155.

[12] J. Luthin, Ch. Linsmeier, Surf. Sci., submitted

[13] J.K. Moulder, W.F. Strickle, P.E. Sobol, K.D. Bomben, Handbook of X-ray Photoelectron Spectroscopy, Perkin Elmer Co., Physical Electronics Co., Physical Electronics Division, Minnesota, 1992

[14] Gmelin, Handbook of Inorganic and Organo-metallic Chemisrty, 8th Ed., Be, Sup. Vol. B4, Springer, Berlin, 1996

[15] K. Ashida, K. Watanabe, Fusion Engineering and Design 37 (1997) 307

[16] MultiPak Ver. 2.2, Physical Electronics, 1996

Plasma Deposition of Beryllium Carbide via Magnetron Sputtering

*Yixiang Xie, Nicholas C. Morosoff, William J. James
Chemistry Department and MRC, University of Missouri-Rola,
P. O. Box 1593, Rolla, MO 65409, 573-341-4405 (fax: 2071)
e-mail: xie@umr.edu.us (*contact person)

Richard B. Stephens, 619-455-3863 (Fax: 2399), Inertial Fusion Technology Division,
Fusion Group, P. O. Box 85608, San Diego, CA 92186-9784, stephens@gav.gat.com

Magnetron sputtering of Be into a methane/argon plasma at an audio frequency has been used to make beryllium carbide films for ICF (inertial confinement fusion) target capsule applications. Based on the AES, Auger electron spectroscopy analysis, films containing 50 to 75 atomic percent of Be and the balance elemental carbon and oxygen (< 2 atomic percent) were obtained by adjusting the methane to argon flow rate ratio in the deposition process. AES and XPS, x-ray photoelectron spectroscopy analyses provide strong evidence that Be_2C is the dominant phase in the films and that "free" beryllium exists in the Be-rich films. XRD, x-ray diffraction patterns of these films and the powder samples prepared from the films show only the presence of Be_2C with no evidence of Be and BeO crystals. The Be in the Be-rich films which is not evidenced in the x-ray patterns must be amorphous Be encapsulated in the beryllium carbide matrix. Additionally the absence of certain peaks corresponding to planes of fcc Be_2C suggests a preference for orientation that places the most densely populated planes parallel to the substrate surfaces. The Scherrer formula was used to calculate the crystal grain size, about 20 nm, by measuring the peak widths of (111) and (220) at half height intensities. SEM, scanning electron microscopy cross-sectional images and AES depth profiles reveal a relatively uniform microstructure and elemental compositions. Film cross-sectional views demonstrate the columnar micro-structure and the tight grain boundaries, and the thicknesses. The densities of the films are 1.94 – 2.14 g/cm^3. The roughness factor as determined by AFM, atomic force microscopy is about 24 nm close to the grain size calculated by the Scherrer formula, which implies a smooth surface. DTA, differential thermal analysis, and TGA, thermogravometric analysis of the Be-rich samples under argon suggest the possibility of Be sublimation at a temperature higher than 750 °C, which further supports the presence of free Be in the Be-rich samples. TGA experiments in dry air and wet air establish the greater resistance of Be_2C to oxidation in dry air as opposed to its behavior in moist air. In some manner the Be_2C matrix inhibits the oxidation of the dispersed Be particles within when the Be-rich films are exposed to air. Furthermore the same TGA experiments at room temperature show no weight change in either environment for a period of 24 hours. The films' exposure in laboratory environments for 30 days without weight change and little or no change in appearance of the samples, confirm that the films are air stable at ambient temperature. The films which come the closest to meeting the ICF capsule requirements have a hydrogen permeation coefficient of 7.0 cm^{3}Acm/cm^{2}AsecAcmHg which would allow the fuels to fill the capsule in less than one hour. The relative hardness to silicon is 1.1. Defect stress analysis and tensile stretching experiments indicate the thin films' tensile strength to be in the range of 10 to 100 thousand psi, which meets the ICF standards for filling the capsules to a 350 atm inner pressure. At room temperature the thermal conductivity is 1.95 W/m°C.

Furthermore experimental studies show that beryllium carbide has an extremely low sputtering rate, which suggests the use of beryllium carbide coating as a MCF reactor first wall material.

Erosion and deuterium retention investigation of mixed W-Be layer on Be in experiments on plasma disruption simulation

S.N. Korshunov[a], V.I. Vasiliev[b], M.I. Guseva[a], V.M. Gureev[a], L.S. Danelyan[a], V.V. Zatekin[c], V.S. Kulikauskas[c]

[a]Russian Research Center «Kurchatov Institute», Kurchatov sq. 1, Moscow, 123182, Russia

[b]TRINITI, Troitsk, Moscow region, Russia

[c]Phisical Department, Moscow State University, Moscow, Russia

The mixed W-Be layers were prepared by depositing of Be and W atoms on Be substrate under simultaneous sputtering of Be and W targets by 20 keV Ar^+-ions. The thickness of the deposited mixed W-Be layer was ~500 nm. The element composition analysis of these layers showed that mixed layer contains up to 35 at.% W, up to 35 at.% Be and up to 30 at.% O. The W-Be films on Be were irradiated by pulsed deuterium plasma flux in the electrodynamic plasma MKT-accelerator at the deuterium plasma concentration of 10^{21} m^{-3}, maximal ion energy of (1-2) keV and with the energy flux density of 0.2 MJ/m^2 per pulse. The pulse duration was equal to 60 μs. After irradiation by two plasma pulses the W-Be film is melted and removed completely from the local surface areas. The element distributions in a mixed layer after an effect of the pulsed plasma are essentially changed. For the surface areas with the removed film the Be concentration is about 75 at.%, W – about 15 at.%, O - about 10 at.% and the penetration of W and O atoms up to 1000 nm in depth of Be substrate is observed. For the surface areas with the retained melted film the Be surface concentration increase up to 90 at.%, tungsten and oxygen concentration decrease about 2-3 times. The method of Elastic Recoil Detection Analysis was used to study D retention. The integral deuterium concentrations are equal to $0.6 \cdot 10^{20}$ and $2.2 \cdot 10^{20}$ m^{-2} for the removed film areas and for the retained melted film ones, correspondingly. Consequently, deposited W-Be film promotes the essential reduction of D retention in Be substrate. Transmission electron microscopy was used to study the erosion product size distribution. The erosion products were collected on basalt filter fibers located in a shadow of the pulsed plasma flux around the exposed W-Be film target. The erosion product size distribution has two maxima located in the ranges 0.1-0.2 μm and 2.5-5.0 μm.

1. INTRODUCTION

Beryllium, tungsten and carbon-fiber composite (CFC) are expected to be used on different plasma-facing components (PFCs) of the International Thermonuclear Experimental Reactor (ITER). Beryllium will exist as the largest area plasma-facing material (PFM) because of its use on the first wall. CFC will exist on the highest power load components in the divertor. Tungsten will exist in other areas of the divertor and in the transition region, the lower baffle, to the first wall. Each of these materials are chosen in certain regions for specific material properties. However, erosion during normal ITER operation, as well as off-normal events (such as disruptions), will tend to distribute each of the materials to areas which were perhaps originally designed for other materials. This combination of materials, or mixed materials, can have substantially different properties than the originally designed for material. Moreover, mixed-material effects, arising from the simultaneous use of different PFMs, introduce significant uncertainties for the operation of ITER.

In spite of the fact that the plasma disruptions in tokamaks are violations of the normal current pulse

production, the development of instability causing the ejection of a practically whole plasma volume on the PFCs has not been prevented yet. In this connection, the experiments on the study of a high power pulsed plasma simulating the ITER operation with plasma disruptions on the plasma facing materials are of interest.

The studies of the effect of a high power deuterium pulsed plasma, simulating the plasma disruptions, on the deuterium retention and erosion of mixed W+Be layers on Be are presented in a given paper.

2. EXPERIMENTAL

Targets of electrolytically-pure tungsten and those of commercial powder-compacted beryllium of TShP-type containing 98.7 wt.% Be, 0.9 wt.% O, 0.2 wt.% Fe and 0.2 wt.% C,N and other elements were used in these experiments. Tungsten and beryllium sample surfaces were polished with diamond paste and then electrical polishing was done. The mixed W-Be layers were produced in the ILU accelerator [1] by simultaneous sputtering of tungsten and that of beryllium with Ar^+-ions having the energy of 20 keV. A special device for production of the deposited and mixed layers by simultaneous ion sputtering of different pair targets was made [2]. In this experiments the beryllium collector, having 15 mm in diameter, was placed at the distance of 25 mm from the tungsten and beryllium targets set at the angle of 60^0 to the ion beam. The temperature in the process of irradiation was sustained at the level of 600 K. The mixed-material samples underwent an irradiation in the electrodynamic plasma MKT-accelerator at the deuterium plasma concentration of 10^{21} m^{-3} and at the maximal ion energy of (1-2) keV. The pulse duration was equal 60 μs. In the experiments with the mixed (W-Be) layers deposited on beryllium the energy flux density was 0.2 MJ/m^2 per pulse and the number of pulses did not exceed two, since the film was completely removed with their increase. The deposited layer thicknesses were determined with a Sloan Instruments Dektax profilometer.

After each treatment by pulsed plasma fluxes the studies of target surface microstructure with the JEOL scanning microscope and element surface composition by the Rutherford back scattering technique in the Van-de Graaf accelerator were done. The back-scattered He^+-ions at the angle of 170^0 with the energy of 1.2 MeV were registered with a surface-barrier detector.

The Van-de-Graaf accelerator was also used for determination of the deuterium depth distribution profiles in the mixed W-Be layers by the method of the elastic recoil detection analysis (ERDA). In these experiments the analyzed He^+-ion beam with the energy of 2,2 MeV was incident on the sample under study at the angle of 15^0 to its surface. The recoil atoms were analyzed with a semiconductor detector at an angle of 30^0 relative to the initial of He^+-ion incidence direction. Deuterium depth distribution was calculated from the energy spectrum of deuterium recoil nuclei. Computed spectra were fitted to the experimental ERDA spectra using a data processing program taking account of the energy resolution power of the method. To determine the absolute values for deuterium atom concentration the experimental set up was calibrated with standard lavsan or milar thin film samples.

Basalt fibre filter as well as the graphite foil were used to collect the erosion and evaporation products. The collectors were located in a shadow of the plasma flux, the configuration of which were determined with the limiter (10x20 mm^2) made from tungsten plate. The morfological characterization and microstructure of erosion particles were investigated by means of transmission and scanning electron microscopy. Some layers, including 2-3 fibre layers with the erosion products deposited on them, were separated and studied with the JEOL transmission electron microscope. One should note that the erosion product morphology study with the transmission electron microscope has a great advantage over the scanning one, since it gives an opportunity to study the erosion product nature by the electron difraction analysis. The identification of the particle composition was done with X-ray spectral microanalyzer.

3. RESULTS AND DISCUSSION

3.1. Deuterium retention in mixed W-Be layer

Some studies of peculiarities in the deuterium retention in coating made of the W-Be mixture on beryllium substrate under pulse plasma effect were done. The thickness of the deposited mixed W-Be layer was about 500 nm. The element composition of the deposited mixed W-Be layer, measured by

RBS technique, is shown in Figure 1a. The coating contains up to 35 at.% W, up to 35 at.% Be and up to 30 at.% O. The W-Be layer irradiation by the pulsed deuterium plasma is done under softer operating conditions in comparison with the plasma parameters under irradiation of tungsten and graphite targets [3].

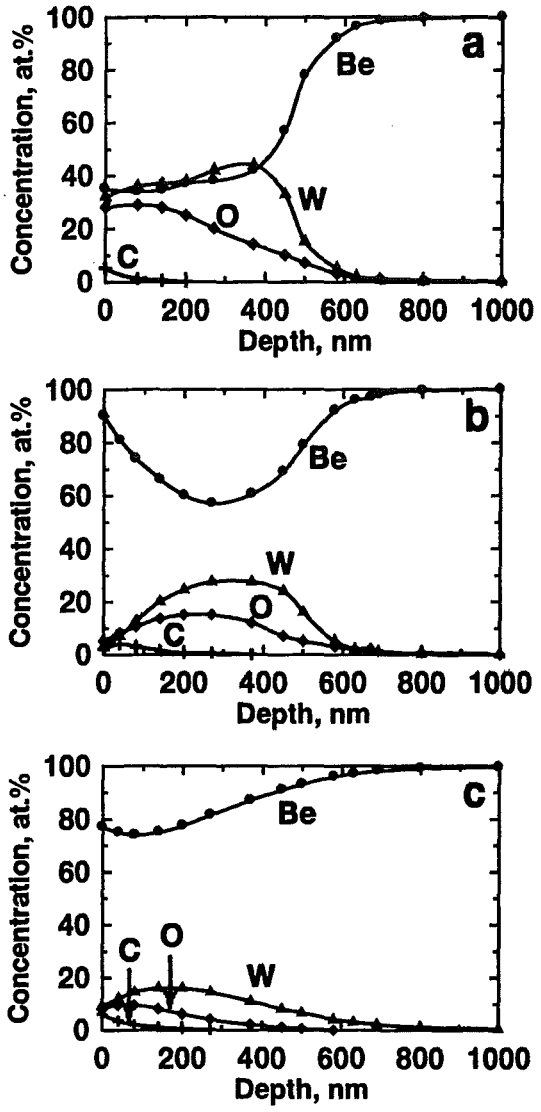

Figure 1. Depth distribution of elements in mixed W-Be layer deposited on Be substrate before (a) and after irradiation by pulsed (0.2 MJ/m^2 per pulse, 60 μs, 2 pulses) deuterium plasma for the areas with the retained (b) and the removed coating (c).

The W-Be coating surface topography before and after an exposure in the pulsed deuterium plasma is shown in Figure 2.

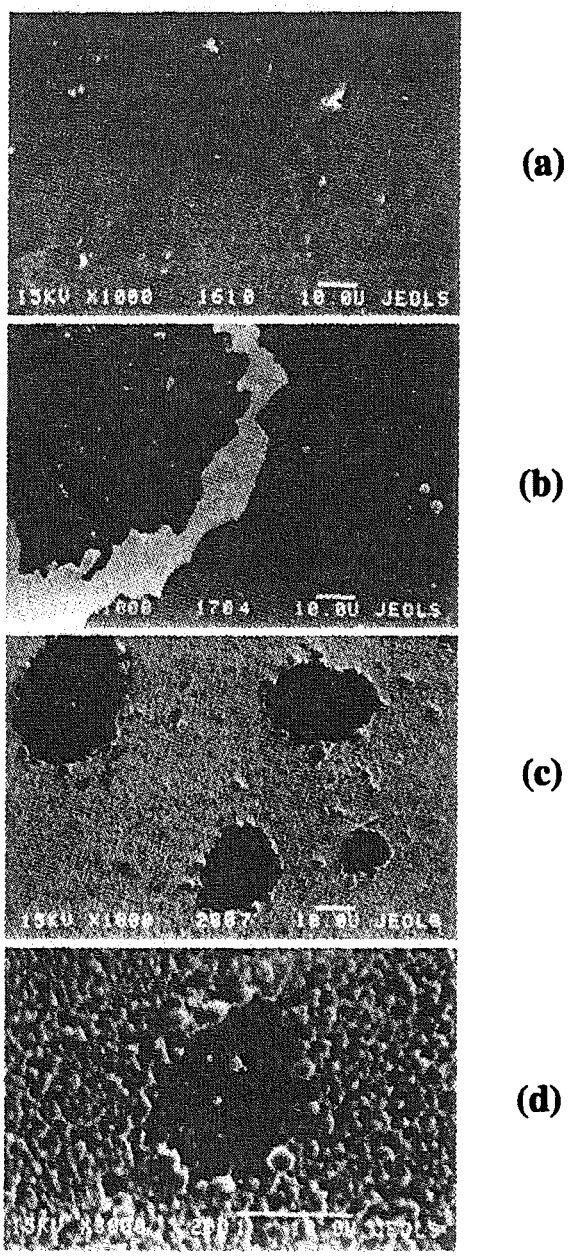

Figure 2. SEM photographs of the mixed W-Be layer surface before (a) and after irradiation by pulsed (0.2 MJ/m^2 per pulse, 60 μs, 2 pulses) deuterium plasma (b,c,d).

As the realized experiments have shown, after irradiation by two plasma pulses at the energy density 0.2 MJ/m^2 per pulse the film is melted (Figure 2c,d) and removed completely from the local surface areas (Figure 2b). According to the observed surface topography, the energy RBS spectra measured at its different parts also confirm the presence of the differencies in the element composition of the target surface layers. The element distributions in a mixed layer after an effect of the pulsed plasma are essentially changed. For the surface areas with the melted film the beryllium diffusion into the coating is observed (Figure 1b). As result, Be surface concentration increase up to 90 at.%, tungsten surface concentration decrease about 3 times and oxygen concentration decrease about 2 times. For the surface areas with the removed film Be surface concentration is about 75 at.%, W – about 15 at.%, O - about 10 at.% and the penetration of W and O atoms up to 1000 nm in depth of Be substrate is observed (Figure 1c). Probably, such an effect can be provided by the leakage of the melted tungsten into the melted beryllium under the pressure produced by a plasma flux under disruption as "viscous fingers" [4].

Some deuterium distribution profiles for various target areas after the plasma effect are shown in Figure 3. The deuterium depth distributions (Figure 3a,b) for different areas correspond to the element distributions shown in Figure 1b,c for the retained melted coating areas and for the removed ones. For retained melted W-Be film the deuterium depth distribution, shown in Figure 3a, is common for deuterium implantation with diffusion into the target. The dose of deuterium achieved at two plasma pulses is equal to $2.5 \cdot 10^{21}$ m^{-2}. Deuterium is situated in surface layer with thickness of 150 nm, i.e. no deuterium diffusion into the beryllium substrate depth is observed. In this modified surface layer the integral deuterium atom concentration is equal to $2.2 \cdot 10^{20}$ m^{-2}. The ratio D/Be atoms in the W-Be target is equal to 0.06, being typical for beryllium containing oxigen and carbon contamination. Deuterium depth distribution for the target region, where mixed W-Be layer is removed, differs from that, where this layer is melted (Figure 3b). Deuterium is almost uniformly distributed in the surface layer of 150 nm in thick, (same thickness is observed for the retained W-Be film areas), its integral concentration decreases up to $0.6 \cdot 10^{20}$ m^{-2} after pulse plasma irradiation.

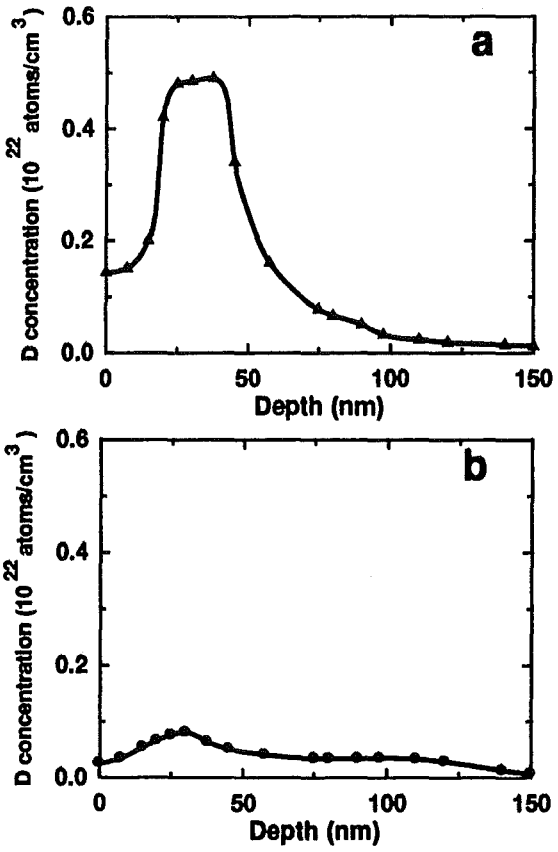

Figure 3. Depth distribution of deuterium in mixed W-Be layer deposited on berylliume substrate after irradiation by pulsed (0.2 MJ/m^2 per pulse, 60 μs, 2 pulses) deuterium plasma for the areas with the removed (a) and retained coating (b).

One should note that the deuterium concentration reduction in the vicinity to the sample surface also means a reduction in the deuterium accumulation in the whole sample, as well as that in its penetrability [5]. In the paper [5] it has been shown that the assigned hydrogen isotope concentration completely determines its concentration in the reactor wall and its penetration throughout the wall.

3.2. Erosion products of mixed W-Be layer

The erosion products were collected upon basalt filter fibres located in the shadow of the pulsed plasma flux around the exposed target of mixed W-Be layer on Be backing. Studies of the erosion product collectors with scanning and transmission

electron microscopes have allowed to register the particles from less 0.1 μm up to 20 μm in size after two deuterium high power plasma pulses in MKT accelerator. The particle size distributions are presented as histograms in Figure 4. Total distribution has two maxima located in the ranges 0.1-0.2 μm and 2.5-5.0 μm, respectively. The results of study of erosion products confirm the melting of the mixed W-Be layer on Be under irradiation by pulsed high power plasma flux. The presence of two maxima in distribution of erosion product sizes is caused by the processes of melting, evaporation and removal of mixed W-Be surface layer. The erosion product size distribution produced as result of W-Be layer irradiation by two high power plasma pulses in comparison with the similar data [6] obtained under simultaneous irradiation of W and CFC by 10 deuterium plasma pulses has the following features.

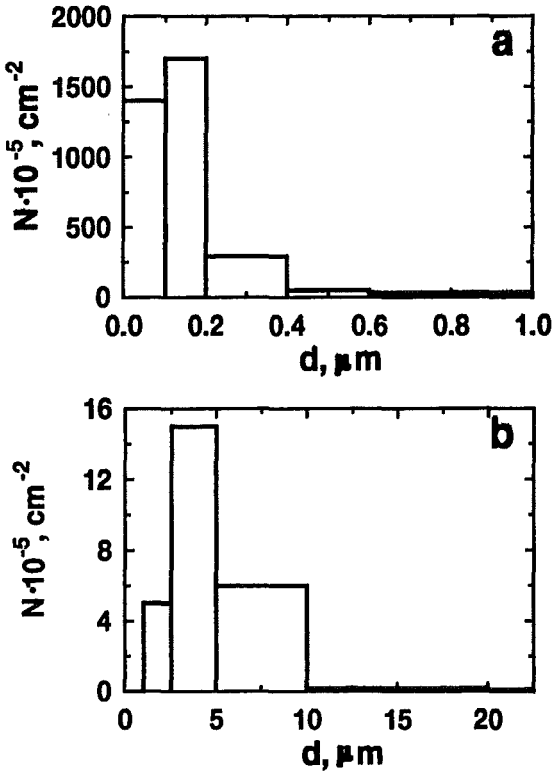

Figure 4. Erosion product size distributions in the ranges 0-1 μm (a) and 1.0-22.5 μm after irradiation of mixed W-Be layer deposited on Be by pulsed (0.2 MJ/m^2 per pulse, 60 μs, 2 pulses) deuterium plasma.

The number of particles is considerably higher than that for W+CFC target: the total number of all size particles collected from 1 cm^2 basalt filter is equal $35 \cdot 10^7$ cm^{-2} for mixed W-Be layer target and $17.5 \cdot 10^7$ cm^{-2} for W+CFC target. The W-Be erosion product size distribution is boarder then that for W+CFC products. The first one spreads from less 0.1 μm up to 20 μm and has two maxima, whereas the second one has the particles in the range 0.7-20 μm and one maximum in the range 0.7-1.0 μm only.

Some typical basalt filter microphotographs with the captured erosion products are shown in Figure 5.

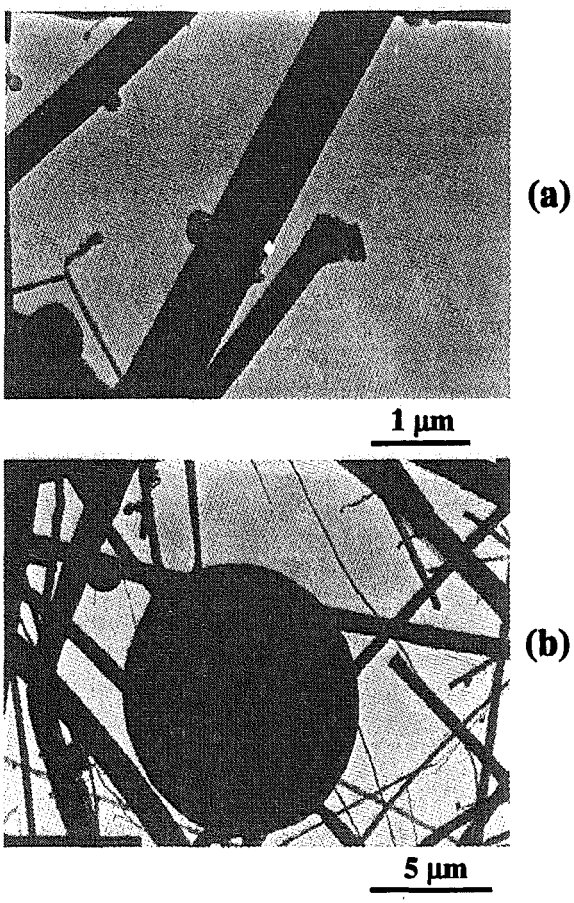

Figure 5. Electron microphotographs of the filters with the small (a) and large (b) erosion product particles after irradiation of mixed W-Be layer deposited on Be by pulsed (0.2 MJ/m^2 per pulse, 60 μs, 2 pulses) deuterium plasma.

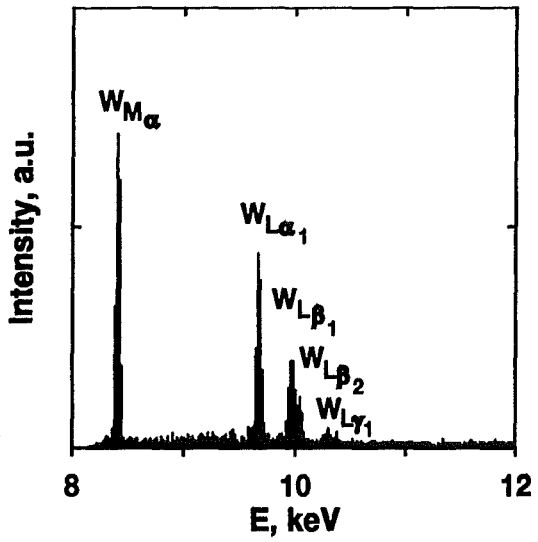

Figure 6. X-ray spectrum of the spherical particle shown in Figure 5b.

Particles have mainly a round drop configuration and an essential difference in size. Along with the droplets, the flakes of an arbitrary configuration are observed on the collectors (see Figure 5a). Probably, such flakes are the pieces of W-Be coating removed from the backing surface after pulse plasma effect. The element and structure identification of the observed droplets and flakes was done with electron diffraction and spectral micro- X-ray analysis. The results of the spectral X-ray analysis of a large round drops (Figure 6) show that such particles are tungsten. The element composition of the large flakes corresponds to that of the mixed W-Be coating after pulsed plasma irradiation. Thus, beryllium and tungsten elements, belonging to the irradiated W-Be coating, were registered among the erosion products.

4. CONCLUSION

1. After high power pulsed deuterium plasma irradiation of mixed W-Be layer on Be backing the deuterium is distributed in a modified surface layer with thickness of 150 nm. The absence of deuterium in Be substrate is provided by the deuterium escape outside during the melting of the mixed layer.
2. Production of W-Be coating on the beryllium at normal operating conditions and its removing under disruptions will assist in a deuterium retention reduction and will prevent the deuterium diffusion into the beryllium substrate depth.
3. The size distribution of W-Be coating target erosion products has two maxima in the ranges 0.1-0.2 μm and 2.5-5.0 μm. The particles attain a maximal size of about 20 μm in diameter and have a drop-like configuration.

ACKNOWLEDGMENTS

This work was supported by the International Atomic Energy Agency.

REFERENCES

1. M.I. Guseva et al., J. Nucl. Mater. 233-237 (1996) 681.
2. S.N. Korshunov et al., Proceedings of the Third IEA Inter. Workshop on Beryllium Technology for fusion, Mito, Japan, 1997, p. 216.
3. Yu.V. Martynenko et al., Nucl. Mater. 258-263 (1998) 1120.
4. Jens Feder, Fractals, Plenum Press, New York & London, 1988.
5. Yu.V. Martynenko, Yu.N. Yavlinskii, Atomic Energy, 1985, v. 58/2, p. 111-113.
6. M.I. Guseva et al. "Morphological features of erosion products for graphite and tungsten targets exposed by powerful plasma flows", Report on JCT/ HT's task related meeting on materials effects of disruptions, TRINITI, Troitsk, Moscow, Russia, February 2-3, 1999.

Deuterium trapping in ion implanted and co-deposited beryllium oxide layers

A.V. Markin[a], A.E. Gorodetsky[a], F. Scaffidi-Argentina[b], H. Werle[b], C.H. Wu[c], A.P. Zakharov[a]

[a] Institute of Physical Chemistry, Russian Academy of Sciences,
Leninsky pr. 31, 117915 Moscow, Russian Federation
[b] Forschungszentrum Karlsruhe, Postfach 3640, 76021 Karlsruhe, Germany

[c] The NET Team, Boltzmannstrasse 2, 85748 Garching, Germany

Deuterium trapping in beryllium oxide films irradiated with 400 eV D ions has been studied by Thermal Desorption Spectroscopy (TDS). It has been found that for thermally grown BeO films implanted in the range 300 - 900 K the total deuterium retention doesn't depend whereas TDS spectra do markedly on irradiation temperature. For R.T. implantation the deuterium is released in a wide range from 500 to 1100 K. At implantation above 600 K the main portion of retained deuterium is released in a single peak centered at about 1000 K. The similar TDS peak is measured for D/BeO co-deposited layer. In addition we correlate our implantation data on BeO with the relevant data on beryllium metal and carbon. The interrelations between deuterium retention and microstructure are discussed.

1. INTRODUCTION

Knowledge of trapping mechanisms of hydrogen isotopes in beryllium oxide is of interest to all beryllium applications for fusion technology. There are evidences that near-surface oxide layers govern the hydrogen permeability through beryllium [1]. Tritium retention in BeO might contribute significantly to the total tritium co-deposition, especially at elevated temperatures [2]. Chemical trapping by BeO inclusions plays essential role in tritium retention and release from neutron irradiated beryllium [3].

In the present work the Thermal Desorption Spectroscopy (TDS) is used to investigate deuterium trapping in ion implanted thin beryllium oxide films, both thermally grown and prepared by ion sputtering technique. The data on deuterium implantation in metallic beryllium are presented for comparison.

2. EXPERIMENTAL

2.1. Samples preparation

Three types of specimens were tested in the present work:

(1) Specimens of $2.5\times2.5\times0.2$ mm^3 in size were cut from a rod of metallic (zone-refined with 0.006 wt.% BeO) beryllium. Before ion irradiation the specimen surface was subjected successively to mechanical polishing and electropolishing followed by annealing at 1000 K for 5 minutes in vacuum 10^{-5} Pa. After above treatment, the Electron Probe Microanalysis (EPMA) showed a low oxygen contamination of the samples that could be corresponded to covering of the sample surface with 4 - 6 nm thin BeO film.

(2) Part of the samples prepared as 'type 1' were deliberately oxidized in 5 kPa dried air at 900 K for 10 minutes. Post-oxidation analysis with Reflected High Energy Electron Diffraction method (RHEED) showed that thin hcp-BeO crystallites of ~20 nm in size are formed on the sample surface. In addition, the Be1s X-ray photoelectron spectrum consisted of a single peak at binding energy of 114 eV suggesting that the beryllium is totally oxidized [4]. This allows to make an estimation of the film thickness by measuring the oxygen areal density with EPMA. Assuming the presence of stoichiometric hcp-BeO phase alone, the oxidation has been proved to result in the formation of oxide layer of 50 nm in thickness on the sample surface.

(3) The BeO films were produced by sputtering the beryllium target with 10 keV Ne ions in deuterium atmosphere at pressure of ~ 1 Pa. The sputtered beryllium reacts on the 0.1 mm tungsten foil substrate surface with residual oxygen to form beryllium oxide layers. Substrates temperature during deposition was kept at temperature of 800 K. Biasing the substrate negatively with respect to the target provides the simultaneous bombardment of the growing film surface with deuterium ions extracted from deuterium plasma generated by Ne^+ - D_2 collisions. An energy of incident ions is estimated to range from 130 to 400 eV per deuteron. Deposition conditions and the film properties are discribed in details elsewhere [5].

Below the specimens of above three types are denoted as *Be*, *tBeO* and *sBeO*, respectively.

2.2. Deuterium ion implantation

The *Be* and *tBeO* samples were irradiated with 4×10^{18} D cm^{-2} s^{-1} flux density of 400 eV D ions produced by RF ion gun. The ion beam of 60 mm in diameter was limited by 20 mm circle Mo diaphragm placed at 30 mm in front of the samples. Special measurements showed that the variation in ion current density of diaphragmed beam at the samples to be not in excess of 20 %. For room temperature irradiation the samples were fitted to Mo plate by W wires. For irradiation at elevated temperatures the samples were clamped in soft 0.1 mm Ni strip heated by electric current. Sample temperature was measured by Cr-Al thermocouple spot welded to the strip. No sensible changes of oxygen areal density on the surface of irradiated samples were detected with EPMA.

2.3. Thermal desorption spectroscopy

Thermal desorption measurements were carried out in UHV chamber with background pressure of 10^{-6} Pa. The specimens were clamped between two nickel strips heated by electric current. The sample temperature was measured by W-Re thermocouple spot-welded to one of the strip. The release of D_2 and HD molecules was monitored by quadrupole mass-spectrometer (QMS). The QMS was calibrated against calibrated H_2 and D_2 leaks. The sensitivity to HD was assumed to be the average of the H_2 and D_2 sensitivities. All spectra were obtained at linear temperature ramping with heating rate of 1 K/s.

3. RESULTS AND DISCUSSION

3.1. Implantation at 300 K

Thermal desorption spectra of D_2 and HD molecules from *Be* samples irradiated at 300 K are shown in Fig.1a. A single peak at 750 K is seen in spectrum of *Be* specimen irradiated to a low fluence of 2×10^{20} D/m^2. The release of practically all the implanted deuterium is registered in this peak. Thus, at low fluence ~100 % retention is observed, in full agreement with results published earlier [6, 7]. It is essential that no measurable desorption was detected from *tBeO* samples irradiated to the low fluence.

An additional peak at 470 K is developed in spectrum of *Be* irradiated to fluence of 2×10^{21} D/m^2 while both position and population of high temperatures peak, characteristic for low fluence irradiation, remain practically unchanged. For this high fluence, a significant desorption is registered also from *tBeO* samples. One feature of *tBeO* is that the spectrum is extended to 1100 K while heating only to 800 K is sufficient to degass fully the *Be* samples.

3.2. Implantation at elevated temperatures

An important information about the nature of trapping sites is obtained from an evolution of TD spectra with increasing of irradiation temperature. The spectrum of *Be* irradiated to a fluence of 2×10^{21} D/m^2 at 600 K is shown in Fig.1b. A narrow peak is developed at 650 K while the peak at 470 K, found after R.T. implantation, is absent. We suggest that the sharpness of both peaks results from the fracture processes occurring in the ion stopping zone at temperatures where trapped deuterium starts to liberate from some deuterium complexes.

For 300 K irradiation, such complexes are deuterium atoms chemisorbed on the inner surfaces [8] and/or the inclusions of amorphous beryllium hydride BeD_2 formed under D ion irradiation [9]. Notice that the desorption of the first and decomposition of the second occur approximately at the same temperature of ~500 K. It is well established that the release of implanted deuterium around 700 - 800 K is controlled by dissociation of deuterium-vacancy complexes formed under D ion irradiation [10]. The nature of peak at 650 K might therefore be in fracture processes caused by

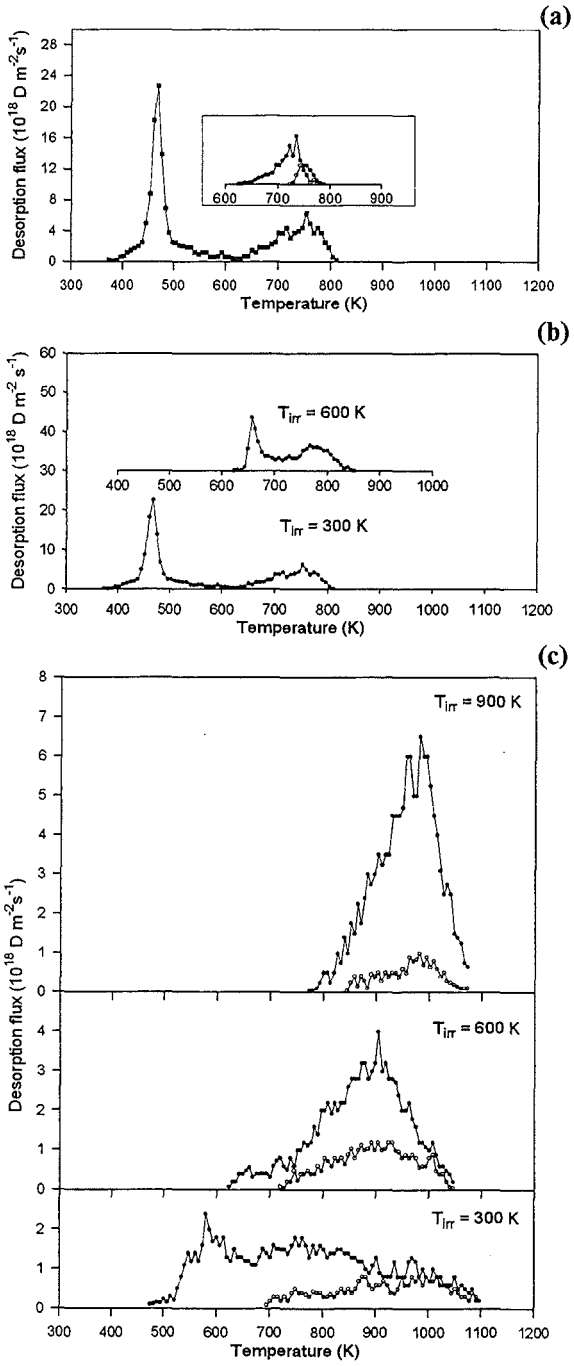

Figure 1. Thermal desorption of D_2 (filled symbols) and HD molecules (open symbols) from *Be* irradiated with 400 eV D ions **(a)** to 2×10^{20} D/m^2 (shown in box) and to 2×10^{21} D/m^2 at 300 K, **(b)** to 2×10^{21} D/m^2 at 600 K and **(c)** from *tBe* irradiated to 2×10^{21} D/m^2 at different temperatures.

deuterium release from the vacancy complexes.

Contrary to metallic beryllium, the *tBeO* samples exhibit the more deep deuterium trapping at elevated irradiation temperatures (Fig.1c). Increasing of irradiation temperature to 600 K and further to 900 K leads to development of a single well-defined peak at 900 - 1000 K that might be ascribed to the formation of additional deep traps for implanted deuterium.

Total amounts of retained deuterium determined by integration of D_2 and HD release spectra, as a function of irradiation temperature are shown in Fig.2. As seen, retained amounts for *Be* are slightly decreased whereas for *tBeO* remain unchanged with irradiation temperature.

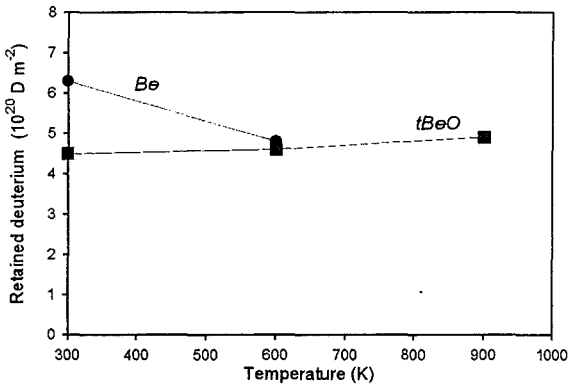

Figure 2. Temperature dependence of deuterium retention in *Be* and *tBeO* irradiated with 400 eV D ions to 2×10^{21} D/m^2.

3.3. Implantation vs co-deposition

It is of interest to analize the results of present work from tritium codeposition standpoint. According to the remark in Ref.[11], hydrogen retention in codeposited layers might be readily related to hydrogen behavior in materials under ion implantation. In Fig.3 are collected the data on thermal stability of hydrogen saturated layers formed on the surface of D ion irradiated beryllium oxide, beryllium and graphite, obtained in present work, by Möller et al. [7] and Doyle et al. [12], respectively. Two dependences are shown for each material: (1) an amount of deuterium retained under RT ion irradiation as function of temperature of the isochronal post-implantation annealing or the linear temperature ramping and (2) the dependence of retained amounts on irradiation temperature. Both

dependences are normalized to R.T. retention.

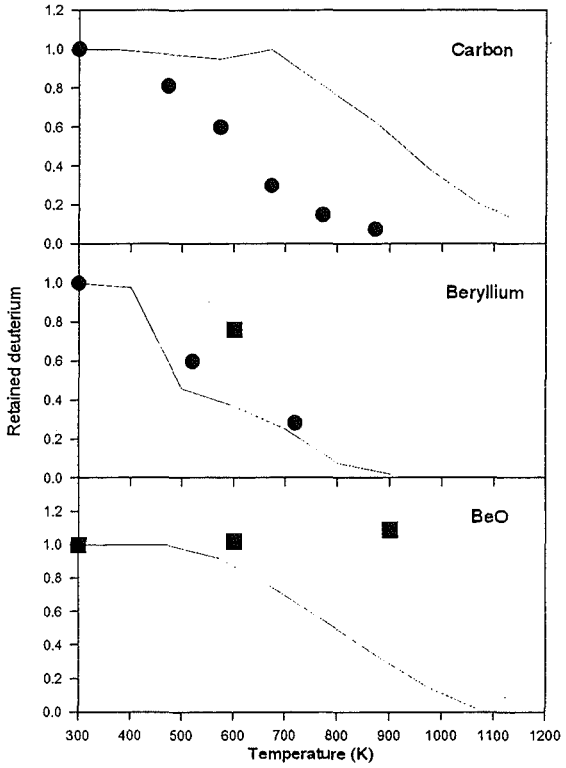

Figure 3. Deuterium retention in carbon [12], beryllium (circles [6] and square [this work]) and beryllium oxide [this work] irradiated with D ions at different temperatures (symbols) as compared with thermal desorption curves measured after 300 K implantation. All data are normalized to retention at 300 K.

As seen from Fig.3, relative positions of (1) and (2) along the temperature axis are specific for each of the materials in question. Dependence (2) for carbon is shifted to left by about 300 K compared to (1) one. For beryllium metal, saturated amounts in the samples irradiated with 3 keV D ions at 520 and 720 K agree well with thermal desorption curve, whereas for beryllium oxide, present work evidences inverse position of the dependences as compared with carbon.

Possible reason for above behavior might be in different microstructures formed in the materials under deuterium implantation. It is well established that re-emission flux from D ion irradiated carbon materials is formed via ion-induced detrapping and recombination processes occurring through the ion stopping zone [13]. In other words, there is a possibility for any deuterium traps to be dissociated followed by fast migration of formed D_2 molecules to the outer surface. Therefore, the binding energy of deuterium and carbon atoms is not the only factor governing retention at elevated temperatures.

For beryllium metal, the significant fraction of retained deuterium is located in the cavities [10]. In this case, close correlation between irradiation points and annealing curve found in Ref.[6] might be the characteristic property of the microstructure that is developed in beryllium under 3 keV D ion implantation. For irradiation with 400 eV D ions, we see that 600 K point lies somewhat higher than thermal desorption curve.

Contrary to both carbon and beryllium, no temperature dependence of the irradiation points for beryllium oxide has emerged from present study. Again, we suggest that this might be the characteristic feature of the ion fluence and the ion energy used. However a general trend seems to be obvious. This behavior is, in the context of TDS method, indicative of increasing in concentration of deep traps with rise of irradiation temperature.

There are evidences that a similar behavior seems to be the case for deuterium trapping in the co-deposited films. Fig.4 shows TDS spectra of deuterium from *sBeO* film deposited - as specified in p.2.1 - at 800 K. As seen the main part of retained deuterium is released in the peak centered at 1000 K. Unfortunately, we failed to produce D/BeO films at 300 K due to technical reason intrinsic for the deposition procedure used in Ref.[5]. For R.T. co-deposition, one can refer to experiments of Mayer et al. [11] where heating to only 800 K was sufficient to complete deuterium release from D/BeO films produced at 300 K.

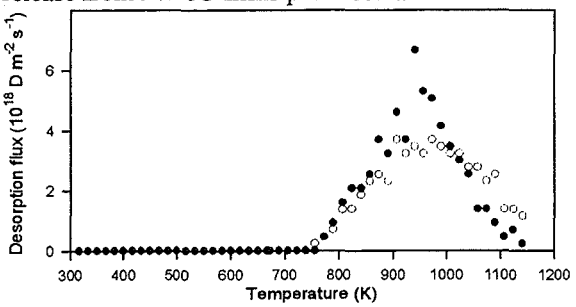

Figure 4. Thermal desorption of D_2 (filled symbols) and HD molecules (open symbols) from *sBe* film.

In conclusion, concerning the existence of phases in hydrogen-beryllium oxide system exhibiting high thermal stability. It is well known that apparent thermal stability of beryllium hydroxide depends strongly on preparation method or, another way, on the original microstructure [14]. While $Be(OH)_2$ starts to decompose at ~ 500K, the heating up to ~ 1100 K is required the reaction to be driven to completion (in terms of weight gain, of course). One possible explanation is that the residual water vapor is collected in closed pores formed in the course of hydroxide decomposition. If so, at the final stage the decomposition is governed by slow permeation of water vapor from the pores, probably, in form of hydrogen. In principle, a qualitatively similar mechanism might be responsible for deep deuterium trapping in beryllium oxide observed in the present work for high temperature irradiation.

4. CONCLUSIONS

Deuterium trapping in beryllium metal and beryllium oxide films irradiated with 400 eV D ions has been studied. The data on beryllium metal are in a good agreement with that published by other researchers for 0.5 - 10 keV D ions. The results of present work are evidences for the existance of deep trapping of deuterium in beryllium oxide. After irradiation at elevated temperatures the implanted deuterium is released in a desorption peak at ~1000 K both from ion implanted thermally grown BeO films and co-deposited D/BeO layers. This suggests that under conditions when oxygen is available in the divertor plasma, the tritium and beryllium co-deposition will contribute significantly to the total tritium retention in the redeposited layers, especially at elevated temperatures.

REFERENCES

1. R.A.Causey, W.L.Hsu, B.E.Mills, J.Ehrenberg, V.Philips, J. Nucl. Mater. 176&177 (1990) 654.
2. M.Mayer, J. Nucl. Mater. 240 (1997) 164.
3. F.Scaffidi-Argentina, H.Werle, Proc. of the Third IAE International Workshop on Beryllium Technology for Fusion, Mito City, 1997, p. 254-260.
4. C.D.Wagner et al., Handbook of X-ray Photoelectron Spectroscopy (Perkin-Elmer Corp., Eden Prairie, Minnesota, 1979).
5. A.V.Markin, V.P.Dubkov, A.E.Gorodetsky, M.A.Negodaev, N.V.Rozhanskii, F.Scaffidi-Argentina, H.Werle, C.H.Wu, R.Kh.Zalavutdinov, A.P.Zakharov, " Codeposition of deuterium ions with beryllium oxide at elevated temperatures", submitted to the ICFRM-9.
6. W.Moller, B.M.V.Scherzer, J.Bohdansky, IPP-JET Report No.26, Garching,(1985).
7. W.R.Wampler, J. Nucl. Mater. 122-123 (1984) 1598.
8. A.V.Markin, V.N.Chernikov, S.Yu.Rybakov, A.P.Zakharov, J. Nucl. Mater. 233 - 237 (1996) 865.
9. B.Tsuchiya, K.Morita, J. Nucl. Mater. 233 - 237 (1996) 898.
10. V.N.Chernikov, V.Kh.Alimov, A.V.Markin and A.P.Zakharov, J. Nucl. Mater. 228 (1996) 47.
11. M.Mayer, R.Behrisch, H.Plank, J.Roth, G.Dollinger, C.M.Frey, J. Nucl. Mater. 230 (1996) 67.
12. B.L.Doyle, W.R.Wampler, D.K.Brice, J. Nucl. Mater. 103 - 104 (1981) 513.
13. W.Möller, J. Nucl. Mater. 162 - 164 (1989) 151.
14. Dupuis T.C. r. Acad. sci., 250 (1950) 957.

HYDROGEN RELEASE FROM DEPOSITED BERYLLIUM LAYERS

V.P.Shestakov, A.Kh.Klepikov, Y.V.Chikhray, I.L.Tazhibaeva

NIIETF of Al Farabi Kazakh State University, Tole bi 96a, Almaty, Kazakhstan, 480012
Phone, FAX: 7(3272)503978, e-mail: istcvova@kazmail.asdc.kz

The analysis of hydrogen retained in deposited beryllium layers deposited by magnetron sputtering was carried out by means of thermodesorption (TDS) technique. Two hydrogen release peaks were clearly seen on the thermodesorption curves at the temperatures 760-800 K and 920-970 K. Hydrogen concentrations in the deposited beryllium layers were calculated from the gas release curves corresponding to the number of Be atoms in the beryllium layer of 100% theoretical density. Average hydrogen concentration in the beryllium samples loaded in the process of magnetron sputtering was equal to 3800±200 appm. The experiments with beryllium layers, enriched with carbon, revealed the increase of retained hydrogen concentration up to 9600±200 appm. Assuming that gas release can be described within the framework of model of diffusion from layer system BeO-Be-BeO, hydrogen diffusion coefficient in BeO and the trapping and detrapping constants for the traps appearing in beryllium in the process of deposition were evaluated.

Introduction

The objective of carrying out experiments on investigation of hydrogen isotopes retention in beryllium layers obtained in the process of magnetron sputtering was the determination of both hydrogen content in deposited layer and possible mechanisms of gas release from it. This task is very important for assessment of tritium content in beryllium dust, being generated during the operation of ITER reactor and also for technologies of beryllium foil fabrication by sputtering technique.

Experimental

The samples for investigation of gas release from beryllium deposited layers were manufactured by Nuclear Physics Institute of NNC RK according to the task on ISTC #K40C project. The samples were deposited in the «Argamak» installation in the mixture of hydrogen and argon with the ratio 50%:50% at the pressure 0.5 Pa. The thickness of deposited beryllium layer was 25 microns, the area of deposition 1×5.5 cm (See Fig. 1). During the following investigations it was found out that the adhesion of beryllium layer deposited on the stainless steel surface was not acceptable, because the deposited layer was detached from the substrate at the elevated temperatures of thermodesorption experiment. Therefore the layer was mechanically removed from the substrate after deposition and the formed «scales» with average size 4 mm^2 were placed into container made of stainless steel foil, previously annealed in a high vacuum at the temperature 1073 K.

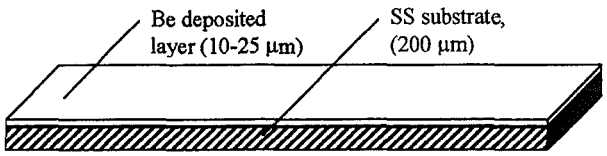

Fig. 1. Beryllium, deposited on stainless steel substrate.

To heat the sample the ohmic heating technique was used. This technique in the conditions of our experimental device allows to achieve the temperatures up to 1475 K with the temperature difference not more than 15 K along the sample.

Experimental installation (EI) "ORHIDEYA" used in the experiments is intended to carry out experiments on hydrogen isotopes release and determination of the parameters of its interaction with structural materials. Fig 2 shows the layout of EI.

The EI consists of high vacuum pumping post connected with water-cooled chamber where the sample is arranged. The sample is arranged on the basic flange of EI in water-cooled high current feedthroughs where it is pressed by screw-nuts between molybdenum washers. The sample is ohmic heated. The control and maintenance of the temperature is realized by means of high accuracy temperature regulator "VRT-3", which is connected with step-down transformer. It allows to maintain the temperature with an accuracy ±1 K in the mode of stable temperature maintaining and ±2 K in a linear heating mode.

The measurement of released hydrogen quantity is carried out by of automated type of partial pressure

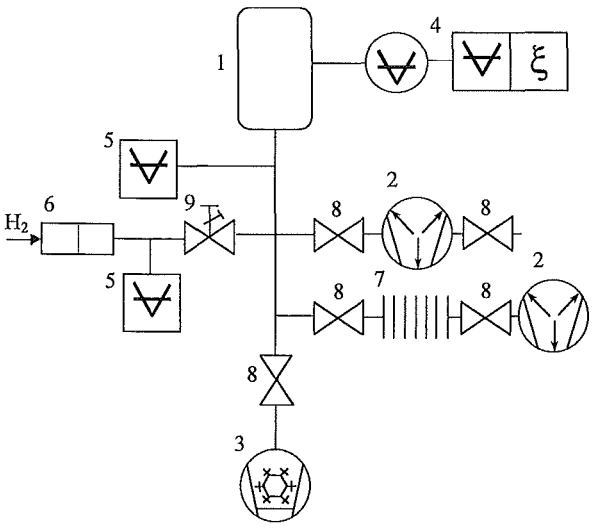

Fig. 2. "ORHIDEYA" experimental installation for the gas release investigation in the linear heating regime. 1-vacuum vessel; 2-ion sputtering pump; 3-adsorption pump; 4-RMO-13 + IPDO + IBM PC AT; 5-PMT-4M; 6-diffusion filter; 7-metal flexible bellows; 8-vacuum valves; 9-mechanical dosing valve.

measuring device with detecting gauge "RMO-13", which is intended to determine the partial pressures of residual gases in high vacuum systems. It allows to determine partial pressures of gases with an accuracy ±10% and to record the curves of gas release in a linear heating mode. This variant of omegatron radio-frequency mass spectrometer is computer controlled and allows to carry out the measurements with necessary rate, quantization and direction of scanning.

After the sample fastening in vacuum chamber, installation was pumped out by rotation pump with liquid nitrogen cooled trap for 1,5 hours to the pressure $\cdot 10^{-1}$ Pa while the chamber was heated by external furnace up to 150°C and the sample temperature increased up to ≈100°C. After that the chamber was pumped by "preliminary" ion sputtering pump "NMD-0,25" and additional annealing of mass spectrometer gauge was carried out at the background pressure $5 \cdot 10^{-4}$ Pa for 1 hour. Then the chamber was pumped by "clear" pump "NMD-0,4" and the annealing was stopped. After the chamber temperature decreased to the room temperature, chamber background pressure was $5 \cdot 10^{-7}$ Pa. The chamber and current feedthroughs were cooled by water with temperature 12-14°C.

To investigate gas release from the sample the thermodesorption technique in a linear heating mode was used. Gas release spectra of the sample can be obtained for 6 gases by means of specially elaborated programmable oscillator. The process of measuring is performed automatically by means of programmable oscillator (PUG-1). After achieving operation vacuum conditions, the mass-spectrometer was adjusted on the hydrogen frequency and the «TDS» control routine for gas release measurements, operating with PC/CAMAC data acquisition system, was run.

Results and discussion

Typical thermodesorption curves of hydrogen release from the scales of deposited beryllium are shown on Fig. 3. The temperature ramp rates are indicated in the figure. The data on gas release rate are in molecules/s*cm^2, effective sample square was taken as 11 cm^2 (doubled square of substrate area).

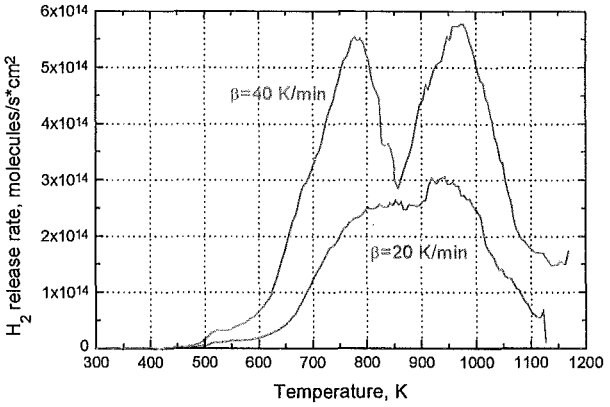

Fig. 3. Typical curves of hydrogen release from the samples of deposited beryllium.

Simultaneously with the measurement of hydrogen release rate the argon release was controlled to determine its release rate in the experiment. We did not succeed to detect argon in our experiments, argon partial pressure retained at the background level during the whole experiment.

Two hydrogen release peaks are clearly seen on the thermodesorption curves at the temperatures 760-800 K and 920-970 K.

Hydrogen concentrations in the deposited beryllium layers were calculated from the gas release curves corresponding to the number of atoms in the beryllium layer of 100% theoretical density with the dimensions 0.025×1×5.5 cm. For the two samples shown on the

Fig. 3., hydrogen concentrations are equal to 3965 appm (the sample with temperature ramp rate 40 K/min) and 3730 appm (the sample with temperature ramp rate 20 K/min). Average hydrogen concentration in the beryllium samples loaded in the process of magnetron sputtering was equal to 3800±200 appm.

The experiments with beryllium layers, enriched with carbon, revealed the increase of retained hydrogen concentration up to 9600±200 appm. Carbon was sputtered simultaneously with beryllium at the same conditions as pure beryllium coatings. The curves of hydrogen release from such coatings, obtained at the temperature ramp rates 20 and 40 K/min, are shown in Fig. 4. The curves are characterized by one gas release peak at the temperature of 700 K. To our regret we could not measure accurately carbon concentration in the deposited beryllium layer, the estimated value was about 5 %.

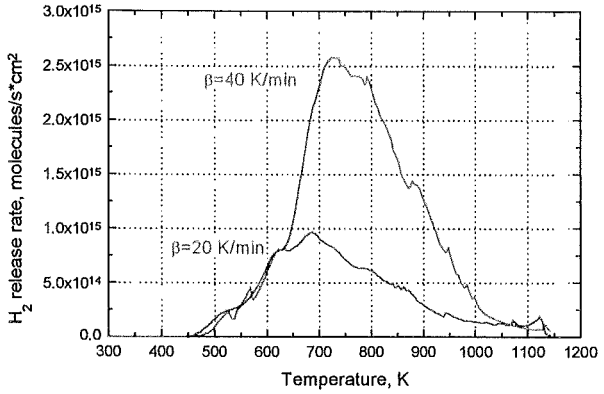

Fig. 4. The curves of hydrogen release from the samples of deposited beryllium enriched with carbon

For modeling of experiments on hydrogen release from deposited beryllium layers the TDSWafer routine created in the Laboratory of Structural Materials of Nuclear Power Devices of NIIETF KazGU was used. The routine is intended for numerical modeling of gas release from the sample, representing a plate both sides of which are covered with layers of substance with hydrogen diffusion coefficients being different from the hydrogen diffusion coefficients in the plate. In our case it was the deposited beryllium layer with the thickness 25 microns, covered from both sides with beryllium oxide layers. The diffusion process for each layer of researched system BeO-Be-BeO can be described within the framework of diffusion in the defect medium, where the diffusion process is described by the system of partial differential equations:

$$\begin{cases} \dfrac{\partial C}{\partial t} = D\dfrac{\partial^2 C}{\partial x^2} - k_1 C + k_2 m \\ \dfrac{\partial m}{\partial t} = k_1 C - k_2 m \end{cases}$$

in the conditions of convertible chemical reaction of first order (Herst-Gaus model) [1, 2], for boundary conditions of first sort.

Here C and m – concentrations of mobile and trapped atoms of hydrogen in the layer, k_1 and k_2 – trapping and detrapping constants in the layer, D – diffusion coefficient in the layer. Besides,

$$D = D_0 \exp\left(\frac{-E_D}{RT}\right)$$

$$k_1 = k_{10} \exp\left(\frac{-E_T}{RT}\right)$$

$$k_2 = k_{20} \exp\left(\frac{-E_R}{RT}\right)$$

where E_D, E_T and E_R – activation energies of diffusion, trapping and detrapping, respectively, T – temperature of the diffusion medium, R – universal gas constant.

Since the thickness of beryllium scales is much less than the other dimensions, the problem of diffusion from infinite plate was solved during the modeling and thus the problem was reduced to one-dimensional one. The temperature difference along the scales was not also taken into account. As a result of modeling it was obtained that for this thickness of beryllium (25 microns) the form of gas release curve depends mainly not on the hydrogen diffusion parameters in beryllium but on its diffusion parameters in beryllium oxide layer. Hydrogen diffusion coefficient in beryllium was assumed to be equal to $D=6.7\times10^{-9}\exp(0.294\text{eV/kT})$ m^2/s, according to recommended value of Abramov [3]. The modeling parameters substituting to the system of equations were selected in such a way that the temperatures of maximums of experimental gas release peaks coincide with the theoretical ones. It was achieved using the following parameters, see Table 1.

The results of modeling by TDSWafer routine using these parameters for temperature ramp rates 20 and 40 K/min are shown on Fig. 5. It is seen that theoretical curves describes the experimental data quite good, but gas release peaks on the experimental curve are wider. It can be explained by the temperature difference along the scales of deposited beryllium and their different size and form.

Table 1. Diffusion parameters of hydrogen for beryllium and beryllium oxide, used in the modeling

Parameter	Be	BeO
Initial concentration	C=50%, m=50%	-
Activation energy of diffusion	30 kJ/mole	165 kJ/mole
Preexponent of diffusion activation energy	7×10^{-9} m^2/s	1×10^{-4} m^2/s
Activation energy of trapping	30 kJ/mole	-
Activation energy of detrapping	270 kJ/mole	-
Trapping constant, k_{10}	0.1 s^{-1}	-
Detrapping constant, k_{20}	10^{13} s^{-1}	-
Thickness	25 microns	4 nm

Table 2. Hydrogen diffusivities in BeO

Beryllium oxide	D_0(m^2/s)	E_d(eV)
single crystal	1.11×10^{-4}	2.28
sintered	7.0×10^{-5}	2.10
powder	3.17×10^{-15}	0.724
best fit	1.3×10^{-10}	1.36
our data	1.0×10^{-4}	1.6

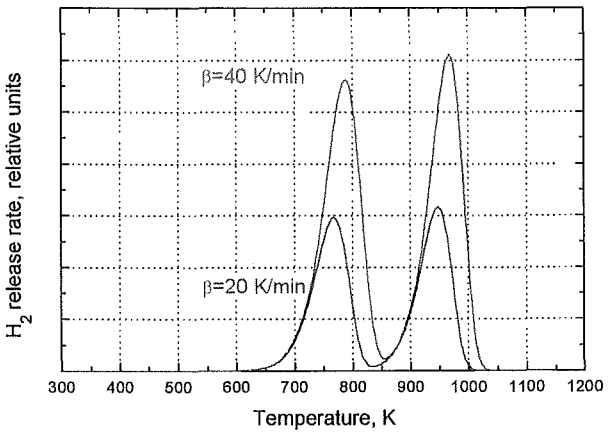

Fig. 5. Theoretical curves, modeling hydrogen release from the scales of deposited beryllium with the thickness 25 microns and the thickness of oxide layer on the surface 4 nm.

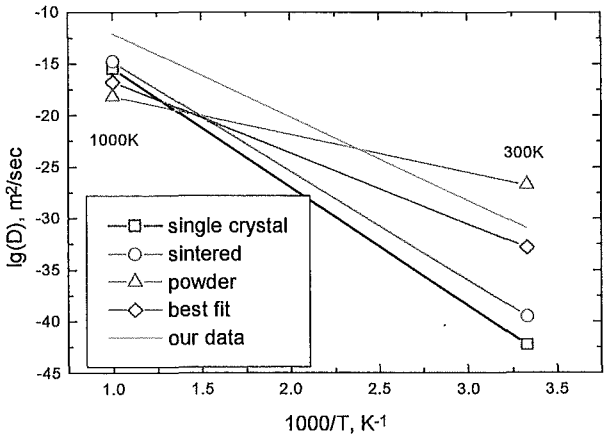

Fig. 6. Temperature dependencies of hydrogen diffusion coefficients in beryllium oxide [4] and the data of modeling.

It is necessary to mention that hydrogen diffusivity in BeO used for fitting theoretical curves to the experimental data, slightly differs from the published data. However the scattering in the values of hydrogen diffusion parameters in beryllium oxide is sufficiently wide and the used values practically do not fall outside the confidence limits in the examined temperature range, that can be clearly seen from Fig. 6.

Fowler data [4] for different BeO samples as a reference ones and our data obtained during the modeling (see Table 2), are depicted on this figure.

The fact that argon is not presented in the spectra of gas release from deposited beryllium layer is not the evidence of its absence in the sample. Since we could not find published data on argon diffusion coefficient in beryllium and BeO, the evaluation of its diffusion path has been carried out using the helium diffusion

coefficients [5] and shows that argon release could be hardly probable registered during our TDS experiments.

Conclusions

Hydrogen concentration in beryllium layers fabricated by magnetron sputtering with the parameters used in our case was about **3800±200 appm.**

Two hydrogen release peaks are clearly seen on the thermodesorption curves at the temperatures 760-800 K and 920-970 K.

Hydrogen concentration in the beryllium layers, enriched with carbon was about 9600±200 appm.

Assuming that gas release can be described within the framework of model of diffusion from layer system BeO-Be-BeO, where the diffusion in BeO is described by classic Fick's diffusion (traps concentration is equal to zero) and in Be – by diffusion in defect medium (Herst-Gaus model) hydrogen diffusion coefficient in BeO and the trapping and detrapping constants for the traps appearing in beryllium in the process of deposition were evaluated.

References

1. Hurst D.G. Diffusion of fission gas. Calculated diffusion from a sphere taking into account trapping and return from the traps. -In: GRRP-1124. Atomic Energy of Canada: I-st Conf., Oct.-Nov.1962.- Walk River,1962,p.129-135.
2. Gaus H. Uber den Einfluss von Fallen auf die Diffusion.- Zeit. Naturforsch, 1965, Bd.20a, S.1298-1308.
3. E.Abramov, M.P.Riehm, D.A.Thompson, and W.W.Smeltzer, "Deuterium permeation and diffusion in high purity beryllium", J. Nucl.Mater, 175, 90-95, 1990.
4. J.D.Fowler et al., «Tritium diffusion in Al_2O_3 and BeO», J.of Amer.Cer. Soc. 60(1977)155-161.
5. J.B.Rich, G.P.Walters In Metallurgy of beryllium, London, Chapman and Hall, 1963.

Negative transferred arc cleaning: a method for roughening and removing surface contamination from beryllium and other metallic surfaces

R.G. Castro[a], K.J. Hollis[a], C. J. Maggiore[a], R.P. Doerner[b], A.Ayala[a], and B.D. Bartram[a]

[a]Los Alamos National Laboratory, Materials Science and Technology Division, Los Alamos, New Mexico 87545, USA
[b] University of California - San Diego, Fusion Energy Research, , La Jolla, CA 92093, USA

TA cleaning has been investigated for preparing the surface of beryllium plasma facing components (PFC's) inside of the International Thermonuclear Experimental Reactor (ITER) prior to depositing beryllium by plasma spraying. Plasma spraying of beryllium was evaluated during the ITER Engineering Design Activity (EDA) for *in-situ* repair and initial fabrication of the beryllium first wall armor. Results have shown that surface roughening of beryllium, during the TA cleaning process, can result in bond strengths greater than 100 MPa between beryllium surfaces and plasma sprayed beryllium. In addition, the TA cleaning process was shown to be an effective method for removing contaminate layers of carbon and tungsten from the surface of beryllium. Investigations have been performed to characterize the different arc-types that occur during the TA cleaning process (Type I, I and III arcs) and the effectiveness of the TA cleaning process for potentially removing co-deposited layers of carbon and deuterium from the surface of beryllium, stainless steel and tungsten.

1. INTRODUCTION

Negative transferred-arc (TA) cleaning has been used throughout the thermal spray community as a method for cleaning and roughening surfaces prior to the deposition of materials during vacuum plasma spraying (VPS). TA cleaning results when a potential difference (voltage) is applied between the front of a DC plasma torch (anode) and a metallic surface to be cleaned (cathode). A cathodic condition is created at the surface of the workpiece that results in the transfer of electrons from the workpiece to the front of the plasma torch during an electric arc discharge. This electron transfer can result in the removal of the oxide surface layer and surface contaminates from metallic materials. One possible application for TA cleaning is the removal of co-deposited layers of carbon and tritium from first wall surfaces inside of a magnetic fusion energy device. Tritium co-deposition is raising significant concern because of operation and safety implications associated with large tritium inventory build-up on the first wall structure of a magnetic fusion energy device [1]. Tritium co-deposition with carbon has been verified in laboratory studies conducted by Hsu and Causey [2-3] and by examination of first wall samples removed from many present-day fusion devices. Due primarily to the safety hazard in some potential accident scenarios (releaseable T-inventory), it is essential to incorporate methods and procedures to detect and efficiently remove tritium from co-deposited layers.

One cleaning method that is being highly considered is the introduction of oxygen into the confinement vessel while heating the first wall. Oxidation of the co-deposited layer can remove both the carbon and hydrogen by eroding the hydrogenated graphite layer producing $(D/T)_2O$ and CO/O_2 which than can be removed by the tritium clean-up system. A major drawback to this approach is that in order to get an acceptable removal rate of the co-deposited carbon layer (> 2 x 10^{-9} m/hr for carbon) the wall temperature of the reactor will need to be heated to 350°C. In addition, this process loads the wall with O_2 that will need to be removed before tokamak operations re-commence.

The use of TA cleaning for removal of co-deposited carbon/tritium layers can provide the following advantages: 1) a non-line-of-sight

process which provides accessibility in shadowed regions, gaps, and recessed areas, 2) non intrusive method requiring short operational shut down times if used in conjunction with plasma spraying for *in-situ* repair, 3) gaseous/vapor residue may be processed by the existing tritium fuel clean-up system, 4) minimal wall conditioning after cleaning and 5) TA cleaning locally heats the surface for removal of contaminates and does not require bulk heating of the first wall.

To better understand the mechanisms of TA cleaning, investigations on the arc characteristics and cleaning efficiency were performed on beryllium, stainless steel and tungsten.

2. EXPERIMENTAL

The TA experiments were carried out in an inert environment plasma spray chamber. In order to purge the air from the system, the chamber was pumped down to 60 Pa and backfilled twice with argon before conducting experiments. The plasma torch used was a commercially available Praxair SG-100 using a 40kW Plasmadyne DC power supply. The torch gas used was argon and the flow rate was 40 standard liters per minute for all experiments. The TA power supply used was a 250 amp constant current DC supply built by Miller Electric, Inc. For all TA cleaning experiments the plasma torch arc was started with the torch away from the substrate. The torch was then moved close to the substrate and the TA power supply engaged manually. For the stainless steel and tungsten samples TA cleaning experiments were captured by a Canon (Canon, Tokyo, Japan) XL-1 digital video camera that was placed in front of a window port in the chamber. Voltage signals from the TA power supply were recorded with a Tektronix (Tektronix, Beaverton, OR) TDS 420A digital oscilloscope and P5200 high voltage differential probe. The TA power supply current was measured with the same oscilloscope using a Tektronix 503S current probe system with a high DC current probe.

The effect of TA cleaning of beryllium surfaces prior to plasma spraying was investigated by cleaning eight beryllium samples (25.4 mm wide x 12.7 mm long x 3.2 mm thick) which had been sputtered coated with 10 to 100 monolayers of tungsten and carbon. This combination of materials was chosen to simulate a contaminated surface similar to what might be expected in the ITER reactor if carbon, tungsten and beryllium are used as plasma facing materials. The sputtered coatings were produced from both tungsten and carbon anodes using 100 eV of Ar and D_2 at a 1:2 ratio, and a current of 100 mA for 30 minutes. The beryllium samples were located 76.2 mm from the sputter targets. Rutherford Backscattering Spectrometry (RBS) using 1.6 MeV He ions was used to characterize the surface of the beryllium before and after TA cleaning. The surface analysis included detection of carbon, tungsten, oxygen, argon and copper.

To investigate the TA removal efficiency of deuterium containing carbon films from stainless steel and tungsten, the PISCES-A device at the University of California, San Diego [4] was used to deposit carbon coatings on stainless and tungsten samples by installing an impurity gas puffing system (CD_4) in the target interaction region of the device. The fraction of impurity gas present was monitored prior to the plasma initiation by use of a quadrupole residual gas analyzer (RGA). Several identical samples were exposed to deuterium plasmas containing varying amounts of impurity fractions (from 0.1% carbon, up to 10% carbon). The temperature of the samples was monitored using thermocouples and an IR pyrometer. All samples were exposed to the deuterium containing plasma for 30 minutes. The radial profile of the plasma was measured using a fast reciprocating Langmuir probe. The ion flux across the face of the sample was measured to be constant within a few percent throughout the duration of the exposure.

The surface compositions of the stainless steel and tungsten samples before and after TA cleaning were measured at the Ion Beam Materials Laboratory using resonant backscattering of alpha particles and elastic recoil detection of the hydrogen isotopes [5]. An incident beam of 5.6 MeV alpha particles was focussed on a 2 x 2 mm^2 spot on the sample and the backscattered yield was measured with a Si solid state detector at a scattering angle of 167 degrees. The samples were tilted at 75 degrees from beam normal and the recoiling hydrogen isotopes were detected at a forward scattering angle of 30 degrees. A combination of Al and mylar absorber foils were used to stop the forward scattered alpha particles but allow transmission of the recoiling hydrogen and deuterium to the detector.

3. RESULTS AND DISCUSSION

3.1. Cathodic Arcing Characteristics on Beryllium, Stainless Steel, and Tungsten

The initiation of an arc at a cathode is though to take place by a combination of thermionic and field-enhanced emission of electrons as described by Juttner *et al.* [6]. Of interest when TA cleaning and roughening a metal surface is the erosion craters that result from the cathodic arc attachments. Figure 1 summarizes the mechanisms that occur during arc attachment and crater formation. A surface explosion, followed by melting and acceleration of molten metal initially forms the crater. After the crater formation, the discharge center is displaced to the rim and the cycle then repeats itself at another localized arc spot. The arcing/crater formation is categorized into one of three spot modes of operation, Types I, II and III. Table 1 gives the spot types and characteristic behavior associated with each.

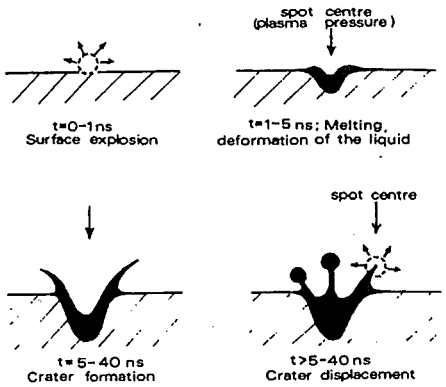

Figure 1. Mechanism for development of erosion craters on clean surfaces in vacuum [7].

Type I spots occur on oxidized or contaminated surfaces. The arc moves relatively quickly from place to place and leaves small, distinct craters while eroding a relative small amount of material per coulomb of electrons conducted. Type I cathode arc spots on stainless steel after TA removal of a carbon surface film are shown in Figure 2a. The arc attachments are discontinuous with a crater radius of less than 1 μm. Type II arc spots are also present in this figure. Type II spots appear on initially clean surfaces or surfaces that have been cleaned by Type I arcs.

Table 1. Cathode spot types and their characteristics[7].

Characteristic	Type I	Type II	Type III
occurrence conditions	oxidized surfaces	clean surfaces	small electrodes, ambient gas, hot cathodes
velocity (m/s)	10-1000	1-150	<1
spot current (A)	<10	5-50	5-50
lifetime (μs)	<0.01	<0.1	>10
crater appearance	discontinuous	overlapping	overlapping
crater radius (μm)	≤1	3-10	>10
erosion rate (μg/C)	<10	10-100	>100

Type II arcs have slower motion and leave connected craters of intermediate size (3-10μm) while eroding material much faster than Type I arcs. Figure 2b shows an example of Type II arc spots on beryllium after TA cleaning. Crater sizes are approximately 2-10 μm.

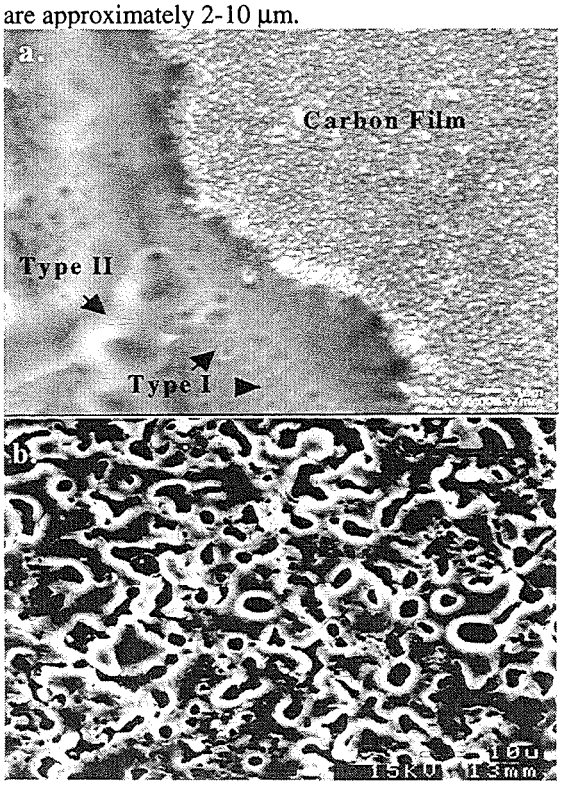

Figure 2. a) Type I and Type II cathode arc spots on stainless steel after TA removal of a carbon film, b) Type II cathode arc spots on beryllium after TA cleaning.

Type III arc spots occur under conditions where the arc is fixed in place by special conditions such as special surface geometries, certain gas pressures, and/or elevated cathode temperatures. These spots move relatively slowly while leaving connected craters of large size (>10μm) and eroding relatively large amounts of material. Type III arc spots on beryllium, stainless steel and tungsten after TA cleaning are shown in Figure 3.

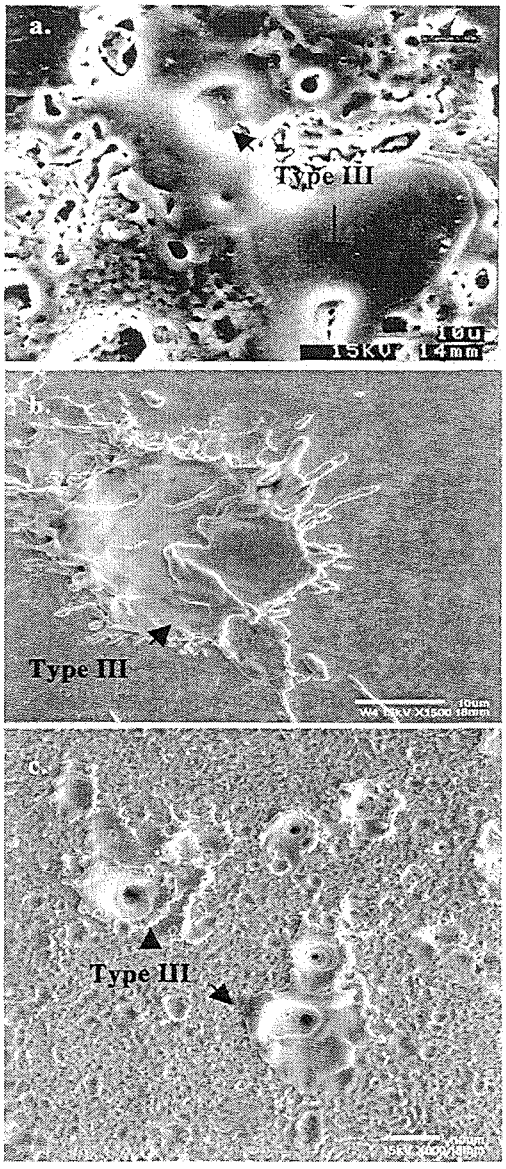

Figure 3. Type III arc spots on a) beryllium, b) tungsten and c) stainless steel after TA cleaning.

A Type III arc attachment is typically desired to maximize the roughness and improve the mechanical interlocking between a plasma spray coating and the TA cleaned surface. Evidence of the mechanical interlocking that occurs between a plasma sprayed beryllium coating on a TA cleaned beryllium surface is shown in Figure 4.

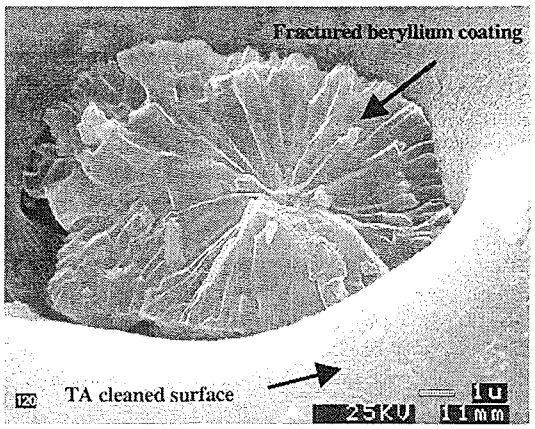

Figure 4. Fracture surface of a beryllium coating entrapped in a surface pore of a TA cleaned beryllium surface.

Surface craters present on the beryllium surface after TA cleaning act as sites where impacting molten beryllium particles can become entrapped during plasma spraying. This results in an interlocking between the coating and the beryllium surface. Bond strengths between plasma sprayed beryllium coatings and beryllium surfaces, which have been roughened by TA cleaning, have been reported to be as high as 250 MPa [8].

Other differences between Type I and II cathode arc spots include the amplitude of arc voltage and arc voltage fluctuations. The arc voltage is typically 20-30% lower for Type I spots and the fluctuation in arc voltage is higher for Type II spots. The lower arc voltage from the Type I spots is due to the presence of the impurity material that acts as a better electron emitter than the base metal. The better electron emission may result from a lower electron work function or the ability to develop a high local electric field due to space charge buildup on the impurity. The higher voltage fluctuation for Type II spots is due to the higher spot current. The fluctuations are due to the extinguishing and restriking of individual arcs. Since the spot current is larger for type II spots than for Type I spots,

there will be more Type I arcs than Type II arcs for a given total arc current. Since there are fewer arcs for Type II spots, the extinguishing and restriking of a single arc causes a larger voltage fluctuation than a single arc extinguishing and restriking for a Type I arc.

The voltage between the plasma torch face (anode) and surface to be cleaned (cathode) has been measured during TA cleaning runs. Figure 5 shows a typical voltage trace recorded during a TA cleaning run for copper. While the TA power supply was engaged with no arc between the torch face and sample, the voltage signal showed a sinusoidal fluctuation between 0 and 85 V with a frequency of 120 Hz (regions I and V in Fig. 5). When the arc attached to the substrate, the current signal increased and the voltage decreased in amplitude. Synchronization of the voltage data to video images allowed the determination of the voltage signal as a function of the observed arc behavior. This allowed, for instance, for the determination of the voltage for cleaning of the thin film contaminants (region II in Fig. 5) and a separate voltage for the arc attached to the base copper substrate (region IV in Fig. 5). Region III in Fig. 5 is the transition from the cleaning arc (Type I) to the metal arc (Type II).

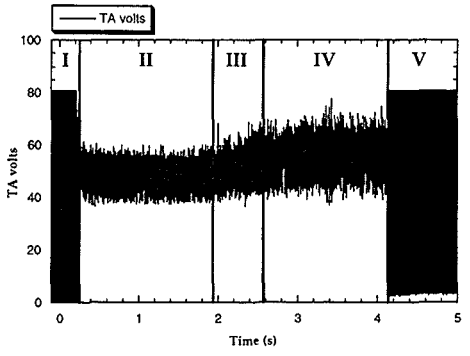

Figure 5 TA voltage during a copper cleaning run [9].

3.2. TA Cleaning Experiments

Beryllium

Results of the RBS analysis (reported in density free units) of the sputtered coated beryllium samples before TA cleaning are given in Table 2. The values reported for the tungsten and carbon correspond to a thickness of 1.0 to 3.5 nm for tungsten, and a thickness of 4.0 to 15.0 nm for carbon at "normal" densities. The detection of argon on the beryllium surface is a result of the argon sputtering process that may also account for the near surface detection of copper. As would be expected oxygen is present as a result of the native oxide that readily forms on the surface of beryllium. Results of the sputtered coated beryllium samples after TA cleaning are given in Table 3.

Table 2. 1.6 MeV He RBS at centerpoint of Be samples prior to TA cleaning (10^{15} atoms/cm^2).

I.D.	C	O	Ar	Cu	W
1	43.49	73.56	0.89	1.28	13.45
2	114.10	149.20	3.35	1.28	15.97
3	50.41	76.00	2.38	0.63	19.12
4	152.10	116.30	1.72	7.72	21.59
5	37.58	79.08	1.84	0.06	17.78
6	96.16	75.05	1.86	0.08	12.73
7	68.55	98.63	1.39	3.45	10.54
8	116.80	83.73	2.02	5.74	6.73

Table 3. 1.6 MeV He RBS at centerpoints of Be samples following TA cleaning (10^{15} atoms/cm^2).

I.D.	C	O	Ar	Cu	W
1	n.d	85.00	n.d.	u.d.	1.10
2	n.d	65.00	n.d	u.d.	0.68
3	n.d	55.00	n.d	u.d.	3.00
4	n.d	93.00	n.d	u.d.	0.41
5	n.d	61.00	n.d.	u.d.	7.00
6	n.d.	43.00	n.d.	u.d	9.60
7	n.d.	83.00	n.d.	u.d	0.71
8	n.d	120.00	n.d.	u.d	1.30

n.d. = not detectable
u.d. = present but undetermined quantity

RBS analysis showed that both the carbon and argon present on the surface of all eight beryllium samples were no longer detectable (minimum detection limit $\leq 10^{13}$ atoms/cm^2). For most of the beryllium samples, the surface tungsten was also reduced by an order of magnitude. An increase in the amount of copper on the surface of the beryllium was detected which extended beyond the range of the RBS analysis (>4.2 x 10^{18} atoms/cm^2). The elevated levels of copper may result from the TA cleaning process which utilizes the copper face of the plasma torch as the anode when cleaning the beryllium surface. Oxygen was still present on all the beryllium samples as a result of air exposure to the samples prior to the RBS analysis.

Table 4. PISCES-A exposure conditions for stainless steel and tungsten.

Sample	Time (s)	Temp (C)	Bias (V)	Carbon %	D+ fluence (cm-2)
Tungsten	1800	325	-150	10	2.20E+20
Stainless Steel	1800	525	-150	5	2.90E+21

Stainless Steel and Tungsten

The exposure conditions for stainless steel and tungsten samples (25.4 mm diameter x 3.175 mm thick) in the PISCES-A device is given in Table 4. The surface analysis of the stainless steel and tungsten samples before and after TA cleaning can be summarized as follows:

- The tungsten sample had a starting deuterium areal density of 53.1 x 10^{16} atoms/cm^2 and an ending value below the backscattering detection limit (~ 1 x 10^{14} atoms/cm^2) after cleaning. This represents a cleaning efficiency of > 1/5310 or 99.98%. The tungsten sample had a 1000 angstrom layer of carbon intermixed with tungsten before TA cleaning and no detectable carbon after cleaning. Surface analysis results for tungsten are shown in Figure 6 before and after TA cleaning.
- The stainless steel sample had a starting deuterium areal density of 7.4 x 10^{16} atoms/cm^2 before cleaning. The amount of deuterium after cleaning was below the backscattering detection limit (~ 1 x 10^{14} atoms/cm^2). A 3000 angstrom surface layer which contained 67% carbon was detected on the stainless steel before TA cleaning. The carbon level was substantially reduced to 27% after cleaning. Surface analysis results for stainless steel are shown in Figures 7 before and after TA cleaning.

The mechanism for removal of deuterium by TA cleaning is most likely a combination of thermal desorption and material removal. Large power densities (~1.5 x 10^9 W/cm^2) can result at the cathode spots as a result of current densities on the order of 10^8 A/cm^2 [7]. Power densities of this order can cause melting and erosion of the surface in addition to producing localized thermal gradients, which promotes the diffusion of deuterium from the sample surface.

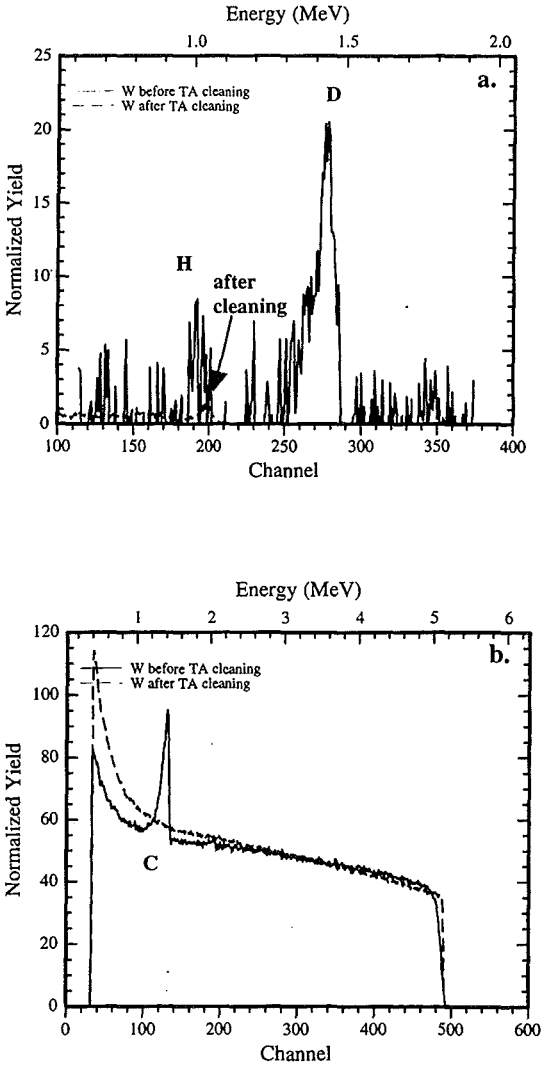

Figure 6. Surface analysis of tungsten before and after TA cleaning. a) hydrogen and deuterium and b) carbon.

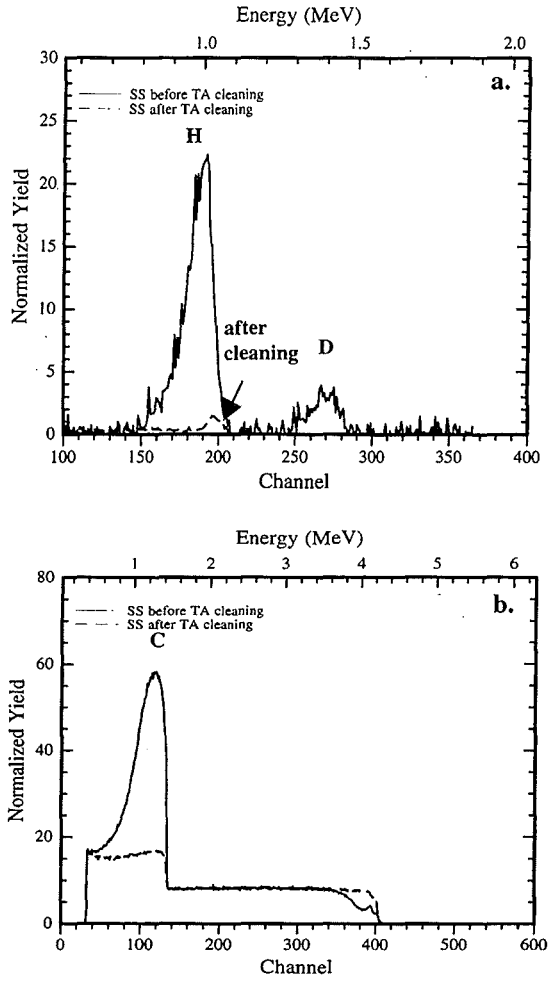

Figure 7. Surface analysis of stainless steel before and after TA cleaning. a) hydrogen and deuterium and b) carbon.

4. CONCLUSION

Results of TA cleaning for roughening and removing surface contamination from beryllium, tungsten and stainless steel can be summarized as follows:

- During TA cleaning arc attachments on the surface of beryllium, tungsten and stainless leaves surface craters that were formed by the displacement of melted material. The arc attachments/craters can be classified as either Type I, II or III cathode spot types as defined by Juttner *et al* [7].
- Type III arc attachments leave large (>10μm) connected craters which is desirable to maximize the mechanical interlocking and bond strength between a plasma sprayed coating and the underlying material.
- TA cleaning was shown to be an effective method for removing carbon and hydrogen isotopes from the surface of beryllium, tungsten and stainless steel.

ACKNOWLEGMENTS

The authors would like to thank Keith Elliott for his contributions on the TA cleaning of beryllium. This research was funded through the Technology Partnership Program Office at Los Alamos National Laboratory and the DOE Office of Fusion Energy.

REFERENCES

1. G. Federici, R. Causey, P.L. Andrew and C.H. Wu, Fusion Engineering and Design 28 (1995) 136-148.
2. W. Hsu and R.A. Causey, J. Vac. Sci. Technol. A, Vol. 5 No.4 (1987) 2768-2772.
3. R.A. Causey, W.L. Chrisman, W.L. Hsu, R. Andrel and B. Wishard, J. Vac. Sci Technol. A, Vol. 7, No. 3 (1989) 1078-1082.
4. D. M. Goebel, J. Bohdansky, R. W. Conn et , Nucl. Fusion 28 (1988) 1041.
5. Handbook of Modern Ion Beam Analysis, Eds. Joseph R. Tesmer and Michael Nastasi, Materials Research Society, Pittsburgh, PA (1995).
6. B. Juttner, V. Puchkarev, E. Hantzsche, I. Beilis, "Cathode Spots", *Handbook of Vacuum Arc Science and Technology*, R. Boxman, P. Martin, D. Sanders, Eds., Noyes Publications, 1995, p 73.
7. A.E. Guile and B. Juttner, IEEE Transactions on Plasma Science, Vol. PS-8, No. 3, Sept 1980, pp. 259-269
8. R.G. Castro, A.H. Bartlett, K.J. Hollis and R.D. Fields, Fusion Eng. and Design 37 (1997) 243-252.
9. K.J. Hollis, R.G. Castro, and B.D. Bartram, Proceedings United Thermal Spray Conf., March 17-19, Dusseldorf, Germany, pp. 202-207.

Studies of re-deposited layers produced at interaction of H and D ions with beryllium

L.S. Danelyan[a], N.G. Elistratov[b], V.M. Gureev[a], M.I. Guseva[a], B.N. Kolbasov[a],V.S. Kulikauskas[c], V.G. Stolyarova[a], N.N. Vasiliev[a], V.V. Zatekin[c] and A.M. Zimin[b]

[a]RRC "Kurchatov Institute", Kurchatov Square 1, Moscow, 123182, Russia

[b]Bauman Moscow State Technical University, Moscow, Russia

[c]Lomonosov Moscow State University, Moscow, Russia

A mode of operation with an effective return of sputtered particles to the Be-target surface under its bombardment by high-rate hydrogen and deuterium ion fluxes was realized to model beryllium re-deposition in conditions similar to those in International Thermonuclear Experimental Reactor ITER. Results of studies of hydrogen isotope accumulation in beryllium, as well as of chemical and physical composition and microstructure of re-deposited and sputtered beryllium layers are presented.

1. INTRODUCTION

Beryllium is the main candidate material for the plasma facing elements of the fusion reactor first wall which has a number of advantages over other materials due to, first of all, its low atomic number, high heat conductivity and isotropy of properties. A great number of papers dealing with the problem of interaction between hydrogen/deuterium plasma and beryllium have been recently published (see, e.g. [1-3]). Some studies [4-9] were devoted to hydrogen isotope accumulation in beryllium layers deposited upon Cu, Si or Al collectors. There is an essential spread in the experimental data in these papers. In one of the first studies deuterium accumulation within the deposited Be-layers under Penning's discharge [4] was negligibly low. On the other hand, according to M. Mayer et al. [5], in Be-layers deposited on Si under sputtering of a Be-target by D_3^+-ions with the energy of 4.5 keV and consisting mainly of BeO, the ratio D/BeO = 0.38, i.e. it is close to the corresponding value for graphite. R. Causey et al. [6-8] have studied deuterium accumulation in Be-layers deposited/re-deposited upon Al, Cu [6] and Si [8] collectors under exposure of Be-targets in a stationary high-flux-density deuterium plasma. The deuterium concentration in the re-deposited layers, according to [6-8], is in the range from 0.02 to 0.35, depending on the experimental conditions [6-7]. The experimental results on hydrogen accumulation in Be-layers deposited on Si in a magnetron discharge [9] under irradiation close to that in [6] practically coincide with the data described in [6].

Re-deposition, i.e. the return of sputtered particles to the wall, will take place under hydrogen isotope particle fluxes onto the wall and plasma electron temperatures expected in ITER. The return of the same nature particles to the surface under sputtering, at ITER conditions, can result in a qualitative change in structure and properties of the surface Be-layer.

In a given study, the mode of operation providing an effective return of the sputtered particles to the Be-target surface under its bombardment by high-density hydrogen and deuterium ion fluxes, described by us earlier [10], have been realized for simulating Be re-deposition in ITER.

2. EXPERIMENTAL TECHNIQUE

The studies of Be sputtering and re-deposition under an effect of hydrogen and deuterium ion fluxes in the range from $3 \cdot 10^{21}$ to $3 \cdot 10^{22}$ m^{-2} s^{-1} were performed at the MAGRAS facility [9-11], where a magnetron sputtering system with permanent

magnets was used as a source of hydrogen ions with the energy of 200 eV. The electric discharges in the magnetron had an annular configuration and were produced under low voltage mode of operation. The experiments were done under a higher hydrogen pressure in the chamber than in [9] for an effective scattering and re-deposition of the sputtered beryllium particles. It varied from 6 to 13 Pa.

The targets of polished beryllium TGP-56, 42 mm in diameter and 2 mm thick, were placed, as sectors, upon the magnetron cathode and clasped to it with a cover. In that case, the return of sputtered atoms occurred mainly upon the target surface. The dose of hydrogen and deuterium ions bombarding the cathode varied from $2.8 \cdot 10^{23}$ to $1 \cdot 10^{26}$ m^{-2}. The beryllium target temperature varied from 350 to 570 K and was measured with a thermocouple.

The thickness of the re-deposited layers and the target sputtering depth were measured with a profilometer STYLUS. The chemical composition of a surface layer was determined by the Rutherford back-scattering technique in the Van-de-Graaf accelerator. For this purpose, helium ions with the energy of 1.5 MeV were used. The angle of scattering was equal to 160^0. The hydrogen isotope accumulation and their distribution within the sputtered and re-deposited layers in depth were determined using the elastic recoil nuclei detection technique, when the helium ions with the energy of 1.8 MeV at the angle of 15^0 were directed to the target surface. The recoil atoms were registered at the angle of 30^0 to the initial direction of the helium ion incidence. An analysis of beryllium microstructure after its bombardment by hydrogen or deuterium ions and studies of the surface topography were performed with a scanning electron microscope, JEOL. A phase composition of the re-deposited beryllium was studied by the electron diffraction and the X-ray structure analysis techniques. A change in the target mass was determined by weighting within the accuracy of 10^{-4} g.

Typical conditions of the beryllium target irradiation by hydrogen and deuterium ions with the energy of 200 eV in the experiments are given in Table 1.

The scheme of the sector target structure consisting of some annular zones symmetrical relative to the centre after the irradiation is shown in Fig. 1. Zone 1 is the central zone where deposition of sputtered beryllium takes place. Zone 2 corresponds to sputtering of beryllium atoms and their deposition. It is separated from the re-deposition zone 4 by a narrow dark zone 3, adjoining the discharge boundary. During the ion bombardment, the external annular sector 5 was screened with a cover.

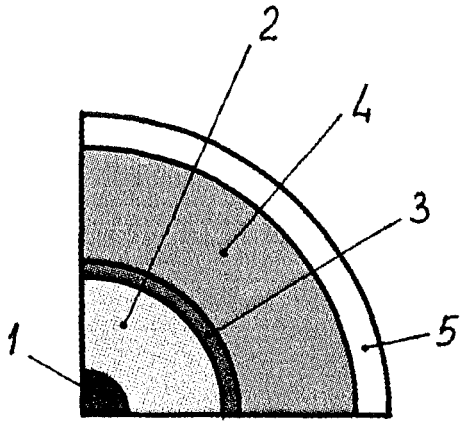

Figure 1. Structure of the sector target after irradiation: 1 - central zone, 2 - sputtering zone, 3 - dark zone, 4 - re-deposition zone, 5 - zone screened with the cover.

3. EXPERIMENTAL RESULTS AND THEIR DISCUSSION

The results of weighting have shown that there were no target mass changes within the accuracy of weighting during the irradiation. It confirms the fact that an effective return of the sputtered atoms to the target has taken place under given conditions. Such a conclusion is also in agreement with the experimental fact that no Be particles were detected at the erosion product collectors made of monocrystalline silicon plates and of glass fibre filters with the fibre diameters in the range from some tenths to tens micrometers (similar to those used by us in [9]) and located at the distance of about 20 cm from the target. A part of beryllium was deposited in zones 1 and 4, outside the area of ion beam effect on the target (zone 2). In these two zones only re-deposition of sputtered beryllium took place. In the zone 2 beryllium deposition onto beryllium surface took place together with the ion bombardment and sputtering.

Table 1
Conditions of experiments with beryllium targets

Target No.	Ion	Irradiation dose, m^{-2}	Target temperature, K
M1	D^+	$8 \cdot 10^{24}$	350
M2	D^+	$2 \cdot 10^{25}$	420
M3	H^+	$1 \cdot 10^{26}$	570

Measurements of the sample surface profiles with the profilometer corroborate the pattern of the sputtering and re-deposition zones. Profilograms show that a different ratio between the sputtering and deposition rates is observed at various annular pieces of a beryllium target under irradiation by both deuterium ions (target M1, Fig. 2) and hydrogen ions (target M3, Fig. 3).

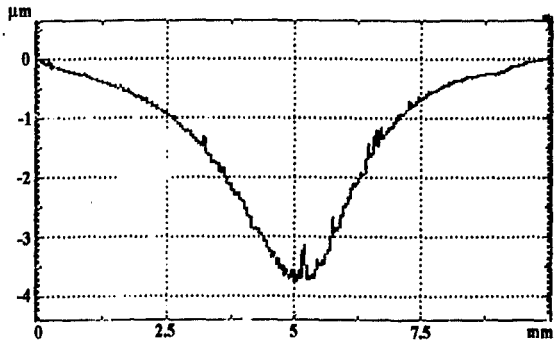

a)

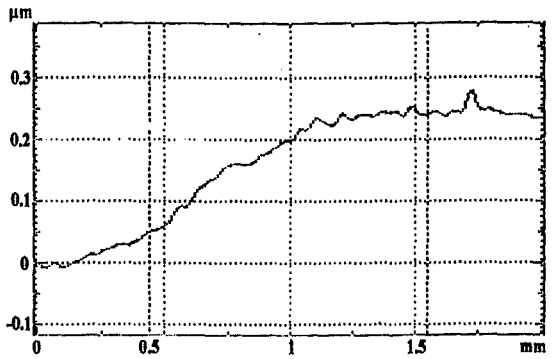

b)

Figure 2. Profilograms of the target M2 surface after irradiation by deuterium ions: a) sputtering zone, b) re-deposition zone.

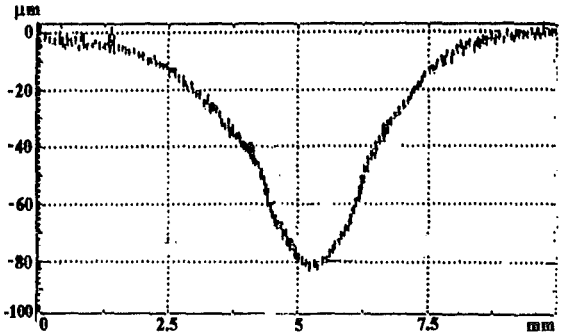

a)

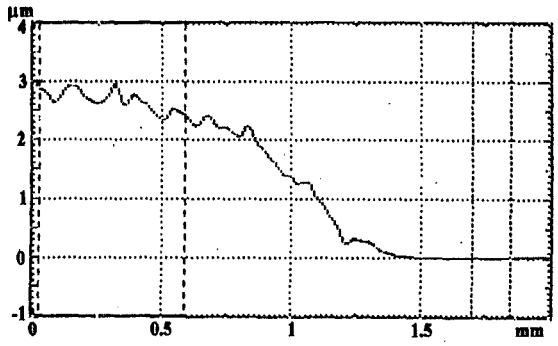

b)

Figure 3. Profilograms of the target M3 surface after irradiation by hydrogen ions: a) sputtering zone, b) re-deposition zone.

The dominant sputtering of a material took place in the zone 2. The sputtering depth reached 78 μm in the target M3 [10]. Meanwhile, only the beryllium re-deposition occurred in the zone 4, where the re-deposited layer thickness varied along the radius and reached in its maximum for the same target about 3 μm. A greater thickness of the deposit is observed in the central zone 1. The target M2, irradiated by deuterium ions, had corresponding sputtering depth and the thickness of the re-deposited layer less than for target M3 (Fig. 2, 3).

A component composition of various beryllium targets zones is shown in Figures 4 and 5. The thickness of re-deposited layers increases with the irradiation dose rise. Atom ratio O/Be is close to 1 in the re-deposition zones produced under target irradiation by both D^+ and H^+ ions, except a narrow surface layer (Fig. 4).

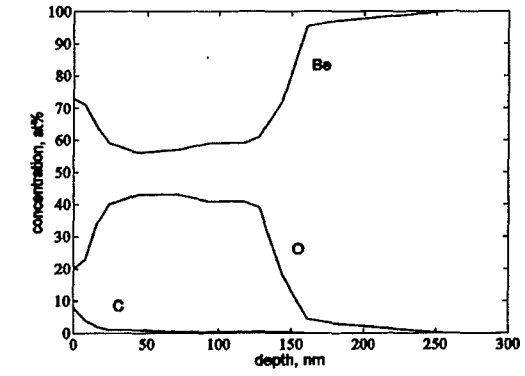

a)

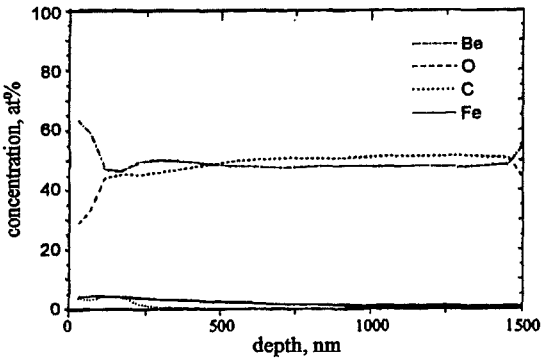

b)

Figure 4. Component composition in the re-deposition zone of targets M2 (a) and M3 (b).

This may confirm that the re-deposition zone of the target consists of BeO, i.e. that the sputtered beryllium atoms entrap oxygen when they are deposited onto the target surface. In contrast to this, the maximum oxygen concentration in the sputtering zone varies in the range from 10 to 15 at.% (Fig. 5). Oxygen distribution in beryllium closed against the irradiation is a table-like (Figure 6).

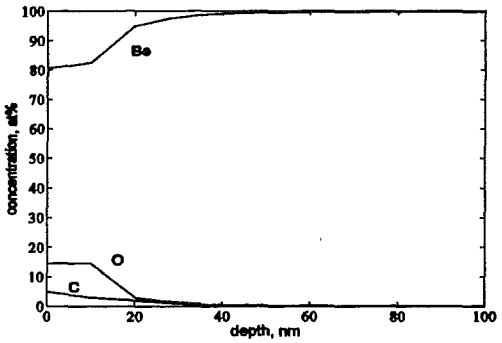

Figure 5. Component composition in the sputtering zone of the target M2.

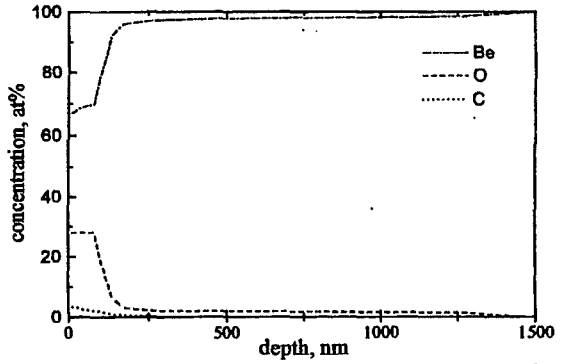

Figure 6. Component composition in the zone of the target M2 screened against irradiation.

A phase analysis of various zones in the beryllium sample M3 performed by the electron diffraction at reflection technique has shown that the sputtering zone is a weakly grain-oriented polycrystalline beryllium (Figure 7a). The electron diffraction patterns of the re-deposition zone surface of the same target demonstrate a diffusive halo (Figure 7b) confirming its amorphous structure. The corresponding spacing of lattice planes is close to that of BeO.

The results of studying the phase composition in the sputtering zone of the sample M2 by the X-ray crystal analysis technique are given in Figure 8. The surface layer in the sputtering zone under deuterium ion bombardment consists mainly of α- and β-beryllium. Along with them, an insignificant amount of BeO, predominantly of α-modification, is observed.

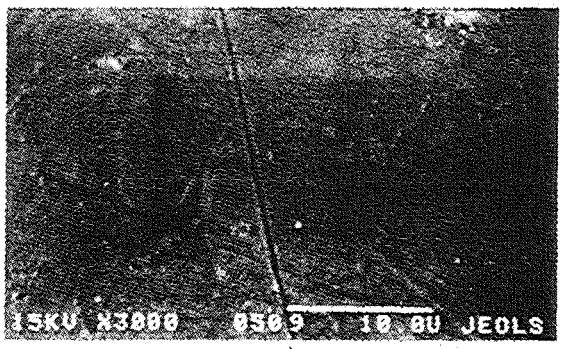

a)

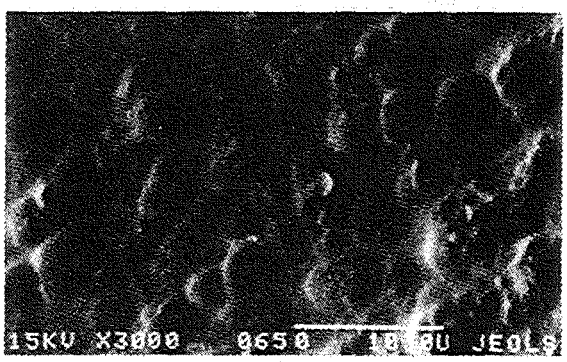

b)

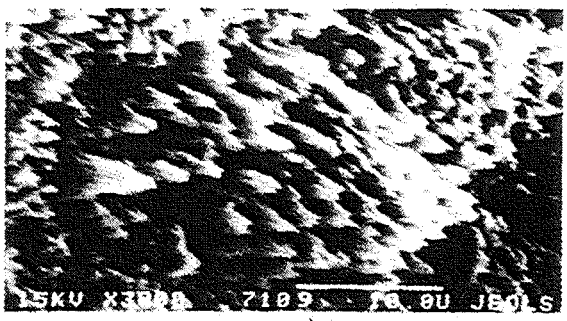

c)

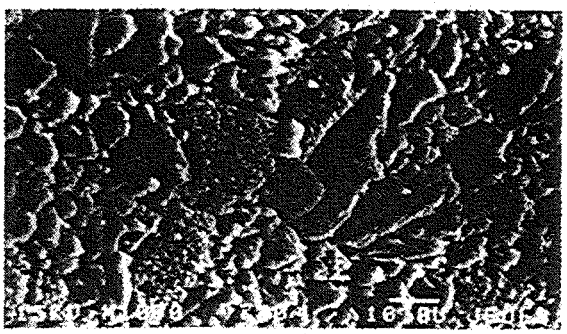

d)

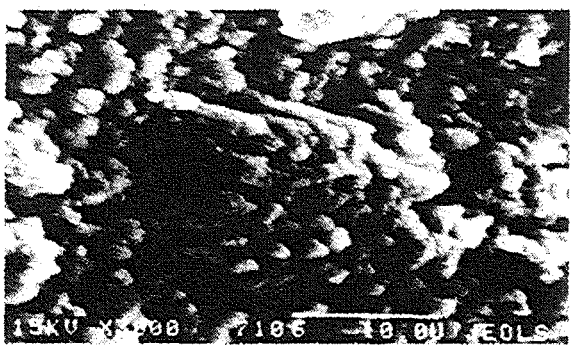

e)

Figure 9. Microstructure of beryllium targets:
a) in the zone screened against irradiation,
b) in the sputtering zone of the target M2,
c) in the sputtering zone of the target M3,
d) in the area of the ionic etching in the sputtering zone of the target M3,
e) in the re-deposition zone of the target M3.

The profiles of deuterium distribution in the surface layers of the sputtering zones of the targets M1 and M2 are shown in Figure 11. They have a table-like configuration, typical for a high irradiation dose.

The integral deuterium concentration in the sputtering zone of samples is in the range from $3.8 \cdot 10^{20}$ to $6.5 \cdot 10^{20}$ m^{-2}, depending on the mode of operation. The ratio of the number of atoms, D/Be, varies from 0.161 at the temperature of 350 K to 0.095 at 420 K. These results are in good agreement with the data of R.Causey [8] measured under a controlled oxygen concentration in deposited films.

Our results of the data analysis on hydrogen isotope accumulation are summarized in Table 2. We would like to emphasize that hydrogen isotope are accumulated not only in the sputtering zone, where a high-rate ion bombardment takes place, but also in the re-deposition zone where ion fluxes are absent. Apparently, the hydrogen/deuterium atoms are carried along from the surrounding medium by the re-deposited beryllium particles. At the same time, ratio D/BeO in our experiments is less than that in [5] where a co-deposition of high-energy gas atoms took place.

Table 2
Characteristics of beryllium layers after irradiation

Target	Ion	Temperature, K	Thickness of re-deposited layer nm	Integral concentration of D (H) in the re-deposition zone, m^{-2}	Integral concentration of D (H) in the sputtering zone, m^{-2}	D/Be (H/Be)	D/BeO (H/BeO)
M1	D^+	350	76	$1.53 \cdot 10^{21}$	$6.52 \cdot 10^{20}$	0.161	0.280
M2	D^+	420	170	$2.54 \cdot 10^{21}$	$3.83 \cdot 10^{20}$	0.095	0.207
M3	H^+	570	~1500	$\sim 6 \cdot 10^{21}$	$2.41 \cdot 10^{20}$	0.060	~0.08

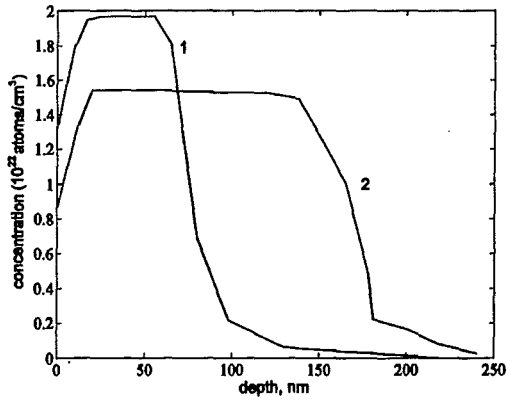

a)

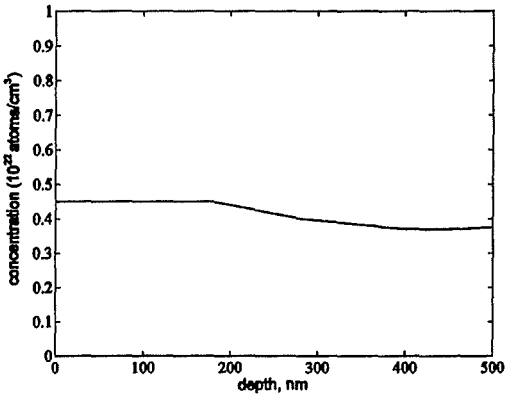

b)

Figure 10. Profiles of hydrogen isotope atoms distribution in re-deposited beryllium layers: a) deuterium in the targets M1 (1) and M2 (2), b) hydrogen in the target M3.

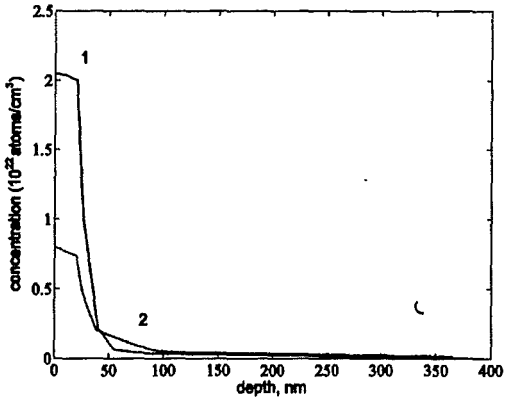

Figure 11. Profiles of deuterium distribution in the sputtering zones of the targets M1 (1) and M2 (2).

4. MATHEMATICAL MODEL OF SPUTTERED ATOMS RE-DEPOSITION

To explain the effective return of sputtered particles and the pronounced annular target structure, observed in the experiments, a numerical model of the main processes which occur under re-deposition has been developed, and it has been numerically realized with an computer.

The mathematical model for calculating the beryllium return to the target surface [12] is based on the fact that one can use a rather simple diffusion model [13] for description of these processes under analysis of an evolution of the sputtering products in a surrounding medium of light atoms (as it takes place in the near-wall plasma of fusion facilities).

The thermalized atoms of the sputtered material, actually the fast atoms knocked-out from the target surface after their scattering on particles of the surrounding medium, participate in the process of diffusion. The volume density of the thermalized particle birth per unit of time is represented by the so-called function of a virtual source, ρ(r,z) [14,15] which is calculated in the approximation of a continuous deceleration from the equation for balance of the particles knocked-out from the target surface and thermalized in a given point, having the current co-ordinates (r,z). Then, the found field of values, ρ(r,z), is used for solving the diffusion equation for thermalized sputtered atoms in the surrounding gas:

$$D\left(\frac{\partial^2 n}{\partial z^2}+\frac{1}{r}\frac{\partial n}{\partial r}+\frac{\partial^2 n}{\partial r^2}\right)=-\rho(r,z),$$

with zero values of concentration at all the boundaries (except the discharge axis, where the symmetry condition is used), which allows to find the distribution of beryllium atoms near the cathode surface and to calculate their fluxes to the target. The thermalization length of the sputtered beryllium atoms for the conditions of the described experiment is about 2 cm. This value practically coincides with the target radius. In this case, the returning particle flux should depend on the radial co-ordinate, and such a dependence is observed in the experiment. Let us consider some results of the calculations for the conditions of the experiment with the target M3. The lines of equal concentration level for sputtered beryllium particles near the target M3 are shown in Figure 12, and the flux of beryllium particles re-depositing upon the surface of the target M3 (in relative units) is plotted as a function of the radius in Figure 13. An absolute value of the beryllium concentration near the surface is rather high. At the maximum, it reaches $3\cdot10^{17}$ m^{-3} at the distance of about 3 cm from the surface, but nevertheless it is noticeably lower than the hydrogen concentration which is of the order of 10^{21} m^{-3} for a given experiment. Figure 13 shows that the flux of returning beryllium atoms has a maximum at the system axis where the discharge is absent, and it decreases about in half to the target periphery.

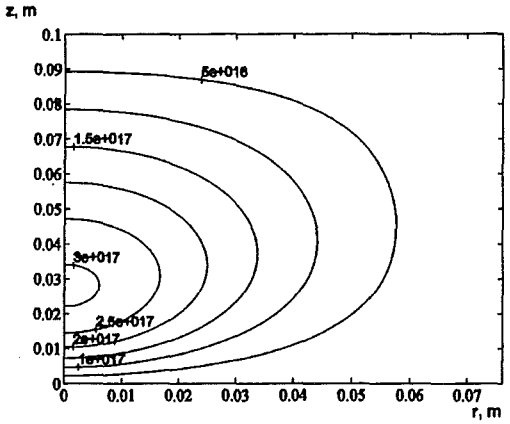

Figure 12. The lines of equal concentration level for sputtered beryllium atoms near the target M3 surface.

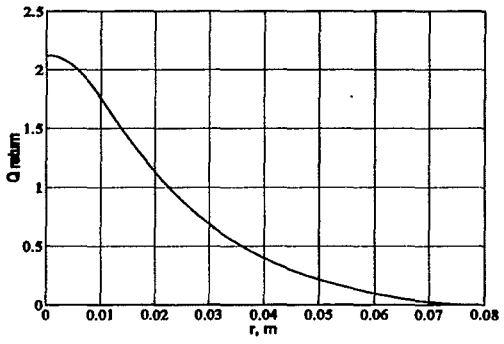

Figure 13. Flux of beryllium atoms re-depositing upon the target M3 against radius.

The received relationships, together with the experimental data, have allowed to estimate the coefficient of beryllium sputtering by hydrogen ions from the rates of two competing processes: sputtering and deposition. The volume of sputtered beryllium has been determined by integration of the product of sputtering depth by an element of an annular surface, being equal ~11 mm^3 for the given experiment what corresponds to 21 mg. Having recalculated this volume for the number of particles and referring them to the number of bombarding ions, we obtain $Y_1 = 0.044$ at./ion.

On the other hand, we can estimate the number of beryllium atoms knocked-out from the surface, using the mass of the deposited sediment and the

calculated relationship of the particle return flux against the radius. Such an estimation for the median part of the re-deposition zone, where the deposited sediment is 1.5 μm thick (see Figure 4b), gives the sputtering yield $Y_2 = 0.058$, somewhat exceeding Y_1. In this case, we took into account that the sediment consists not of pure beryllium but of its oxide. If we take into account the return of beryllium in the zone of sputtering, the value of Y_1 somewhat rises and the values Y_1 and Y_2 become almost equal to each other.

The Be sputtering yield, found in such a way, exceeds the known values for H^+-ions with the energy of 200 eV (~ 0.02 at./ion) [16], including our data received for beryllium deposited on the Si collector [10]. Apparently, this is connected with the fact that in the given experiment, the discharge plasma is located near the target surface. In this plasma, the charge exchange and ionization of the sputtered Be-atoms take place, and the beryllium self-sputtering yield is greater by an order of magnitude than that for beryllium sputtering by hydrogen ions [17].

The produced calculated data, together with those received experimentally, explain the annular structure of the target after its irradiation by an ion flux in the magnetron. The central zone is characterized by the maximum of a returning particle flux onto inactive cathode surface, where the discharge and sputtering are absent. In the next, respective to the centre, annular zone both the sputtering and the deposition take place. The intensity of the latter process decreases towards the target periphery. Therefore, the sputtering profile in this zone is asymmetric in respect to the symmetry axis of the discharge contact area, and the sputtering depth maximum is shifted regarding of it towards the periphery. Finally, in the re-deposition zone separated from the ion flux effect zone by a narrow dark zone, 3 (Figure 1), the beryllium particle re-deposition only takes places.

5. CONCLUSION

1. At the MAGRAS facility the mode of operation with beryllium re-deposition onto beryllium, using the magnetron discharge, was realized under beryllium bombardment by high rate hydrogen and deuterium ion beams.

2. Concentration of oxygen atoms in the sputtering zone is 10-15 at.%, and in the re-deposition zone it is 40-50 at.%.

3. Beryllium exists in the crystalline state as a metal in the sputtering zone, and predominantly as an amorphous oxide in the re-deposition zone.

4. Microstructure of beryllium is changed essentially under ion irradiation. Blisters or cones are formed in the sputtering zone depending on the irradiation dose. Cones are formed due to a difference in the sputtering yields of BeO and Be. In the re-deposition zone, a growth of columnar structure occurs under high hydrogen ion irradiation doses.

5. Ratio of number of atoms D/Be or H/Be is 0.06-0.16 decreasing with the target temperature rise in the sputtering zone.

6. Hydrogen and deuterium entrapping takes place in the whole re-deposition zone, where the flux of bombarding ions is absent. Ratio D/BeO (H/BeO) decreases from 0.28 to 0.08 with the temperature growth.

7. Calculations of the beryllium deposition using experimental sputtering and re-deposition profiles explain the annular target structure after irradiation. Estimation of the beryllium sputtering yield shows a necessity to take into account beryllium self-sputtering.

REFERENCES

1. H. Kawamura, E. Ishitsuka, A. Sagara, et al., J. Nucl. Mater., 176-177 (1990) 661-665.
2. Proceedings 2nd IEA Int. Workshop on Beryllium Technology for Fusion (Editor G.R. Longhurst), Jackson Lake Lodge, Wyoming, USA, 1995.
3. Proceedings 3rd IEA Int. Workshop on Beryllium Technology for Fusion (Editors H. Kawamura, M. Okamoto), Mito-city, Japan, 1998.
4. K.L. Wilson, R.A. Causey, W.L. Hsu, et al., J. Vac. Sci. Technol., A8 (1990) 1750.
5. M. Mayer, R. Behrish, H. Plank, et al., J. Nucl. Mater., 230 (1996) 67.
6. J.N. Brooks, R.A. Causey, G. Federici, G. Ruzic, J. Nucl. Mater., 241 - 243 (1997) 294-298.

7. R.A. Causey, G.R. Longhurst, W. Harbin, J. Nucl. Mater., 241-243 (1997) 1043-1046.
8. R.A. Causey, D.S. Walsh, J. Nucl. Mater., 254 (1998) 84-86.
9. D.V. Andreev, A.Yu. Biryukov, L.S. Danelyan, et al., Fusion Eng. Des. 39 - 40 (1998) 465 -475.
10. V.M. Gureev, M.I. Guseva, L.S. Danelyan, et al., Proc. 3rd IEA Int. Workshop on Beryllium Technology for Fusion (Editors H. Kawamura, M. Okamoto), Mito-city, Japan, 1998, p. 74-83.
11. N.N. Vasiliev, B.N. Kolbasov, D.K. Kurbatov, et al., Abstracts 2nd IEA Int. Workshop on Beryllium Technology for Fusion (Editor G.R. Longhurst), Jackson Lake Lodge, Wyoming, USA, 1995, p. 38.
12. N.G. Elistratov, A.M. Zimin, Problems of Atomic Science and Engineering, ser. Thermonuclear Fusion, No. 1 (1999) 8-16 (in Russian).
13. J.A. Valles-Abarca, A. Gras-Marti, J. Appl. Phys., 55/5 (1984) 1370-1378.
14. A.G. Zhiglinskij, V.V. Kuchinskij, Mass-transfer under plasma-surface interaction, Moscow, Energoatomizdat, 1991 (in Russian).
15. G.G. Bondarenko, A.P. Korzhavy, V.I. Kristya, et al., Proc. 13th Int. Conf. on Ion Interaction with Surface, Moscow, 1997, v. 2, p. 81-84 (in Russian).
16. W. Ekstein, C. Garcia-Rosales, J. Roth, W. Ottenberg, Sputtering Data, IPP 9/82, Garching, 1993.
17. M.I. Guseva, V.M. Gureev, S.N. Korshunov, et al., J. Nucl. Mater., 220-222 (1995) 957-960.

TRITIUM LOSS IN MOLTEN FLIBE SYSTEMS[a]

Glen R. Longhurst and Robert A. Anderl
Idaho National Engineering and Environmental Laboratory
P.O. Box 1625, Idaho Falls, Idaho 83415-3860, USA
208-526-9950, Fax 208-526-2930, gxl@inel.gov

R. Scott Willms
Los Alamos National Laboratory, MS C-348
Los Alamos, NM 87545

ABSTRACT

An emerging issue relative to beryllium technology in fusion involves tritium interactions with molten beryllium-bearing salts. Innovative designs for fusion reactors, both magnetic and inertially confined, feature the molten salt mixture $2LiF \bullet BeF_2$, commonly called Flibe, as a tritium breeder and coolant. Tritium is bred in the Flibe as neutrons from the plasma are absorbed by Li atoms, which then transmute to tritium and helium. Transmutation of tritium from Be also occurs. Among the issues to be resolved for such coolant systems is the potential loss of tritium from the Flibe coolant to the walls of the system, particularly through heat exchanger tubes, and from there into secondary coolants or working fluids and the environment. Effectively removing tritium from Flibe in clean-up units is also important.

In quiescent or low Reynolds number flow, tritium movement through Flibe is governed by diffusion. For Flibe in turbulent flow, as in heat exchanger tubes, transport is by turbulent mixing, and the same flow conditions and structural design features that maximize heat transfer to the heat exchanger walls will enhance the transport of tritium to those same surfaces. Analyses have been performed to estimate the fractional loss of tritium through heat exchanger tubes and release rates from Flibe droplets in vacuum disengagers in molten Flibe systems. The calculations suggest unacceptably large losses of tritium through heat exchanger tubes. The gravity of the implications of these estimates calls for experimental verification to determine if tritium losses through molten Flibe heat exchangers or other Flibe systems can really be so high and whether vacuum disengagers will really work. There is also a need for better information on evolution of tritium from Flibe droplets in a vacuum.

Several experiments are presently being planned to address these issues and are discussed. These include experiments to induce tritium in Flibe using spontaneous fission neutrons, experiments in flowing loops to evaluated tritium losses through heat exchanger walls, and exploration of schemes for tritium extraction from molten Flibe.

[a] Work performed for U.S. Department of Energy, Office of Science, under DOE Idaho Operations Office Contract DE-AC07-94ID13223.

INTRODUCTION

The molten salt mixture $2LiF \bullet BeF_2$, commonly referred to as Flibe, is under consideration for use in fusion reactors. In magnetic fusion energy (MFE) reactor designs, the Flibe has been considered as a renewable surface for interfacing with the plasma in high plasma-flux regions and as a tritium-breeding coolant. In inertial fusion energy (IFE) designs, it has been considered as a shielding medium from both neutrons and the hydrodynamic blast of IFE targets. In this report, we consider issues associated with tritium production in and release from Flibe in fusion reactor systems and experiments planned to examine those issues. These issues include chemical and radiological concerns as well as those associated with operational and environmental hazards.

2. FLIBE APPLICATIONS

The use of molten Flibe as a coolant for fusion reactors has several engineering and safety advantages. Flibe serves as a high temperature heat transfer fluid that achieves high thermal efficiencies, acts as a good radiation shield, and has modest to good fluid flow properties.[1]

Flibe is used at high temperature, but low pressure. Any ex-vessel cracks in the coolant piping are expected to produce small leaks, due to the low coolant pressure. Only a low frequency pipe rupture event (i.e., less than 10^{-4}/year) should lead to a large coolant spill.

One of the early applications of Flibe in fusion reactor designs was in HYLIFE-II.[2] In that IFE design, Flibe is circulated at the rate of about 60 m^3/s through a set of fixed and oscillating jets and serves to shield the first wall from the blast and neutrons as well as to breed tritium. Two banks of movable jets, oscillating sinusoidally but 180° out of phase with each other, provide a moving cavity into which a target pellet can be fired (as from a rifle) and ignited by either laser or heavy ion beam drivers. The stationary jets complete the coverage for the shielding function.

Since then, Flibe has been considered as a coolant and as a plasma-facing material by the Advanced Liquid Plasma Surface (ALPS) and Advanced Power Extraction (APEX) projects within the U.S. DOE Office of Fusion Energy Sciences, and for the Force Free Helical Reactor (FFHR).[3] Studies are presently underway to develop methods of getting molten Flibe to conform to the desired shapes in dynamic flow situations and to investigate tritium breeding and extraction, chemical compatibility, and other issues relevant to the application of Flibe in advanced magnetic fusion designs.[4–7]

TRITIUM PRODUCTION AND LOSS

The HYLIFE-II inertial fusion design concept using Flibe was investigated for activation. Principal radioisotopes created from neutron activation of pure Flibe are ^{10}Be, ^{3}H, and ^{18}F.[8] The dominant activation product is ^{18}F.[8,9] More tritium will be bred in the lithium if ^{6}Li enrichment is used to enhance tritium fuel production in the coolant. During a spill, gaseous tritium, in the form of TF or HT, may be released.

One of the inducements for Flibe in fusion reactors is its inherent ability to produce the fusion fuel tritium from the reaction of fusion neutrons with the lithium in the Flibe. Beryllium will also generate tritium by neutron transmutations. Figure 1 shows the activation and decay schemes associated with tritium production in Flibe.[10]

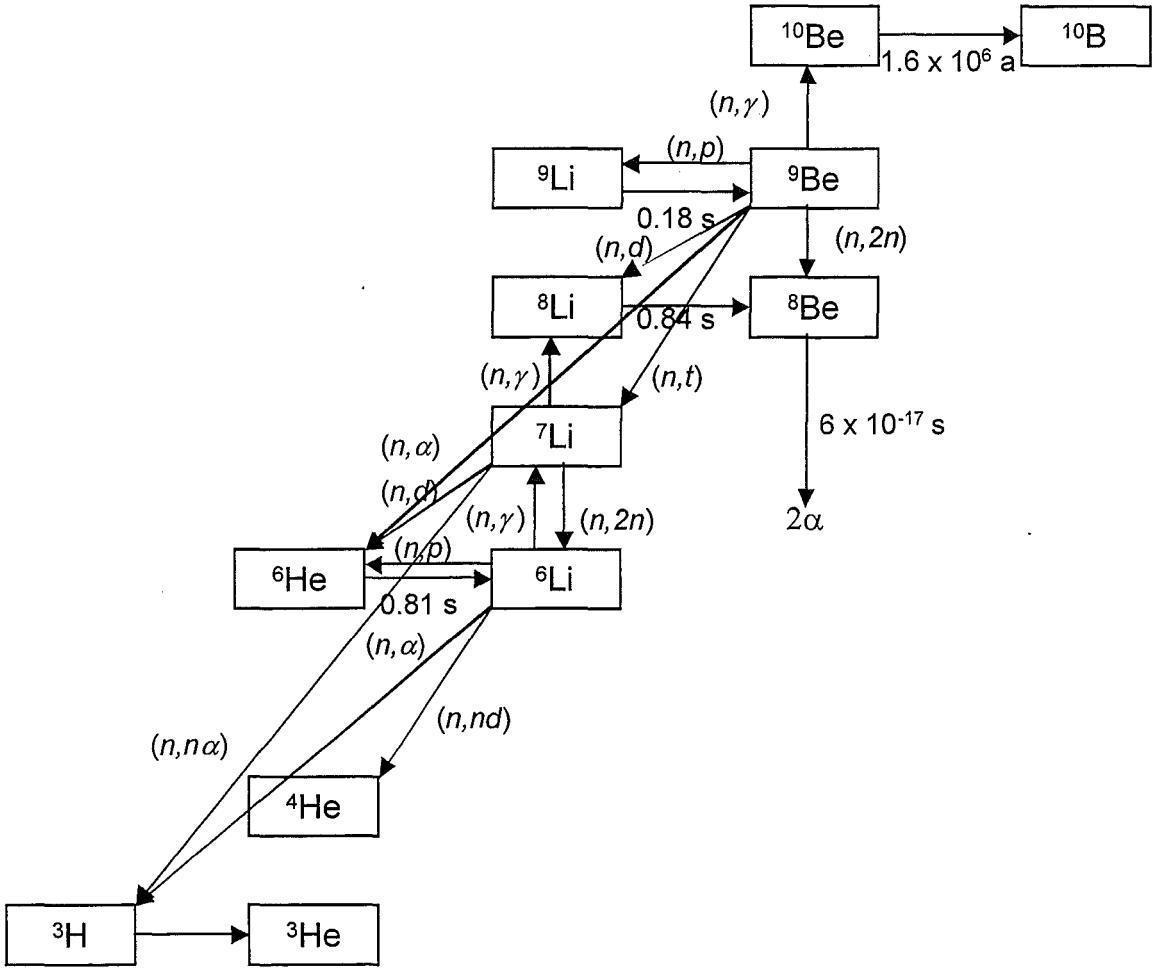

Figure 1. Activation and decay paths for lithium and beryllium in Flibe.

An important concern regarding tritium produced in Flibe is its propagation to other parts of a fusion system. Solubility of hydrogen isotopes in Flibe is very low.[11] That means that even a small concentration of tritium produced in the Flibe by neutron transmutations will have a very high chemical potential and will readily exit the Flibe by whatever means are available. A particular concern in this regard is its ability to pass through the walls of heat exchanger tubes or other structures and enter the atmosphere or a secondary coolant stream. Transport of tritium in Flibe flowing in heat transfer systems is largely by convection. Therefore, the same design configurations that will be used to maximize heat transfer from the Flibe will also maximize the transport of tritium.[12] During an accidental spill, gaseous tritium in the form of TF or HT may be released from the Flibe as well.

A second concern for Flibe is the ability to remove tritium from the Flibe at the locations desired in the Flibe loop and in a time sufficiently short to be practical. For the HYLIFE II design, the method chosen for tritium removal was a vacuum disengager in which tiny droplets are created and allowed to fall through a vacuum.[12] During the fall, tritium evolves from the droplets by diffusion. Key design considerations then were associated with the time required to remove the desired amount of tritium, the droplet size, and vacuum pumping requirements.

ANALYSIS

Two analytical investigations were performed in an attempt to evaluate the significance of these issues in the context of the HYLIFE II design study. They are reviewed here, but the reader is invited to review the detailed reports for a full description of the methods and results.

Loss in Tubes

The first analysis explored the rate at which tritium produced in Flibe may permeate through heat exchanger tubes.[13,14] Flibe was assumed to pass through a long 316 stainless steel tube of fixed diameter. The flow was assumed to be turbulent and well developed over the entire length of the tube. Under those circumstances, transport of energy, momentum, and dissolved hydrogen molecules is governed by turbulent diffusion. Hence, energy density (represented by temperature), momentum density (velocity), and tritium concentration were assumed to have similar profiles in the radial direction.[15] For simplicity it was assumed that tritium was the only hydrogen species present. The tube was assumed to be in a counter-flow heat exchanger such that the bulk temperature of the Flibe varied linearly over the length of the tube, and the wall temperature was taken to be lower than the local Flibe bulk temperature by a constant increment, ΔT.

At the tube wall, tritium diffuses in the boundary layer with assumed diffusivity[16]

$$\mathbf{D}\left(\frac{\mathbf{m}^2}{\mathbf{s}}\right) = 2.137\times10^{-6}\exp\left(-\frac{0.462\mathrm{eV}}{\mathbf{kT}}\right) \qquad (1)$$

where **k** is Boltzmann's constant and **T** is temperature. At the wall surface, the concentration of tritium in the Flibe was assumed to equate to an equivalent gas pressure or chemical potential through Henry's law according to [11]

$$\mathbf{S}\left(\frac{\mathbf{atom}}{\mathbf{m}^3\mathbf{Pa}}\right) = 2.58\times10^{17}\exp\left(-\frac{0.457\mathrm{eV}}{\mathbf{kT}}\right) \qquad (2)$$

That equivalent pressure, in turn, implied uptake in stainless steel through a Sieverts' law solubility[17]

$$S\left(\frac{\text{atom}}{\text{m}^3\text{Pa}^{1/2}}\right) = 5.14\times10^{23}\exp\left(-\frac{0.144\text{eV}}{\text{kT}}\right) \quad (3)$$

involving a recombination rate-limited surface exchange process.[18] It was not known whether molecules would form at the interface and then dissociate to enter the tube walls or whether the tritium would go in directly. It was optimistically assumed that T_2 molecules diffused through the Flibe such that the exchange rate was second order in the Flibe tritium concentration. In reality the tritium atoms exist mainly as ions in the Flibe [5] and HT should be considered as well, because some protium will also be present. If a Sieverts'-law solution boundary condition were assumed, or if molecular recombination followed by dissociation were not involved, loss rates of tritium from the Flibe would be faster yet. If the molecules are mostly TF, then the process would exhibit yet different results.

Tritium entering the stainless steel was then assumed to move by diffusion through the tube wall and to recombine on the outer side, again in a second-order process. Because of turbulent mixing outside the tube, the partial pressure of T_2 outside the tube was assumed to be a constant. These processes are illustrated in Figure 2.

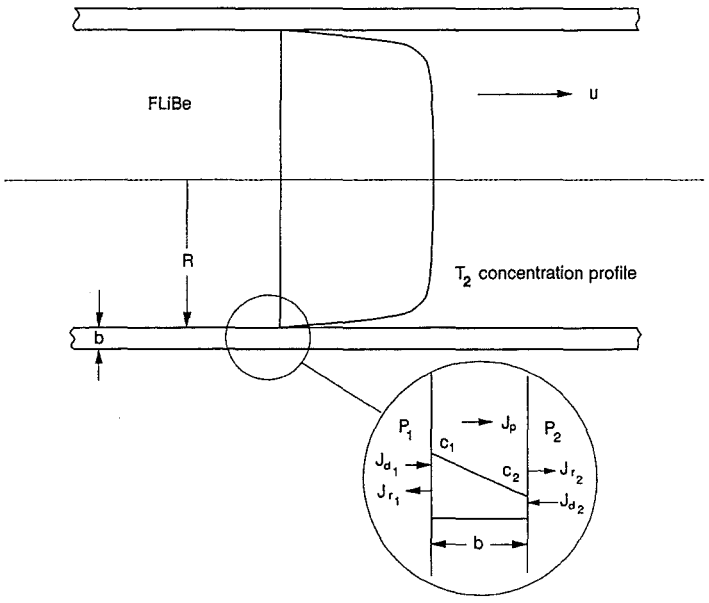

Figure 2. Relationships between various parameters considered in analysis of tritium loss through heat exchanger tube wall.

Making use of the Reynolds-Lewis analogy,[15] it was then possible to numerically calculate tritium concentration profiles over the length of the tube and the resulting permeation fraction. Figure 3 shows calculated radial concentration profiles inside the tube. The concentration has been made dimensionless by normalizing to a concentration defined in terms of the wall permeation flux and a reference velocity given by the wall shear stress and the Flibe density.

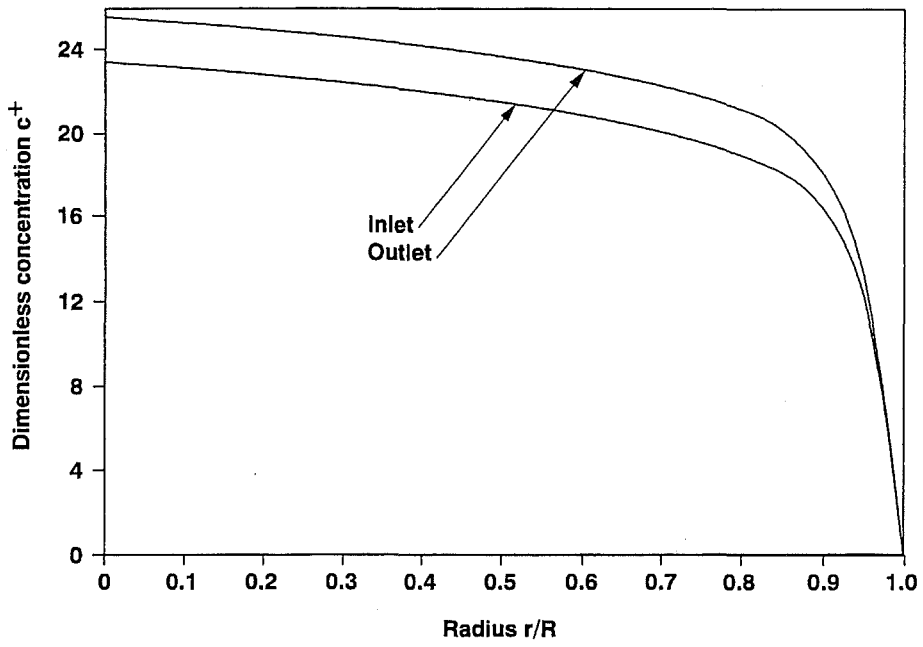

Figure 3. Normalized tritium concentrations calculated for molten Flibe flowing through a tube 2 cm in diameter and 10 m long. The actual (non-normalized) outlet concentration is only a small fraction of that at the inlet.

Figure 4 shows axial concentration profiles for various assumptions regarding the effectiveness of a dissociation/ recombination barrier on the inside wall of a heat exchanger tube 2 cm in diameter and 10 m long with Flibe flowing at 1.8 m/s and an inlet temperature of 943 K. It may be seen there that a very substantial permeation barrier is needed to prevent almost the entire tritium content of the Flibe from being lost through the tube wall. Such barriers for use in Flibe systems have not yet been developed. This highlights the significance of the problem associated with tube wall loss.

Detritiation of Droplets

With the continual buildup of tritium in the Flibe by neutron transmutation, there is a need for a means of removing the tritium in controlled ways to prevent its dispersion through heat exchanger tubes. In the HYLIFE II design, that was accommodated using tritium disengagers, columns through which small Flibe droplets could fall under vacuum.[19] The concept required tritium in the droplets to diffuse to the surface and recombine, coming off as free molecular gas that could be pumped away to separation and storage. A key issue in the design was the rate at which such tritium evolution could occur. That obviously impacted the required droplet size and the height through which the droplets would have to fall. The detailed solution for the amount of dissolved solute retained in a spherical droplet where diffusion governs is [20]

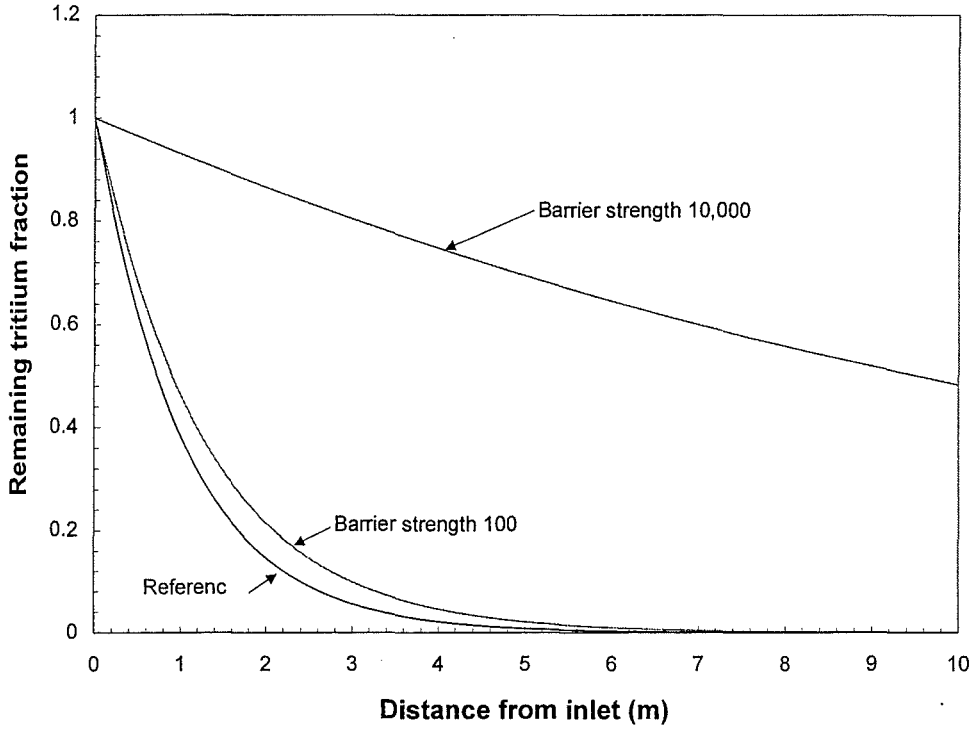

Figure 4. Axial tritium concentration profiles calculated for Flibe flowing at 1.8 m/s in a 10-m long x 2-cm diameter heat exchanger tube for various permeation barrier strengths (inhibitions to dissociation/recombination) on the inner tube wall.

$$\Phi = \frac{p_\infty}{p_0} + 6\left(1 - \frac{p_\infty}{p_0}\right)\sum_{m=1}^{\infty} \exp\left(-\lambda_m^2 \, Fo\right)\frac{[\sin(\lambda_m) - \lambda_m \cos(\lambda_m)]^2}{[\lambda_m - \sin(\lambda_m)\cos(\lambda_m)]} \tag{4}$$

where P_∞ and P_0 are the ultimate and initial tritium concentrations, respectively, **Fo** is a dimensionless time or Fourier number based on diffusivity **D** and droplet radius **r**

$$Fo = \frac{tD}{r^2} \tag{5}$$

and the λ_m are solutions to the characteristic equation

$$\lambda_m \cot(\lambda_m) = 1 - Bi \tag{6}$$

Here **Bi** is a Biot number

$$Bi = \frac{hr}{D} \tag{7}$$

where **h** is the surface mass transfer coefficient for the tritium.

Time evolution histories were found for a range of Biot numbers. These are shown as functions of the dimensionless time **Fo** in Figure 5.

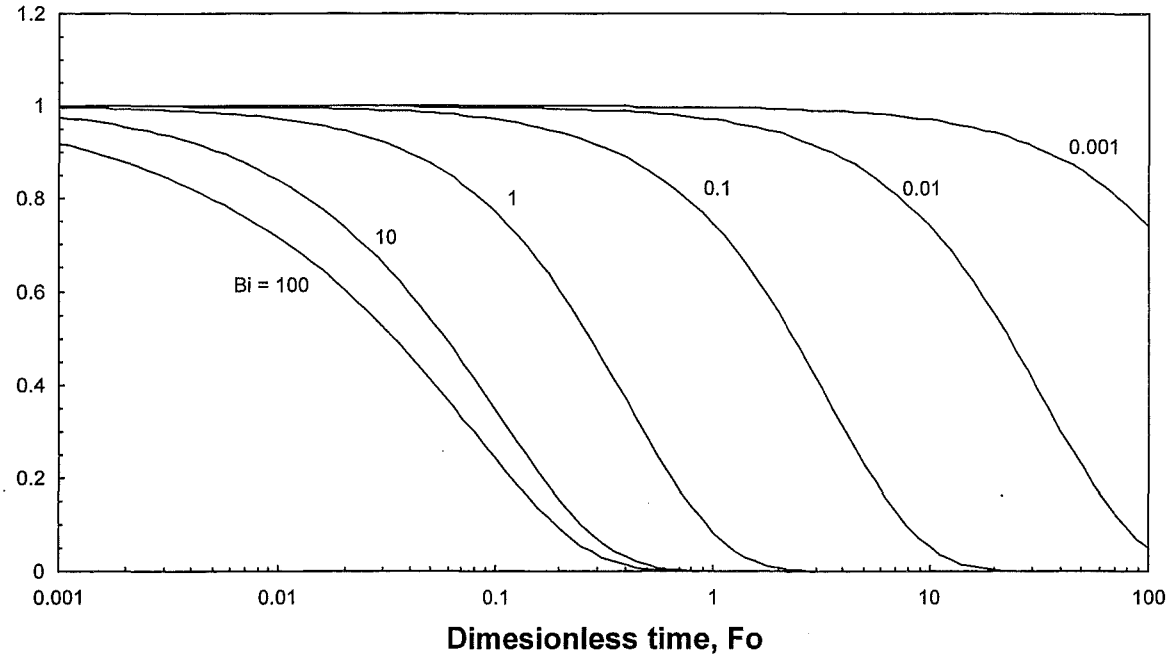

Figure 5. The fraction of tritium remaining in a droplet subject to idealized diffusion to the surface depends on the diffusivity, surface mass transfer coefficient, and droplet radius as they appear in the **Fo** and **Bi** numbers. The tritium does not come out faster at higher **Bi** numbers.

Therefore, if one has good values for diffusivity of tritium in the Flibe and the surface mass transfer coefficient, it should be possible to determine the optimum droplet diameter and vacuum residence time for effective removal of the tritium in this way.

Not included in this analysis was the extent to which internal flows within the droplets, induced by the droplet formation process, could accelerate transport of tritium from within the droplet to the droplet surface. We also did not have a reliable value for the mass transfer coefficient for tritium from the surface. Further, we were not sure of the chemical form of the tritium in the droplet.

These unknowns and uncertainties point out the need for detailed experiments to be conducted with Flibe to evaluate key parameters involved with tritium production in and release from molten Flibe in the dynamic environments of a fusion reactor.

EXPERIMENTS

Several experiments are in progress or are being considered for exploring tritium safety issues in Flibe. Many of these are concerned with the mobilization of tritium from Flibe.[21,22] It is not clear whether there are reasonable means for getting tritium into Flibe for such experiments other than actual neutron irradiation. This is because of the complex chemistry of the various reactions involving the fluorine, beryllium, lithium, and the tritium produced. One priority in the forthcoming research should be to develop a successful tritiating procedure for Flibe.

Reactor Test

Suzuki and co-workers [5] described work to determine mechanisms for the change of chemical species of tritium in Flibe. In that work, a container of molten Flibe was placed in an irradiation position of the YAYOI reactor at the University of Tokyo. Tritium was produced in the Flibe by fission neutrons, released from the Flibe as HT or TF, and swept by a mixture of helium and hydrogen in a purge gas stream to analysis stations. The TF fraction was determined by converting TF to HT on an aluminum reduction bed followed by ion chamber counting and comparing the total tritium count from that stream with the count from another ion chamber on a stream in which the TF had been absorbed by a molecular sieve bed.

They found that for H_2 concentrations in the purge gas of 1 percent or less, the rate of HT release from the Flibe was controlled by the H_2 partial pressure. At very low H_2 partial pressures (100 Pa or 1000 appm or less), the tritium coming from the Flibe was mainly as TF. For H_2 concentrations of 10 percent or more, they found release was first order in tritium concentration and that HT release rate was controlled by diffusion to the surface.

One aspect not clear in the work at YAYOI was the extent to which recombination of T^+ ions with surface H was responsible for HT formation as opposed to formation of HT in the Flibe fluid, as they postulated, with subsequent diffusion of HT molecules through the Flibe. Likewise, it could not be determined whether TF molecules were formed in the bulk Flibe or at the surface. In light of the very low solubility for hydrogen isotopes in Flibe, the surface recombination pathway seems more likely.

It is evident from Figure 1 above that some protium will be present in the Flibe mixture from (n,p) reactions. Some deuterium may also be present. These hydrogenic species will probably be as prevalent as will the tritium. These appear not to have been considered in the model presented, and the rates of HF and DF formation were not measured.

If there is a free Flibe surface with available hydrogenic species, then this process of flooding with protium to reduce TF release and the attendant corrosion problems will be applicable, and the rates measured will be very useful. For the HYLIFE-II vacuum disengager, where no sweep gas is present, or for flow in heat exchanger tubes, it is not clear what the release rates or species will be.

FLIQURE

One experiment presently being initiated at the Idaho National Engineering and Environmental Laboratory is the Fusion Liquid Release Experiment (FLIQURE). This experiment, shown schematically in Figure 6, was initiated in response to the need to understand the chemistry and mechanisms for mobilization of beryllium or fluorine compounds and activation products, including tritium, resident in molten Flibe. As discussed previously, tritium may be produced in Flibe by the reaction of a neutron with a lithium atom, the destruction of which would effectively liberate a fluorine atom. Tritium may also be produced by interaction of a neutron with a beryllium atom, as shown in Figure 1. Other hydrogenic species will also be produced.

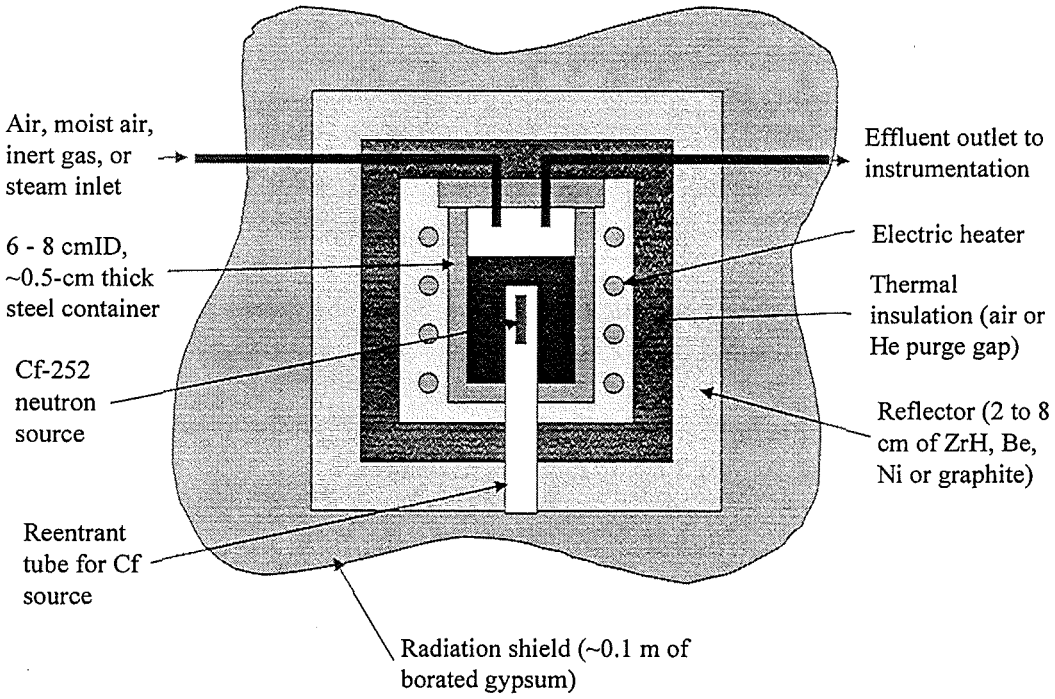

Figure 6. FLIQURE experiment for investigation of tritium interactions with molten Flibe.

The FLIQURE experiment will have many of the same features and limitations as the YAYOI experiment, but it has the benefit of not requiring installation in a fission reactor. A modification to allow tritium permeation measurements through the inner vessel wall with only a small amount of inert cover gas over the Flibe would be useful in evaluating the direct transfer of tritium from the Flibe to structures.

The FLIQURE experiment is presently in design. Analyses have indicated tritium production rates may be on the order of 10^{12} tritium atoms per hour from a 1.0 mg Cf-252 source acting on a 200-mL Flibe volume with a 40-cm Be reflector. Improved tritium production rates may be achieved with a ZrH_{16} moderator and a more optimal reflector configuration.

Tritium-Flibe Chemistry Experiments

The lack of tritium-Flibe chemistry data has prompted a proposal as part of the US-Japan fusion collaboration. Specifically this proposal is between the Japanese University Community (Monbusho) and the U.S.-DOE. The general issues that this collaboration will seek to address are:

- Fundamental parameters
  - Equilibrium
  - Kinetics
  - Chemical reactions
- Tritium removal
  - Technology choice
  - Product characterization
- Heat Exchanger Interactions
  - T permeation
  - Permeation barrier testing
  - Corrosion
- Materials corrosion testing
- Impurity control
  - Be screen
  - Other
- Chemistry control
  - H_2 addition for TF control
  - Other addition for control and makeup
- Tritium product purification
  - Technology choice
  - Waste issues
- Coolant tritium removal
  - Characterize stream

The collaboration will begin with the construction of a number of experiments in which the Flibe is not flowing. These experiments will be designed to measure a specific physical or chemical property such as solubility and mass transfer coefficient. The results of these experiments will lead to the construction and testing of an integrated tritium-Flibe handling loop. The loop will include sections of Flibe storage and supply, tritium addition, chemical addition, tritium extraction, heat exchanger mockup, and corrosion test sections. It is also proposed to include sections for tritium purification and heat exchanger coolant characterization. Analysis points throughout the loop will facilitate characterization of the Flibe at all points in the loop. If funded, this work is expected to begin in the 2001 time frame. The experiments will be conducted in the U.S., mostly likely at Los Alamos National Laboratory.

CONCLUSIONS

Use of Flibe in fusion reactors offers new and interesting possibilities for coping with heat loads to walls as well as breeding tritium directly in the coolant. With those possibilities come concerns for adequate tritium management. It will be important to extract tritium from the Flibe

in an efficient and controlled way at appropriate locations in the Flibe circuit and to prevent tritium from penetrating fusion reactor structures, especially coolant system structures, in other areas.

Relatively little has been done experimentally to determine the properties and parameters needed for adequate assessment of these tritium management issues. It will be important to understand thoroughly the chemistry of tritium and other hydrogenic species in the Flibe as well as that of the fluoride ions that will be liberated by neutron transmutations. Other issues of importance are the determination of the mechanisms by which tritium moves through the Flibe and where and how it recombines to leave the Flibe.

These issues are beginning to be addressed by experiments in the U.S. and Japan. These experiments are beginning with static pool experiments. It is important to generate the tritium and other reactive species in the Flibe by neutron transmutation since uptake in other ways is difficult and will probably not give the appropriate fidelity to chemical reactions and transport processes involving those species. It is hoped that experiments will eventually evolve to dynamic loop experiments to evaluate loss of tritium through heat exchanger tubes and related issues of barrier effectiveness and detritiation mechanisms.

REFERENCES

1. R. W. Moir, "HYLIFE-II Inertial Confinement Fusion Reactor Design," *Fusion Technology, 19* (May 1991) pp. 617-624.

2. R. W. Moir et al., "HYLIFE-II: A molten-salt inertial fusion energy power plant design—Final Report," *Fusion Technology, 25* (1994) 5–25.

3. A. Sagara et al., "Materials design and related R&D issues for the force-free helical reactor (FFHR)," *Journal of Nuclear Materials, 258-263* (1998) pp. 2079-2082.

4. H. Moriyama et al., "Molten salts in fusion nuclear technology," *Fusion Engineering and Design, 39-40* (1998) pp. 627-637.

5. A. Suzuki et al., "Change of tritium species in Li_2BeF_4 molten salt breeder under neutron irradiation at elevated temperature," *Journal of Nuclear Materials, 258-263* (1998) pp. 519-524.

6. T. Terai et al., "Compatibility of structural materials with Li_2BeF_4 molten salt breeder," *Journal of Nuclear Materials, 258-263* (1998) pp. 513-518.

7. A. Suzuki et al., "Mechanism on Change of Tritium species in Li_2BeF_4 Molten Salt Breeder under Neutron Irradiation at Elevated Temperature," *Fusion Technology, 34* (Nov 1988) pp.526-530.

8 . M. T. Tobin, "Neutronics Analysis for HYLIFE-II," *Fusion Technology, 19* (May 1991) pp. 763-769.

9 . T. J. Dolan and G. R. Longhurst, *Safety and Environmental Issues of HYLIFE-II*, EGG-FSP-8653, Idaho National Engineering Laboratory (October 1989).

10 . F. W. Walker et al., eds., *Nuclides and Isotopes*, 14th Ed., General Electric Company, San Jose, CA (1989).

11 . A. P. Malilnauskas and D. M. Richardson, "The solubilities of hydrogen, deuterium and helium in molten Li_2BeF_4," *Industrial and Engineering Chemistry. Fundamentals, 13* (1974) pp. 242-245.

12 . G. R. Longhurst and T. J. Dolan, *HYLIFE-II Tritium Management System*, EGG-FSP-9971, Idaho National Engineering and Environmental Laboratory, Idaho Falls, Idaho (1993).

13 . G. R. Longhurst, *Permeation of Tritium through HYLIFE-II Heat Exchanger Tubes*, EGG-FSP-8678, Idaho National Engineering and Environmental Laboratory, Idaho Falls, Idaho (September 1989).

14 . G. R. Longhurst and T. J. Dolan, "Tritium Permeation Losses in HYLIFE-II Heat Exchanger Tubes," *Fusion Technology, 19* (May 1991) pp. 820-825.

15 . R. B. Bird, W. E. Stewart, and E. N. Ligfhtfoot, *Transport Phenomena*, John Wiley & Sons, New York (1960) pp. 630, 384, 186.

16 . J. Oishi et al., "Tritium recovery from molten LiF-BeF_2 salt," *Fusion Engineering and Design, 8* (1989) pp. 317-321.

17 . T. Tanabe et al., "Hydrogen Transport in Stainless Steels," *Journal of Nuclear Materials, 122 & 123* (1984) pp. 1568-1572.

18 . M. I. Baskes, "A Calculation of the Surface Recombination Rate Constant for Hydrogen Isotopes on Metals," *Journal of Nuclear Materials, 92* (1980) p. 3.18

19 . T. J. Dolan, G. R. Longhurst, and E. Garcia-Otero, *A Vacuum Disengager for Tritium Removal from HYLIFE-II reactor Flibe*, EGG-M-91508, Idaho National Engineering and Environmental Laboratory, Idaho Falls, Idaho (March 1992).

20 . G. R. Longhurst, *Gas Evolution from Spheres*, EGG-FSP-9634, Idaho National Engineering and Environmental Laboratory, Idaho Falls, Idaho (April 1991).

21 . Y. Asaoka et al., "Equilibrium Distributions of Tritium in Liquid Lithium/Molten Salt Systems," *Journal of Nuclear Materials, 179-181* (1991) pp. 879-881.

22 . J. Oishi et al., "Tritium Recovery from Molten LiF-BeF_2 Salt," *Fusion Engineering and Design, 8* (1989) pp. 317-321.

BERYLLIUM RESEARCH ON FFHR MOLTEN SALT BLANKET

Takayuki TERAI and Satoru TANAKA
Department of Quantum Engineering & Systems Science
University of Tokyo
7-3-1 Hongo, Bunkyo-ku, Tokyo 113-8656, Japan
(Phone) +81-3-5841-7010 (FAX) +81-3-5689-7349
(e-mail) tera@q.t.u-tokyo.ac.jp

Akio SAGARA
National Institute for Fusion Science
Oroshi, Toki 509-5292, Japan

Dai-Kai SZE
Argonne National Laboratory
9700 South Cass Av. Argonne, IL, USA

Force-Free Helical Reactor, FFHR, is a demo-relevant heliotron-type D-T fusion reactor based on the great amount of R&D results obtained in the LHD project. Since 1993, collaboration works have made great progress in design studies of FFHR with standing on the major advantage of current-less steady operation with no dangerous plasma disruptions. There are two types of reference designs, FFHR-1 and FFHR-2, where molten Flibe (LiF-BeF2) is utilized as tritium breeder and coolant. In this paper, we present the outline of FFHR blanket design and some related R & D topics focusing on Be utilization.

Beryllium is used as a neutron multiplier in the design and Be pebbles are placed in the front part of the tritium breeding zone. In a Flibe blanket, HF (TF) generated due to nuclear transmutation will be a problem because of its corrosive property. Though nickel-based alloys are thought to be intact in such a corrosive environment, FFHR blanket design does not adopt the alloys because of their induced radioactivity. The present candidate materials for the structure are low-activated ferritic steel (JLF-1), V-4Cr-4Ti, etc. They are capable to be corroded by HF in the operation condition, and Be is expected to work as a reducing agent in the system as well. Whether Be pebbles placed in a Flibe flow can work well or not is a very important matter. From this point, Be solubility in Flibe, reaction rate of the Redox reaction with TF in the liquid and on the surface of Be pebbles under irradiation, flowing behavior of Flibe through a Be pebble bed, etc. should be investigated. In 1997, in order to establish more practical and new data bases for advanced design works, we started a collaboration work of R&D on blanket engineering, where the Be research above mentioned is included. Preliminary dipping-test of Be sheets and in-situ tritium release experiment from Flibe with Be sheets have got started.

4th IEA INTERNATIONAL WORKSHOP ON BERYLLIUM TECHNOLOGY FOR FUSION

FORSCHUNGSZENTRUM KARLSRUHE
KARLSRUHE, GERMANY
SEPTEMBER 15-17, 1999

Name	Organization/Address	Country	Tel	Fax	E-mail
E. Abramov	Ben-Gurion University of the Negev Dept. for Materials Science and Eng. P.O. Box 653, Beer-Sheva	Israel	+972-7-6461821		abramov@bgumail.bgu.ac.il
E. Alves	Instituto Tecnológico e Nuclear, EN. 10 P-2685 Sacavém, Portugal	Portugal	+351-1-9550021	+351-1-9941525	ealves@itn1.itn.pt
R.A. Anderl	Idaho National Engineering and Environmental Laboratory PO Box 1625, Idaho Falls, ID 83415-7113	USA	+1-208-5334153	+1-208-533-4207	raa@inel.gov
V. Barabash	ITER Garching JWS, Materials Group Boltzmannstraße 2, D-85748 Garching	Germany	+49-89-3299-4144	+49-89-3299-4163	barabav@sat.ipp-garching.mpg.de
M. Bitenbayev	Physics Technical Institute 480012 Almaty	Kazakhstan		+7-327-2-50-39-78	
N. Bitkolov	Research Institute of Industrial and Marine Medicine, Gagarina ave. 65/67 St. Peterburg, 196143	Russia	+7-812-1272000	+7-812-126-7583	bitkolov@vozduh.spb.ru
L. Boccaccini	Forschungszentrum Karlsruhe, IKET Hermann-von-Helmholtz Platz 1 D-76344 Eggenstein-Leopoldshafen	Germany	+49-7247-822415	+49-7247-82-5987	lorenzo.boccaccini@iket.fzk.de
A. Cardella	ITER Joint Central Team Boltzmannstraße 2, D-85748 Garching	Germany	49-89-3299-4100	+49-89-32994422	cardela@ipp.mpg.de

4th IEA INTERNATIONAL WORKSHOP ON BERYLLIUM TECHNOLOGY FOR FUSION

FORSCHUNGSZENTRUM KARLSRUHE
KARLSRUHE, GERMANY
SEPTEMBER 15-17, 1999

Name	Organization/Address	Country	Tel	Fax	E-mail
R.G. Castro	Los Alamos National Laboratory, Materials Science and Technology Division Los Alamos, New Mexico 87545	USA	+1-505-667-5191	+1-505-667-5268	rcastro@lanl.gov
J.-M. Cayphas	Physique des Solides Irradiés Univ. Libre de Bruxelles, CP 234 Bld. du Triomphe, B-1050 Brussels	Belgium	+32-2-650-5740	+32-2-650-5227	jmcaypha@ulb.ac.be
V.P. Chakin	SSC RF RIAR, 433510, Dimitrovgrad, Uljanovsk region	Russia			fae@omv.niiar.simbirsk.ru
R. Chaouadi	SCK•CEN, Boeretang 200, 2400 Mol	Belgium	+32-14-332231	+32 14 321529	rchaouad@sckcen.be
V. Chernov	SSC RF-A.A. Bochvar Research Institute of Inorganic Materials (VNIINM) Berzarina St. 38, 123060 Moscow	Russia			
Y. Chikhray	Scientific Research Institute of Experimental and Theoretical Physics State University of Kazakhstan Tole Bi 96A, 480012 Almaty	Kazakhstan		+7-327-2-50-3978	
L. Coheur	ULB- Physique des Solides Irradiés CP234, Bld. du Triomphe, 1050 Bruxelles	Belgium	+32-2/6505738	+32-2-650-5227	lcoheur@ulb.ac.be
M. Dalle Donne	Forschungszentrum Karlsruhe, IKET Hermann-von-Helmholtz-Platz 1 D-76344 Eggenstein-Leopoldshafen	Germany	+49-721-822335	+49-721-825987	
G. Dell'Orco	ENEA Brasimone, P.O. Box 1 40032 Camugnano-Bologna	Italy	+39-0534-801129	+39-0534-801244	dellorco@brasimone.enea.it

4th IEA INTERNATIONAL WORKSHOP ON BERYLLIUM TECHNOLOGY FOR FUSION

FORSCHUNGSZENTRUM KARLSRUHE
KARLSRUHE, GERMANY
SEPTEMBER 15-17, 1999

Name	Organization/Address	Country	Tel	Fax	E-mail
A. Di Maio	Dipartimento di Ingegneria Nucleare, Università degli Studi di Palermo Viale delle Scienze, 90128 Palermo	Italy	+39-91-232215	+39-91-232215	dimaio@din.din.unipa.it
D.E. Dombrowski	Brush Wellman Inc. 17876 St. Clair Avenue Cleveland, OH 44110	USA	+1-216-383-4007	+1-216-481-5480	david_dombrowski@brushwellman.com
F. Druyts	SCK-CEN, Boeretang 200, 2400 Mol,	Belgium	+32-14-33-3238	+32 14 32 35 53	fdruyts@sckcen.be
A. Fiege	Forschungszentrum Karlsruhe, PKF Hermann-von-Helmholtz Platz 1 D-76344 Eggenstein-Leopoldshafen	Germany	+49-7247-82-5465	+49-7247-82-5467	albert.fiege@pkf.fzk.de
U. Fischer	Forschungszentrum Karlsruhe, IKET Hermann-von-Helmholtz Platz 1 D-76344 Eggenstein-Leopoldshafen	Germany	+49-7247-82-3407	+49-7247-82-4837	ulrich.fischer@iket.fzk.de
N. Franz	NGK Deutsche Berylco GmbH Postfach 1620, D-61406 Oberursel	Germany	+49-6171-639941	+49-6171-6399-50	nf.dbg@ngkdbg.com
V. Gervash	Efremov Institute, 189631 St. Petersburg,	Russia	+7-812-4627872	+7-812-4644623	gervash@sintez.niiefa.spb.su
R. Giniaytulin	Efremov Institute, Sovetskiy pr.1, Metallostroy, 189631 St. Petersburg,	Russia	+7-812-4627834	+7-812-4644623	ginirn@niiefa.spb.su

4th IEA INTERNATIONAL WORKSHOP ON BERYLLIUM TECHNOLOGY FOR FUSION

FORSCHUNGSZENTRUM KARLSRUHE
KARLSRUHE, GERMANY
SEPTEMBER 15-17, 1999

Name	Organization/Address	Country	Tel	Fax	E-mail
P. Goldstrass	Max-Planck-Institut für Plasmaphysik Boltzmannstraße 2, D-85748 Garching	Germany	+49 89 3299 2285	49 89 3299 2279	peter.goldstrass@ipp.mpg.de
A. Goraieb	Goraieb Versuchstechnik, In der Tasch 4a, 76227 Karlsruhe	Germany	+49-7247-823640	+49-7247-22513	
V. Gorokhov	A.A. Bochvar Research Institute of Inorganic Materials (VNIINM) Rogova Street 5a, Box 369 123060 Moscow	Russia	+7-095-190-6344	+7-095-196-6701	vniinm.400@g23.relcom.su
D. Harries	9A Cumnor Rise Road, Cumnor Hill Oxford, 0X2 9HD	U.K.	+44-1865-863176	+44-1865-863176	
S. Hermsmeyer	Forschungszentrum Karlsruhe, IRS Hermann-von-Helmholtz Platz 1 D-76344 Eggenstein-Leopoldshafen	Germany	+49-7247-82-4997		hermsmeyer@irs.fzk.de
G. Hofmann	Forschungszentrum Karlsruhe, IKET Hermann-von-Helmholtz Platz 1 D-76344 Eggenstein-Leopoldshafen	Germany	+49-7247-82-4407	+49-7247-82-4837	
T. Ishida	Nuclear Fusion Section, Nuclear Plant Department, Power Plant Division Kawasaki Heavy Industries, LTD. 6-5, 2-chome, Minamisuna Koto-ku Tokyo 136-8588	Japan	+81-3-3615-5147	+81-3-3640-9497	ishida_toshi@khi.co.jp
T. Iwadachi	NGK INSULATORS, LTD., 1 Maegata-cho, Handa-city Aichi-ken 475-0825	Japan	+81-569-23-5806	+81-569-23-5856	iwadachi@ngk.co.jp

4th IEA INTERNATIONAL WORKSHOP ON BERYLLIUM TECHNOLOGY FOR FUSION

FORSCHUNGSZENTRUM KARLSRUHE
KARLSRUHE, GERMANY
SEPTEMBER 15-17, 1999

Name	Organization/Address	Country	Tel	Fax	E-mail
H. Kawamura	Japan Atomic Energy Research Institute Narita-cho, Oarai-machi Higashi Ibaraki-gun, Ibaraki-ken 311-1394	Japan	+81-29-264-8360	+81-29-264-8480	kawamura@oarai.jaeri.go.jp
A.M. Khomutov	State Scientific Center of Russian Federation—A.A. Bochvar All-Russia Research Inst. of Inorganic Materials (VNIINM), P.O. Box 369, 123060 Moscow	Russia	+7-095-190-6344	+7-095-196-6701	vniinm.400@g23.relcom.su
A. Korshunov	Russian Research Center "Kurchatov Institute" Kurchatov sq. 1, 123182 Moscow	Russia	+7-95-196-7367	+7-95-943-0073	kolbasov@qq.nfi.kiae.su
H. Kleykamp	Forschungszentrum Karlsruhe, IMF I, Hermann-von-Helmholtz-Platz 1 D-76344 Eggenstein-Leopoldshafen	Germany	+49-721-822888	+49-721-824567	heiko.kleykamp@imf.fzk.de
B.N. Kolbasov	Russian Research Center "Kurchatov" Institute, Nuclear Fusion Institute Kurchatov sq. 1, 123182 Moscow	Russia	+7-95-196-7583	+7-95-943-0073	kolbasov@qq.nfi.kiae.su
A. Kolbayenkov	Institute of Atomic Energy of Kazakhstan, Semipalatinsk-21 Krasnoarmeiskya 10	Kazakhstan		+7-327-2-33-8585	
I.B. Kupryianov	A.A.Bochvar All-Russia Reseach Institute of Inorganic Materials (VNIINM) P.O. Box 369, 123060 Moscow	Russia	+7-95-1908015	7-95-925-5972	vniinm.400@g23.relcom.ru

4th IEA INTERNATIONAL WORKSHOP ON BERYLLIUM TECHNOLOGY FOR FUSION

FORSCHUNGSZENTRUM KARLSRUHE
KARLSRUHE, GERMANY
SEPTEMBER 15-17, 1999

Name	Organization/Address	Country	Tel	Fax	E-mail
C. Linsmeier	Max-Planck-Institut für Plasmaphysik Boltzmannstraße 2, 85748 Garching	Germany	+49-89-3299-2285	+49-89-3299-2279	linsmeier@ipp.mpg.de
A. Lodato	ITER Joint Central Team Boltzmannstraße 2, D-85748 Garching	Germany	49-89-3299-4109	+49-89-32994422	lodato@itereu.de
G.R. Longhurst	Idaho National Engineering and Environmental Laboratory P.O. Box 1625, Idaho Falls Idaho 83415-3860	USA	208-526-9950	208-526-2930	gxl@inel.gov
S. Malang	Forschungszentrum Karlsruhe, IKET Hermann-von-Helmholtz Platz 1 D-76344 Eggenstein-Leopoldshafen	Germany	+49-7247-82-4101	+49-7247-82-4837	siegfried.malang@iket.fzk.de
A. Markin	Institute of Physical Chemistry, Russian Academy of Sciences, Leninsky pr. 31, 117915 Moscow	Russia	+7-95-330-2192	+7-95-334-8531	Markin@ipcras.msk.ru
W. Maschek	Forschungszentrum Karlsruhe, IKET Hermann-von-Helmholtz Platz 1 D-76344 Eggenstein-Leopoldshafen	Germany	+49-7247-82-2468	+49-7247-82-5987	werner.maschek@iket.fzk.de

4th IEA INTERNATIONAL WORKSHOP ON BERYLLIUM TECHNOLOGY FOR FUSION

FORSCHUNGSZENTRUM KARLSRUHE
KARLSRUHE, GERMANY
SEPTEMBER 15-17, 1999

Name	Organization/Address	Country	Tel	Fax	E-mail
I. Mazul	Efremov Institute of Electrophysical Apparatus Sovetsky pr. 1, Metallostroy 189631 St. Petersburg	Russia	+7-812-462-7643	+7-812-464-4623	mazuliv@niiefa.spb.su
T. Mc Kechnie	Plasma Process. Inc. 4914 D Moores Mill Road Huntsville, Alabama 37811	USA	+1-256-851-7653	+1-256-859-4134	tim.mck@plasmapros.com
M. Merola	EFDA-CSU Boltzmannstraße 2, 85748 Garching	Germany	+49-89-3299-4220	+49-89-3299-4198	merolam@ipp.mpg.de
M. Miyakawa	NGK Instulators Ltd., New Metals Division Yebisu Garden Place Tower 25F, 4-20-3 Ebisu, Shibuya-ku, Tokyo 155-6025	Japan	+81-3-5488-8913	+81-3-5488-8973	miyakawa@ngk.co.jp
Y. Nishi	NGK Deutsche Berylco GmbH, Tabaksmühlenweg 28, D-61440 Oberursel	Germany	+49-6171-639928	+49-6171-639950	nnishi@ibm.net
K. Nojiri	NGK Berylco France S.A. Quai Emile Paraf, BP 17 F-44120 Coueron	France	+33-2-4038-6755	+33-2-4038-0995	nojiri@ngkbf.com
B.C. Odegard, Jr.	Sandia National Laboratories–California P.O. Box 969 Livermore, CA 94551–0969	USA	+1-510-294-2789	+1-510-294-3410	odegard@ca.sandia.gov
A. Peacock	EFDA CSU Garching Boltzmannstraße 2, 85748 Garching	Germany	+49-89-3299-2789	+49-89-3299-4198	peacoca@ipp.mpg.de
G. Piazza	Forschungszentrum Karlsruhe, IKET Hermann-von-Helmholtz-Platz 1 D-76344 Eggenstein-Leopoldshafen	Germany	+49-721-822937	+49-721-825987	giovanni.piazza@iket.fzk.de
A. Polyakov	Physics Technical Institute, Almaty 82	Kazakhstan		+7-327-2-50 39 78	

4th IEA INTERNATIONAL WORKSHOP ON BERYLLIUM TECHNOLOGY FOR FUSION

FORSCHUNGSZENTRUM KARLSRUHE
KARLSRUHE, GERMANY
SEPTEMBER 15-17, 1999

Name	Organization/Address	Country	Tel	Fax	E-mail
J. Reimann	Forschungszentrum Karlsruhe, IKET Hermann-von-Helmholtz-Platz 1 D-76344 Eggenstein-Leopoldshafen	Germany	+49-721-823498	+49-721-824837	joerg.reimann@iket.fzk.de
M. Roedig	Forschungszentrum Jülich, IWV-2 D-52425 Jülich	Germany	+49-2461-61 63 83	+49-2461-61 3687	m.roedig@fz-juelich.de
F. Scaffidi-Argentina	Forschungszentrum Karlsruhe, IKET Hermann-von-Helmholtz-Platz 1 D-76344 Eggenstein-Leopoldsghafen	Germany	+49-7247-82-2047	+49-7247-82-5987	francesco.scaffidi@iket.fzk.de
D. Schmidt	NGK Deutsche Berylco GmbH Tabaksmühlenweg 28, D-61440 Oberursel	Germany	+49-6171-63 99 31	+49-6171-63 99 51	ds.dbg@ngkdbg.com
V.P.Shestakov	NIIETF of Kazakh State University Tole bi 96a, Almaty, 480012	Kazakhstan	+7-3272-676775	+7-3272-503978	istcvova@asdc.kz
M. Simoncini	ENEA Brasimone P.O. Box 1, 40032 Camugnano-Bologna	Italy	+39-0534-801129	+39-0534-801244	msimoncini@brasminone.enea.it
I. Tazhibaeva	Scientific Research Institute of Experimental and Theoretical Physics State University of Kazakhstan Tole Bi 96A, 480012 Almaty	Kazakhstan		+7-327-2-50 39 78	

4th IEA INTERNATIONAL WORKSHOP ON BERYLLIUM TECHNOLOGY FOR FUSION

FORSCHUNGSZENTRUM KARLSRUHE
KARLSRUHE, GERMANY
SEPTEMBER 15-17, 1999

Name	Organization/Address	Country	Tel	Fax	E-mail
L. Tikhomirov	National Nuclear Center Republic of Kazakhstan Semipalatinsk-21 (Kurchatov City)	Kazakhstan		+7-3272-338585	
J. van der Laan	NRG, 3 Westerduinweg, NL-1755 ZG Petten	Netherlands	+31+224+564744	+31-224-561883	vanderlaan@nrg-nl.com
G. Vella	Dipartimento di Ingegneria Nucleare, Università dedli Studi di Palermo Viale delle Scienze 90128 Palermo	Italy	+39-91-232215	+39-91-232215	Vella@din.din.unipa.it
J. Vetter	Forschungszentrum Karlsruhe, PKF Hermann-von-Helmholtz-Platz 1 D-76344 Eggenstein-Leopoldshafen	Germany	+49-7247-82-5460	+49-7247-82-5467	joerg.vetter@pkf.fzk.de
M. Yamada	ITER JCT Garching Boltzmannstr. 2, D-85748 Garching	Germany	+49-89-3299-4305	+49-89-3299-4422	yamadam@ipp.mpg.de
A. Zimin	Nuclear Fusion Institute, Russian Research Center "Kurchatov" Institute Kurchatov sq. 1, 123182 Moscow	Russia			